pennsylvania
DEPARTMENT OF TRANSPORTATION

A Study of Highway Subsidence due to Longwall Mining using data collected from I-79

FINAL REPORT

April 30th, 2010

By
Juan J. Gutierrez, Ph.D., E.I.T.
Luis E. Vallejo, Ph.D.
Jeen-Shang Lin, Sc.D., P.E.

University of Pittsburgh

COMMONWEALTH OF PENNSYLVANIA
DEPARTMENT OF TRANSPORTATION

CONTRACT # 510601
WORK ORDER # PIT 015

Technical Report Documentation Page

Form DOT F 1700.7 **(8-72)** **Reproduction of completed page authorized**

1. Report No. FHWA-PA-2010-009-PIT015	**2. Government Accession No.**	**3. Recipient's Catalog No.**
4. Title and Subtitle A Study of Highway Subsidence Due to Longwall Mining Using Data Collected From I-79		**5. Report Date** April 30th 2010 **6. Performing Organization Code**
7. Author(s) Juan Jose Gutierrez, Ph.D., E.I.T. Luis E. Vallejo, Ph.D. Jeen-Shang Lin, Sc.D., P.E.		**8. Performing Organization Report No.**
9. Performing Organization Name and Address University of Pittsburgh Swanson School of Engineering Department of Civil and Environmental Engineering 943 Benedum Hall Pittsburgh, PA 15260		**10. Work Unit No. (TRAIS)** **11. Contract or Grant No.** 510601
12. Sponsoring Agency Name and Address The Pennsylvania Department of Transportation Bureau of Planning and Research Commonwealth Keystone Building 400 North Street, 6th Floor Harrisburg, PA 17120-0064		**13. Type of Report and Period Covered** Final Report May 2008 - April 2010 **14. Sponsoring Agency Code**
15. Supplementary Notes		

16. Abstract

Longwall mining is a common underground coal extraction technique in Appalachia. The extraction takes the form of panels whose width and length can reach approximately 1450 ft and 13000 ft; the coal seam thickness is roughly about 7.0 ft. Typical mine depth ranges from 640 ft to 830 ft. Longwall panels were mined underneath highway I-79 in the Cumberland and Emerald mines in southwestern Pennsylvania, causing large subsidence in the range of 4.5 ft to 5.5 ft that affected traffic safety and could have potentially damaged highway structures such as pavements, culverts, and bridge abutments. Mining under the highway prompted the close monitoring by the Pennsylvania Department of Transportation of the impact of mining on the highway sections above the mines. A substantial amount of data was collected that formed the basis of this work. The data included time series of surveying data and inclinometer data in selected points. With the aid of a genetic algorithm, a three dimensional subsidence model was developed. The model gives the spatial and temporal distribution of surface subsidence in terms of the depth of mining, the panel width, the thickness of extraction, and the location relative to the face of the panels. A FEM model was developed in order to better understand the mechanisms of subsidence. The results of both empirical and numerical modeling are presented.

17. Key Words Highway, subsidence, SDPS, Finite Element Method, Longwall mining, Coal, Mining		**18. Distribution Statement** No restrictions. This document is available from the National Technical Information Service, Springfield, VA 22161	
19. Security Classif. (of this report) Unclassified	**20. Security Classif. (of this page)** Unclassified	**21. No. of Pages** 426	**22. Price**

PennDOT / University of Pittsburgh Intergovernmental Agreement
Contract No. 510601

Work Order 015: A Study of Highway Subsidence due to Longwall Mining using data collected from I-79

Final Report

Juan J. Gutierrez Ph.D., E.I.T.

Luis E. Vallejo Ph.D.

Jeen-Shang Lin Sc.D., P.E.

Submitted to:

Pennsylvania Department of Transportation

Pittsburgh, April 30th 2010

A Study of Highway Subsidence due to Longwall Mining using data collected from I-79

Abstract

Longwall mining is a common underground coal extraction technique in Appalachia. The extraction takes the form of panels whose width and length can reach approximately 1450 ft and 13000 ft, respectively; the coal seam thickness is roughly about 7.0 ft. Typical mine depth ranges from 640 ft to 830 ft. Longwall panels were mined underneath highway I-79 in the Cumberland and Emerald mines in southwestern Pennsylvania, causing large subsidence in the range of 4.5 ft to 5.5 ft that affected traffic safety and could have potentially damaged highway structures such as pavements, culverts, and bridge abutments. Mining under the highway prompted the close monitoring by the Pennsylvania Department of Transportation of the impact of mining on the highway sections above the mines. A substantial amount of data was collected that formed the basis of this work. The data included time series of surveying data and inclinometer data in selected points. With the aid of a genetic algorithm, a three dimensional subsidence model was developed. The model gives the spatial and temporal distribution of surface subsidence in terms of the depth of mining, the panel width, the thickness of extraction, and the location relative to the face of the panels. A FEM model was developed in order to better understand the mechanisms of subsidence. The results of both empirical and numerical modeling are presented.

TABLE OF CONTENTS

LIST OF TABLES

LIST OF FIGURES

1.0 TASK 1: LITERATURE REVIEW AND EVALUATION OF GEOLOGICAL MATERIALS

1.1 THE LONGWALL MINING PROCESS

Mine Subsidence Engineering Consultants (Mine Subsidence Engineering Consultants 2007) presents a succinct and clear description of the longwall mining process. This section draws heavily from it. The typical dimensions of a longwall panel are: Width between 500 and 1000 ft, length between 3000 and 12000 ft, and extracted seam thickness between 6 and 15 ft. A shearing machine travels the whole face length (width of the panel) back and forth and deposits the coal on a face conveyor, which is installed along the whole face length. The face conveyor transports coal into a belt conveyor, which takes coal out of the mine (Mine Subsidence Engineering Consultants 2007). The advance direction of the mining process is thus parallel to the length of the mine panel.

The narrow space where the shearing equipment, the face conveyor and the personnel are located is protected against roof collapse by hydraulic supports and a rigid canopy. Once the shearing machine has advanced a certain distance towards the intact coal, the canopy, hydraulic supports, and the shearing machine are moved in the advance direction. Ideally, the overburden behind the support structure collapses against the gob as support is lost. Figure 1-1 (Mine Subsidence Engineering Consultants 2007) shows a typical longwall mine with its main

components. Figure 1-2 shows a typical mining face with the collapsed overburden, hydraulic supports, shearer and the intact coal seam. Deformation of the upper strata illustrates how deformation of the ground takes place as the process continues. Figure 1-3 shows an actual view of the equipment at the mining face (Mine Subsidence Engineering Consultants 2007).

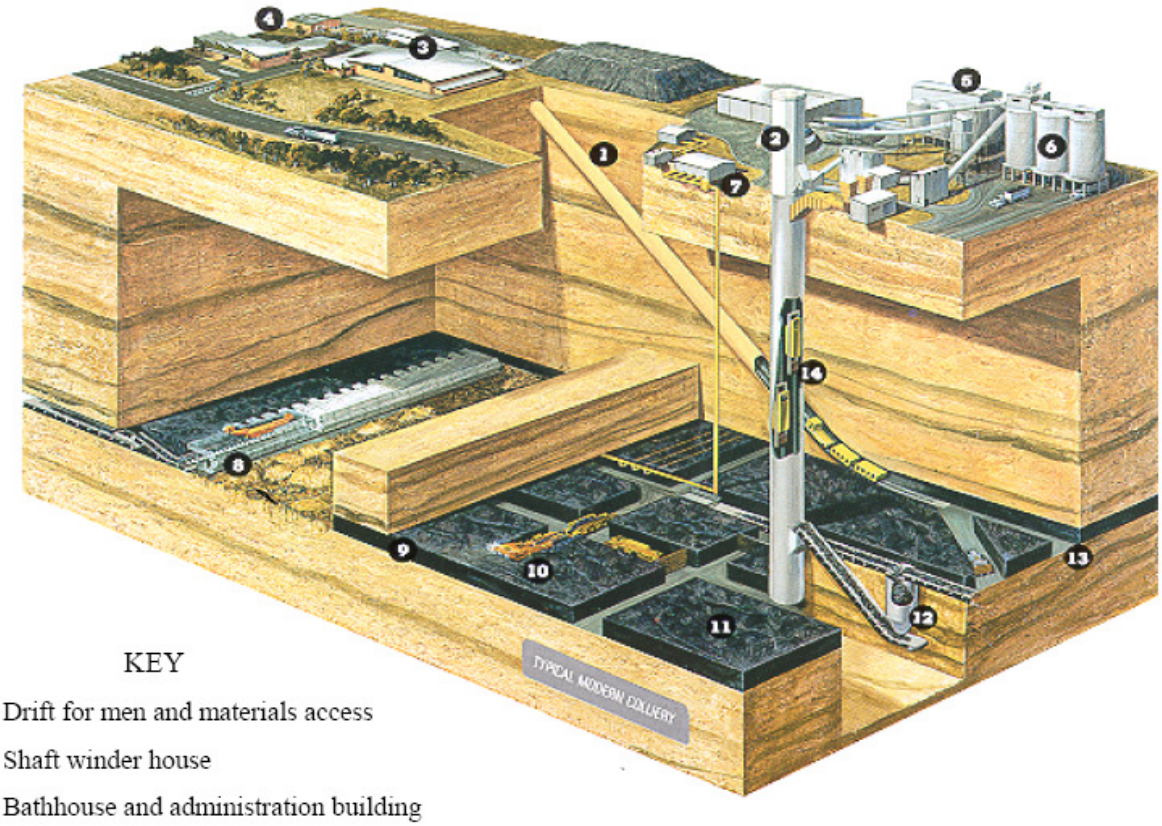

KEY

1. Drift for men and materials access
2. Shaft winder house
3. Bathhouse and administration building
4. Workshops
5. Coal preparation plant
6. Coal storage bins
7. Gas drainage system
8. Longwall face equipment
9. Coal seam
10. Continuous miner unit
11. Coal pillar
12. Underground coal bin
13. Main roadway or heading
14. Coal skips to carry coal to the surface

Figure 1-1. View of a typical longwall mine

(Mine Subsidence Engineering Consultants 2007)

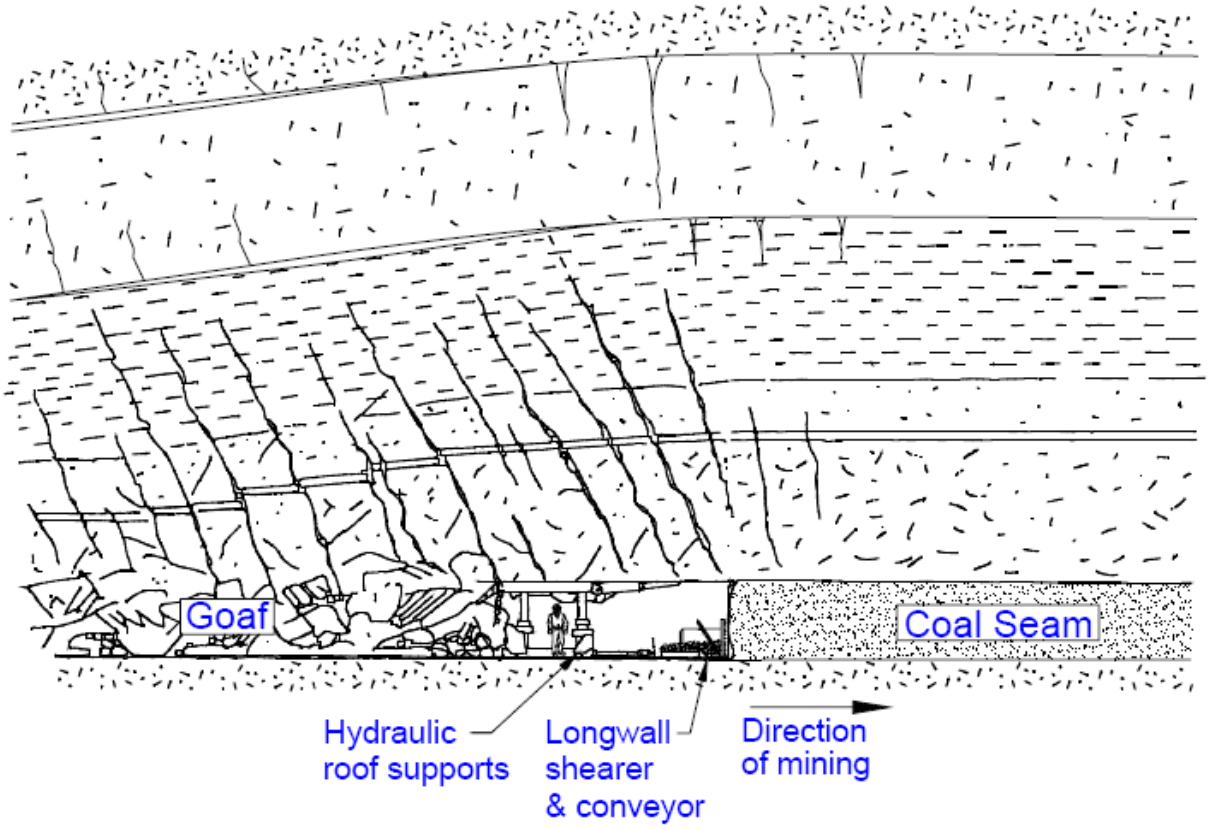

Figure 1-2. Typical longwall face

(Mine Subsidence Engineering Consultants 2007)

Figure 1-3. Face equipment

(Mine Subsidence Engineering Consultants 2007)

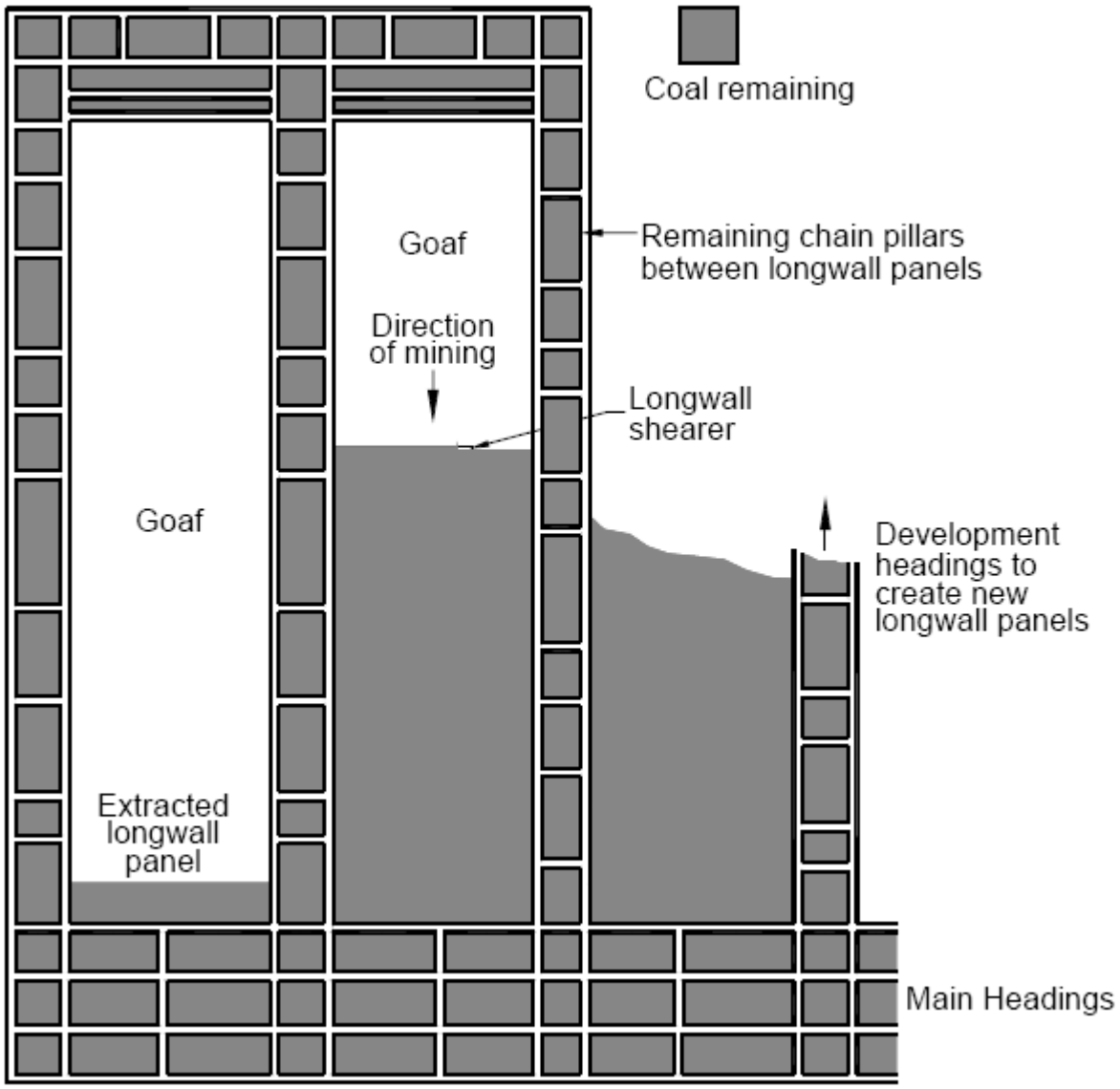

Figure 1-4. Typical plan view of a series of longwall panels

(Mine Subsidence Engineering Consultants 2007)

Typically, several panels are mined that are adjacent. In order to have access to each of the panels, several roadways are constructed with continuous mining equipment surrounding each panel. At the entrance side of the mine, these roadways are called main headings. Parallel to the length of the panels the roadways are called development headings. Other functions of these

roadways are to provide access to machinery, workers, and utilities such as pumped water pipes, gas extraction pipes, compressed air, electrical supply, and communication systems. The typical advance direction is toward the main or entrance headings, which is called retreat mining. In order to protect the headings, pillars of coal are left in place. The pillars in the development headings are called chain pillars.

In the process of longwall mining (refer to Figure 1-2), as the face advances and the roof left behind collapses, bending and sagging of the near strata takes place. Farther layers closer to the surface will not fracture but will bend causing subsidence. If the width of a longwall panel is too narrow, there is a chance that subsidence will not develop in the surface or it will be very small if it takes place at all. However, the current practice is to extract wider widths in order to make the process more economical. Therefore, maximum potential subsidence takes place in most practical cases (Mine Subsidence Engineering Consultants 2007).

1.1.1 The subsidence mechanism

As the process of mining advances and the void created in the seam becomes larger, the collapse of the mine roof into the gob and the sagging of deep layers above it cause the surface to deform into a subsidence trough. The area of deformed ground in the surface is greater than the area of the mined out panel. The angle formed by the vertical above the edge of the panel and the point on the surface where subsidence becomes negligible is called the angle of draw, γ, and is a function of the strength of the overburden.

The subsidence at the surface is in most cases smaller than the extracted coal thickness due to voids left in the collapsed strata. Therefore, the magnitude of subsidence, S^*, with respect to the extracted thickness, m, or subsidence factor, S^*/m , is a function of the material above the

coal seam (Kratzsch 1983; OSMRE 1986; Whittaker and Reddish 1989; Peng 1992; Mine Subsidence Engineering Consultants 2007; Kratzsch 2008; Agioutantis and Karmis 2009).

If the extracted width, *W*, of a panel is small with respect to the depth of the panel, *H*, it is possible that an arching effect takes place in the layers above the roof, which creates a stable dome and shortens the magnitude of subsidence in the surface. This condition is called subcritical. As the width is increased, the layers above the roof of the mine are not capable of arching and the collapse is complete, thus causing the maximum potential subsidence to take place. The panel width for which maximum potential subsidence takes place is called critical width. If the width is further increased, no larger subsidence will take place. Any width above that threshold is called supercritical (OSMRE 1986; Whittaker and Reddish 1989; Peng 1992; Mine Subsidence Engineering Consultants 2007; Agioutantis and Karmis 2009).

It has been mentioned that the typical configuration of a mine includes more than one panel. Also, the area of influence of subsidence in the surface above a panel is greater than the area of the panel itself. This means that the areas of influence of adjacent panels have overlapping zones, and as a consequence differential subsidence is experienced above a panel when a neighboring panel is extracted, therefore increasing the total subsidence as compared to a single extracted panel (Mine Subsidence Engineering Consultants 2007).

1.1.2 Subsidence parameters

Figure 1-5 shows the principal parameters in mine subsidence. The mathematical and physical relationship between these parameters is well known and is presented below.

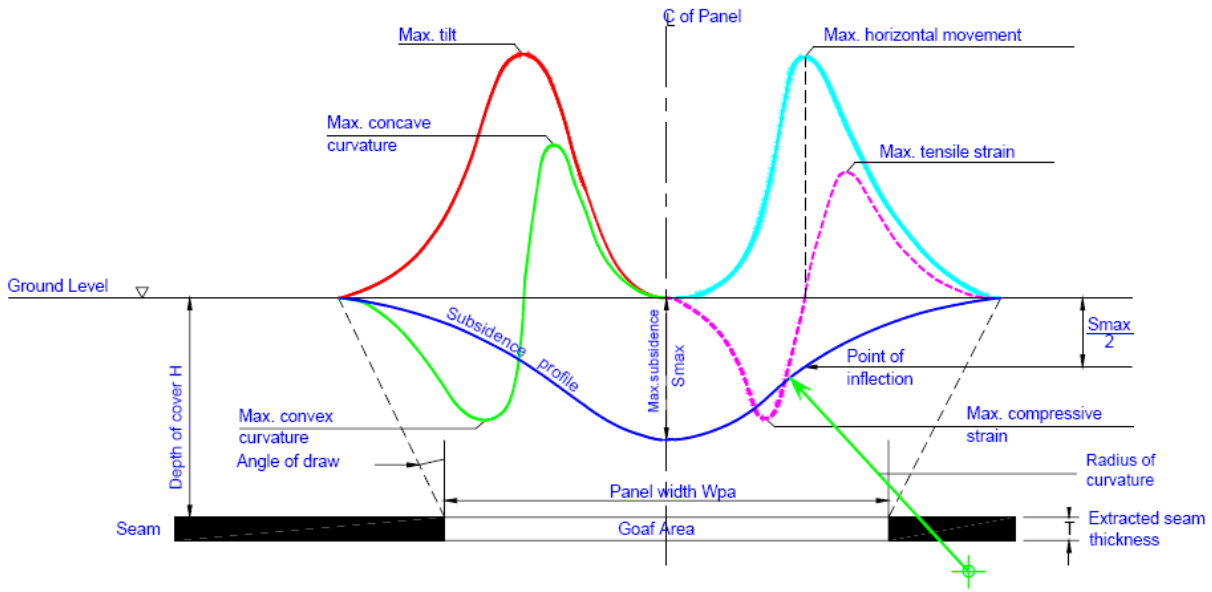

Figure 1-5. Subsidence parameter profiles

(Mine Subsidence Engineering Consultants 2007)

1.1.2.1 Subsidence

Subsidence is generally understood as the vertical ground movement at the surface, even though horizontal displacements are also a component of the deformation called subsidence (Mine Subsidence Engineering Consultants 2007). It is measured in units of length. If subsidence is expressed through a mathematical function (e.g. a profile function), it often accounts for vertical subsidence as a function of horizontal distance.

1.1.2.2 Tilt

Tilt is the slope of the deformed profile. It is mathematically computed as the first derivative of subsidence and reaches its maximum magnitude at the point of inflection of the subsidence profile, where the curvature changes from concave downward to concave upward. It is expressed in units of length over length (Mine Subsidence Engineering Consultants 2007).

1.1.2.3 Horizontal displacement

The magnitude of horizontal displacement is often related to the magnitude of tilt in a linear way. The magnitude of horizontal displacement reaches its peak where the magnitude of tilt is highest and becomes zero at the edge of the subsidence trough and at the center of the trough. Its units are those of length (Mine Subsidence Engineering Consultants 2007).

1.1.2.4 Curvature

Curvature is the second derivative of the subsidence profile or the first derivative (rate of change) of tilt. It is concave downward toward the edge of the trough (usually defined as positive) and concave upward toward the center of the subsidence trough (negative). The units of curvature are 1/length (Mine Subsidence Engineering Consultants 2007).

1.1.2.5 Horizontal strain

Horizontal strain is often related to curvature since peak strains correspond to peak curvature magnitudes. Strain is defined as the change in length with respect to original length and therefore its units are that of length over length. At the point of maximum curvature in the concave downward portion of the trough, maximum tensile strains take place. At the point of maximum

curvature in the concave upward portion of the trough, maximum compressive strains take place (Mine Subsidence Engineering Consultants 2007).

1.1.3 Subsidence impacts at the surface

Figure 1-6 shows how subsidence parameters affect surface structures at various portions of the subsidence trough. A structure in the surface can be safe or exposed to damage depending on its location inside the subsidence trough. A structure located in the central portion of the subsidence trough will experience permanent vertical settlement but no residual tilt or strains since these parameters become zero in this zone of the trough. The structural damage caused in the dangerous portions of the trough depends on which parameter becomes dangerously high in magnitude at a given location. If a structure is located at the maximum tilt point, it will be permanently tilted but will not be exposed to residual strains. In the case of residual strains, a structure could experience tensile strains or compressive strains depending on whether it is located in the concave downward or concave upward zone of the trough (Mine Subsidence Engineering Consultants 2007).

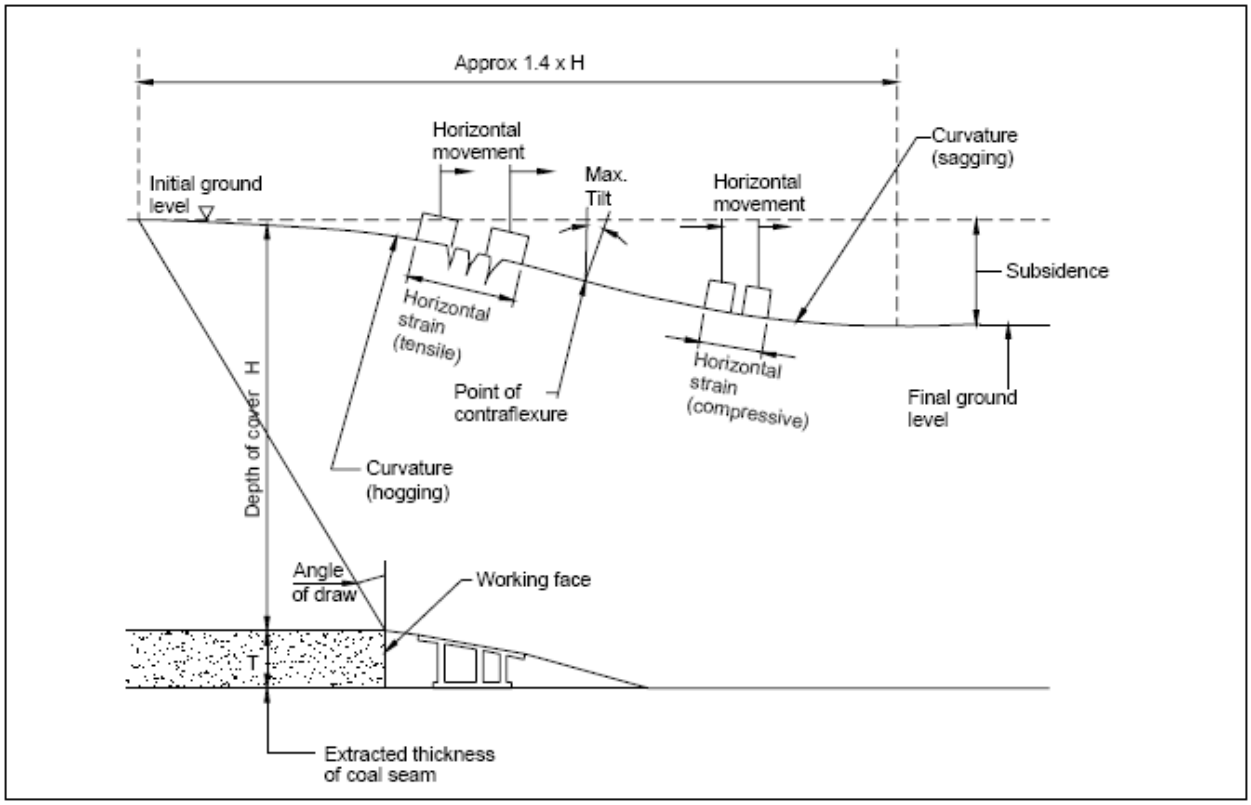

Figure 1-6. Development of subsidence trough

(www.minesubsidence.com 2007)

1.2 GEOLOGY OF THE REGION UNDER STUDY

Figure 1-7 shows the location of the Emerald and Cumberland mines southeast of Waynesburg, Pennsylvania, below interstate I-79.

Figure 1-7. Location of Emerald and Cumberland mines below I-79

(Adapted from Steve Thomas/Post-Gazette, source: Consol)

The following paragraphs on the description of the geology of the Greene County quote extensively from Stone (Stone 1932) and from the online archives of the PennState Libraries (PennState 2000). These descriptions are consistent with stratigraphic columns provided by Edmunds et al (Edmunds 1999; Edmunds, Skema et al. 1999) shown in Figure 1-8 and Figure 1-9. The PennState archives rely on an older source: *A geological hand atlas of the sixty-seven counties of Pennsylvania: embodying the results of the field work of the survey, from 1874 to*

1884, by J. P. Lesley. (Report of progress, Geological Survey of Pennsylvania, v. X, Harrisburg, PA, Board of commissioners for the second geological survey, 1885).

Green County occupies the southwest corner of the Commonwealth of Pennsylvania. It is bounded on the South and west by West Virginia, on the North by Washington County, and on the East it terminates at Monongahela River, the boundary of Fayette County. It has an area of 574 square miles or 367360 acres. Green County is hilly with few broad flat areas either in valley bottoms or on hilltops. It is all slope and for the most part rather steep slopes. The whole area is intricately and deeply dissected by streams, the valley bottoms are narrow, as are also the ridge tops. Elevations range from 750 feet on Monongahela River and 850 feet on the streams crossing the western boundary to 1660 feet, the highest point on the Monongahela-Ohio divide. The divide is in the western part of the county and along it there are many hilltops over 1550 feet in elevation. From the divide eastward there is a general slope or decrease in elevation of the ridge crests to about 1300 feet near Monongahela River. Differences in elevation of 500 feet within half a mile occur just below the mouth of Dunkard Creek on Monongahela River and at Eno on the north boundary of Richhill Township. Hills rising 400 feet in half a mile are common.

The rocks in Greene County are all in layers or beds ranging from a fraction of an inch to many feet thick and for the most part lying nearly horizontal. The surface rocks in Greene County belong to the Upper Carboniferous system. According to Stone (Stone 1932), there are four main groups, the Conemaugh, Monongahela, Washington, and Greene.

The Conemaugh group lies underneath the Pittsburgh Coal, the first 50 to 80 feet usually being shale with thin beds of limestone.

The Monongahela group extends from the base of the Pittsburgh coal to the top of the Waynesburg coal. The group ranges in thickness in this county from 279 feet to 405 feet,

according to the record of wells that passed through it. An average for the county is about 330 feet, and the range for Whiteley Township is: Least 313 ft, greatest 363 ft, and average 332 ft. The Monongahela group differs from the Conemaugh group below and the Washington group above it in having much more coal and limestone. It contains over 100 ft of limestone, some heavy beds of sandstone, shales, and five persistent coal beds. The Pittsburgh coal, which is at the base of the group, is the thickest bed, probably the least variable, and has the shortest outcrop line of all the workable coals in the county.

The Washington group underlies much of the surface of the county east of Waynesburg. The Washington group is composed of shales, sandstones, and thin beds of limestone and coal.

The Greene group has a maximum thickness of 700 to 800 feet. The Greene group is composed of such soft rocks that good exposures of more than a few feet of strata are rare. In the eastern half of the county the beds are so variable and so poorly exposed that the sequence of strata can scarcely more than be guessed at. In most places it consists of shales and shaly sandstones. A few of the sandstones are massive but not persistently so. Thin beds of red shale, several thin limestones and coal beds are interspersed throughout the group.

PennState University Libraries online (PennState 2000): “It is, in fact, a great flat dome-shaped country between the Monongahela and Ohio rivers, underlain by the almost perfectly flat uppermost coal measures on top of the Pittsburgh bed, the edge of which appears in the Monongahela valley only in front of Clarksville, and for 2 miles below Greensboro, and 8 miles above Greensboro, rising slowly into W. Virginia. The coal beds above it outcrop along both sides of Ten-mile run (south fork) up to Waynesburg, up Muddy creek 2 ½ miles, White Creek 1 ½ miles, Whitely Creek 4 miles, and Dunkard’s Creek 5 miles. At the three high divides, where Aleppo, Jackson, Gilmore, and Springhill townships join each other, the land is so elevated that

it would be necessary to sink 1200` to reach the *Waynesburg coal bed* and 1700` to reach the *Pittsburgh coal bed*. The section of these highest Paleozoic rocks in Pennsylvania, as exhibited along Fish Creek, begins with 80` of concealed rocks on the *14th limestone* (4`;) shale, 25`, on bituminous shale (2`) representing the latest of the coal beds; shale, 30`; *Gilmore sandstone* (forming cliffs) 30`; shale, 20`, on the *13th limestone*, (1`;) sandstone and shale 225`, on the *Nineveh coal bed*, (2 ½`;) sandstone and shale, 30`, on the *10th limestone*, (6`;) the *Fish Creek sandstone*, on a *coal bed* (?`;) shale and sandstone, 45`, on a *limestone* (1`;) sandstone, 20`; and then ferriferous shale, 10`. On the *Dunkard coal bed* (1`;) shale, including 10` of sandstone, 63`, on a *coal bed* (1`;) shale and sandstone, 45`, on a *coal bed* (1`) lying upon the *Upper Washington* or *6th limestone*. The 7th, 8th, 9th, 11th, and 12th limestone, all of them thin, are exposed along Ten-mile run in Centre township. On Dunkard Creek there are two limestones (25` apart) between the 8th and 10th. There is an evident increase in thickness of all the intervals going south across the county into W. Virginia. The next lower group *underlying* the *Upper Washington (6th) limestone* (3`) consists of shaly sandstone, 20`, on the *5th limestone* (5`;) shale and sandstone, 30` to 45`, on the *Jollytown coal bed* (1`;) shale and sandstone, 180`, on the *3d limestone* (3`;) sandstone, 18`, on black shale (3`,) on the *2d* or *Lower Washington limestone* (3 ½`;) shale, 6`, on the *Washington coal bed* (2 ½`;) clay and thin sandstone, 18`, on the *Little Washington coal bed* (with shale, 7`;) sandstone, 20`, on the *Waynesburg "B" coal bed* (1`;) sandstone and shale, 18` on the *1st limestone* (with shale, 13`) on the *Waynesburg "A" coal bed* (1 ';) variegated shale, 10`, on the Waynesburg sandstone which tops the Upper Productive Coal measures. The *6th limestone* in Washington County becomes a group of alternate lime and shale beds, 30` thick. Its middle layers are full of minute *Crustaceans*, as also in all the other limestones. Under it is a plant bed. The *4th limestone* is rich in minute forms of *Bellerophon* and *Euomphalus* and *Bryozoa*; fish teeth

and spines are found. Under the 2d limestone is a crustacean and fish bed. The Washington or Brownsfield coal bed extends into Ohio and north as far as Eldersville in Allegheny County; its thickness varies from *six inches to eleven feet* in the Washington county mines. The Upper Productive Coal Measures embrace the *Washington sandstone* 70`; shale 0` to 12`, on the *Waynesburg main coal bed* (6`,) with its under clay (3`;) sandstone 20`, on limestone (5`;) sandstone and shale 60`, on the *Uniontown coal bed* (1` to 3`;) the *Upper Great limestone* 18`; sandstone and shale, 60`; *Lower Great limestone* 55`; sandy shale 40`, on the *Sewickley coal bed* (1` to 6`;) sandstone 10`; the *Fishpot limestone* 18`; sandstone and shale, 25`, on the *Redstone coal bed* (1` to 4`;) limestone 10`; Pittsburgh upper sandstone 40`; shale 0` to 10`, on the *Pittsburgh coal bed* (5` to 12`.) The shale cover to the Waynesburg coal bed has preserved the finest *leaf impressions* yet obtained from these upper series. The coal bed covers at least 15,000 square miles in the two States, and has a parting which fluctuates in thickness from 0` to 6` in a few yards of distance. The coal is sometimes 8` thick, and the great overlying sandstone often descends into it, even to its floor…."

Table 1-1 contains an approximated layered representation of the description above for 750 feet of overburden on top of the Pittsburgh coal bed. Figure 1-8 and Figure 1-9 provide boring logs similar to the description above.

Table 1-1. Tabular summary of the first 750 feet down to Pittsburgh coal bed

Layer No.	Min. Thickness [ft]	Max. Thickness [ft]	Hardrock	Rock Type
1		118		Shale and sandstone
2		3	x	Limestone
3		18	x	Sandstone
4		3		Shale
5		3.5	x	Lower Washington limestone
6		6		Shale
7		2.5		Washington Coal Bed
8		18	x	Clay and sandstone
9		20	x	Sandstone
10		1		Waynesburg "B" Coal Bed
11		18		Sandstone and shale
12		1		Waynesburg "A" Coal Bed
13		10		Shale
14		30	x	Limestone
15	6	11		Washington Coal Bed
16		70	x	Washington Sandstone
17	0	12		Shale
18		6		Waynesburg Main Coal Bed
19		3		Clay
20		20	x	Sandstone
21		5	x	Limestone
22		60		Sandstone and shale
23	1	3		Uniontown Coal Bed
24		18	x	Upper Great Limestone
25		60		Sandstone and shale
26		55	x	Lower Great Limestone
27		40		Sandy shale
28	1	6		Sewickley Coal Bed

Table 1-1 (continued)

Layer No.	Min. Thickness [ft]	Max. Thickness [ft]	Hardrock	Rock Type
29		10	x	Sandstone
30		18	x	Fishpot limestone
31		25		Sandstone and shale
32	1	4		Redstone Coal Bed
33		10	x	Limestone
34		40	x	Pittsburgh Upper Sandstone
35	0	10		Shale
36	5	12		Pittsburgh Coal Bed
Total Depth [ft]		750		
Hardrock percentage by thickness		45%		

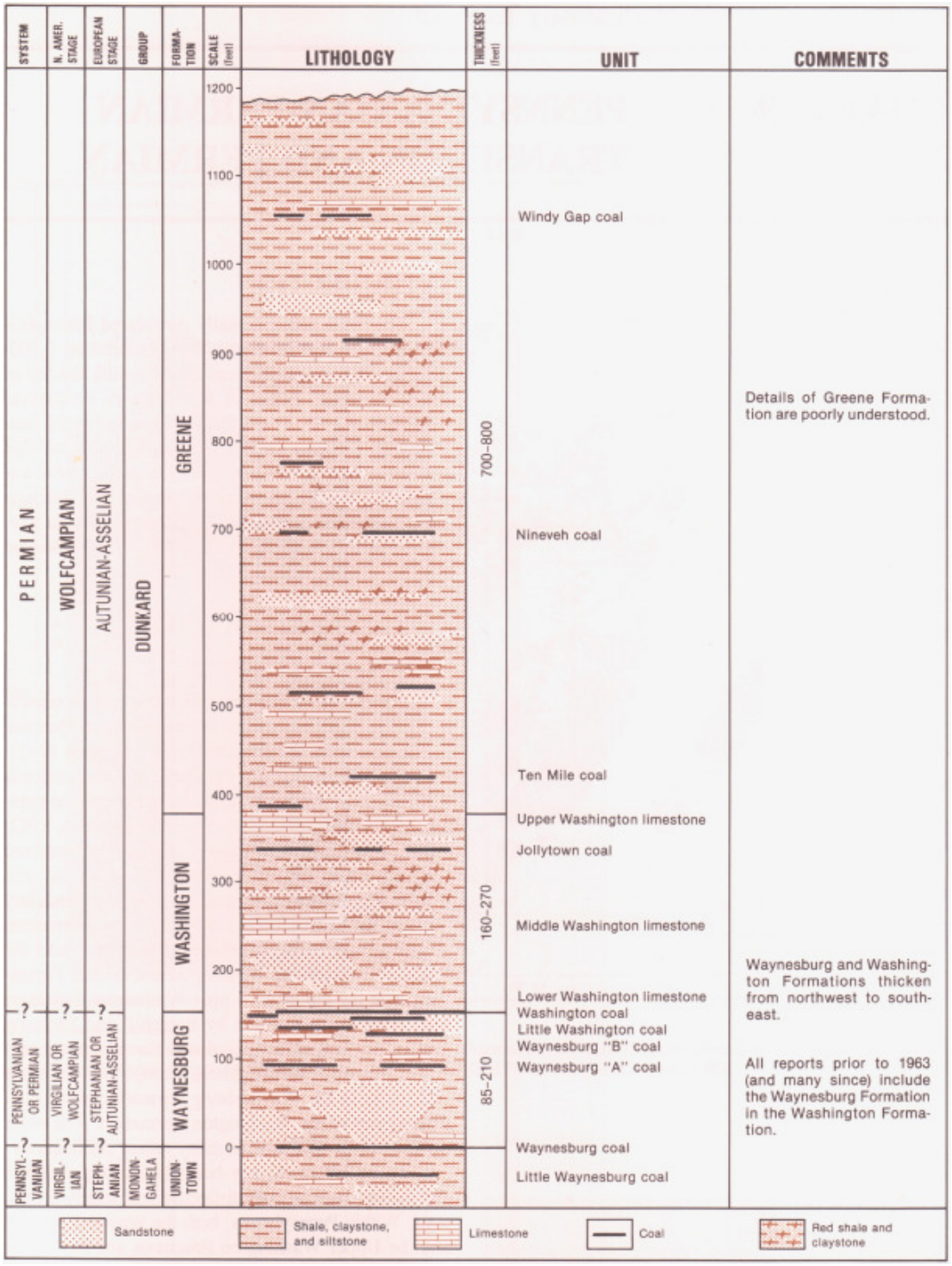

Figure 1-8. Stratigraphic column of the Pennsylvanian-Permian and Permian sequence of southwestern Pennsylvania

(Edmunds 1999)

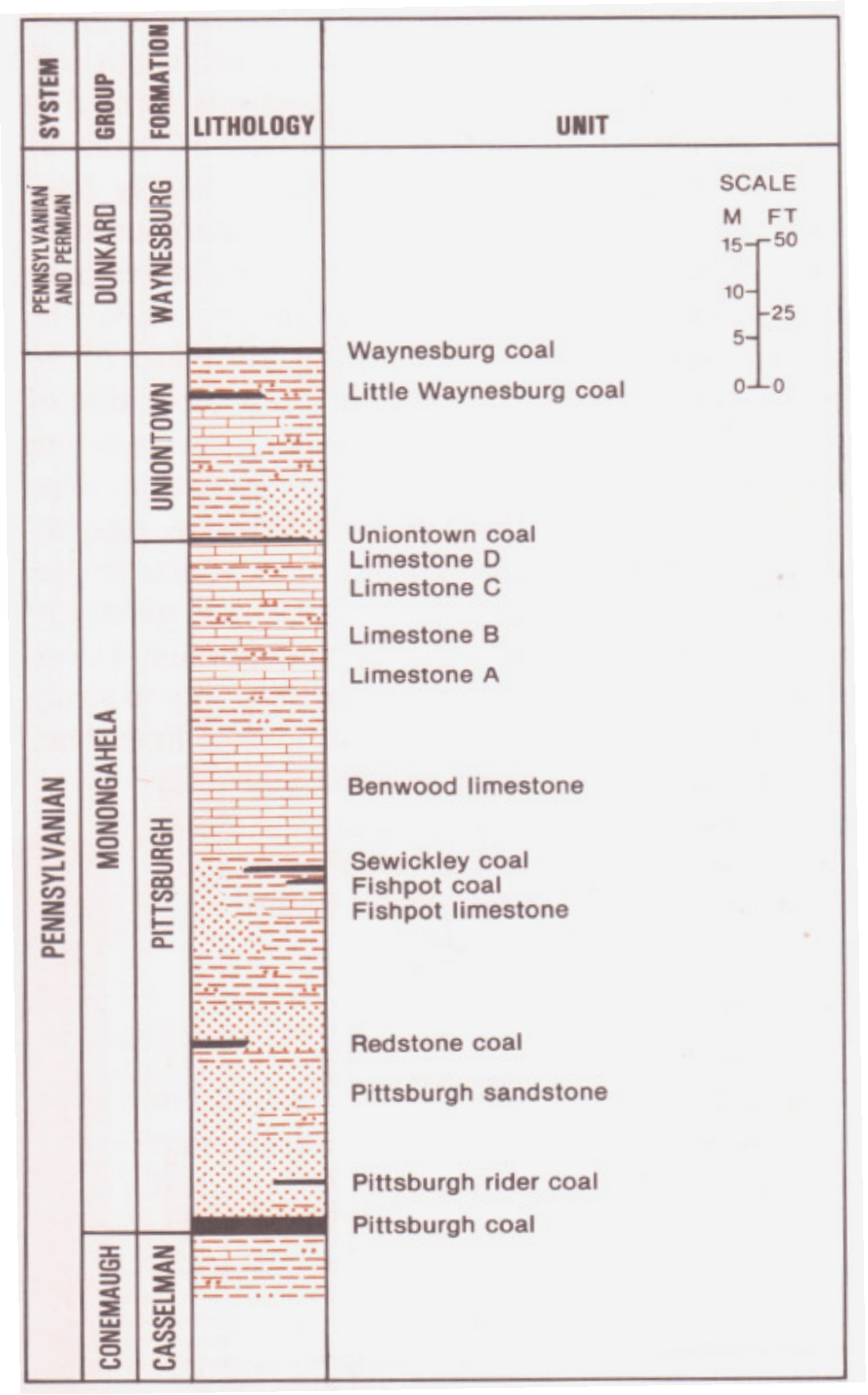

Figure 1-9. Stratigraphic column of the Monongahela Group of Western Pennsylvania

(Edmunds, Skema et al. 1999)

Jeran and Adamek (Jeran and Adamek 1988) provide two columnar diagrams of core test holes of the Pittsburgh Coalbed in southwestern Pennsylvania (Figure 1-10). We concluded that these two diagrams are the most detailed stratigraphic data available from the region where the Cumberland and Emerald mines are located. Table 1-2 and Table 1-3 show the approximate thickness readings taken from Figure 1-10.

A detailed stratigraphy of the roof and first few layers above a longwall panel in southwestern Pennsylvania up to 5.5 meters is given in Figure 1-11 (Oyler, Mark et al. 2004). For most layers, the Rock Quality Designation (RQD) percentage and the unconfined compressive strength are provided.

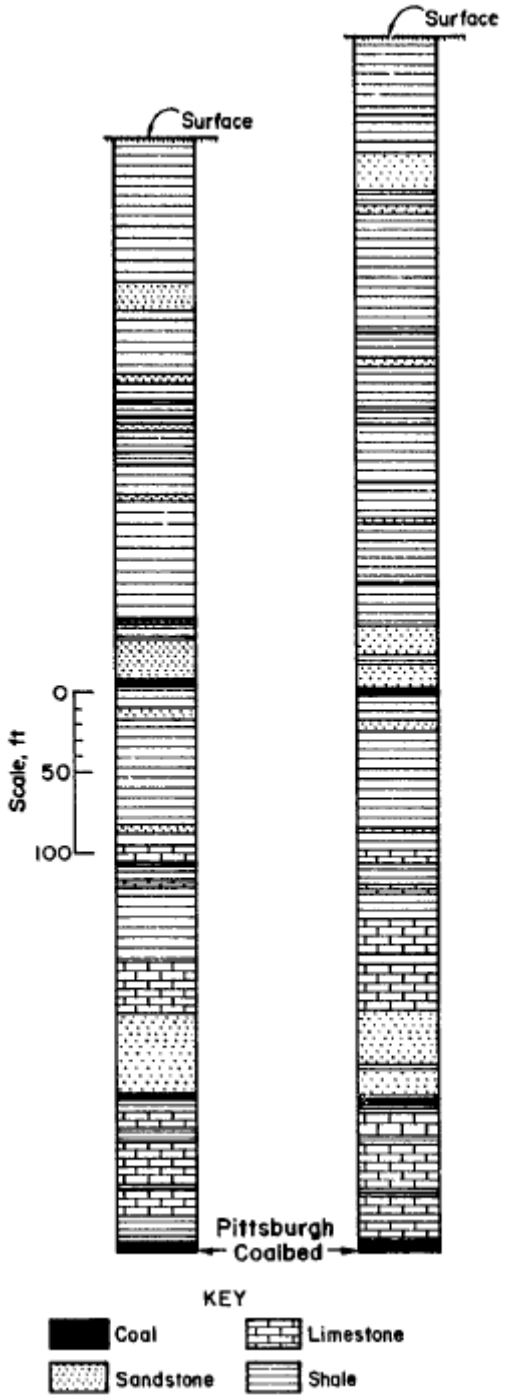

Figure 1-10. Columnar diagrams of two core test holes in southwestern Pennsylvania

(Jeran and Adamek 1988)

Table 1-2. Typical layer thickness read from core test hole No. 1

Layer No.	Approx. Layer Thickness [ft]	Rock type
1	90	Shale
2	17	Sandstone
3	35	Shale
4	5	Sandstone
5	10	Shale
6	3	Coal
7	10	Shale
8	2	Coal
9	3	Shale
10	5	Sandstone
11	10	Shale
12	2	Coal
13	8	Shale
14	2	Coal
15	17	Shale
16	5	Sandstone
17	70	Shale
18	4	Coal
19	2	Sandstone
20	10	Shale
21	2	Coal
22	25	Sandstone
23	5	Coal
24	10	Shale
25	10	Sandstone
26	67	Shale
27	7	Sandstone
28	7	Shale
29	10	Limestone
30	2	Coal
31	7	Shale
32	5	Sandstone
33	50	Shale
34	33	Limestone
35	50	Sandstone
36	5	Coal
37	8	Shale
38	10	Limestone
39	10	Shale
40	30	Limestone
41	3	Shale
42	20	Limestone
43	20	Shale

Table 1-2 (continued)

Layer No.	Approx. Layer Thickness [ft]	Rock type
44	8	Coal
Total Overburden Thickness	714	
Hardrock Cumulative Thickness	234	
Percent Hardrock	33%	

Table 1-3. Typical layer thickness read from core test hole No. 2

Layer No.	Approx. Layer Thickness [ft]	Rock type
1	75	Shale
2	25	Sandstone
3	10	Shale
4	7	Sandstone
5	80	Shale
6	3	Sandstone
7	15	Shale
8	5	Sandstone
9	25	Shale
10	3	Sandstone
11	3	Shale
12	3	Sandstone
13	60	Shale
14	3	Sandstone
15	40	Shale
16	3	Coal
17	20	Shale
18	20	Sandstone
19	5	Shale
20	15	Sandstone
21	8	Coal
22	15	Shale
23	8	Sandstone
24	37	Shale
25	3	Sandstone
26	10	Shale
27	10	Limestone
28	10	Shale
29	10	Limestone
30	15	Shale
31	20	Limestone
32	5	Shale

Table 1-3 (continued)

Layer No.	Approx. Layer Thickness [ft]	Rock type
33	30	Limestone
34	40	Sandstone
35	5	Shale
36	15	Sandstone
37	8	Coal
38	15	Limestone
39	5	Sandstone
40	35	Limestone
41	5	Sandstone
42	25	Limestone
43	8	Coal
Total Overburden Thickness	762	
Hardrock (limestone and sandstone) Cumulative Thickness	305	
Percent Hardrock	40%	

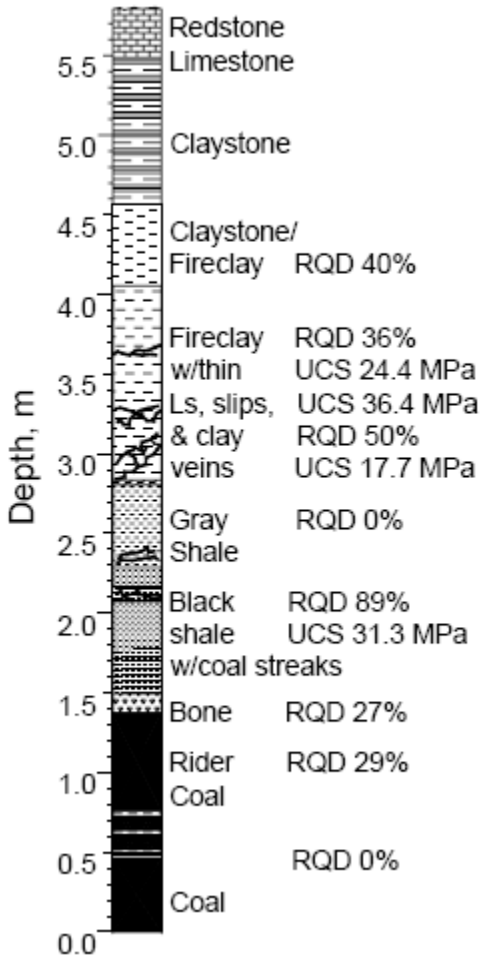

Figure 1-11. Composite core log from a study site in southwestern Pennsylvania

(Oyler, Mark et al. 2004)

1.3 SUBSIDENCE PREDICTION MODELS

Some basic definitions and terminology necessary for the subsidence prediction models are presented in Figure 1-12 (OSMRE 1986), which shows a sketch of a typical subsidence trough together with some of the most commonly used parameters. Figure 1-13 presents a graphical comparison of subcritical, critical, and supercritical mining subsidence situations.

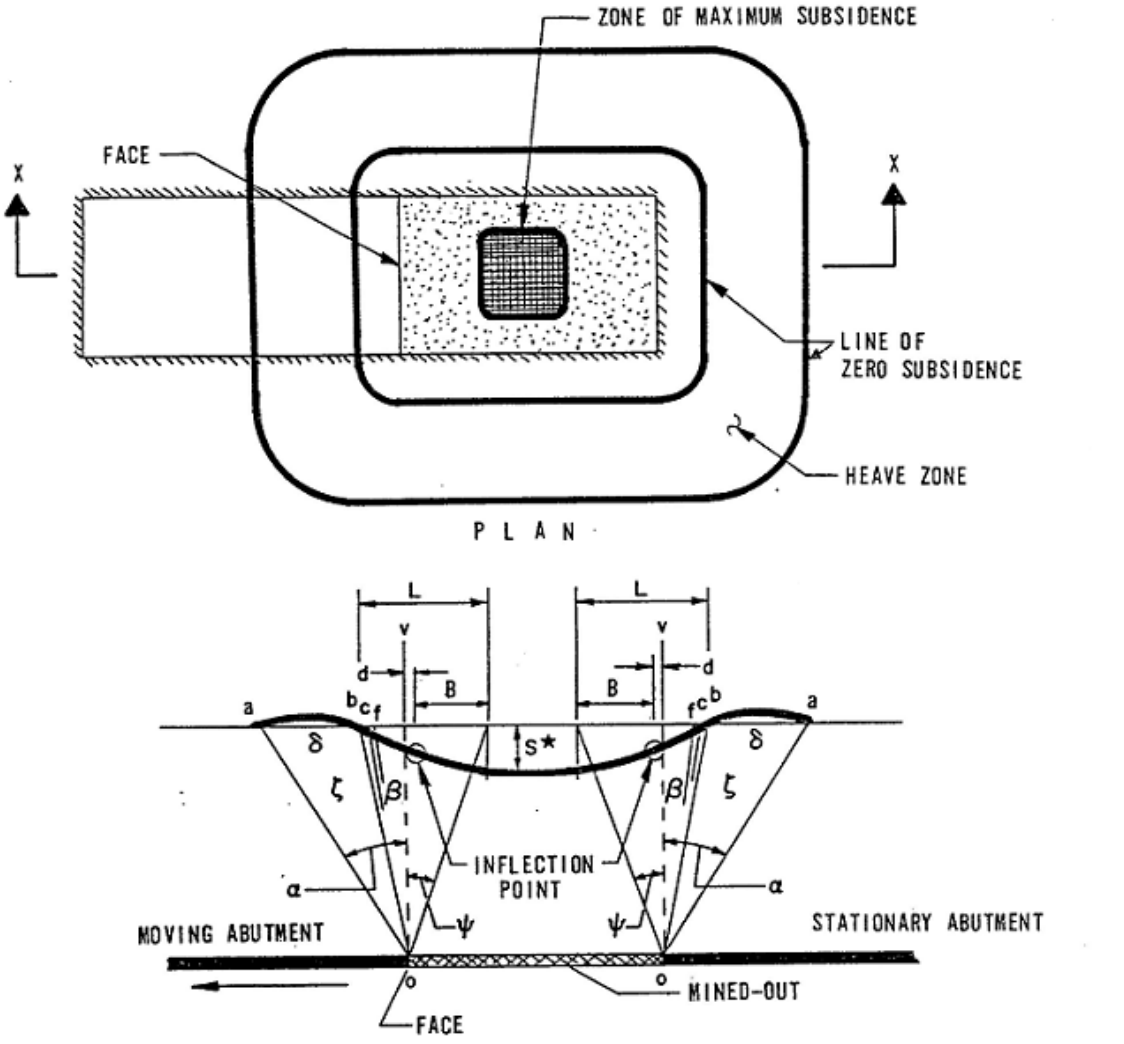

Figure 1-12. Principal parameters that characterize the subsidence trough

(OSMRE 1986)

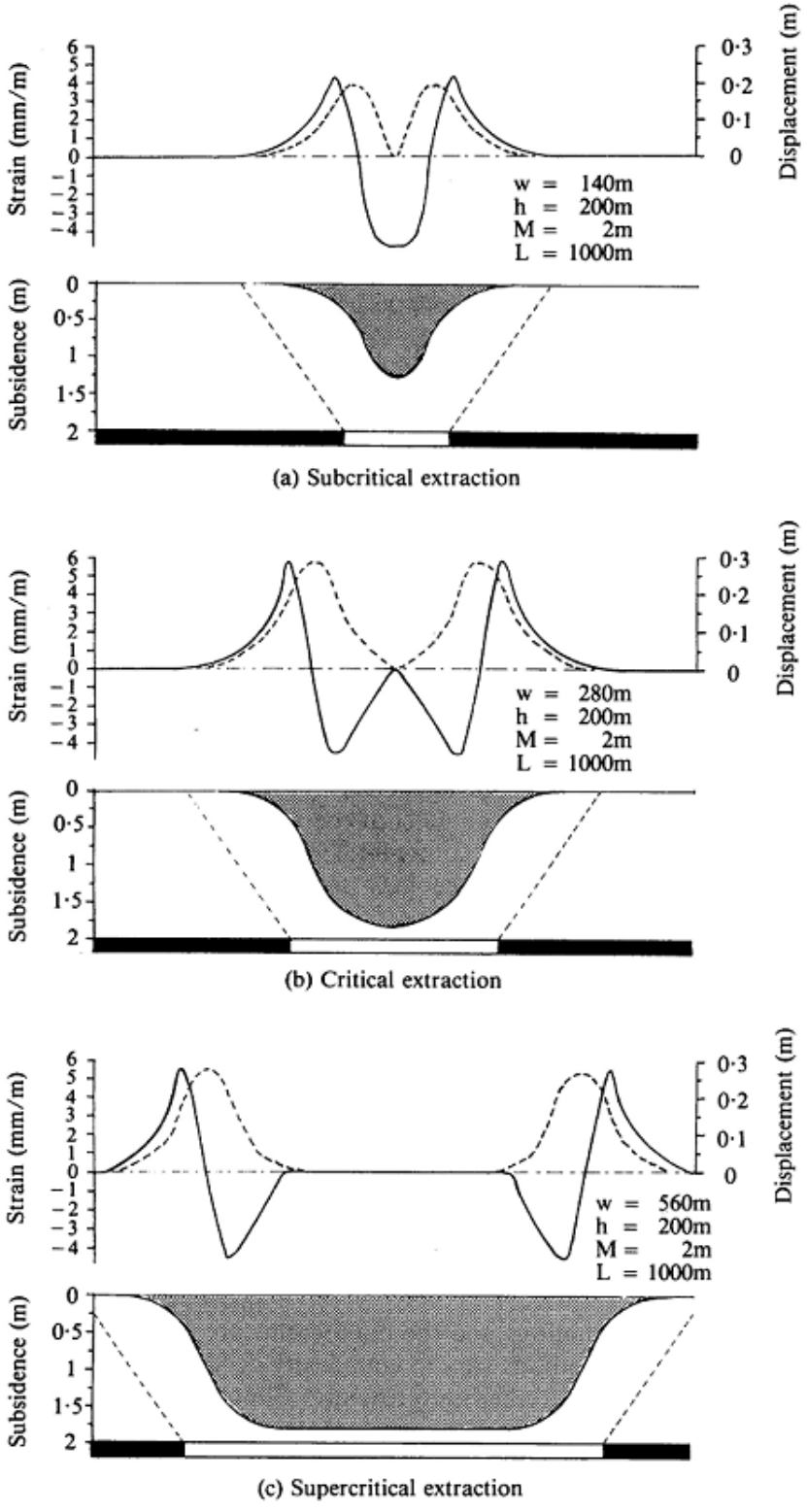

Figure 1-13. Comparison of subcritical, critical and supercritical mining subsidence situations

(Whittaker and Reddish 1989)

In the development of subsidence prediction models two major assumptions are commonly made (Karmis, Haycocks et al. 1992). The first simply suggests that subsidence is proportional to the mined seam thickness. The second implies that subsidence at a point on the surface is a function of its coordinates with respect to the mined area, and that the maximum value of subsidence is observed above the geometrical center of the excavation.

Whittaker and Reddish (Whittaker and Reddish 1989) consider five main groups of subsidence prediction methods, namely empirically derived relationships, profile functions, influence functions, analytical models, and physical models.

Karmis et al (Karmis, Haycocks et al. 1992) consider three main groups of subsidence prediction methods, namely theoretical models, numerical methods, and empirical or semi-empirical methods. Among the latter are the Profile Function Method, the Influence Function Method, and the Zone Area Method. Among numerical methods is the Finite Element Method. The VPI&SU (Virginia Tech) research group integrated profile function, influence function, zone area, and finite element techniques in the Surface Deformation Prediction System (SDPS). The Zone Area Method was initially developed in Britain for non-regular longwall or room-and-pillar panels (Karmis, Haycocks et al. 1992). It is assumed that movement of a specific point on the surface is affected by the excavation of a circular underground area.

1.3.1 National Coal Board Graphical Method

The UK Subsidence Engineers' Handbook (SEH) graphical method is based on observations at around 200 sites from different coalfields. This work had two main publications, one in 1965 and the final one in 1975 (Whittaker and Reddish 1989).

1.3.1.1 Prediction of maximum subsidence

SEH 1975 presents Figure 1-14 and Figure 1-15 as the two graphical tools to find maximum subsidence. One of the conditions that Figure 1-14 complies with is that the panel length should be at least 1.4 times the depth of excavation. If this is not the case, Figure 1-15 provides with a correction factor as a function of the ratio of face advance to depth. The correction factor must be applied to the subsidence magnitude found through Figure 1-14. The SEH 1975 (Subsidence Engineers' Handbook (SEH), 1975) stresses that "when considering workings of any w/h value in a virgin area the prediction from Figure 1-14 (which was derived from cases of multi-seam working) should be reduced by a multiplying factor of 0.9".

1.3.1.2 Prediction of complete subsidence profiles

SEH 1975 presents Figure 1-16 as a normalized graph of subsidence contours as a function of the width to depth ratio and the distance from the center of the panel in terms of the depth. The use of Figure 1-14, Figure 1-15, and Figure 1-16 together are sufficient in order to produce complete subsidence profiles accounting for magnitude, shape and extension.

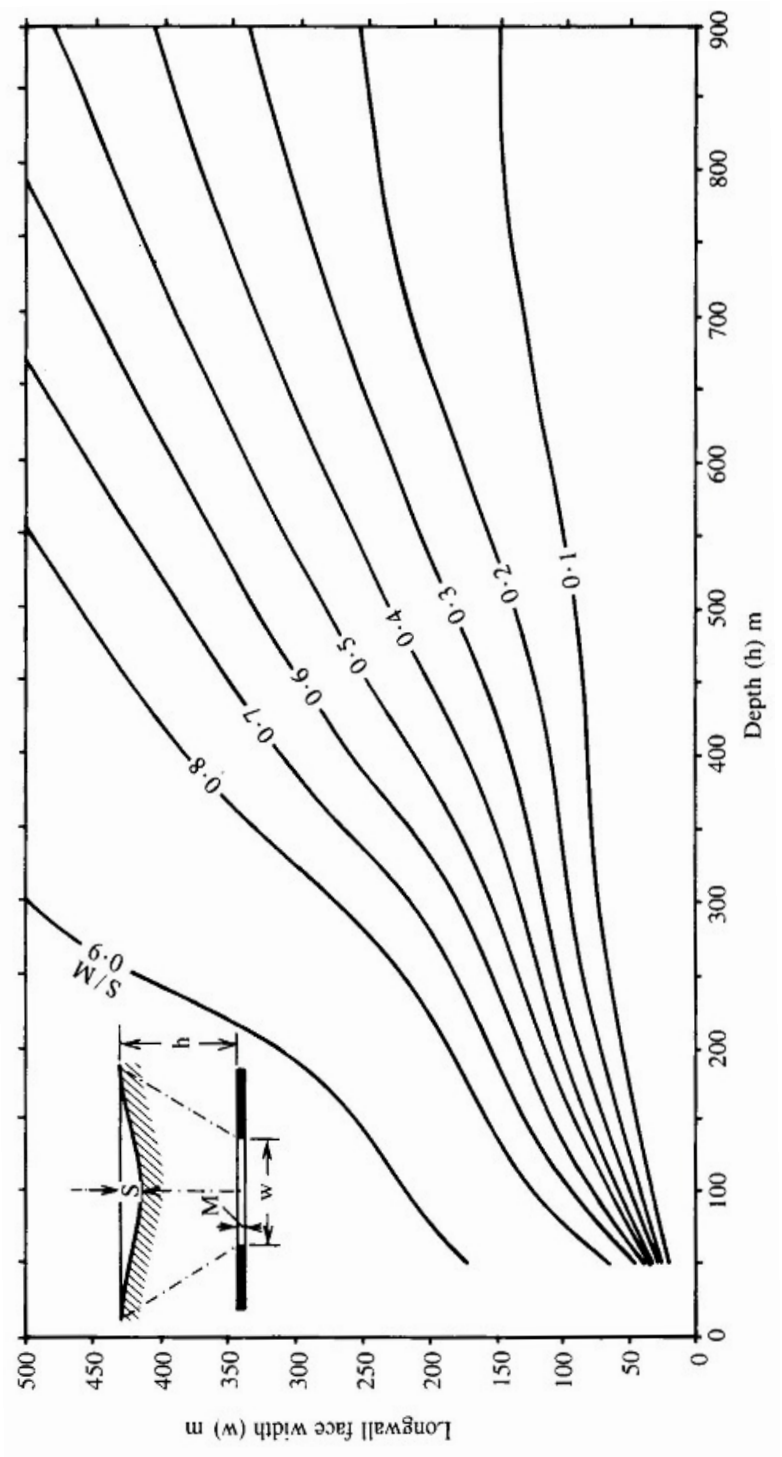

Figure 1-14. Relationship of subsidence to extraction width and depth after NCB 1965

(Whittaker and Reddish 1989)

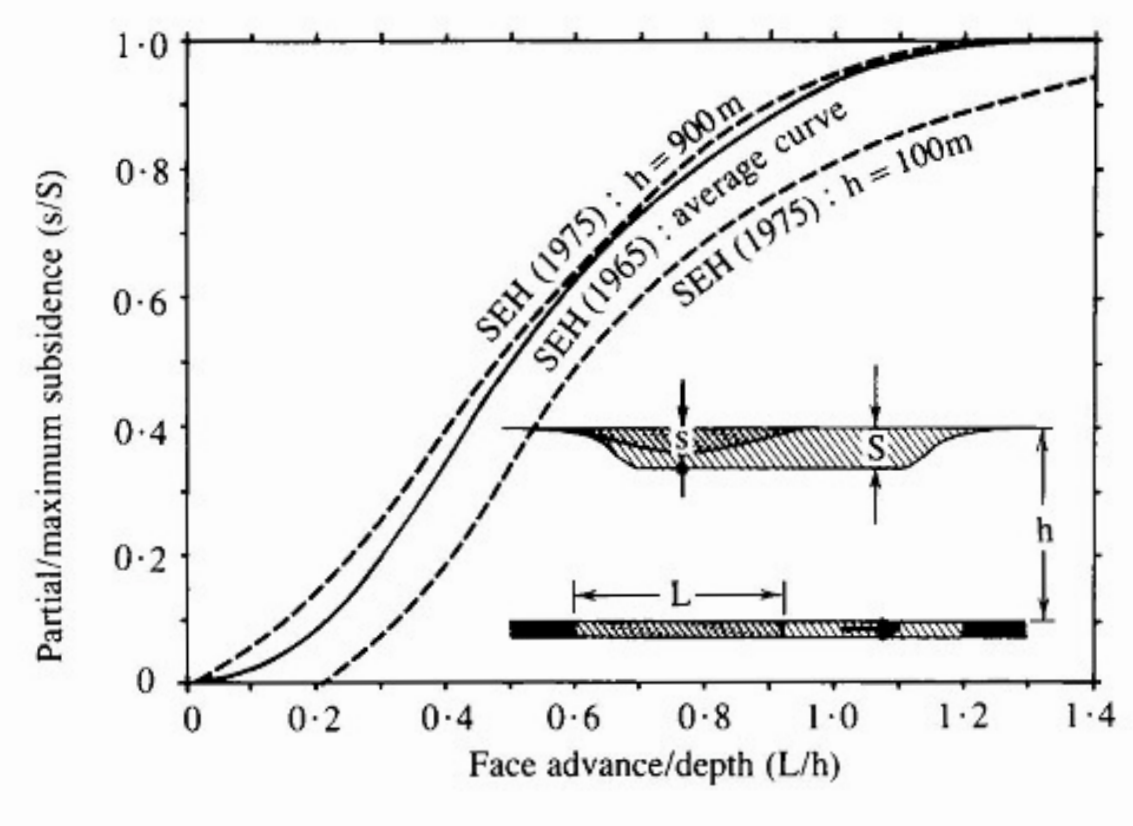

Figure 1-15. Correction graph for limited face advance after SEH 1965 and 1975

(Whittaker and Reddish 1989)

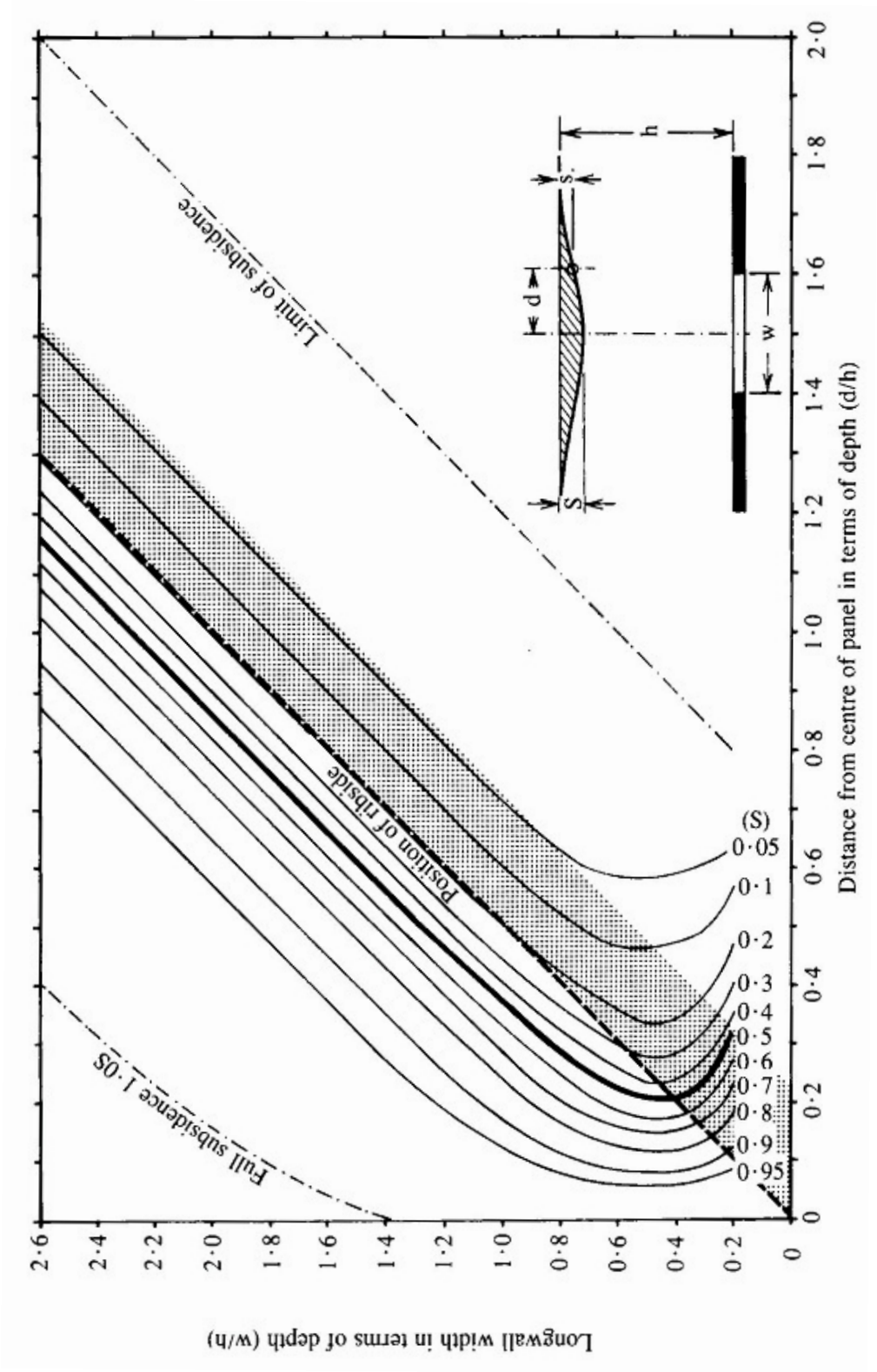

Figure 1-16. Design graph for prediction of subsidence profiles after SEH 1975

(Whittaker and Reddish 1989)

1.3.1.3 Prediction of strain profiles

In determining strain profiles, the first step is to evaluate the maximum strains, which are expressed in terms of the subsidence to depth ratio as a function of the width to depth ratio as shown in Figure 1-17, the same way maximum slope is dealt with. After maximum magnitudes of strains are obtained, a graph containing contours of strain may be used as illustrated in Figure 1-18.

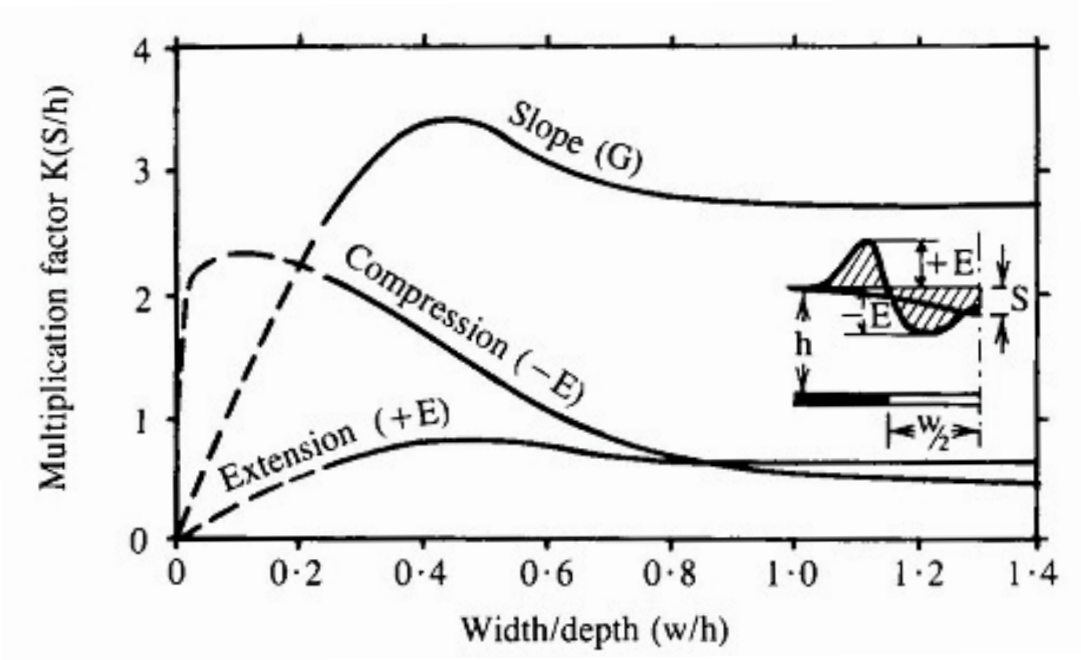

Figure 1-17. Multiplication factor K (S/h) for determining maximum values of slope and strain at various width to depth ratios after SEH 1965 and 1975

(Whittaker and Reddish 1989)

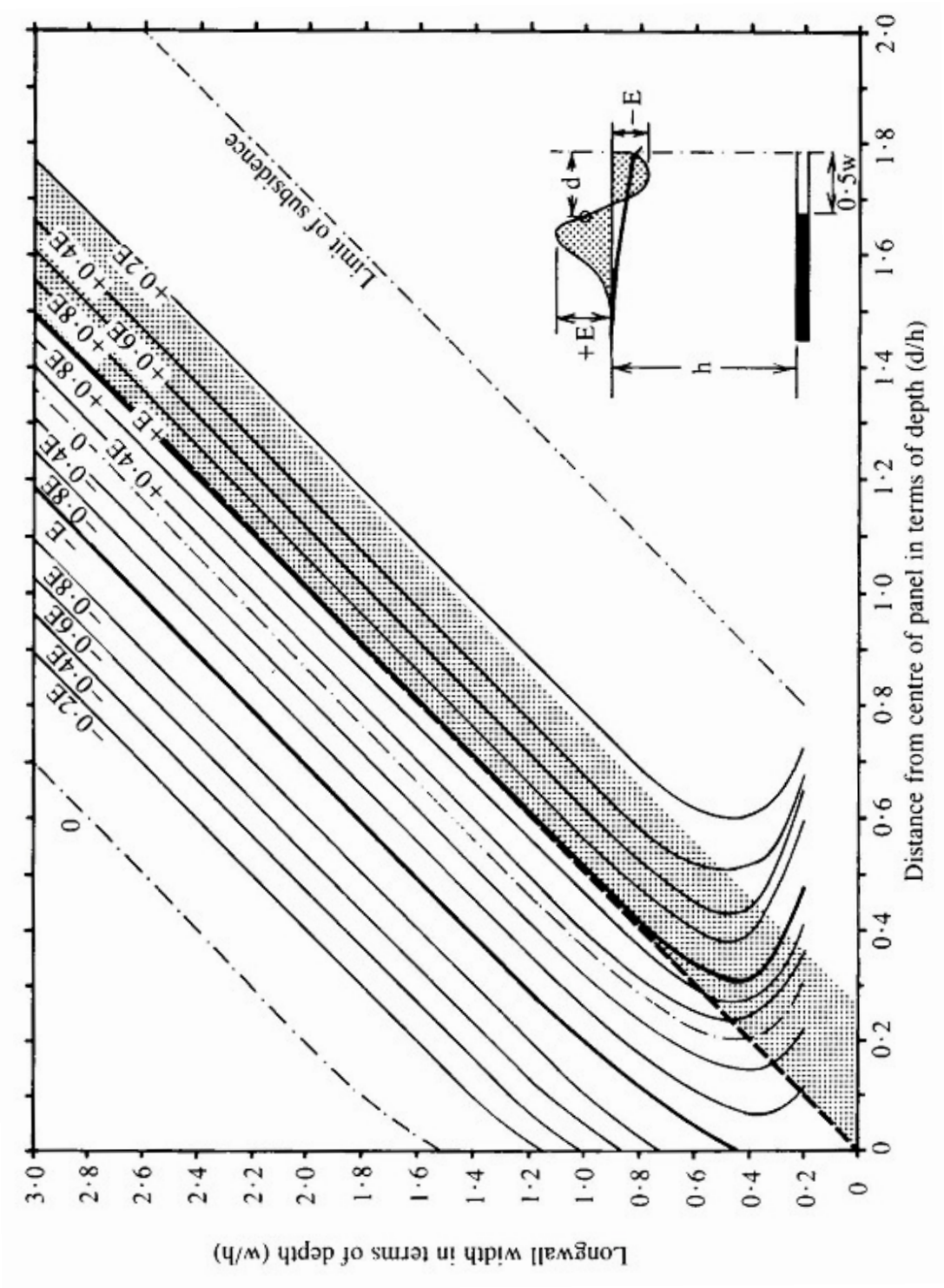

Figure 1-18. Design graph for prediction of strain profiles after SEH 1965

(Whittaker and Reddish 1989)

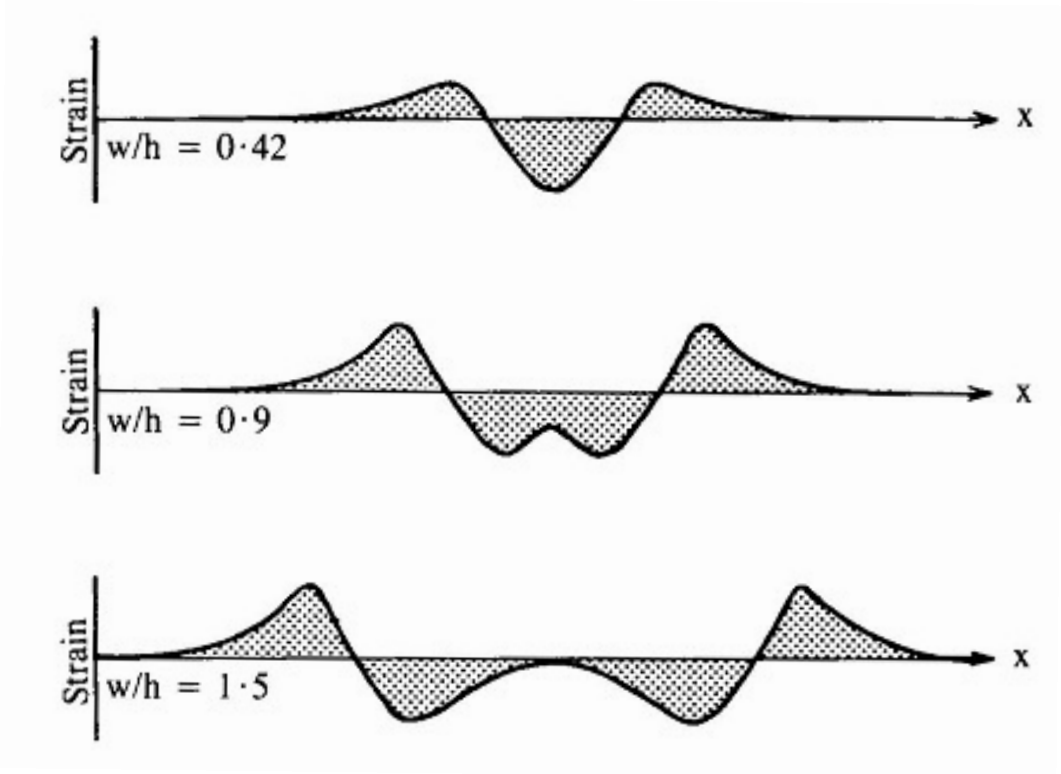

Figure 1-19. Illustration of the three principal types of strain profile after SEH 1975

(Whittaker and Reddish 1989)

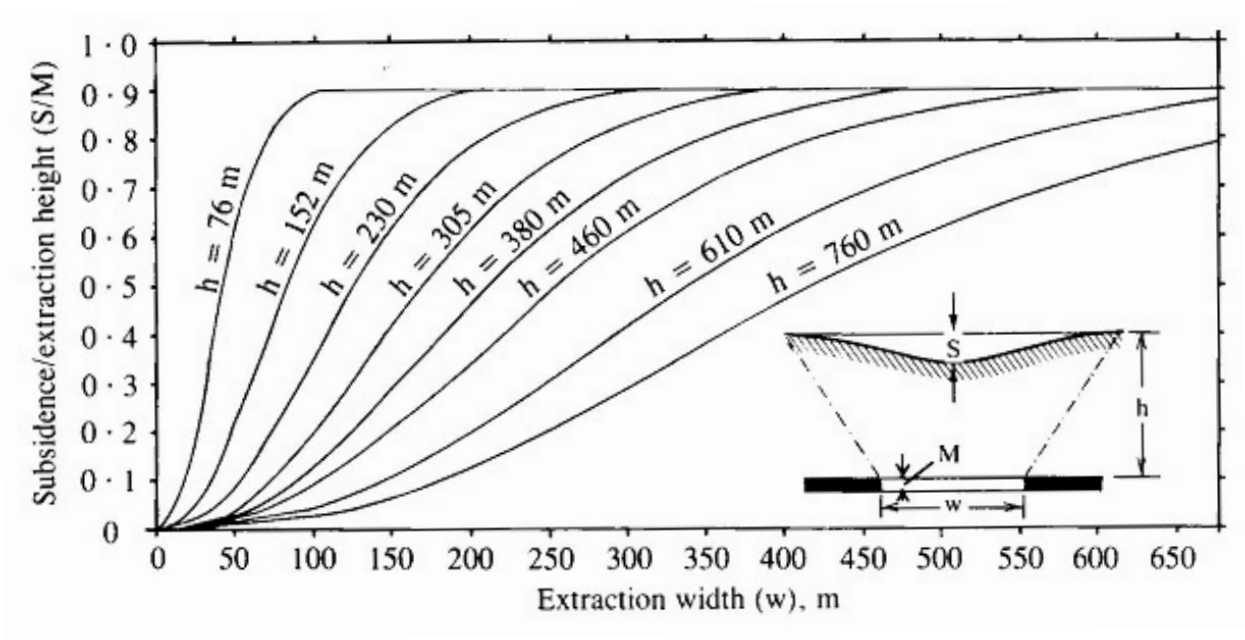

Figure 1-20. Effect of increasing depth and extraction width on the resulting subsidence after SEH 1965

(Whittaker and Reddish 1989)

1.3.2 Profile Functions

Profile functions generally use the geometry of the excavation along with equations or tables of data to predict a longitudinal or transverse profile for subsidence or strains. The constants for the equations and the nomograms are all derived empirically from local observations (Whittaker and Reddish 1989). There is a wide variety of profile functions developed in many parts of the world. The present report focuses on two profile functions that have been successfully employed in the Northern Appalachian Coal Field. The first profile function is a hyperbolic-tangent type of function, proposed by Karmis. The second profile function is an exponential function proposed by Peng and Cheng.

The following description of two profile function methodologies for the prediction of subsidence relies heavily on the Guidance Manual on Subsidence Control of the Office of Surface Mining Reclamation and Enforcement (OSMRE 1986).

1.3.2.1 Estimation of maximum subsidence

The present section is a review of the subsidence profile prediction models that have yielded successful results in the Northern Appalachian Coal Field. The first step considered in both models is the estimation of maximum subsidence in relation to the mined thickness of coal.

$$S^* = a \cdot m \qquad 1\text{-}1$$

where:

S^*: Maximum subsidence, in units of length

a: Dimensionless, $a \leq 1$

m: Mined thickness of coal, in units of length

1.3.2.2 The Hyperbolic Tangent Profile Function

Effect of the Width-to-Depth ratio and overburden on factor a

The subsidence factor '*a*' increases as the ratio width-to-depth increases. The maximum potential magnitude of '*a*' is achieved in critical conditions for a certain width. The magnitude of '*a*' is not only a function of the width-to-depth ratio, but also of the mechanical characteristics of the overburden, both of which are accounted for by Karmis' research group (Karmis, Triplett et al. 1983). These researchers considered 34 longwall cases from the Northern Appalachian Coalfield and produced the nomogram in Figure 1-21.

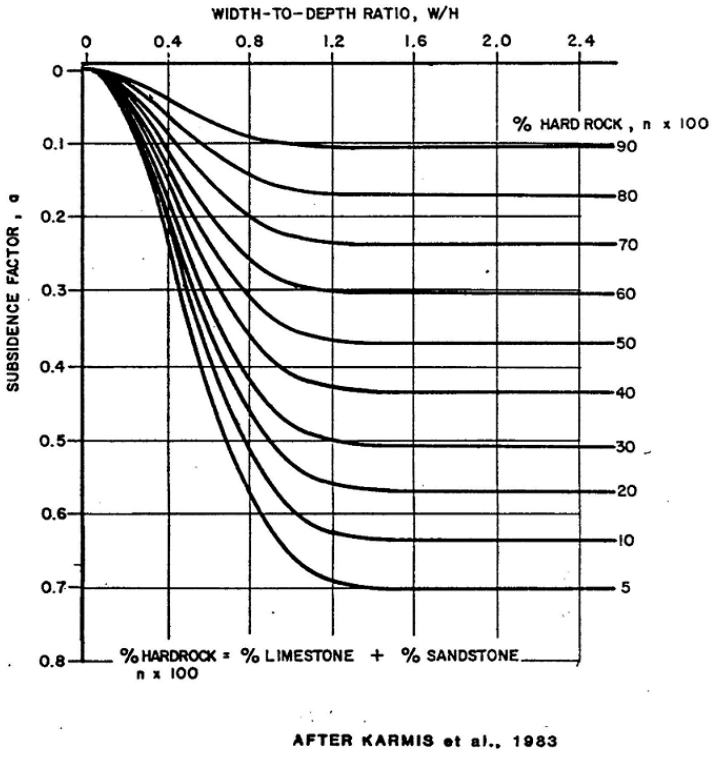

Figure 1-21. Subsidence factor as a function of width-to-depth ratio of the mine panel and the percent hardrock in the overburden

(OSMRE 1986)

Ground surface profile

The group lead by Karmis (Karmis, Triplett et al. 1984) propose the use of a hyperbolic tangent function[1]:

$$S(x) = 0.5S^* \left[1 - \tanh\left(\bar{C}\, x / B \right) \right] \qquad 1\text{-}2$$

where:

x: Horizontal distance between a point on the profile and the inflection point

S^*: Maximum subsidence for the profile

B: Distance between the inflection point and the nearest point of maximum subsidence S*, and depends upon the W/H ratio of the panel (Figure 1-27)

$\bar{C}$: Constant equaling 1.4 for subcritical panels and 1.8 for critical and supercritical panels

Angle of draw γ

Karmis et al (Karmis, Triplett et al. 1983) produced Figure 1-22 for the dependence of the angle of draw upon the ratio width-to-depth. The angle of draw increases with increasing ratio width-to-depth and reaches a constant value when critical conditions are achieved.

[1] This profile function is implemented in the Surface Deformation Prediction System (SDPS) developed by VPI&SU

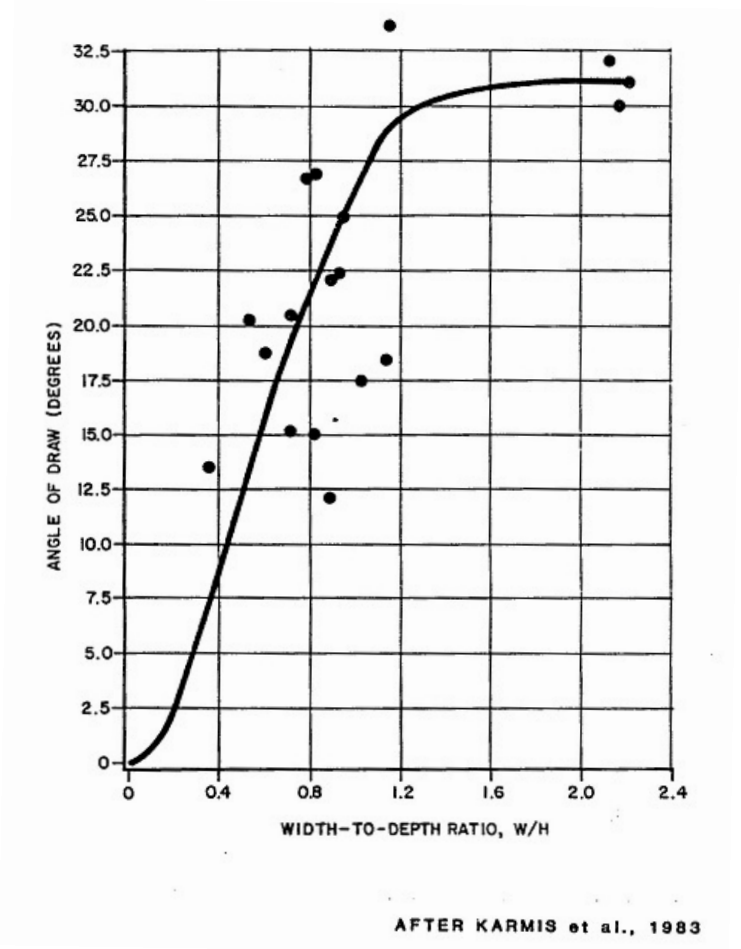

Figure 1-22. Relationship of angle of draw to width-to-depth ratio of the mine panel

(OSMRE 1986)

1.3.2.3 The Exponential Profile Function

Effect of Width-to-Depth Length-to-Depth Ratios on factor a

Peng and Geng (Peng and Geng 1983) considered forty cases from the Northern Appalachian Coalfield and produced the following expression to account for the overburden properties:

$$a_0 = 0.5(0.9 + P) \qquad 1\text{-}3$$

where

a_0: Absolute maximum subsidence factor

P: Combined Strata Coefficient,

$$P = \frac{\sum hQ}{\sum h} \qquad 1\text{-}4$$

where

Q: Stratum Property Coefficient (Figure 1-23)

h: Thickness of each stratum in the overburden.

Subsidence, understood as vertical displacement, has not reached a maximum value when conditions are subcritical. Peng and Geng (Peng and Geng 1983) propose the following expression for estimating maximum subsidence when conditions are subcritical:

$$S^* = a' \cdot m \qquad 1\text{-}5 \quad \text{(a)}$$

$$a' = a_0 \cdot C \qquad \text{(b)}$$

$$C = \left[\left(\frac{L_L}{L_C}\right)\left(\frac{L_W}{L_C}\right)\right]^{1/2}\left[1.8\left(\frac{L_W}{L_C^{-0.1}}\right)\right]^{1/2} \qquad \text{(c)}$$

where

a': Subsidence factor adjusted for geometry

m: Mined thickness of coal

L_L: Length of the mined-out area

L_W: Width of the mined-out area

L_C: Critical dimension (for both width and length) required for maximum potential subsidence

C: Parameter that is used to adjust the subsidence factor for panel geometry, with the condition that L_I/L_C and $L_W/L_C \leq 1$. Values of C are presented graphically in Figure 1-25. For $L_W/L_C > 0.65$, the second of the two terms in brackets equals unity (OSMRE 1986).

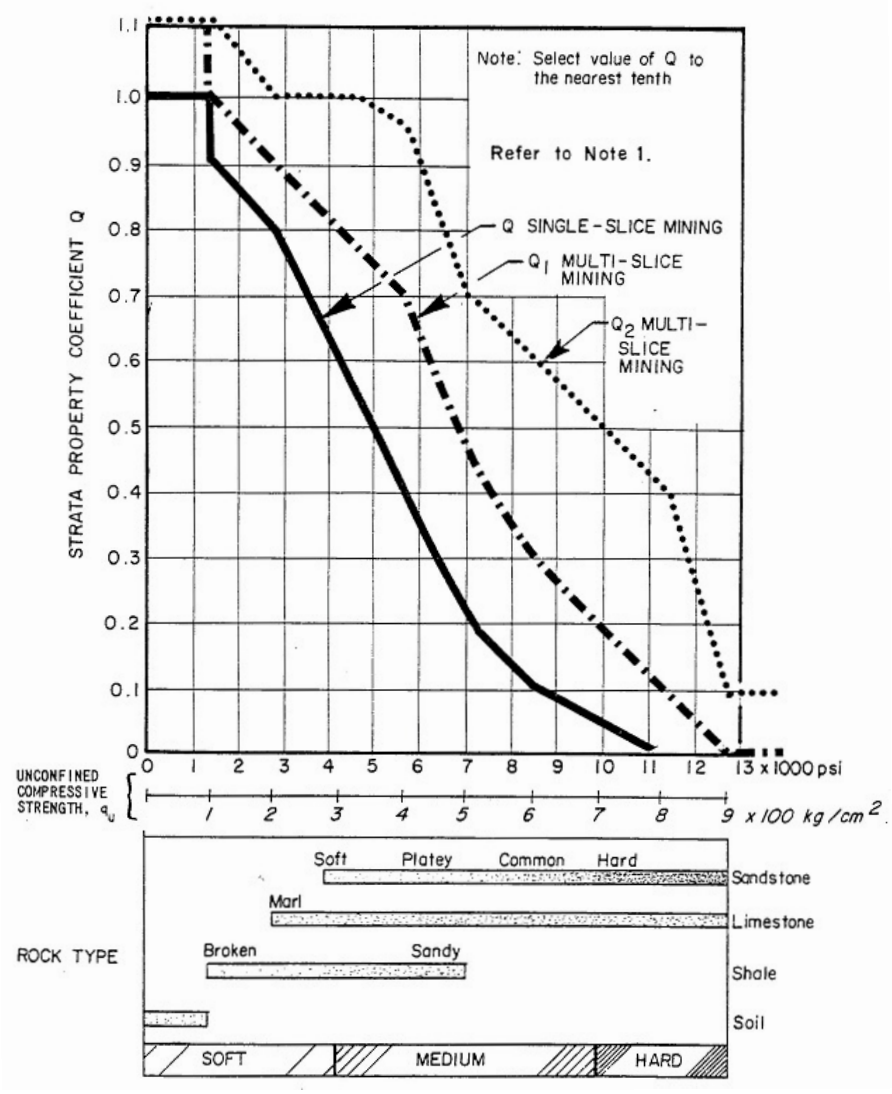

Figure 1-23. Stratum property coefficient as a function of rock type and strength (OSMRE 1986)

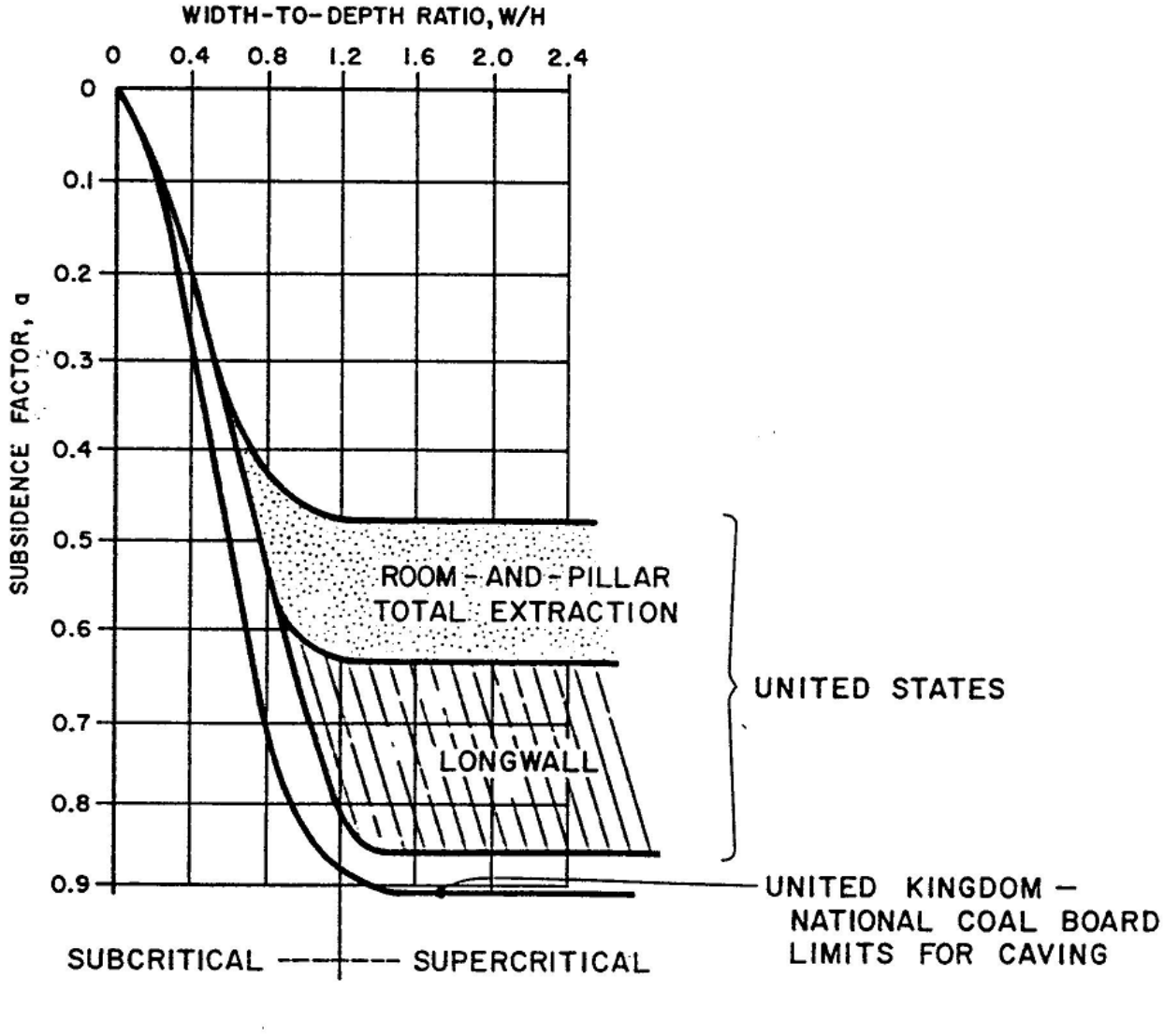

Figure 1-24. General relationship between subsidence factor and width-to-depth ratio of mine panel

(OSMRE 1986)

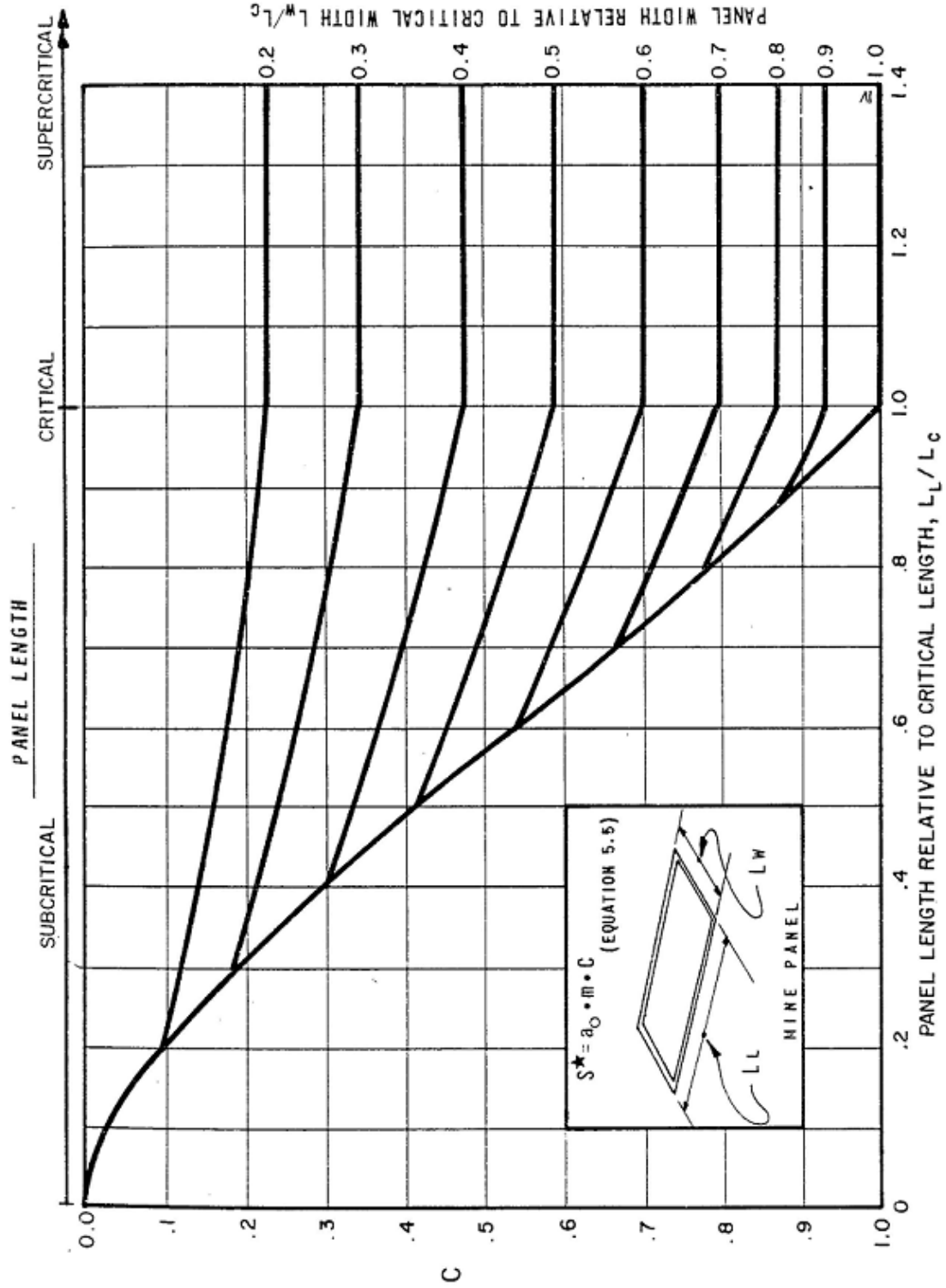

Figure 1-25. Relationship of subsidence to width and length of mine panel

(OSMRE 1986)

Ground surface profile

Chen and Peng (Chen and Peng 1981) use an exponential function:

$$S(x) = S * \exp\left[- a_{pf} (x/L)^b \right] \qquad 1\text{-}6$$

where:

a_{pf}, b: Empirical constants, which Chen and Peng found to be equal to (a_{pf} , b) = (8.97, 2.03) based on longwall profiles from the Northern Appalachian Coal Field.

x: Horizontal distance between a point on the profile and the origin, which is located at the point of maximum subsidence nearest the edge of the panel

L: Horizontal distance between the lip of the trough (zero subsidence) and the point of maximum subsidence nearest the edge of the panel (OSMRE 1986).

Critical panel dimensions

Chen and Peng (Chen and Peng 1981) report a value of $W = 1.1H$ for critical conditions in the Northern Appalachian Coalfield, whereas Karmis et al. (Karmis, Haycocks et al. 1981) report $W = 1.2H$, which compares to $1.4H$ in the U.K (OSMRE 1986).

Peng and Geng (Peng and Geng 1983) suggest a nearly linear relationship between maximum subsidence factor a_0 and ratio of critical panel dimension to mine depth L_C/H, as shown in Figure 1-26 for the Northern Appalachian Coal Field (OSMRE 1986). With H and a_0 known, the critical dimension L_C can be obtained.

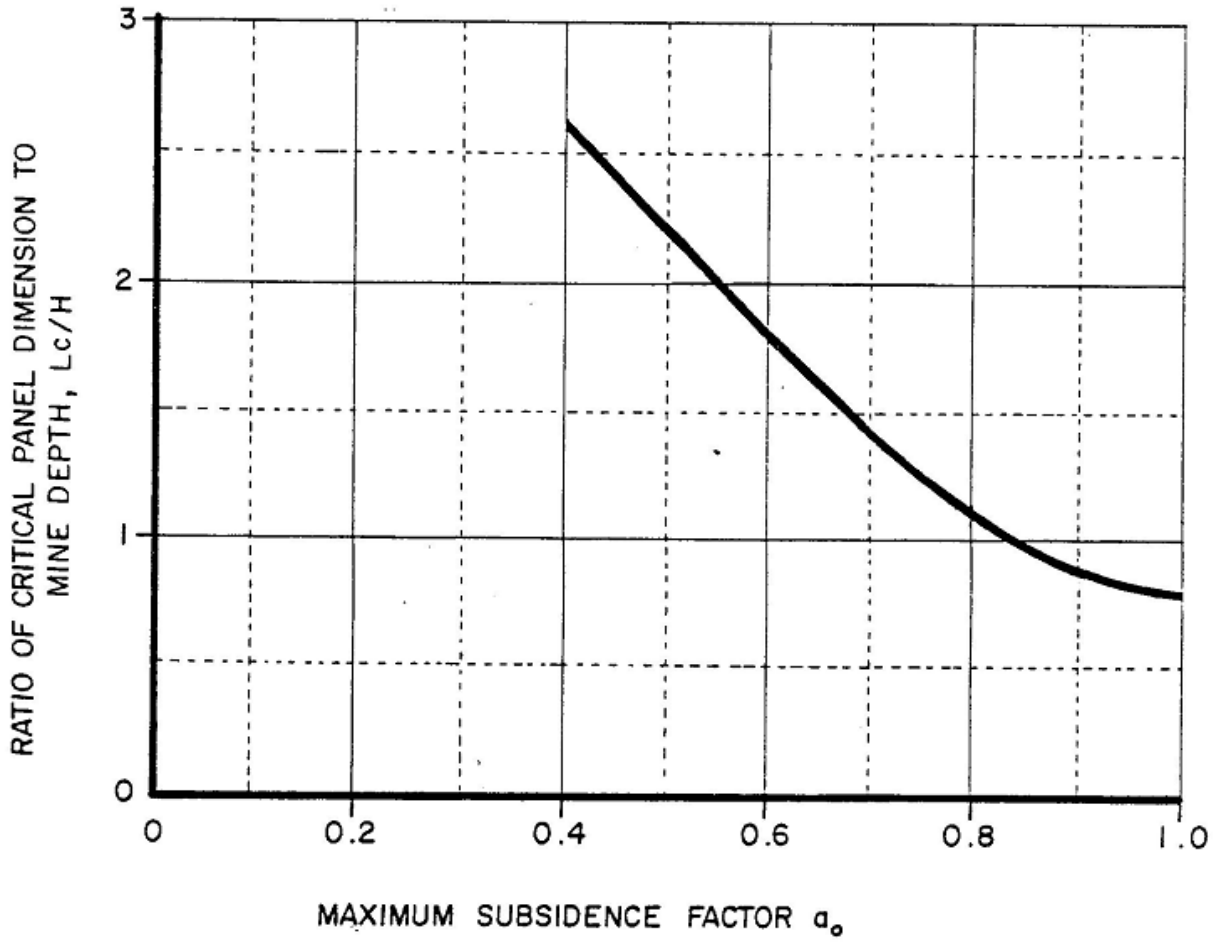

Figure 1-26. Relationship of critical panel dimension to maximum subsidence factor and mine depth (OSMRE 1986)

Angle of draw γ

Peng and Geng (Peng and Geng 1983) attempt to account for lithology of the overburden by including the subsidence factor in the estimation of the angle of draw. They propose two different expressions. They first consider a panel whose length and width are critical or supercritical:

$$\gamma = 44 - 6a - 0.015H \qquad 1\text{-}7$$

where:

a: Subsidence factor

H: Overburden thickness

The second case is for a panel whose length is critical or supercritical, but whose width is between 0.55 and 0.85 times the critical dimension:

$$\gamma = 38 - 6a - 0.015H \qquad 1\text{-}8$$

The researchers claim that the error obtained with the above expressions is less than 2 degrees. However, the Guidance Manual on Subsidence Control (OSMRE 1986) observes the fact that these expressions predict higher values of angle of draw the more competent the overburden is, which is not consistent with the conventional knowledge. The Guidance Manual on Subsidence Control continues to stress that "in general, published data have not shown a strong correlation between angle of draw and lithology" and attempts to explain this fact by speculating that "one or more of the following factors might be responsible for the lack of a strong correlation: non-representative or poor information concerning lithology, poor measurements of angle of draw, failure to account for position of the strata in the rock sequence, failure to assess the weighted average overburden composition, failure to account for the dimensions of the mine panel, or failure to recognize that the angle of draw can vary with position around a panel even without significant variations in lithology."

1.3.2.4 Comments on the hyperbolic tangent (Karmis et al) and exponential (Chen and Peng) profile function methods

According to the Guidance Manual on Subsidence Control (OSMRE 1986), "both the hyperbolic tangent and the exponential functions can be considered equally satisfactory for sketching anticipated subsidence profiles for sites in the Northern Appalachian Coal Field".

1.3.2.5 Derived parameters of subsidence

Ground surface slope

The slope of surface *i(X)* is given by the first derivative with respect to *X* of the subsidence function *S(X)*:

$$i(X) = S'(X) \qquad 1\text{-}9$$

Ground surface curvature

The curvature of the surface *K(X)* is the rate of change of slope and is calculated through the second derivative with respect to *X* of the subsidence function *S(X)*:

$$K(X) = S''(X) \qquad 1\text{-}10$$

Horizontal ground displacement

The horizontal movement *u(X)* of a point *X* on the subsidence profile is related to the slope *i(X)* by an empirical constant *J* (OSMRE 1986):

$$u(X) = Ji(X) \qquad 1\text{-}11$$

Horizontal strain

The horizontal strain *e(X)* is the elongation or shortening of the ground surface in the immediate vicinity of a surface point *X* relative to an initial reference length. $e(X) = \Delta L/L$.

Karmis et al (Karmis, Triplett et al. 1984), see Figure 1-29, propose the following expression for horizontal strain as a function of curvature:

$$e_0 = 0.92\sqrt{K_0} \qquad 1\text{-}12$$

The Guidance Manual on Subsidence Control (OSMRE 1986) stresses two points when using profile function prediction methods:

1. “The subsidence profile and associated parameters represent the configuration of the ground surface through the point of maximum subsidence for the particular panel geometry, mine depth and overburden lithology. The profile does not account for the presence of any heave zone around the perimeter of the panel".

2. "The subsidence profile and associated parameters can be sensitive to the estimated angle of draw. Note that the angle of draw is used in the calculation of the half width of the subsidence profile, which in turn, governs the shape of the subsidence profile. The use of a small angle of draw tends to yield a conservative (that is, high) estimate of maximum slope, curvature, horizontal displacement and strain. However, the areal extent of the subsidence trough may be underestimated. The use of a more liberal estimate of the angle of draw tends to provide a more conservative estimate of the size of the subsidence trough but at the same time may underestimate the maximum values of slope, curvature, horizontal displacement and strain. Given the uncertainties inherent in all computational methods, consideration should be given to presenting a range of values for the subsidence trough and its parameters.”

PROFILE FUNCTION FACTORS

Hyperbolic Tangent Function
C = 1.4 Subcritical

x/B	Subsidence A= S/S*	Slope A'= 1B/S*	Curvature A"= kB²/S*	Horizontal Displacement cA'= u/S*	Strain cA"= eB/S*
-1.00	.943	-.151	-.375	.050	.125
-.95	.935	-.171	-.416	.057	.139
-.90	.926	-.193	-.460	.064	.153
-.85	.915	-.217	-.505	.072	.168
-.80	.904	-.243	-.551	.081	.184
-.75	.891	-.272	-.596	.091	.199
-.70	.877	-.303	-.639	.101	.213
-.65	.861	-.336	-.678	.112	.226
-.60	.843	-.371	-.712	.124	.237
-.55	.823	-.407	-.737	.136	.246
-.50	.802	-.444	-.752	.148	.251
-.45	.779	-.482	-.753	.161	.251
-.40	.754	-.519	-.739	.173	.246
-.35	.727	-.556	-.707	.185	.236
-.30	.698	-.590	-.655	.197	.218
-.25	.668	-.621	-.585	.207	.195
-.20	.636	-.648	-.495	.216	.165
-.15	.603	-.670	-.388	.223	.129
-.10	.570	-.686	-.267	.229	.089
-.05	.535	-.697	-.136	.232	.045
0.00	.500	-.700	0.000	.233	0.000
.05	.465	-.697	.136	.232	-.045
.10	.430	-.686	.267	.229	-.089
.15	.397	-.670	.386	.223	-.129
.20	.364	-.648	.495	.216	-.165
.25	.332	-.621	.585	.207	-.195
.30	.302	-.590	.655	.197	-.218
.35	.273	-.556	.707	.185	-.236
.40	.246	-.519	.739	.173	-.246
.45	.221	-.482	.753	.161	-.251
.50	.198	-.444	.752	.148	-.251
.55	.177	-.407	.737	.136	-.246
.60	.157	-.371	.712	.124	-.237
.65	.139	-.336	.678	.112	-.226
.70	.123	-.303	.639	.101	-.213
.75	.109	-.272	.596	.091	-.199
.80	.096	-.243	.551	.081	-.184
.85	.085	-.217	.505	.072	-.168
.90	.074	-.193	.460	.064	-.153
.95	.065	-.171	.416	.057	-.139
1.00	.057	-.151	.375	.050	-.125

Hyperbolic Tangent Function
C = 1.8 Subcritical

x/B	Subsidence A= S/S'*	Slope A'= 1B/S*	Curvature A"= kB²/S*	Horizontal Displacement cA'= u/S*	Strain cA"= eB/S*
-1.00	.973	-.093	-.318	.031	.106
-.95	.968	-.110	-.372	.037	.124
-.90	.962	-.131	-.435	.044	.145
-.85	.955	-.154	-.505	.051	.168
-.80	.947	-.181	-.583	.060	.194
-.75	.937	-.212	-.668	.071	.223
-.70	.926	-.248	-.760	.083	.253
-.65	.912	-.289	-.856	.096	.285
-.60	.897	-.334	-.953	.111	.318
-.55	.879	-.384	-1.046	.128	.349
-.50	.858	-.438	-1.130	.146	.337
-.45	.835	-.496	-1.197	.165	.399
-.40	.808	-.557	-1.238	.186	.413
-.35	.779	-.620	-1.245	.207	.415
-.30	.746	-.681	-1.209	.227	.403
-.25	.711	-.740	-1.124	.247	.375
-.20	.673	-.793	-.985	.264	.328
-.15	.632	-.837	-.795	.279	.265
-.10	.589	-.871	-.559	.290	.186
-.05	.545	-.893	-.288	.298	.096
0.00	.500	-.900	0.000	.300	0.000
.05	.455	-.893	.288	.298	-.096
.10	.411	-.871	.559	.290	-.186
.15	.368	-.837	.795	.279	-.265
.20	.327	-.793	.985	.264	-.328
.25	.289	-.740	1.124	.247	-.375
.30	.254	-.681	1.209	.227	-.403
.35	.221	-.620	1.245	.207	-.415
.40	.192	-.557	1.236	.186	-.413
.45	.165	-.496	1.197	.165	-.399
.50	.142	-.438	1.130	.146	-.377
.55	.121	-.384	1.046	.128	-.349
.60	.103	-.334	.953	.111	-.318
.65	.088	-.289	.856	.096	-.285
.70	.074	-.248	.760	.083	-.253
.75	.063	-.212	.668	.071	-.223
.80	.053	-.181	.583	.060	-.194
.85	.045	-.154	.505	.051	-.168
.90	.038	-.131	.435	.044	-.145
.95	.032	-.110	.372	.037	-.124
1.00	0.27	-.093	.318	.031	-.106

Figure 1-27. Profile function factors (1)

(OSMRE 1986)

Exponential Function
a = 8.97
b = 2.03

X/L	Subsidence A= S/S*	Slope A= 1L/S*	Curvature A"= kL/S*	Horizontal Displacement cA'= u/S*	Strain cA"= eL/S*
0.00	1.000	0.000	-18.000	0.000	-2.117
.05	.980	-.815	-16.117	-.096	-1.924
.10	.920	-1.563	-13.442	-.184	-1.605
.15	.826	-2.132	-9.140	-.251	-1.091
.20	.710	-2.465	-4.141	-.290	.494
.25	.584	-2.550	.630	-.300	.075
.30	.459	-2.419	4.440	-.284	.530
.35	.345	-2.129	6.884	-.250	.822
.40	.248	-1.754	7.912	-.206	.945
.45	.170	-1.358	7.756	-.160	.926
.50	.111	-.992	6.800	-.117	.812
.55	.070	-.685	5.452	-.080	.651
.60	.042	-.447	4.046	-.053	.483
.65	.024	-.277	2.800	-.033	.334
.70	.013	-.163	1.816	-.019	.217
.75	.007	-.091	1.107	-.011	.132
.80	.003	-.048	.637	-.006	.076
.85	.002	-.024	.346	-.003	.041
.90	.001	-.012	.178	-.001	.021
.95	0.000	-.005	.086	-.001	.010
1.00	0.000	-.002	.040	0.000	.005

Figure 1-28. Profile function factors (2)

(OSMRE 1986)

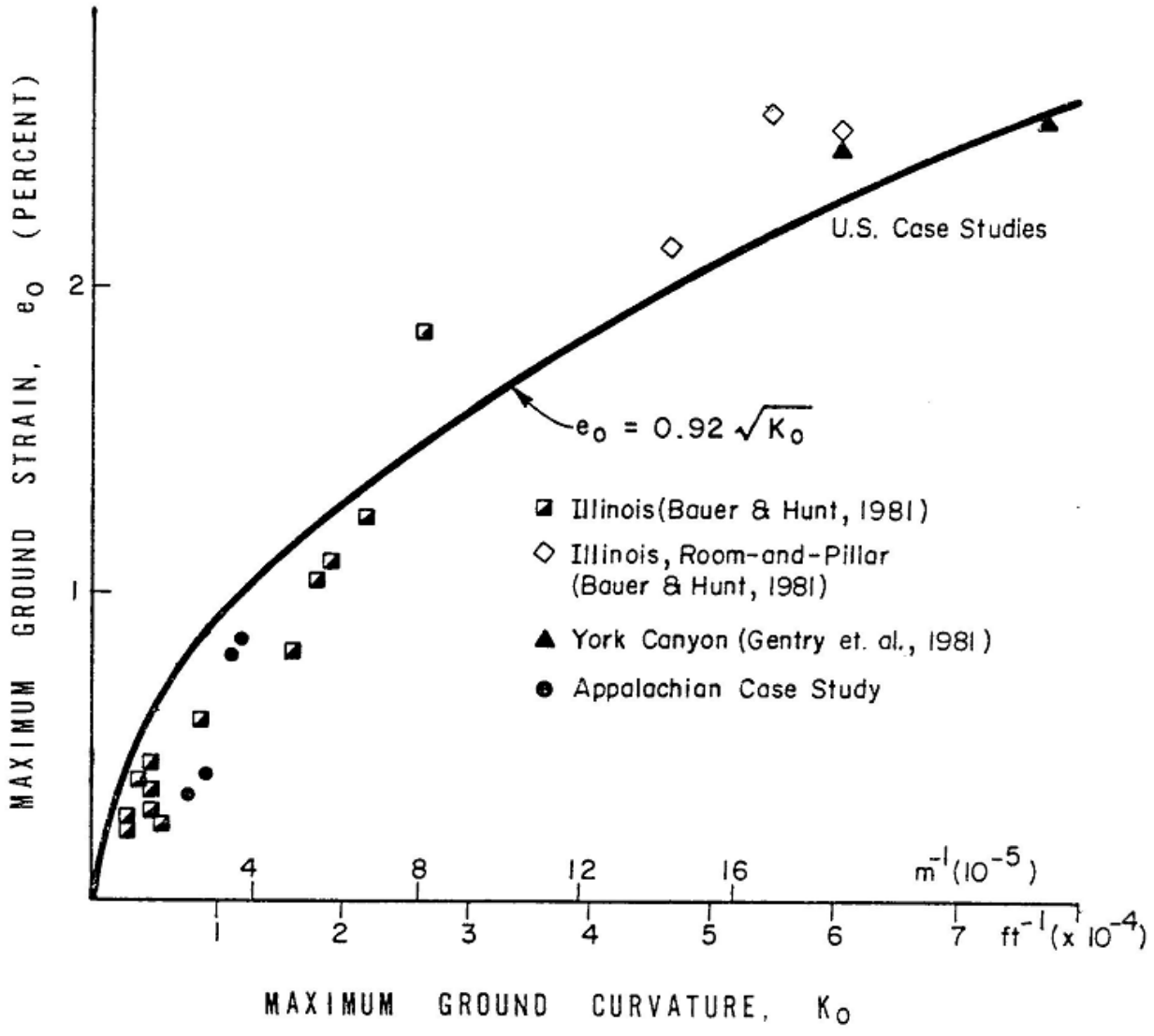

Figure 1-29. General relationship between maximum ground strain and maximum ground curvature

(OSMRE 1986)

1.3.3 Influence Functions

Karmis et al (Karmis, Haycocks et al. 1992): "An influence function describes the distribution of ground movement, i.e. subsidence or strain, caused by an infinitesimal ground excavation." Influence functions were originally developed for the central and eastern European Coalfields.

1.3.3.1 Bell-shaped Gaussian Function (Knothe's Method)

Karmis et al (Karmis, Haycocks et al. 1992) report that after reviewing the functions available in the literature, they chose the bell-shaped Gaussian function, often also referred to as the Budryk-Knothe method of prediction. The method assumes that the influence function, $f(x)$, can be expressed in a two-dimensional coordinate system as:

$$f(x) = \frac{1}{r} exp\left[-\pi \frac{x^2}{r^2}\right] \qquad 1\text{-}13$$

where

r: Average radius of influence, $H/tan(\beta)$

H: Mining height

β: Angle of influence

x: Horizontal distance from the origin (inflection point)

The subsidence $S(x)$ at any point (Karmis, Haycocks et al. 1992), for a half-infinite horizontal plane excavation can be expressed as a function of the maximum subsidence, $S_{\max}$, as follows:

$$S(x) = \frac{S_{\max}}{r} \int_{x}^{\infty} \exp\left[-\pi \frac{x^2}{r^2}\right] dx \qquad 1\text{-}14$$

The horizontal strain, $E(x)$, can be calculated from the expression:

$$E(x) = RK(x) \qquad 1\text{-}15$$

where

R: Strain correlation coefficient, in units of length

K(x): Curvature, i.e. the second derivative of subsidence

Karmis et al (Karmis, Haycocks et al. 1992): "The influence function is a much more versatile and flexible formulation compared to the profile function and can be applied to complex mining conditions…This technique can be applied to irregularly shaped mine sections, areas of different mining height, extraction ratio and seam elevation, multi-seam mining or where prediction of ground deformation is required on individual surface control points."

The integral in equation 1-14 can also be solved in polar coordinates (see Figure 1-30).

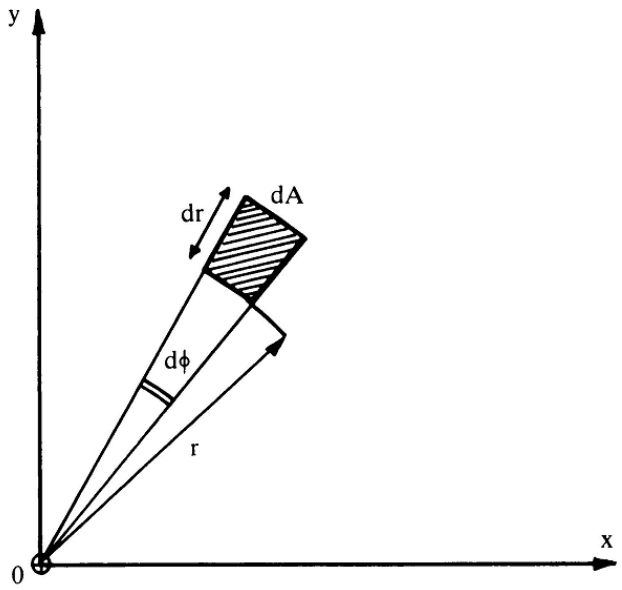

Figure 1-30. Polar coordinates in Knothe's method

(Whittaker and Reddish 1989)

1.3.3.2 Bals' Method

Bals based his theory on the assumption that the influence caused on a point *P* by an infinitesimal extracted particle is inversely proportional to the square of the distance between the extracted particle and *P*. The extent of the complete area of influence is determined by the magnitude of the angle of draw, γ, as seen in Figure 1-31.

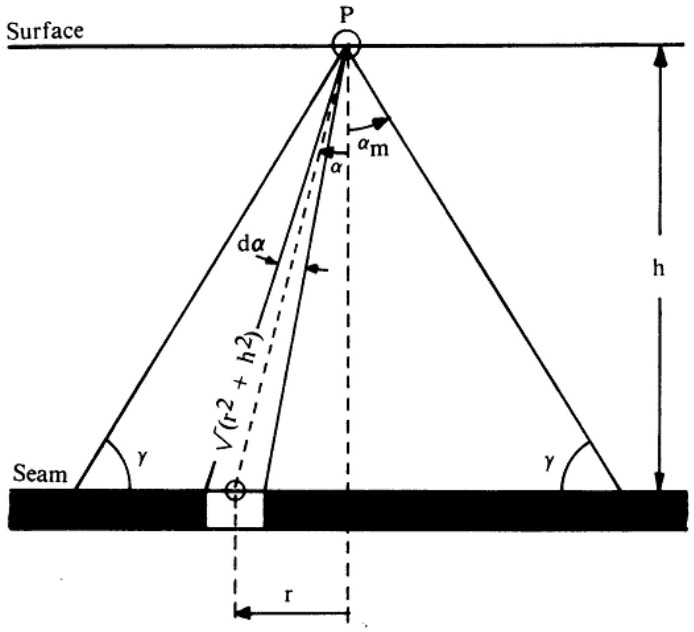

Figure 1-31. Representation of Bals' influence function

(Whittaker and Reddish 1989)

Adamek and Jeran (Adamek and Jeran 1981) express the subsidence of any surface point as:

$$S = m \cdot a \cdot z \cdot e \qquad 1\text{-}16$$

where

S: Subsidence magnitude

m: Coal seam thickness

a: Subsidence factor (determined empirically)

z: Time coefficient (for complete subsidence z = 1)

e: Efficiency coefficient

A function k_Z is defined as (Whittaker and Reddish 1989):

$$k_Z = \frac{const}{h^2}\cos^2\alpha d\alpha \qquad 1\text{-}17$$

where

$\frac{h}{\cos\alpha}$: Distance between extracted particle and point *P*.

const: A constant

α: Angle between the vertical and the line joining point *P* and the extracted particle

Integrating equation 1-17 yields:

$$K_Z = \frac{const}{h^2}\int_0^{\alpha m}\cos^2\alpha d\alpha$$
$$K_Z = \frac{const}{h^2}\frac{1}{4}\left(\sin 2\alpha m + 2\alpha m\right) \qquad 1\text{-}18$$

The angle α_m must be expressed in radians. The term $const/(4h^2)$ is a constant in the case of flat seams, therefore it can be neglected. Adamek and Jeran (Adamek and Jeran 1981) redefine a function k as:

$$k = \sin 2\alpha m + 2\alpha m \qquad 1\text{-}19$$

The function expressed in equation 1-19 is illustrated in Figure 1-32.

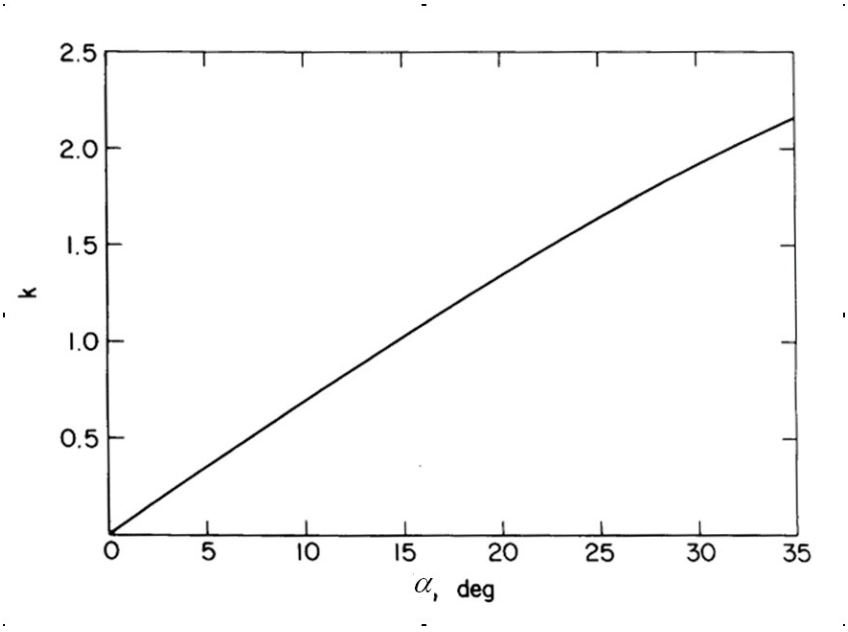

Figure 1-32. The k function in Bals' method

(Adamek and Jeran 1981)

The next step in Bals' method was to produce a chart that consists of annular areas of equal influence. The possible number of zones is unrestricted. However, the most common configuration has five annular zones and it can be further divided by any number of diameters, producing several concentric areas whose influence is exactly the same, making it a straightforward graphical method. Whittaker and Reddish (Whittaker and Reddish 1989) show the five zones of Bals' method with 8 diameters for a total weight of 1/80 for each area element (Figure 1-33). Adamek and Jeran (Adamek and Jeran 1981) use 4 diameters for a total weight of 1/40 per area element (Figure 1-34). The coefficient of efficiency '*e*' for point P in the example of Figure 1-34 is the product of all area units or partial area units and the weight of each, i.e. 1/40 or 2.5% in this case.

Irregular shapes can be analyzed with this method as illustrated in Figure 1-35 (Whittaker and Reddish 1989). Figure 1-36 shows some other charts from different influence function methods.

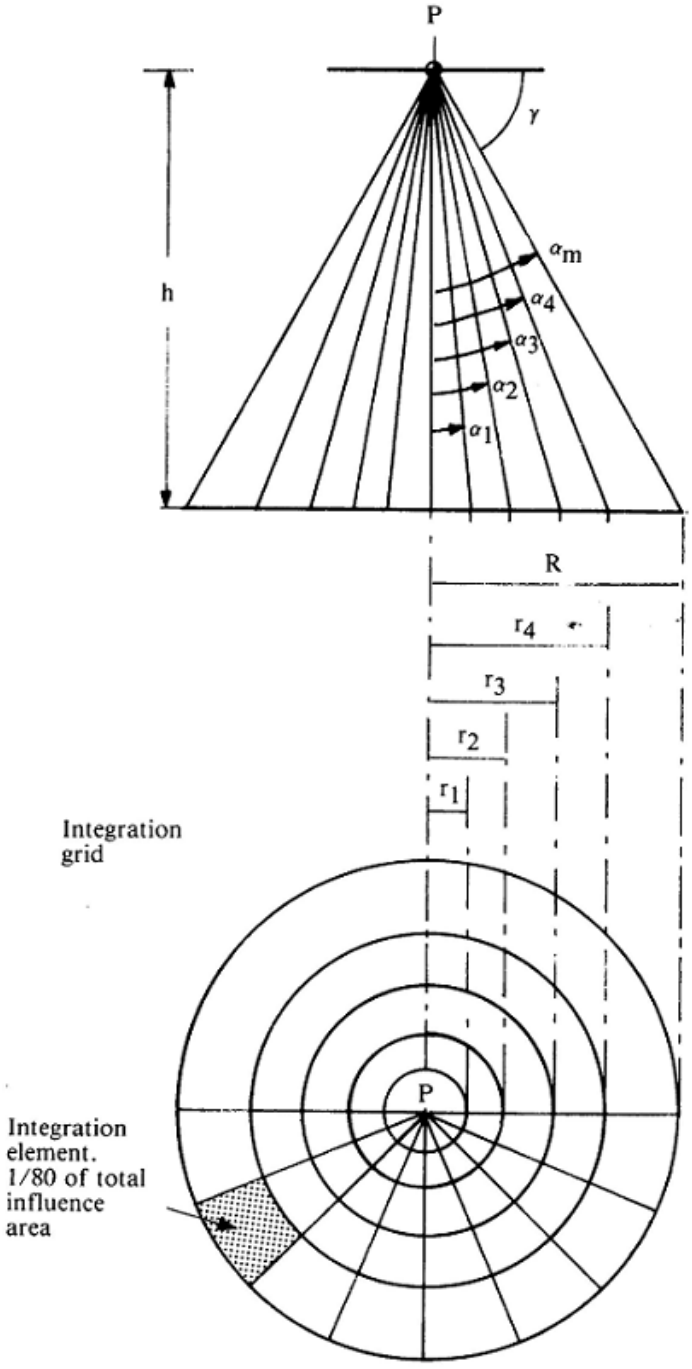

Figure 1-33. Illustration of the Bals' graphical method for the estimation of subsidence (Whittaker and Reddish 1989)

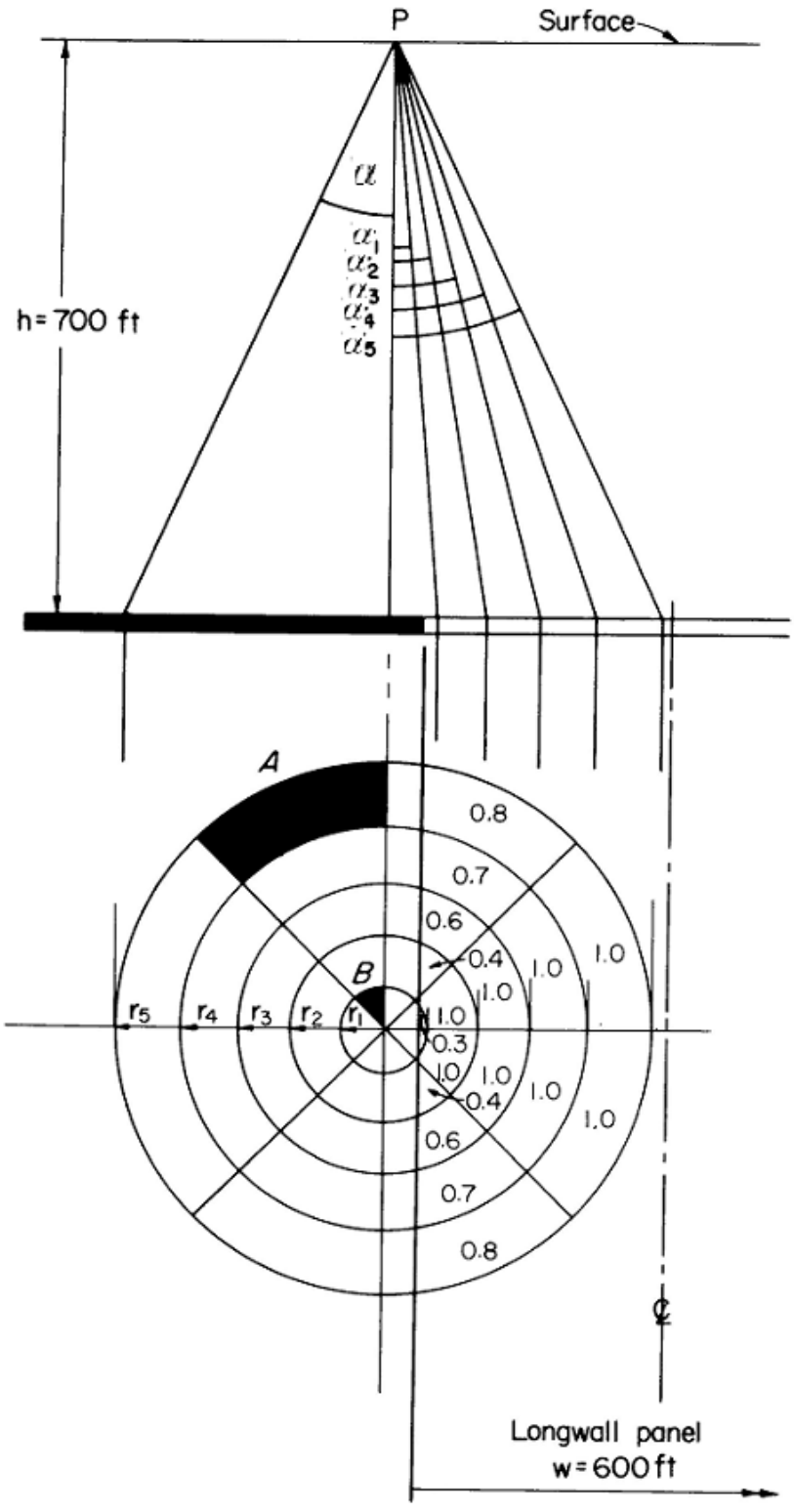

Figure 1-34. An example of the estimation of subsidence at point P

(Adamek and Jeran 1981)

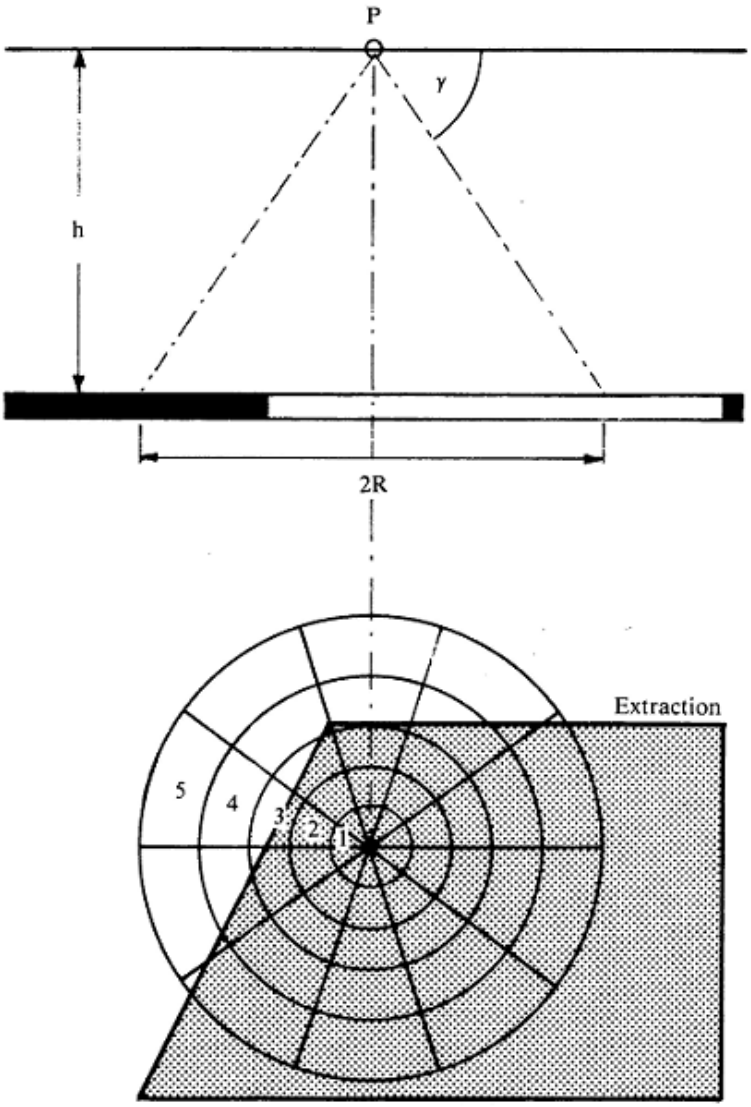

Example:

Annular zone	Number of influence elements	Influence (%)
1	10	20
2	10	20
3	9	18
4	6	12
5	5	10
	Total	80%

Subsidence at point P = 0·8 S

Figure 1-35. Another example of the estimation of subsidence at point P

(Whittaker and Reddish 1989)

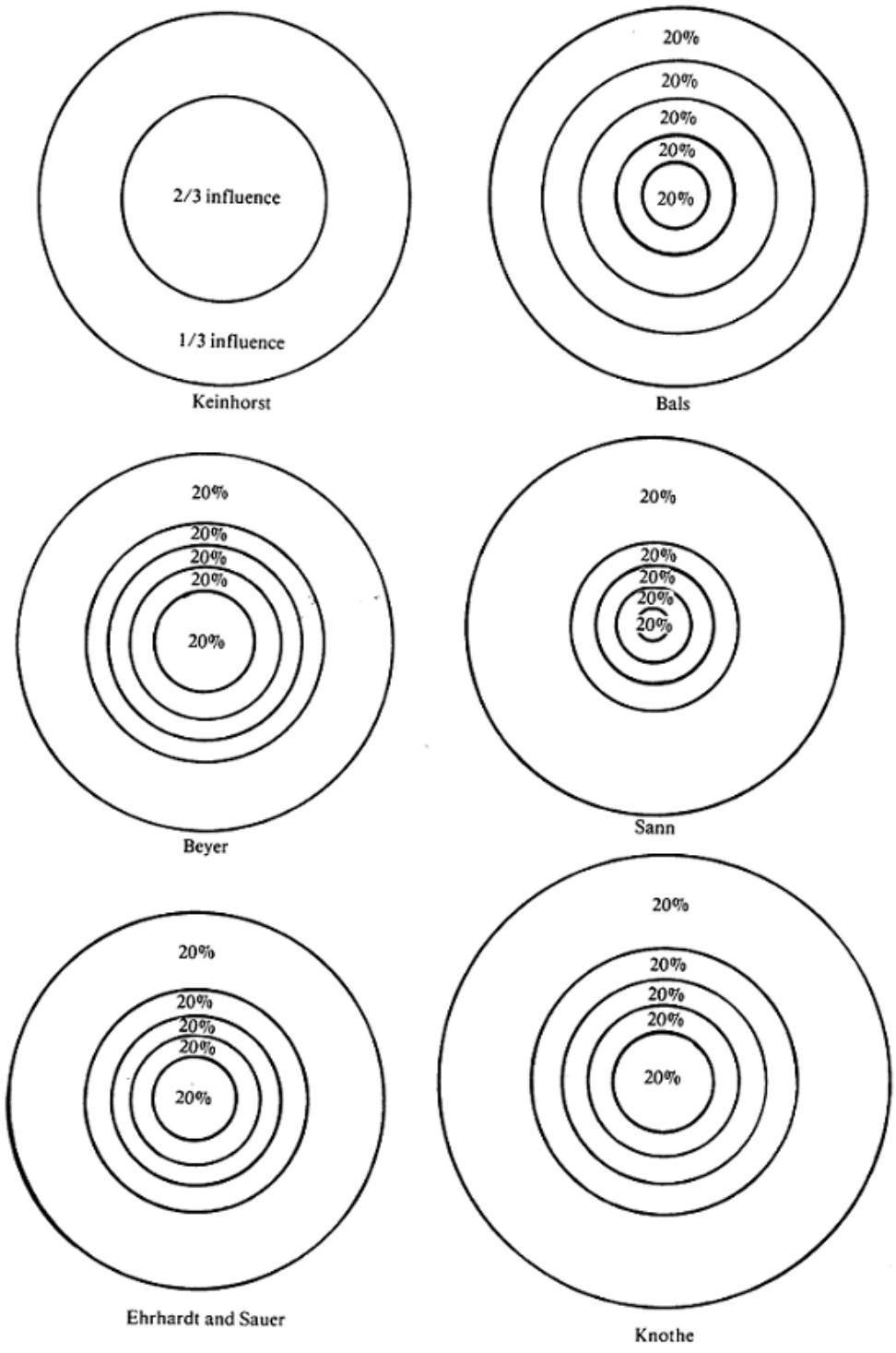

Figure 1-36. Illustration of different charts from various influence function methods

(Whittaker and Reddish 1989)

In the configuration of five annular zones, Adamek and Jeran (Adamek and Jeran 1981) report the following values of k and α_m for an angle of draw $\gamma = 25°$:

Table 1-4. Zone area parameters

(Adamek and Jeran, 1981)

Zone No.	k	αm
1	0.3276	4.6°
2	0.6552	9.5°
3	0.9828	14.4°
4	1.3104	19.5°
5	1.6380	25°

1.3.4 A methodology incorporating both profile and influence functions

Adamek et al (Adamek, Jeran et al. 1987) proposed a novel methodology for prediction of subsidence in the Northern Appalachian Coalfield by incorporating elements of profile and influence function methods. Field data used in their study were collected by the Bureau of Mines in 11 longwall panel studies (Adamek, Jeran et al. 1987). The conditions at each study site were different with respect to underground geometry, overburden thickness, and geology. Figure 1-37 shows parameters at the various test sites of the panel studies.

Test site	H, ft		m, ft	w, ft	sF at centerline, ft	a at centerline for $\gamma = 25^{\circ}$	$\bar{a}$ (VS/VE)	w/H
	Range	At centerline						
1.....	520-706	650	5.5	460	-2.62	0.513	0.30	0.71
2.....	677-700	700	5.5	600	-3.25	.597	.35	.86
3.....	645-700	700	5.5	600	-3.25	.597	.32	.86
4.....	509-624	615	5.5	605	-3.65	.604	.44	.98
5.....	652-781	652	5.5	605	-3.55	.645	.39	.93
6.....	740-795	795	5.5	600	-3.09	.587	.32	.75
7.....	732-795	795	5.5	600	-3.09	.587	.32	.75
8.....	913-995	913	6.0	630	-3.42	.614	.40	.69
9.....	803-913	913	6.0	630	-3.42	.614	.38	.69
10.....	802-855	855	6.0	630	-3.12	.547	.34	.74
11.....	717-780	717	6.0	630	-3.72	.623	.34	.88
12.....	702-719	717	6.0	630	-3.72	.623	.34	.88
13.....	368-402	402	6.0	940	-4.04	.673	.37	2.34
14.....	345-402	402	6.0	940	-4.04	.673	.39	2.34
15.....	700-845	845	5.5	600	-2.95	.571	.31	.71
16.....	747-866	747	5.5	510	-2.79	.547	.34	.68

a Subsidence coefficient.
$\bar{a}$ Average subsidence coefficient.
H Specific overburden thickness.
m Extracted thickness.
sF Measured subsidence.
VE Volume of coal extracted.
VS Volume of subsidence trough.
w Width of panel.
w/H Ratio of panel width to overburden thickness.
γ Angle of draw.

Figure 1-37. Overview of basic site parameters for the development of the Bureau of Mines prediction methodology

(Adamek, Jeran et al. 1987)

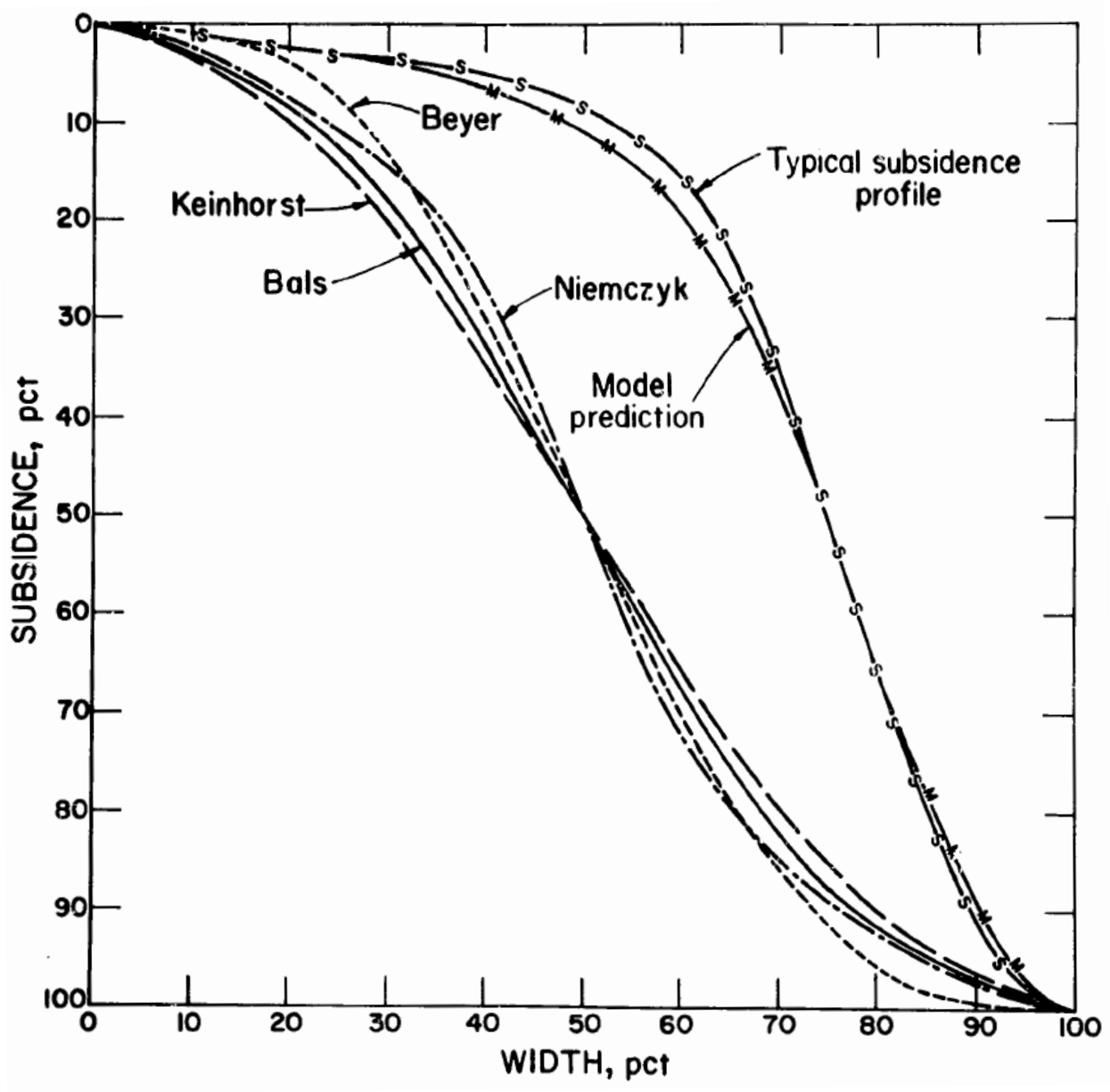

Figure 1-38. Comparison of measured and calculated subsidence profiles

(Adamek, Jeran et al. 1987)

Figure 1-38 shows that the typical subsidence profile in the Northern Appalachian Coalfield differs dramatically from profiles calculated through some European influence function methods. Adamek et al (Adamek, Jeran et al. 1987) incorporate the angle of draw as a functional parameter by considering a hypothetical homogeneous overburden and introduce a novel

procedure to account for different lithologic conditions. Adamek et al (Adamek, Jeran et al. 1987): "For homogeneous overburden (overburden without resistant rock units) or overburden behaving homogeneously, from the point of view of subsidence, the concept of the angle of draw as a functional parameter for predictive methodologies based on the principle of the area of influence has been proven valid". These authors found that the most appropriate angle of draw value for the Northern Appalachian Coalfield is 25°. The influence function component of the methodology is based on Bals' theory, which assumes that displacement of any surface point is determined by the cumulative effects of the individual elementary parts of the extracted areas (Adamek, Jeran et al. 1987): "Based on Newton's law governing the attraction of masses, Bals assumes that each differential part of the mined-out area exerts an influence on the surface point inversely proportional to the square of its distance from it. The influence is quantified by the efficiency coefficient *e*". The Bureau developed a computer algorithm to compute and tabulate the values of *e* for different mining conditions.

The next step in the methodology was to account for lithologic conditions. For this purpose the researchers defined the subsidence coefficient a_v as:

$$a_{vi} = \frac{sF_i}{m \cdot e_i} \qquad 1\text{-}20$$

where

sF_i: Measured subsidence

m: Extracted coal seam thickness

e_i: Efficiency coefficient for each point

For each surface point at all 11 study sites (16 half profiles or test sites) the value of the variable subsidence coefficient was defined. Figure 1-41 and Figure 1-42 show the variation of

subsidence coefficient for each of the 16 half profiles. Regression analyses of the subsidence coefficients from all test sites on the location relative to the edge of the panel have yielded a third-degree polynomial equation for a 25° angle of draw:

$$a_v = AX^3 + BX^2 + CX + D \qquad 1\text{-}21$$

$$A = -3.587x10^{-8}$$
$$B = 1.628x10^{-5}$$
$$C = -9.105x10^{-5}$$
$$D = 1.359x10^{-1}$$

where

a_v: Variable subsidence coefficient

X: Distance from the edge of the panel toward the centerline, ft

For points located outwards from the edge of the panel, X = 0. Then, the subsidence of any point toward the centerline will be (Adamek, Jeran et al. 1987):

$$s_i = m \cdot e_i \cdot a_{vi} \qquad 1\text{-}22$$

and outwards from panel edge

$$s_i = m \cdot e_i \cdot 0.1359 \qquad 1\text{-}23$$

Figure 1-43 shows variable subsidence coefficients along individual profiles for 25° draw angle, with average values and standard deviations. The standard deviation of predicted subsidence can be found using the following:

$$\pm \sigma_i [ft] = \pm \sigma_i \cdot m \cdot e_i \qquad 1\text{-}24$$

Figure 1-44 shows the differences between measured and computed subsidence (Δ_i) in comparison with standard deviations (Adamek, Jeran et al. 1987). The differences are far below standard deviations within the area of the panel and are about the same outside the panel.

w/H	Distance inward from edge of panel as fraction of panel width										
	0.50	0.45	0.40	0.35	0.30	0.25	0.20	0.15	0.10	0.05	0.00
0.1.....	0.289	0.289	0.289	0.286	0.286	0.280	0.277	0.268	0.258	0.250	0.237
0.2.....	.473	.471	.468	.466	.460	.449	.440	.428	.415	.389	.361
0.3.....	.609	.609	.606	.599	.590	.577	.563	.542	.520	.487	.439
0.4.....	.722	.719	.714	.706	.692	.676	.654	.629	.594	.554	.487
0.5.....	.811	.808	.801	.788	.772	.749	.723	.686	.643	.588	.500
0.6.....	.879	.877	.868	.853	.833	.803	.765	.720	.667	.600	.500
0.7.....	.934	.931	.919	.899	.870	.833	.793	.744	.686	.609	.500
0.8.....	.973	.969	.952	.927	.896	.858	.818	.765	.703	.622	.500
0.9.....	.998	.988	.972	.949	.920	.882	.841	.786	.720	.633	.500
1.0.....	1.000	.999	.987	.967	.939	.903	.861	.804	.737	.644	.500
1.1.....	1.000	1.000	.997	.982	.957	.921	.879	.823	.751	.656	.500
1.2.....	1.000	1.000	1.000	.992	.972	.939	.896	.841	.765	.667	.500
1.3.....	1.000	1.000	1.000	.999	.983	.953	.913	.855	.780	.677	.500
1.4.....	1.000	1.000	1.000	1.000	.992	.966	.927	.870	.793	.686	.500
1.5.....	1.000	1.000	1.000	1.000	.999	.977	.939	.884	.804	.692	.500
1.6.....	1.000	1.000	1.000	1.000	1.000	.986	.952	.896	.818	.703	.500
1.7.....	1.000	1.000	1.000	1.000	1.000	.987	.963	.909	.828	.711	.500
1.8.....	1.000	1.000	1.000	1.000	1.000	.993	.972	.920	.841	.720	.500
1.9.....	1.000	1.000	1.000	1.000	1.000	.999	.979	.929	.851	.728	.500
2.0.....	1.000	1.000	1.000	1.000	1.000	1.000	.987	.939	.861	.737	.500
2.1.....	1.000	1.000	1.000	1.000	1.000	1.000	.992	.949	.870	.744	.500
2.2.....	1.000	1.000	1.000	1.000	1.000	1.000	.997	.957	.879	.751	.500
2.3.....	1.000	1.000	1.000	1.000	1.000	1.000	1.000	.964	.888	.758	.500
2.4.....	1.000	1.000	1.000	1.000	1.000	1.000	1.000	.972	.896	.765	.500
2.5.....	1.000	1.000	1.000	1.000	1.000	1.000	1.000	.978	.906	.772	.500
2.6.....	1.000	1.000	1.000	1.000	1.000	1.000	1.000	.983	.913	.780	.500
2.7.....	1.000	1.000	1.000	1.000	1.000	1.000	1.000	.988	.920	.786	.500
2.8.....	1.000	1.000	1.000	1.000	1.000	1.000	1.000	.992	.927	.793	.500
2.9.....	1.000	1.000	1.000	1.000	1.000	1.000	1.000	.996	.934	.799	.500
3.0.....	1.000	1.000	1.000	1.000	1.000	1.000	1.000	.999	.939	.804	.500

Figure 1-39. Table of efficiency coefficients e for 25° angle of draw (1)

(Adamek, Jeran et al. 1987)

w/H	Distance outward from edge of panel as fraction of panel width										
	0.00	-0.05	-0.10	-0.15	-0.20	-0.25	-0.30	-0.35	-0.40	-0.45	-0.50
0.1.....	0.237	0.222	0.213	0.201	0.191	0.184	0.180	0.177	0.171	0.166	0.160
0.2.....	.361	.332	.304	.288	.274	.261	.246	.234	.224	.214	.203
0.3.....	.439	.392	.357	.331	.305	.286	.263	.244	.227	.209	.194
0.4.....	.487	.418	.375	.333	.297	.263	.235	.207	.182	.159	.139
0.5.....	.500	.412	.356	.308	.263	.228	.196	.166	.139	.116	.094
0.6.....	.500	.400	.333	.280	.235	.196	.159	.130	.104	.080	.061
0.7.....	.500	.391	.314	.256	.207	.166	.130	.099	.073	.051	.033
0.8.....	.500	.378	.297	.235	.182	.139	.104	.073	.048	.028	.013
0.9.....	.500	.367	.280	.214	.159	.116	.080	.051	.028	.012	.001
1.0.....	.500	.356	.263	.196	.139	.094	.061	.033	.013	.001	.000
1.1.....	.500	.344	.249	.177	.121	.077	.043	.018	.003	.000	.000
1.2.....	.500	.333	.235	.159	.104	.061	.028	.008	.000	.000	.000
1.3.....	.500	.323	.220	.145	.087	.046	.017	.001	.000	.000	.000
1.4.....	.500	.314	.207	.130	.073	.033	.008	.000	.000	.000	.000
1.5.....	.500	.308	.196	.116	.061	.022	.001	.000	.000	.000	.000
1.6.....	.500	.297	.182	.104	.048	.013	.000	.000	.000	.000	.000
1.7.....	.500	.289	.172	.091	.037	.007	.000	.000	.000	.000	.000
1.8.....	.500	.280	.159	.080	.028	.001	.000	.000	.000	.000	.000
1.9.....	.500	.272	.149	.071	.021	.000	.000	.000	.000	.000	.000
2.0.....	.500	.263	.139	.061	.013	.000	.000	.000	.000	.000	.000
2.1.....	.500	.256	.130	.051	.008	.000	.000	.000	.000	.000	.000
2.2.....	.500	.249	.121	.043	.003	.000	.000	.000	.000	.000	.000
2.3.....	.500	.242	.112	.036	.000	.000	.000	.000	.000	.000	.000
2.4.....	.500	.235	.104	.028	.000	.000	.000	.000	.000	.000	.000
2.5.....	.500	.228	.094	.022	.000	.000	.000	.000	.000	.000	.000
2.6.....	.500	.220	.087	.017	.000	.000	.000	.000	.000	.000	.000
2.7.....	.500	.214	.080	.012	.000	.000	.000	.000	.000	.000	.000
2.8.....	.500	.207	.073	.008	.000	.000	.000	.000	.000	.000	.000
2.9.....	.500	.201	.066	.004	.000	.000	.000	.000	.000	.000	.000
3.0.....	.500	.196	.061	.001	.000	.000	.000	.000	.000	.000	.000

w/H Ratio of panel width to overburden thickness.

Figure 1-40. Table of efficiency coefficients e for 25° angle of draw (2)

(Adamek, Jeran et al. 1987)

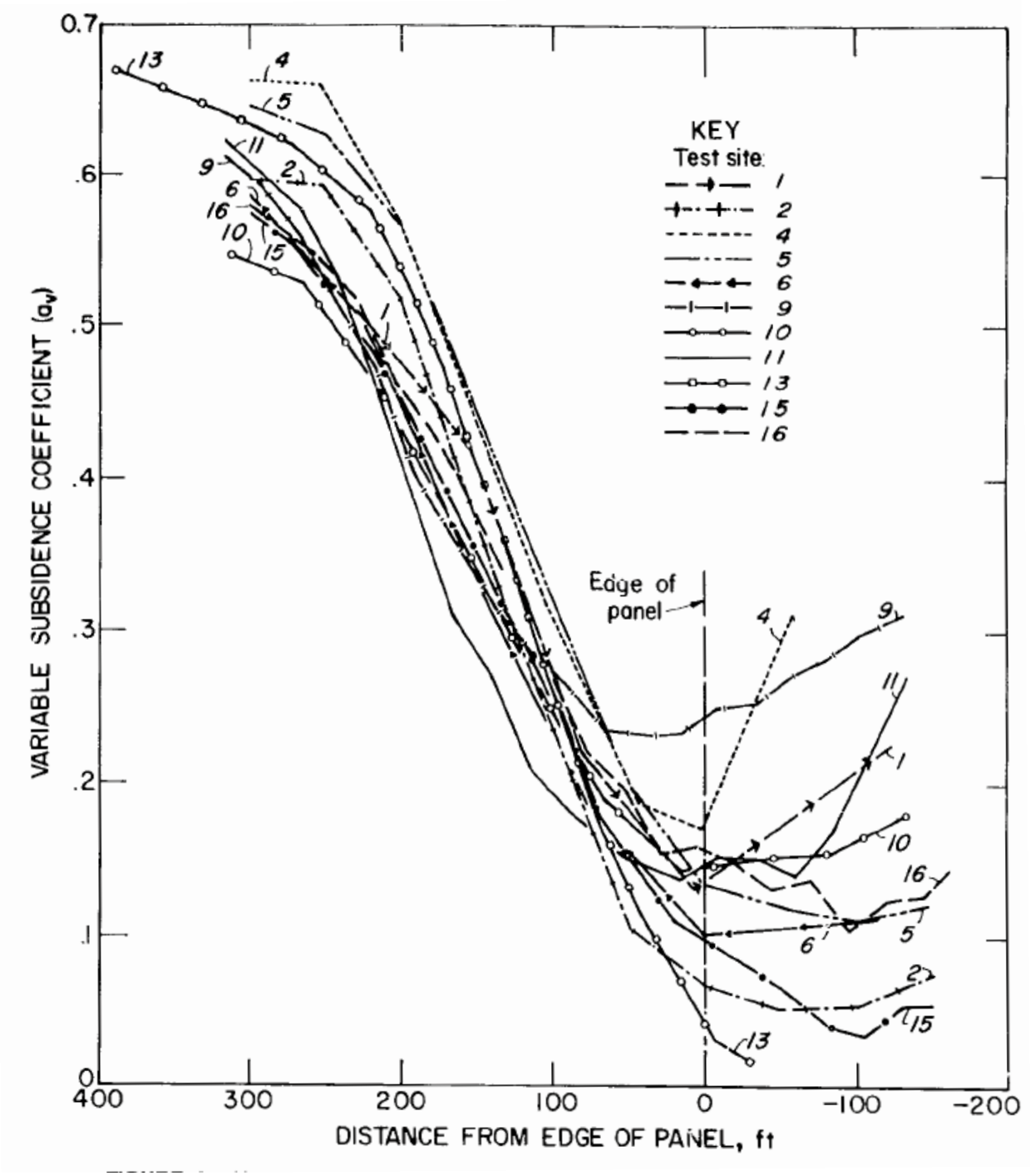

Figure 1-41. Variable subsidence coefficient for 25° draw angle, left half profiles

(Adamek, Jeran et al. 1987)

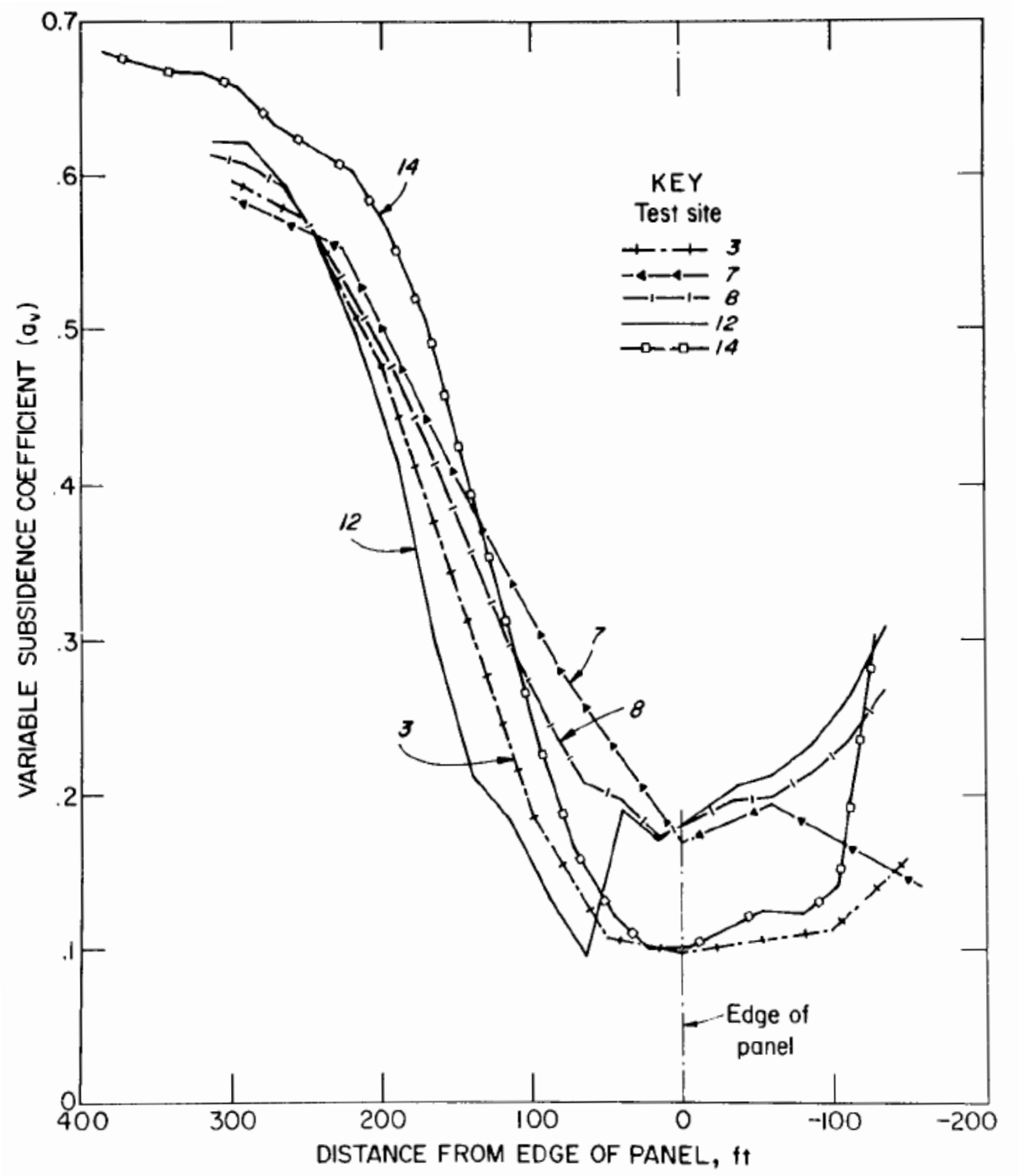

Figure 1-42. Variable subsidence coefficient for 25° draw angle, right half profiles

(Adamek, Jeran et al. 1987)

Test site	Distance inward,[1] ft--						Edge of panel (0 ft)	Distance outward,[1] ft--		
	300	250	200	150	100	50		-50	-100	-150
1.....	NAp	NAp	0.480	0.410	0.275	0.182	0.135	0.170	0.210	0.240
2.....	0.597	0.590	.515	.370	.235	.207	.068	.053	.055	.075
3.....	.597	.571	.475	.335	.186	.106	.098	.105	.110	.150
4.....	.662	.655	.565	.435	.308	.205	.175	.295	.230	.230
5.....	.645	.627	.565	.440	.318	.200	.135	.120	.112	.124
6.....	.587	.530	.445	.335	.230	.155	.100	.105	.112	.115
7.....	.586	.564	.502	.405	.315	.235	.167	.190	.170	.150
8.....	.600	.530	.425	.335	.270	.234	.245	.265	.295	.320
9.....	.610	.571	.487	.380	.267	.200	.180	.196	.225	.225
10.....	.542	.505	.430	.340	.245	.175	.145	.153	.165	.190
11.....	.610	.545	.410	.285	.193	.152	.145	.145	.200	.300
12.....	.622	.571	.445	.250	.154	.150	.180	.210	.248	.248
13.....	.635	.600	.535	.405	.255	.130	.042	.015	NAp	NAp
14.....	.660	.621	.572	.432	.250	.128	.100	.122	.137	.300
15.....	.575	.525	.450	.350	.255	.152	.098	.065	.065	.055
16.....	NAp	.540	.460	.375	.265	.192	.157	.135	.110	.135
$\bar{a}_v$.....	.609	.570	.485	.368	.251	.169	.136	.147	.163	.191
$\pm\sigma_1$.....	.033	.043	.053	.054	.045	.041	.050	.074	.070	.083

NAp Not applicable. [1]From edge of panel.

Figure 1-43. Variable subsidence coefficients along individual profiles for 25° draw angle, with average values and standard deviations

(Adamek, Jeran et al. 1987)

	Distance inward,[1] ft--						Edge of panel (0 ft)	Distance outward,[1] ft--		
	300	250	200	150	100	50		-50	-100	-150
$\bar{a}_v$.....	0.606	0.567	0.485	0.368	0.251	0.169	0.136	0.146	0.163	0.190
$\pm\sigma_{\|}$.....	0.032	0.042	0.053	0.054	0.045	0.041	0.055	0.074	0.070	0.083
$e_{\|}$.....	0.990	0.971	0.933	0.878	0.802	0.692	0.500	0.309	0.198	0.121
$\sigma_{\|}e_{\|}$.....	0.032	0.041	0.049	0.047	0.036	0.028	0.027	0.022	0.014	0.010
$\pm\sigma_{\|}$...ft..	0.180	0.220	0.270	0.260	0.200	0.160	0.150	0.130	0.080	0.060
sF....ft..	3.250	3.170	2.650	1.800	1.040	0.410	0.190	0.090	0.060	0.050
sP....ft..	3.300	3.040	2.470	1.770	1.120	0.640	0.370	0.230	0.150	0.090
$\pm\Delta_{\|}$...ft..	0.050	-0.130	-0.180	-0.030	0.080	0.230	0.180	0.140	0.090	0.040

$\bar{a}_v$ Average variable subsidence coefficient.
$e_{\|}$ Efficiency coefficient.
sF Measured subsidence.
sP Computed subsidence.
$\Delta_{\|}$ Differences between measured and computed subsidences.
$\sigma_{\|}$ Standard deviation of average value of subsidence coefficient for individual conceptions.
$\sigma_{\|}$(ft) $me_{\|}\sigma_{\|}$, where m = extracted thickness.
[1]From edge of panel.

Figure 1-44. Comparison of measured and computed subsidence for 25° draw angle

(Adamek, Jeran et al. 1987)

1.3.5 Comparison of Profile Functions and Influence Functions

Whittaker and Reddish (Whittaker and Reddish 1989) report some remarkable points about profile and influence functions separately. The first list refers specifically to profile functions:

1. "Field observations can be easily employed to derive profile functions.
2. Profile functions can be readily applied to a wide range of subsidence problems, including subcritical situations.
3. Profile functions are easier to calibrate to field data and are generally more accurate in subsidence predictions.
4. The range of subsidence problems to which profile functions can be applied is mainly limited to relatively straightforward two-dimensional mining extraction situations involving essentially rectangular geometrical configurations.

5. Profile functions can be adapted to take into account the effects of small pillars in modifying the surface subsidence profile."

The following comments refer specifically to influence functions:

1. "Shape of extraction is not a limiting factor in respect of influence functions, since they can be applied to any shape of extraction in one or more seams.
2. The method is more mathematically rigorous than that involved with profile functions, and consequently requires more detailed assessment when performing subsidence predictions.
3. Influence functions are based on the principle of superposition and consequently assume complete validity of applying the principle to any mining situation.
4. Since influence functions depend mainly upon the radius of influence (r), they can be readily adapted to take different geological conditions into account.
5. Accuracy in subsidence prediction with influence functions tends to be reduced in preference to increased flexibility of application particularly regarding extensive extractions of irregular configuration.
6. Prediction of displacement with influence functions tends to be more complicated than with profile functions; for increased accuracy of prediction of subsidence and displacements, corrections require to be made to the basic method in the form of edge zones of incomplete closure around extraction areas."

1.3.6 Other models found in the literature

Whittaker and Reddish (Whittaker and Reddish 1989) list some additional profile models, most of which have limited applications since they have been produced out of site-specific data from various countries.

1.3.6.1 Other Profile Function Models

Among other profile function models that have been produced in various countries are the one proposed by Kowalczyk in Poland in 1966, Martos in Hungary in 1958, Niederhofer's model in 1962 which can be applied to inclined seams, and the one proposed by Kumar, Saxena and Singh in India in 1983. Two similar profile function methods to those thoroughly discussed in this report appear below (Whittaker and Reddish 1989).

Donets Trigonometrical Function

Developed in 1958, this model gives similar results to the hyperbolic profile function.

$$S = \left(\frac{S}{2}\right)\left[1 - \frac{x}{R} - \frac{1}{\pi}\sin\left(\frac{\pi x}{R}\right)\right] \qquad 1\text{-}25$$

Trigonometrical Function

Proposed by Hoffman in 1964, this model gives similar results to the hyperbolic profile function.

$$S = S\sin^2\left[\frac{\pi}{4}\left(\frac{x}{R} - 1\right)\right] \qquad 1\text{-}26$$

1.3.6.2 Other Influence Function Models

Keinhorst's method

Another influence function method is Keinhorst's method proposed in 1928 and 1934 which uses a different influence function:

$$k_Z = \frac{2}{3\pi}\frac{\tan^2\beta}{\tan^2\gamma}\frac{S}{R^2} \qquad \text{1-27}$$

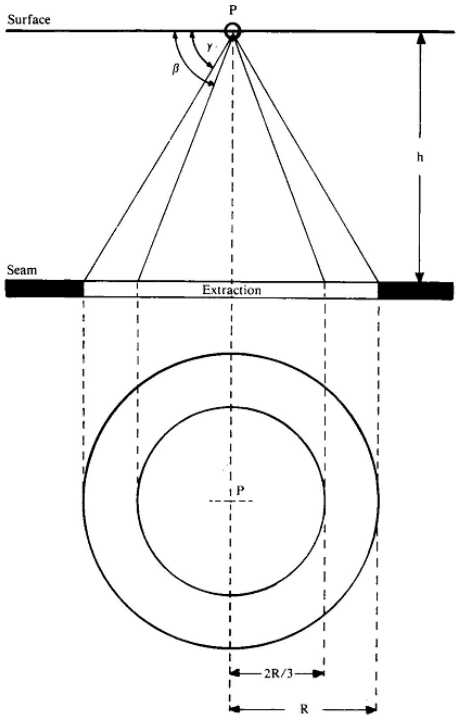

Figure 1-45. Keinhorst's influence function

(Whittaker and Reddish 1989)

Beyer's method

$$k_Z = \frac{3S}{\pi R^2}\left[1-\left(\frac{r}{R}\right)^2\right]^2 \qquad \text{1-28,}$$

after Beyer in 1945 (Whittaker and Reddish 1989).

Sann's method

$$k_Z = \frac{2S}{\pi\sqrt{\pi}R}\frac{1}{r}\exp\left[-4\left(\frac{r}{R}\right)^2\right] \quad \text{1-29,}$$

after Sann in 1949 (Whittaker and Reddish 1989).

Litwiniszyn's method

$$k_Z = \frac{nS}{R^2}\exp\left[-n\pi\left(\frac{r}{R}\right)^2\right] \quad \text{1-30,}$$

after Litwiniszyn in 1957 (Whittaker and Reddish 1989), where n is an independent parameter which is usually equal to 1.

Table 1-5 contains a chronological summary of the various prediction methods.

Table 1-5. Chronological summary of subsidence prediction methods

Subsidence Prediction Method	First proposed by	General Type	Specific type	Author who implemented method in Appalachia	Year of implementation in Appalachia
Keinhorst's method	Keinhorst (1928, 1934)	Influence function method	N/A	N/A	N/A
Bals' method	Bals (1931/1932), Zenc (1969)	Influence function method	N/A	N/A	N/A
Beyer's method	Beyer (1945) and Niemczyk (1949)	Influence function method	N/A	N/A	N/A
Sann's method	Sann (1949), Bräuner (1973)	Influence function method	N/A	N/A	N/A
Knothe's method (also called Budryk-Knothe)	Knothe (1953, 1957), Zenc (1969)	Influence function method	Bell-shaped Gaussian function	Karmis et al*	1980-1992
Hyperbolic function	King and Whetton (1957)	Profile function method	Hyperbolic function	Karmis et al*	1983
Litwiniszyn's method	Litwiniszyn (1957)	Influence function method	N/A	N/A	N/A
Exponential function	Martos (1958)	Profile function method	Exponential function	Cheng and Peng	1981
Donets trigonometrical function	GIMS (1958)	Profile function method	Trigonometrical function	N/A	N/A
Trigonometrical function	Hoffman (1964)	Profile function method	Trigonometrical function	N/A	N/A
Subsidence Engineer's Handbook (SHE)	National Coal Board (NCB), UK 1975	Empirical /Graphical	Graphical	N/A	N/A
Bureau of mines method	Adamek et al (1987)	Empirical	Combines elements of both profile and influence function methods	Adamek et al	1987

*SDPS is based on these techniques.

2.0 TASK 2: EVALUATION OF SUBSIDENCE PROFILES

This chapter is mainly concerned with the transformation of subsidence data supplied by PennDOT, which will be useful to construct a predictive model for the area of interest. A detailed explanation of the transformation process is described, and detailed information on each panel is given.

2.1 OVERVIEW OF PANELS

Figure 2-1 and Figure 2-2 show the Emerald and Cumberland mine panels that are part of this study. Some of the panels shown are documented with subsidence data; a few of them are useful as far as the development of subsidence prediction tools is concerned. Some of the panels are partially documented, still providing very useful information. Table 2-1 contains basic information from the project panels.

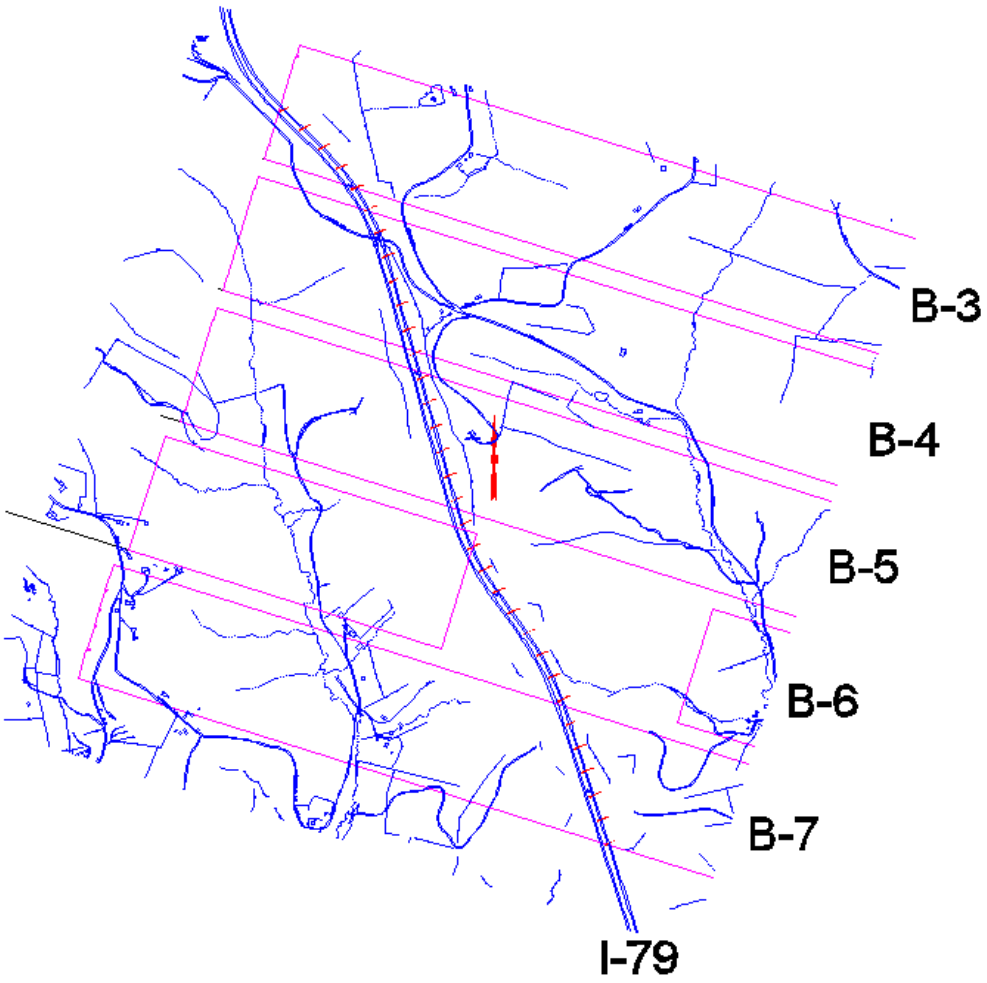

Figure 2-1 Overview of the Emerald mine panels under study

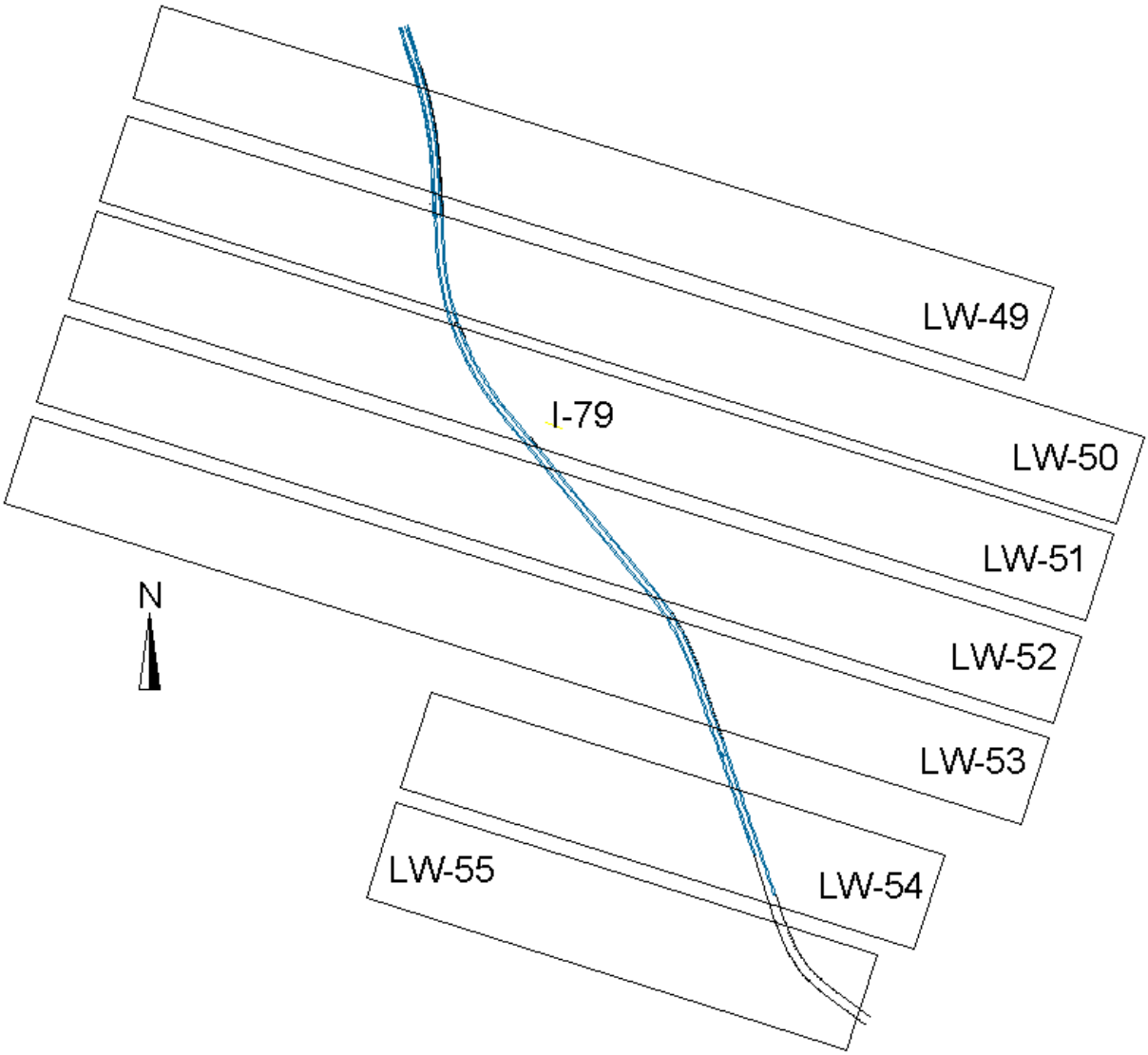

Figure 2-2 Overview of the Cumberland mine panels under study

Table 2-1 Panel basic geometric parameters and maximum measured subsidence

Panel	*S** [ft] ([m])	*m*[ft] ([m])	*S*/m*	*H* [ft] ([m])	1000x*H* [ft] ([m])	Width, *W* [ft] ([m])	*W/H*
B-4	3.949 (1.204)	6.33 (1.93)	0.624	768 (234)	0.768 (0.234)	1455 (443)	1.9
LW-49	4.589 (1.399)	7.40 (2.26)	0.620	786 (240)	0.786 (0.240)	1239 (378)	1.6
LW-50	4.546 (1.386)	7.40 (2.26)	0.614	800 (244)	0.800 (0.244)	1231 (375)	1.5
B-3	4.692 (1.430)	6.56 (2.00)	0.715	723 (220)	0.723 (0.220)	1431 (436)	2
LW-52	4.929 (1.502)	7.40 (2.26)	0.666	763 (233)	0.763 (0.233)	1239 (378)	1.6
LW-53	5.311 (1.619)	7.70 (2.35)	0.690	736 (224)	0.736 (0.224)	1234 (376)	1.7
LW-51	4.676 (1.425)	7.40 (2.26)	0.632	766 (233)	0.766 (0.233)	1239 (378)	1.6
LW-55	5.438 (1.658)	7.70 (2.35)	0.706	640 (195)	0.640 (0.195)	1350 (411)	2.1

2.2 NATURE AND USES OF THE DATA

The process of subsidence prediction, whether it is based on profile function type models or influence function type models, can be viewed as being carried out in two main steps:

1. Estimation of maximum subsidence, often represented by *S**.
2. Construction of a subsidence profile (or trough) based on *S** and other parameters.

After we carefully evaluated the electronic files and hard copy information provided by PennDOT, it was determined that the data sets that best serve the purpose of subsidence prediction are the surveying data that were collected during the time when the panel mine face was approaching, passing underneath, and leaving the projected I-79 highway segment for each

of the panels under study. Good quality and a large amount of this type of data are very useful for performing both steps of the subsidence prediction. Most panels in this study contain limited data that contribute to the first step only. Table 2-2 contains an inventory of panels describing the usefulness of each of the panel data sets.

Table 2-2 Inventory of panels and their suitability for model building

Panel	Useful for step 1?	Useful for step 2?	Comments
LW-51	Yes	Yes, to a high degree	Best data
LW-49	Yes	Yes, to a high degree	Best data
LW-52	Yes	Yes	Good data
LW-55	Yes	Yes, limited	Good but limited data
B-4	Yes	Yes, limited	Good but limited data
LW-50	Yes	No	No Easting, Northing provided
LW-53	Yes	No	No surveying data
B-3	Yes	No	Subcritical profiles only
LW-54	No	No	No surveying data
B-5	No	No	No surveying data
B-6	No	No	No surveying data

2.3 DATA FOR SUBSIDENCE PROFILE (TROUGH) EVALUATION

Highways are rarely parallel or perpendicular to the direction of mining, and we have devised a data transformation scheme in order to obtain subsidence profiles as a function of distance from the mine face. This procedure yields spatial subsidence profiles in 2D and troughs in 3D. A step-by-step explanation of the transformation process is detailed in section 2.5 of this report. Figures employed for that explanation were based upon data taken from panel LW-51 of the Cumberland mine, with a total of 9 different dates of surveying data during the process of mining.

Critical information employed in the study includes the following:

- Mine panel geometry (overburden depth, coal seam thickness, panel location with respect to the highway)
- Coordinates of stations along the highway, in form of Easting, Northing, and Elevation
- Dates at which surveying was carried out at predetermined stations
- Mine face rate of advance

2.4 SUPERCRITICAL SUBSIDENCE TROUGHS AND THEIR SIGNIFICANCE

From the geometric conditions of the panels depicted in Figure 2-1 and Figure 2-2 it can be appreciated that the highway I-79 crosses the various panels in regions where the deformation in the longitudinal and transversal directions is expected to be supercritical. Most of the data we have been able to process did exhibit supercritical deformation characteristics in the longitudinal direction. One set of data, from panel LW-55, however, also exhibited subcritical subsidence in the longitudinal profile. The mining of this panel started right underneath I-79, providing us with the only case with edge boundary effect in the longitudinal direction (i.e., a starting edge of a mining operation in this case).

To illustrate the role of the supercritical region in our construction of the longitudinal profile, a conceptual model is presented in Figure 2-3. The drawing is not at scale and the level of subsidence exaggerated.

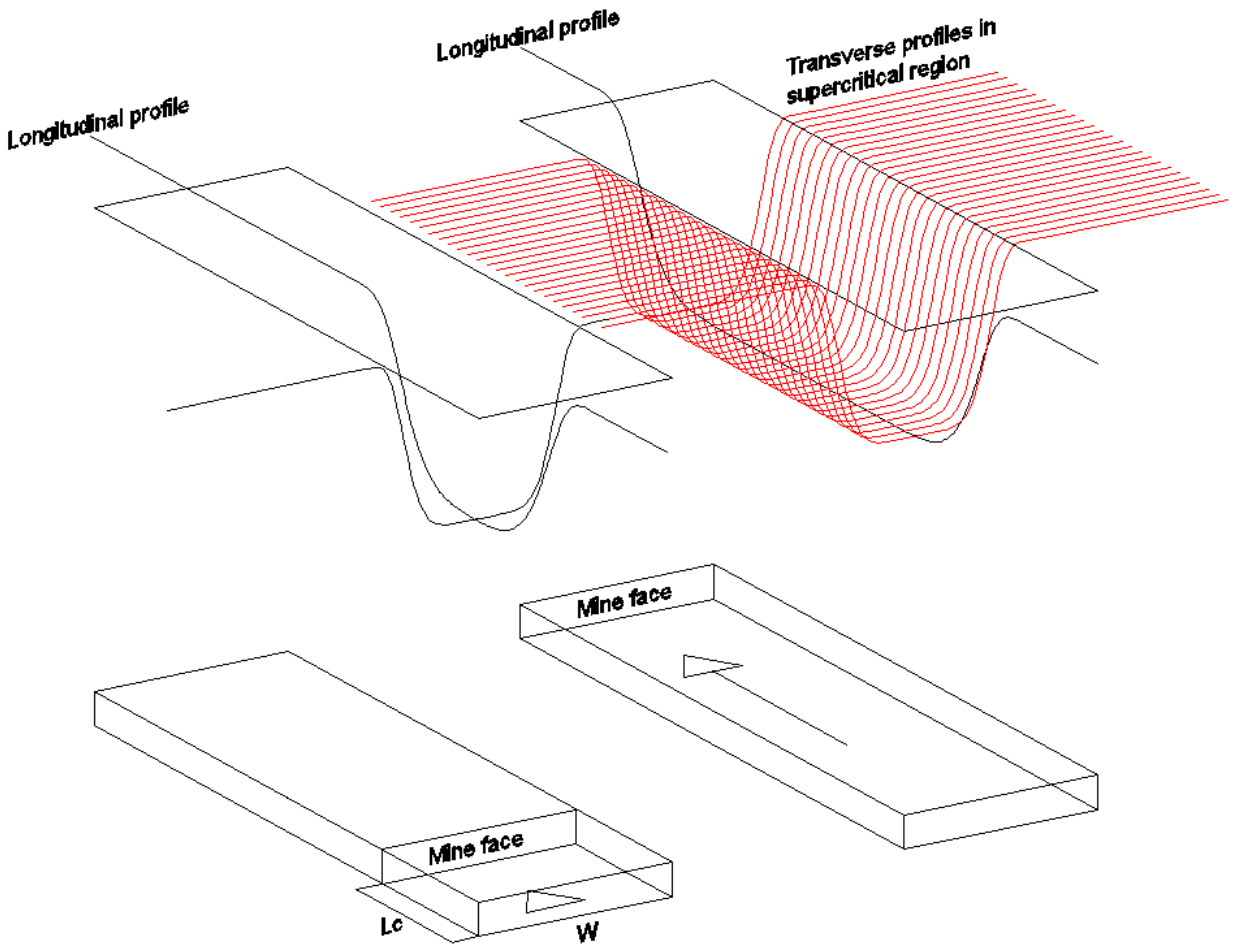

Figure 2-3 Illustration of a supercritical trough above a longwall panel

After a mining operation reaches a critical length *Lc* the subsidence exhibits supercritical characteristics. Once this critical length is surpassed, the trough front that is formed above the mine face will propagate like a wave in the direction of mining preserving its shape and traveling at roughly the same speed at which the mine face advances. This assumes that the ground is homogeneous and the mining operation remains steady. The reasonableness of the assumption is addressed in the data analysis.

Figure 2-4 further illustrates this point. The figure shows two positions 1 and 2, representing, respectively, two mine face positions with Position 2 farther advanced than

Position 1. Both positions were reached after the critical length had been surpassed. The assumption of the unchanged trough front advance is reflected in the shift of the longitudinal profile.

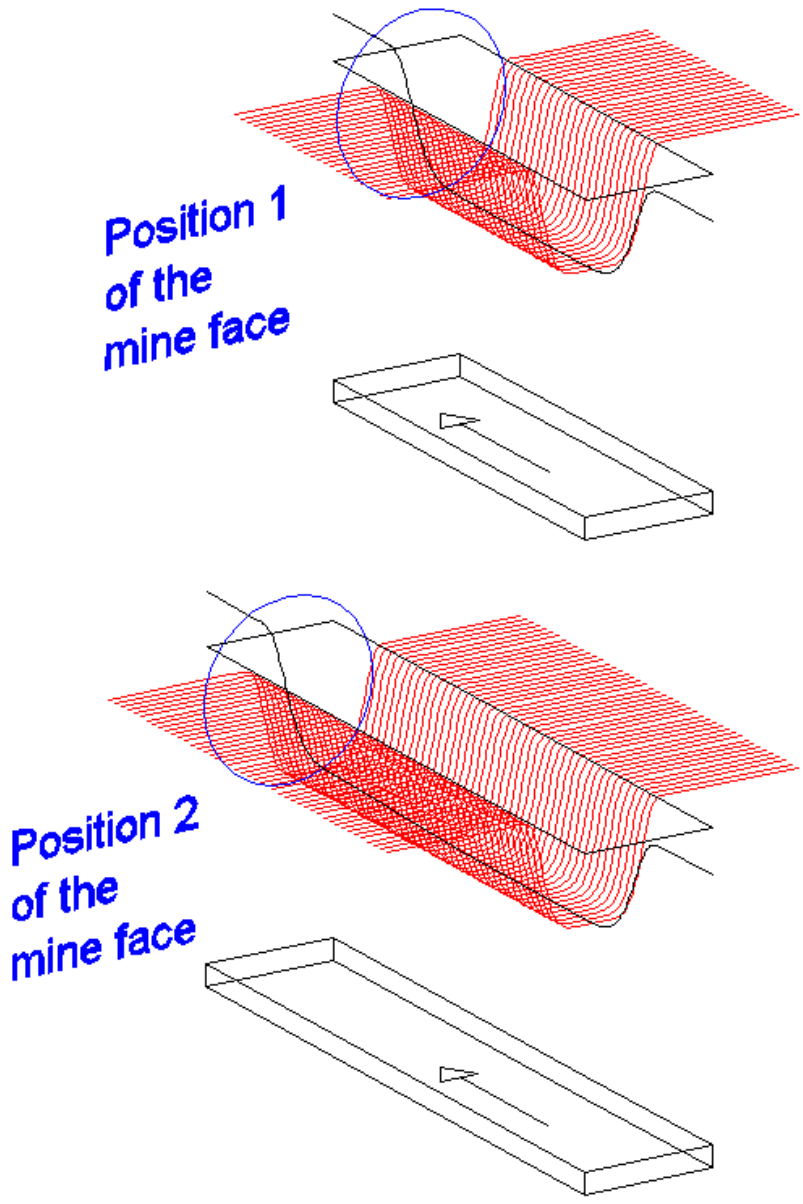

Figure 2-4 The trough front in the supercritical region is always the same for an observer traveling at the same speed

2.5 DATA TRANSFORMATION

Along the highway segment above each panel of interest, a series of stations (points parallel to the highway direction) were surveyed (Easting, Northing, and Elevation) at various dates with respect to a predetermined coordinate system covering the period of time during which the mine face approached, passed underneath, and left the given highway segment. Stations were surveyed along the northbound and southbound highway shoulders and for some panels along the central axis of the highway (central line between northbound and southbound) also. Below is an example of raw data for panel LW-51 for three consecutive stations.

Table 2-3 Surveying raw data sample for three consecutive stations

Station		East	North	Elevation		East	North	Elevation
		Baseline				3/25/2006		
481+0NB		1306604.3	188855.18	1178.6417		1306604.3	188855.18	1178.773
481+50NB		1306572.4	188893.8	1178.3465		1306572.4	188893.8	1178.5433
482+0NB		1306540.6	188932.38	1178.0512		1306540.6	188932.38	1178.2808

Table 2-3 shows the basic surveying raw data for three consecutive stations. The baseline coordinates were obtained from AutoCAD files of the highway at the panel sites obtained long before mining. Figure 2-5 shows an overview of panel LW-51, the position of the mine face at the dates shown, and the surveying stations along I-79. This graph is a zoomed result in the highway portion observable in Figure 2-2 for LW-51. It is clear that this area is well within the supercritical region in the longitudinal direction. Using the raw data that are only partially shown in Table 2-3, the deformation (initially heave) experienced by the three stations with respect to the baseline on March 25 2006 were the differences between the elevation column of the

baseline and the elevation column on 03/25/2006. After all subsidence values were obtained for each and every single station and coupled with the position of the mine face for each surveying date, a transformation of the data was performed. A step-by-step description of the procedure is presented herein:

1. For every single station and every single date of surveying, the vertical subsidence, *S*, was computed by subtracting the elevation from the original (baseline) elevation.
2. For every single date, the position of the mine face was noted.
3. From the East, North, Elevation coordinate system, data was transformed into a rotated coordinate system whose axes are parallel and perpendicular, respectively, to the panel longitudinal direction (see Figure 2-5). The origin of this coordinate system is the same as the East, North, Elevation, since the transformation involves only rotation (clockwise at an angle of 17°32'53"). This coordinate system has axes 1, 2, as shown in Figure 2-5.
4. In order to express point position locally for each panel in a convenient way, a local coordinate system *x*, *z*, *S*, whose origin is located at the left extreme of the mine face projected to the ground surface, was applied to all stations available for each surveying date (see Figure 2-6). The local *x*, *z*, *S* system moves as the mine face advances. For the troughs that were within the supercritical region in the longitudinal direction, with the adoption of homogeneous assumption, all these data were combined in a 3D single *x*, *z*, *S* set.

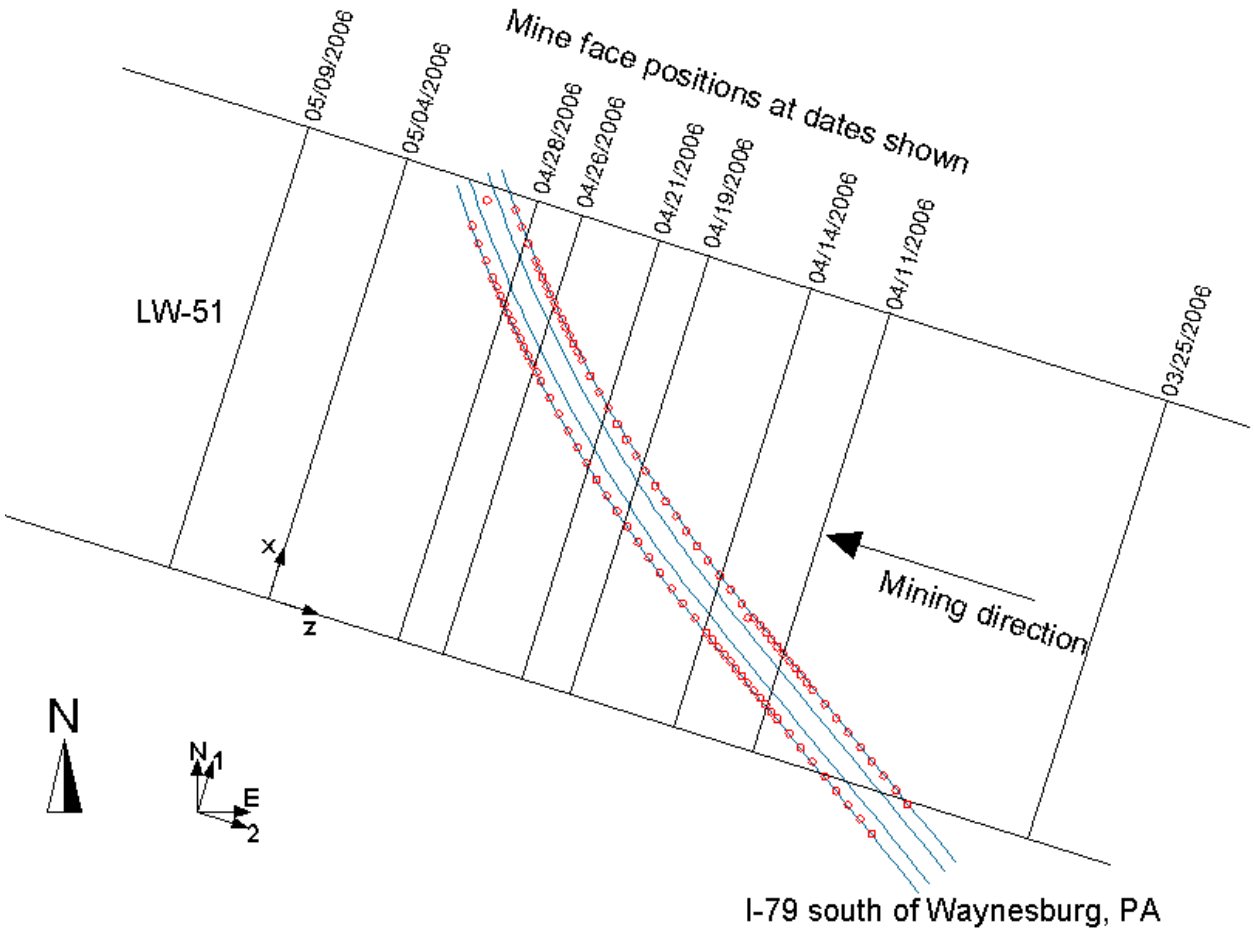

Figure 2-5 Overview of a section of Cumberland mine panel LW-51 intersecting I-79

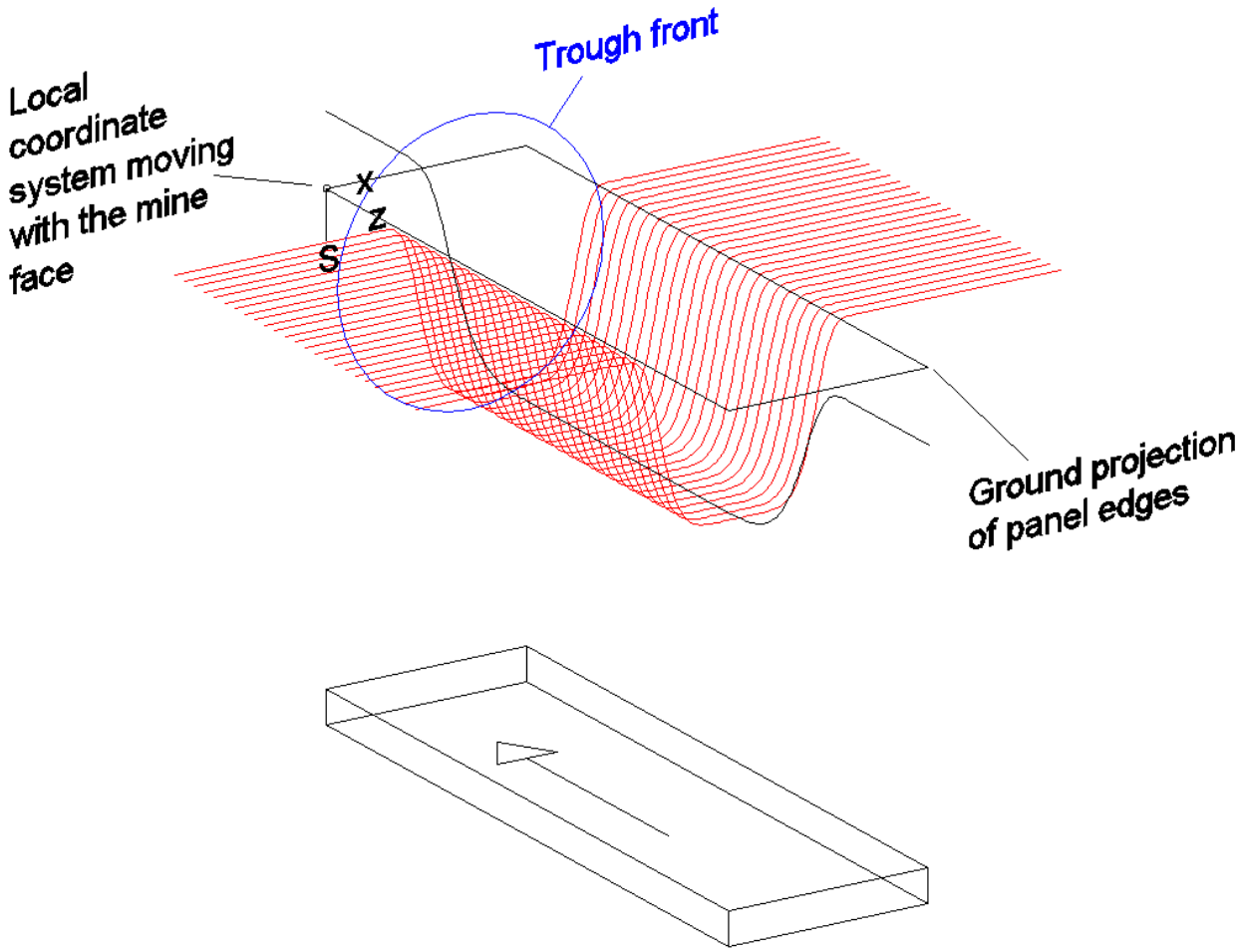

Figure 2-6 Local coordinate system moving at the same rate as the mine face

2.6 USE OF AN ADEQUATE BASELINE FOR SUBSIDENCE PROFILE ESTIMATION

Early on, we realized that the correct baseline for subsidence calculations may not be assumed to be the one corresponding to the first surveying date (e.g. 03/25/06 for LW-51) because of the proximity of the mine face to the highway such that heave may have already occurred when the surveying was first carried out. Instead, we developed the baseline based upon digitized AutoCAD map files for each panel that were prepared long before the mining operation. Subsidence was then estimated with respect to this original reference. However, we have not as yet applied this baseline correction to the tiltmeter data because their locations are often far from where dense data are available for interpolation. This explains why the subsidence estimated from tiltmeters is often larger.

2.7 PANEL DATA

2.7.1 Emerald mine

2.7.1.1 Panel B-3

Emerald mine panel B-3 ends where the x, z coordinate system origin is located in Figure 2-7. This is the only panel in this study that ends where it intersects the highway. Figure 2-7 shows how close the highway section is to the panel corner. As a result, profiles in this area are mainly subcritical, as depicted in Figure 2-8 and Figure 2-9. The farthest points from the panel corner

are located at distances from the edges where critical or supercritical profiles may be reached. However, from the limited surveying data, which contains data until February 28, 2006, critical or supercritical profiles could not be observed. Due to the lack of data, profiles at the ending edge could not be obtained, as can be appreciated in Figure 2-10. Figure 2-11 shows the location of 8 tiltmeters along I-79. Since tiltmeter data provide elevation differences and tiltmeter data are available from dates after the panel was completely mined out, these were checked and the elevation changes were plotted against *x*, as shown in Figure 2-12. From the data, it cannot be concluded that B-3 reached a critical or a supercritical shape.

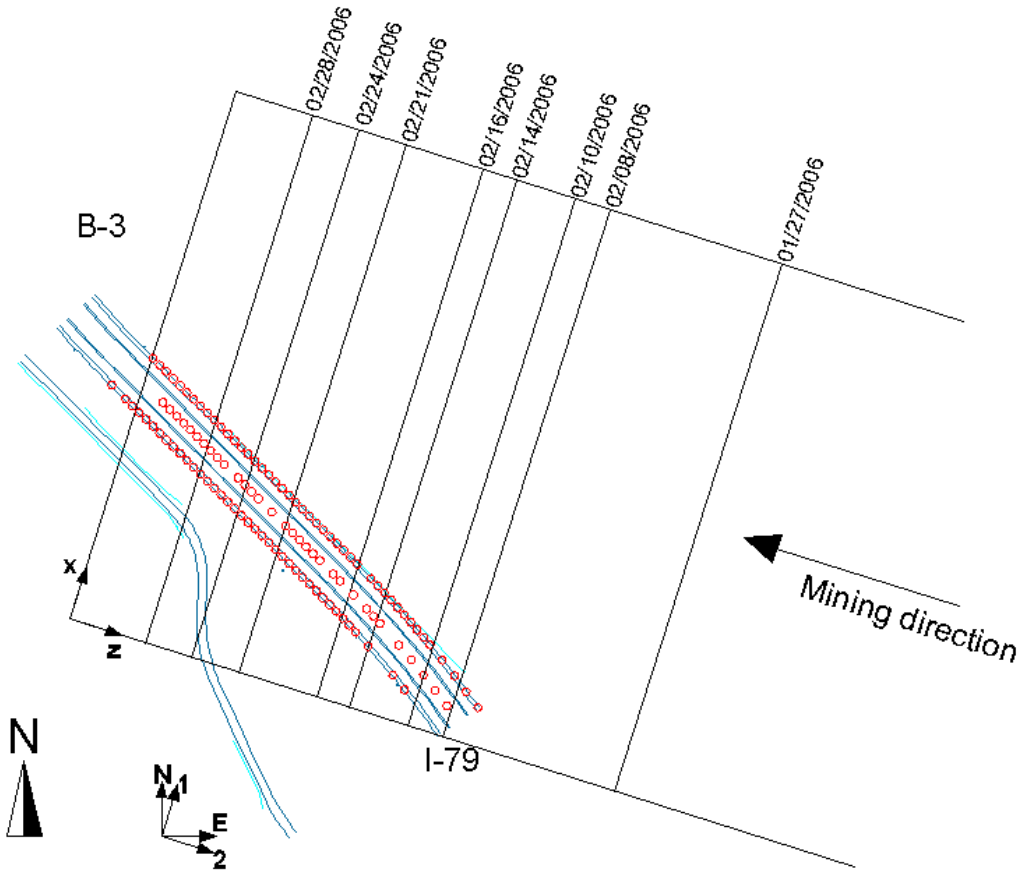

Figure 2-7 Overview of the West end of Emerald mine panel B-3 intersecting I-79

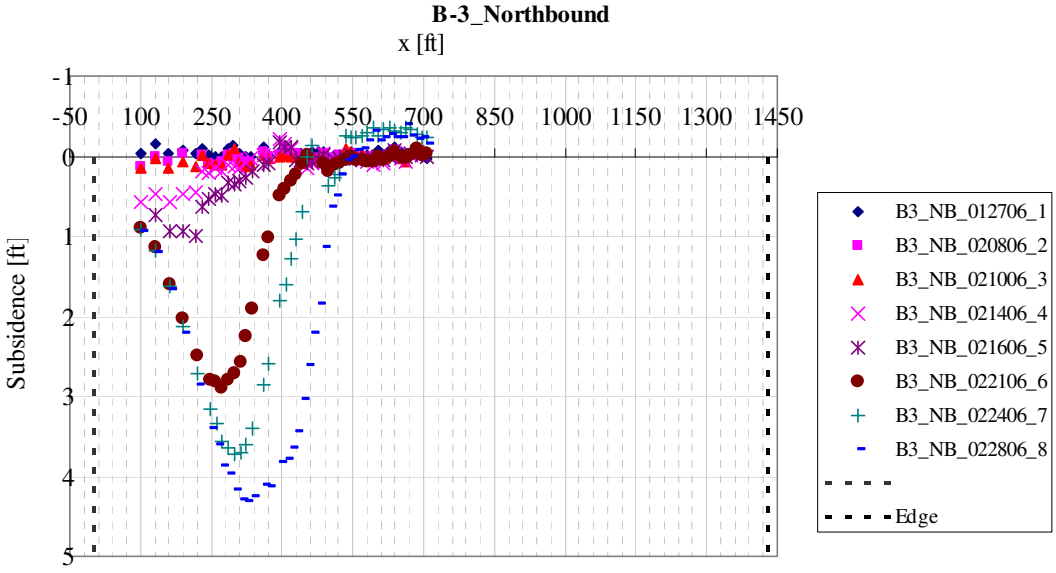

Figure 2-8 Emerald mine panel B-3 *z*-plane (transversal) projection of northbound station surveying data for different times showing subcritical profiles

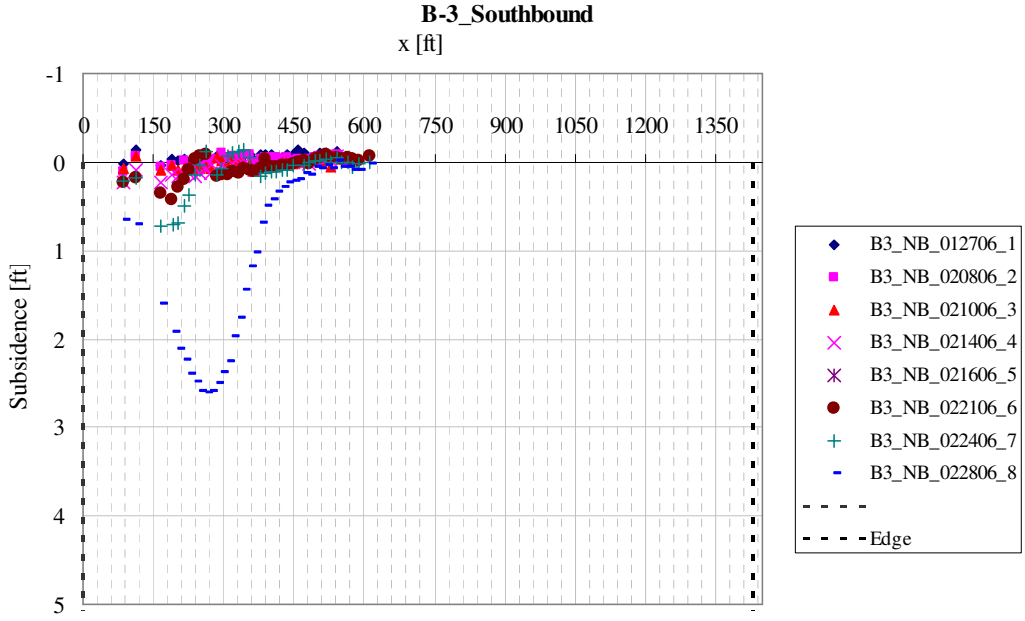

Figure 2-9 Emerald mine panel B-3 *z*-plane (transversal) projection of southbound station surveying data for different times showing subcritical profiles

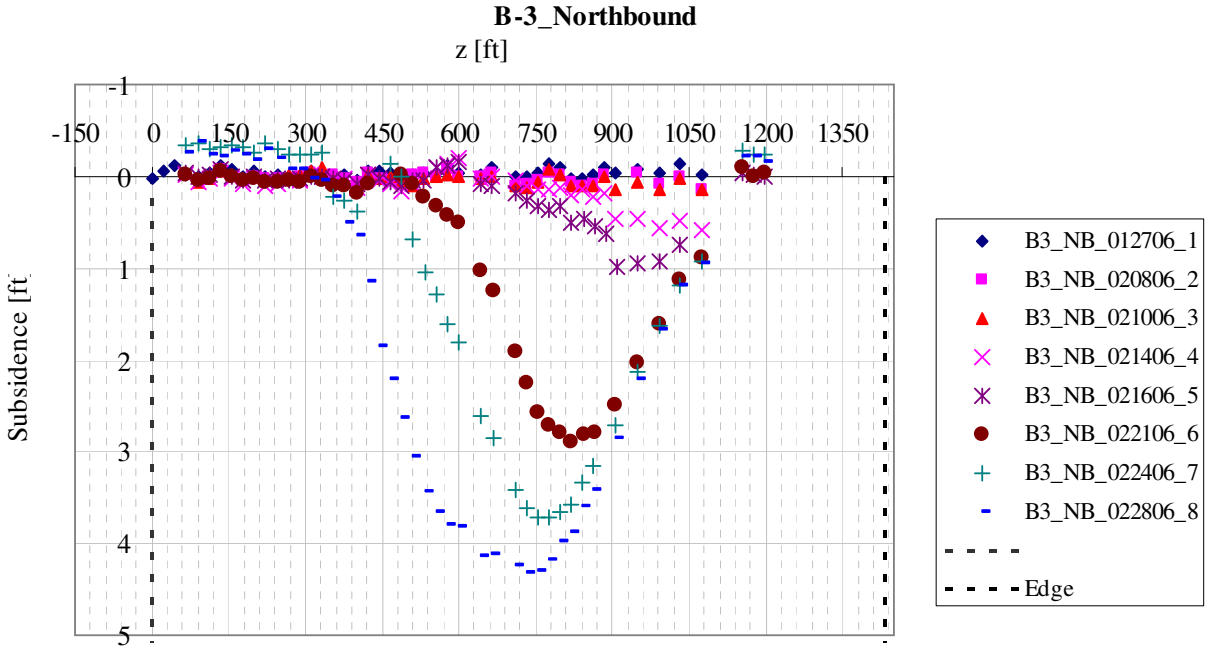

Figure 2-10 Emerald mine panel B-3 *x*-plane (longitudinal) projection of southbound station surveying data for different times showing subcritical profiles

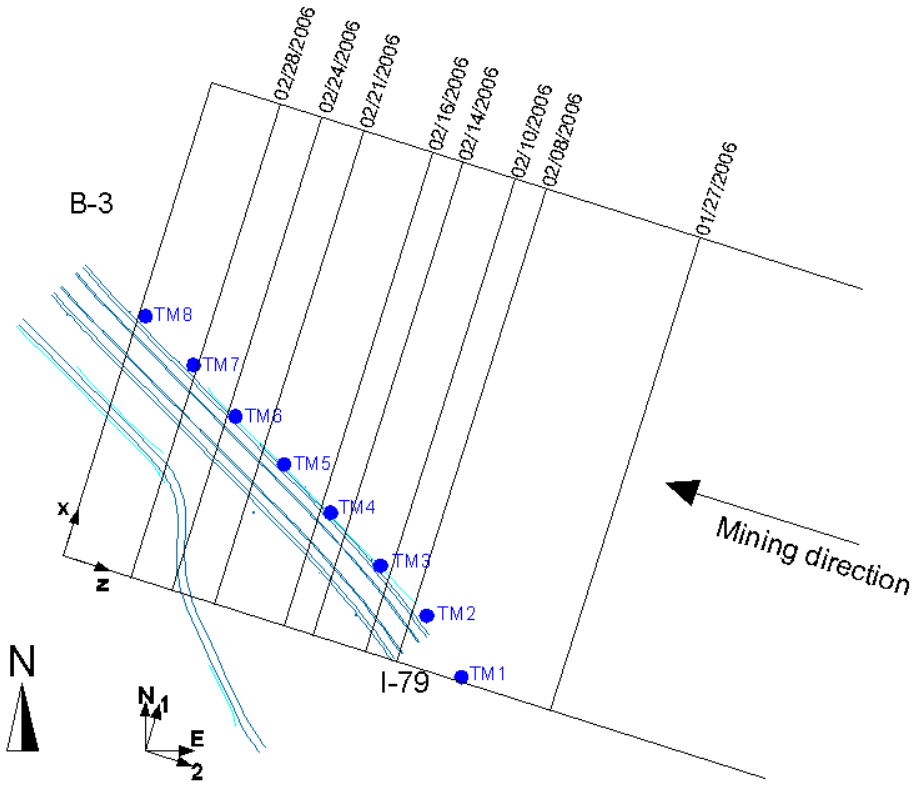

Figure 2-11 Tiltmeter location at Emerald mine panel B-3

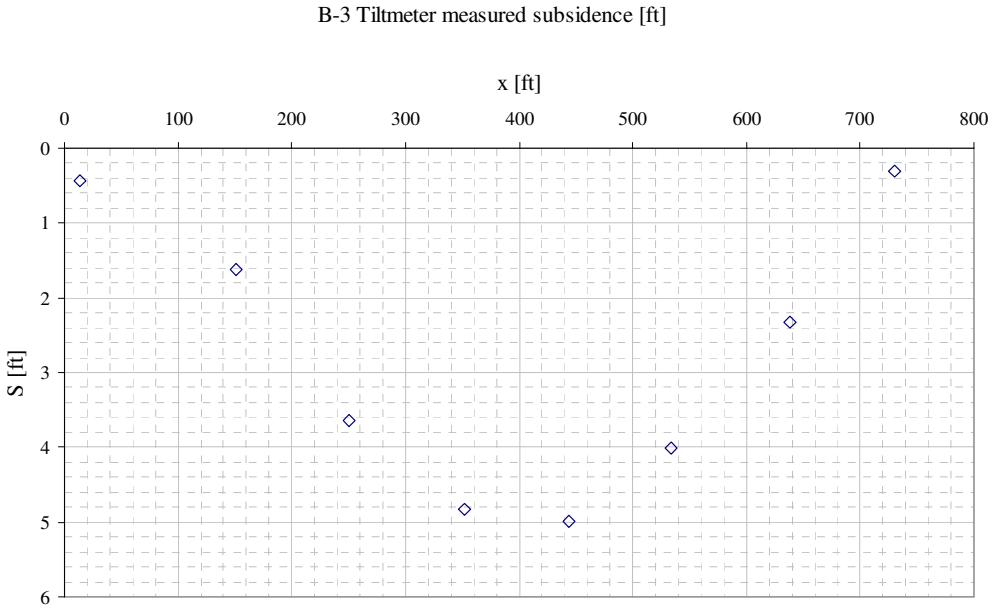

Figure 2-12 B-3 Tiltmeter subsidence readings

2.7.1.2 Panel B-4

Emerald B-4 panel is located next to B-3 panel to the south. The highway intersects this panel in a region where the final longitudinal subsidence profile is supercritical. Figure 2-13 shows the panel, the highway and the data points along the northbound side of the highway. The southbound data points cannot be plotted due to a lack of Northing data (the Northing data were mistakenly replaced by the Easting data in the raw data). Another factor that limits the amount of data for B-4 is the fact that only 4 surveying dates are available. Figure 2-14 shows the location of tiltmeters. Figure 2-15 shows a transversal projection of all surveying data sorted by surveying date. This data is not transformed data and it should not be understood as transverse profiles, just as a projection of the highway points on a plane normal to the z-axis. This is the first type of plot we produced for every single panel. From this plot of B-4, a few important and unusual characteristics of subsidence evolution can be readily observed:

- The heave recorded in areas adjacent to panel edges and ahead of the mine face, reaching a magnitude of roughly 1 ft with an affecting distance up to 1350' from the mine face.
- The subsidence profile was lower for 11/21/2006 than it was for 12/06/06 by a magnitude of roughly 0.5 ft.
- Three low points are observed on the right portion of the graph. These three points lie on bridge structures that were removed ahead of the advance of the longwall face, according to the October 2006 report on panel B-4 presented to PennDOT by Earth Inc.

We double-checked the subsidence magnitudes with the tiltmeter elevation data which are plotted in Figure 2-16. Tiltmeter 3 had problems during surveying and data for this tiltmeter is missing, and that resulted in a gap in the plot. From the figure, it is apparent that tiltmeters

followed a supercritical profile. The magnitude of subsidence read from the tiltmeters is higher than that obtained from the surveying data (as explained in section 2.6) by roughly 0.3 ft.

The surveying data for this panel were only available for four dates which lead to gaps in the profile both in transversal and longitudinal directions as seen in Figure 2-17 (longitudinal profile) and in the figures in Appendix A1, which correspond to transversal data.

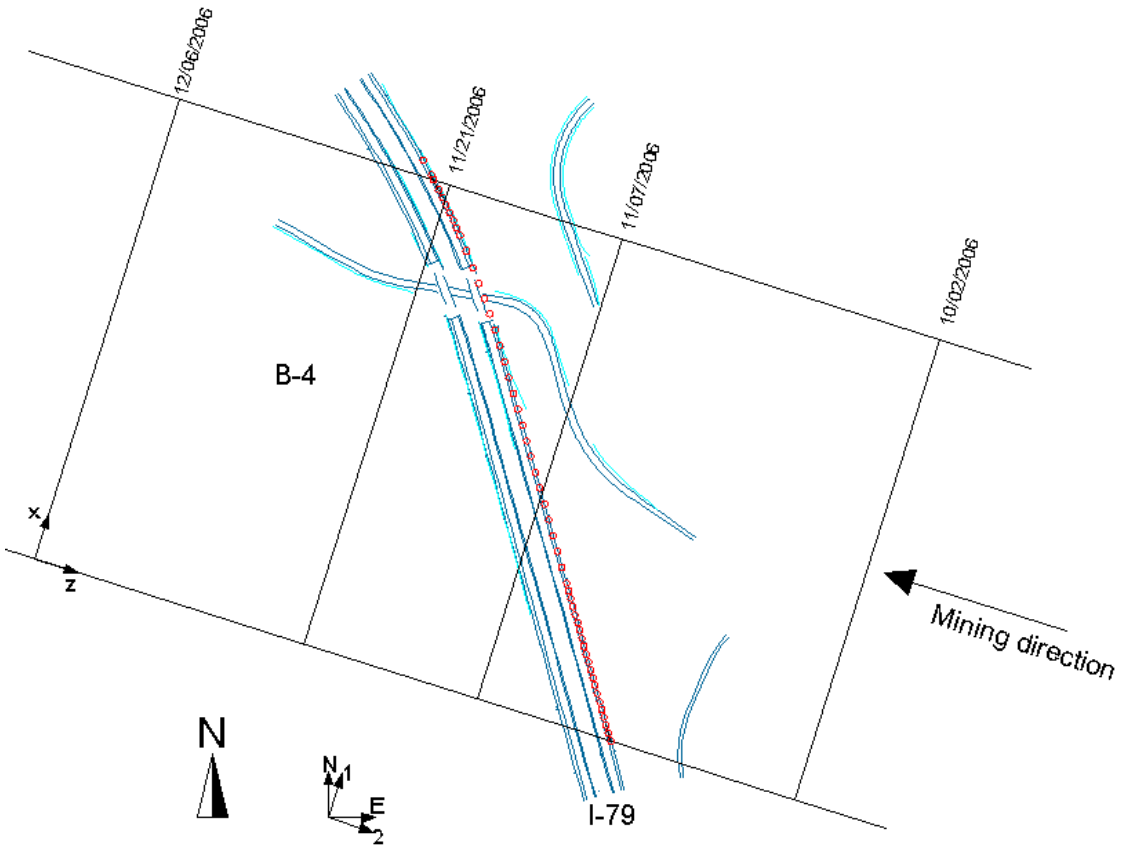

Figure 2-13 Overview of Emerald mine panel B-4 intersecting I-79

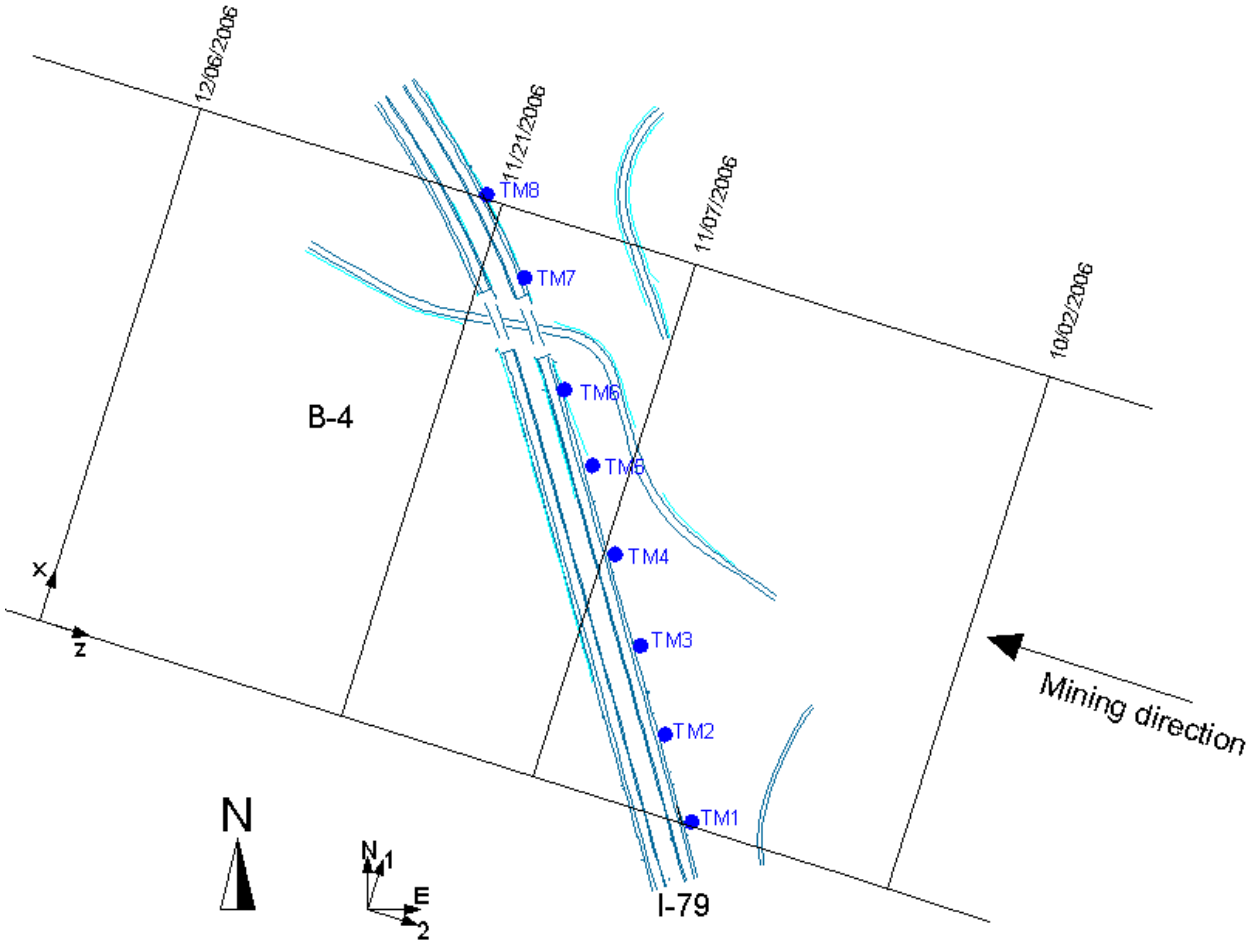

Figure 2-14 Tiltmeter location at Emerald mine panel B-4

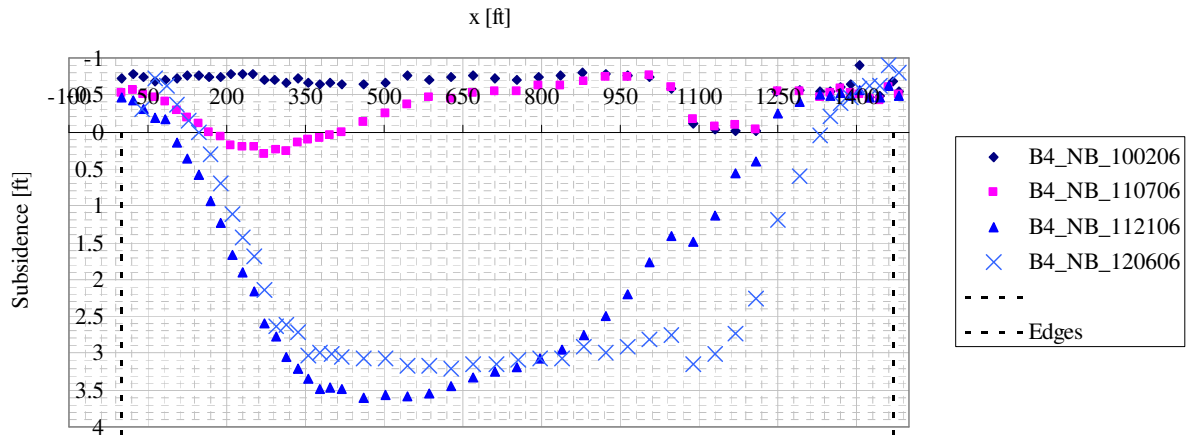

Figure 2-15 Emerald mine panel B-4 z-plane (transversal) projection of station surveying data for different dates

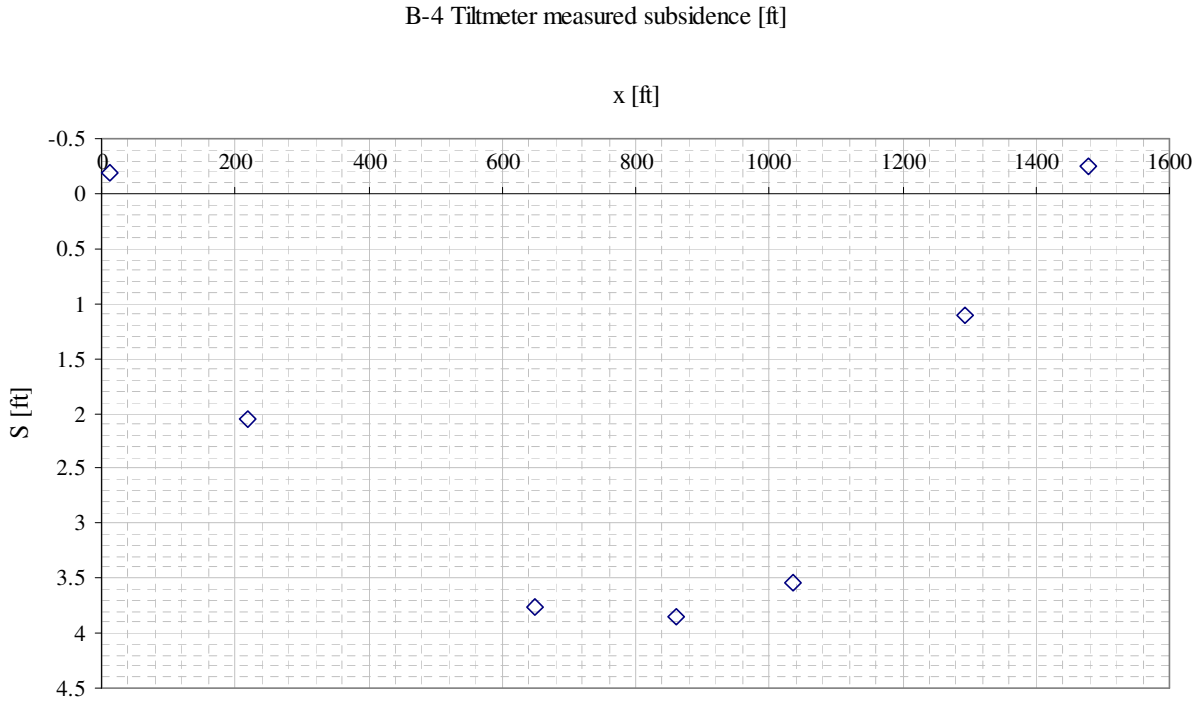

Figure 2-16 B-4 Tiltmeter subsidence readings

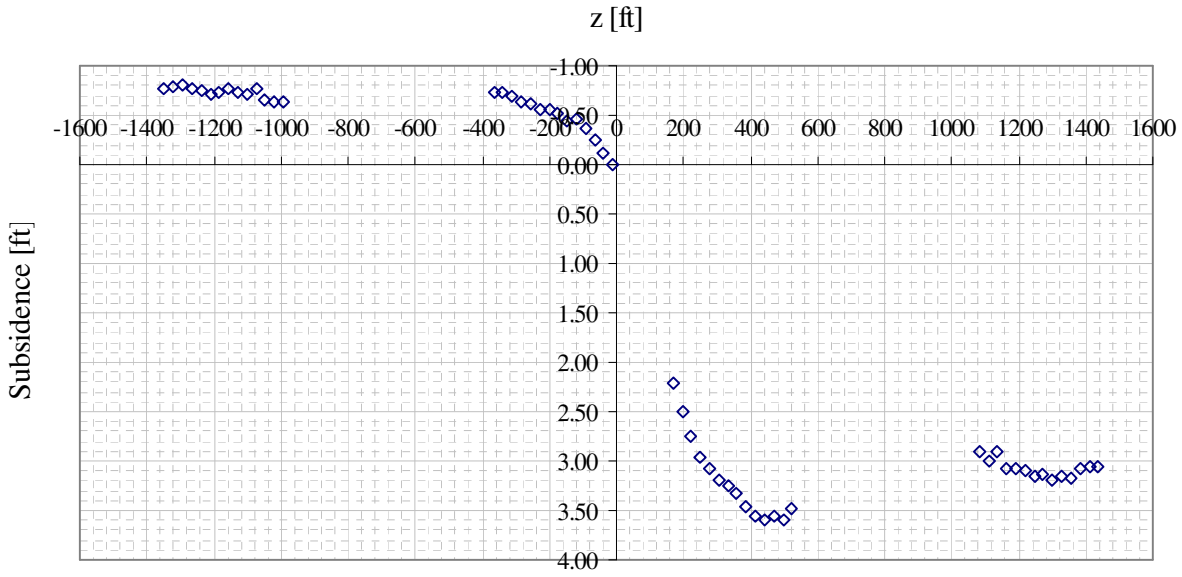

Figure 2-17 B-4 longitudinal subsidence profile in the central 600 ft

2.7.2 Cumberland Mine

2.7.2.1 Panel LW-49

The segment of I-79 above panel LW-49 began to be surveyed after the mine face had passed underneath it, as observed in Figure 2-18. Figure 2-18 and Figure 2-20 show transversal projection of subsidence data for different dates. Figure 2-21 depicts the longitudinal profile taken from the central 400 ft of the panel width after data transformation. Transversal transformed data can be observed in sequence in Appendix A2.

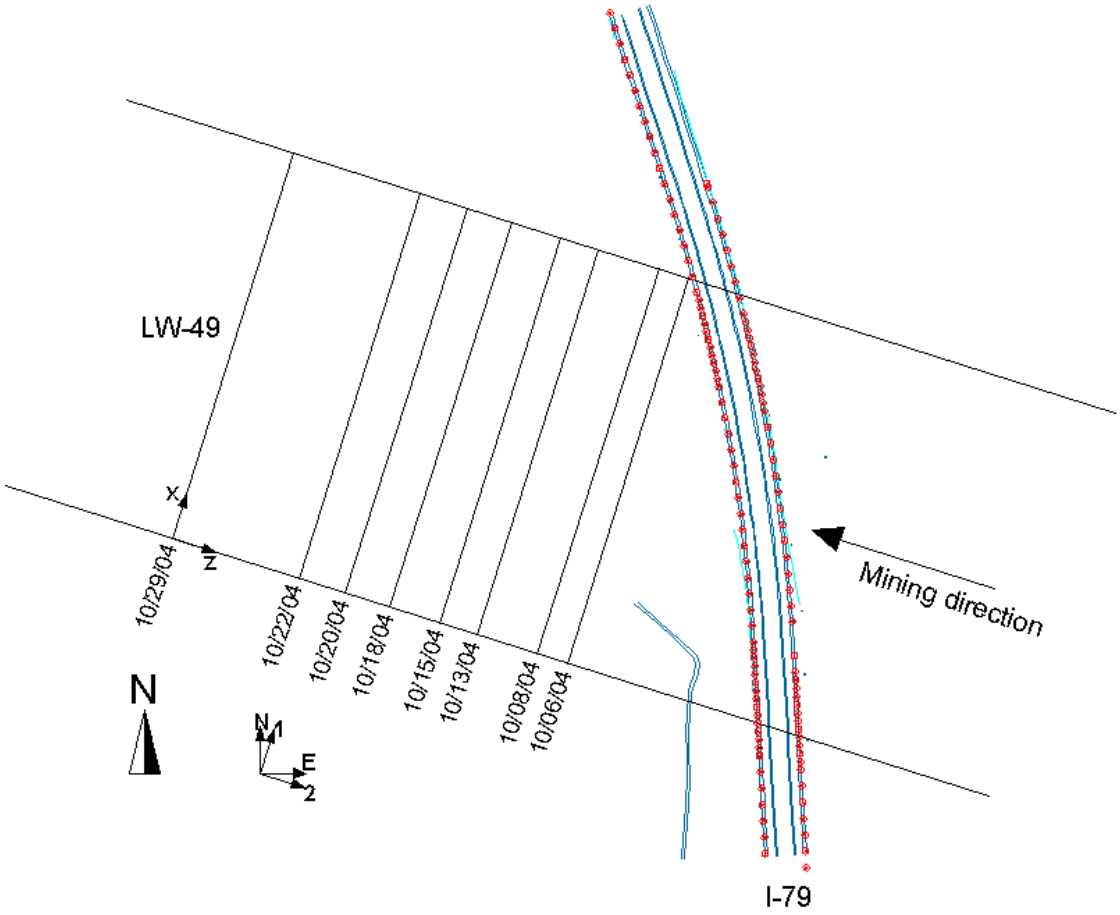

Figure 2-18 Overview of Cumberland mine panel LW-49 intersecting I-79

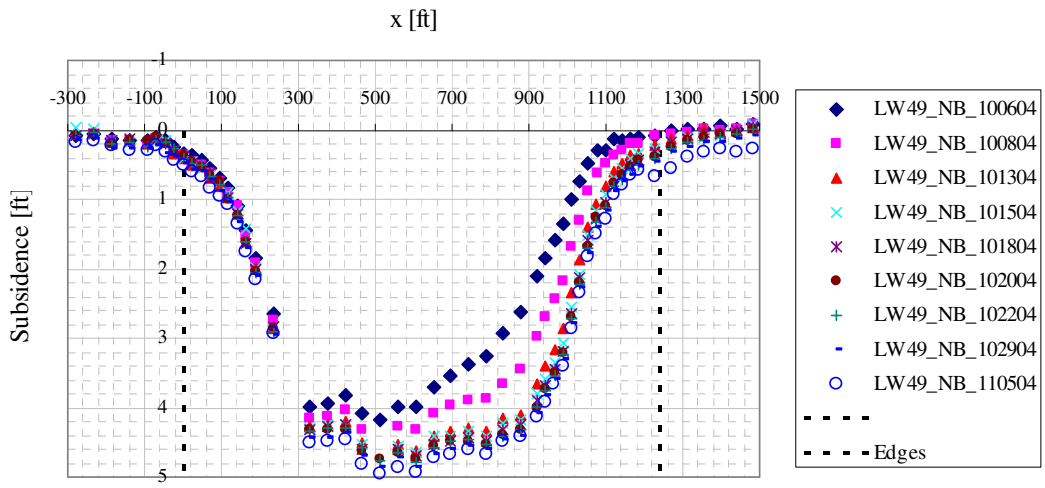

Figure 2-19 Cumberland mine panel LW-49 *z*-plane (transversal) projection of northbound station surveying data for different dates

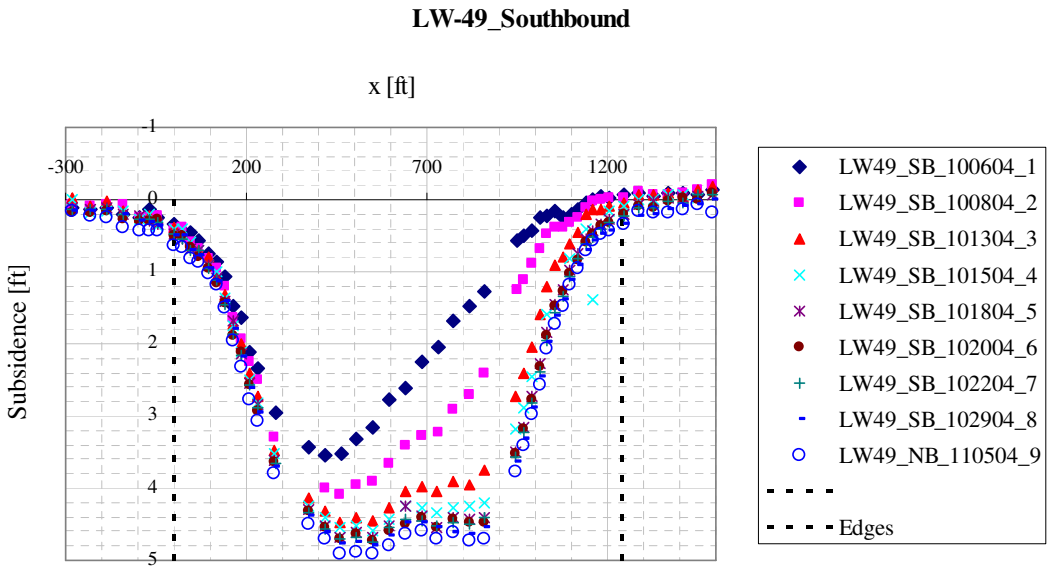

Figure 2-20 Cumberland mine panel LW-49 *z*-plane (transversal) projection of southbound station surveying data for different dates

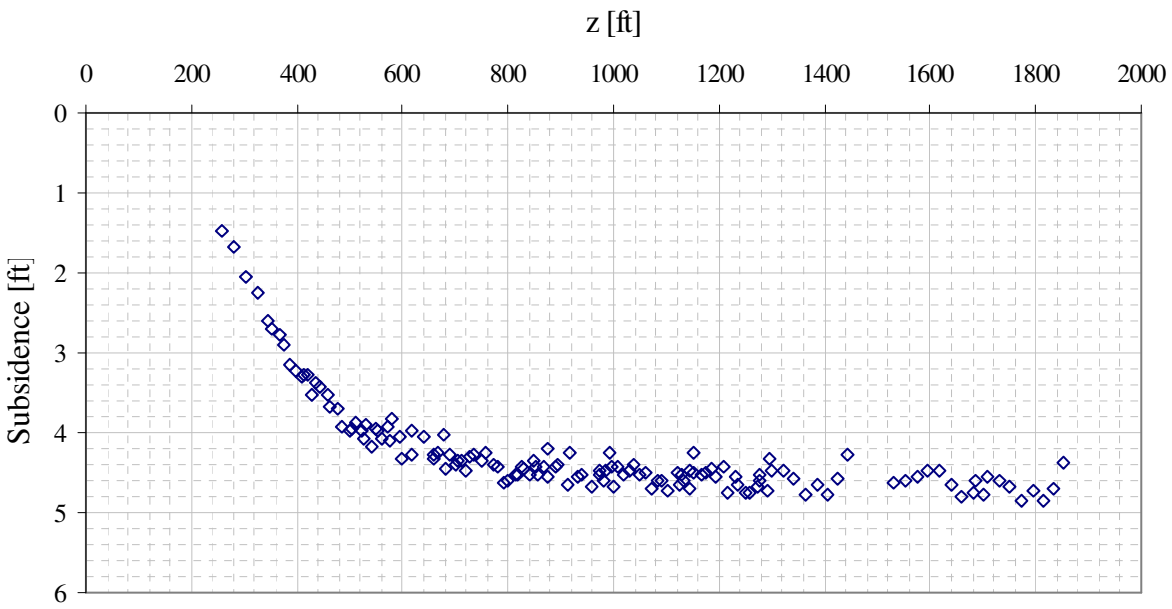

Figure 2-21 Cumberland mine panel LW-49 longitudinal profile for the central 400 ft

2.7.2.2 Panel LW-51

Panel LW-51 is the best documented panel of this study. This fact is apparent from Figure 2-22 and Figure 2-23, showing a total 9 different surveying dates, well spaced and corresponding to mine face positions behind the highway, at locations underneath the highway, and ahead of it, as illustrated in Figure 2-5. The southbound data corresponding to 05/04/2006 seems to differ from the general smooth pattern. The data showed some abrupt change in the surface elevation as observed in Figure 2-23 and Figure 2-24. This could very well be a result of deformation of highway fills. Appendix A3 shows transverse transformed data.

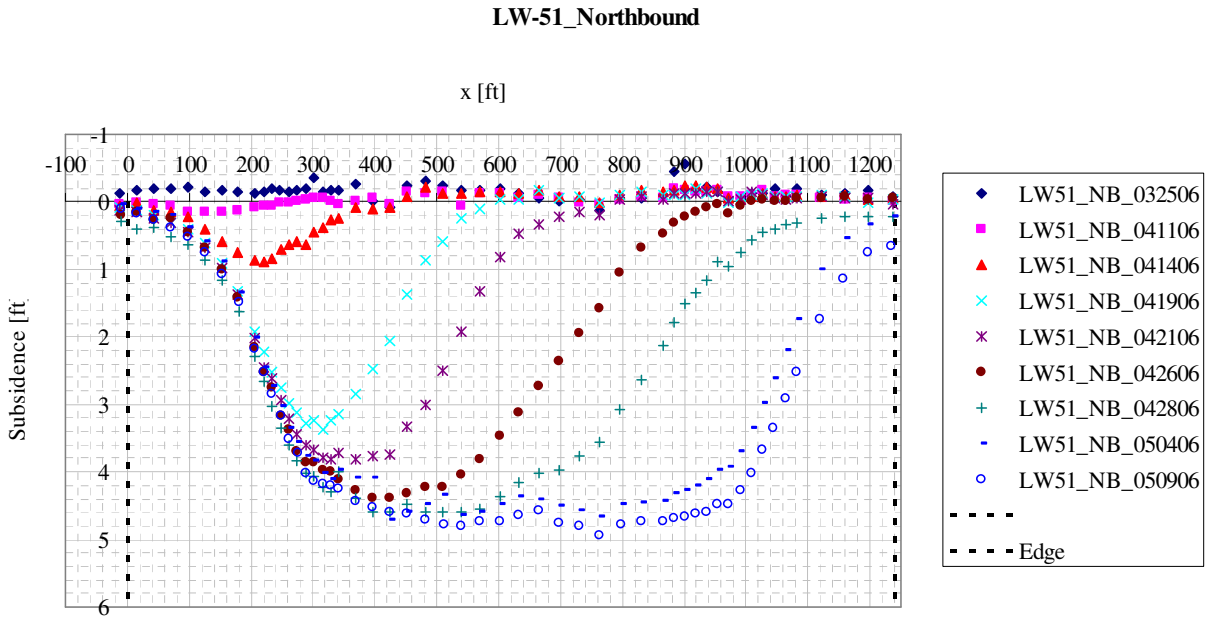

Figure 2-22 Cumberland mine panel LW-51 *z*-plane (transversal) projection of northbound station surveying data for different dates

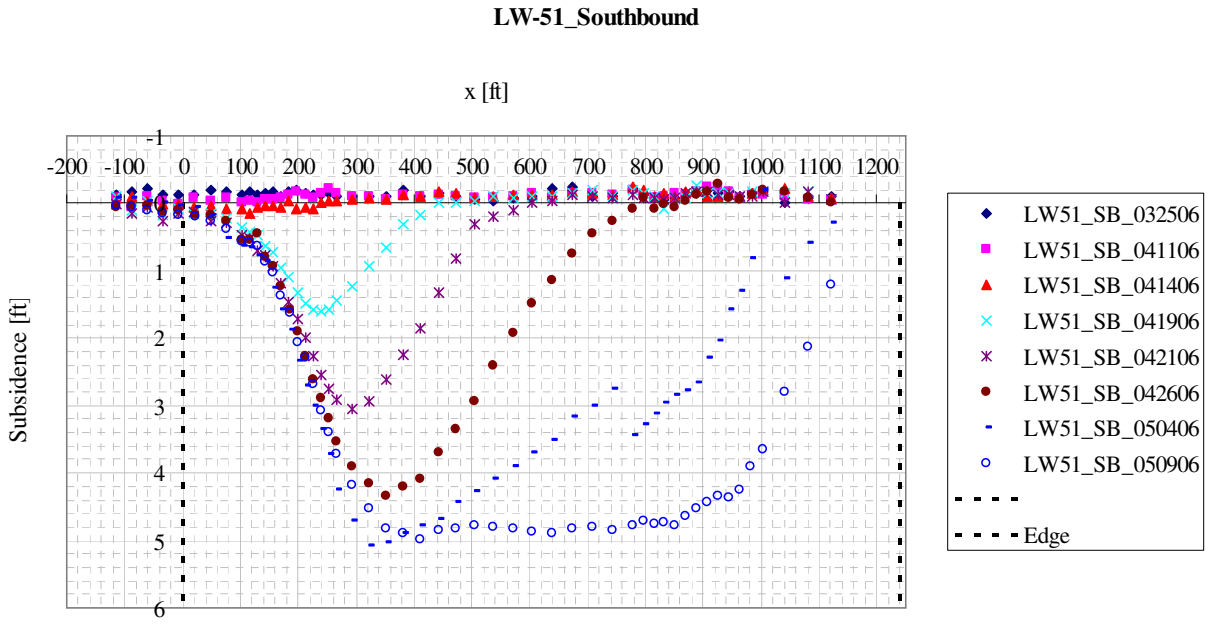

Figure 2-23 Cumberland mine panel LW-51 *z*-plane (transversal) projection of southbound station surveying data for different dates

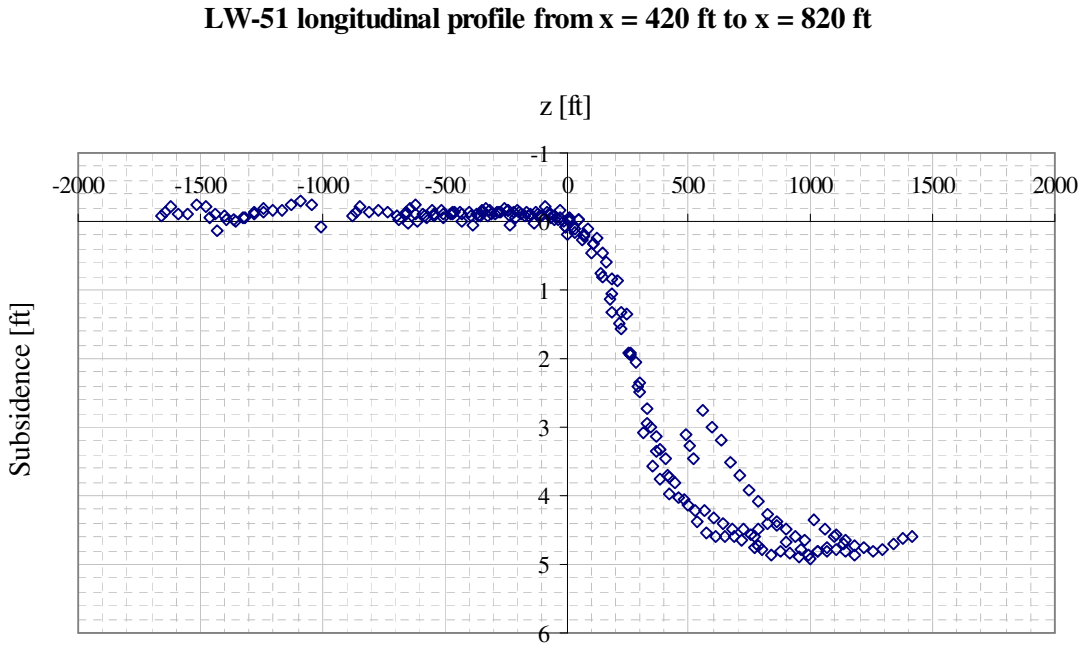

Figure 2-24 Cumberland mine panel LW-51 longitudinal profile for the central 400 ft

2.7.2.3 Panel LW-52

The large gap observed between the last two survey dates produces an equally large gap in the transformed data of LW-52, as can be appreciated in Figure 2-25 and Figure 2-28. Figure 2-27 depicts profiles from different dates on the southbound of I-79. Substantial differences in maximum subsidence are apparent if the last profile of this figure is compared to that of the northbound in Figure 2-27. The shape of the final transversal profile for the southbound does not resemble a typical supercritical profile, which would be presumed to be flat in the central region along the panel width. Instead, on the right side of the panel a sharp rise in subsidence occurred giving an unusually high maximum subsidence equal to 5.5 ft.

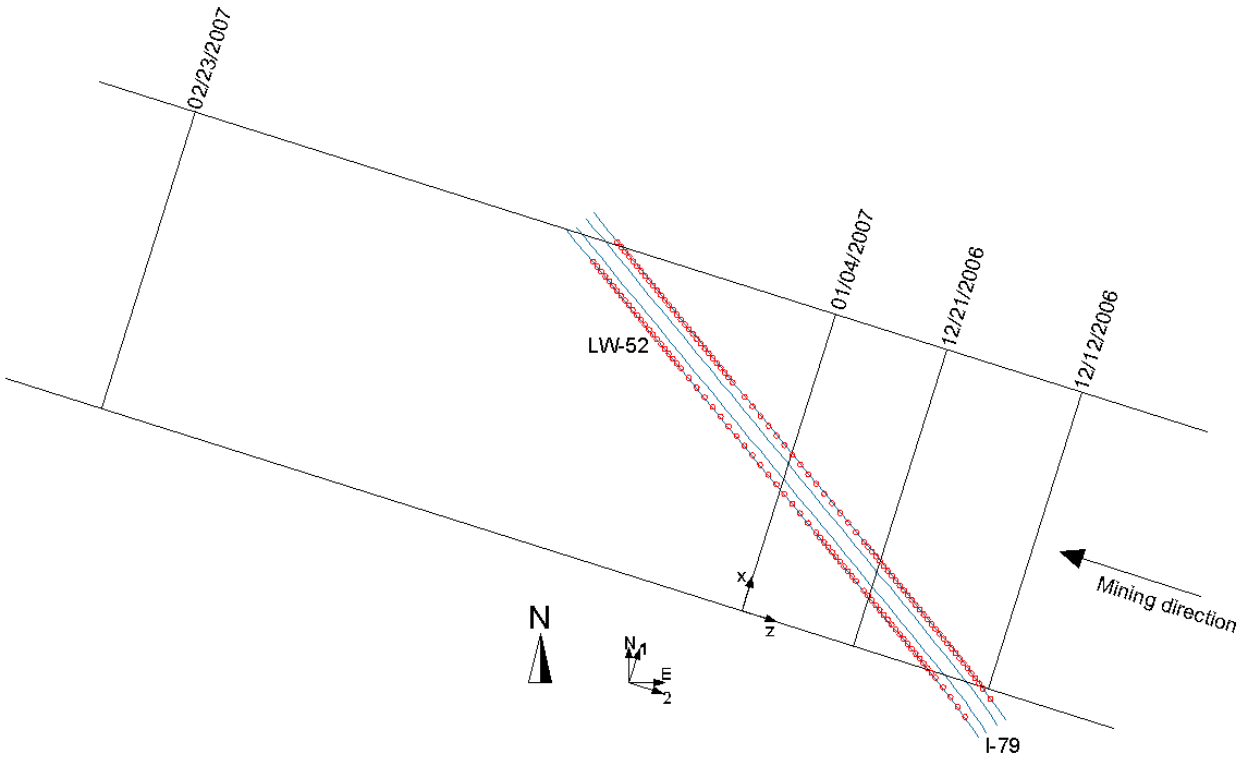

Figure 2-25 Overview of Cumberland mine panel LW-52 intersecting I-79

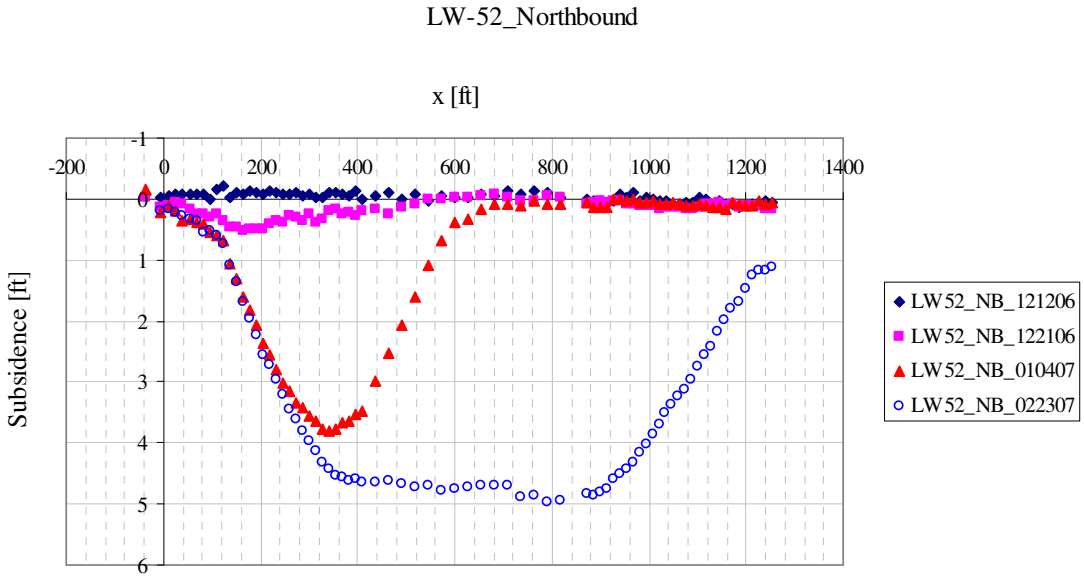

Figure 2-26 Cumberland mine panel LW-52 *z*-plane (transversal) projection of northbound station surveying data for different dates

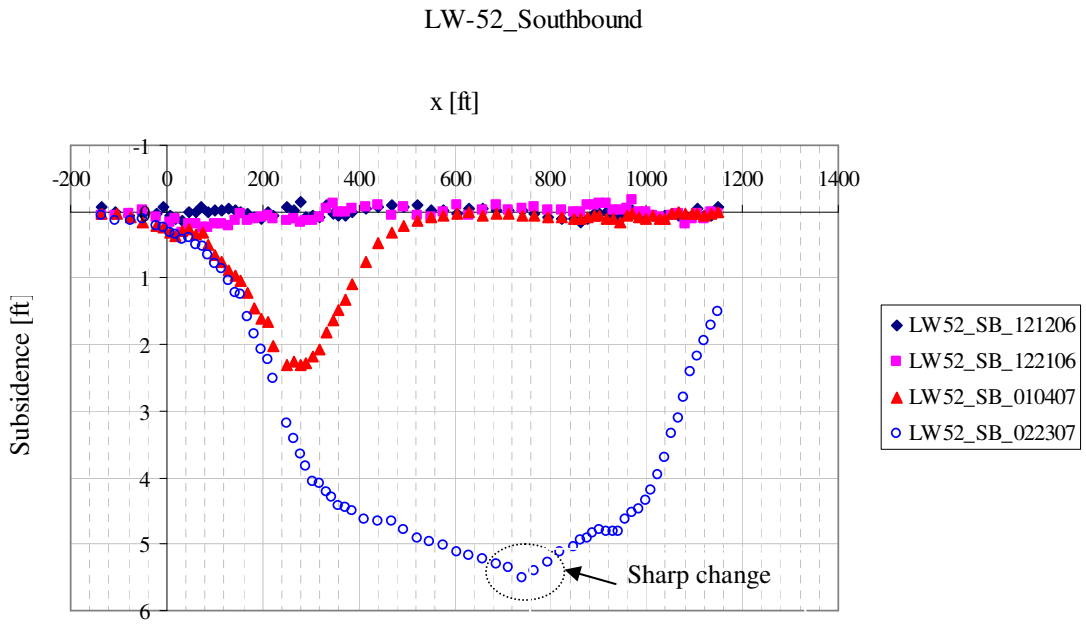

Figure 2-27 Cumberland mine panel LW-52 *z*-plane (transversal) projection of southbound station surveying data for different dates

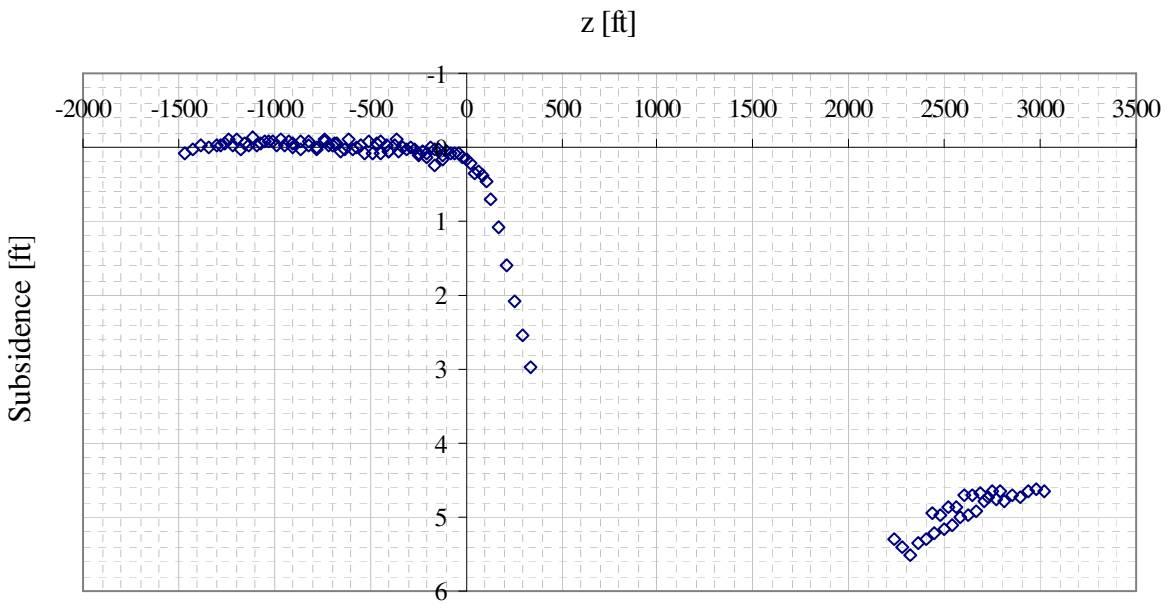

Figure 2-28 Cumberland mine panel LW-52 longitudinal profile for the central 400 ft

2.7.2.4 Panel LW-55

Panel LW-55 was added to the project as data became available during and after mining, on the month of October 2008. This panel is unique in that it starts right at the area of concern. Transformation of this data is not relevant because a complete history until profiles become supercritical could not be obtained. One reason is that the highway does not completely cross the panel and crosses it at a predominant subcritical deformation region. Another reason is the limitation of data, which were only measured until October 27 2008, as shown in Figure 2-29. However, a small region of supercritical deformation may be observed in Figure 2-30 and Figure 2-32, thus providing a valuable maximum subsidence magnitude. Figure 2-32 and Figure 2-33 show excessive heave taking place from 10/03/08 to 10/06/08 for the southbound. A double-check of tiltmeter data seems to show no such drastic changes in elevation, as depicted in Figure 2-35 and Figure 2-36.

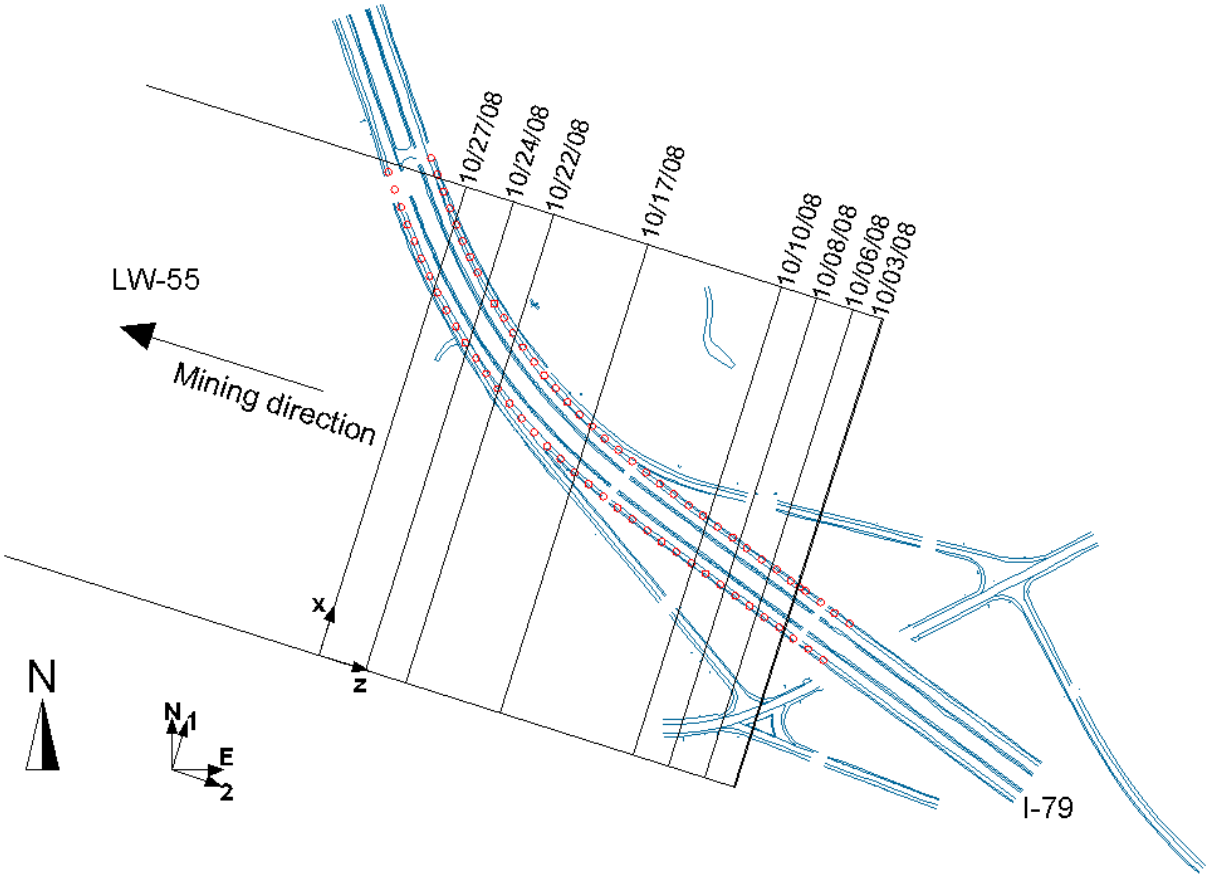

Figure 2-29 Overview of Cumberland mine panel LW-55

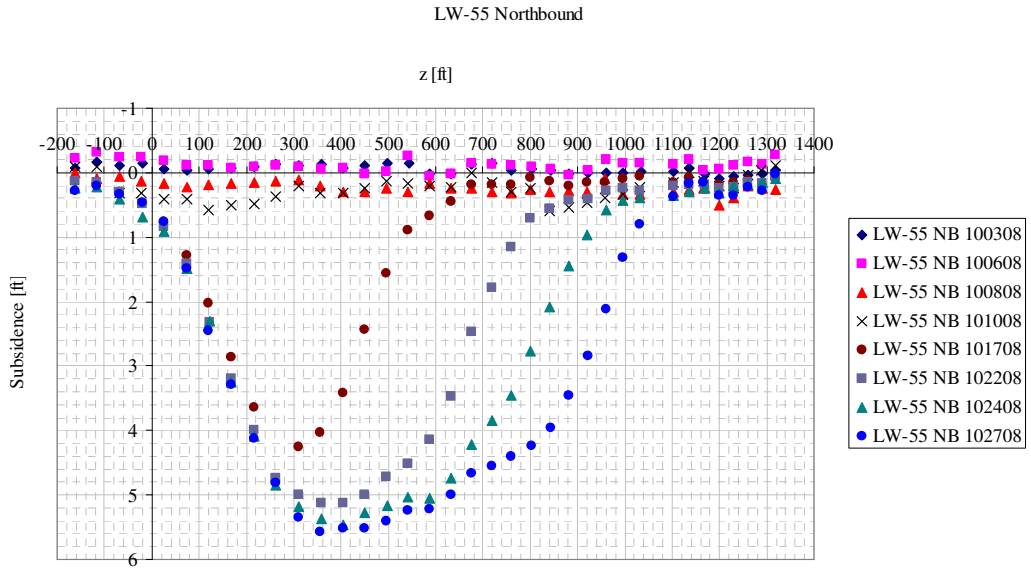

Figure 2-30 Cumberland mine panel LW-55 *x*-plane (longitudinal) projection of northbound station surveying data for different dates

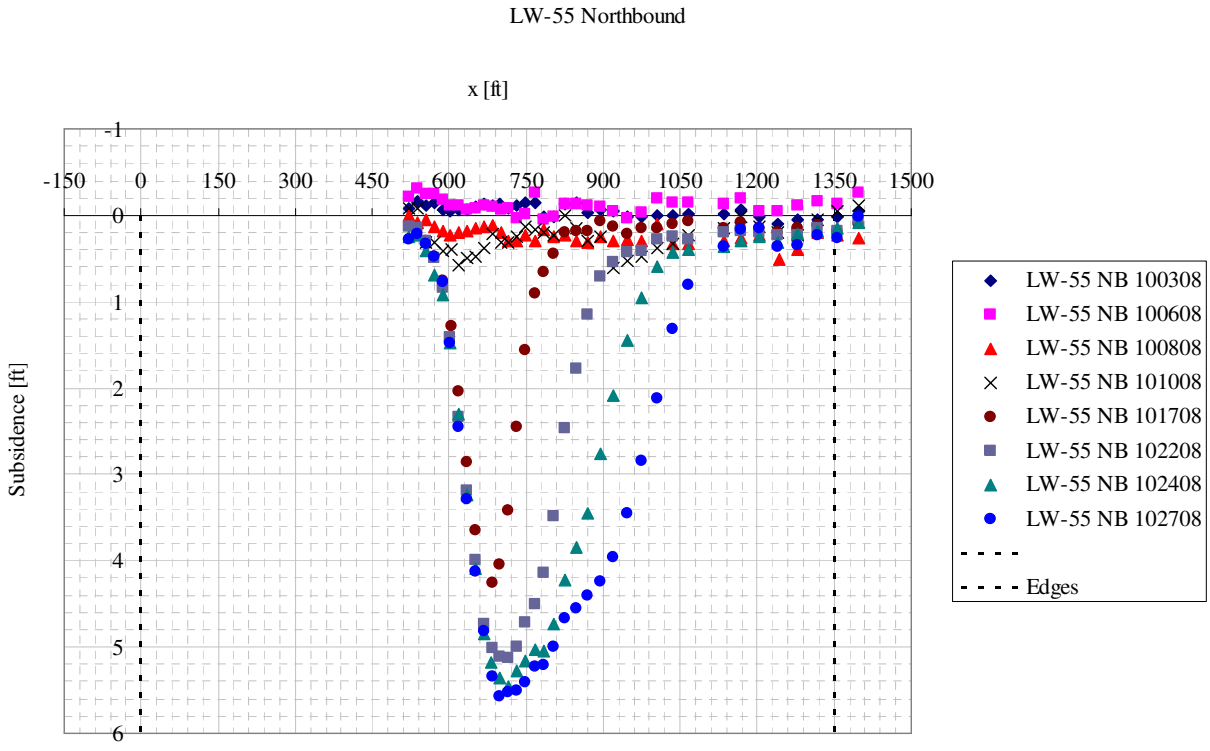

Figure 2-31 Cumberland mine panel LW-55 *z*-plane (transversal) projection of northbound station surveying data for different dates

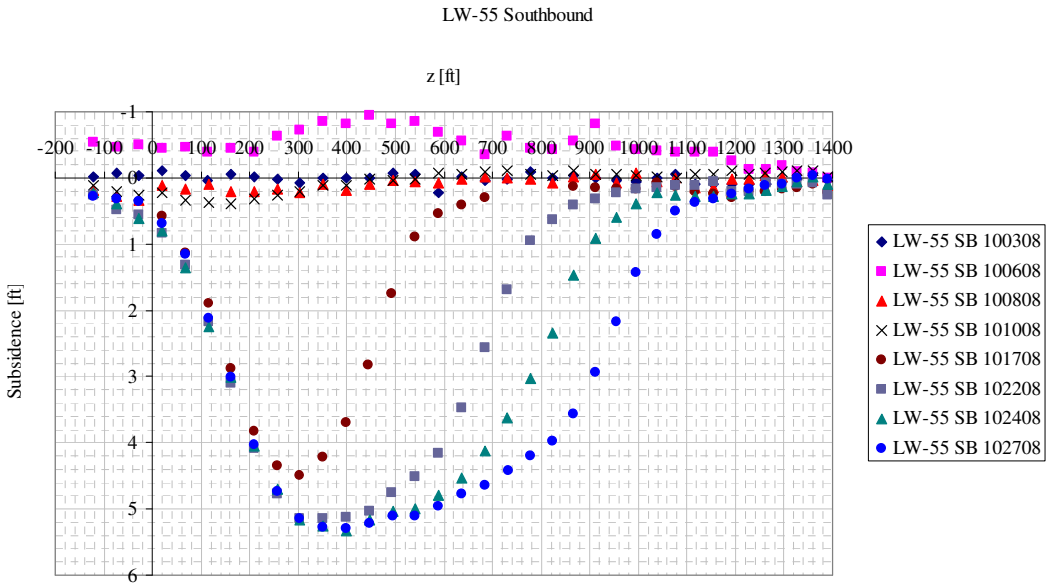

Figure 2-32 Cumberland mine panel LW-55 *x*-plane (longitudinal) projection of southbound station surveying data for different dates

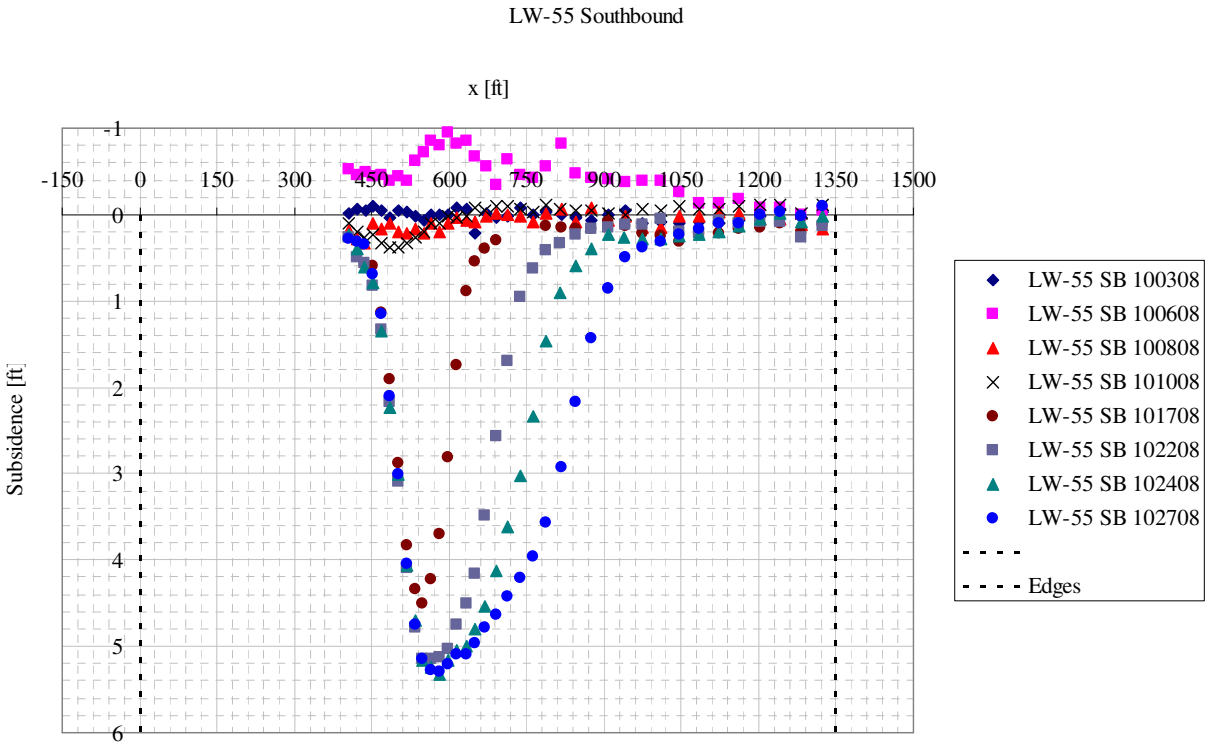

Figure 2-33 Cumberland mine panel LW-55 *z*-plane (transversal) projection of southbound station surveying data for different dates

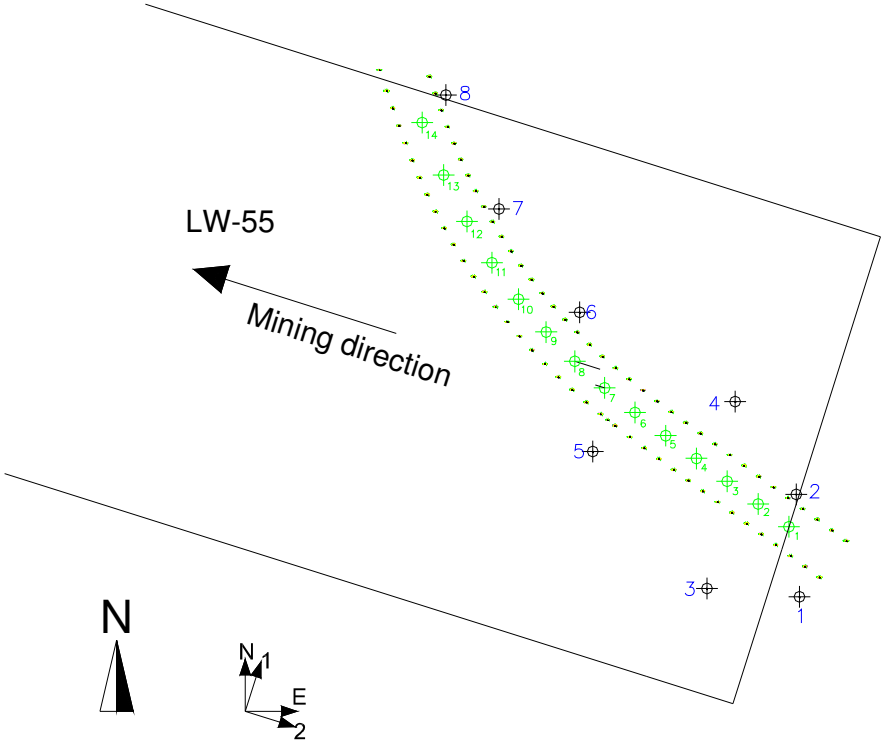

Figure 2-34 Overview of LW-55 tiltmeters

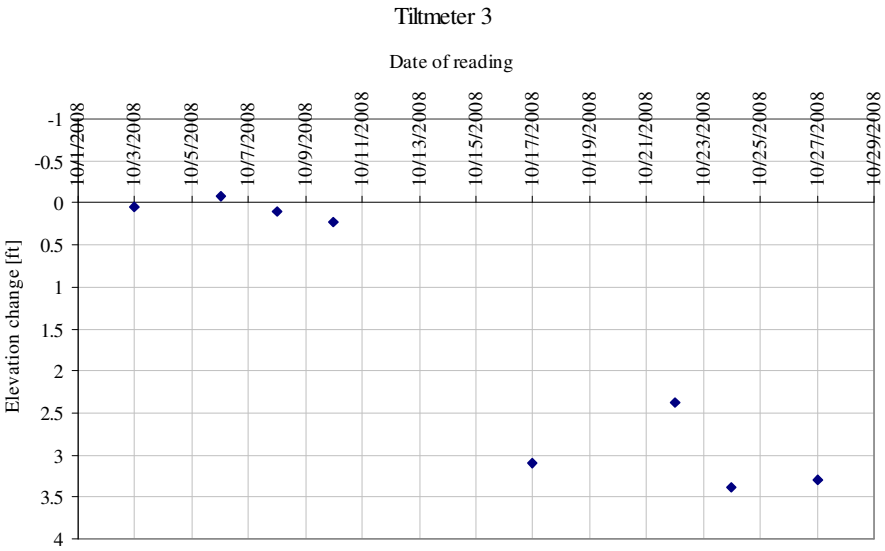

Figure 2-35 Cumberland mine panel LW-55 tiltmeter 3 elevation change readings

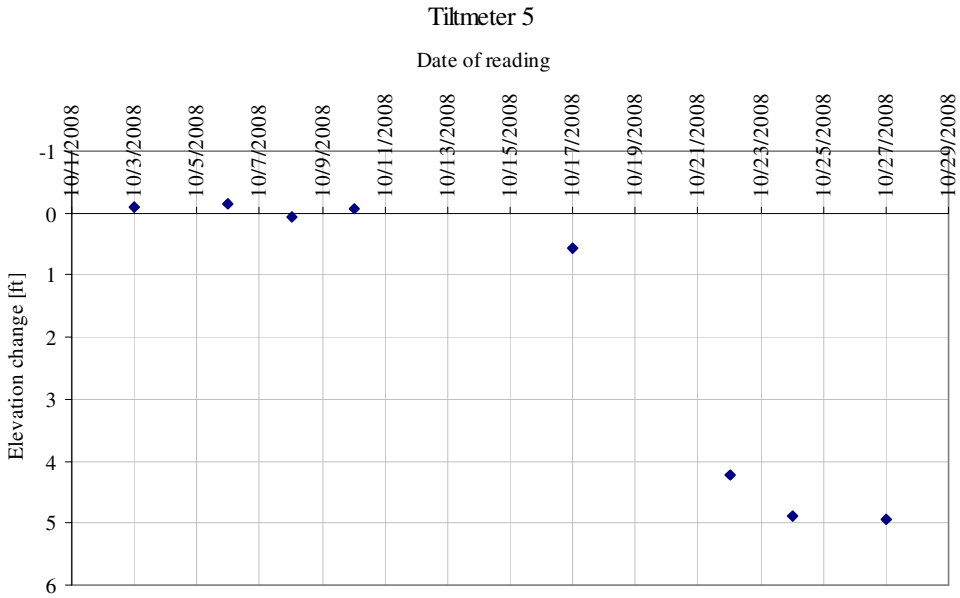

Figure 2-36 Cumberland mine panel LW-55 tiltmeter 5 elevation change readings

2.7.2.5 Panels LW-50 and LW-53

From panels LW-50 and LW-53 only the maximum subsidence could be estimated from elevation changes, since no East, North coordinates were available. The subsidence magnitude is contained in Table 2-1 and is greatly valuable for the development of a model of maximum subsidence.

3.0 TASK 3: MODELING SUBSIDENCE PROFILES

In the modeling of subsidence profiles, we focused only on the panels that provide sufficient data. We first focused on the evaluation of the prediction model of the Surface Deformation Prediction System (SDPS 5.0 and 6.0) software. As the software does not capture all the essential characteristics of the observed subsidence profile, we continued to work beyond the proposed scope of the project and explored new subsidence profile equations to fit the panel data.

The original SDPS was developed by Dr. Michael Karmis' group at the Department of Mining and Minerals Engineering at Virginia Tech. The Windows version was developed by Dr. Zach Agioutantis and Dr. Michael Karmis under a contract from the Office of Surface Mining Reclamation and Enforcement (OSMRE).

We used SDPS 5.0 and 6.0 to predict subsidence profiles for panels B-4, LW-49, LW-51, LW-52, and LW-55. We found that one of the drawbacks of SDPS is that the predicted maximum subsidence in the region under study (using the best estimate of hard rock percentage of overburden to be 37%), was substantially lower than observed values. This report concludes that this drawback may be ameliorated using a relationship of S*/M (Maximum subsidence normalized by the seam thickness) versus overburden depth, H, developed based on the data collected by PennDOT that were provided to Pitt.

Section 3.2 contains the SDPS predictions of final subsidence for panels LW-49, LW-51, LW-52, LW-55, and B-4, together with the measured data.

3.1 INSIDE SDPS – BRIEF SUMMARY OF STEPS, FORMULAE AND CRITERIA USED IN LONGWALL SUBSIDENCE PREDICTION

This section introduces SDPS and its ability to predict subsidence due to underground coal mining. We have found that the main source of error or uncertainty in subsidence estimation using SDPS comes from the estimate of maximum subsidence. The details of this finding are discussed in subsections 3.1.1. Subsection 3.1.2 presents the theory behind SDPS profile function method and the main steps involved in the use of SDPS, and subsection 3.1.3 deals with the theory behind SDPS influence function method and the steps involved in its application.

3.1.1 Maximum subsidence prediction model

SDPS uses a maximum subsidence prediction model (Figure 3-1) that results from combining the regressions shown in Figure 3-2 and Figure 3-3, respectively. We have shown that the SDPS maximum subsidence model underestimates maximum subsidence for the specific case of the area of concern. The average relative error produced was 22%, which would for example lead to an estimation of 3.9 ft maximum subsidence instead of 5.0 ft. This was derived from using the best estimate of the average hard percentage of rock equal to 37%. The discrepancy between predicted maximum subsidence factors and those based on measured data is illustrated in Figure 3-4. In an informal talk with a specialist working for one of the coal companies in the area of concern, we learned that a rule of thumb for the typical value of maximum subsidence factor in the area of concern is equal to 0.67. The average value calculated by the Pitt team is 0.68, with values as high as 0.74 and as low as 0.61. The agreement between our data and the vast

experience of many subsidence cases for the area leading to the reference value of 0.67 contrasts sharply with the SDPS prediction of 0.53.

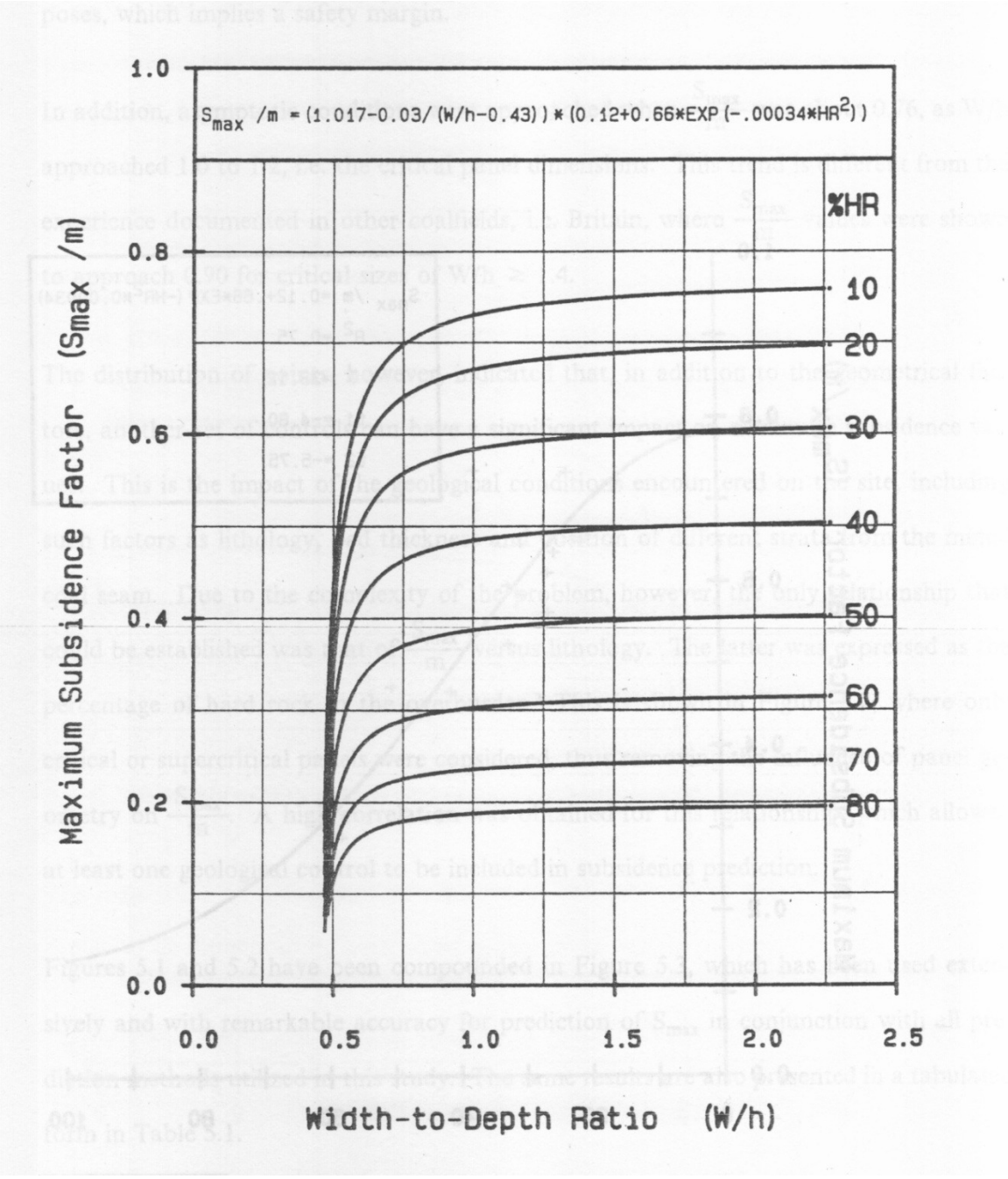

Figure 3-1 SDPS maximum subsidence model

(Karmis 1987)

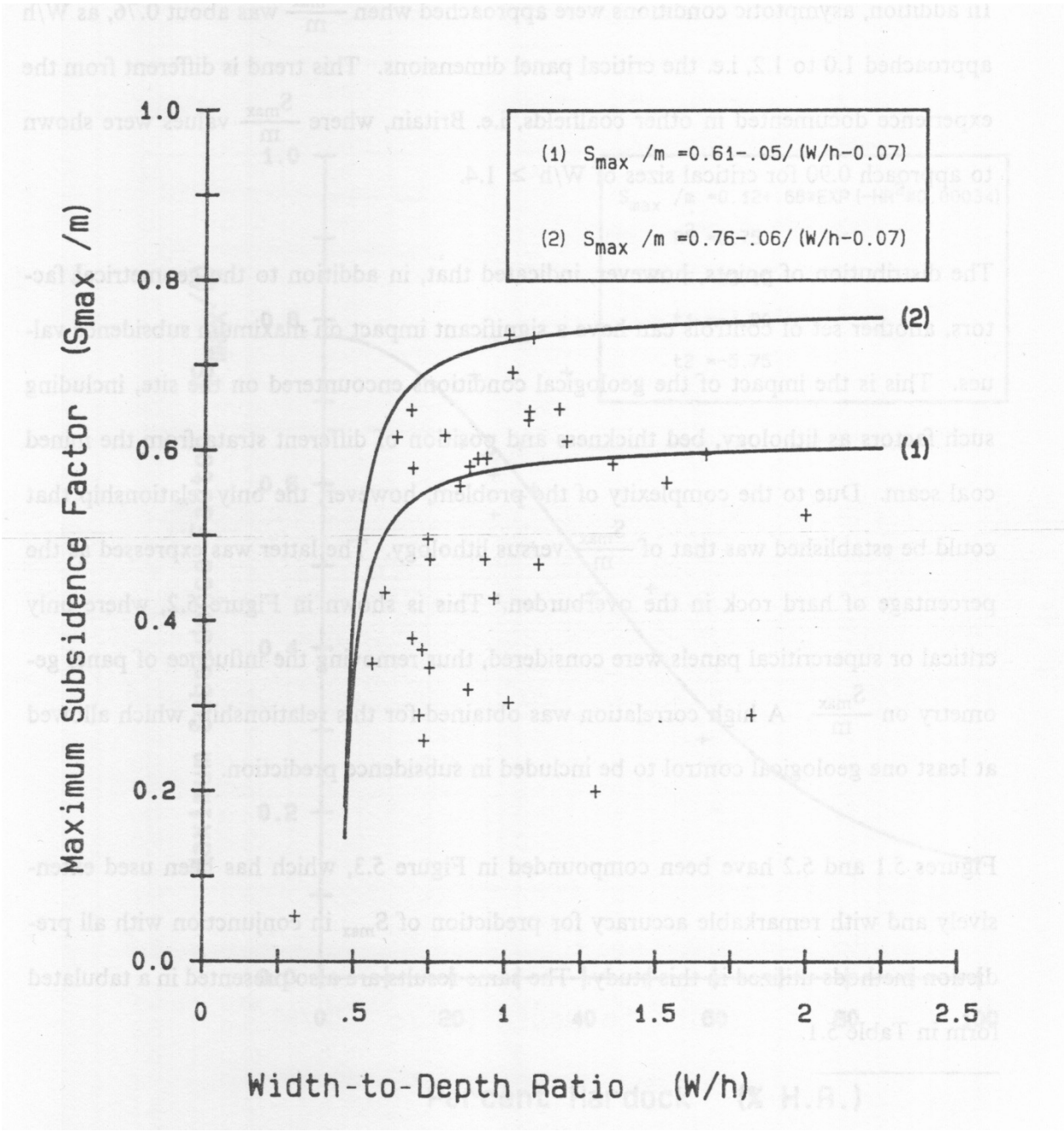

Figure 3-2 SDPS maximum subsidence factor as a function of geometry

(Karmis 1987)

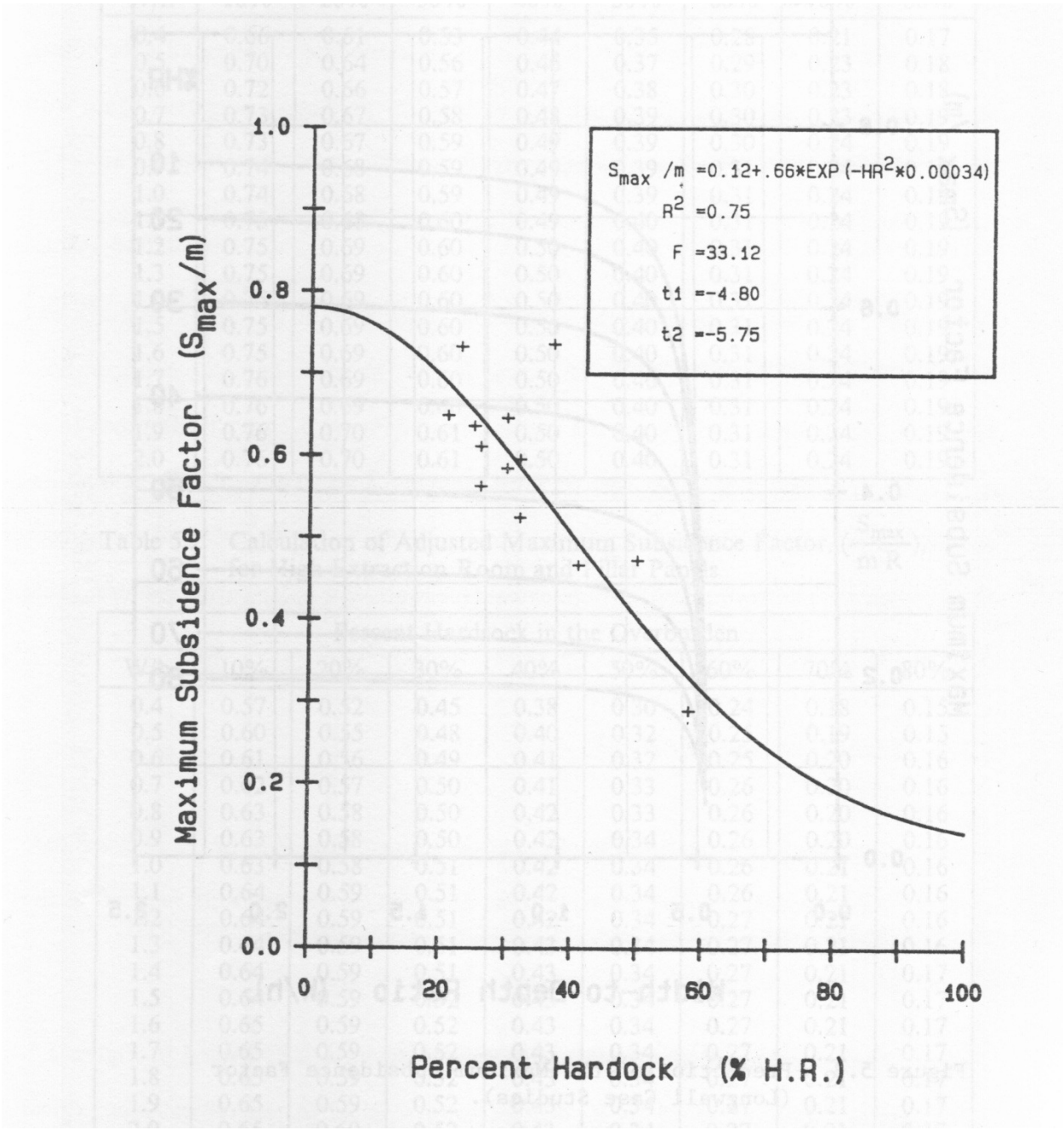

Figure 3-3 SDPS maximum subsidence factor as a function of geology

(Karmis 1987)

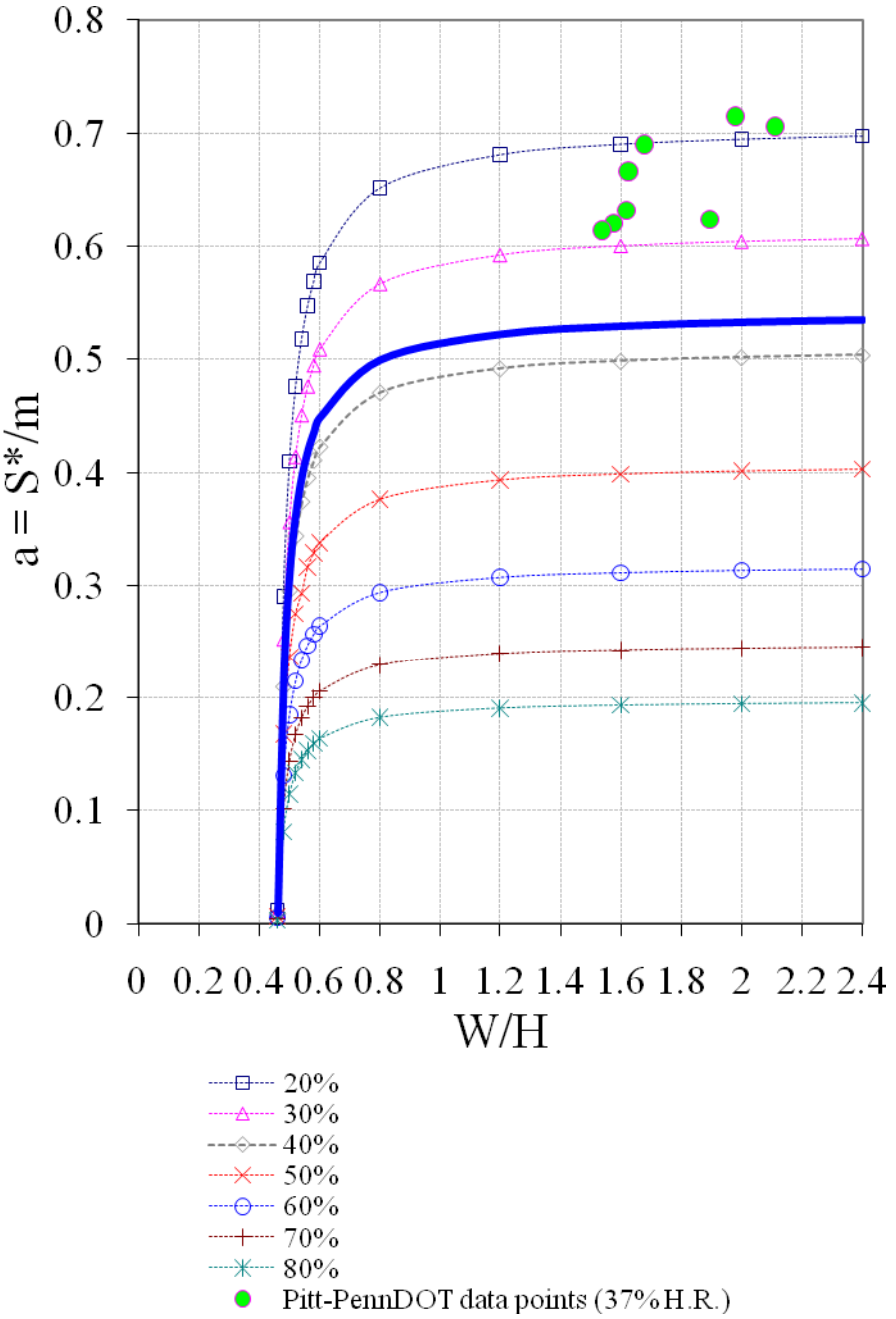

Figure 3-4 Discrepancy between measured maximum subsidence factors and SDPS prediction

The last column in Table 2-1 shows that the ratios *W/H* in all panels we studied far exceed the threshold of 1.2 which has been proposed in SDPS as a threshold that settlement ratio becomes almost constant. In other words, *W/H* of 1.2 is being used in SDPS as the criterion to determine whether a subsidence profile is subcritical (<1.2) or supercritical (>1.2). Since hard rock percentage for the area of the project is a constant, predictions based on the SDPS maximum subsidence model would basically return a more or less constant factor (flat portion of the branch of the SDPS nomogram corresponding to 37%). However, *S*/M* values of the data being studied do not seem to be constant or nearly constant, as can be read from Table 2-1. Rather, a trend was found to exist between the maximum subsidence factor and the overburden depth, *H*, as shown in Figure 3-5. The deeper the mine panel, the less subsidence is to be expected.

The use of the ratio *W/H*, as SDPS does, fails to account for the direct influence the overburden depth *H* has on the magnitude of maximum subsidence. The problem of the SDPS approach to relate maximum subsidence factor to the ratio of *W/H* is illustrated in the following example. Consider two cases that have a similar *W/H* value (such as LW-50 and LW-52), one should expect that the overburden depth, *H*, itself influences the magnitude of maximum subsidence as long as the geology remains the same. Figure 3-6 and Figure 3-7 are further illustrations that help to demonstrate how SDPS fails to account for the direct influence the overburden depth has on the magnitude of maximum subsidence. SDPS would predict the same maximum subsidence in the two cases of Figure 3-6 where *W/H* ratios are the same, while our observations indicate that a lesser maximum subsidence results from the deeper mine panel of Figure 3-7.

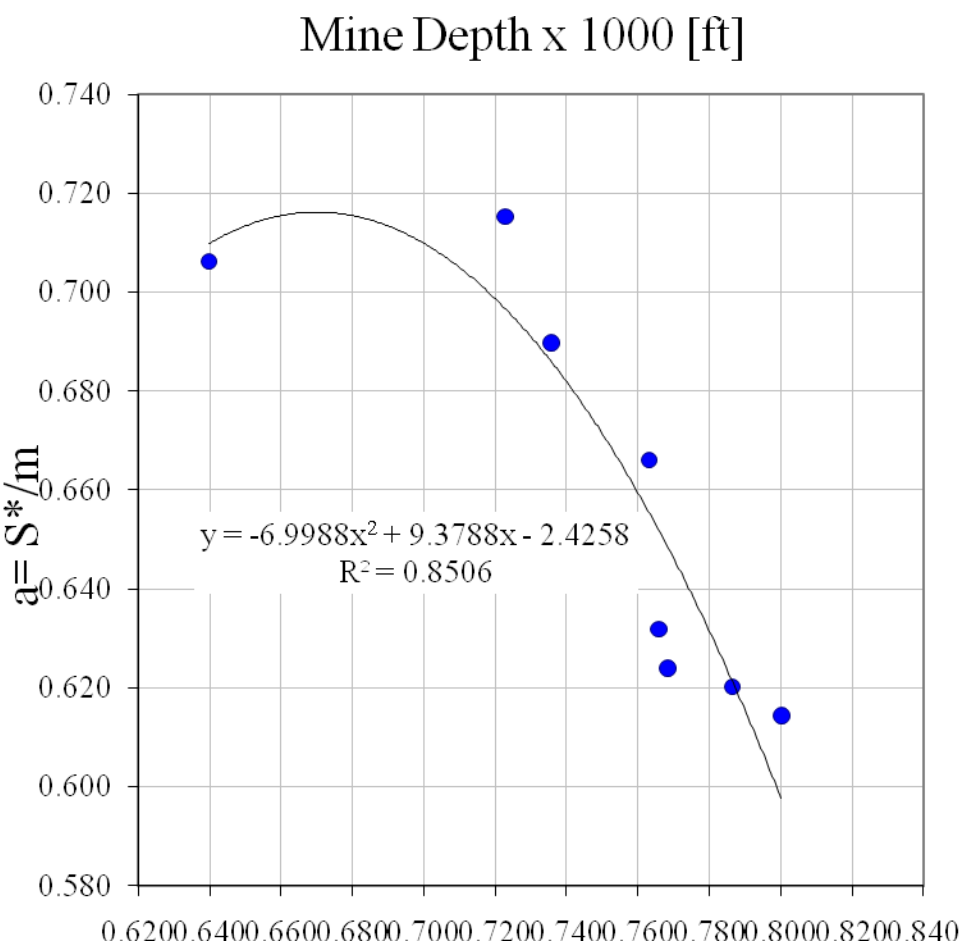

Figure 3-5 Pitt-PennDOT model for maximum subsidence factor prediction

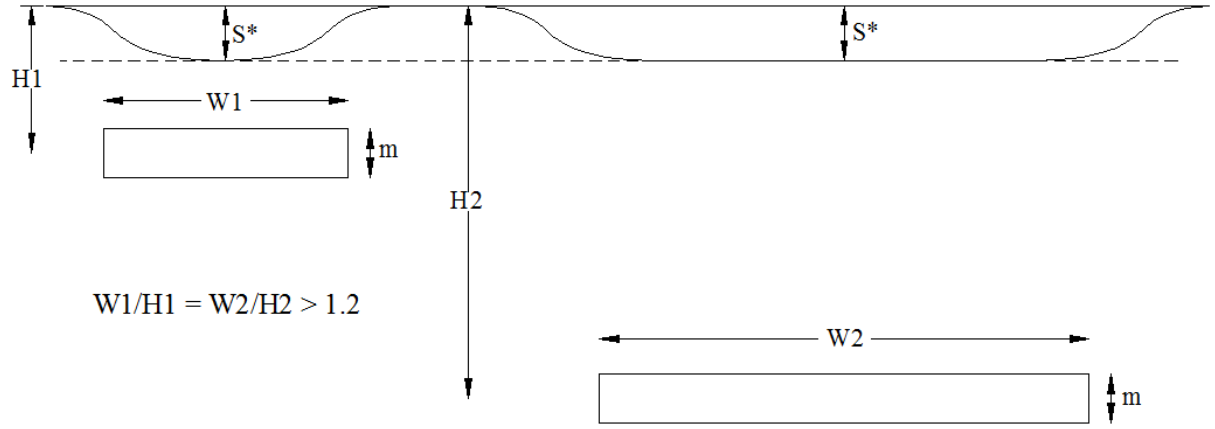

Figure 3-6 Schematic depiction of SDPS prediction of maximum subsidence (same geology)

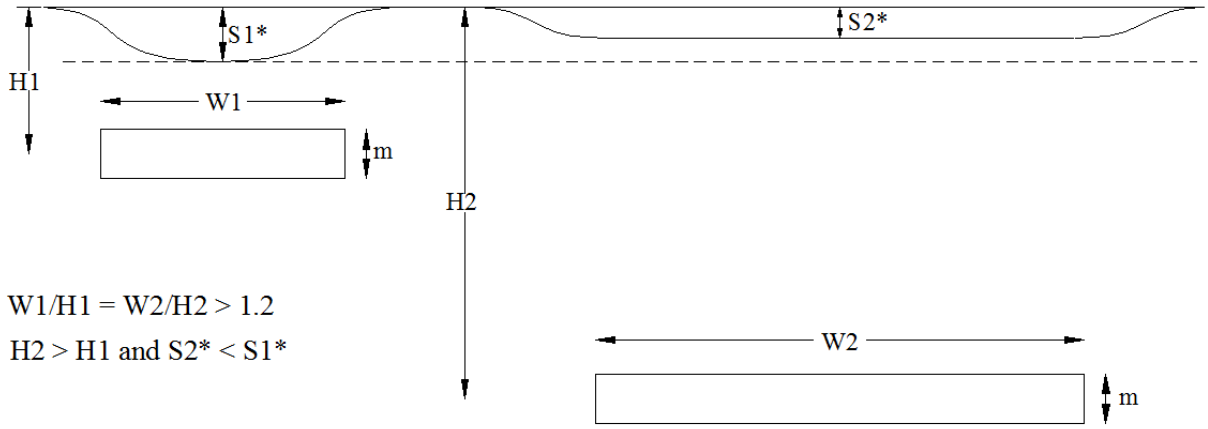

Figure 3-7 Schematic depiction of empirical maximum subsidence prediction (same geology)

In general, the maximum subsidence estimation is a very important first step for any empirical prediction approach, whether it is of the profile function or influence function type. The magnitude of maximum subsidence affects the magnitude of the whole profile and the subsequent indices that can be derived from it, such as slope, curvature, horizontal deformation, and strain estimations. Therefore, a poor estimation of maximum subsidence affects not only the

estimation of deformation, but all the useful index estimations that may be derived from it, which are truly the ultimate purpose of subsidence prediction. Fortunately, a simple empirical relationship like the one we developed as depicted in Figure 3-5 can be used in overcoming the limitation and makes it possible to use SDPS and take advantage of its useful features, such as indices prediction, graphical visualization, tabular outputs, and compatibility with useful CAD tools.

3.1.2 Theory behind SDPS profile function method

The SDPS profile function method is based on a hyperbolic function that defines the shape of the profile as follows:

$$S = 0.5S^* \left[1 - \tanh\left(\frac{cx}{B} \right) \right] \qquad 3\text{-}1$$

where

S^* = maximum subsidence

c = 1.8 for critical and supercritical profiles, 1.4 for subcritical profiles

x = distance from the inflection point (positive towards the rib)

B = distance from the inflection point to the point with maximum subsidence

The nature of the hyperbolic tangent function is such that the maximum subsidence, S^*, is not located at the center of a panel. This is particularly so for subcritical profiles. A correction is therefore needed for maximum subsidence, given by:

$$S'_{\max} = \frac{S^*}{S_{center}} S^* \qquad 3\text{-}2$$

where

S'_{max} = corrected maximum subsidence

S_{center} = magnitude of subsidence at panel center before correction

S^* = estimated maximum subsidence

The distance B from the inflection point to the point of maximum subsidence is obtained using the fact that critical conditions occur when $W/H = 1.2$. Based on this threshold, the distance between the rib and the point of maximum subsidence is equal to $0.6H$ (or half $1.2H$). All that remains to be known in order to estimate B is the distance between the rib and the inflection point (edge effect), which is obtained from Figure 3-8. B is then given by:

$$B = 0.6H - d \qquad 3\text{-}3$$

where

B = distance between inflection point and point of maximum subsidence

d = distance between the rib and the inflection point

H = overburden depth

The SDPS profile function that accounts for a corrected maximum subsidence magnitude, the edge effect (given by the parameter d) and with $x = 0$ being at the panel center instead of at the inflection point, is then given by:

$$S(x) = 0.5S'_{\max}\left\{1 - \tanh\left[\frac{c(x - 0.5W + d)}{B}\right]\right\} \qquad 3\text{-}4$$

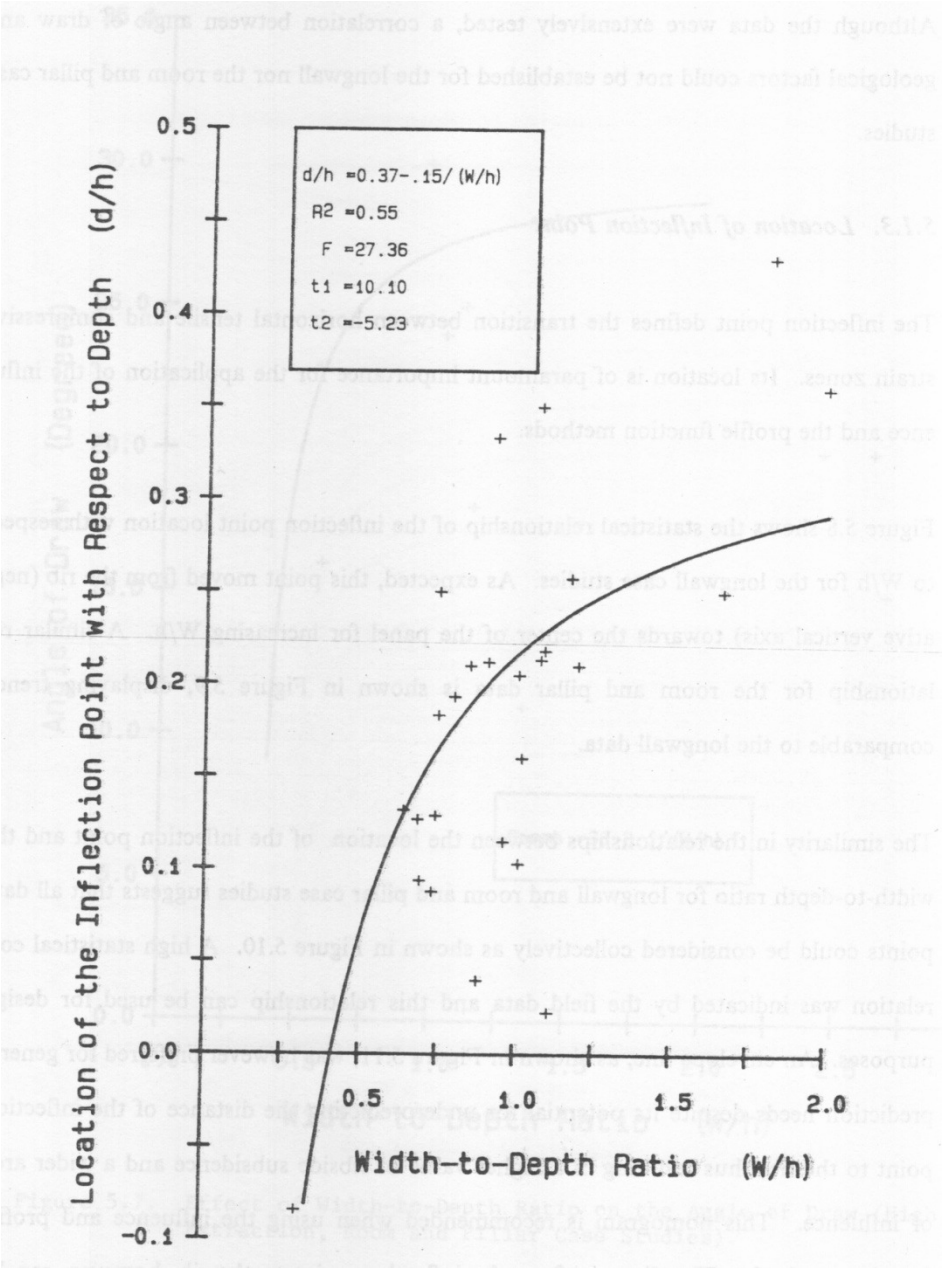

Figure 3-8 SDPS nomogram for inflection point location

A step-by-step procedure for longwall subsidence prediction using SDPS profile function (Karmis 1987) is as follows:

1. Input *m*, *W*, *H*, *% H.R.*
2. Estimate $S^* = S^*(m, W, H, H.R.)$ and $d = d(W, H)$
3. If $W / H \geq 1.2$, then use $c = 1.8$, else $c = 1.4$
4. If $W / H < 1.2$, then use $B = 0.5W - d$, else $B = 0.6H - d$
5. $x' = x - 0.5W + d$
6. $$S'_{\max} = \frac{S^*}{S_{center}} S^*$$
7. $$S(x) = 0.5S'_{\max}\left[1 - \tanh\left(\frac{cx'}{B}\right)\right] = 0.5S'_{\max}\left\{1 - \tanh\left[\frac{c(x - 0.5W + d)}{B}\right]\right\}$$

3.1.2.1 Screenshots of the step-by-step profile function procedure in SDPS 5.0

Screenshots of SDPS version 5.0 are included in this section in order to tutor the use of the profile function method. At the time this part of the work was performed, version 6.0. had not yet been released. However, we double-checked and found that the only difference between versions 5.0 and 6.0 was that 6.0 incorporated dynamic subsidence. Therefore, the static results obtained with either version are the same.

The important input parameters are required in the Project Parameters menu, which contains both the Subsidence Parameters required to perform the calculations and the Output Options (see Figure 3-9 and Figure 3-10). Figure 3-9 contains the Subsidence Parameter window where the basic geometry and geology parameters need to be input. The hard rock percentage *H.R.* used was equal to 37%. A zero-subsidence definition is required in order to compute the

angle of draw. The user can define it as an absolute value (e.g. 0.001 ft) or as a percentage of maximum subsidence (e.g. 0.1% of S^*). The value of 0.001 ft has been used in the present report.

Conservative Profile and Average Profile are also options available in the input parameters as shown in Figure 3-9. The conservative profile is an envelope of the database, whereas the average profile is obtained as the mean of the database.

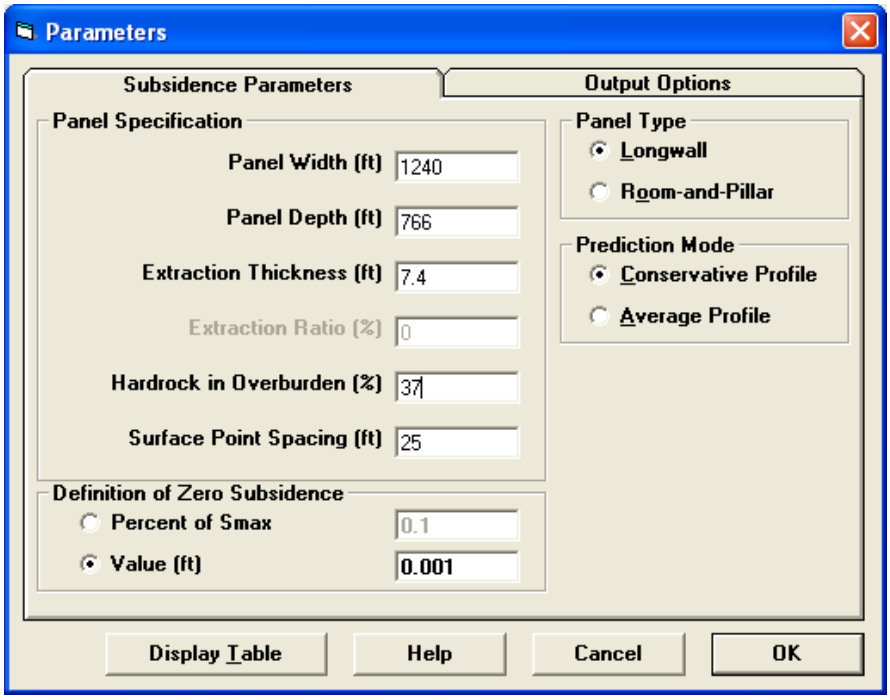

Figure 3-9 SDPS profile function parameter input

Figure 3-10 contains the window of Output Options, where it can be chosen between tabular or graphical output. Display of angles from rib at different values of subsidence approaching zero may be chosen. A typical graphical output display is shown in Figure 3-11, and a typical tabular output is displayed in Figure 3-12 and Figure 3-13, the latter figure showing the angles from the ribs, which are basically the angles of draw as the magnitude of subsidence approaches zero.

The predicted subsidence that resulted based on a hard rock percentage of 37% is underestimated if compared to the measured value which is close to 5.0 ft. This is a consequence

of the use of the default maximum subsidence model, as discussed in section 3.1.1. If the Pitt-PennDOT regression is used instead, a correct magnitude of maximum subsidence may be obtained. Figure 3-14 shows the parameter input with a lowered value of hard rock percentage equal to 23%, which was found by trial and error until the value *S*/m* (maximum subsidence over extraction thickness) matched 0.67 obtained with the Pitt-PennDOT regression. A comparison of the two cases before and after the correction is given in Figure 3-15. Figure 3-16 depicts a graphical display of subsidence and the angle of draw based on the 0.001 ft-zero-subsidence definition.

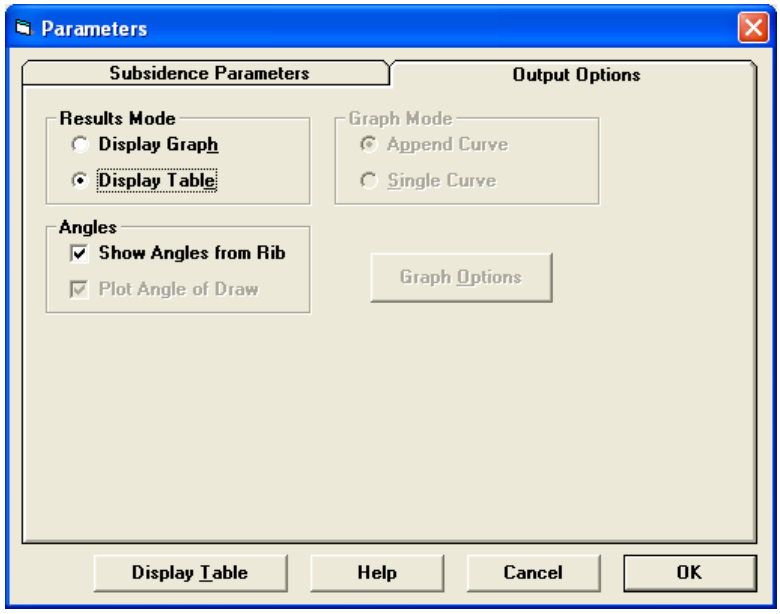

Figure 3-10 SDPS profile function output options menu

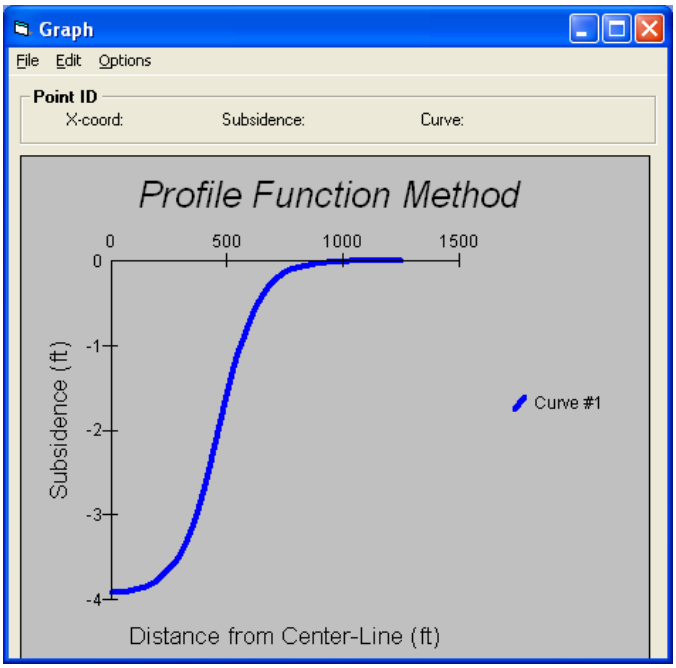

Figure 3-11 SDPS profile function half-panel graphical output

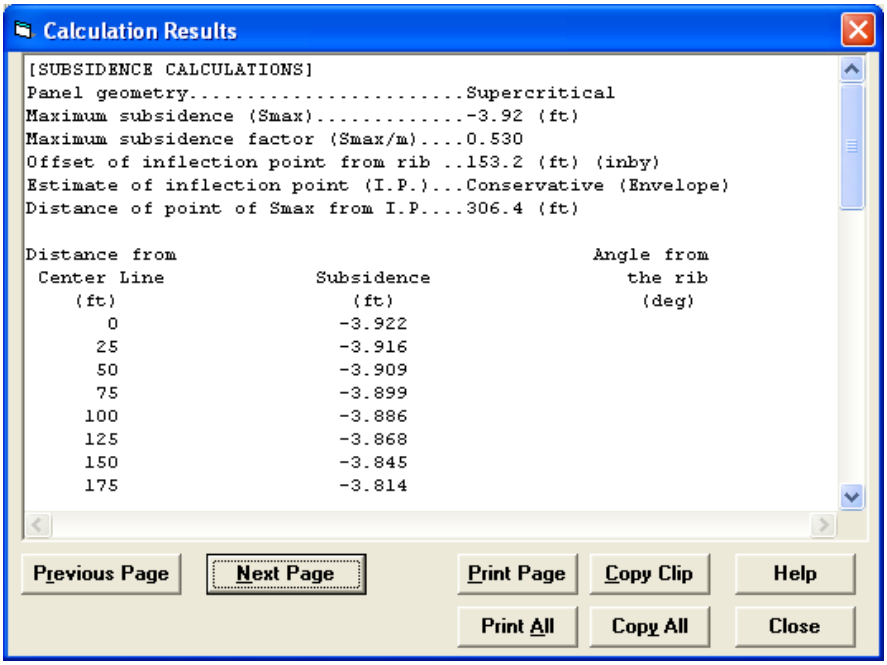

Figure 3-12 SDPS profile function tabular output

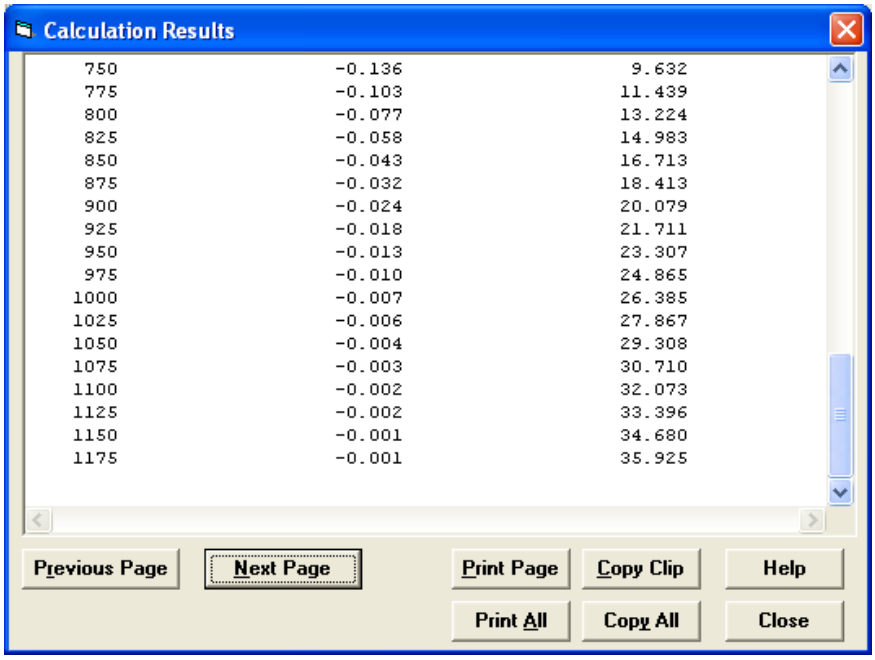

Figure 3-13 SDPS profile function tabular output showing angle of draw (lat row, last column)

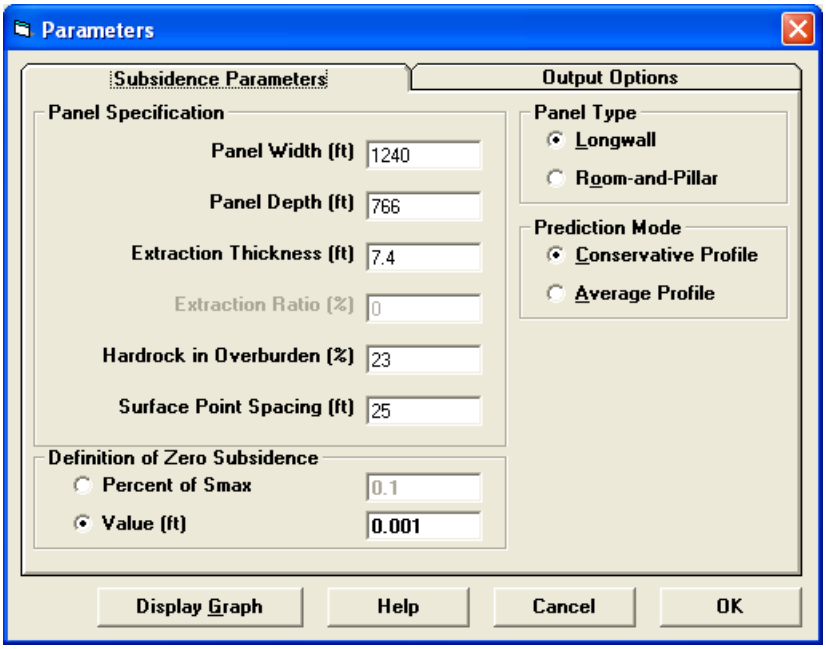

Figure 3-14 SDPS profile parameter input showing a lowered hard rock percentage of 23%

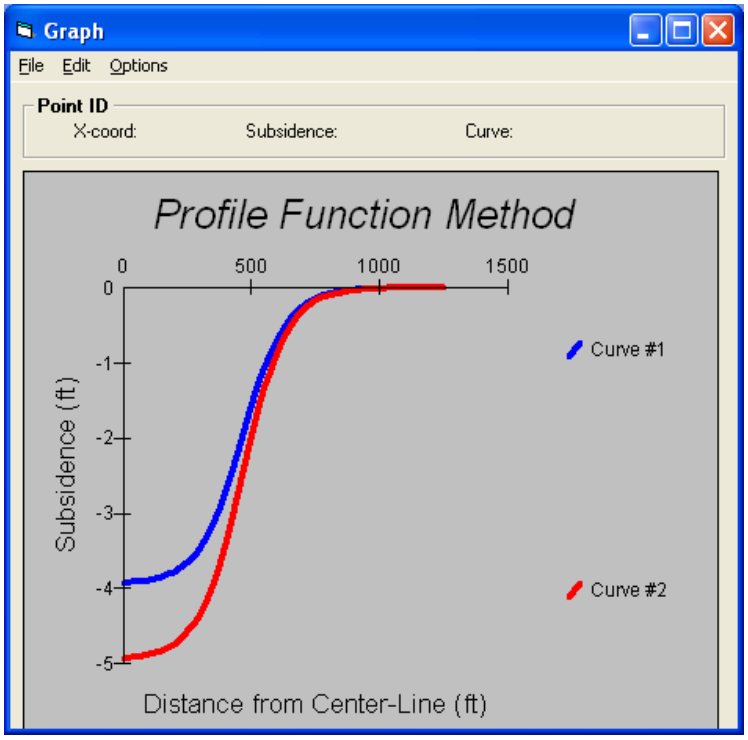

Figure 3-15 SDPS profile function graphical output showing both underestimated and correct predictions

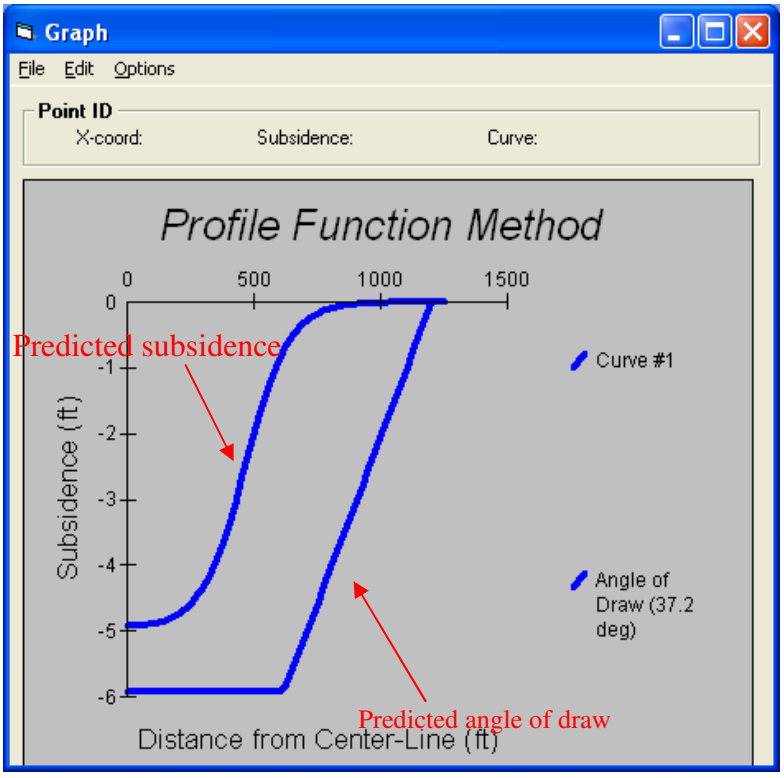

Figure 3-16 SDPS profile function graphical output and angle of draw

3.1.3 SDPS Influence Function Method

The SDPS also included another approach called the influence function method. It is used for three-dimensional subsidence prediction, as the influence function is expressed in terms of the two horizontal coordinates *x*, *y*, and the subsidence magnitude is the third dimension or vertical component.

The influence function utilized in SDPS is the bell-shaped Gaussian function employed in the Budryk-Knothe influence function method. The function is given by:

$$g(x, y, s, t) = \frac{1}{r^2} e^{-\pi \frac{(x-s)^2 + (y-t)^2}{r^2}} \qquad 3\text{-}5$$

where

x, y = location of an infinitesimal element of excavation

s, t = location of a point $P(s,t)$ where subsidence is considered

r = radius of principal influence, $r = \frac{h}{\tan \beta}$

β = angle of principal influence, complement of the angle of draw, γ

Subsidence at a point $P(s.t)$ can be expressed as a definite integral:

$$S(x, y, s, t) = \frac{1}{r^2} \iint_A S_O(x, y) e^{-\pi \frac{(x-s)^2 + (y-t)^2}{r^2}} dxdy \qquad 3\text{-}6$$

where

A = area of excavation

$S_o(x,y)$ = function of roof convergence of the excavation area

If the excavation area is of rectangular shape, the origins of the surface and the excavation area are common at *P*(0,0), and the convergence of the roof is constant and $S_O(x, y) = S*$, the above function can be expressed as:

$$S(x, y) = \frac{S*}{r^2} \int_{x1}^{x2} e^{-\pi \frac{x^2}{r^2}} dx \int_{y1}^{y2} e^{-\pi \frac{y^2}{r^2}} dy \qquad 3\text{-}7$$

A step-by-step procedure for longwall subsidence prediction using SDPS influence function may be summarized as:

1. Input percent *H.R.*, principal influence angle, β $(90° - \gamma)$, strain coefficient
2. Input coordinates, panel elevation, extraction thickness
3. Input prediction points
4. Estimate *S** = *S**(*m*, *W*, *H*, *H.R.*) and *d* = *d*(*W*, *H*) or input alternative *S*/m* factor
5. Calculate $r = \frac{H}{\tan \beta}$, where *r* is the radius of principal influence, *H* is the overburden depth, and β is the angle of principal influence.
6. Calculate subsidence using expression 3-7

The influence function method in SDPS can also provide estimates of deformation indices such as slope, curvature, horizontal deformation, and horizontal strain.

3.1.3.1 Screenshots of the step-by-step influence function procedure in SDPS 5.0

Screenshots of the process using the influence function method for prediction are presented herein. In the Project Description (Figure 3-17), a choice of units, type of mine, points of calculation, angle of influence, percent hard rock, and strain coefficient, can be made. Figure

3-18 shows the Mine Plan input, where the panel geometry can be defined. The influence function method in version 5.0 or 6.0 gives the user the choice to directly define a value of *S*/m* or calculate it automatically using the default maximum subsidence model discussed in detail in section 3.1.1. This option is convenient as it lets the user define an alternative value of *S*/m*, in which case the hard rock percentage value is not taken into account in the calculations. The Mine Plan menu also has Adjustment Options, which refer to edge adjustments.

Adjustments of edge effect are required in SDPS influence function method because it would return a value of subsidence exactly equal to half maximum subsidence at the edge. This basic output of the influence function is illustrated in Figure 3-27 together with the shifted version accounting for the edge effect. SDPS 5.0 or 6.0 have three options to deal with the edge effect. One option is to adjust automatically. A second option is to adjust manually, and a third option is to not adjust.

Prediction points can be set up considering the needs of a project and taking into account that some adjustments to account for the edge effect are required. The SDPS edge effect calculation option returns the magnitude the profile or trough needs to be shifted toward the center of the panel. Accordingly, the user needs to account for the calculation boundaries. The Prediction Points menu is depicted in Figure 3-19.

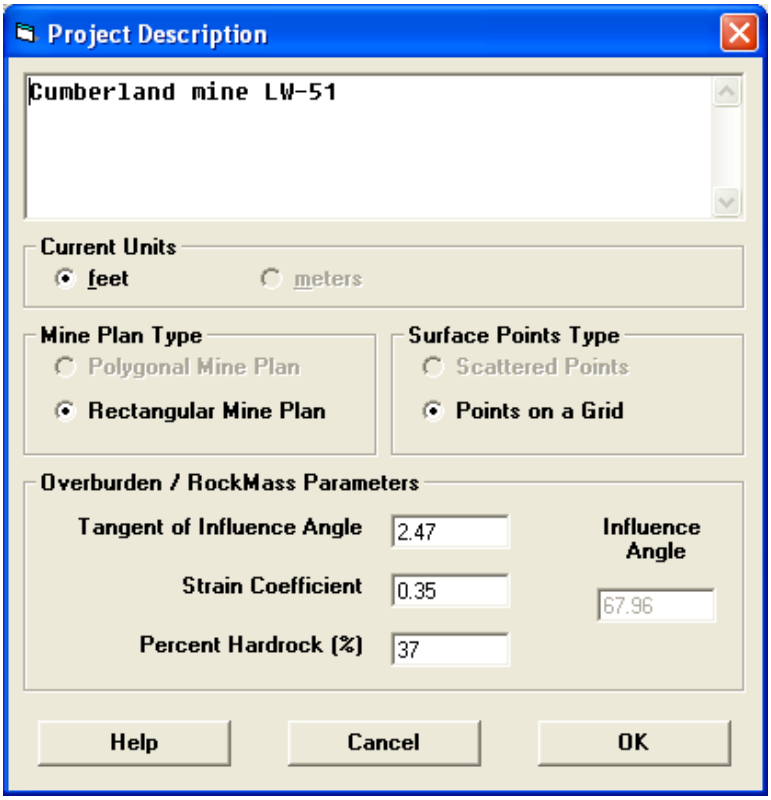

Figure 3-17 SDPS influence function project description input

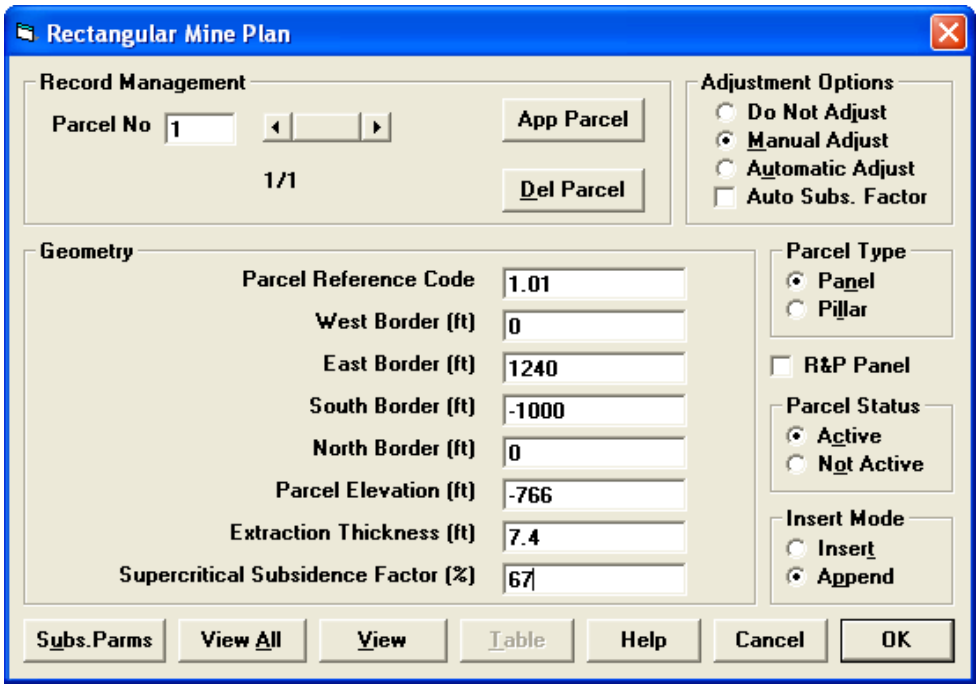

Figure 3-18 SDPS influence function mine plan input

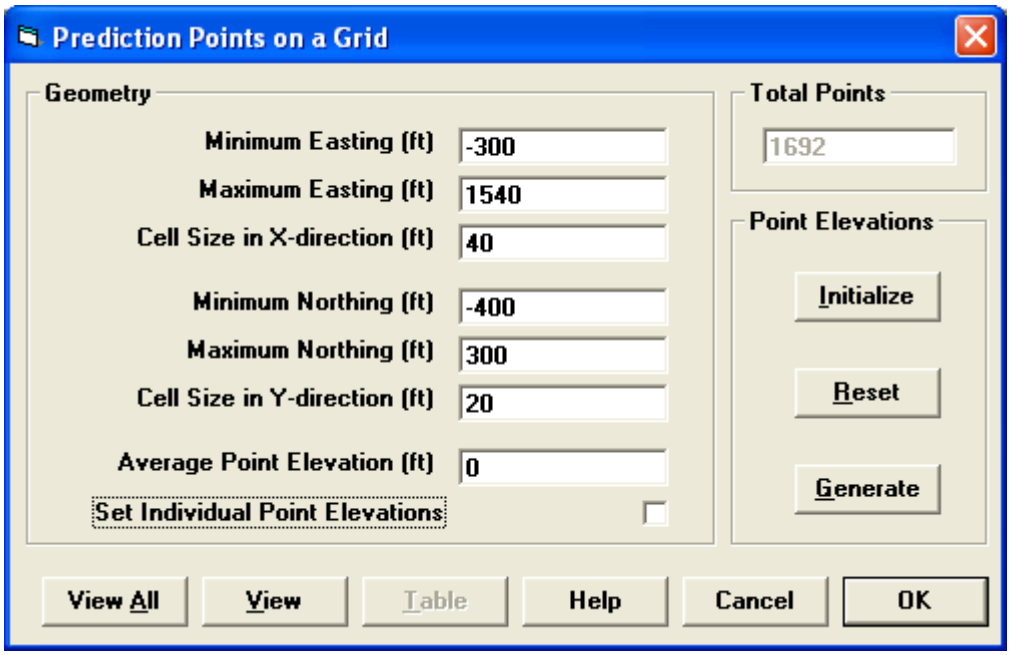

Figure 3-19 SDPS influence function prediction points input

Figure 3-20 shows the output options where the desired deformation indices are selected. In this report, the main concern is subsidence magnitude, but as discussed in chapter 1.0 of this report, the slope, curvature, horizontal displacement, and horizontal strain may also be obtained. Other output options such as *X*, *Y*, *Z* data output, headers, and files that need to be generated may be selected in this window.

A tabular *X*, *Y*, *Z* output is shown in Figure 3-21. Figure 3-22 shows the graph module that is linked to the influence function method and several display options. Figure 3-23 shows the resulting trough in 2D, where maximum or final subsidence profiles are far away from mine face position and the deformations decrease toward the mine face. Figure 3-24 and Figure 3-25 are

3D plots that may be rotated. Figure 3-26 shows the edge effect calculation option, which is based on Figure 3-8.

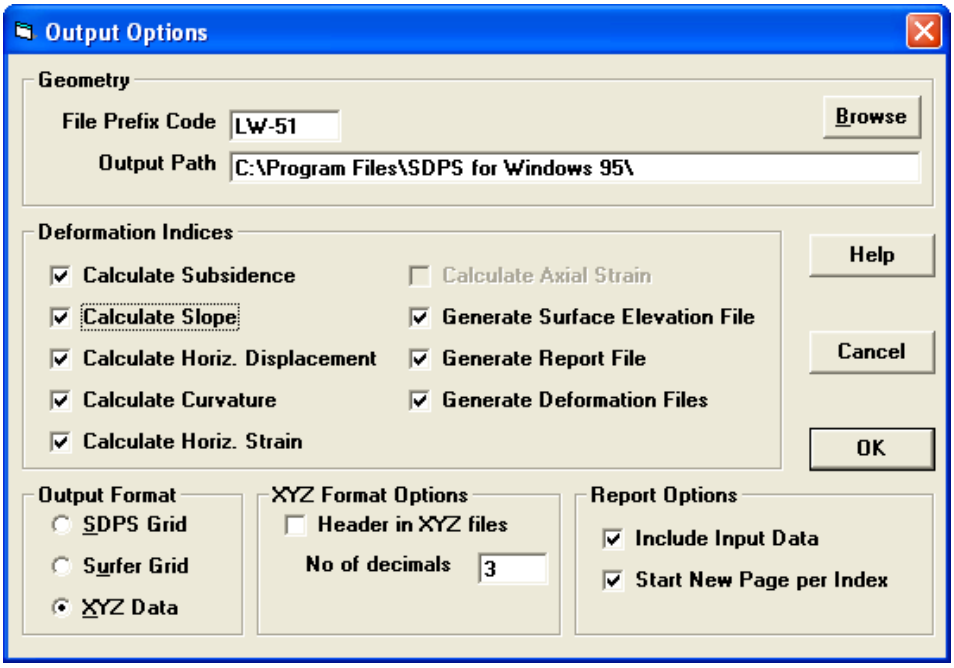

Figure 3-20 SDPS influence function output options menu

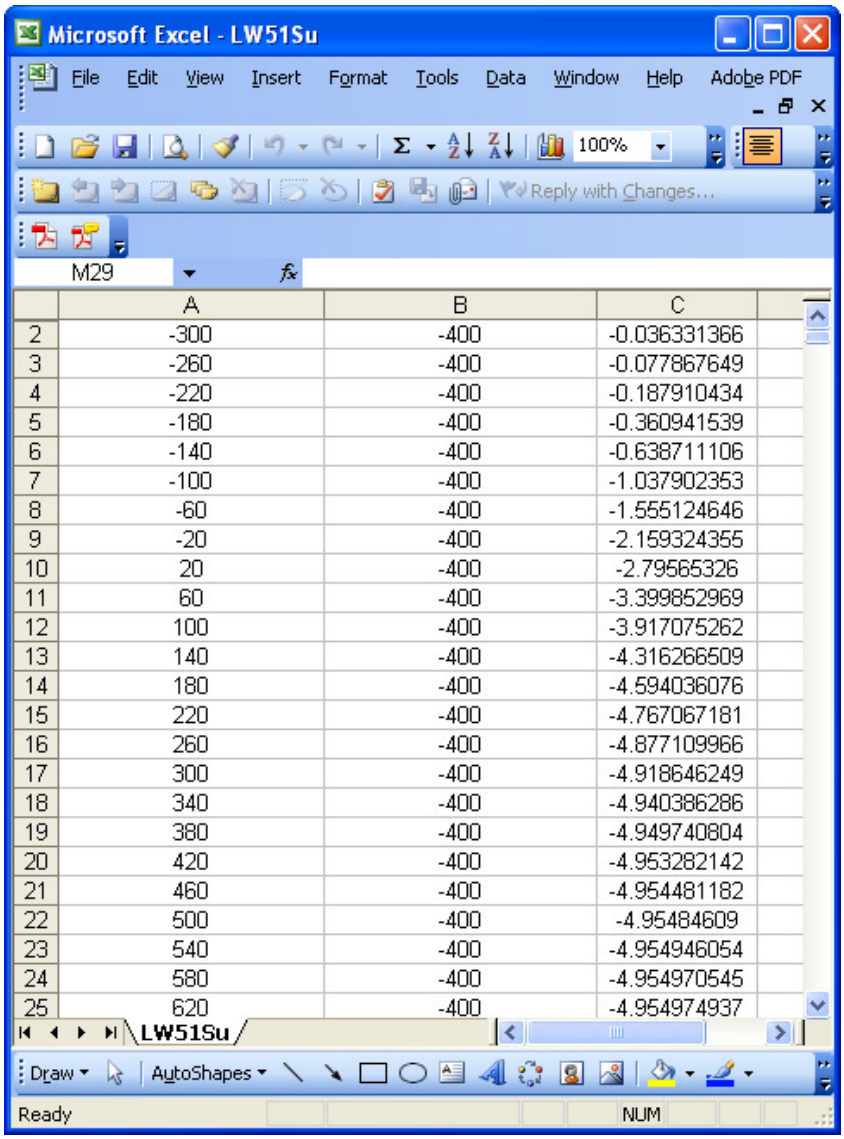

	A	B	C
2	-300	-400	-0.036331366
3	-260	-400	-0.077867649
4	-220	-400	-0.187910434
5	-180	-400	-0.360941539
6	-140	-400	-0.638711106
7	-100	-400	-1.037902353
8	-60	-400	-1.555124646
9	-20	-400	-2.159324355
10	20	-400	-2.79565326
11	60	-400	-3.399852969
12	100	-400	-3.917075262
13	140	-400	-4.316266509
14	180	-400	-4.594036076
15	220	-400	-4.767067181
16	260	-400	-4.877109966
17	300	-400	-4.918646249
18	340	-400	-4.940386286
19	380	-400	-4.949740804
20	420	-400	-4.953282142
21	460	-400	-4.954481182
22	500	-400	-4.95484609
23	540	-400	-4.954946054
24	580	-400	-4.954970545
25	620	-400	-4.954974937

Figure 3-21 SDPS influence function results file X, Y, Z as viewed using Excel

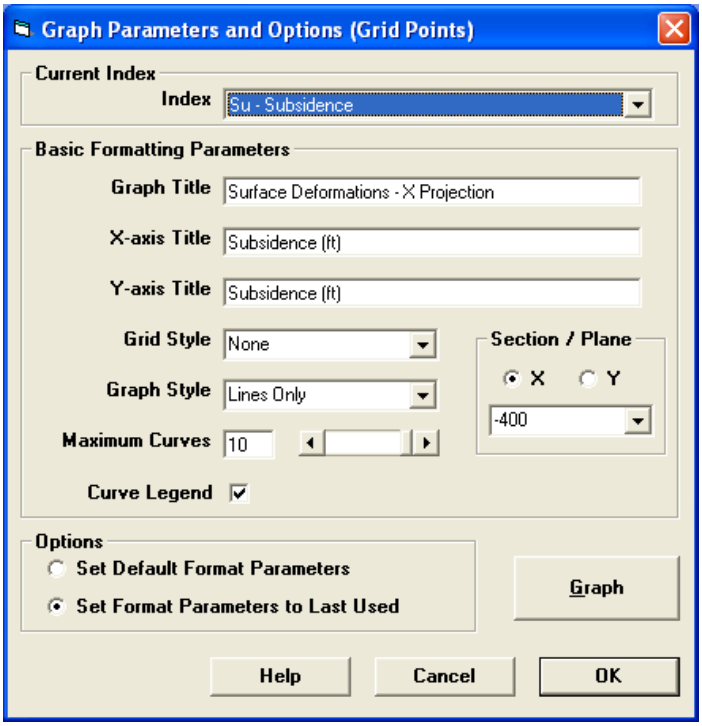

Figure 3-22 SDPS influence function graphing options menu

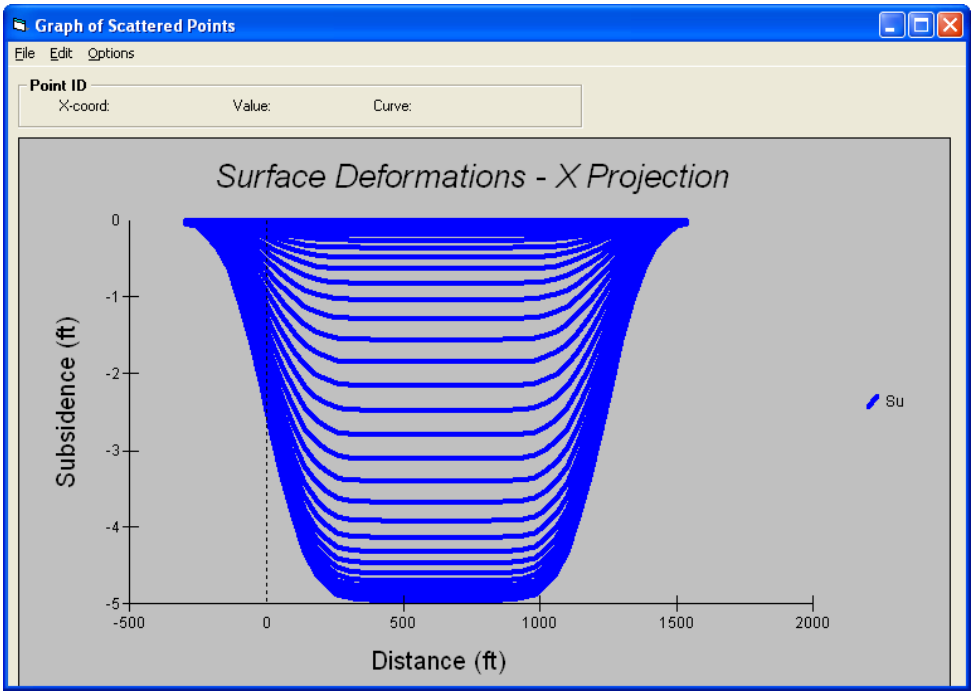

Figure 3-23 SDPS 2D graph showing example LW-51 from maximum subsidence toward mine face

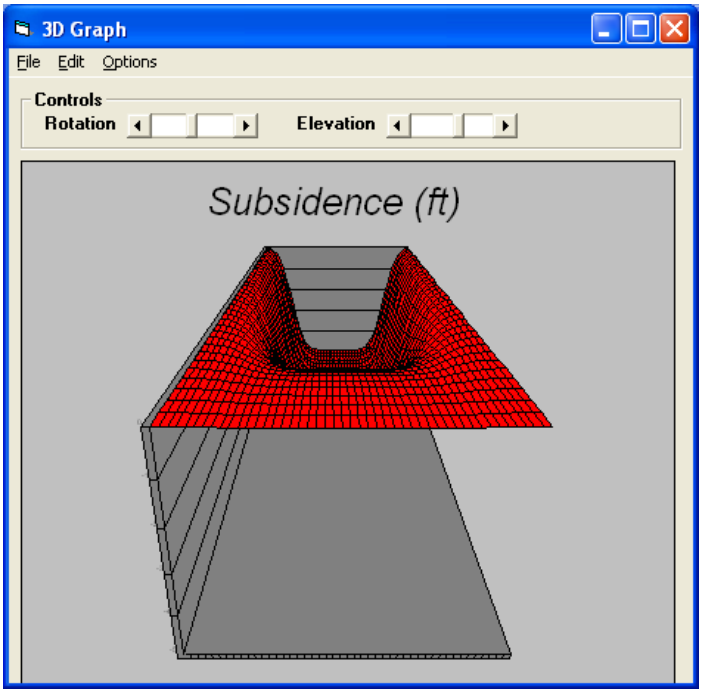

Figure 3-24 SDPS 3D graph showing example LW-51 (from mine face toward maximum subsidence)

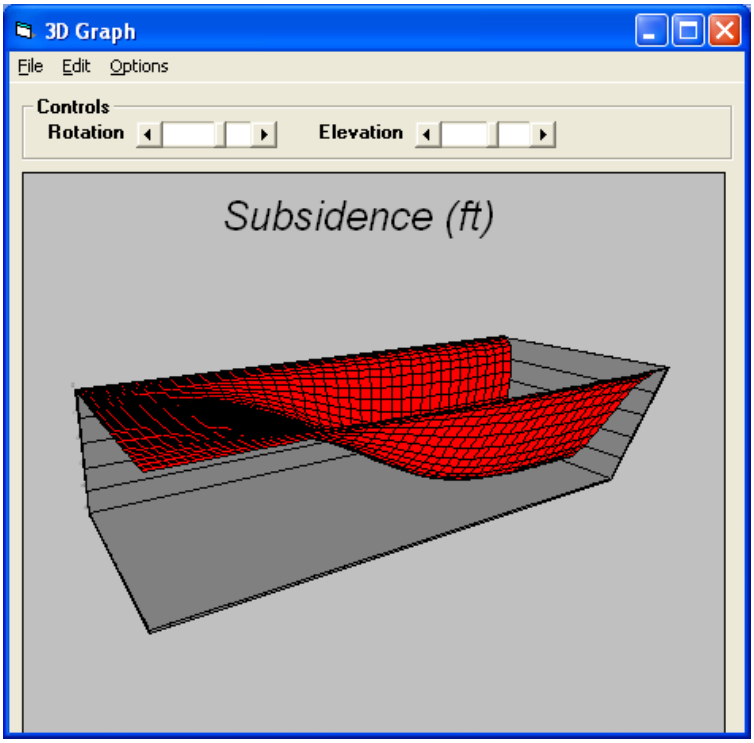

Figure 3-25 SDPS 3D graph showing example LW-51 (mine face on the left)

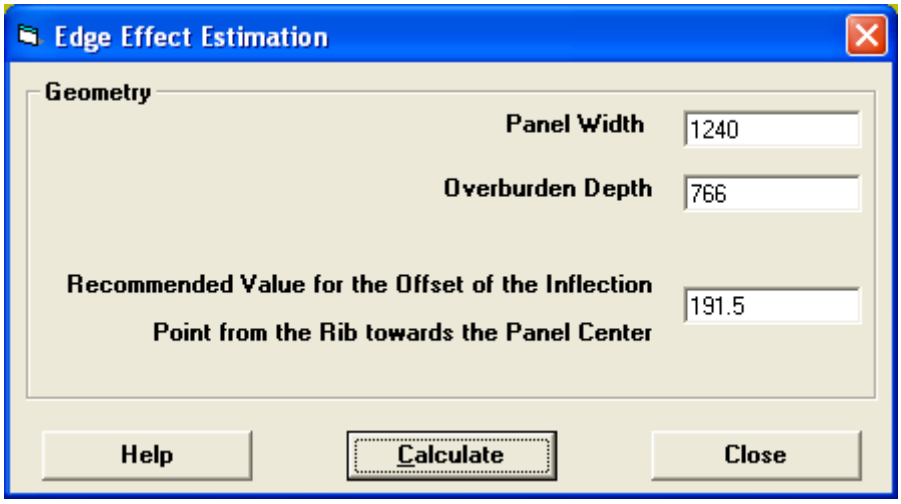

Figure 3-26 SDPS edge shift estimation

3.1.3.2 Edge effect adjustments in SDPS

The profile function method directly accounts for the edge effect in the profile function, as shown in section 3.1.2, but the influence function method produces the result depicted in Figure 3-27 with the example labeled as "SDPS LW-51 Influence F", where the result needs to be shifted to adjust for edge effect. A feature of influence functions, given its mathematical nature, is that subsidence at the edge is exactly equal to half of the maximum subsidence. Therefore, an edge correction is required in order to successfully reproduce the actual shape of the trough in the vicinity of the edges. It has been shown that according to SDPS 5.0. and 6.0., a set of adjustment options have been apparently included in the software that basically let the user choose between automatic adjustment, manual adjustment and no adjustment. The series labeled "SDPS LW-51 Influence F shifted" in Figure 3-27 corresponds to post-processed data after reading the value of adjustment that is produced in the edge effect option depicted in Figure 3-26.

We were particularly interested in the case when there are two panels located close to each other. As an illustrating example we look at two adjacent panels LW-52 and LW-51. The legend in Figure 3-28 shows how the "no adjustment" option from SDPS returns the profile with half-maximum subsidence at the edges. Since the middle between the two panels is in the intersection of the two zones of influence, SDPS accounts for the interaction and predicts a lesser magnitude of subsidence than at either external edge.

Figure 3-28 shows how the edge adjustment was carried out. In this particular problem, the interaction between the two panels is not strong according to SDPS. This can be appreciated in the difference in subsidence magnitudes between the left and right edges of either panel being almost negligible in contrast with the measured data, which shows that the right side edge undergoes substantially higher subsidence than the left one. However, the large difference in subsidence showed by the measured data is affected by the deformation and failure of the coal pillars left in place between the two panels, a factor that is not accounted for in the influence functions.

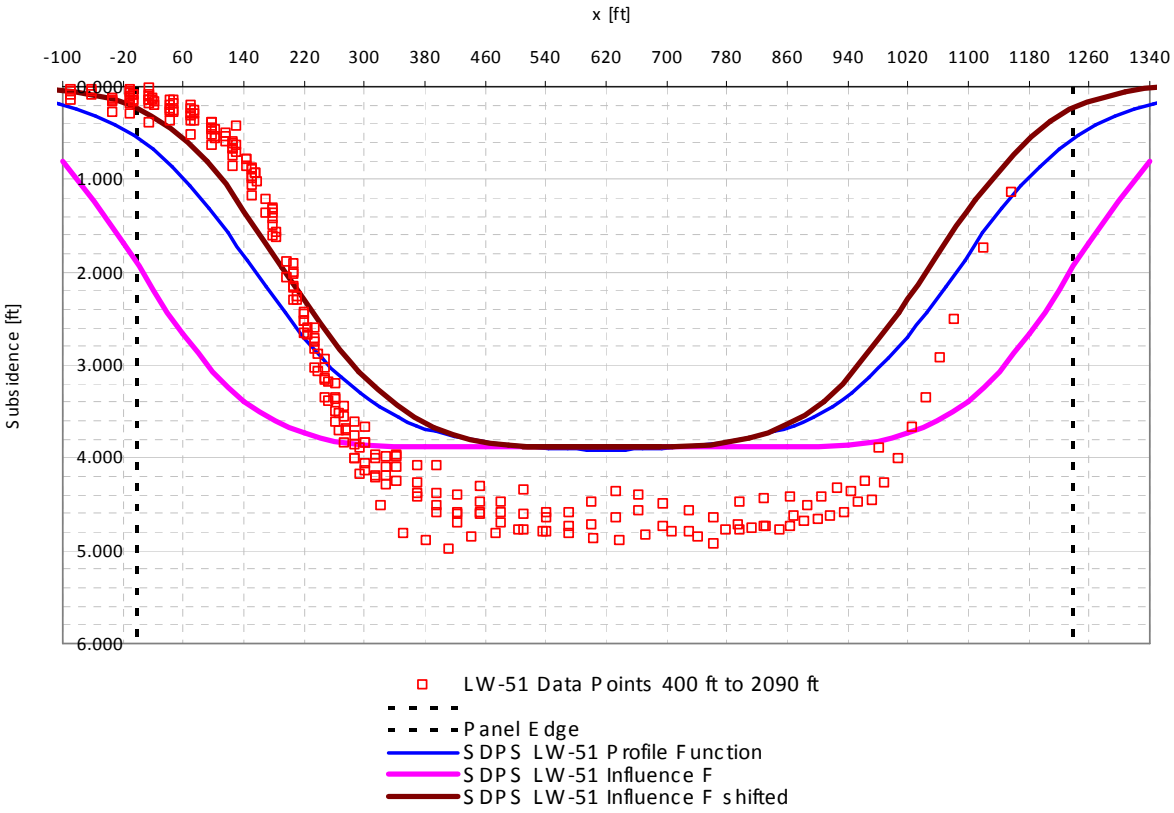

Figure 3-27 SDPS LW-51 output using default S*/m model embedded in SDPS

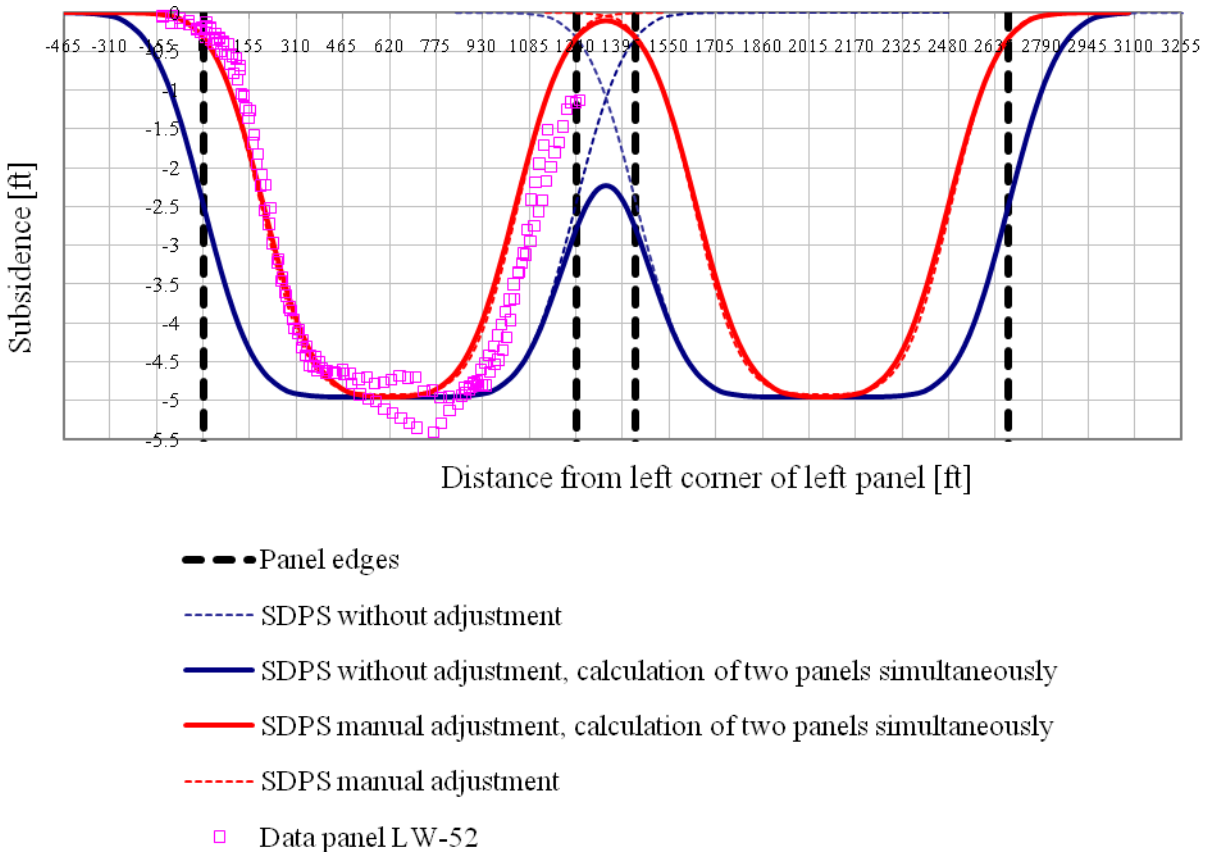

Figure 3-28 SDPS simultaneous calculation of two panels using influence function method

3.2 SDPS PREDICTION OF SUBSIDENCE IN THE GREENE COUNTY

This section deals with a graphical depiction of SDPS final subsidence predictions comparing the predictions obtained when the default maximum subsidence model is used and those using the alternative maximum subsidence model that we proposed. The legends are consistent for Figure 3-29 through Figure 3-33. What is apparent from these figures is that a prediction using the default maximum subsidence model of SDPS introduces error, which has been discussed before

and whose magnitude would be underestimated by 22% on average. Once the alternative maximum subsidence model we proposed is used, the SDPS predictions are substantially improved:

- The shifted influence function profile and the average profile function profile are very close to each other and to the data they are expected to predict.
- The conservative profile function profile is below the other predictions, consistently with the fact that it accounts for the database envelope.
- The data may be asymmetric, a feature that SDPS cannot deal with, as opposed to the potential capabilities of the Pitt-PennDOT approach, which we introduce later in this report.

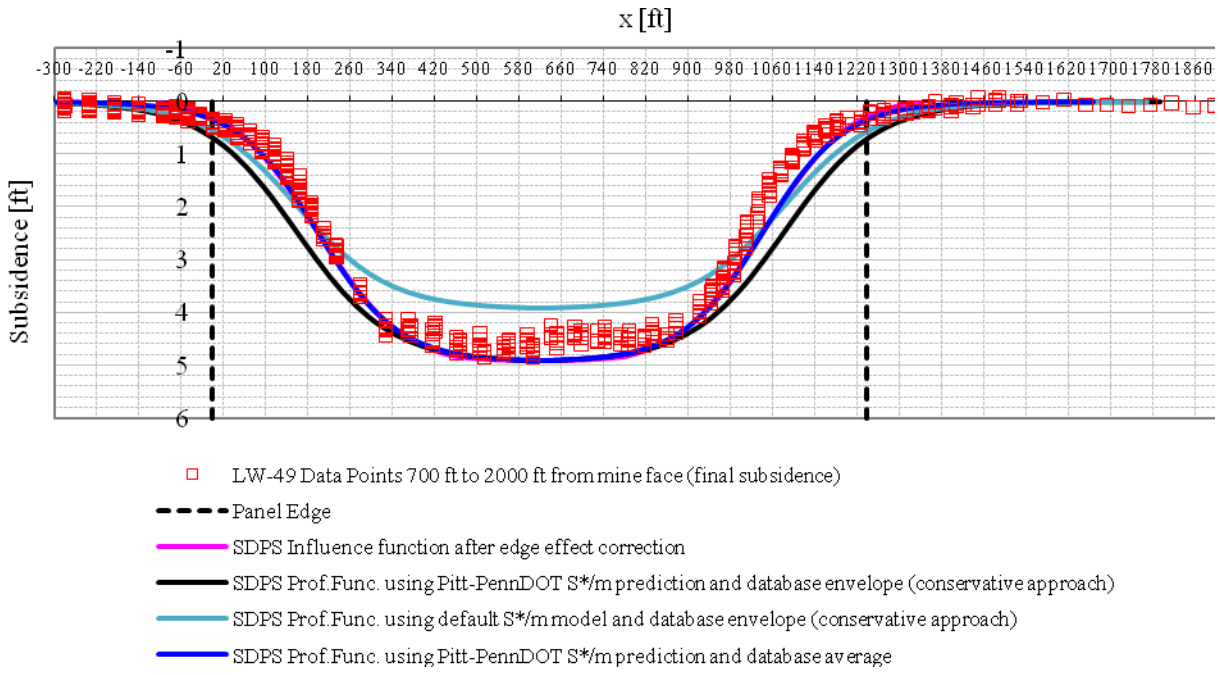

Figure 3-29 SDPS transversal view of prediction of final subsidence for LW-49

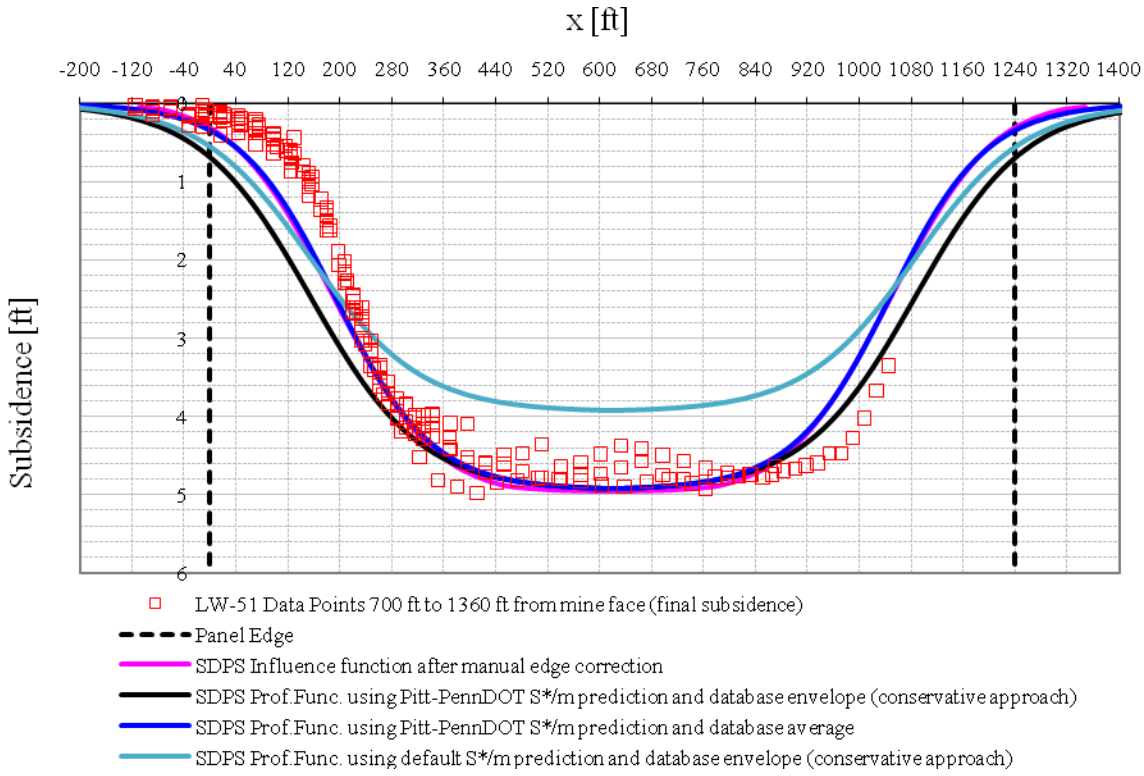

Figure 3-30 SDPS transversal view of prediction of final subsidence for LW-51

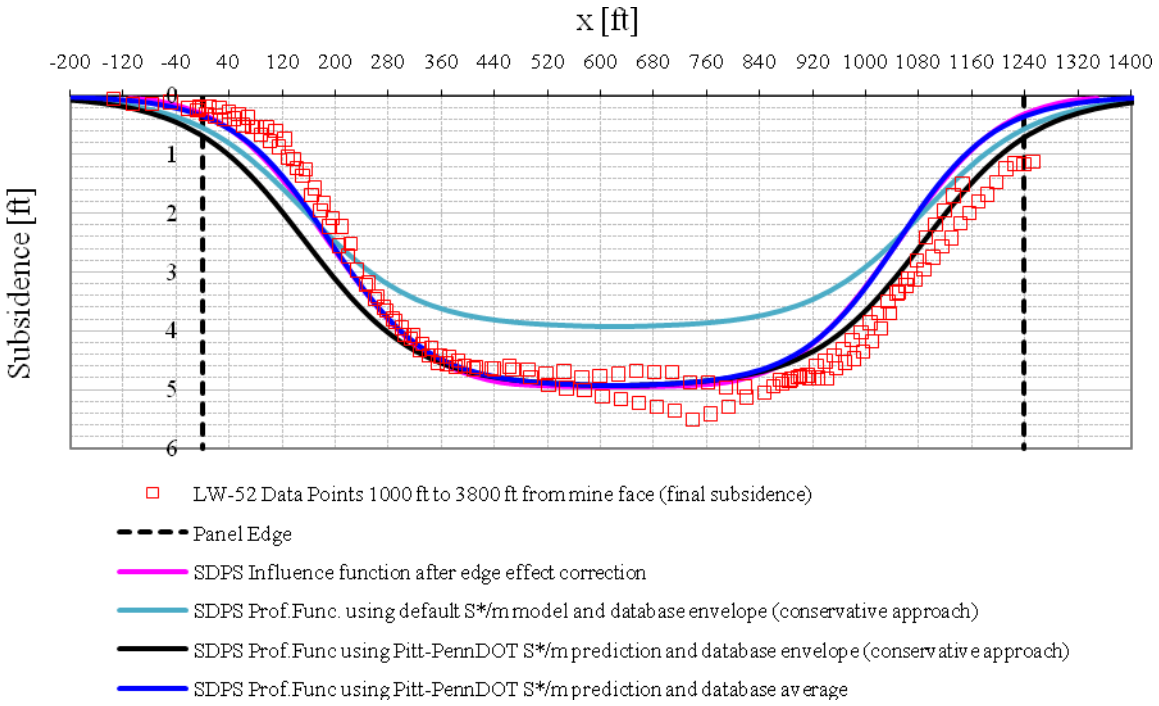

Figure 3-31 SDPS transversal view of prediction of final subsidence for LW-52

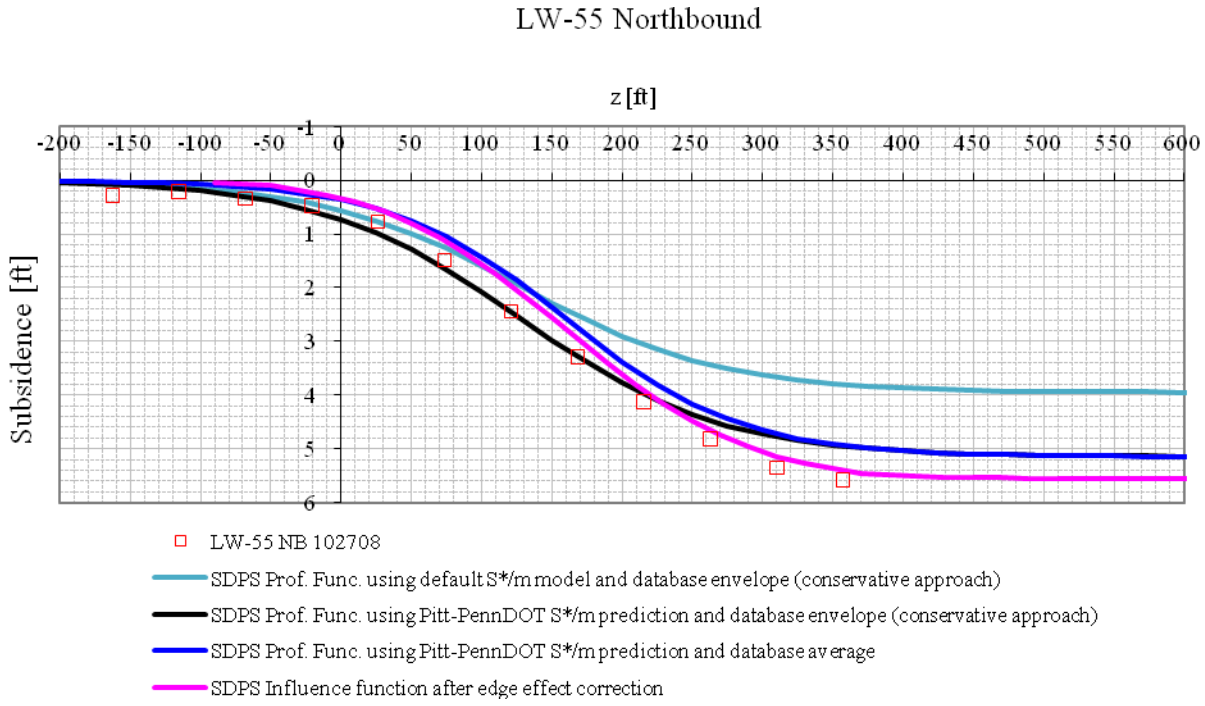

Figure 3-32 SDPS transversal view of prediction of final subsidence for LW-55

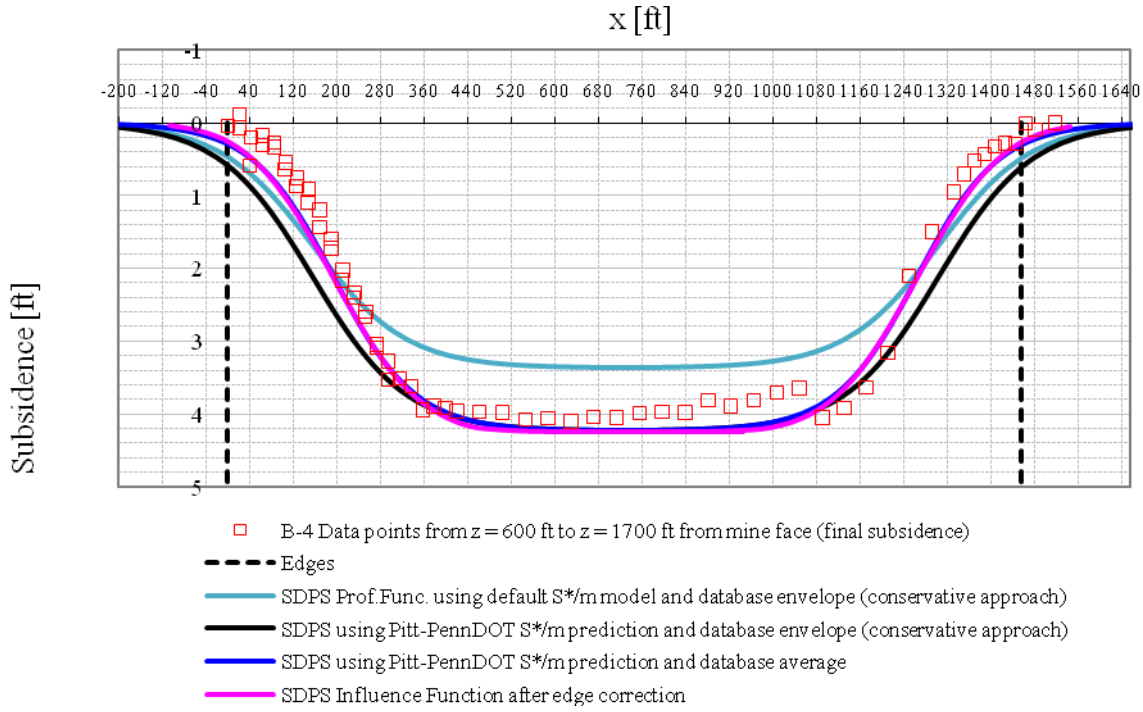

Figure 3-33 SDPS transversal view of prediction of final subsidence for B-4

The three-dimensional output of SDPS can be visualized in 2D sections for panels LW-49, LW-51, and LW-52 in the Appendix 4, 5, and 6 respectively. Appendix 7 contains profile function output tables containing angles of draw.

4.0 TASK 4: COMPARISON OF MEASURED AND PREDICTIVE SUBSIDENCE PROFILES

The present chapter compares the subsidence data obtained from detailed surveys of the longwall mined area under highway I-79, with subsidence predictions obtained from the current version of the Surface Deformation Prediction System (SDPS 6.0), and the Pitt-PennDOT highway subsidence model developed as part of this research.

In chapter 3.0 , we presented the measured trend between maximum subsidence factor and overburden thickness, and pointed out the misleading results obtained from the SDPS maximum subsidence model for the zone of interest. Motivated by this finding and by the good quality of the data provided by PennDOT, we developed a predictive tool for the zone of interest, which we called the Pitt-PennDOT highway subsidence prediction model. A detailed description of this model is presented in this chapter. The basic steps to use this model are given in Appendix A.9.

The previous chapter also presented a detailed description of the Surface Deformation Prediction System (SDPS) and the prediction results obtained using that tool. An important feature of SDPS 6.0 with respect to SDPS 5.0, is the incorporation of dynamic subsidence prediction. It will be described at the end of this report, given its usefulness.

4.1 PITT-PENNDOT HIGHWAY SUBSIDENCE PREDICTION MODEL

The previous chapters provided a general description of surveying data and a description of a transformation process that allows us to represent the subsidence trough as a spatial function in supercritical subsidence deformation regions along the longwall panel.

This chapter introduces a methodology to empirically obtain any supercritical subsidence trough based on the overburden thickness, extraction thickness, and panel width. It is important to emphasize at this point that this empirical model shall serve as a prediction tool only for the region from which the data were obtained.

The proposed methodology involves two main stages: The first stage is concerned with the development of a maximum subsidence model; the second stage with a normalized subsidence distribution model.

4.1.1 Maximum subsidence prediction

All panels are considered to reach supercritical subsidence conditions, which implies that maximum potential subsidence fully develops. Researchers report that the subsidence factor, a, defined as the ratio of the maximum subsidence, S^*, over the coal seam thickness being extracted, m, reaches a constant value for the case of supercritical conditions, provided the geology does not change (NCB 1975; Whittaker and Reddish 1989; Agioutantis and Karmis 2009). Peng, however, provides an inverse relationship between maximum potential subsidence factor and overburden depth based upon several Appalachian sites (Peng 1992), which suggests that the depth of the mine has a direct influence on the magnitude of subsidence. An accompanying explanation by Peng on this relationship claims that as depth increases, the area of

influence of the extraction increases, producing milder subsidence and also decreased deformation indices that result along with subsidence. The relationship found in this study (Figure 3-5) is consistent with Peng's relationship.

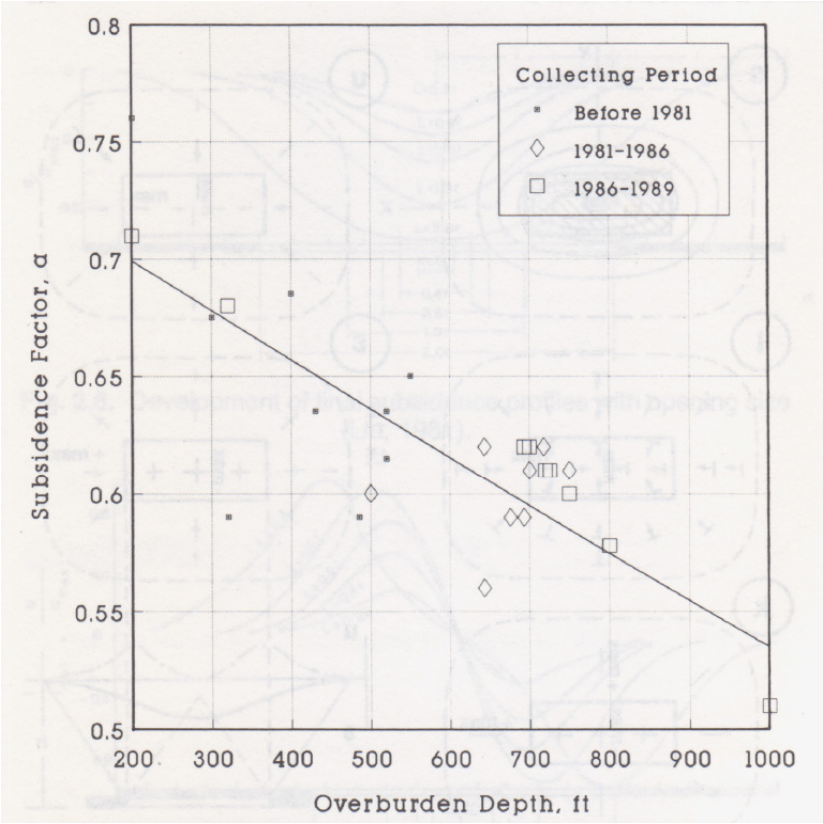

Figure 4-1 Peng's relationship between subsidence factor and overburden depth for Appalachia

4.1.2 Normalized subsidence distribution model

For the second part of the subsidence trough prediction, a surface distribution of normalized subsidence is required. To obtain a useful distribution, both the magnitude of subsidence at a point and its surface location need to be normalized.

4.1.2.1 Subsidence normalization

Given a distribution of absolute subsidence readings, all readings may be normalized with respect to the maximum subsidence, S^*.

4.1.2.2 Lateral position normalization or edge effect

The lateral or edge effect normalization is obtained by normalizing the perpendicular lateral distance from the panel edges to every point where subsidence was measured. The parameter by which this lateral normalization is carried out is the overburden depth, H. Performing the normalization of lateral distance x, z, with respect to H, is equivalent to considering the edge effect of subsidence deformation, as we explain below.

The lateral normalization can be performed in supercritical cases in the light of Figure 4-2, which shows the distance between the edge and the inflection point, d, as a function of the ratio W/H in SDPS (Agioutantis and Karmis 2009). Beyond $W/H = 1.2$, which corresponds to our cases, d/H becomes a constant. This means that normalizing our data's abscissas of supercritical profiles with respect to the overburden depth, H, will necessarily bring all supercritical profiles together in the inflexion point. This normalization made it possible for us to predict any supercritical trough.

The normalization of our data with respect to *H* produces Figure 4-3 and Figure 4-4, which depict the transversal and longitudinal normalized subsidence profiles, respectively. Notice that the ordinates (subsidence) are normalized with respect to *S**, as explained in section 4.1.2.1.

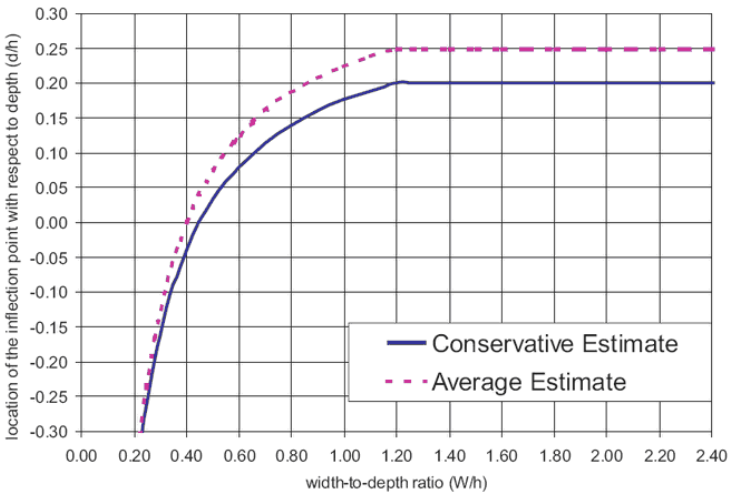

Figure 4-2 Edge effect estimation

(Agioutantis and Karmis 2009)

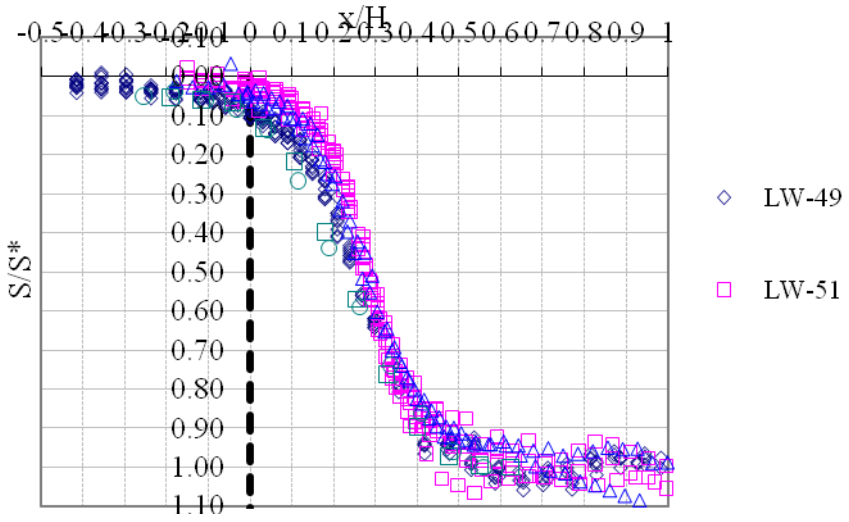

Figure 4-3 Normalized subsidence and normalized location in the transverse direction

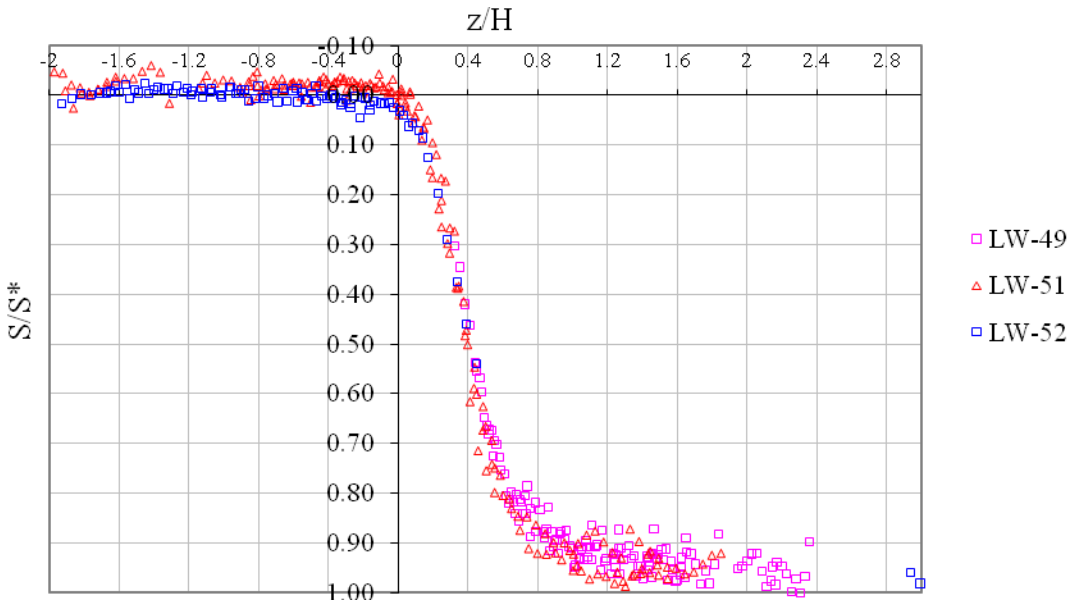

Figure 4-4 Normalized subsidence and normalized location in the longitudinal direction

4.1.3 Fitting a 3D model

The previous subsection described how data can be normalized both vertically and horizontally and showed that the data available follow convenient trends when normalized. That is, narrow bounds are formed in normalized data as the inflexion points are forced to come together. This leads to the next step, which is fitting a three-dimensional normalized subsidence model to the data.

In order to obtain a 3D model, a transverse 2D model and a longitudinal 2D model will be multiplied. Two-dimensional models are common in the literature. Two of them were described in chapter 1.0 .

A transversal view of 3D data for all panels is shown in Figure 4-5. The view presented is from the mined area toward the mine face. Each point is at a unique distance away from the mine face (direction toward the paper). The procedure to obtain data in x, z, S (transversal, longitudinal, subsidence) has been explained in chapter 2.0 . In summary, what can be visualized in this figure is the subsidence trough to which a 3D function can be fitted. The function, or model, will have to address the following factors:

- Panels do not have the same width.
- Some panels are symmetric in the case that no adjacent panel has been previously mined out in the immediate neighborhood (e.g. LW-49).
- Most panels exhibit asymmetry, that is, the side adjacent to a mined-out panel is more subsided than the opposite side.

These features, however, may be dealt with as long as a good model can be found to describe the complex shape of the typical edge deformations, whether these are adjacent to mined-out or not mined-out panels. Figure 4-6 through Figure 4-7 show data according to its use as symmetric side (without mined-out adjacent panel) or asymmetric side (with mined-out panel adjacent).

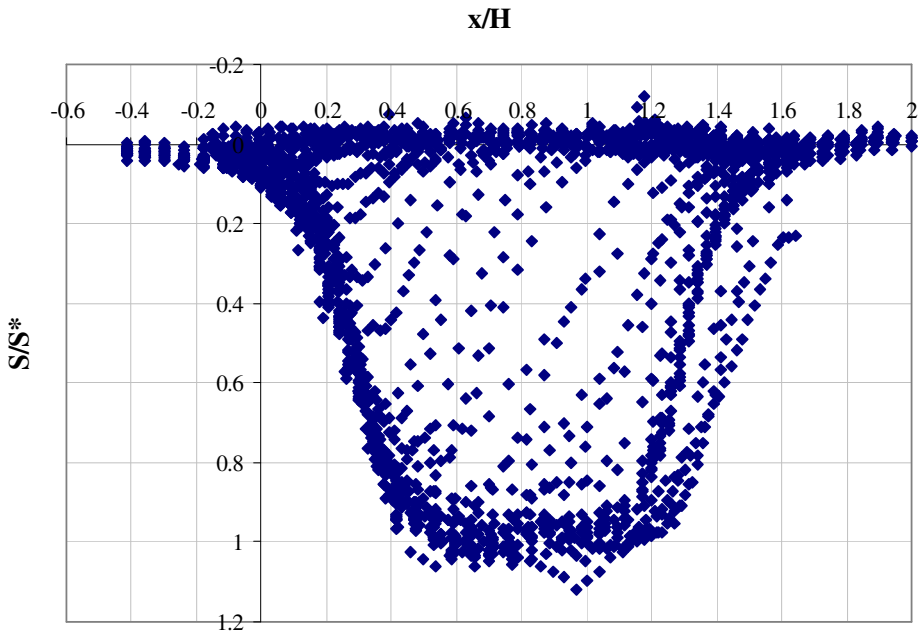

Figure 4-5 Transversal view of data from all panels

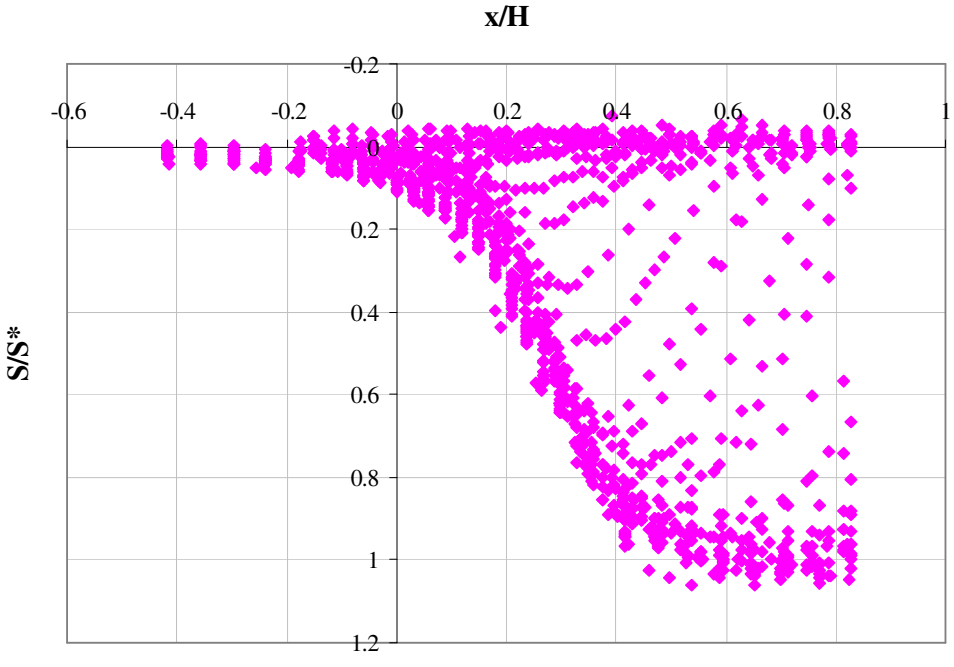

Figure 4-6 Transversal view of panels LW-49, 51, 52 data adjacent to non-mined-out panel

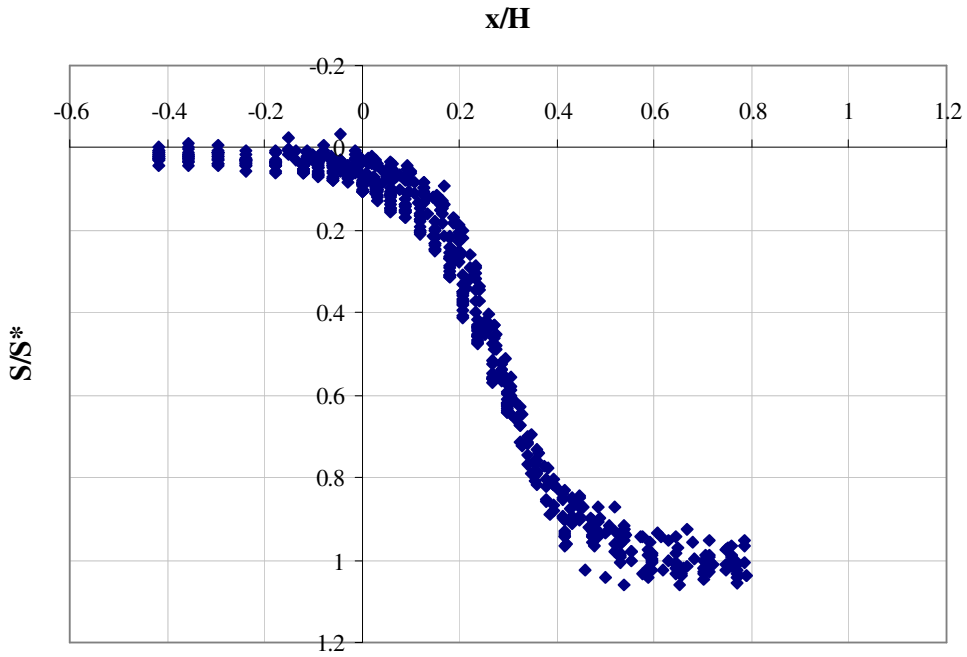

Figure 4-7 Transversal view of panels LW-49, 51, 52 final deformation data adjacent to non-mined-out panel

The problem of fitting data with a 3D profile function requires a non-linear regression technique. Since the data trends are clear, the search for functions to fit the data is relatively straightforward. For the non-linear regression, the Genetic Algorithm (GA), a robust technique in determining the parameters of the proposed model, will be used. After specifying a profile function, an objective function, and giving a range of possible parameter values, the GA finds parameter values that provide a global minimum fit according to the objective functions.

For this model, the objective is to find the parameters of the model such that the sum of square errors between the model and data is minimum. Thus, the objective function is simply a function that defines the sum of squared errors.

Four 3-D profile models were considered in this research. The first model has the following form:

$$\frac{S}{S*} = e^{a_1\left|a_2-\frac{x}{H}\right|^{a_3}} e^{a_4\left|a_5-\frac{z}{H}\right|^{a_6}} \qquad 4\text{-}1$$

The model in 4-1 is similar to the model proposed by Chen and Peng of West Virginia University (OSMRE 1986).

The second model (4-2) is called the Gompertz model in its 2D version (Graybill and Iyer 1994) and can be written as,

$$\frac{S}{S*} = e^{-e^{-\left(a_1+a_2\frac{x}{H}\right)}} e^{-e^{-\left(a_3+a_4\frac{z}{H}\right)}} \qquad 4\text{-}2$$

Gompertz model has not been used in subsidence prediction, it comes from the area of logistics. The third model (4-3) would be the 3D version of the subsidence profile function used by SDPS (Agioutantis and Karmis 2009):

$$\frac{S}{S*} = 0.25\left[1-\tanh\left(a_1+a_2\frac{x}{H}\right)\right]\left[1-\tanh\left(a_3+a_4\frac{z}{H}\right)\right] \qquad 4\text{-}3$$

The fourth model (4-4) is known as Richard's model (Graybill and Iyer 1994) in its 2D version. As the Gompertz model, this model has not been used in subsidence prediction either, it comes from the area of logistics.

$$\frac{S}{S*} = \frac{1}{\left[1+e^{-\left(a_1+a_2\frac{x}{H}\right)}\right]^{a_3}\left[1+e^{-\left(a_4+a_5\frac{z}{H}\right)}\right]^{a_6}} \qquad 4\text{-}4$$

All the previous models in their 2D version are capable of profile fitting in the problem of subsidence. Usually the 2D problem involves estimation of maximum or final subsidence, for which a supercritical final deformed profile is fit usually by taking the transversal coordinate as the horizontal distance. However, the 3D problem that arises from the data depicted in Figure 4-5

through Figure 4-7 poses the challenge of describing both final deformations (large and far from mine face) and dynamic deformations (small and close to mine face) through a single 3D regression model. Runs of the GA algorithm for each of the above four models show that two of the models, i.e. models 1 and 4, each having 6 model parameters (namely models equation 4-1 and equation 4-4) best fit the data. This is not surprising since representing the 3D nature of the data requires a level of detail that only the 6-parameter models can provide. Table 4-1 and Table 4-2 contain the output of parameters for the various regression models, together with the objective function value and standard deviations. Trial function number 4 (4-4) proved to best fit the data due to its low sum of squared error and standard deviation.

Table 4-1. Genetic algorithm output for side without adjacent panel

Trial function	a_1	a_2	a_3	a_4	a_5	a_6	Sum of squared error	n	p	Standard Deviation
1	-1.889E-4	1.93	16.04	-7.403E-4	2.42	9.67	10.2	1264	6	0.090
2	-2.72	2.57	-0.35	-0.19			87.2	1264	4	0.263
3	1.32	-5.58	1.94	-2.81			111.3	1264	4	0.297
4	-2.79	11.60	1.24	-1.94	6.00	1.23	8.5	1264	6	0.082

Table 4-2. Genetic algorithm output for side with adjacent panel

Trial function	a_1	a_2	a_3	a_4	a_5	a_6	Sum of squared error	n	p	Std. Dev.
1	-1.74E-4	2.06	13.23	-1.28E-3	2.14	10.87	0.89	628	6	0.038
4	-1.83	10.34	1.11	-1.45	6.73	2.23	0.73	628	6	0.034

When the asymmetrical model is used, however, it is still desired that the two model halves match along a central line smoothly. Therefore, the parameters a_4, a_5, a_6 may be set equal to those of the symmetric model (longitudinal, z, parameters), leaving only the transversal parameters a_1, a_2, a_3 as variables. Setting the former constant and equal to -1.94, 5.99, and 1.23, and re-running the genetic algorithm, the results in Table 4-3 are obtained, which are still very good results.

Table 4-3. Genetic algorithm output for side with adjacent panel Trial function 4

Trial function	a_1	a_2	a_3	a_4	a_5	a_6	Sum of squared error	n	p	Std. Dev.
4	-2.77	12	0.73	-1.94	5.99	1.23	0.92	628	6	0.038

4.1.4 Spatial distribution of subsidence

To apply the model derived, a step by step procedure can be summarized as follows:

1. *S*/m* is read as a function of *H*. *S** is thus obtained by multiplying *S*/m* with *m*.
2. The non-linear model (e.g. without mined adjacent panel) is evaluated by plugging in *H* and *S**:

$$\frac{S}{S^*} = \frac{1}{\left[1+e^{-\left(-2.79+11.60\frac{x}{H}\right)}\right]^{1.24}\left[1+e^{-\left(-1.94+6.00\frac{z}{H}\right)}\right]^{1.23}} \qquad 4\text{-}5$$

4.1.5 Temporal distribution of subsidence

One apparent feature of the way the trough is obtained is that the trough front, as it is described, experiences the dynamic effect of subsidence. In other words, if a central longitudinal profile is obtained from the non-linear regression that describes the trough, that longitudinal profile is nothing but the dynamic subsidence profile in 2D. Provided the geology is the same, the shape of the dynamic subsidence profile is influenced by the rate of advance of the mine face and it can be gentle for high rates of advance or sharp for slow rates (Kratzsch 1983; Jarosz, Karmis et al. 1990; Kratzsch 2008; Agioutantis and Karmis 2009).

The data upon which the 3D model is based comes from three panels, LW-49, LW-51, and LW-52, which experienced an average constant rate of advance of roughly 57 ft/day. As a result, the non-linear regression here obtained represents the magnitude of or close magnitudes to that rate of advance. The difference between the dynamic profile shape and the permanent deformation shapes on the sides of the panel, or static profiles as they are often called, is clear if Figure 4-3 and Figure 4-4 are compared. One way to deal with intermediate values of rate of advance between 0 and 57 ft/day would be to consider profiles within these two limits through linear interpolation. For advancing rate higher than 57 ft/day, a prediction through extrapolation could be less reliable, although conclusions on this may not be drawn due to a lack of data.

In temporal subsidence prediction, a useful task is to predict deformation for a given point in terms of a time scale that can be set to zero for the position of the mine face. The basic assumption for both spatial and temporal subsidence prediction is that the rate of mine face advance is constant, and in this case equal to 57 ft/day. Therefore, the longitudinal coordinate, z, can be expressed as a function of the rate of advance, v, as $z = vt$.

$$\frac{S}{S^*} = \frac{1}{\left[1 + e^{-\left(-2.79+11.60\frac{x}{H}\right)}\right]^{1.24}\left[1 + e^{-\left(-1.94+342\frac{t}{H}\right)}\right]^{1.23}} \qquad 4\text{-}6$$

Since v = 57 ft/day, the spatial coordinate z is replaced by 57t, and the model in 4-6 is obtained. Since t = 0 corresponds to the mine face position, t < 0 corresponds to points ahead of the mine face, whereas t > 0 corresponds to points behind the mine face. For example, if there are concerns about a point P that is estimated to be reached by the mine face in 4 days, its deformation can be predicted for the days before and after the mine face passes by plugging in t = -3, -2, -1, 0, 1, 2, 3, etc. It is important to note that model 4-6 has the spatial coordinate x as one of its independent variables. The point P of concern could be located anywhere within the width of the panel, even outside the edges. Also, complete transverse profiles could be predicted for different times. Even though the Pitt-PennDOT model can perform temporal subsidence prediction, it is currently limited by the constant rate of advance common to the whole dataset on which this capability was based, that is, 57 ft/day. However, we have explored the alternative new version of SDPS (SDPS 6.0), which incorporated dynamic subsidence as we will describe later in this chapter. The SDPS 6.0 requires the input of a time constant, c, that we can obtain from the PennDOT data and employ it for future predictions regardless of the mine face rate of advance.

Another way the temporal subsidence may be looked at is in the prediction of long-term subsidence, for which researchers have proposed decay functions (Whittaker and Reddish 1989). This research is not concerned with this type of prediction since the available data was limited to a very narrow time duration that was terminated soon after the mine face passed the surveyed stations.

4.1.6 Subsidence deformation indices

Definitions of subsidence deformation indices were introduced in chapter 1.0 . Deformation indices are important for damage prediction. If the subsidence profile or trough is known, these can be easily obtained.

From the general model,

$$S = \frac{S^*}{\left[1+e^{-\left(a_1+a_2\frac{x}{H}\right)}\right]^{a_3}\left[1+e^{-\left(a_4+a_5\frac{z}{H}\right)}\right]^{a_6}} \qquad 4\text{-}7$$

the following parts may be defined:

$$C_X = \frac{S^*}{\left[1+e^{-\left(a_1+a_2\frac{x}{H}\right)}\right]^{a_3}},\ C_Z = \frac{S^*}{\left[1+e^{-\left(a_4+a_5\frac{z}{H}\right)}\right]^{a_6}} \qquad 4\text{-}8$$

$$S_X = \frac{1}{\left[1+e^{-\left(a_1+a_2\frac{x}{H}\right)}\right]^{a_3}},\ S_Z = \frac{1}{\left[1+e^{-\left(a_4+a_5\frac{z}{H}\right)}\right]^{a_6}} \qquad 4\text{-}9$$

The first and second derivatives of 4-9 are required for the deformation indices. The expressions for the case of the transversal direction, *x*, are:

$$S'_X = \frac{a_2 a_3}{H}\frac{e^{-\left(a_1+a_2\frac{x}{H}\right)}}{\left[1+e^{-\left(a_1+a_2\frac{x}{H}\right)}\right]^{a_3+1}} \qquad 4\text{-}10$$

$$S''_X = -\frac{{a_2}^2 a_3}{H^2} e^{-\left(a_1+a_2\frac{x}{H}\right)}\left[1+e^{-\left(a_1+a_2\frac{x}{H}\right)}\right]^{-a_3-1} + \ldots$$

$$\ldots + \frac{(a_3+1){a_2}^2 a_3}{H^2} e^{-2\left(a_1+a_2\frac{x}{H}\right)}\left[1+e^{-\left(a_1+a_2\frac{x}{H}\right)}\right]^{-a_3-2} \qquad 4\text{-}11$$

For the right half of the trough, the equations are:

$$S'_X = -\frac{a_2 a_3}{H}\frac{e^{-\left(a_1+a_2\frac{W-x}{H}\right)}}{\left[1+e^{-\left(a_1+a_2\frac{W-x}{H}\right)}\right]^{a_3+1}} \qquad 4\text{-}12$$

$$S''_X = -\frac{{a_2}^2 a_3}{H^2} e^{-\left(a_1+a_2\frac{W-x}{H}\right)}\left[1+e^{-\left(a_1+a_2\frac{W-x}{H}\right)}\right]^{-a_3-1} + \ldots$$

$$\ldots + \frac{(a_3+1){a_2}^2 a_3}{H^2} e^{-2\left(a_1+a_2\frac{W-x}{H}\right)}\left[1+e^{-\left(a_1+a_2\frac{W-x}{H}\right)}\right]^{-a_3-2} \qquad 4\text{-}13$$

The same expressions may be obtained for the longitudinal direction, *z*. Based on these, the deformation indices are obtained as follows:

$$Slope_X = -\frac{\partial S}{\partial x} = -C_Z S'_X$$

$$Curvature_X = -\frac{\partial^2 S}{\partial x^2} = -C_Z S''_X$$

As discussed in chapter 1.0 , horizontal displacements are correlated to slope through a constant. The SDPS developers (Agioutantis and Karmis 2009) use a factor B_f defined as $B_f = B\frac{H}{tan\beta}$, where B is a fitting constant and $\frac{H}{tan\beta}$ is the radius of influence, where H is the overburden thickness and β is the angle of influence. The SDPS uses B = 0.35 for Northern

Appalachia. From horizontal displacement figures obtained for the highway I-79, and taking the resulting subsidence trough into account, a preliminary value for this constant B is set here equal to 0.15. Graphical results of the Pitt-PennDOT model are given in Figure 4-8 through Figure 4-16.

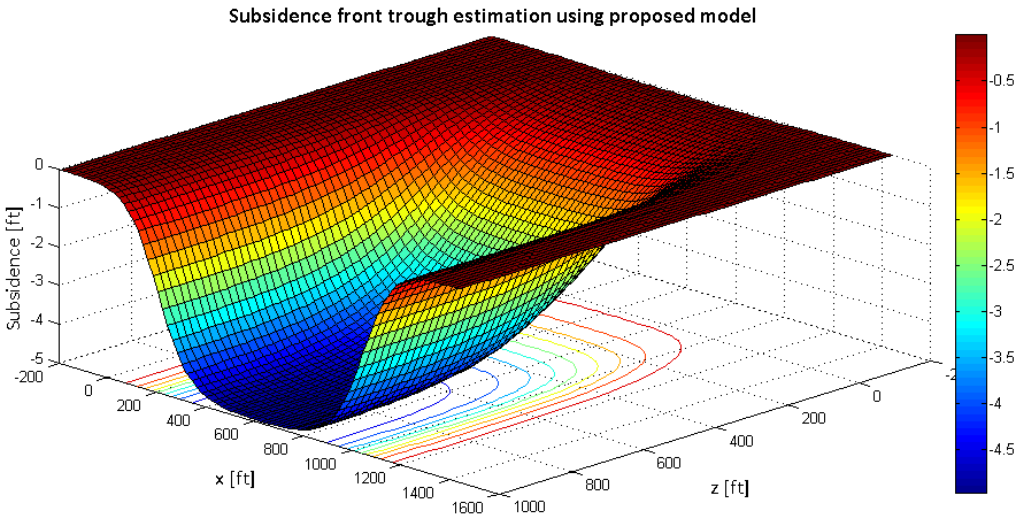

Figure 4-8 Example of 3D view of predicted trough with H = 766 ft, S^* = 5 ft, W = 1240 ft

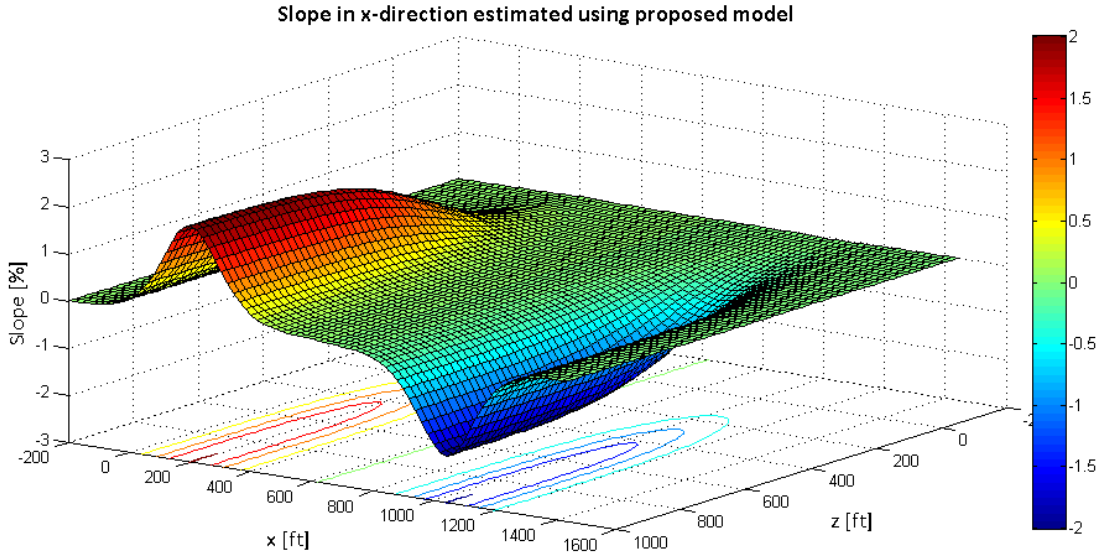

Figure 4-9 Example of 3D view of slope magnitude for H = 766 ft, S^* = 5 ft, W = 1240 ft

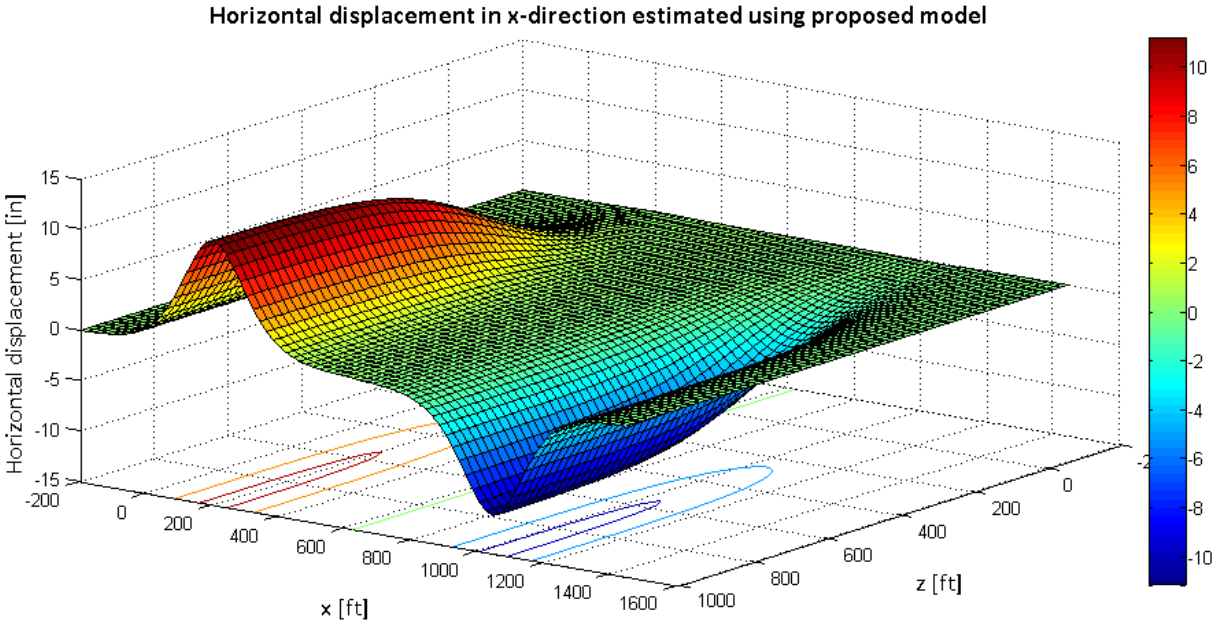

Figure 4-10 3D view of horizontal displacement for H = 766 ft, S^* = 5 ft, W = 1240 ft, β = 68°, B = 0.15

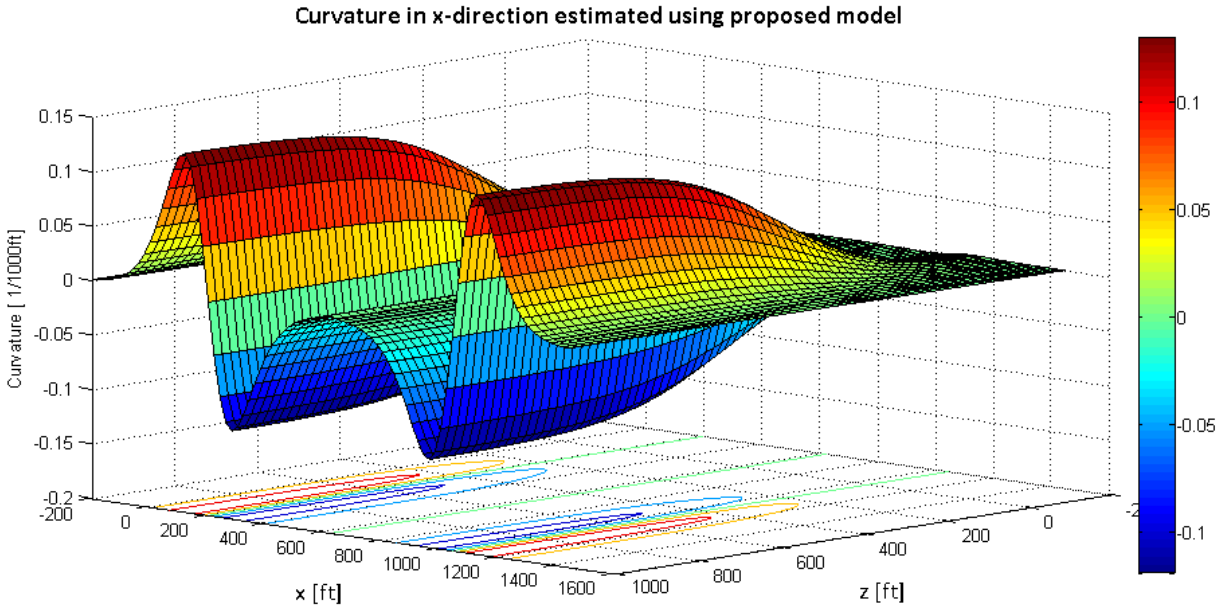

Figure 4-11 3D view of curvature for H = 766 ft, S^* = 5 ft, W = 1240 ft, β = 68°, B = 0.15

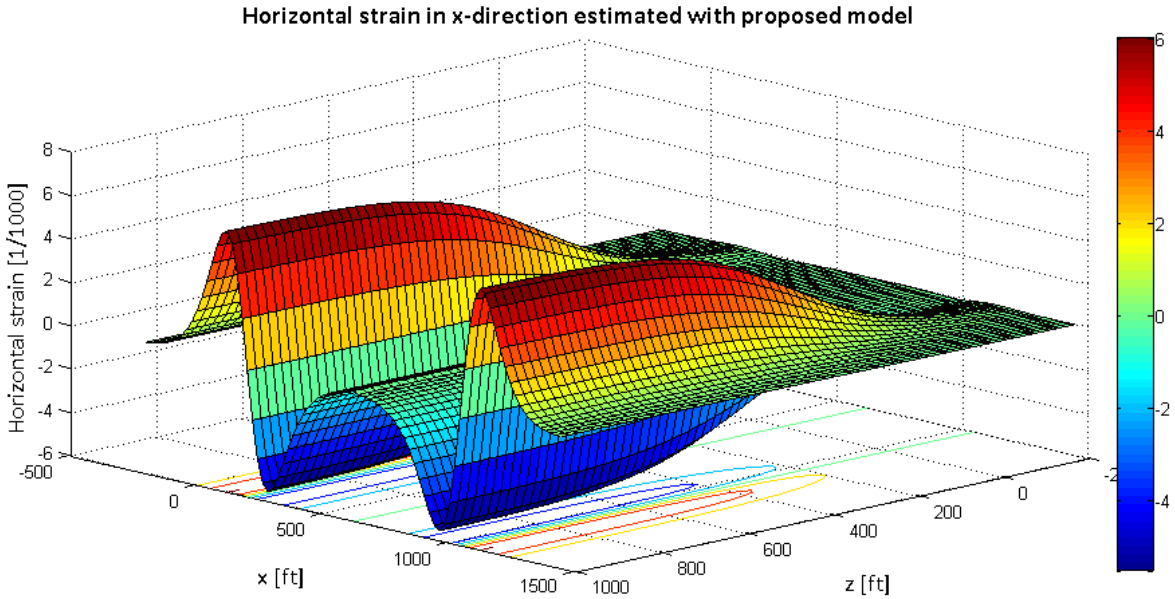

Figure 4-12 3D view of horizontal strain for H = 766 ft, S^* = 5 ft, W = 1240 ft, β = 68°, B = 0.15

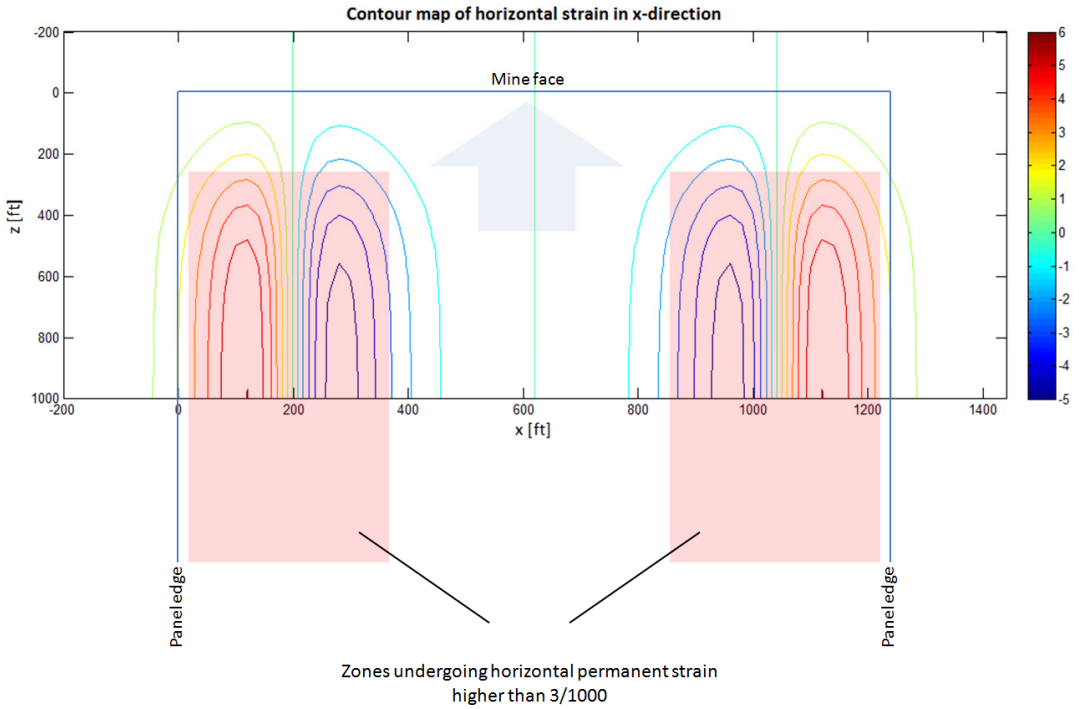

Figure 4-13 Contour map of horizontal strain for H = 766 ft, S^* = 5 ft, W = 1240 ft, β = 68°, B = 0.15

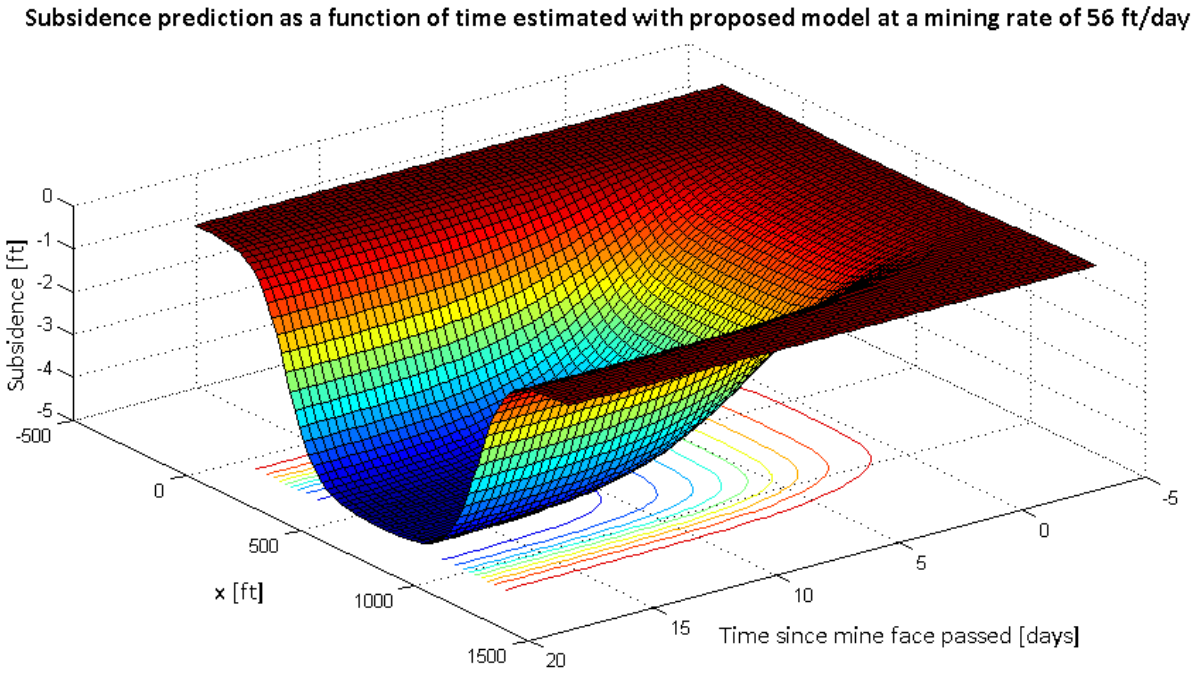

Figure 4-14 Subsidence as a function of time for H = 766 ft, S^* = 5 ft, W = 1240 ft, v = 56 ft/day

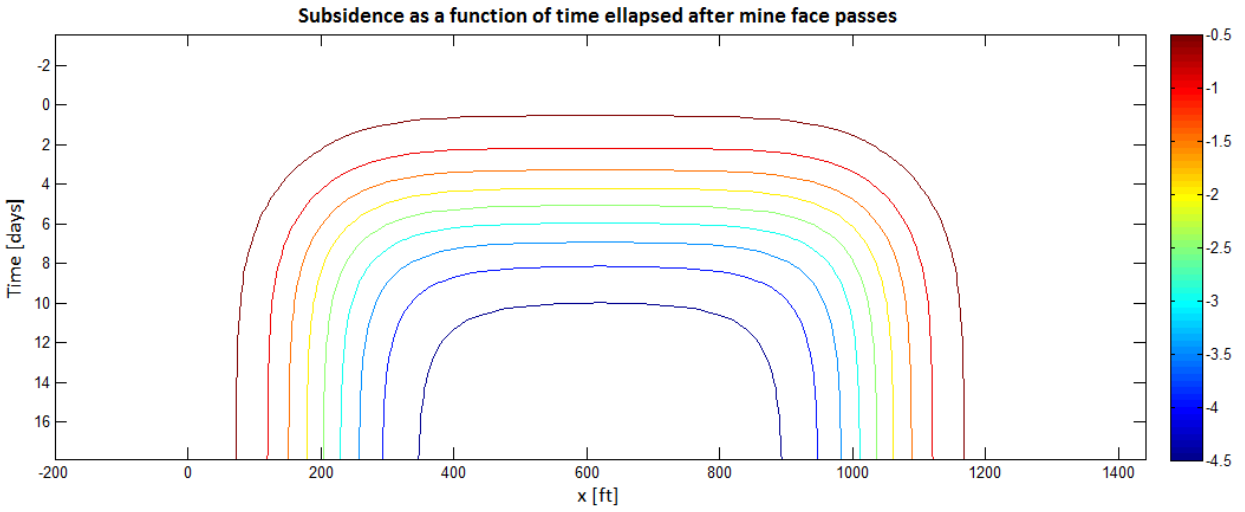

Figure 4-15 Subsidence contours as a function of time for H = 766 ft, S^* = 5 ft, W = 1240 ft, v = 56 ft/day

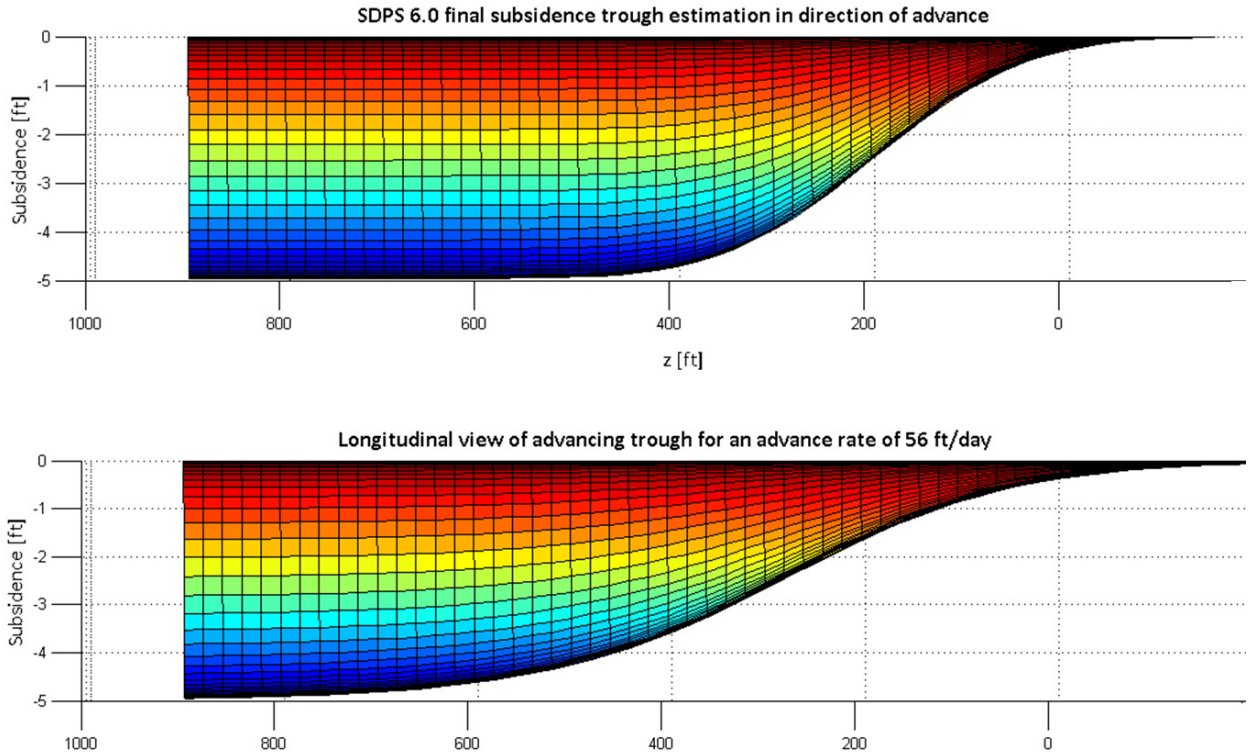

Figure 4-16 Comparison of lateral view of subsidence troughs obtained by SDPS 6.0 and Pitt-PennDOT

4.1.7 Comments on horizontal displacements

A three-dimensional trough subsidence may be predicted as described in previous sections of this chapter. Subsection 4.1.6 introduced the traditional way horizontal displacements are dealt with. A linear correlation to slope yields horizontal displacement, an assumption that seems to have worked well for relatively flat terrain. However, researchers have brought up the fact that this assumption is less reliable when hilly terrain is dealt with (Luo and Peng 1999), and have proposed methodologies to account for the inclination of terrain and its impact both on subsidence and horizontal displacements. Luo and Peng consider the proportionality factor *G*, which is the reciprocal of the safety factor against sliding of an infinite slope. Their paper shows an example where this assumption seems to work. Basically, a relatively shallow topsoil above the bedrock is considered, and its tendency to slide as a function of the terrain slope, represented by the *G* factor, is considered in adjusting the subsidence movements caused by a flat terrain.

the massive fill embankments seem to play a role in the horizontal deformation of the highway. In general, it may be observed that those displacements are sensitive to very gentle highway gradients of the order of 1 to 3 degrees.

In cases where the direction of highway gradient is constant, that is, the whole highway segment above the panel width going uphill or downhill, it is even possible that a majority of all surveyed points move in a single direction, namely the downhill direction. This behavior, strongly asymmetric, cannot be captured by the assumption that horizontal displacements may be correlated to the trough slope, which yields symmetric results. Also, considering infinite slope stability in the way Luo and Peng do (Luo and Peng 1999) does not seem to be the best approach in the case of highway embankments since the behavior is dominated by their complex irregular

three-dimensional geometry. The complex behavior of horizontal displacements on top of highway foundations will be addressed through numerical modeling in the next chapter.

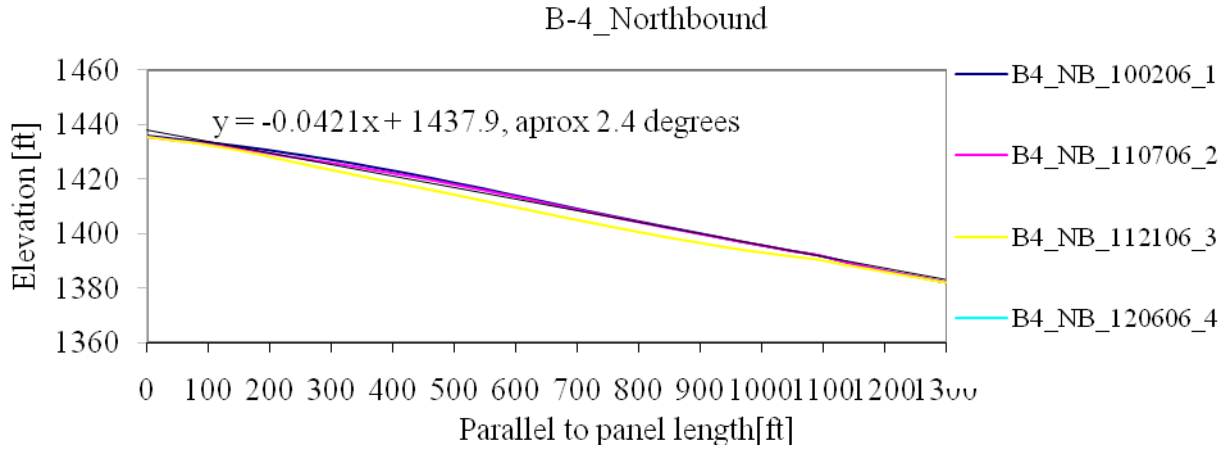

Figure 4-17 Highway elevation in the z-plane projection for B-4

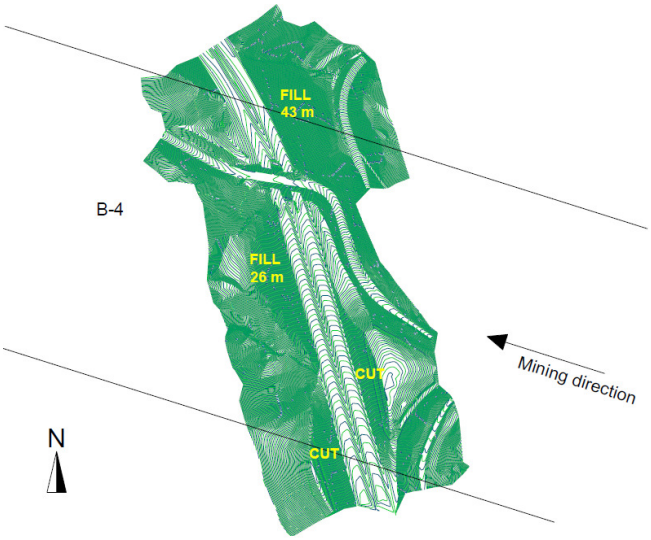

Figure 4-18 Emerald mine panel B-4 cut and fill zones

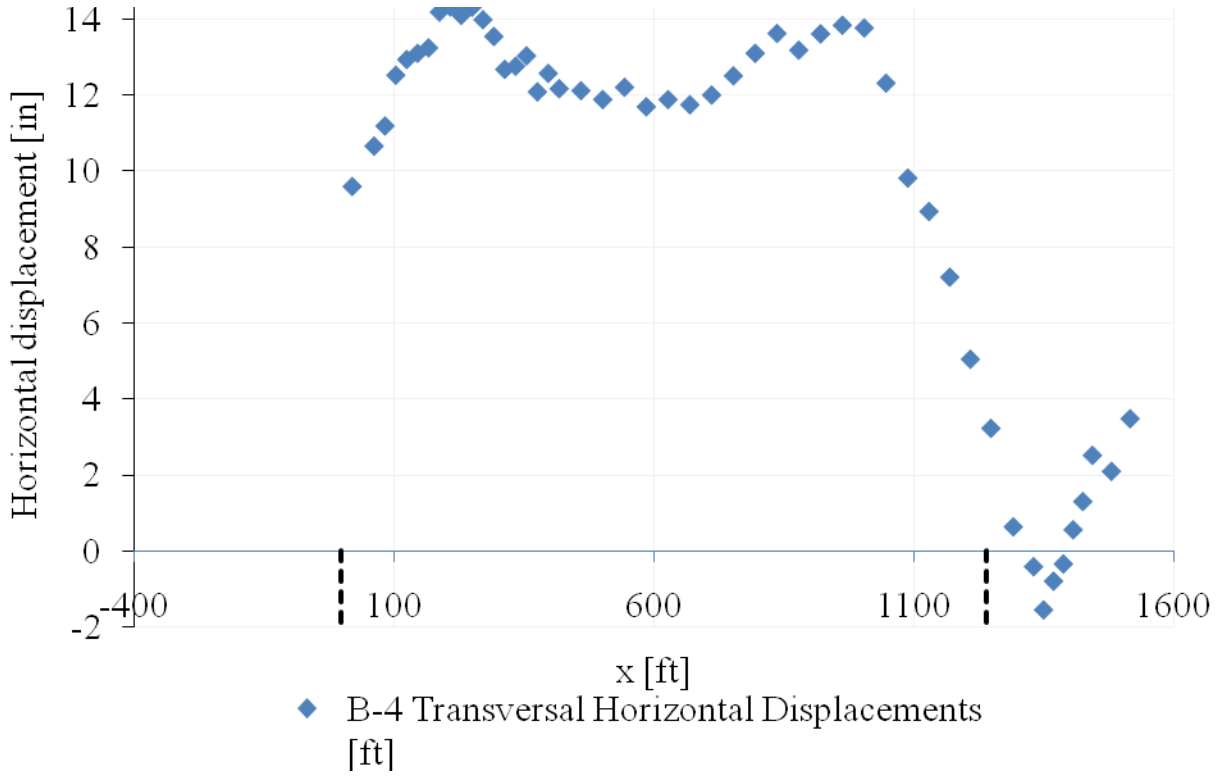

Figure 4-19 Emerald mine panel B-4 z-plane projection of northbound horizontal displacements

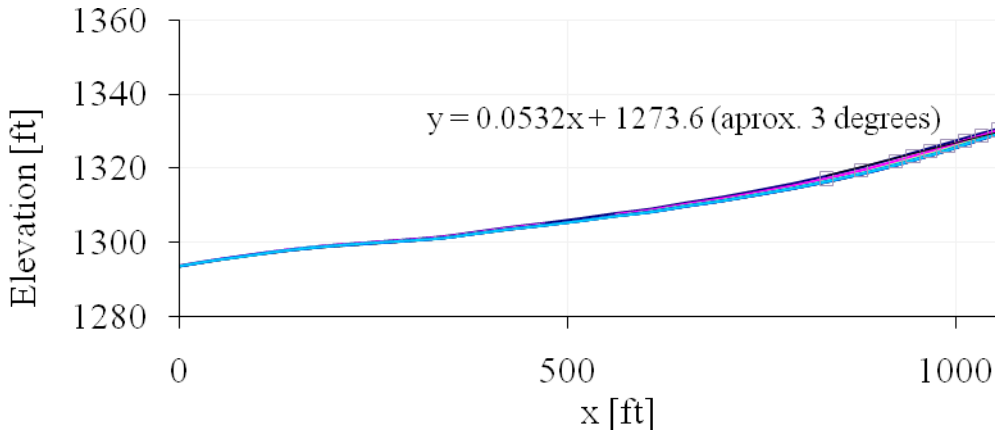

Figure 4-20 Highway northbound elevation in the z-plane projection for LW-49

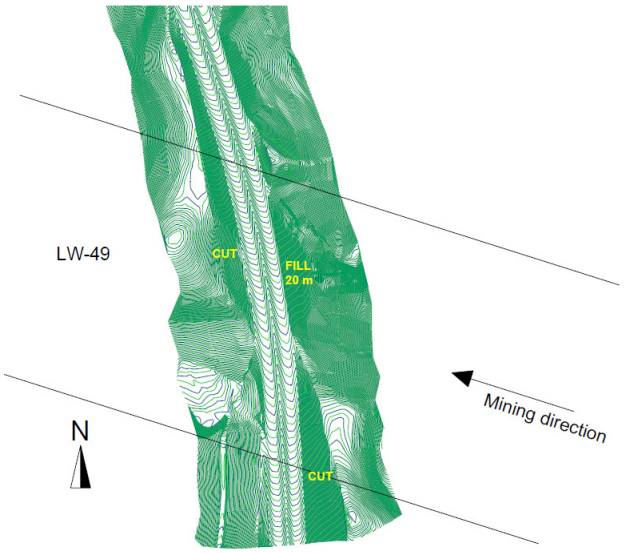

Figure 4-21 Cumberland mine panel LW-49 cut and fill zones

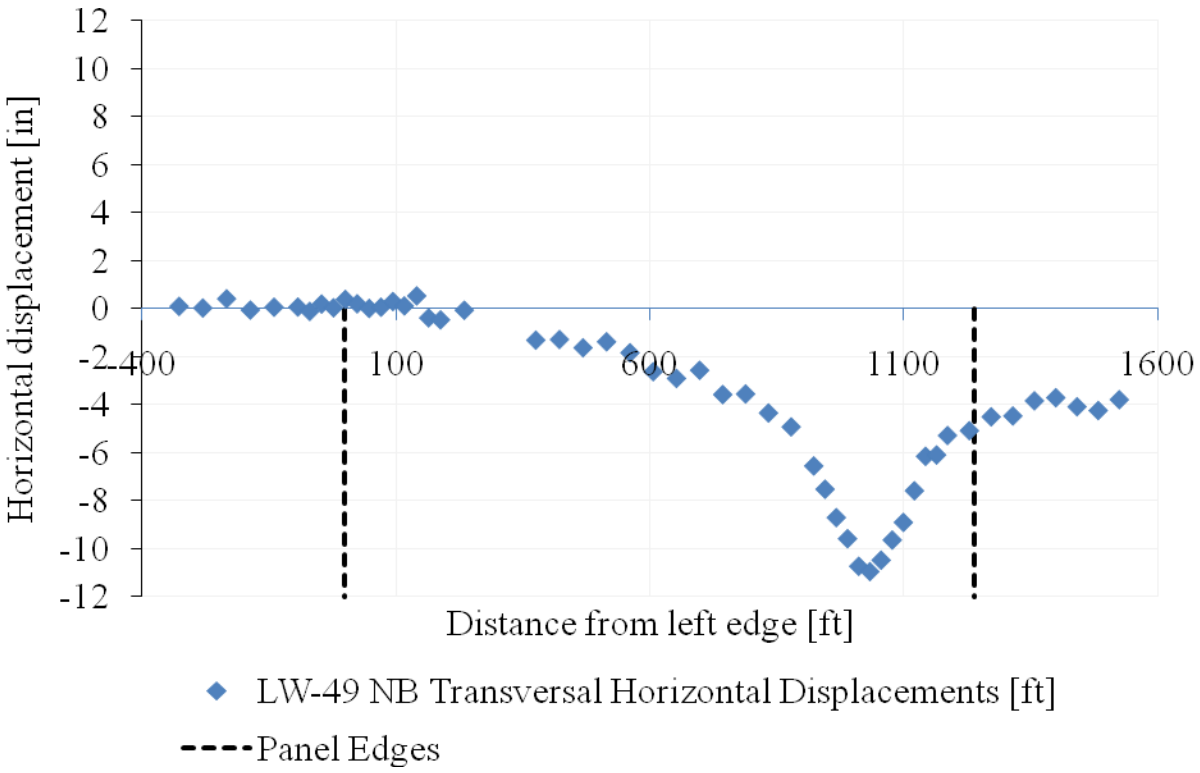

Figure 4-22 Cumberland mine panel LW-49 z-plane projection of northbound horizontal displacements

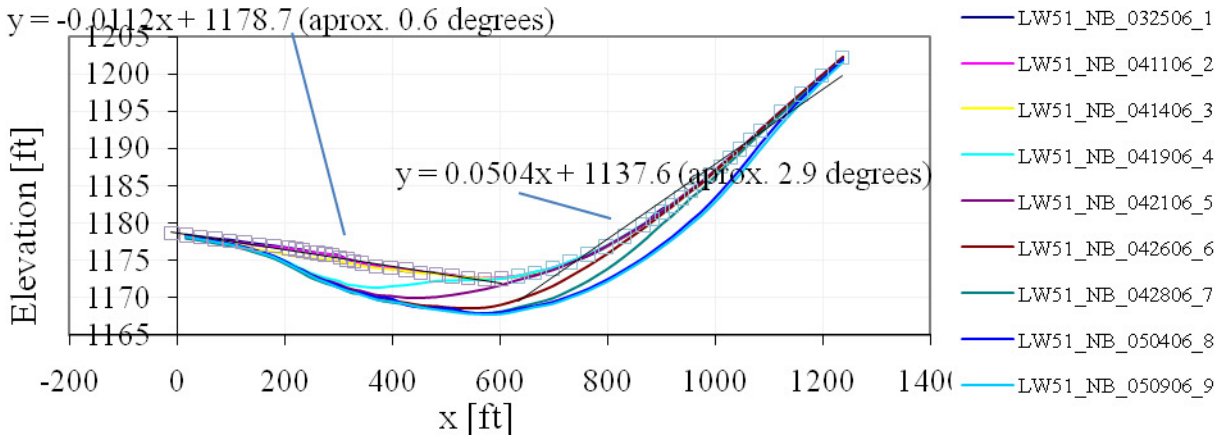

Figure 4-23 Highway northbound elevation in the z-plane projection

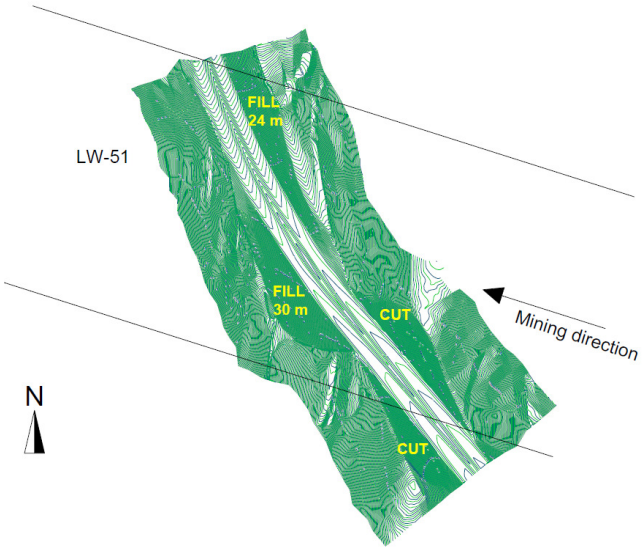

Figure 4-24 Cumberland mine panel LW-51 cut and fill zones

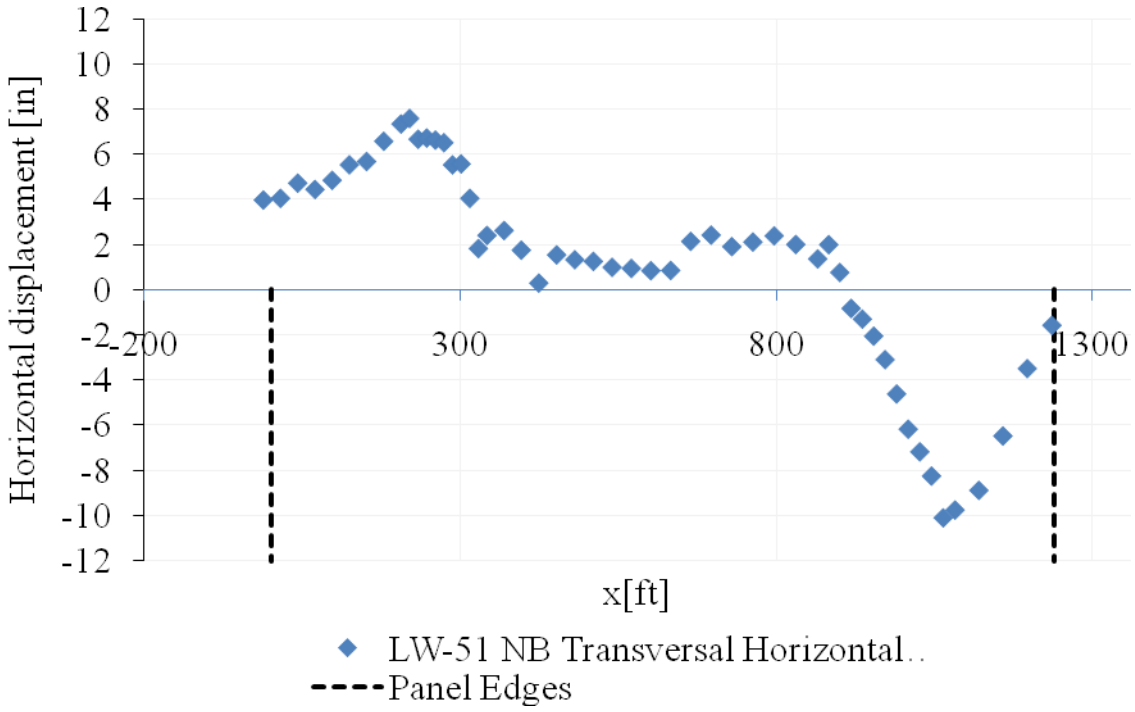

Figure 4-25 Cumberland mine panel LW-51 z-plane projection of northbound horizontal displacements

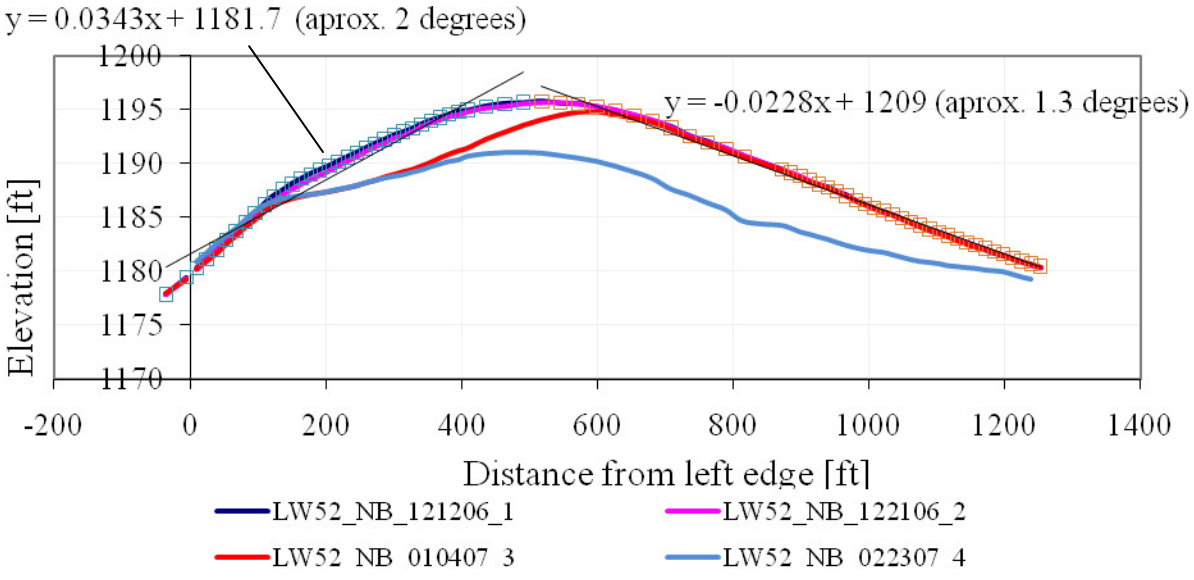

Figure 4-26 Highway northbound elevation in the z-plane projection

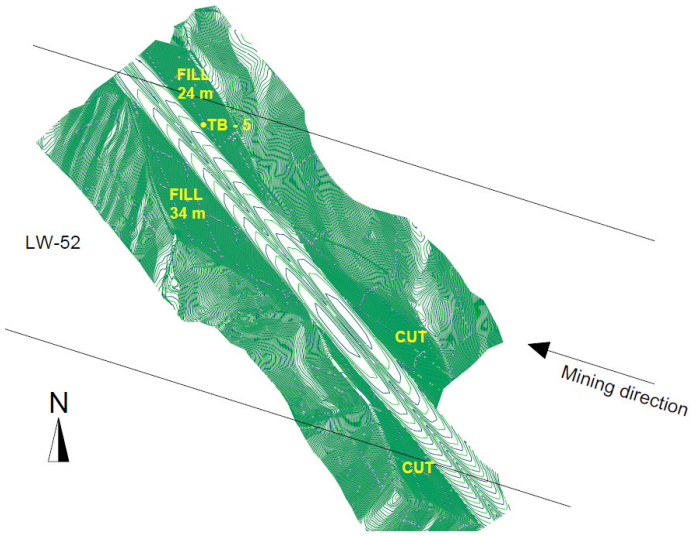

Figure 4-27 Cumberland mine panel LW-52 cut and fill zones

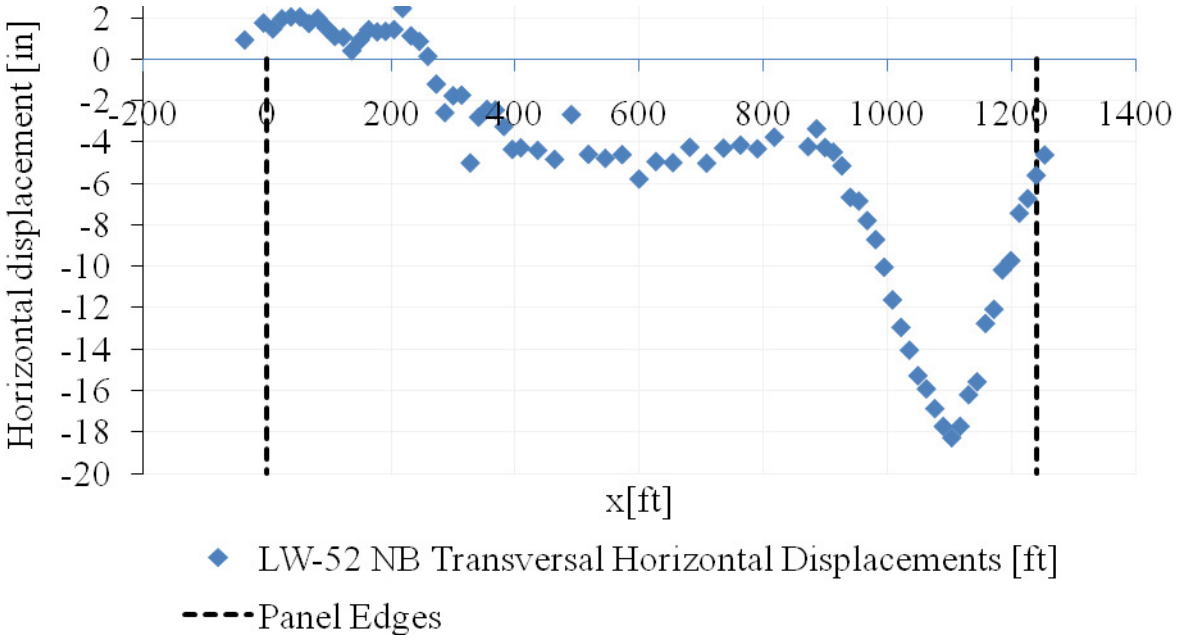

Figure 4-28 Cumberland mine panel LW-52 z-plane projection of northbound horizontal displacements

4.2 GRAPHICAL COMPARISON OF FINAL SUBSIDENCE

A comparison of the two final subsidence prediction tools described is presented herein in a graphical way. The ability of the Pitt-PennDOT model to consider the asymmetry of the subsidence profiles is manifested in the following results. It is noteworthy that the results for LW-49 are almost the same. This is because LW-49 was the only symmetric panel of this study, in that it did not have any previously mined-out neighbor panel. On the other hand, we have panel LW-52, which had the previously mined-out LW-51 panel to its right side, and panel LW-51, which had the previously mined-out LW-50 panel. In these cases substantial differences exist between SDPS and the Pitt-PennDOT models. The latter appears to work better.

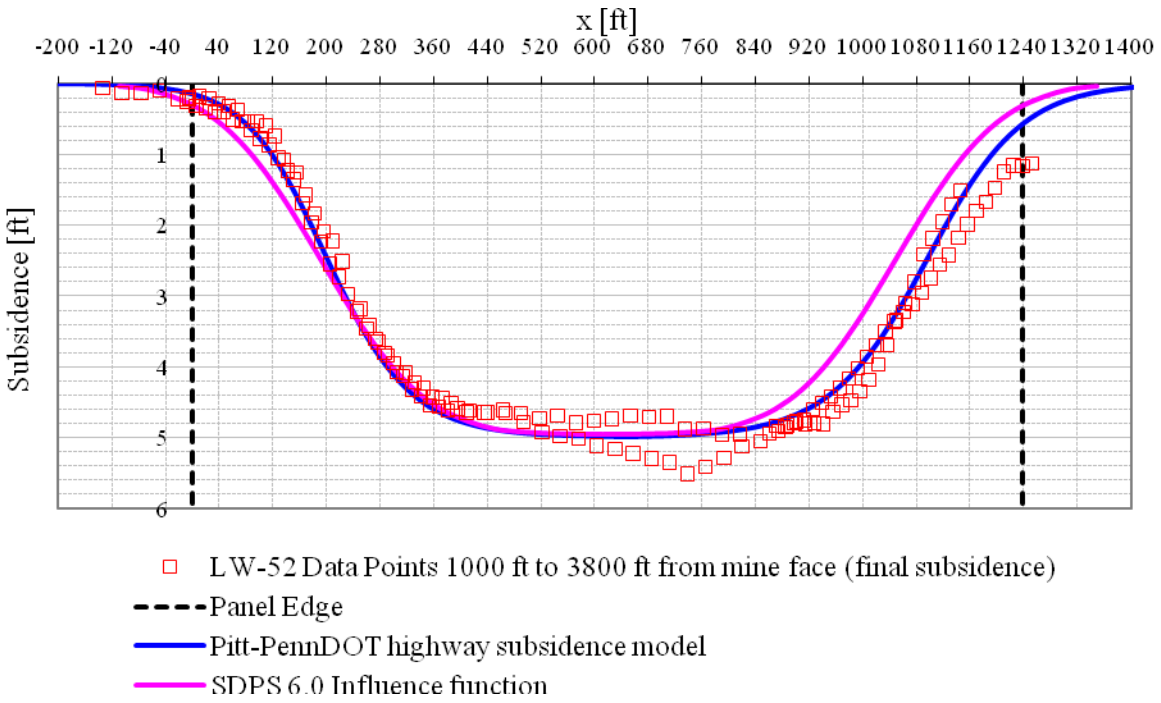

Figure 4-29 Comparison of final subsidence data, Pitt-PennDOT model, and SDPS 6.0 for LW-52

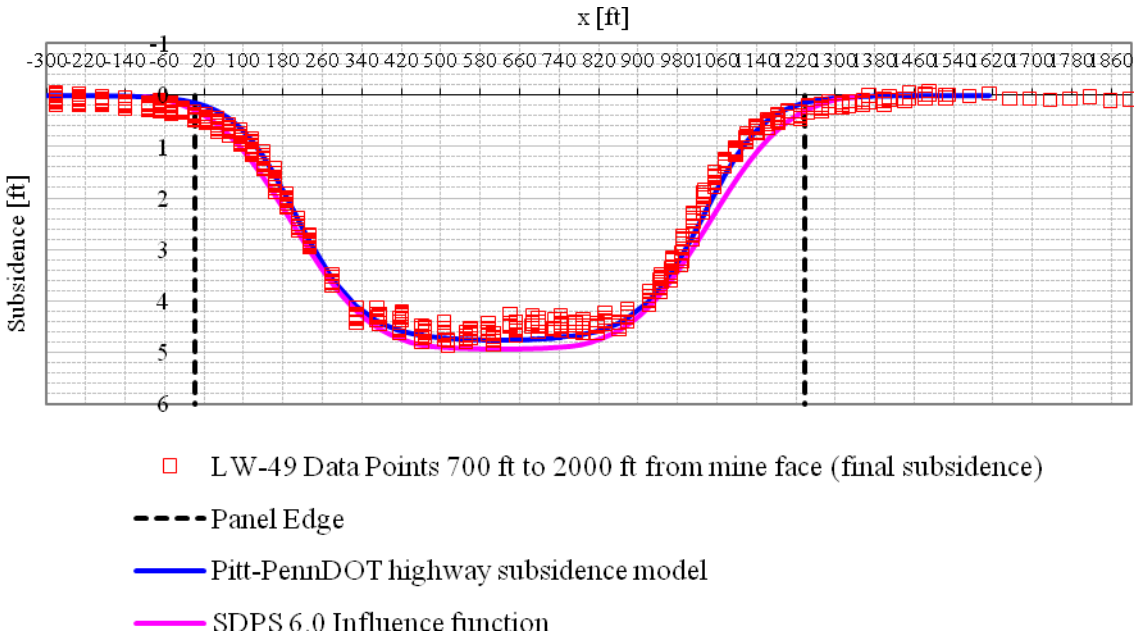

Figure 4-30 Comparison of final subsidence data, Pitt-PennDOT model, and SDPS 6.0 for LW-49

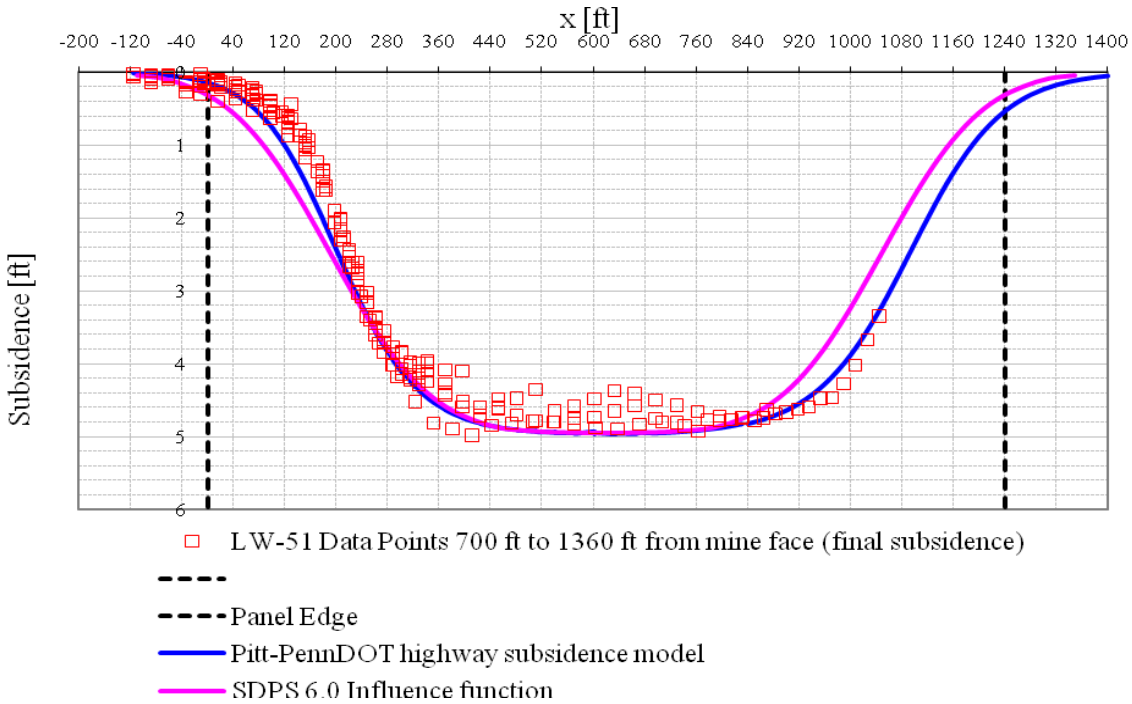

Figure 4-31 Comparison of final subsidence data, Pitt-PennDOT model, and SDPS 6.0 for LW-51

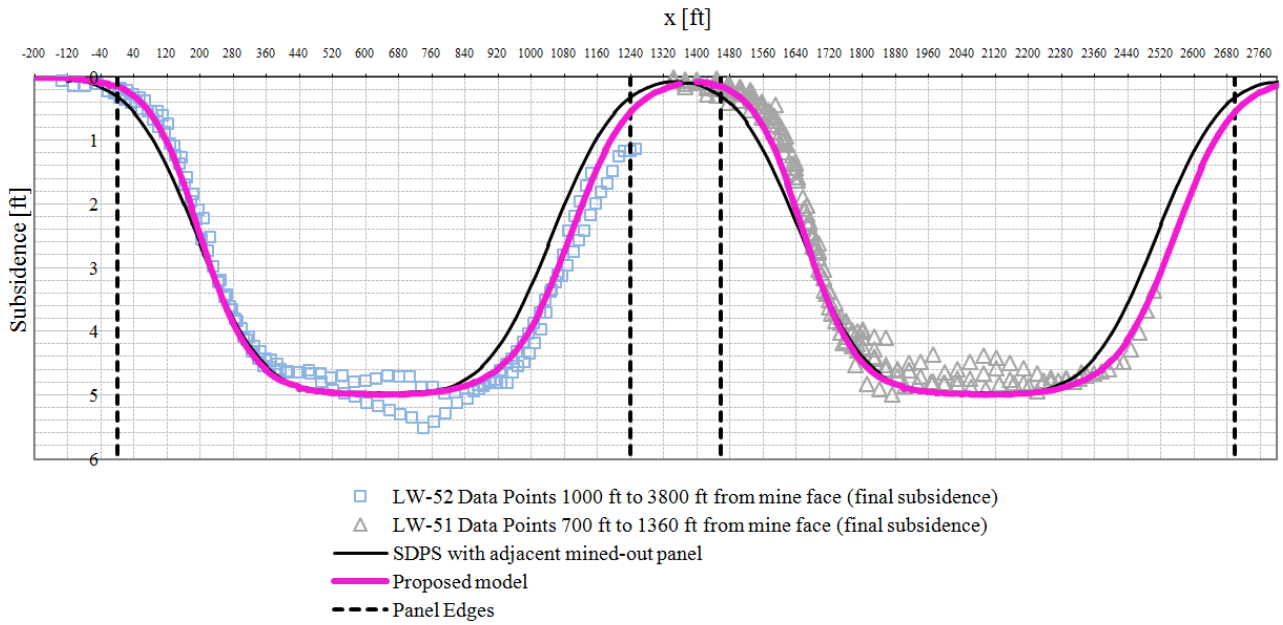

Figure 4-32 Comparison of final subsidence data, Pitt-PennDOT model, and SDPS 6.0 for LW-51 and LW-52

4.3 SDPS 6.0 – DYNAMIC SUBSIDENCE

The current version of the Surface Deformation Prediction System (SDPS 6.0) incorporated dynamic subsidence modeling. The treatment of dynamic subsidence relies heavily on the paper by Jarosz et al (Jarosz, Karmis et al. 1990). Dynamic subsidence refers to the development of surface subsidence as a function of time. The process of dynamic subsidence covers the time span between zero-subsidence and final or static subsidence. The evolution of subsidence as a function of time is characteristic of the mechanical behavior of the rocks in the mine overburden. Kratzsch (Kratzsch 2008) has considered the visco-elastic behavior to describe dynamic subsidence.

The dynamic subsidence prediction method used in SDPS 6.0 is based on Knothe's differential equation proposed in 1951:

$$\dot{S}(t) = c\left[S^f(t) - S(t)\right] \qquad 4\text{-}14$$

where

$\dot{S}(t) =$ Subsidence development rate.

$S^f(t) =$ Final subsidence if mine face stopped at time *t*.

$S(t) =$ Actual subsidence at time *t*.

$S^f(t) - S(t) =$ Subsidence potential at time *t*.

$c =$ Time constant.

The solution for time-dependent subsidence is then obtained from subtracting a virtual (translated) area *A'* –caused subsidence (multiplied by a factor) from the final subsidence caused by real area *A* (see Figure 4-33 and Figure 4-34). Equation 4-15 expresses it mathematically. The last term is considered after the mine face has stopped:

$$S(x_t, x_0, y_1, y_2, z, \Delta t) = S^f(x_t, x_0, y_1, y_2, z)$$

$$- \exp\left(\frac{{u_z}^2}{4\pi}\right)\exp\left(\frac{u_z x_t}{r_z}\right) S^f\left(x_t + \frac{r_z u_z}{2\pi}, x_0 + \frac{r_z u_z}{2\pi}, y_1, y_2, z\right)$$

$$+ \Delta S^f(x_t, x_0, y_1, y_2, z)\left[1 - \exp(-c\Delta t)\right] \qquad 4\text{-}15$$

where

$u_z = \frac{c_z r_z}{v}$, a factor.

$c_z =$ Time coefficient for horizon *z*.

Δt = Time elapsed since excavation has stopped (zero for continuously advancing face)

r_z = Radius of influence

v = Rate of advance

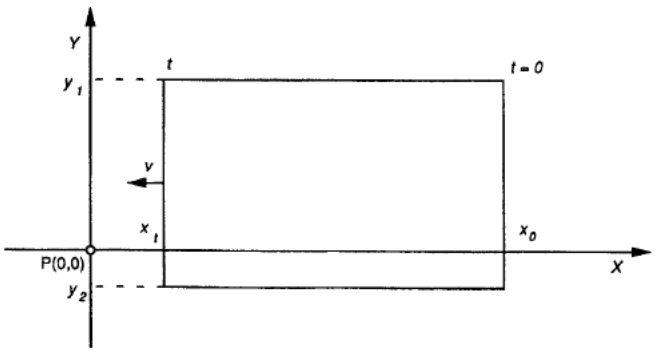

Fig. 1. Geometry of a longwall panel with one advancing side

Figure 4-33 Geometry for the method by Jarosz et al

(Jarosz, Karmis et al. 1990)

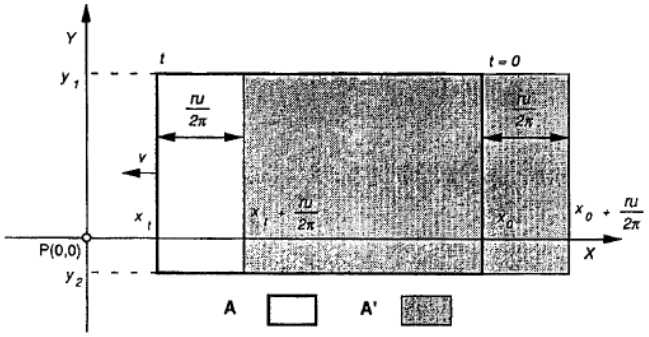

Fig. 2. Translation of an extraction contour (*A* – real contour of extraction, *A'* – translated contour)

Figure 4-34 Translation of extraction in the method by Jarosz et al

(Jarosz, Karmis et al. 1990)

Jarosz et al. (Jarosz, Karmis et al. 1990) used a value of 0.075/day for the time constant *c* for cases in Virginia and West Virginia, with average rates of advance equal to 20 ft/day. Using this value (default SDPS 6.0) for our cases would yield wrong results, as shown in Figure 4-35.

Cui et al. (Cui, Wang et al. 2001) proposed a relationship between the critical dimension *Lc*, the rate of advance, *v*, and the time coefficient, *c*:

$$c = -\frac{v}{L_c} \ln 0.02 \qquad 4\text{-}16$$

Reading from our data, our critical dimension is roughly 800 ft and our rate of advance is 57 ft/day, thus yielding c = 0.29/day. Using this value in SDPS shows that it is consistent with our data, although 0.2/day seems to be even closer (see Figure 4-35).

Once the correct value of the constant *c* is known for the region of interest, the application of dynamic subsidence prediction within SDPS 6.0 is straightforward. The user chooses a point of interest and its location with respect to the panel edges. The rate of advance is specified, and subsidence evolution can be predicted for the point of interest as a function of the distance between the point and the mine face. Positive distances correspond to positions before the mine face has reached the point of interest, whereas negative distances correspond to mine face positions passed the point of interest.

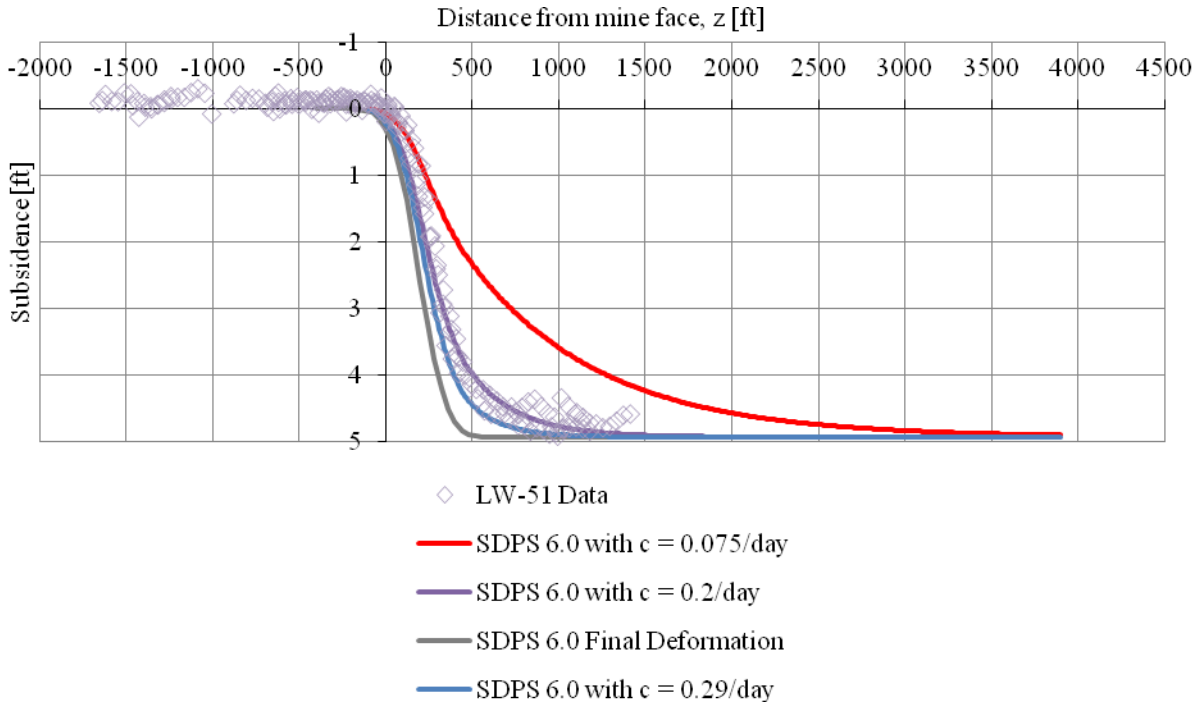

Figure 4-35 Determining the magnitude of the time constant *c*

4.3.1 An example of dynamic subsidence in SDPS 6.0 - Panel LW-51

Here we work out an example of dynamic subsidence that shows the input interface and step-by-step use of the program. This feature of SDPS 6.0 is very useful for subsidence prediction, especially while the mining face approaches and passes underneath the highway. Beside the important question of how much final subsidence the highway will be subjected to, this tool aids in answering another important question, that is, how that deformation will evolve in the time span between a few days before the mine face reaches the point of interest and a few days after. Ideally, dynamic deformation output would also aid in the correlation between the subsidence trough slopes and horizontal strains, which may be compared to well established damage

thresholds. This correlation is indeed provided in SDPS. However, in the case of highway structures these correlations do not apply, as we demonstrate in subsection 4.1.7 of this report.

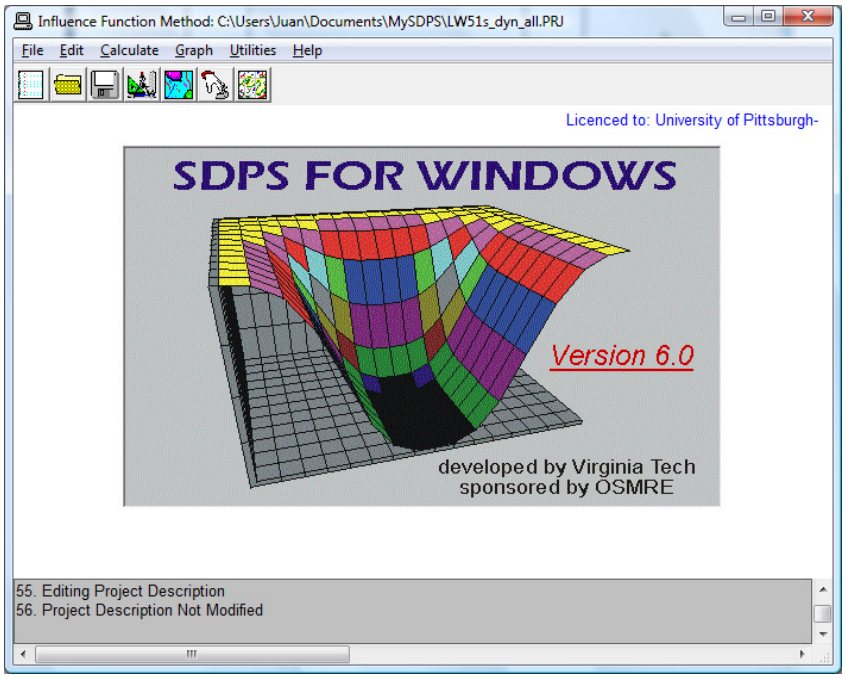

Figure 4-36 Interface of the new SDPS 6.0 version

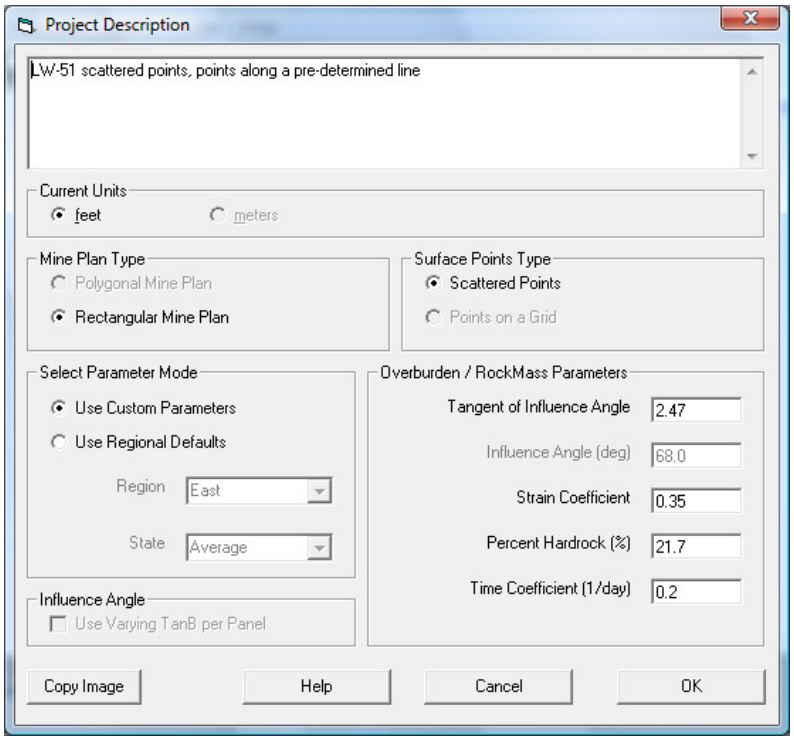

Figure 4-37 Project description input

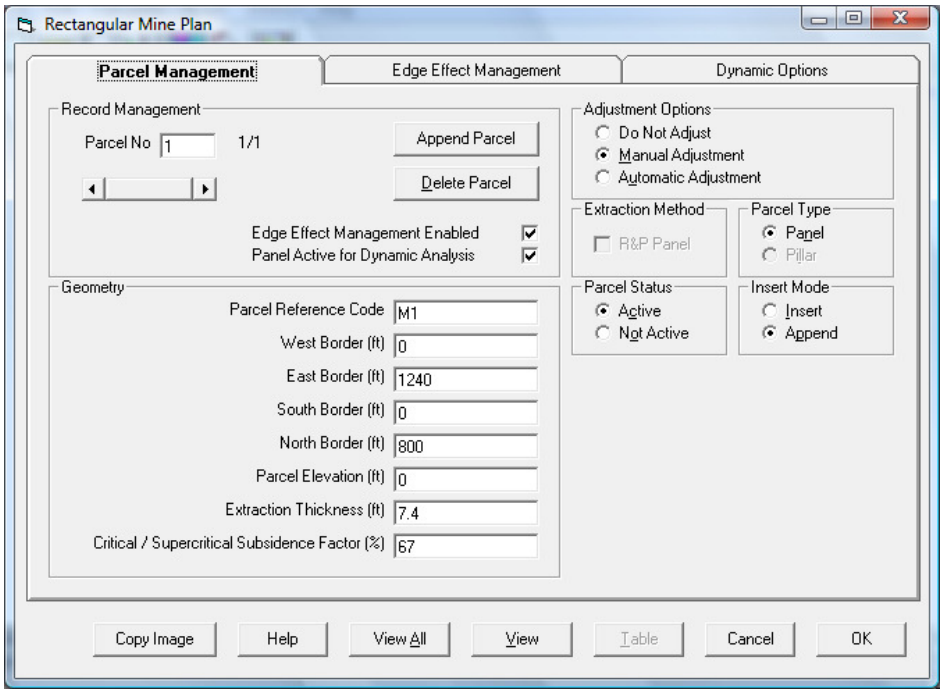

Figure 4-38 Panel geometry input

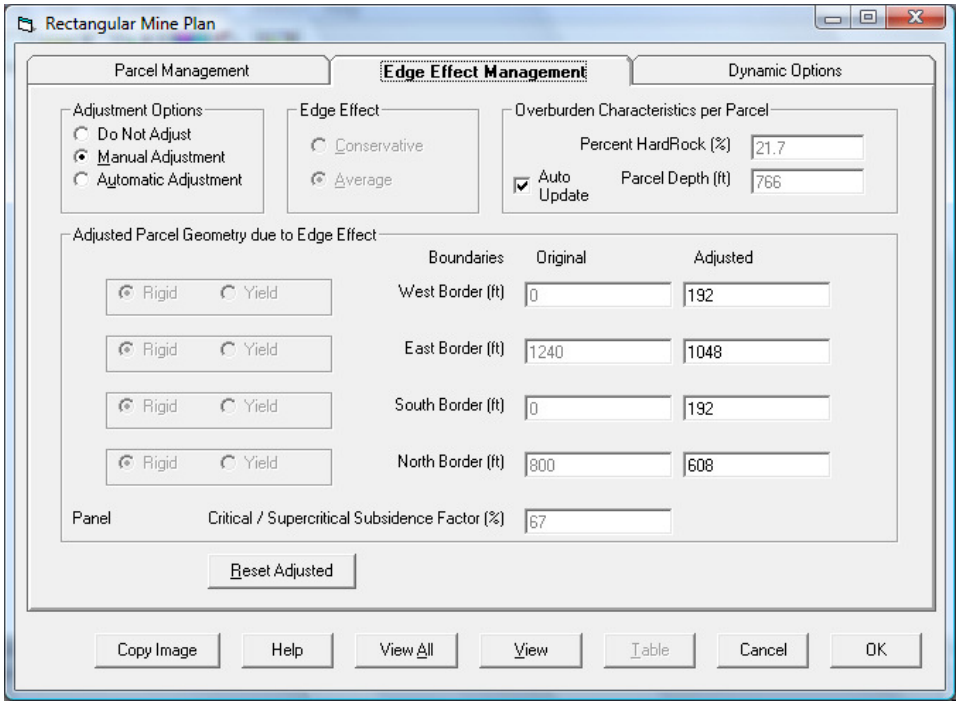

Figure 4-39 Edge effect input

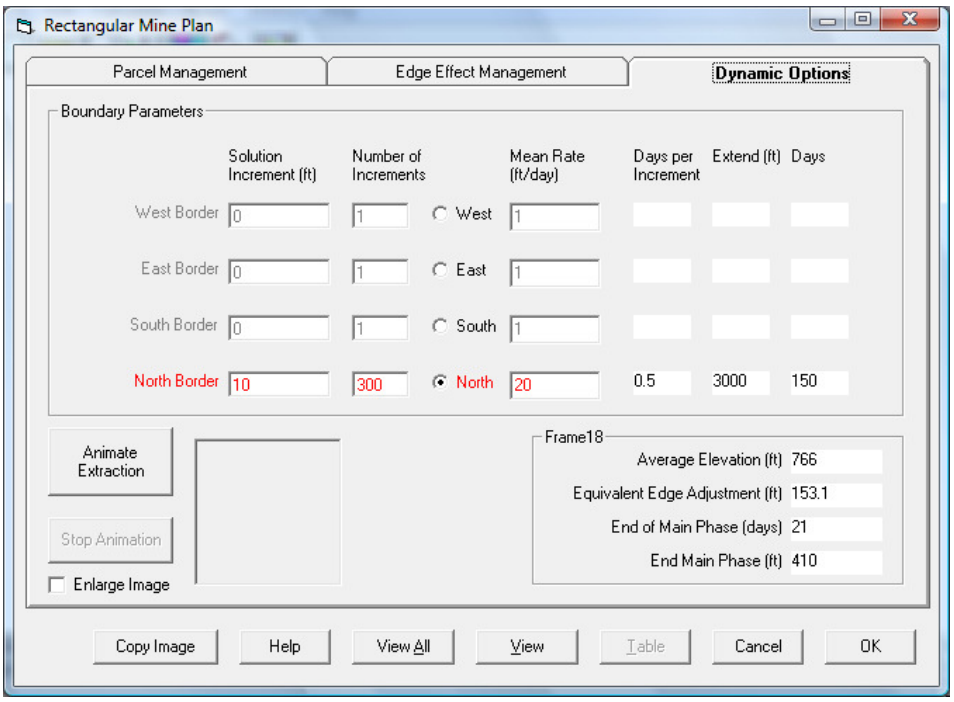

Figure 4-40 Dynamic options input

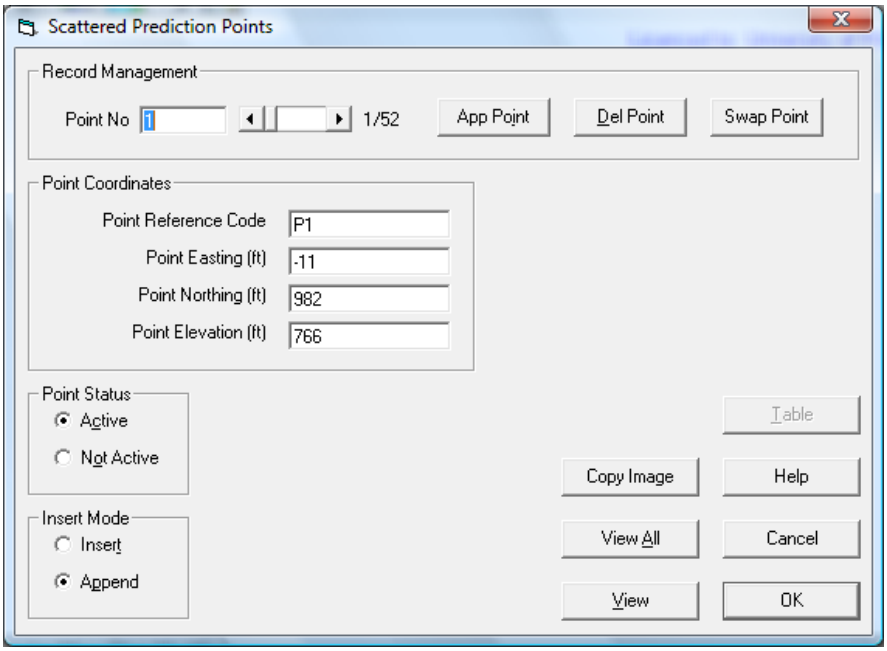

Figure 4-41 Input of coordinates for points of interest

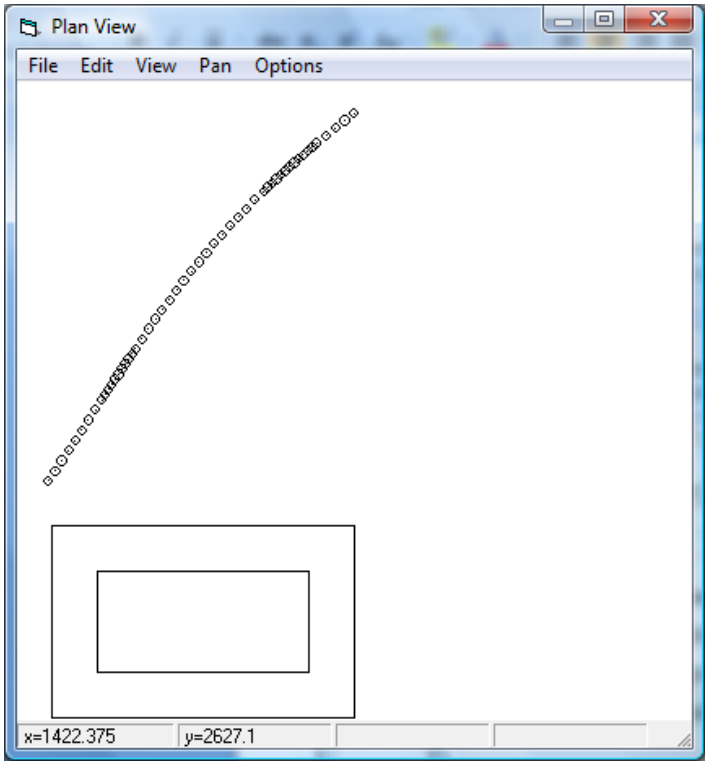

Figure 4-42 View of mining simulation

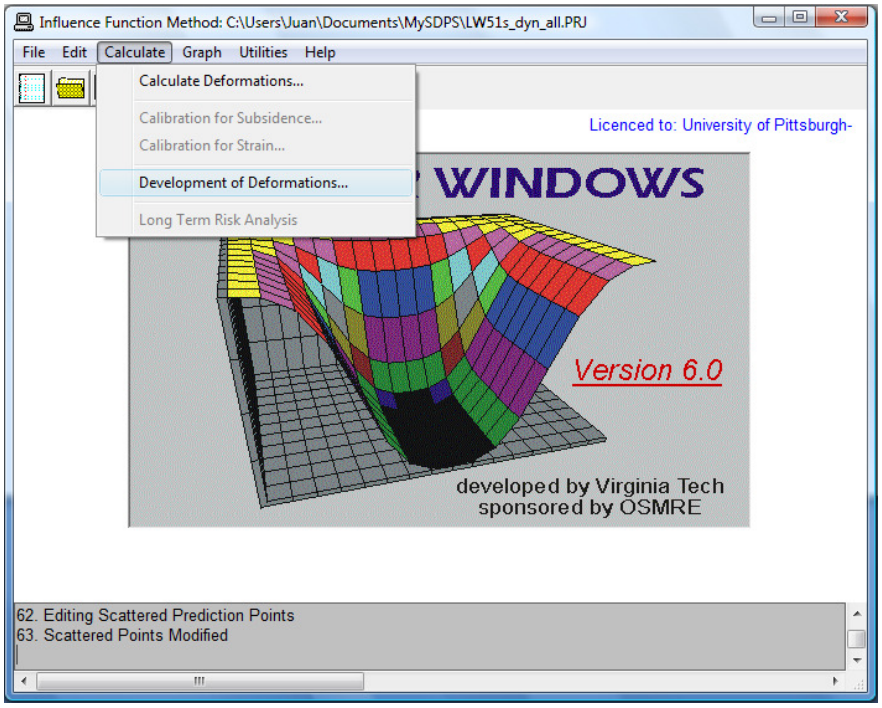

Figure 4-43 Interface of calculation options

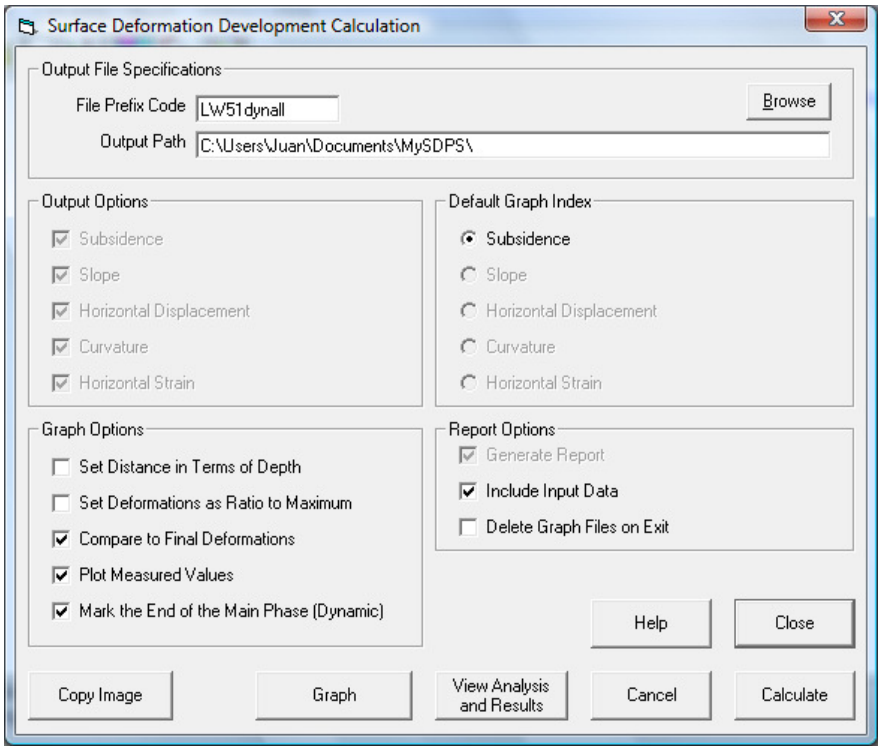

Figure 4-44 Deformation development options

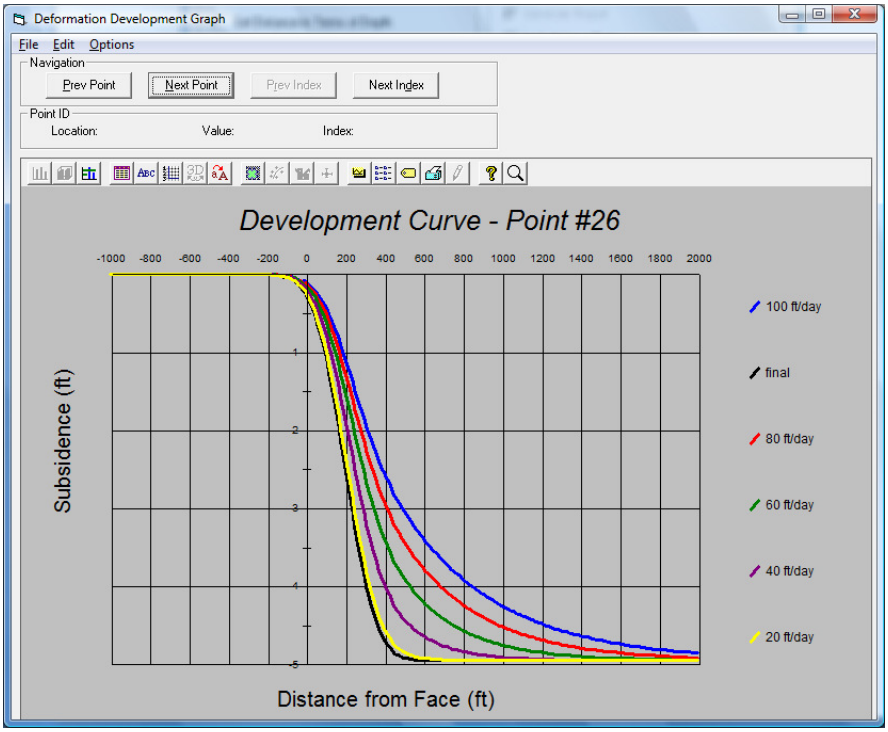

Figure 4-45 Deformation development for a central point with varying face advance rates

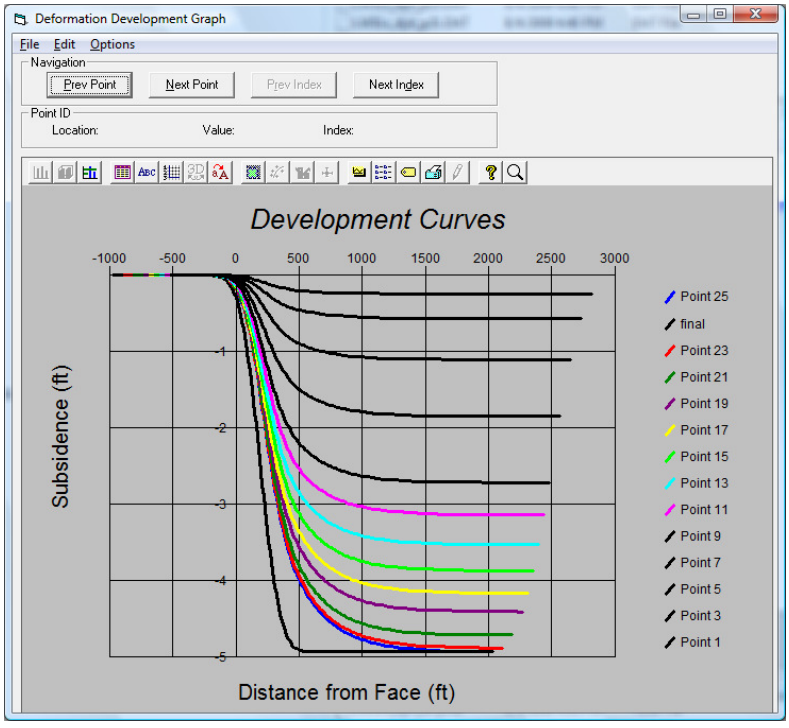

Figure 4-46 Deformation development for various points across panel width using v = 57 ft/day

4.4 GENERAL TRENDS AND FINDINGS

The data provided by PennDOT was used to better understand longwall mine subsidence through trends and new findings, which we summarize in the next few points:

- In the study region, the terrain ahead of the mine face experienced heave of roughly 0.2 ft during mining, and this behavior extended to as far as 1500 ft from the mine face.
- A clear trend was found to exist between the subsidence factor and the overburden thickness, whereby the subsidence factor decreased with increasing overburden thickness. This finding showed that even in supercritical subsidence conditions, the subsidence factor can still vary, as opposed to the SDPS method, whose maximum subsidence model yields almost constant subsidence factors in the supercritical region ($W/H > 1.2$).
- Highway embankments are extremely sensitive to horizontal movements, as these are influenced by highway grade slopes, irregular embankment cross sections with non-uniform mass distribution within the embankments, and the location and orientation of embankments in relation to the mine panels. This special behavior of embankments cannot be captured by existing subsidence tools such as SDPS, unless the geometry is symmetric and the highway grade is flat, which is rarely the case.
- There is a very clear difference between subsidence of the side of a panel that is adjacent to a previously mined panel, and one that is located in a virgin area. This behavior cannot be captured by influence functions, but can be captured by regression models such as the ones developed in this project.

5.0 TASK 5: PREDICTION OF FUTURE SUBSIDENCE TAKING PLACE UNDER HIGHWAY I-79

The present chapter has two parts. The first part gives a description of data obtained from Emerald mine's panel B-7 and discusses the differences between the results of this panel and those of previously studied panels. The second part discusses a finite element model (FEM) for highway subsidence that was not originally planned within the scope of the first phase of this project. The FEM gives promising results and can be extended to a broader study of embankment behavior due to mining subsidence. Detailed non-linear soil models can be implemented in this model in the future.

5.1 PANEL B-7

The results of Emerald mine's panel B-7 are presented here. Figure 5-1 gives the position of B-7 in the maximum subsidence model. It is evident that if B-7 would have followed the trend we found from previous panels, it would have subsided less than it did, since B-7 is the deepest of all panels we have. Figure 5-2 shows Peng's database of subsidence factor as a function of depth (Peng 1992) where subsidence factor for the deepest panel (depth of 1000 ft) is smallest. Figure 5-3 gives the relative location of our points with respect to Peng's points. The apparent departure of our points from Peng's trend may be explained by different conditions between the sites in his

database and our site at Cumberland and Emerald mines. Our average subsidence factor, however, equal to roughly 0.68, is very consistent with a rule of thumb value of 0.67 suggested by an expert familiar with the zone of southwestern Pennsylvania, as we have mentioned before in this report. As far as Peng's database is concerned, the exact locations were not provided. Regardless of the magnitude in subsidence factor, both trends are consistent in that this factor decreases with relative increases of the overburden depth, and this is where B-7 falls out of the expected zone.

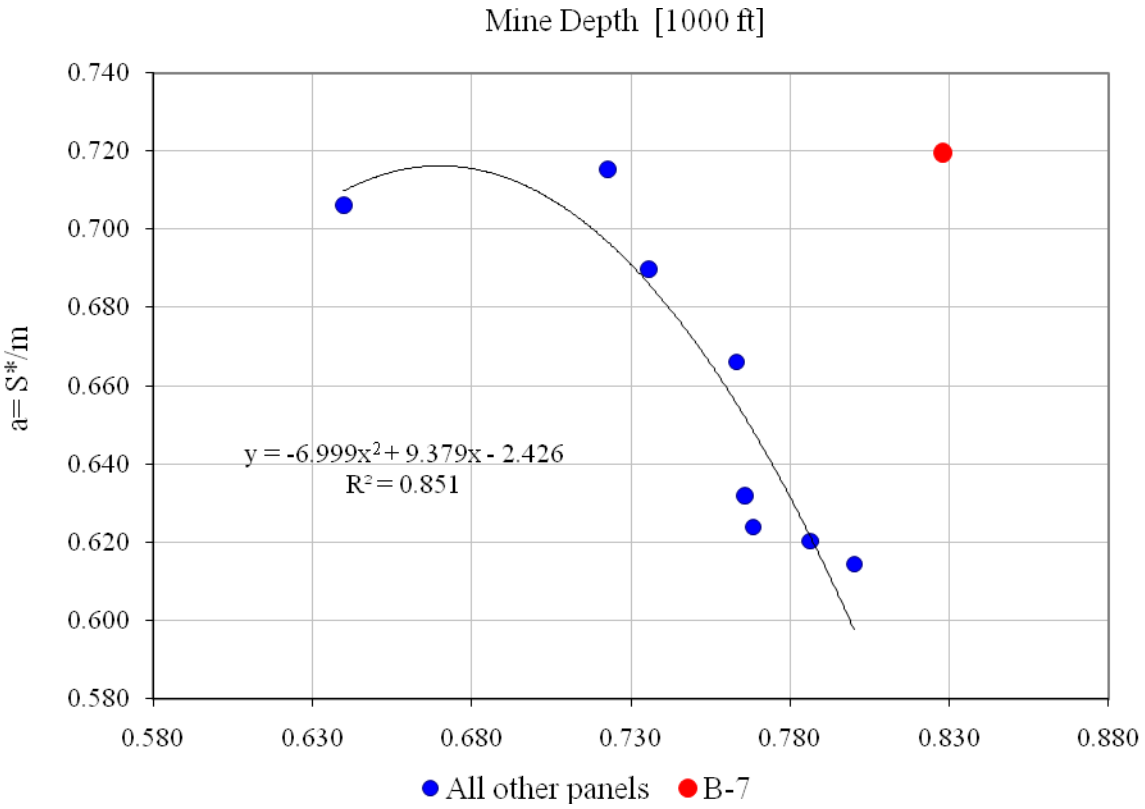

Figure 5-1 Maximum subsidence model and B-7

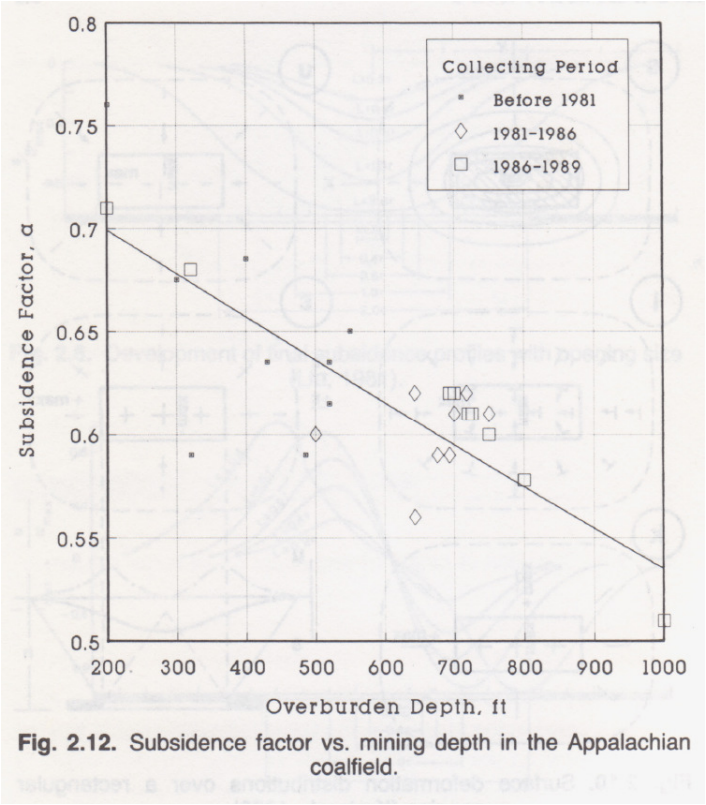

Fig. 2.12. Subsidence factor vs. mining depth in the Appalachian coalfield.

Figure 5-2 Peng's database of subsidence factor as a function of depth in Appalachia

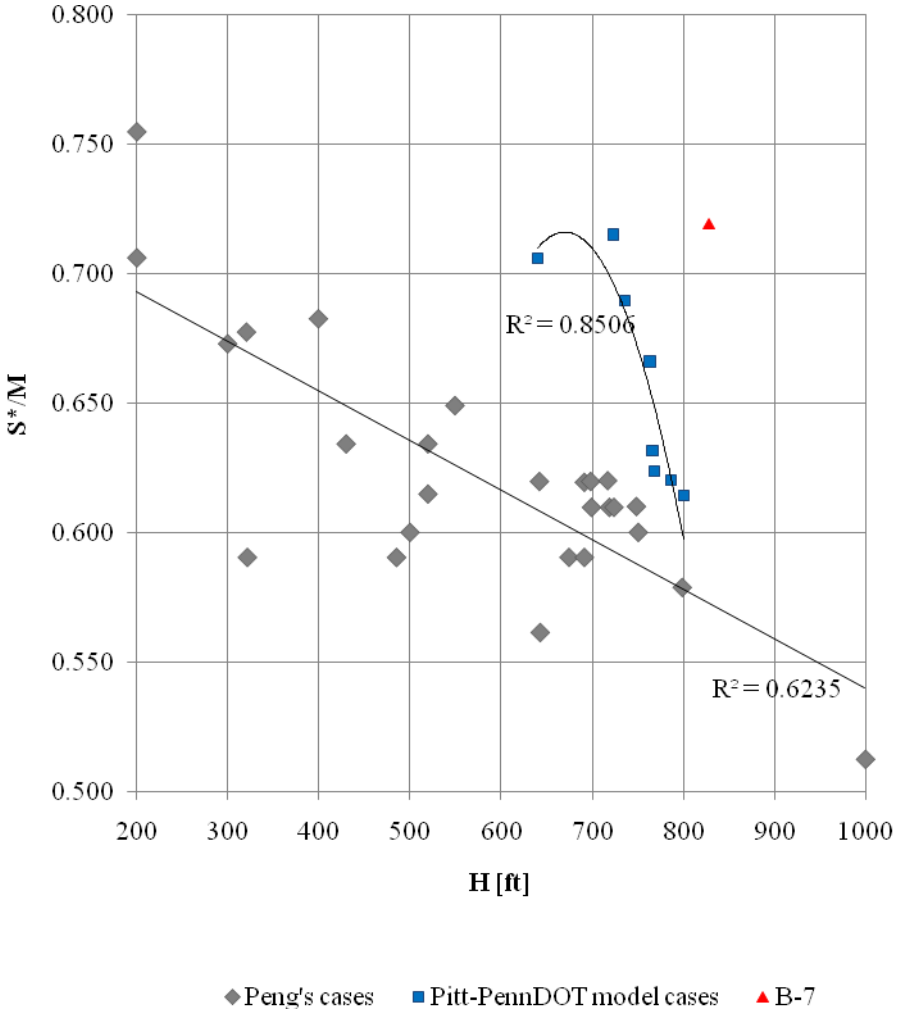

Figure 5-3 Location of project points with respect to Peng's database

We have reported previously that heave of roughly 0.3 ft took place before the rock overburden subsided in previous panels. This heave seems to be an indication of the strength and soundness of the overburden rock. This behavior could not be observed in the case of B-7, as can be seen in Figure 5-4 and Figure 5-5. These data show that even for earlier dates, when the highway had not yet been reached, the movement of the overburden was in a downward direction.

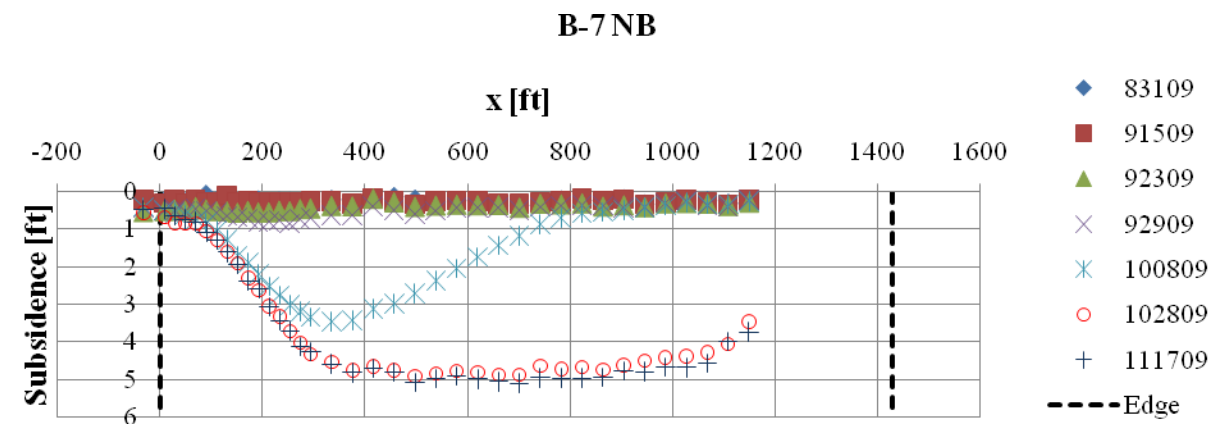

Figure 5-4 Transversal view of I-79 northbound station subsidence for different dates above B-7

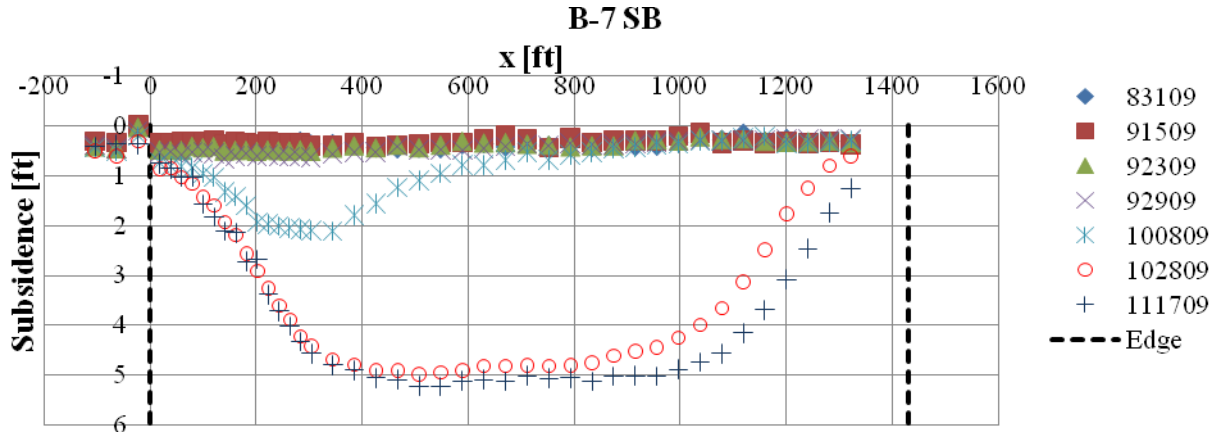

Figure 5-5 Transversal view of I-79 southbound station subsidence for different dates above B-7

In regard to the dynamic subsidence behavior, B-7 was mined-out at an average rate of advance of 24 ft/day as opposed to the average 57 ft/day in previous panels. This suggested that we could find differences in the subsidence development curves, specifically a sharper shape given the reduction in rate of advance. However, while B-7 was mined out slowly, it also happened to be substantially deeper than previous panels. Since deeper panels produce flatter development shapes, and slower mining produces sharper development shapes , these two factors seem to have

interacted in this case, producing a net effect that could not be differentiated from the previous cases. Figure 5-6 gives the measured development curves, while Figure 5-7 gives a prediction using SDPS 6.0. It turns out that SDPS is very sensitive to the rate of advance in its dynamic subsidence methodology and almost insensitive to the overburden thickness. Therefore, SDPS 6.0 predicts a much sharper shape for the case of 24 ft/day than for 57 ft/day. This, as demonstrated in Figure 5-6, is not what we find in the field. Figure 5-6 gives a clear comparison between a panel that experienced some degree of heave ahead of the mine face (LW-51) and B-7, which experienced downward movements ahead of the panel.

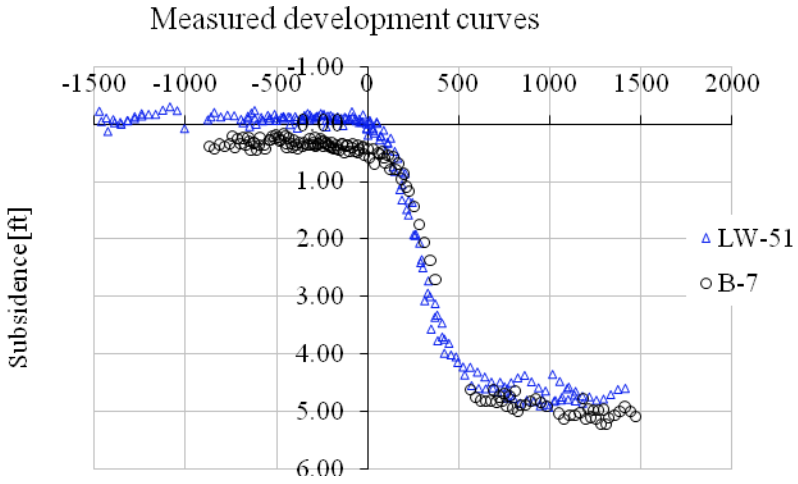

Figure 5-6 Measured subsidence development curves for B-7 and LW-51

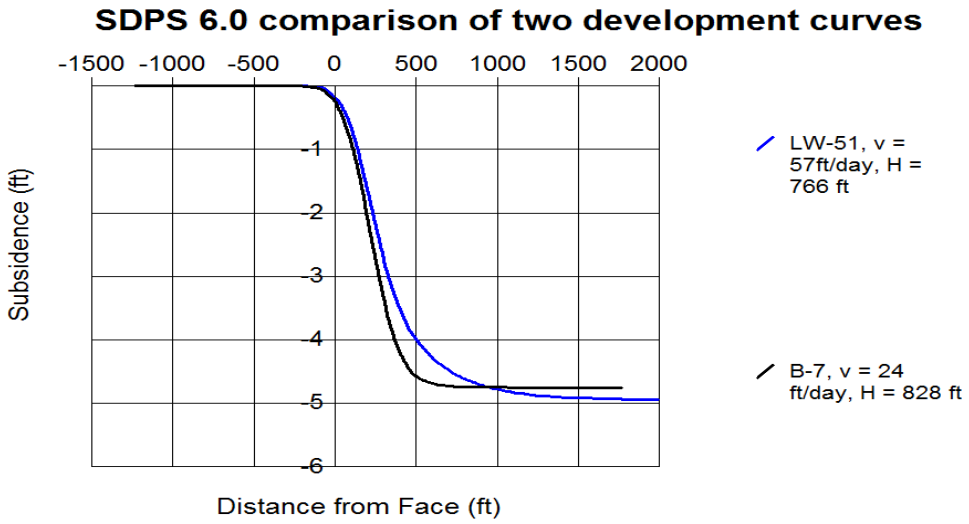

Figure 5-7 SDPS predicted subsidence development curves for B-7 and LW-51

5.2 HIGHWAY SUBSIDENCE FINITE ELEMENT MODEL

A Finite Element Model (FEM) for the problem of highway subsidence is proposed here. Table 5-1 gives a list of the actual rock layers encountered in the field, according to a 1955 boring log by Mott Core Drilling Company in Perry Township, Greene County, and their thicknesses, as well as a set of layers used in the finite element model.

Table 5-1 Boring log and FEM model layer thicknesses

Sub-layer No. (bottom-up)	Approx. thickness of individual layers [ft]	Approx. thickness of individual layers [m]	Depth [m]	Rock type	FEM Layer (bottom-up)	Total layer thickness [m]
55	5.0	1.5	1.5	Surface	29	4.0
54	6.0	1.8	3.4	Brown clay		
53	12.0	3.7	7.0	Gray shale	28	4.0
52	40.5	12.3	19.4	Gray sandy shale	27	12.0
51	17.5	5.3	24.7	Dark shale	26	5.0
50	3.4	1.0	25.7	Sandy shale	25	3.0
49	6.5	2.0	27.7	Gray shale		
48	1.4	0.4	28.1	Coal		
47	20.0	6.1	34.2	Dark shale	24	8.0
46	1.0	0.3	34.5	Coal	23	5.0
45	12.6	3.8	38.4	Sandy shale		
44	3.5	1.1	39.4	Dark shale		
43	52.5	16.0	55.4	Sandy lime	22	18.0
42	7.2	2.2	57.6	Sandstone		
41	10.3	3.1	60.8	Gray lime	21	7.0
40	2.5	0.8	61.5	Sandy lime		
39	7.0	2.1	63.7	Gray lime		
38	3.7	1.1	64.8	Coal		

Table 5-1 (Continued)

Sub-layer No. (bottom-up)	Aprox. thickness of individual layers [ft]	Aprox. thickness of individual layers [m]	Depth [m]	Rock type	FEM Layer (bottom-up)	FEM Total layer thickness [m]
37	4.6	1.4	66.2	Green lime	20	4.0
36	10.0	3.0	69.3	Green soft lime		
35	35.7	10.9	80.1	Sandstone	19	11.0
34	20.0	6.1	86.2	Dark shale	18	8.0
33	7.2	2.2	88.4	Coal		
32	10.0	3.0	91.5	Sandy shale	17	6.0
31	3.2	1.0	92.4	Sandstone		
30	5.0	1.5	94.0	Dark shale		
29	15.5	4.7	98.7	Gray lime	16	5.0
28	10.3	3.1	101.8	Green lime	15	5.0
27	5.5	1.7	103.5	White lime		
26	15.4	4.7	108.2	Green lime	14	5.0
25	10.3	3.1	111.3	White lime	13	7.0
24	14.2	4.3	115.7	Gray lime		
23	36.0	11.0	126.6	White lime	12	11.0
22	25.5	7.8	134.4	Sandy lime	11	8.0
21	7.3	2.2	136.6	White lime	10	12.0
20	32.7	10.0	146.6	Lime shale streaks		
19	12.0	3.7	150.3	White lime	9	4.0
18	4.4	1.3	151.6	Dark shale	8	9.0
17	10.4	3.2	154.8	Gray lime		
16	3.2	1.0	155.8	Green lime		
15	12.0	3.7	159.4	Gray lime		
14	13.0	4.0	163.4	Sandy shale	7	6.0
13	4.4	1.3	164.7	Dark shale		
12	3.8	1.2	165.9	Coal		
11	17.0	5.2	171.1	Dark shale	6	5.0
10	24.5	7.5	178.5	Sandy shale	5	7.0
9	3.0	0.9	179.4	Dark shale	4	5.3
8	2.0	0.6	180.0	Soft clay		
7	1.1	0.3	180.4	Coal		
6	2.0	0.6	181.0	Dark shale		
5	6.6	2.0	183.0	Gray lime	3	5.3
4	14.2	4.3	187.3	Dark shale		
3	7.6	2.3	189.6	Bone coal streaks		
2	7.4	2.3	191.9	Coal	2	2.4
1	131.2	40.0	231.9	Floor	1	40.0

5.2.1 General description of FEM model

The coal extraction in the following variants of the FEM model was done at a depth of 623 ft. The extraction magnitude was 7.9 ft, and the model took on the form of a block with a length of 3280 ft, width of 1640 ft, and height of 1083 ft. The layer partition of the FEM model was done such that the number of layers could be reduced for the ease of building and running the model. The use of a stack of layers in subsidence modeling is important because the relative displacement between layers and the relatively low bending stiffness of individual layers allow for realistic subsidence trough shapes. Su built a FEM with several layers and obtained accurate shape of the subsidence trough (Su 1991). Besides FEM, a laminated Boundary Element model also considered a stack of layers and was used in subsidence modeling (Heasley and Barton 1998).

The FEM model proposed here was developed using the software LS-DYNA. The model has been implemented mainly for linear elastic material, although in some cases a basic elasto-plastic material was used. Between layers, a tiebreak contact definition and friction angle can be used. The basic strength parameters used in the tiebreak definition are tensile strength and shear strength. A contact failure criterion involves these two parameters. When the failure criterion is met, the bonds between the layers are broken and relative displacements occur between them.

5.2.2 FEM calibration criteria in the context of subsidence

Calibration of the FEM model was planned based on three criteria that are important in a subsidence model. The criteria are: subsidence trough shape, maximum subsidence magnitude, and post-mining vertical stress distribution in the panel abutment and gob areas of the panel.

Obtaining reasonable results of these three characteristics is the main motivation behind the development of the model. A brief description of each of these is given here. The next sub-section explores the trade-offs between these criteria.

5.2.2.1 Subsidence trough shape

The shape of the subsidence trough is a very important feature in a prediction model. Underground extractions in materials that behave somewhat elastically will produce S-shapes in the surface when the extractions reach certain dimensions. However, the S-shaped subsidence curve needs to be accurate if the model is intended to serve prediction of surface deformations, as the exact location of critical deformations needs to be known. The key to the correct shape of subsidence troughs is the stacking of several thin layers that represent the geologic strata in the overburden rock. The correct shape of a subsidence trough can be calibrated trough appropriate number of layers, relative thickness of the layers with respect to overburden depth, mechanical properties of the layer material, and strength of the bonding between layers.

5.2.2.2 Maximum subsidence

The problem of predicting maximum subsidence has been discussed and a maximum subsidence model for the region has been proposed (see Figure 3-5). For this purpose, the ratio of maximum subsidence to extraction thickness, *S*/M*, was used, which is always less than 1.0 and in the vicinity of 0.67 in southwestern Pennsylvania. An important factor that contributes to this ratio being always less than 1.0 is the bulking factor. Peng defines the bulking factor as "the ratio of the volume of the broken rock strata to the original volume of the same strata before they are broken and cave." It continues: "Since the volume of the broken strata is always larger than that of the original intact strata, bulking factor is usually larger than one" (Peng 2008).

The average value of bulking factor measured by Peng was 1.28. The bulking behavior of broken rock is a feature not considered in the present FEM model. Even though LS-DYNA has the capabilities necessary to model damage in rock materials, its implementation in the problem of three-dimensional subsidence would be computationally extremely expensive and impractical. Obtaining magnitudes of subsidence in supercritical troughs that are less than the extracted thickness is a very difficult task without considering the bulking factor. Even though it is still possible to get the correct value of the *S*/M* ratio if the roof of the extracted cavity is not allowed to touch the floor, the resulting distribution of vertical stress in the panel abutment and gob areas and the trough shape so obtained are not completely satisfactory.

5.2.2.3 Post-mining vertical stress distribution in the panel abutment and gob areas

The model would be expected to give not only correct subsidence magnitude and shape, but also a reasonably correct redistribution of post-mining vertical stresses in the panel abutment and gob areas. This would consistently connect the mechanics in the mine with the deformations on the surface. Otherwise, many different combinations of parameters could be used to produce correct subsidence magnitudes and shapes without truly representing the mechanics of the problem. Typical panel abutment and gob stress distributions are given in Figure 5-8 and Figure 5-9 (Morsy and Peng 2002).

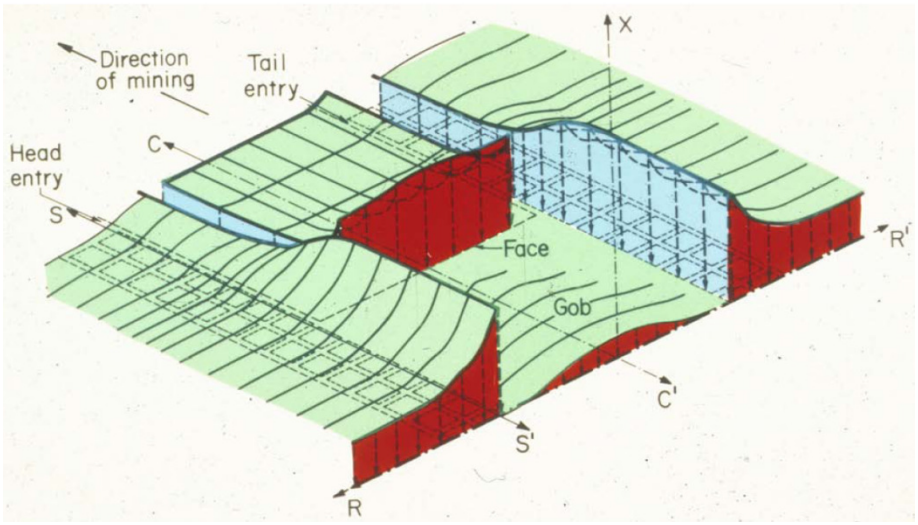

Figure 5-8 Qualitative panel abutment stress distribution

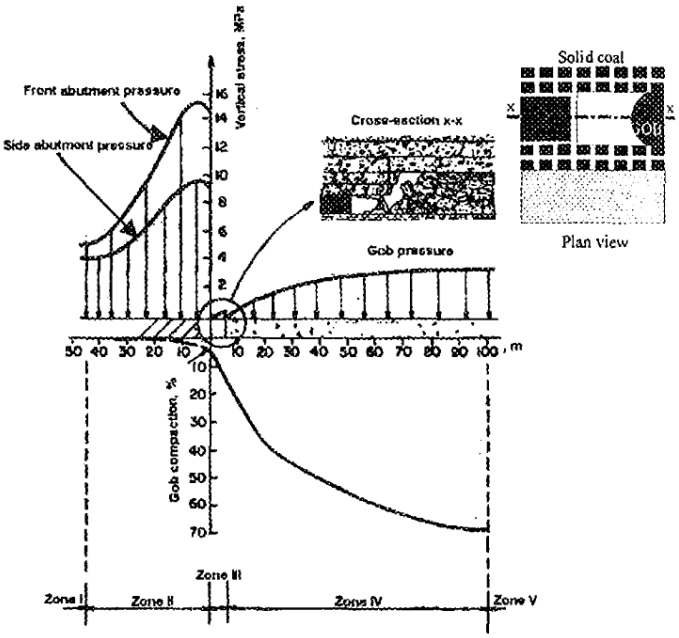

Figure 5-9 Probable distribution of strata pressure in the vicinity of the longwall face

(Morsy and Peng 2002)

5.2.3 Trade-off between subsidence shape, subsidence magnitude, and post-mining vertical stress redistribution

The first model investigation begins with a stack of relatively thin layers whose thicknesses are given in Table 5-1. Several cases will be explored in which each of the three calibration criteria is analyzed.

5.2.3.1 Case 1

The modulus of elasticity for all layers is equal to 2.14×10^6 psi (1.48×10^{10} Pa) and the Poisson's ratio is equal to 0.22. These are average values based on the values used by Su (Su 1991). The tensile and shear interface bond strengths were varied linearly from the top to the bottom in the range 340 psi (2.35×10^6 Pa) to 803 psi (5.55×10^6 Pa), for an average of 572 psi (3.95×10^6 Pa) for the first case, roughly 10% of the compressive strength of a typical rock encountered in this region. This first model is given in Figure 5-10. *S*/M* turned out to be equal to 1.09 because the layers fall into the created extraction, thus fully closing the vertical gap. The readings of subsidence were corrected by subtracting the initial settlement due to the application of gravity to the whole model.

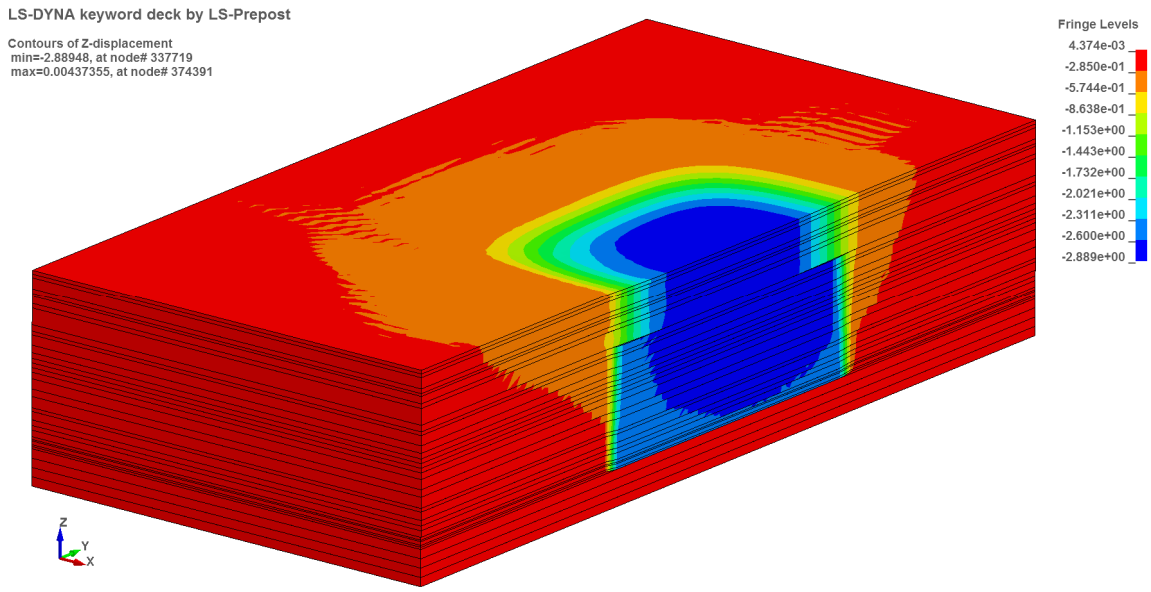

Figure 5-10 Subsidence for case 1

The shape of the trough obtained with this first model is given in Figure 5-11. In terms of shape, it can appreciated that the stacking of thin layers is very effective and a very accurate shape may be obtained.

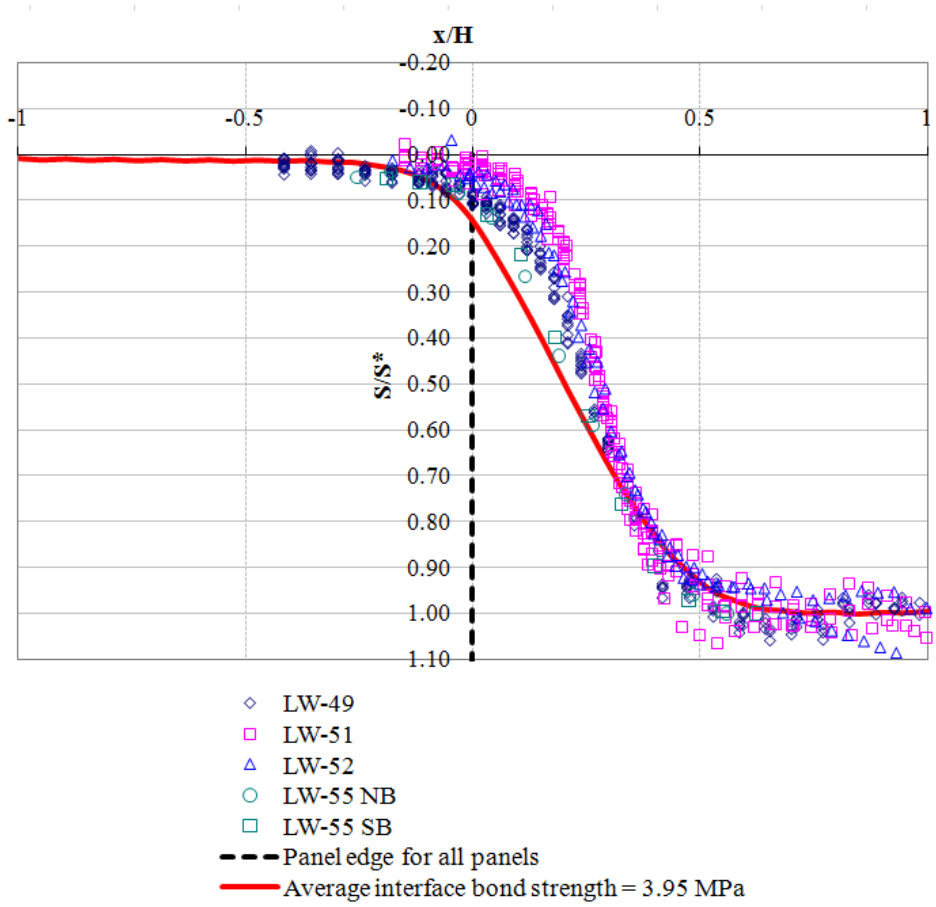

Figure 5-11 Shape of subsidence trough for case 1

The post-mining redistribution of stresses is given in Figure 5-12. Since the central portion of the stack of layers is allowed to fall downward with all of its weight applied on the floor of the cavity, the magnitude of the stresses is essentially the same in the gob as in the panel abutments.

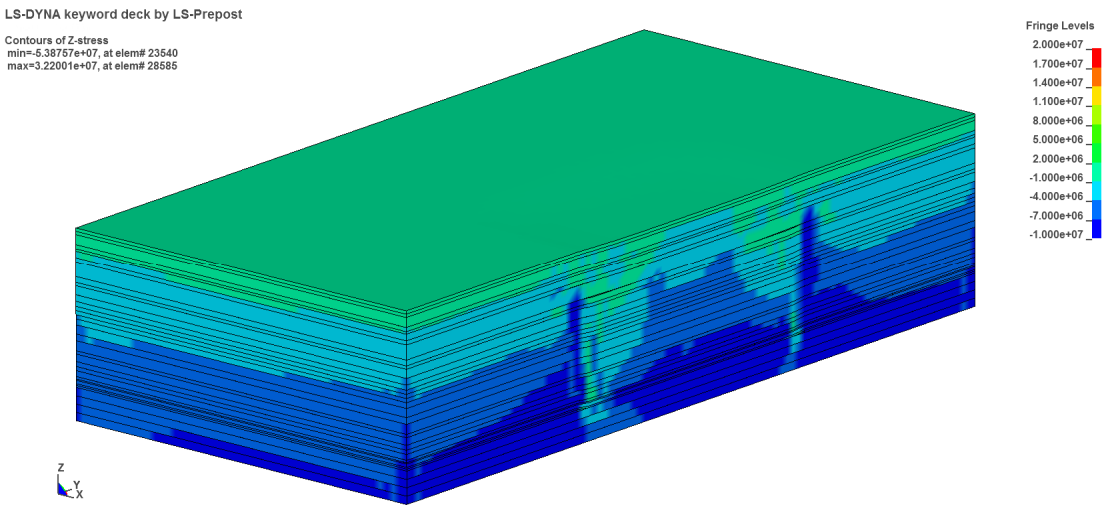

Figure 5-12 Post-mining vertical stress redistribution for case 1

5.2.3.2 Case 2

In case 2, the modulus of elasticity for all layers is also equal to 2.14x10^6 psi (1.48x10^{10} Pa) and the Poisson's ratio is equal to 0.22. The tensile and shear interface bond strengths were varied linearly from the top to the bottom in the range 347 psi (2.40x10^6 Pa) to 810 psi (5.60x10^6 Pa), for an average of 579 psi (4.00x10^6 Pa) for the first case, just a slight increase with respect to case 1. This second model is given in Figure 5-13. *S*/M* turned out to be equal to 1.07 because the layers fall into the created extraction, thus fully closing the vertical gap. The readings of subsidence were corrected by subtracting the initial settlement due to the application of gravity to the whole model. The shape of the trough obtained with the second model is given in Figure 5-14.

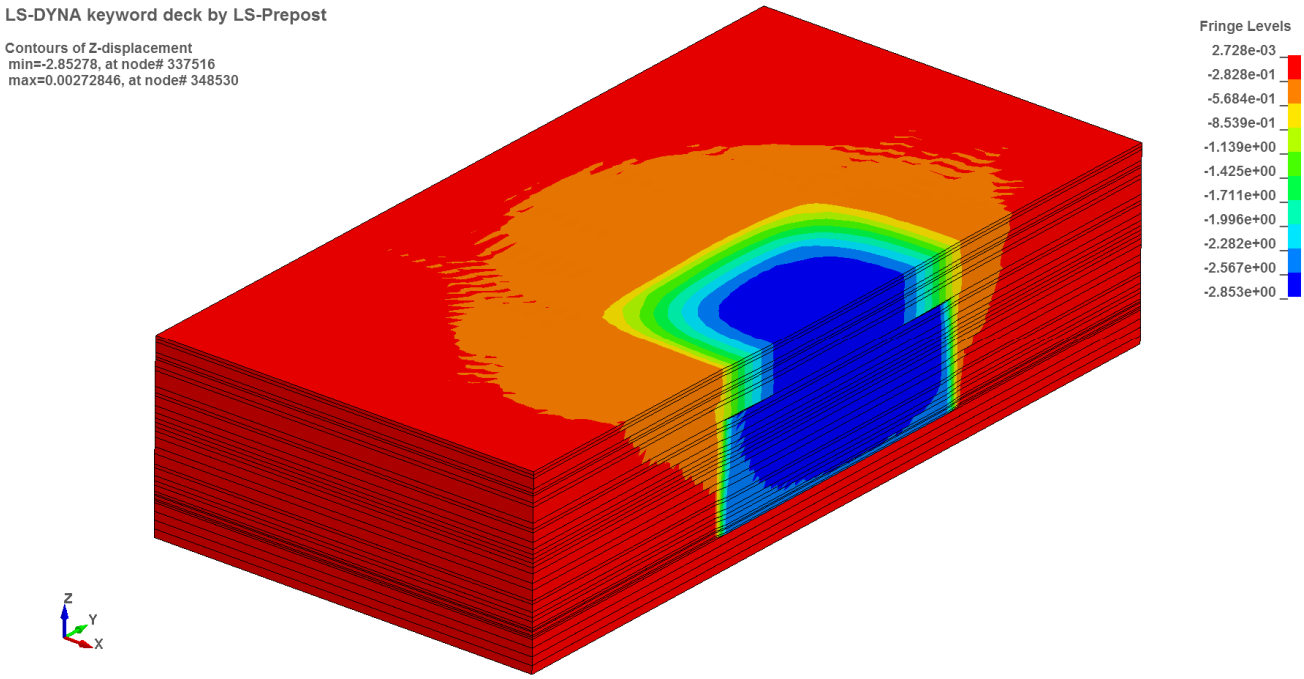

Figure 5-13 Subsidence for case 2

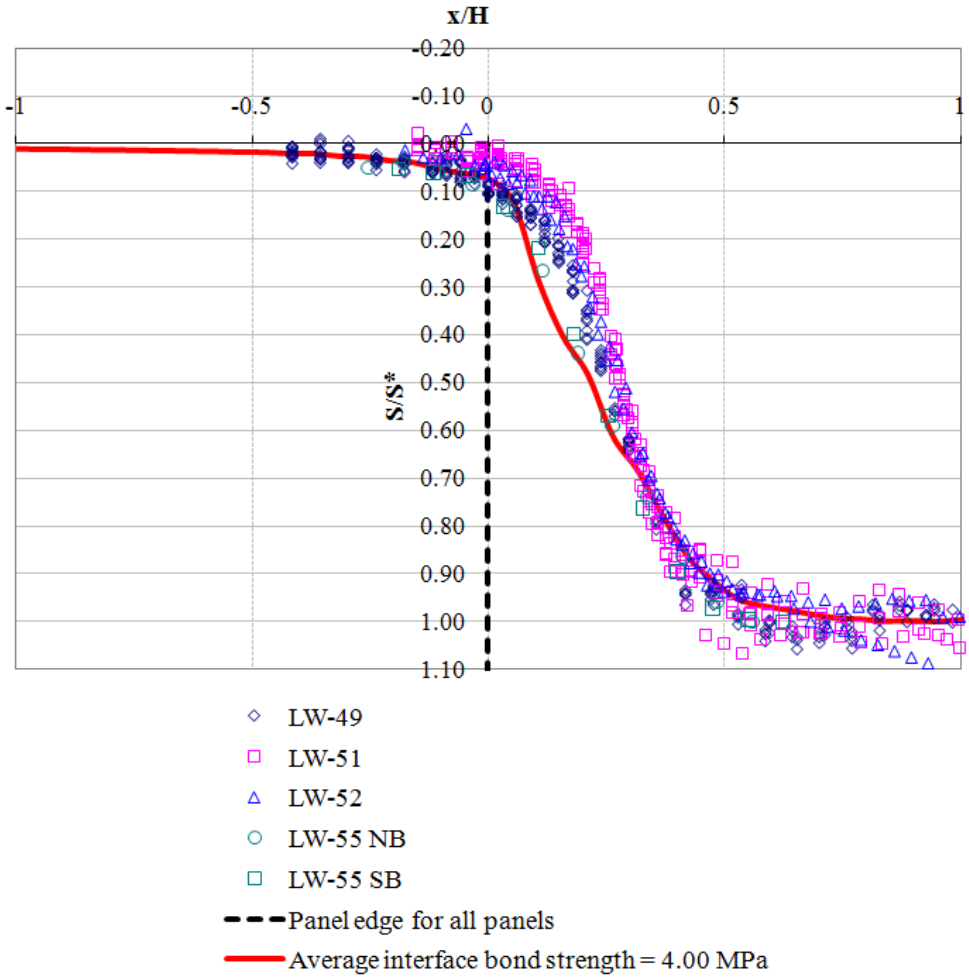

Figure 5-14 Shape of subsidence trough for case 2

The post-mining redistribution of stresses is given in Figure 5-15. Since the central portion of the stack of layers is allowed to fall downward with all of its weight applied on the floor of the cavity, the magnitude of the stresses is essentially the same in the gob as in the panel abutments.

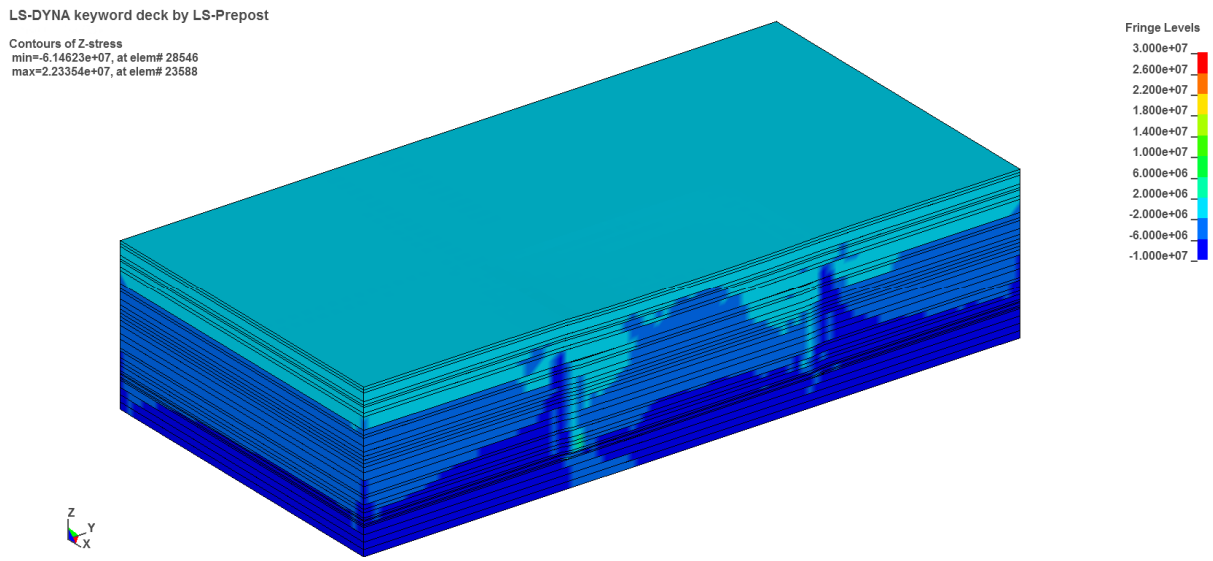

Figure 5-15 Post-mining vertical stress redistribution for case 2

5.2.3.3 Case 3

In case 3, the modulus of elasticity for all layers is also equal to 2.14×10^6 psi (1.48×10^{10} Pa) and the Poisson's ratio is equal to 0.22. The tensile and shear interface bond strengths were varied linearly from the top to the bottom in the range 355 psi (2.45×10^6 Pa) to 818 psi (5.65×10^6 Pa), for an average of 586 psi (4.05×10^6 Pa) for the first case, again a very slight increase with respect to case 2. This third model is given in Figure 5-16. *S*/M* in this model goes abruptly down to 0.24 as the whole stack of layers remains hanging in the central portion and supported only in the panel abutments. The readings of subsidence were corrected by subtracting the initial settlement due to the application of gravity to the whole model. The shape of the trough obtained with the third model is very flat, as given in Figure 5-17.

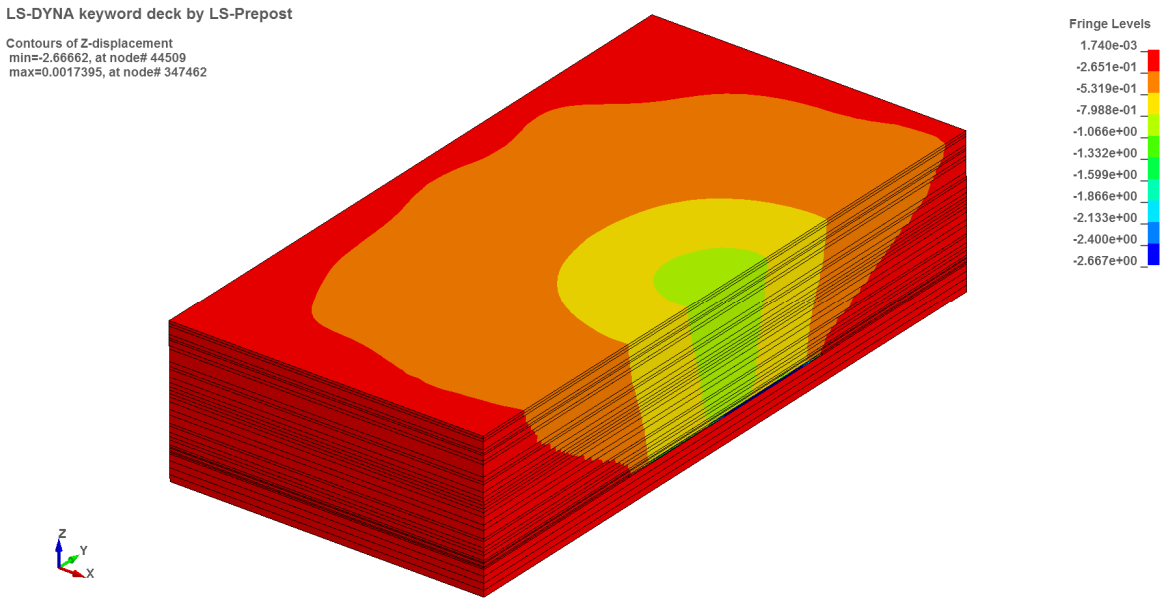

Figure 5-16 Subsidence for case 3

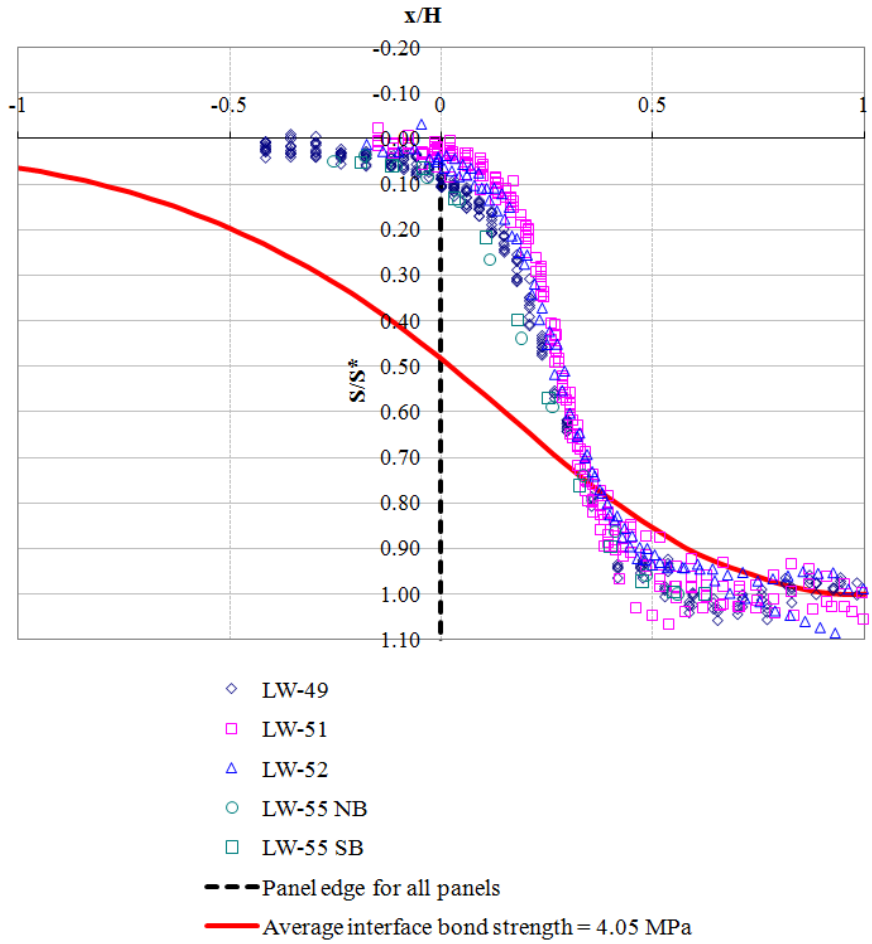

Figure 5-17 Shape of subsidence trough for case 3

The post-mining redistribution of stresses is given in Figure 5-18. Since the central portion of the stack of layers is not touching the floor of the cavity, the magnitude of the stresses in the panel abutments is high whereas the central part of the overburden is in tension.

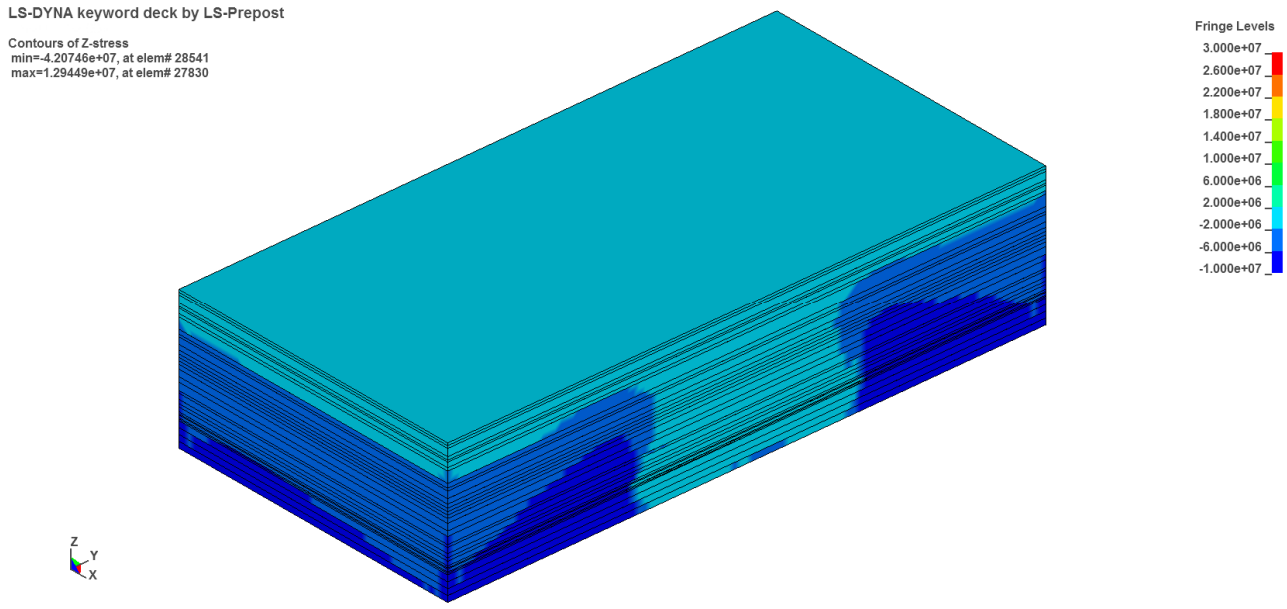

Figure 5-18 Post-mining vertical stress redistribution for case 3

5.2.3.4 Case 4

In case 4, the modulus of elasticity for all layers is also equal to 2.14×10^6 psi (1.48×10^{10} Pa) and the Poisson's ratio is equal to 0.22. A different treatment is given to the interface bonding. A sequence is used in which every third pair of layers are allowed to freely slide with respect to each other, whereas the layers in between are bonded through a high strength of 1.4×10^5 psi (100 MPa). The sequence of sliding allowance in terms of 1 and 0 is 1001001 where 1 means "allowed to slide" and 0 gets the high bond strength of 1.4×10^5 psi (100 MPa). The fourth model is given in Figure 5-19. *S*/M* in this model turns out to be equal to 1.12 as the whole stack of

layers is allowed to fall on the central floor. The readings of subsidence were corrected by subtracting the initial settlement due to the application of gravity to the whole model.

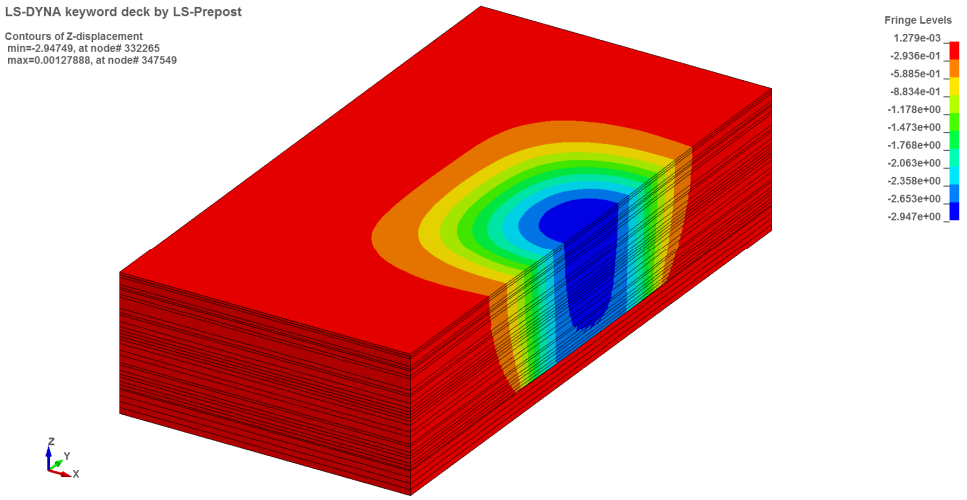

Figure 5-19 Subsidence for case 4

The shape of the trough obtained with the fourth model is given in Figure 5-20. The shape is not correct because only the central portion of the overburden roof is in contact with the floor.

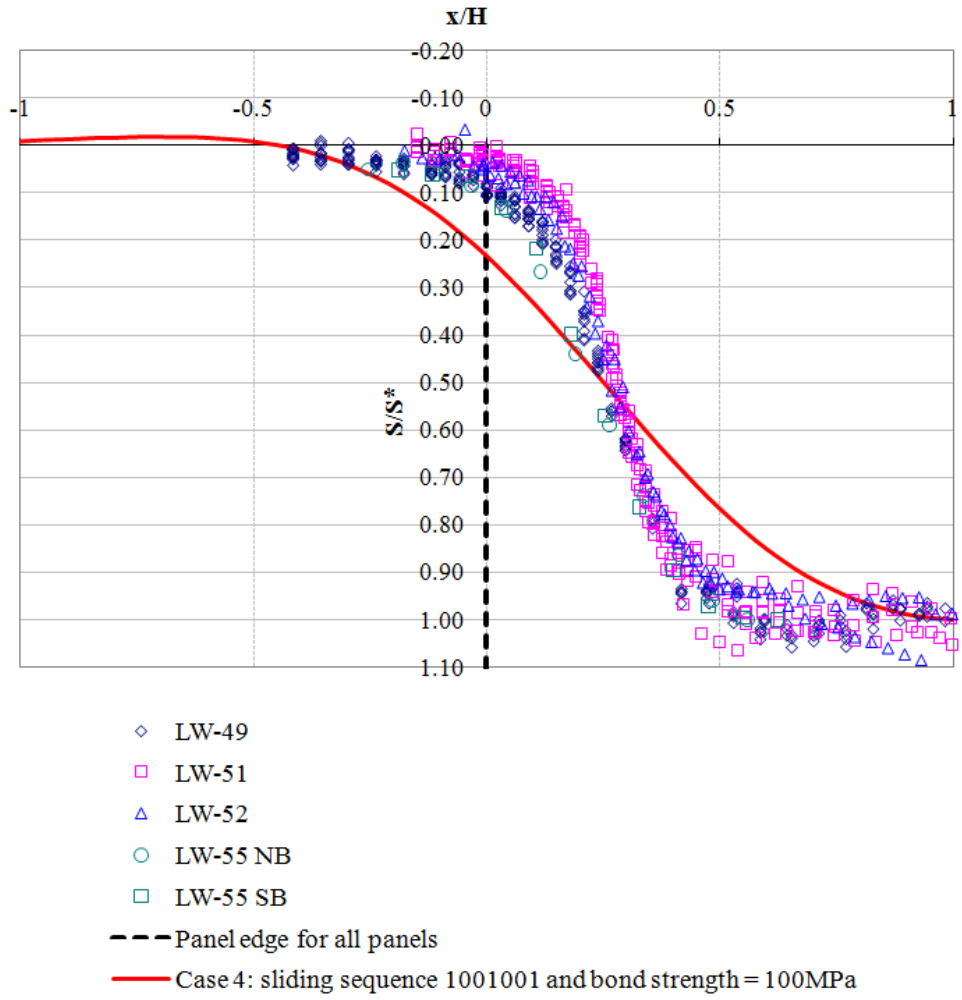

Figure 5-20 Shape of subsidence trough for case 4

The post-mining redistribution of stresses is given in Figure 5-21. Since the central portion of the stack of layers is allowed to fall downward with all of its weight applied on the floor of the cavity in the central portion, the magnitude of the stresses is essentially the same in the center of the gob as in the panel abutments.

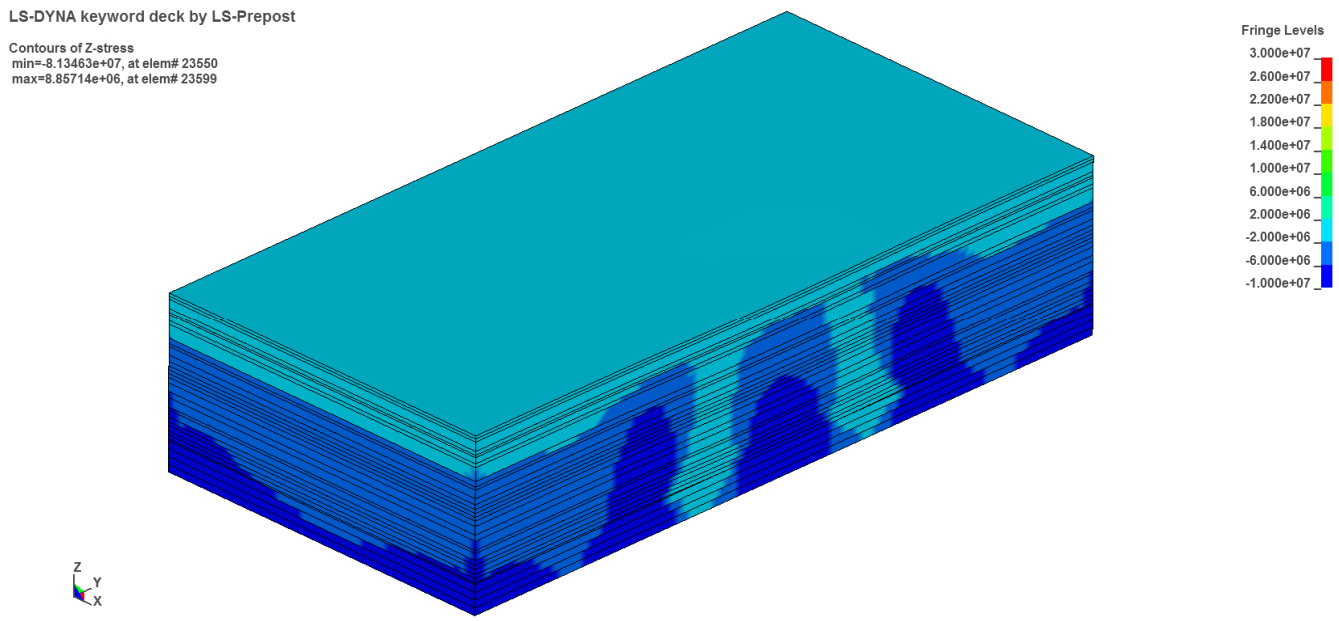

Figure 5-21 Post-mining vertical stress redistribution for case 4

5.2.3.5 Case 5

Case 5 is like case 4, except for the sequence of sliding allowance. In this case, this sequence is 100010001. The fifth model is given in Figure 5-22. *S*/M* in this model turns out to be equal to 1.06 as the whole stack of layers is still allowed to fall on the central floor. The readings of subsidence were corrected by subtracting the initial settlement due to the application of gravity to the whole model.

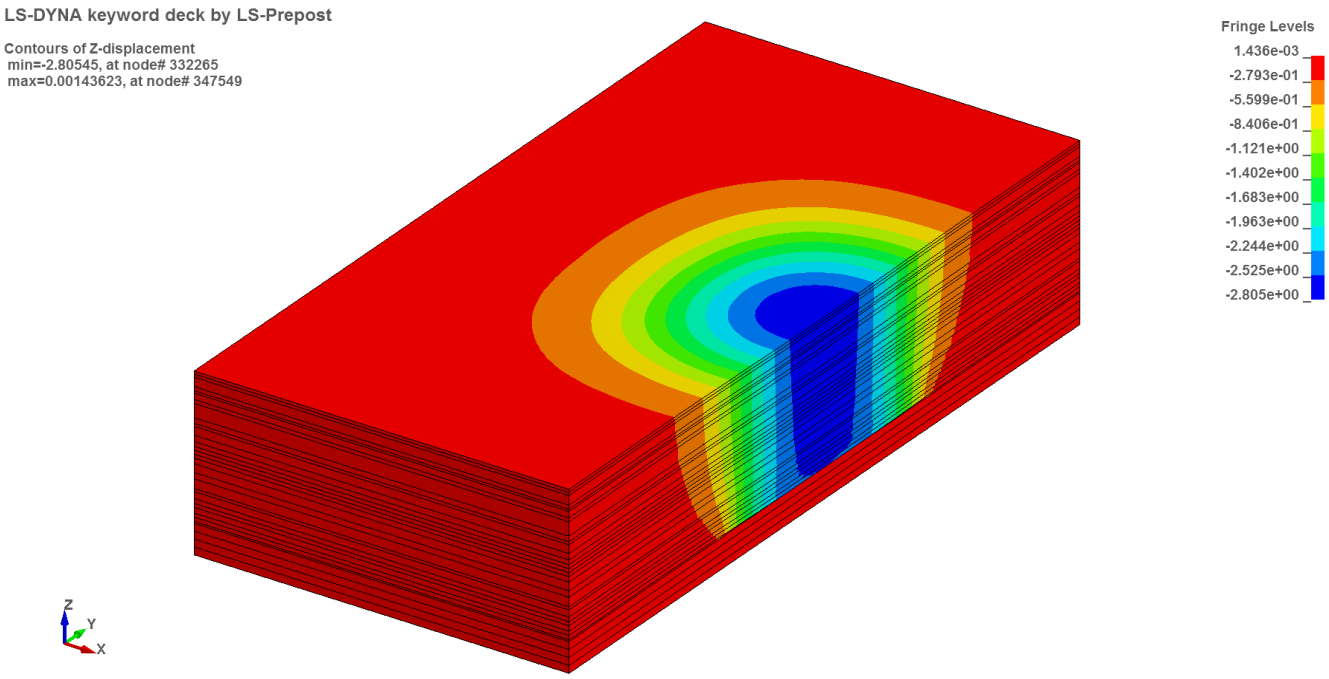

Figure 5-22 Subsidence for case 5

The shape of the trough obtained with the fifth model is given in Figure 5-23. The shape again looks like in case 4, as only the central portion of the roof is in full contact with the floor.

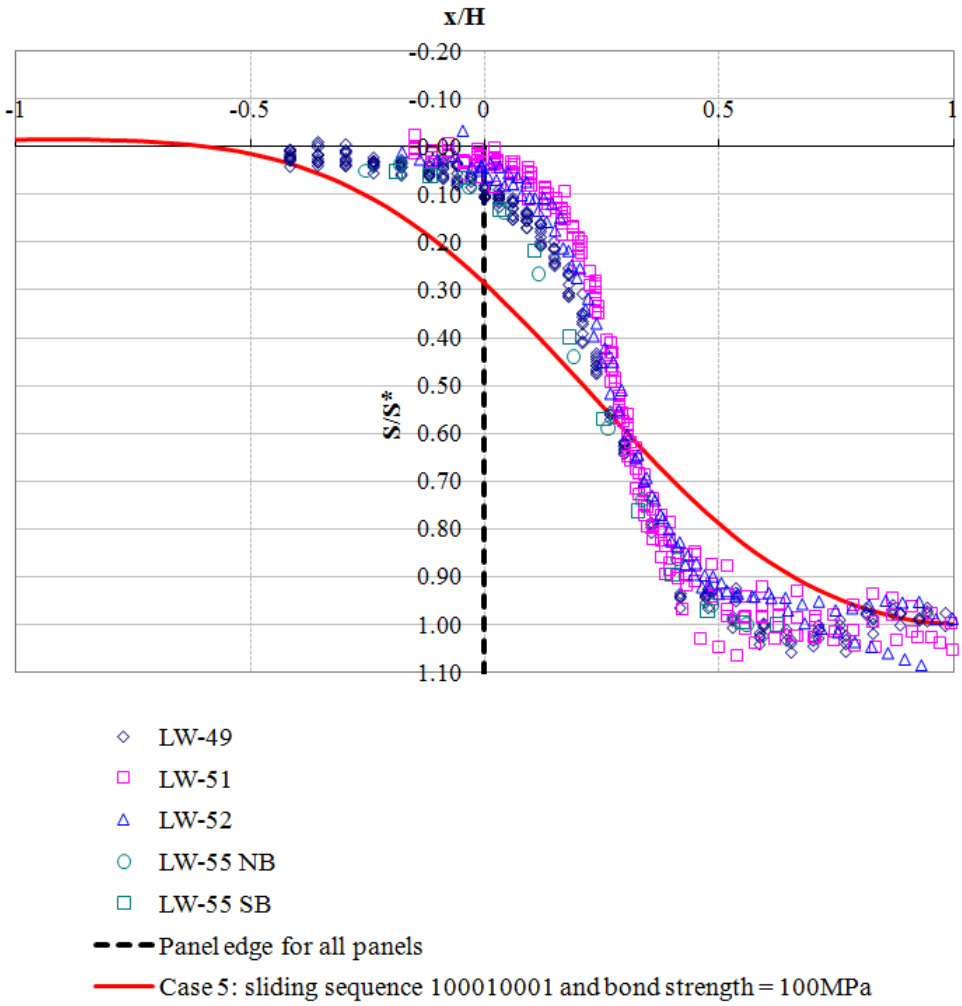

Figure 5-23 Shape of subsidence trough for case 5

The post-mining redistribution of stresses is given in Figure 5-24. Since the central portion of the stack of layers is allowed to fall downward with all of its weight applied mainly on the central portion of the floor of the cavity, the magnitude of the stresses is essentially the same in the gob as in the panel abutments. However, since the overall stiffness of the system was increased by increasing the spacing of interfaces with sliding allowance, the central region where stresses were high is smaller than in case 4.

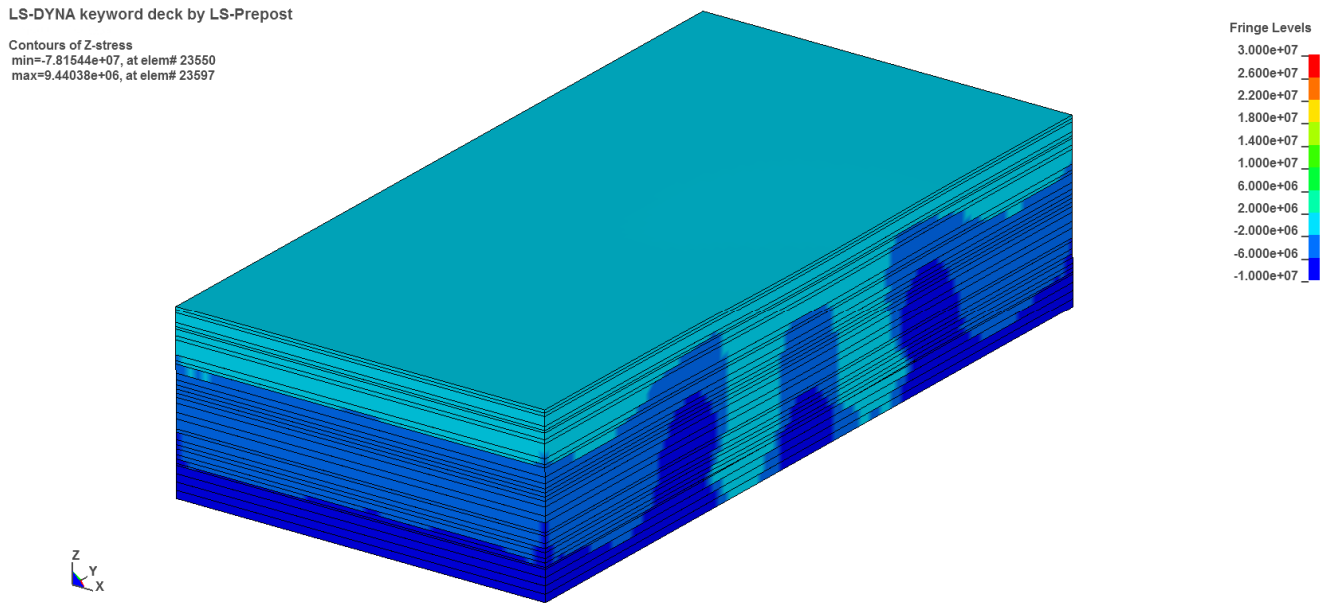

Figure 5-24 Post-mining vertical stress redistribution for case 5

5.2.3.6 Case 6

Case 6 differs from all previous cases in that the Young's modulus was increased to 4.3×10^6 psi (30 GPa). All other features are those of case 5, including the sliding sequence of 100010001. This sixth model is given in Figure 5-25. *S*/M* in this model turns out to be equal to 0.66 as the whole stack of layers does not touch the floor. The readings of subsidence were corrected by subtracting the initial settlement due to the application of gravity to the whole model.

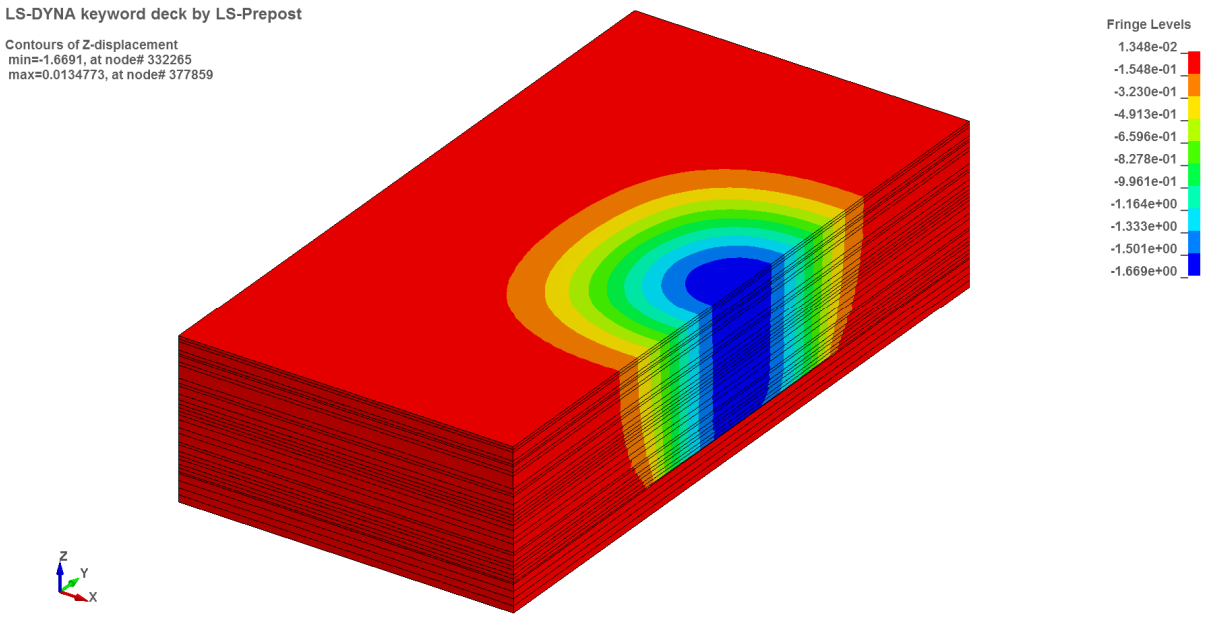

Figure 5-25 Subsidence for case 6

The shape of the trough obtained with the sixth model is given in Figure 5-26. The shape is not optimal but it is reasonable as sliding is allowed in some interfaces and the central portion of the rock falls into the ground.

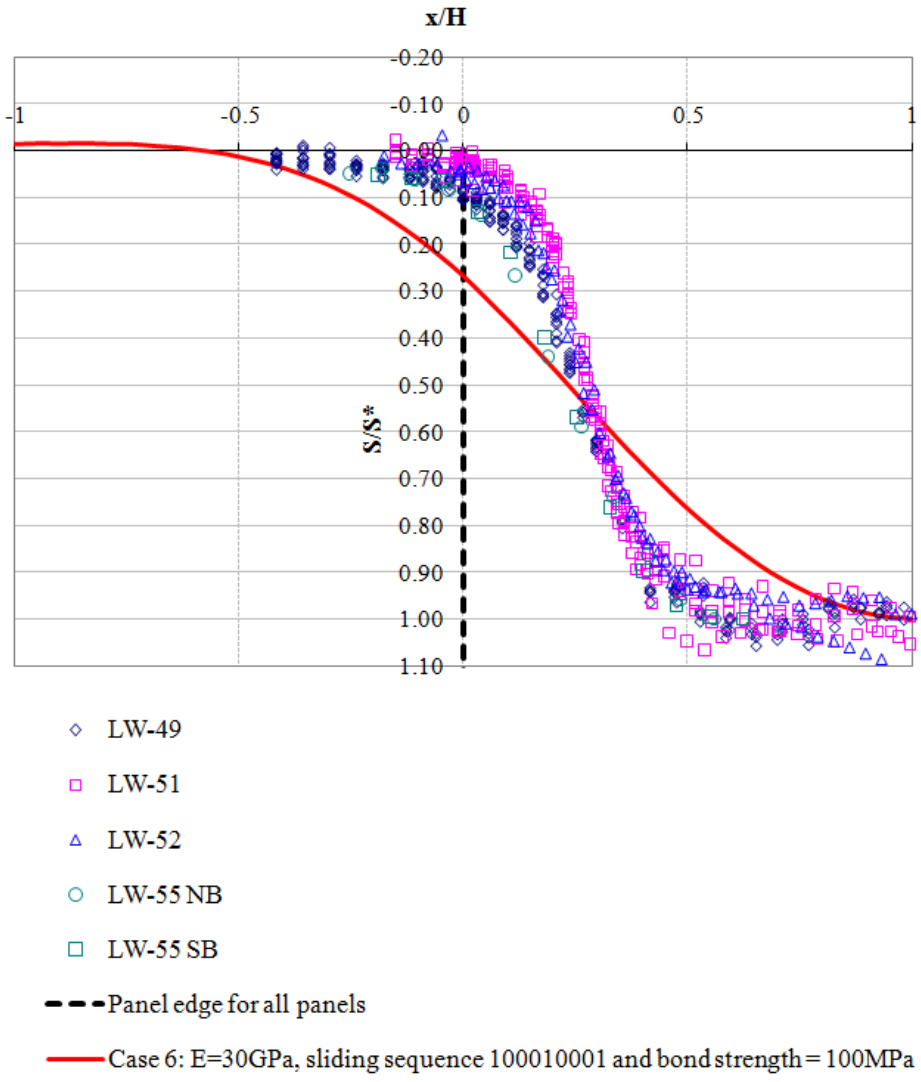

Figure 5-26 Shape of subsidence trough for case 6

The post-mining redistribution of stresses is given in Figure 5-27. Since the central portion of the stack of layers is not allowed to fall downward, the magnitude of the stresses is concentrated at the panel abutments. The magnitude of stress concentration is roughly 6 times higher than the pre-mining, roughly equal to 4340 psi (30 MPa), and the magnitude at the central hanging portion is roughly zero.

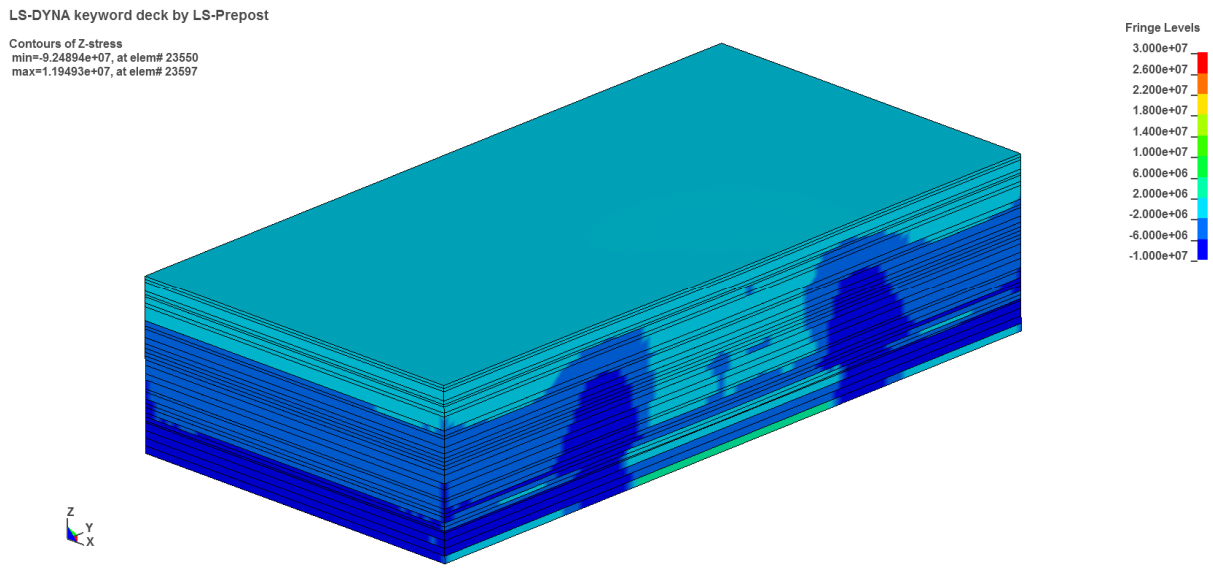

Figure 5-27 Post-mining vertical stress redistribution for case 6

5.2.3.7 Case 7

In case 7, tuning of the Young's modulus was done in order to improve the *S*/M* to approach the one measured in the field roughly equal to 0.7. The modulus was set equal to 3.3×10^6 psi (23 GPa). All other features are those of case 6, including the sliding sequence of 100010001. This seventh model is given in Figure 5-28. *S*/M* in this model turns out to be equal to 0.7 as the whole stack of layers does not touch the floor. The readings of subsidence were corrected by subtracting the initial settlement due to the application of gravity to the whole model. The shape is reasonably good as in the previous case and the stresses have the same limitations as in the previous model.

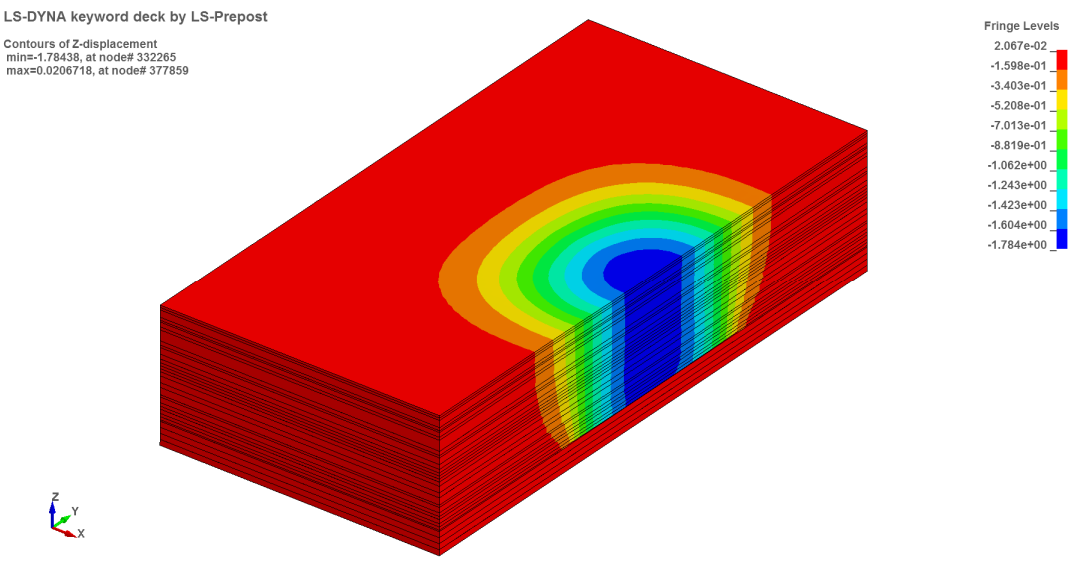

Figure 5-28 Subsidence for case 7

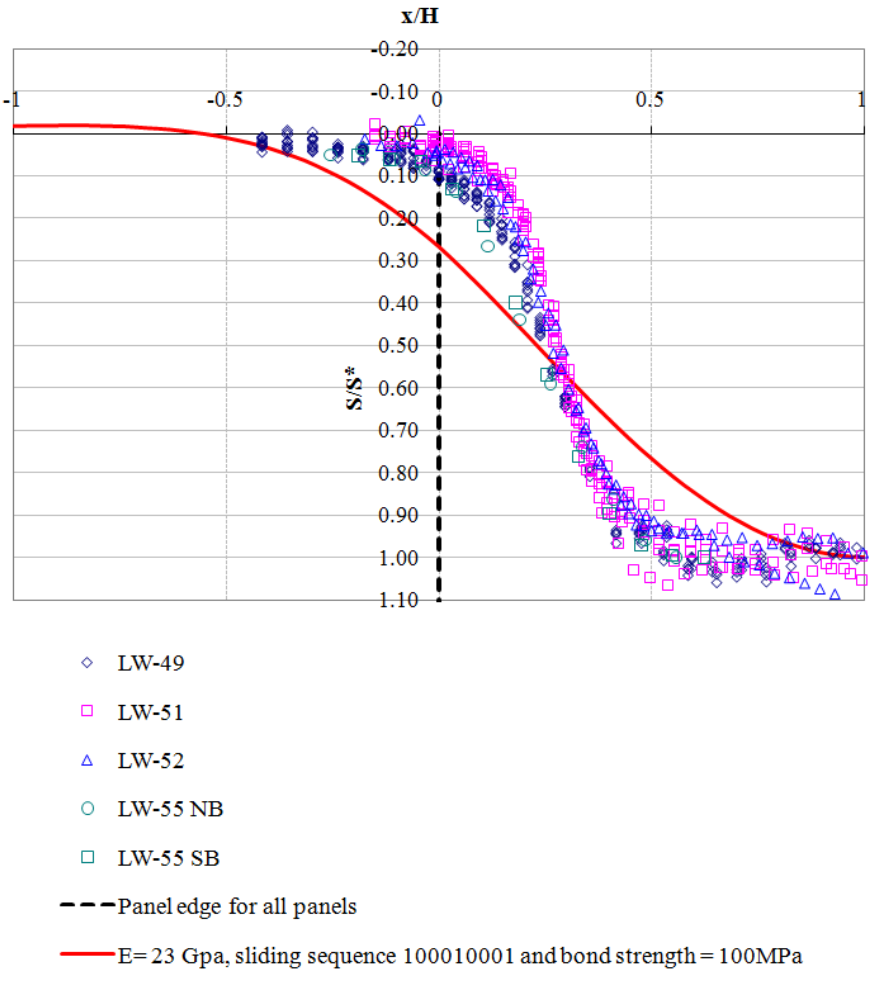

Figure 5-29 Shape of subsidence trough for case 7

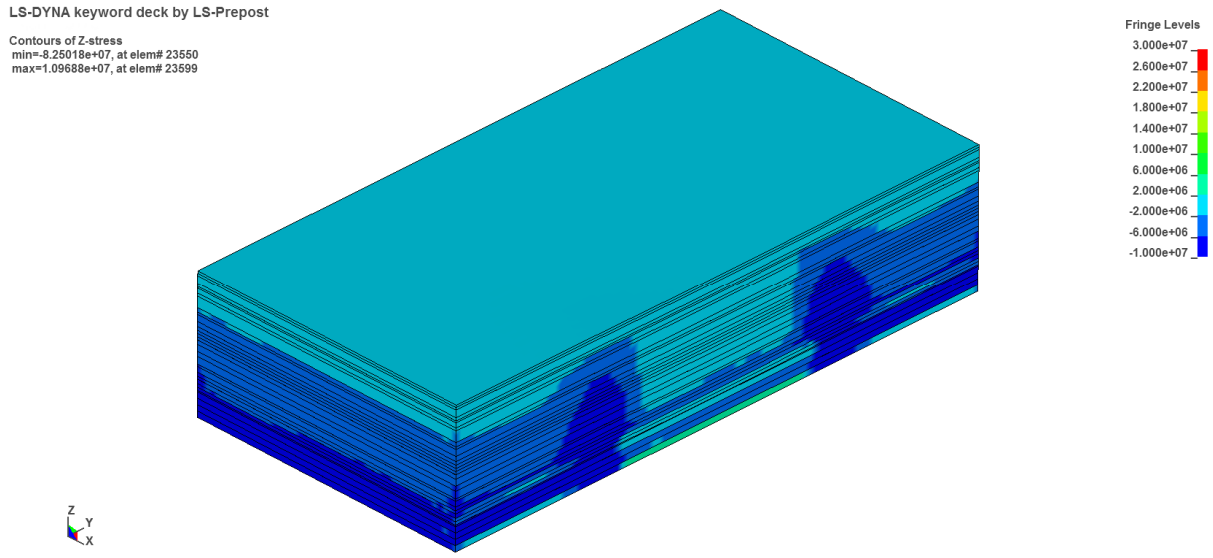

Figure 5-30 Post-mining vertical stress redistribution for case 7

5.2.4 The effect of horizontal in-situ stresses

Horizontal in-situ stresses can be extremely high in southwestern Pennsylvania, in cases reaching a ratio of 5:1 when compared to vertical stresses as illustrated in Figure 5-31 (Mark and Gadde 2008), where the circled data points correspond to eastern United States cases. A model with the properties contained in Table 5-2 is given in Figure 5-32. Figure 5-33 and Figure 5-34 provide details of the influence of the large horizontal pressure. The thin layers tend to warp, thus exerting a lifting effect that keeps the upper layers from freely falling downward. The subsidence factor obtained with this model was 0.64, and the vertical stress distribution and trough shape are given in Figure 5-35 and Figure 5-36, respectively.

It is interesting that the consideration of in-situ horizontal stresses produces correct subsidence magnitude and trough shape. The distribution of vertical stress is less comparable to

typical results seen in the literature. Also, the ratio of horizontal versus vertical stress of 5:1 could be in the upper end of the range. Nevertheless, this factor had not been considered in previous models, and it suggests that it is a very important factor that should not be ignored.

Table 5-2 Mechanical properties of model considering horizontal stresses

Shear Modulus, G [psi (GPa)]	$6.6x10^5$ (4.6)
Density [pcf (kg/m^3)]	165 (2650)
Yield stress, σ_y [psi (MPa)]	4052 (28)
Plastic stiffness, E_p [psi (MPa)]	15 (0.1)
Bulk Modulus, K [psi (GPa)]	$1.1x10^6$ (7.7)
Young's Modulus, E [psi (GPa)]	$1.66x10^6$ (11.5)

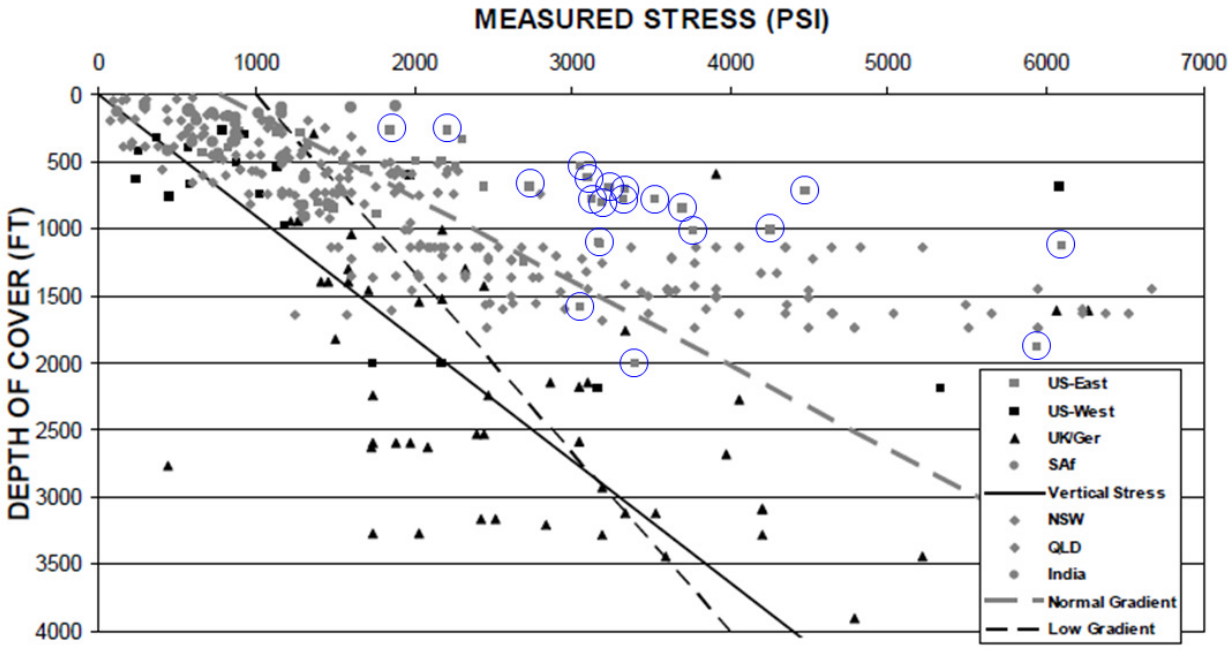

Figure 5-31 Horizontal in-situ stress database (Mark and Gadde 2008)

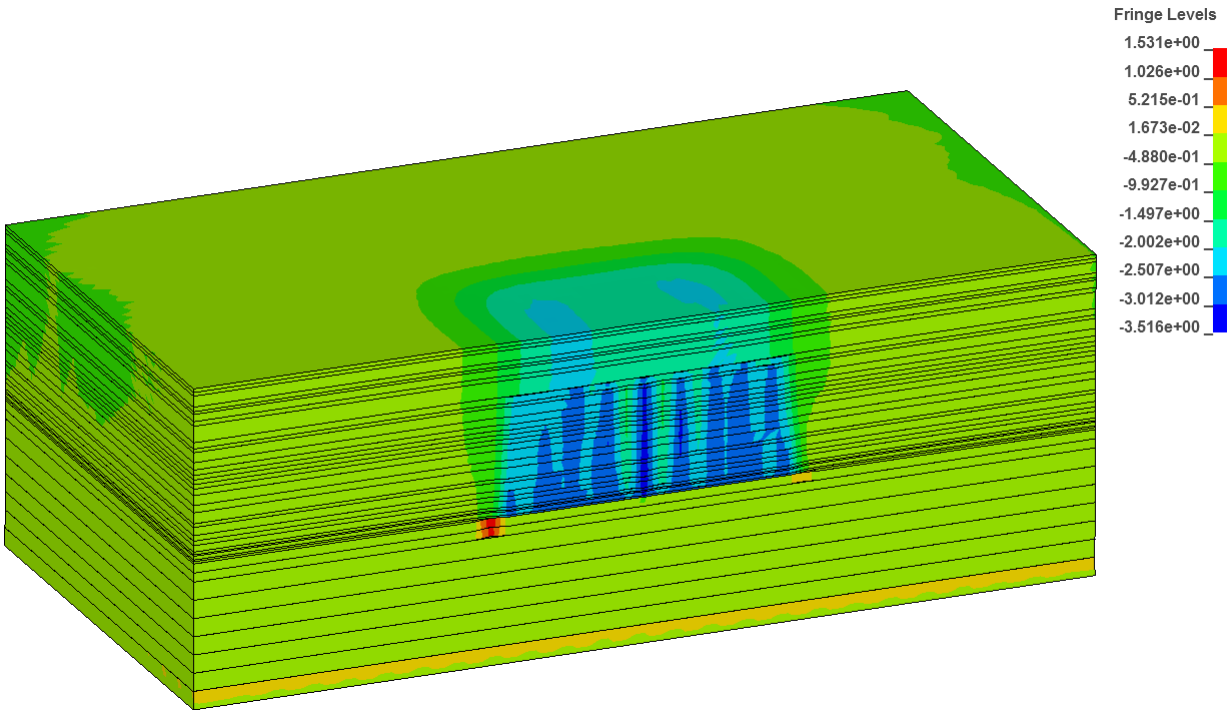

Figure 5-32 Subsidence considering the effect of horizontal in-situ stresses

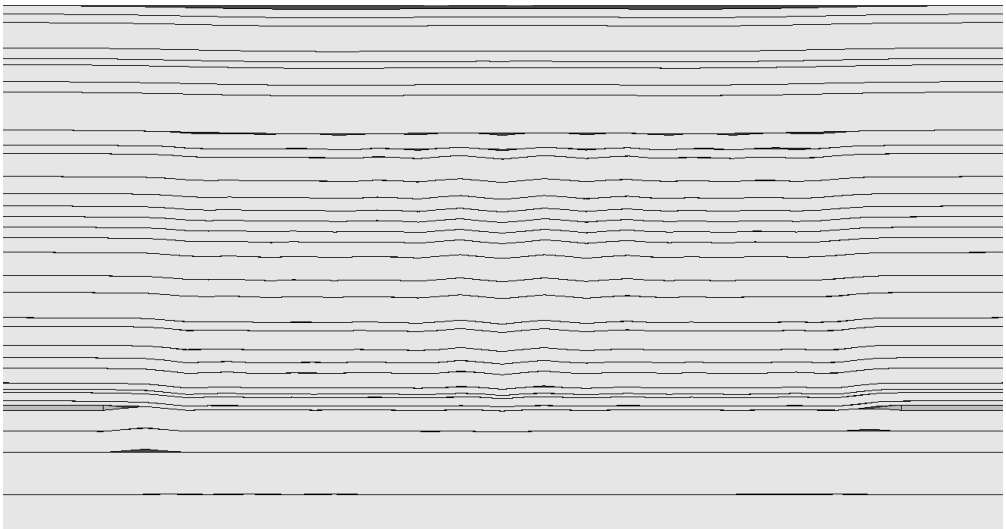

Figure 5-33 View of post-mining warped layers and deformed surface

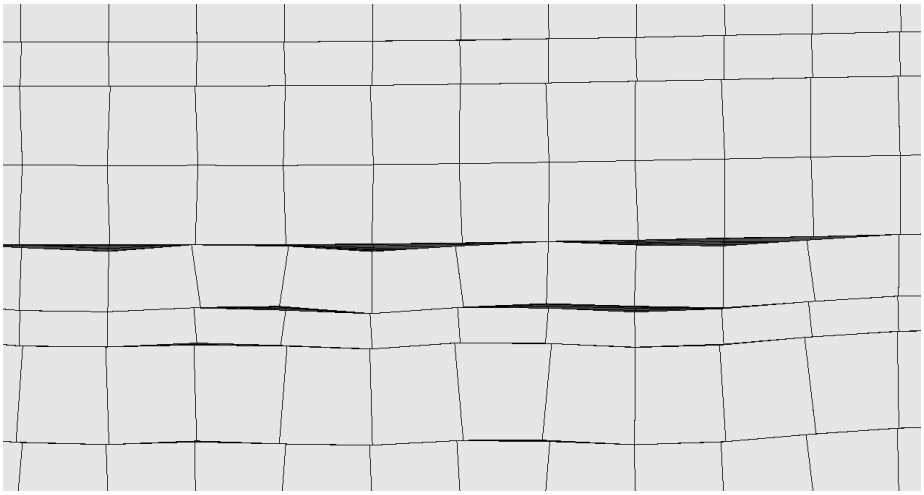

Figure 5-34 Detail of warped layers and gaps created

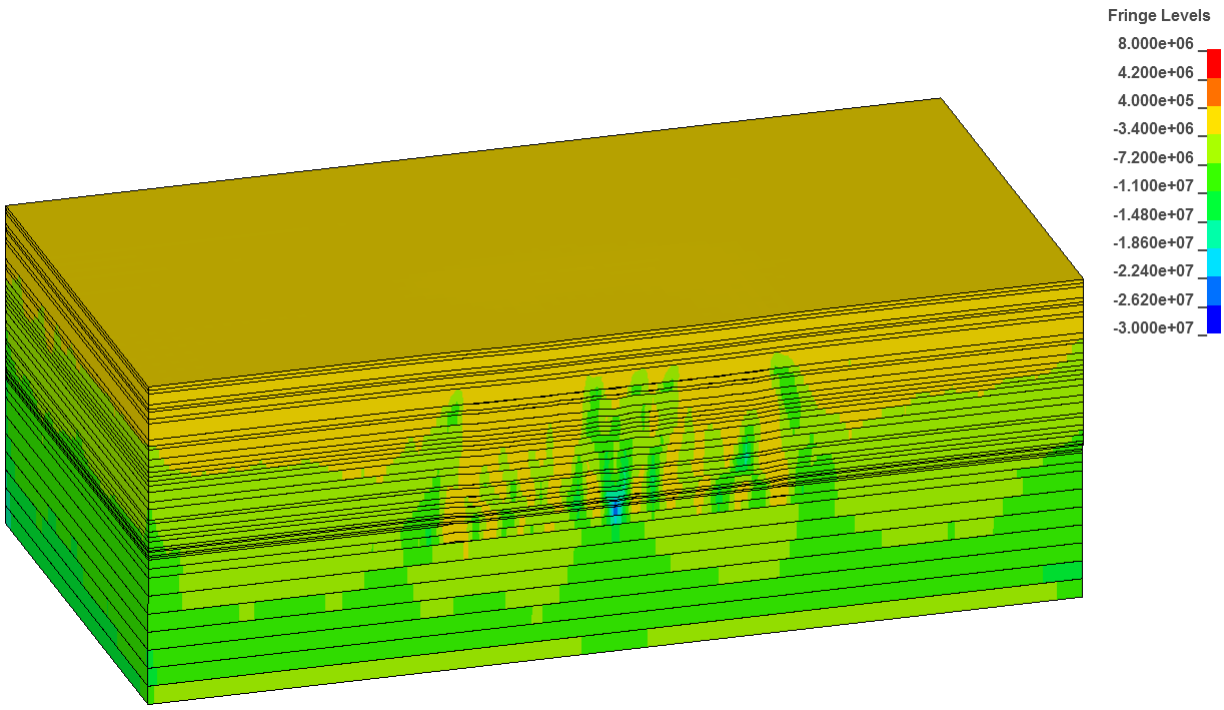

Figure 5-35 Vertical stresses at the end of extraction

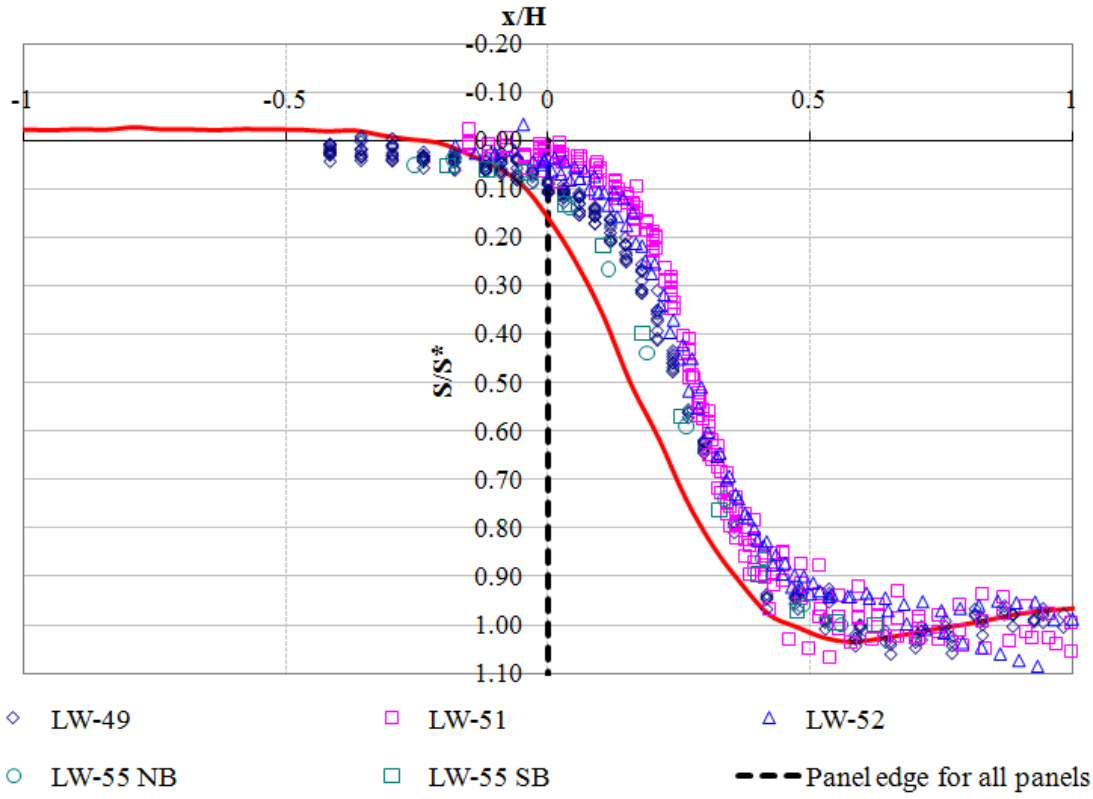

Figure 5-36 Normalized subsidence profile for model with in-situ stresses

5.2.5 An indirect way to consider the bulking factor

In subsection 5.2.2.2, the definition of bulking factor was introduced. The bulking factor is fundamental for the maximum subsidence magnitude, as it keeps the roof and floor from fully closing the gap created by mining. The degree and extent of fracturing of the gob, among other parameters, determine the magnitude of bulking. In FEM modeling, directly simulating the process of rock fracturing is a very challenging problem and quite expensive computationally. In order to overcome this problem, elements with a height of 3.28 ft and sides of 32.8 ft are left in place with a separation of 65.6 ft from center to center, in order to keep the roof from fully closing the cavity. While the extraction magnitude is still at 7.9 ft, the magnitude of maximum

subsidence reaches 5.48 ft and a reasonable subsidence factor of 0.7 is obtained. However, the shape reveals a shift of the trough outward from the mined area. This shift can be attributed to the fact that the whole overburden was kept from moving downward against the gob, and thus the resulting bending of the overburden was not as strong as it was when full closing of the 7.9 ft took place. In this model, all layers were allowed to freely slip with respect to other layers, and horizontal in-situ stresses were not accounted for. The mechanical properties of the rock were a Young's modulus of $1x10^6$ psi (7 GPa), Poisson's ratio of 0.22, and density equal to 165 pcf (2650 kg/m^3). The boundary conditions were defined by rollers on all sides.

A graphical depiction of subsidence is given in Figure 5-37 . Figure 5-38 gives a detail of the 1-m-elements left in place, with the overburden being able to close the cavity only by a limited amount. A substantial shift of the trough in an outward direction can be appreciated in Figure 5-39, which could be due to the restriction in the height of drop of the overburden, affecting also the magnitude of bending of the rock mass. If the rock mass were allowed to bend more strongly, as in the case of full closure, then the trough would probably be displaced inward, as seen in other models.

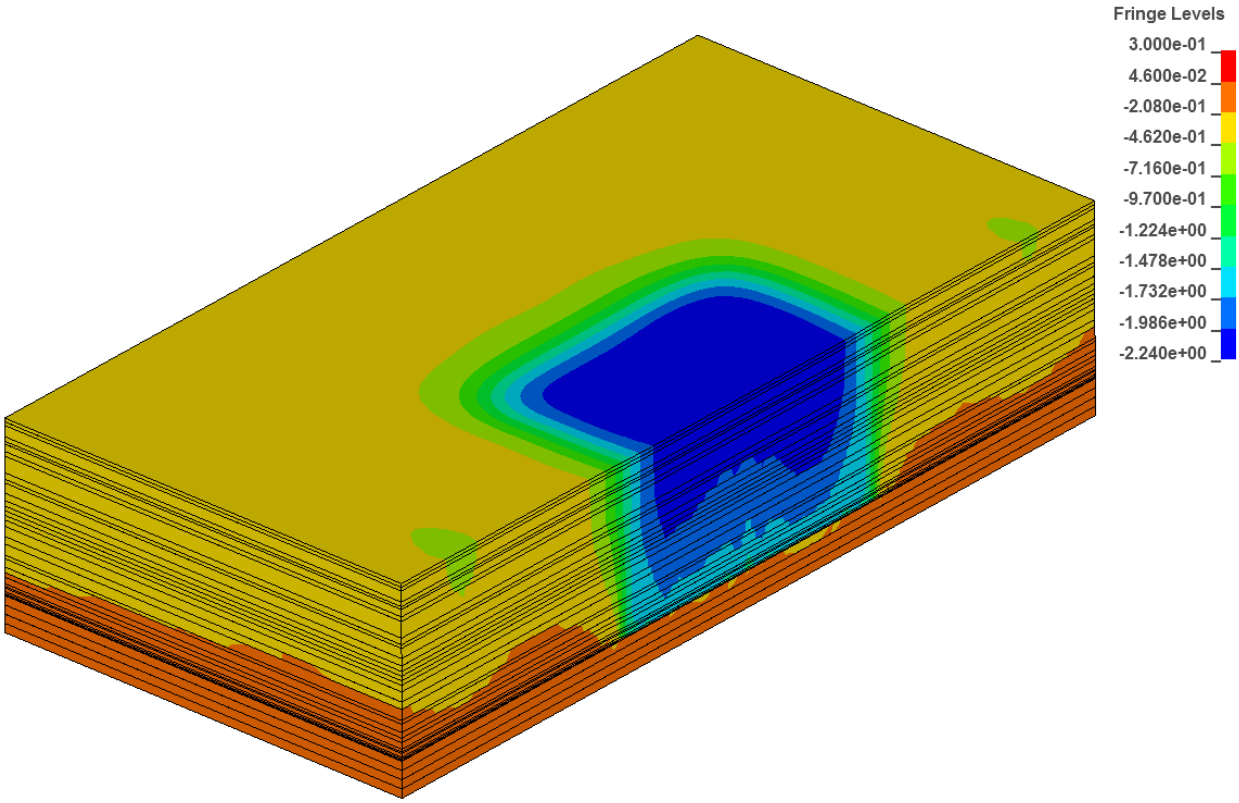

Figure 5-37 Subsidence in model with 1-m-elements left in place

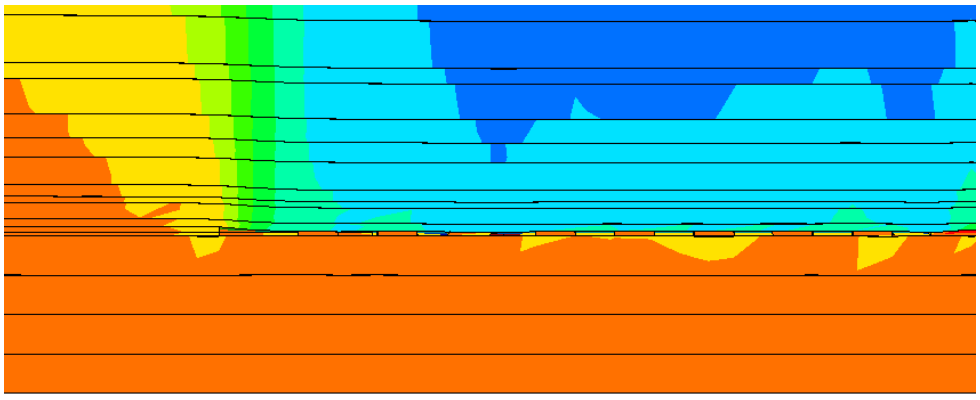

Figure 5-38 Detail of left in place 1-m-elements

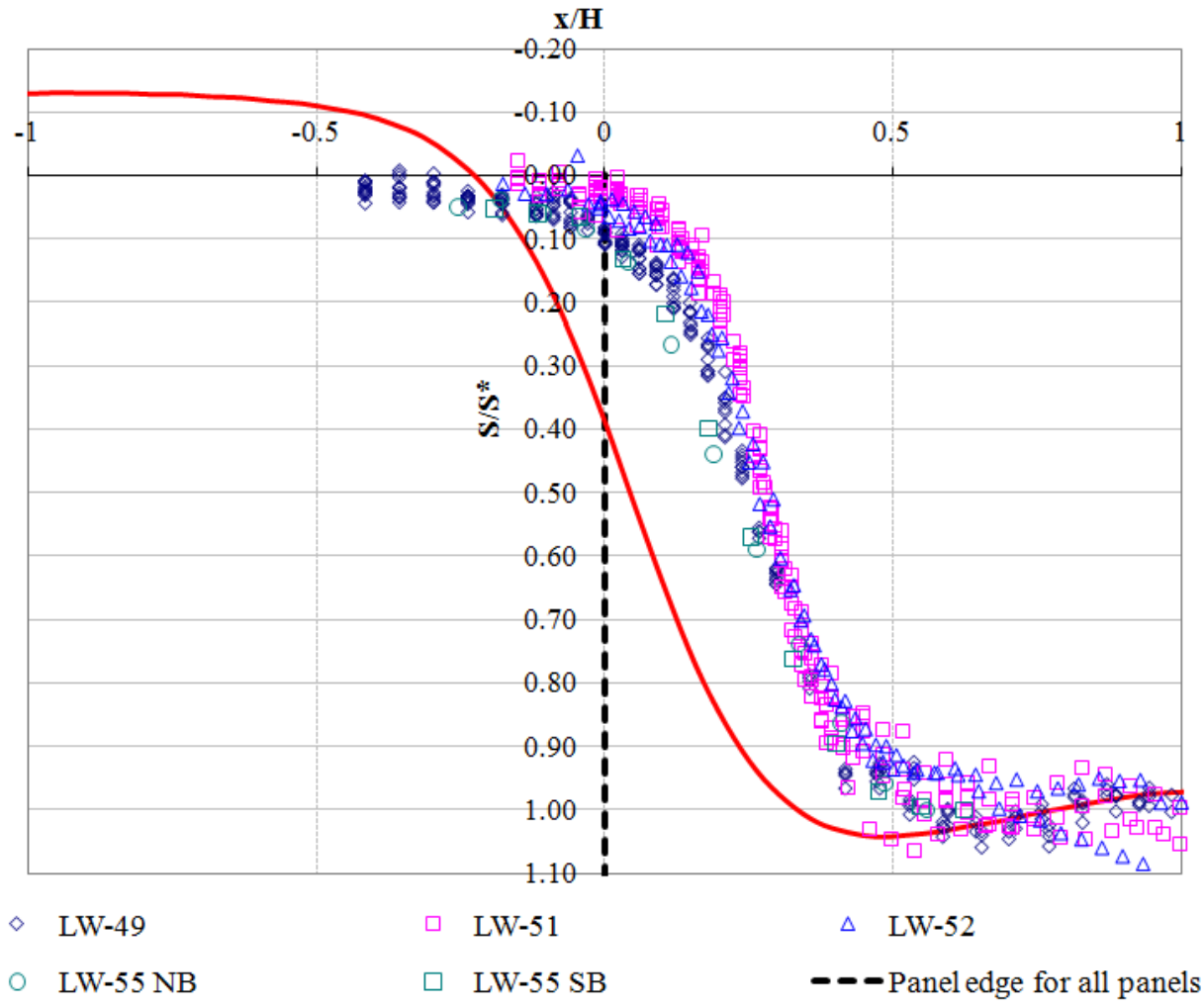

Figure 5-39 Normalized subsidence profile for model with 1-m-elements left in place

5.2.6 Results including a highway embankment

For the general visualization of embankment behavior, a model with the properties shown in Table 5-3 and Table 5-4 was developed. Figure 5-41 shows that subsidence or vertical deformation is essentially independent of the presence of the embankment. This has been known to the subsidence community in that vertical deformations are not sensitive to hilly conditions. This fact also made it possible to develop the empirical model described in chapter 4.0 . On the other hand, horizontal deformations are very sensitive to the irregular shape of the highway embankment, and the asymmetry in horizontal deformation distribution is evident in Figure 5-42. This asymmetry is cause here by a sloping grade of the embankment in a magnitude of 5 degrees.

Figure 5-43 shows two lines along which subsidence and horizontal deformations were calculated. The results are given in Figure 5-44 and Figure 5-45 and they demonstrate that under the special conditions of highway embankments, the general assumption that trough slope and horizontal deformation are linearly correlated, is generally not valid. The symmetry in subsidence is clear from Figure 5-44, while asymmetry in horizontal displacements is demonstrated in Figure 5-45. Also, even though the embankment underwent a less steep deformation, the horizontal deformation was substantially higher than on the overburden. This would be explained by the fact that the overburden is formed by strong, confined rock, whereas the embankment is weaker, formed by compacted soils, and unconfined. The asymmetry in horizontal displacements given by the FEM is conservative. Extreme cases were actually documented and are depicted for example in Figure 4-22 or Figure 4-23. This suggests that prediction of horizontal deformations along earthen structures of irregular shapes needs to be aided with detailed numerical modeling calibrated to account for the behavior of the actual materials encountered in the field. Figure 5-40 gives a transition from subcritical to supercritical

conditions, which takes place somewhere between W/H = 1.0 and W/H = 1.3. This result is consistent with the literature. Also, it is interesting to note that heave in the outer parts of the trough increased as the conditions evolved from subcritical to supercritical.

Table 5-3 Mechanical properties of model overburden

Shear Modulus, G [psi (GPa)]	1.36×10^6 (9.4)
Density [pcf (kg/m^3)]	165 (2650)
Yield stress, σ_y [psi (MPa)]	5500 (38)
Plastic stiffness, E_p [psi (MPa)]	15 (0.1)
Bulk Modulus, K [psi (GPa)]	1.98×10^6 (13.7)
Young's Modulus, E [psi (GPa)]	3.32×10^6 (23)

Table 5-4 Mechanical properties of embankment

Shear Modulus, G [psi (GPa)]	2.9×10^5 (0.2)
Density [pcf (kg/m^3)]	165 (2650)
Yield stress, σ_y [psi (MPa)]	275 (1.9)
Plastic stiffness, E_p [psi (MPa)]	15 (0.1)
Bulk Modulus, K [psi (GPa)]	7.9×10^5 (0.55)
Young's Modulus, E [psi (GPa)]	7.7×10^5 (0.535)

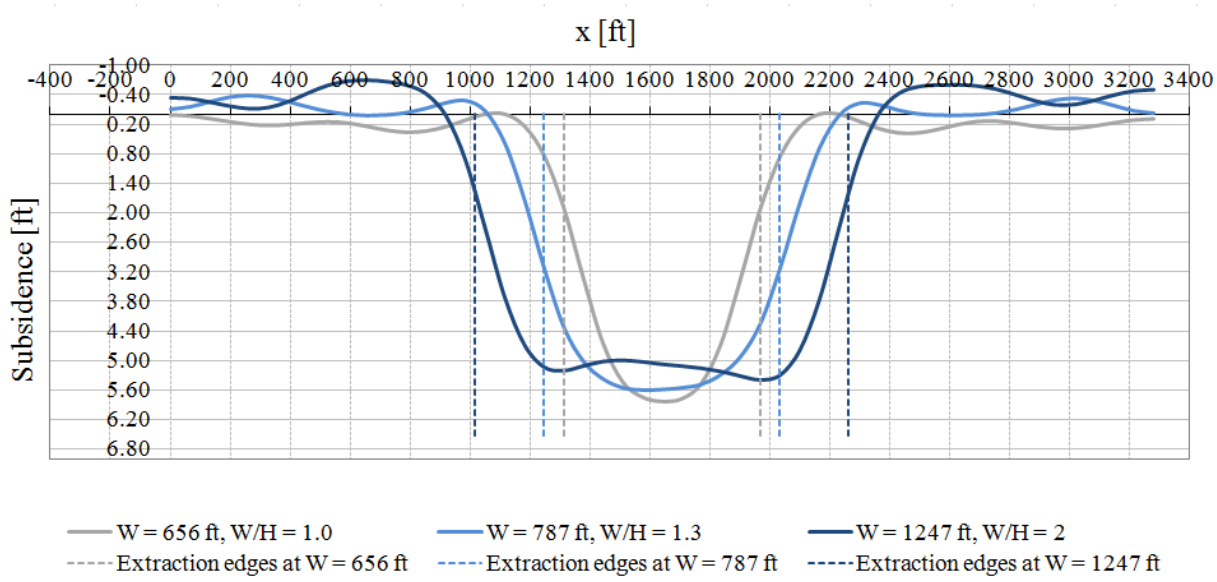

Figure 5-40 Transition from subcritical to supercritical subsidence profiles

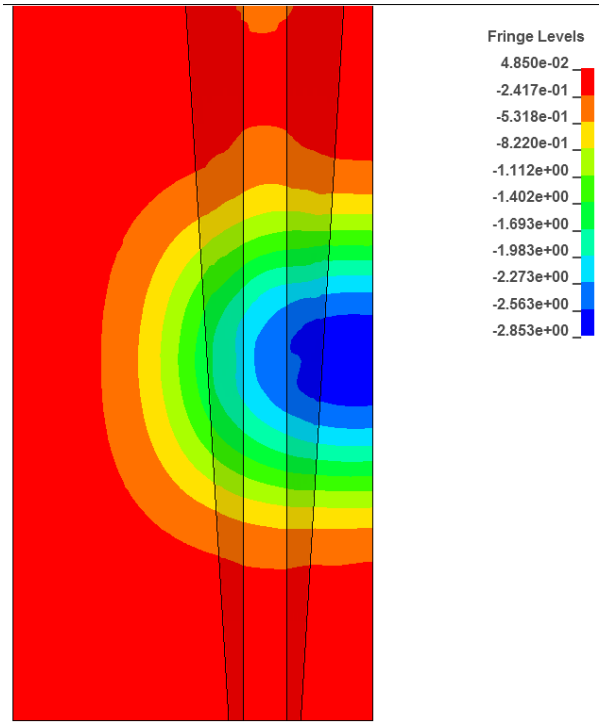

Figure 5-41 Top view of subsidence in 3D FEM model with embankment on top

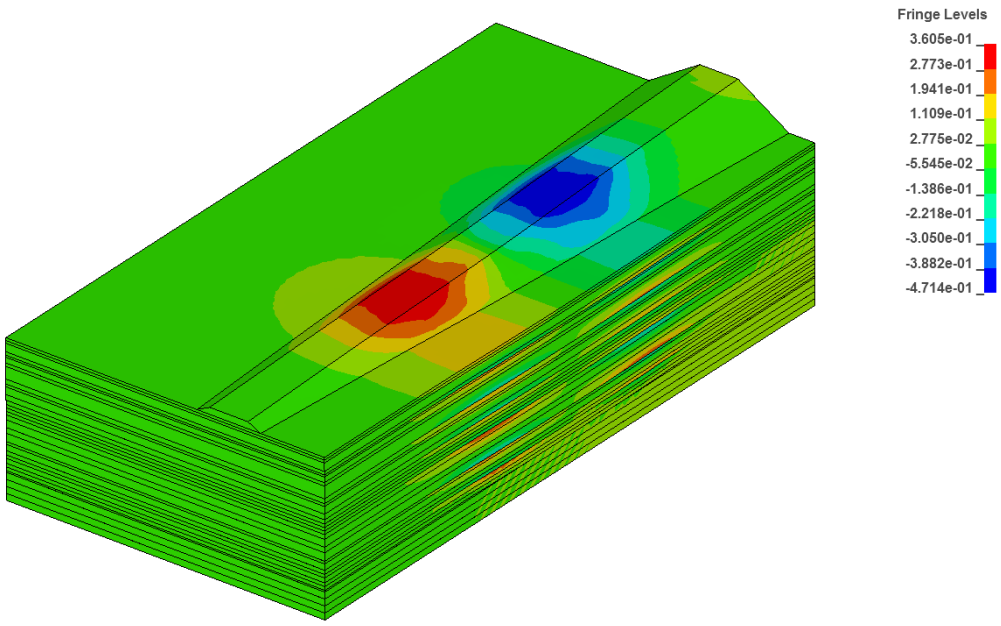

Figure 5-42 Lateral deformation distribution

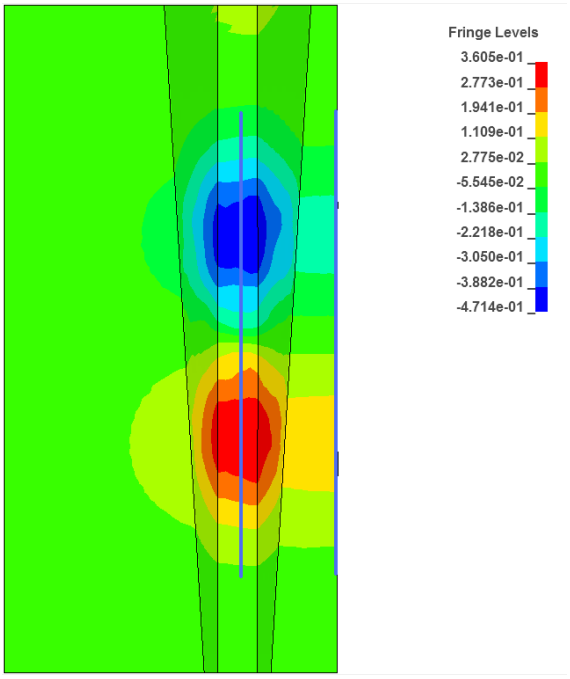

Figure 5-43 Profile lines on embankment and terrain for horizontal deformation

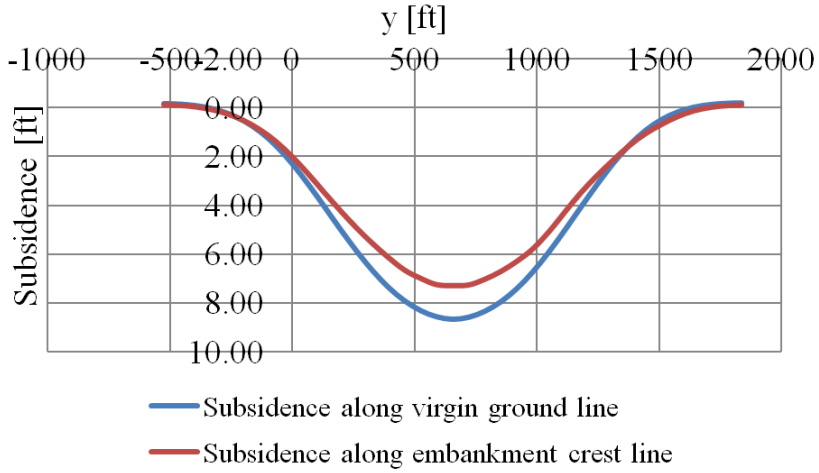

Figure 5-44 Subsidence profiles along embankment and virgin ground lines

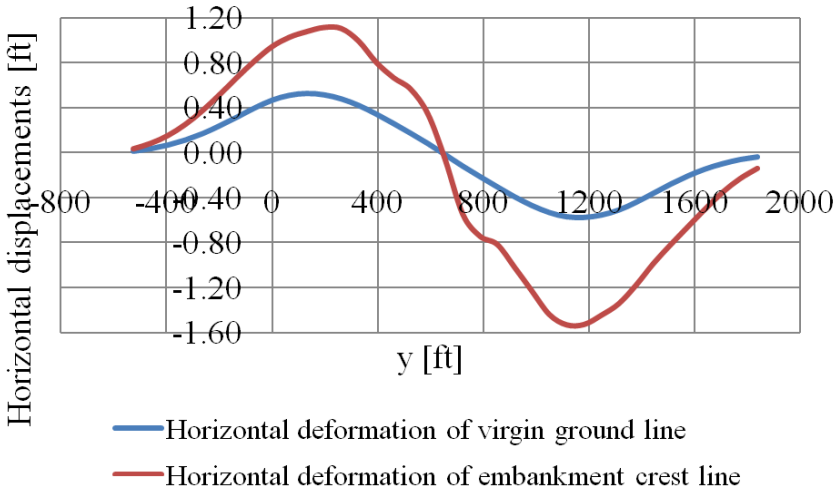

Figure 5-45 Horizontal deformation along embankment and virgin ground lines

6.0 CONCLUSIONS

The following conclusions are relevant to this project:

- The trend followed by the maximum subsidence factor was found to be inversely related to the overburden depth. This finding is consistent with broader studies performed by Peng (Peng 1992). Since the maximum subsidence factor is used in the SDPS software, it has been established and emphasized throughout this report, that a successful use of the software SDPS relies on the correct prediction of maximum subsidence, which is suggested by the model described in section 4.1.1.
- The Pitt-PennDOT model has an advantage over the SDPS model in that asymmetry can be considered. Asymmetry in the subsidence profiles arises from the fact that usually a panel is mined-out next to a previously mined-out panel, with the side next to the old panel usually experiencing more subsidence than the side next to intact overburden.
- A simultaneous description of the so called static and dynamic subsidence was made through the methodology described. This was possible because the data were both spatially and temporally considered. This is useful in that a complete final and in-progress description of the subsidence trough can be made in three dimensions in a single model.
- The use of mathematical functions made it possible to derive the subsidence information indices.

- Even though the Pitt-PennDOT model has the potential to incorporate more rates of advance as data may continue to be collected, a dynamic subsidence analysis at this point can be alternatively performed using SDPS 6.0, as described in this report. The methodology can be incorporated into Pitt-PennDOT Model, but considering the scarcity of the time rate data, it is not recommended.
- The complex effect of horizontal ground deformation due to subsidence on large highway embankments has been described in this report. An analysis of this effect is only possible through the use of numerical methods (such as the finite element method), on a case-by-case basis.
- The FEM demonstrated a connection between the large horizontal in-situ stresses and subsidence magnitude and shape.
- In order for a FEM model to correctly simulate the complete mechanism associated to mine subsidence, fracturing of the material would need to be implemented. This would be the best way to reproduce the so-called bulking factor that has a remarkable influence on the subsidence factor. Since this is impractical due to the extremely expensive computational cost, some conditions need to be imposed, such as the remaining elements on the floor that account for the bulking factor in an indirect way.
- The horizontal in-situ stresses seem to play an important role on the subsidence factor, especially when they are very high. These stresses seem to be particularly high in this region of the world, where the typical subsidence factors also happen to be very low. The observed results would suggest that there is a connection between in-situ stresses and subsidence magnitudes.
- The behavior of horizontal deformations of earthen structures was demonstrated through a simple hypothetical case. This quick result is in good agreement with observations and

suggests that the use of current empirical subsidence tools to predict lateral deformations would be extremely unreliable when applied to embankments or earth dams. In such cases, detailed numerical models should be implemented.

- The application of the FEM presented in this study validated previous published field research findings on subsidence which was evaluated as either a two or a three dimensional phenomena. The FEM could be further used to analyze the behavior of structures other than embankments (covered in this study) when they are located on the ground surface right above longwall mines.

7.0 REFERENCES

1. Adamek, V. and P. W. Jeran (1981). Evaluation of existing predictive methods for mine subsidence in the U.S. *Workshop on Surface Subsidence due to Underground Mining* Morgantown, WV, Department of Mining Engineering, West Virginia University.
2. Adamek, V., P. W. Jeran, et al. (1987). Prediction of surface deformations over longwall panels in the Northern Appalachian Coalfield, Bureau of Mines, United States Department of the Interior.
3. Agioutantis, Z. and M. Karmis (2009). Surface Deformation Prediction System for Windows Virginia Polytechnic Institute and State University.
4. Chen, D. W. and S. S. Peng (1981). Analysis of surface subsidence parameters due to underground longwall mining in the Northern Appalachian Coalfield. Morgantown, WV, West Virginia University.
5. Cui, X., J. Wang, et al. (2001). "Prediction of progressive surface subsidence above longwall coal mining using a time function." *International Journal of Rock Mechanics and Mining Sciences* **38**(7): 1057-1063.
6. Edmunds, W. E. (1999). Chapter 11: Pennsylvanian-Permian Transition and Permian. *Geology of Pennsylvania*. C. H. Schultz. Harrisburg, Pittsburgh, Pennsylvania Geological Survey Pittsburgh Geological Society**:** 171-177.
7. Edmunds, W. E., V. W. Skema, et al. (1999). Chapter 10: Pennsylvanian. *Geology of Pennsylvania*. C. H. Schultz. Harrisburg, Pittsburgh, Pennsylvania Geological Survey Pittsburgh Geological Society**:** 156.
8. Graybill, F. A. and H. K. Iyer (1994). *Regression Analysis: Concepts and Applications*. Belmont, California, USA, Dusbury Press An Imprint of Wadsworth Publishing Company.
9. Heasley, K. A. and T. M. Barton (1998). Subsidence Prediction Using a Laminated, Boundary-Element Program. *3rd North American Rock Mechanics Symposium*. Cancun, Mexico**:** 381-390.
10. Jarosz, A., M. Karmis, et al. (1990). "Subsidence development with time - experiences from longwall operations in the Appalachian coalfield." *International Journal of Mining and Geological Engineering*: 261-273.
11. Jeran, P. and V. Adamek (1988). Subsidence due to undermining of sloping terrain: A case study. *Report of Investigations*, United States Department of Interior Bureau of Mines.

12. Karmis, M. (1987). Prediction of ground movements due to underground mining in the Eastern United States coalfields. Blacksburg, VA, USA, Virginia Polytechnic Institute and State University.
13. Karmis, M., C. Haycocks, et al. (1992). The prediction of ground movement caused by mining. *3rd Subsidence Workshop Due to Underground Mining*, Morgantown, WV, USA, West Virginia University.
14. Karmis, M., T. Triplett, et al. (1983). Mining Subsidence And Its Prediction In The Appalachian Coalfield. *The 24th U.S. Symposium on Rock Mechanics (USRMS)*. College Station, TX, The Association of Engineering Geologists. Permission to Distribute - American Rock Mechanics Association.
15. Karmis, M. C., C. Haycocks, et al. (1981). A study of longwall subsidence in the Appalachian coal region using field measurements and computer modeling techniques. *First Annual Conference on Ground Control in Mining*, Morgantown, WV, West Virginia University.
16. Karmis, M. C., T. Triplett, et al. (1984). Recent developments in subsidence prediction and control for the Eastern U.S. Coalfields. *25th U.S. Symposium on Rock Mechanics*, Northwestern University, Illinois, SME-AIME.
17. Kratzsch, H. (1983). *Mining Subsidence Engineering*. Berlin Heidelberg New York, Springer-Verlag.
18. Kratzsch, H. (2008). *Bergschadenkunde*. Bochum, Deutscher Markscheider-Verein e.V.
19. Luo, Y. and S. S. Peng (1999). "Integrated approach for predicting mining subsidence in hilly terrain." *Mining Engineering*: 100-104.
20. Mark, C. and M. Gadde (2008). Global Trends in Coal Mine Horizontal Stress Measurements. *27th International Conference on Ground Control in Mining*, Morgantown, WV, West Virginia University.
21. Mine Subsidence Engineering Consultants (2007). "Introduction to longwall mining and subsidence." Retrieved 08/19/2009, 2009, from www.minesubsidence.com.
22. Morsy, K. and S. S. Peng (2002). Numerical modeling of the gob loading mechanism in longwall coal mines. *21st International Conference on Ground Control in Mining*, Morgantown, WV, West Virginia University.
23. NCB (1975). *Subsidence Engineer's Handbook*, National Coal Board.
24. OSMRE (1986). Guidance manual on subsidence control, United States Department of Interior.
25. Oyler, D., C. Mark, et al. (2004). Performance of roof support under high stress in a U.S. coal mine, NIOSH.
26. Peng, S. S. (1992). *Surface Subsidence Engineering*. Littleton, CO, USA, Society for Mining, Metallurgy, and Exploration, Inc.
27. Peng, S. S. (2008). *Coal Mine Ground Control*. Morgantown, WV, Department of Mining Engineering, College of Engineering and Mineral Resources, West Virginia University.
28. Peng, S. S. and D. Y. Geng (1983). The Appalachian Field: General characteristics of surface subsidence and monitoring methods. *Surface mining environmental monitoring and reclamation handbook*. L. V. A. Sendlein, H. Yazicigil, C. L. Carlson and H. K. Russel, Elsevier**:** 627-646.
29. PennState (2000, 2001). "Description of the geology of Greene County, Pennsylvania." 2008, from http://www.libraries.psu.edu/emsl/guides/X/greene.htm.

30. Stone, R. W. (1932). *Geology and mineral resources of Greene County Pennsylvania*. Harrisburg, Pennsylvania, USA, Pennsylvania Geological Survey.
31. Su, D. (1991). Finite element modeling of subsidence induced by underground coal mining: The influence of material nonlinearity and shearing along existing planes of weakness. *10th International Conference on Ground Control in Mining*, Morgantown, WV, USA, West Virginia University.
32. Whittaker, B. N. and D. J. Reddish (1989). *Subsidence: Occurrence, Prediction, and Control*, Elsevier Science Publisher B.V.

APPENDIX

A.1 EMERALD MINE PANEL B-4 TRANSFORMED DATA

Given the scarcity of date for panel B-4, ranges of 100 ft were chosen for the visualization of transverse data. The distance is measured from the mine face.

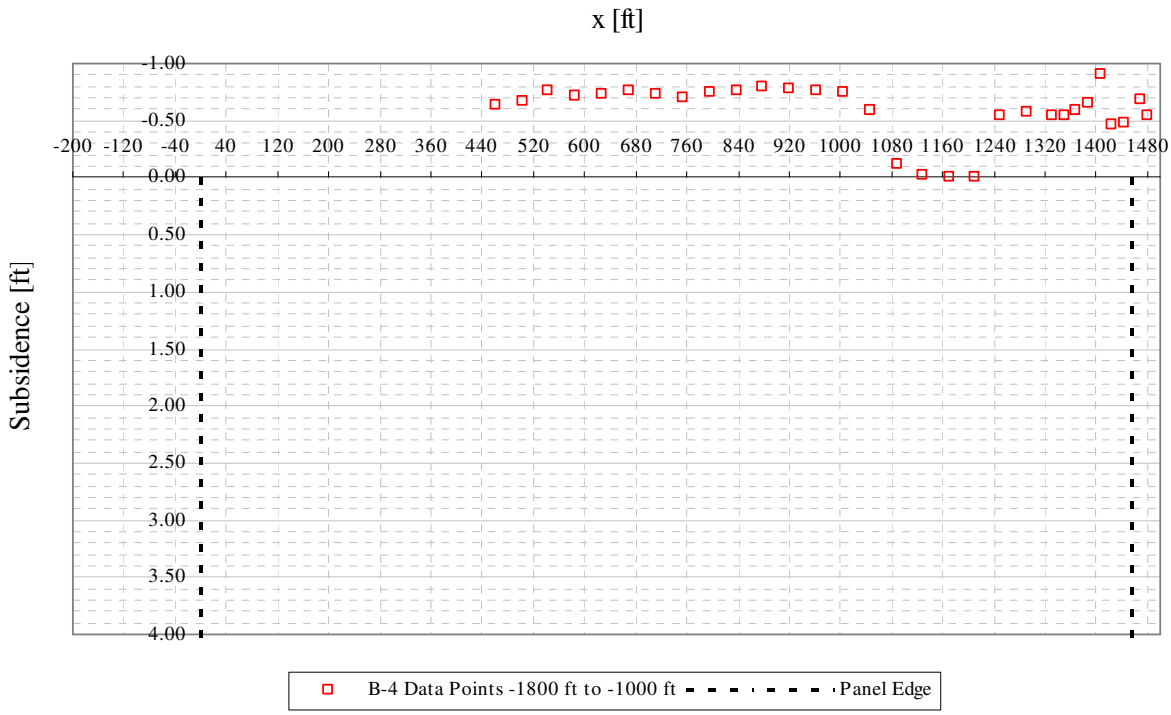

Figure A1- 1 B-4 transverse view of data points from -1800 ft to -1000 ft from mine face

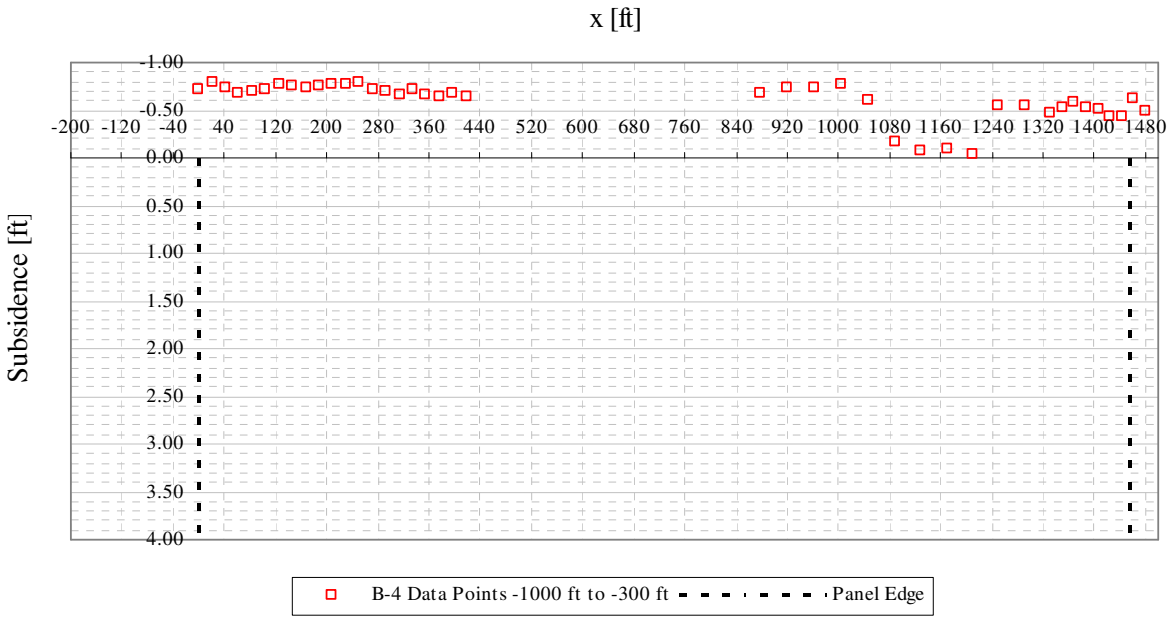

Figure A1- 2 B-4 transverse view of data points from -1000 ft to -300 ft from mine face

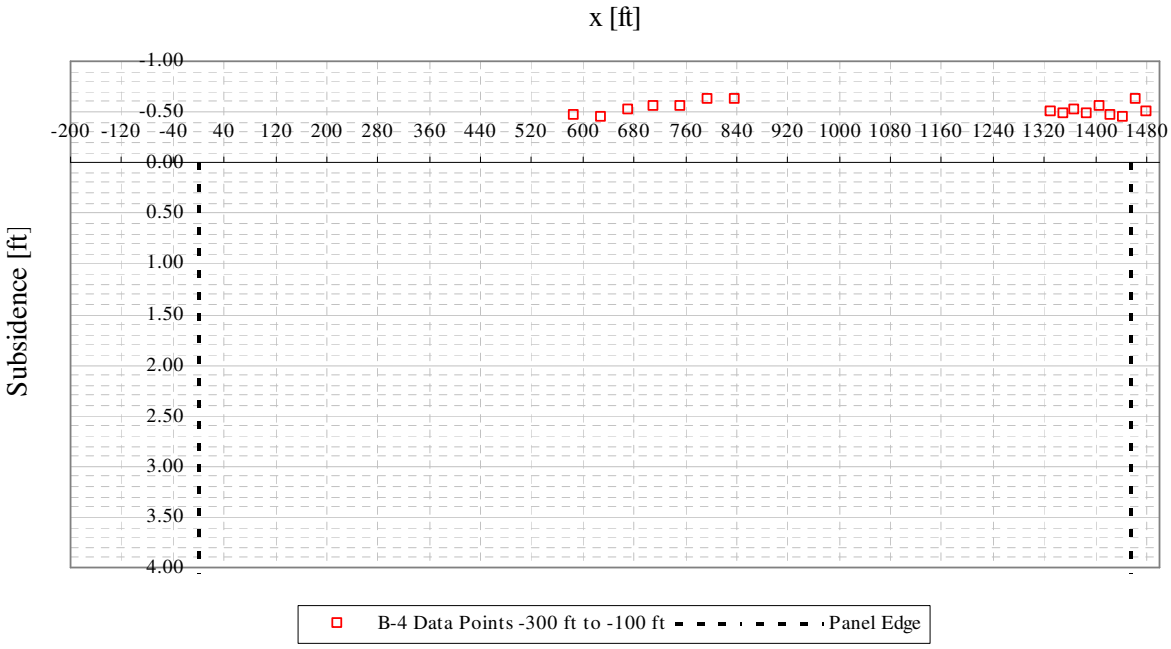

Figure A1- 3 B-4 transverse view of data points from -300 ft to -100 ft from mine face

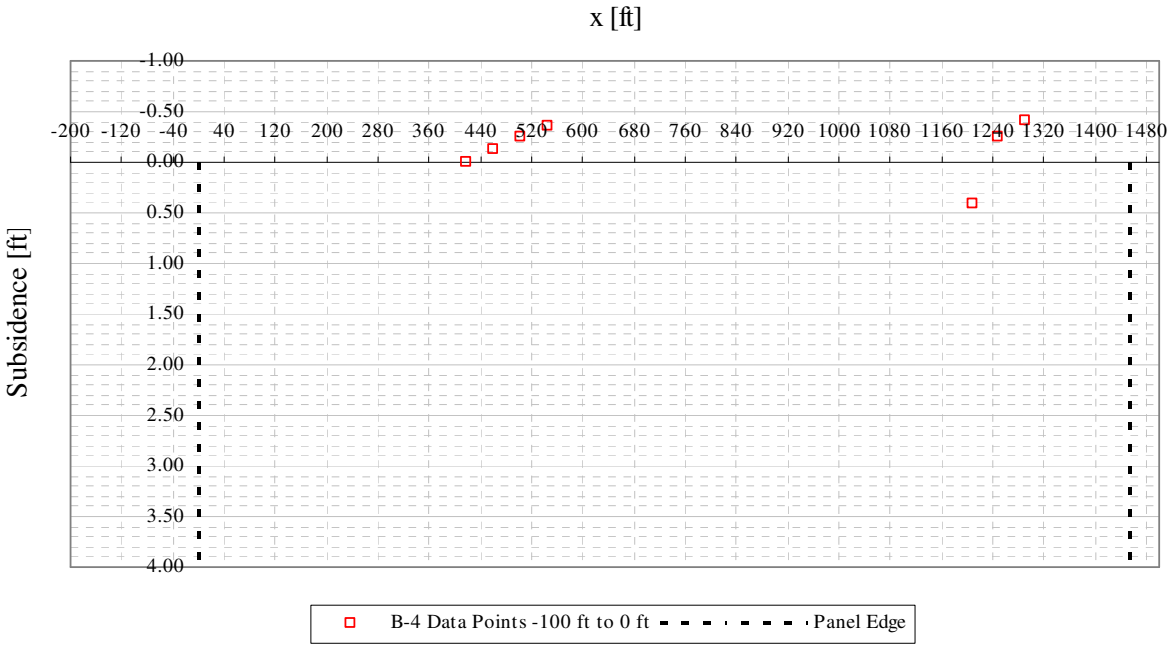

Figure A1- 4 B-4 transverse view of data points from -100 ft to 0 ft from mine face

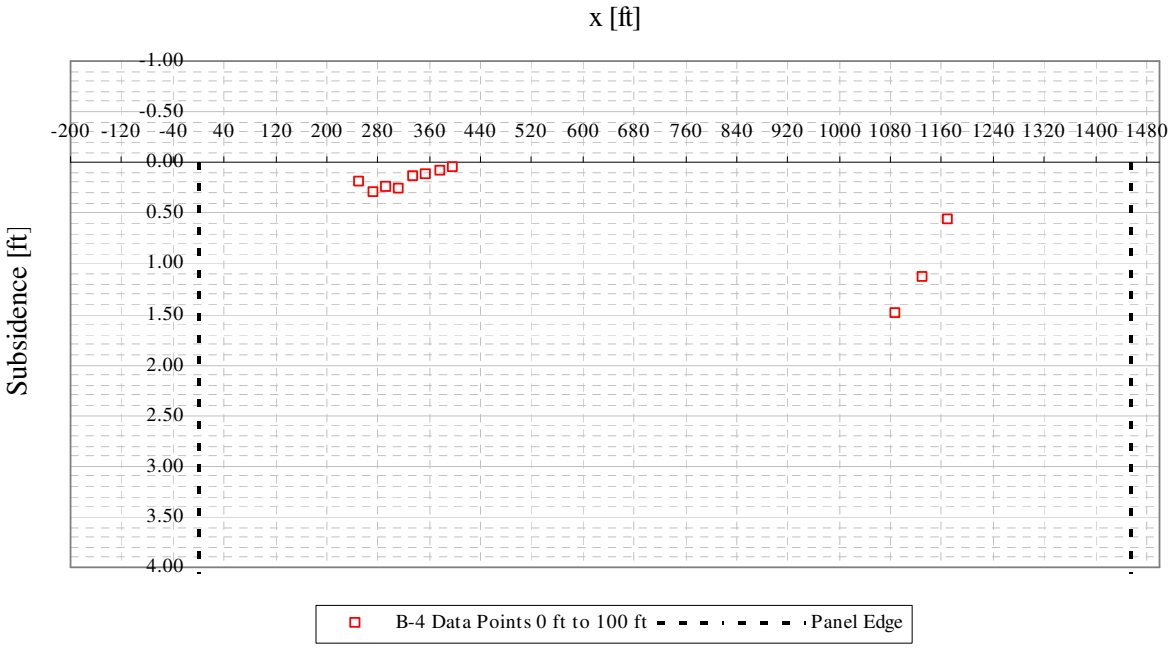

Figure A1- 5 B-4 transverse view of data points from 0 ft to 100 ft from mine face

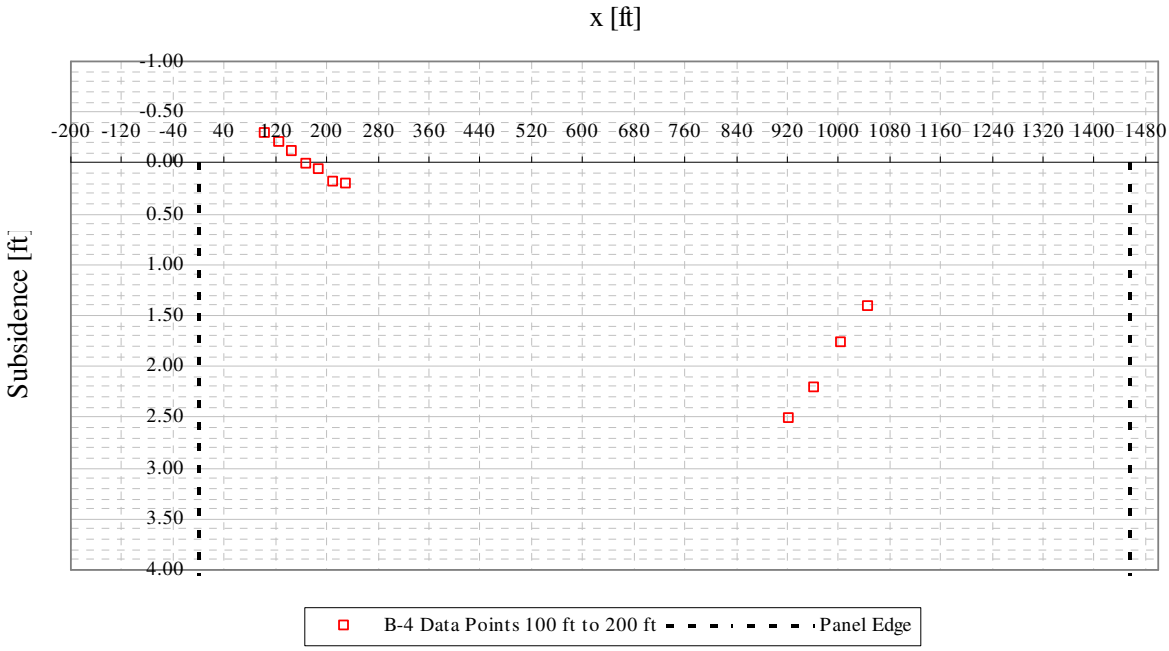

Figure A1- 6 B-4 transverse view of data points from 100 ft to 200 ft from mine face

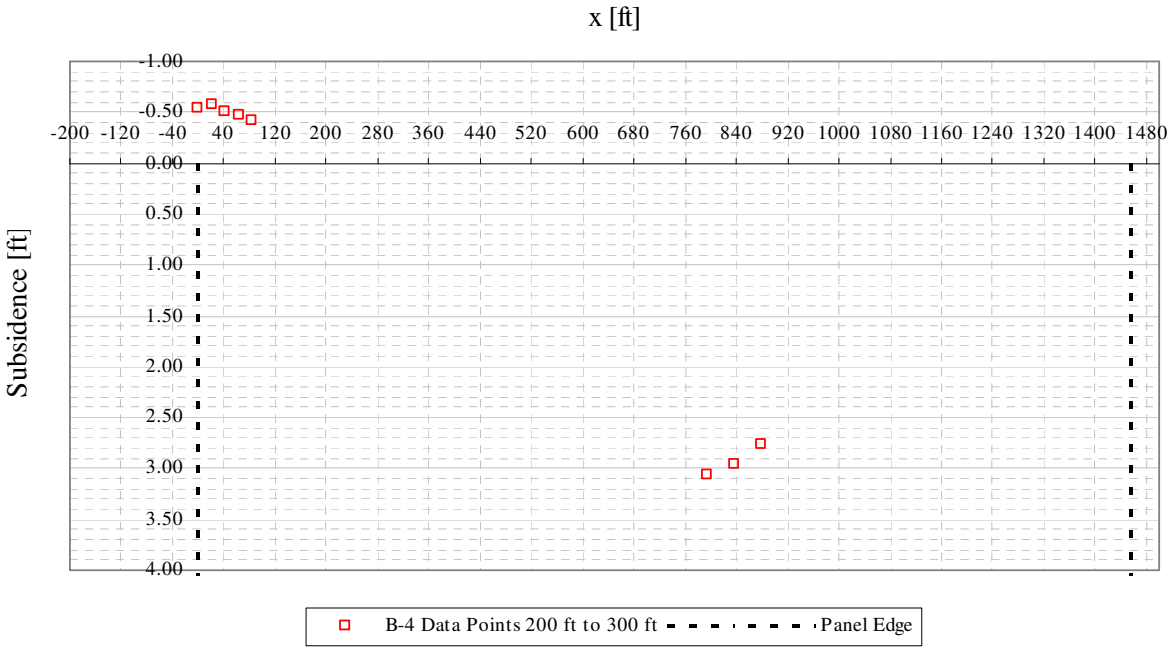

Figure A1- 7 B-4 transverse view of data points from 200 ft to 300 ft from mine face

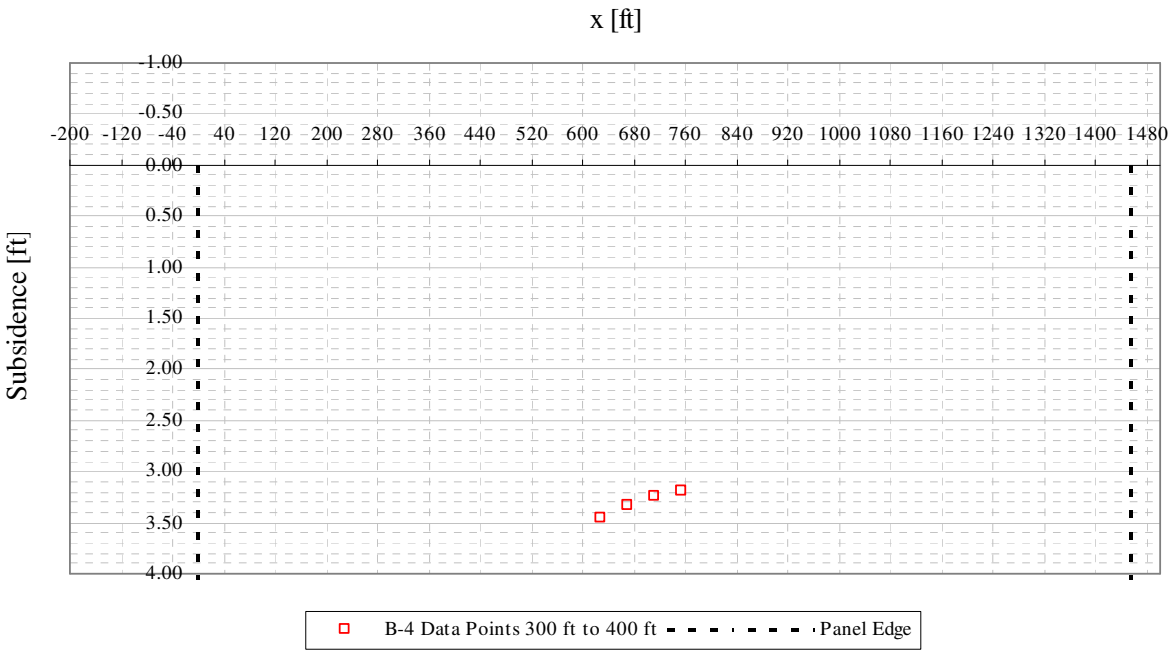

Figure A1- 8 B-4 transverse view of data points from 300 ft to 400 ft from mine face

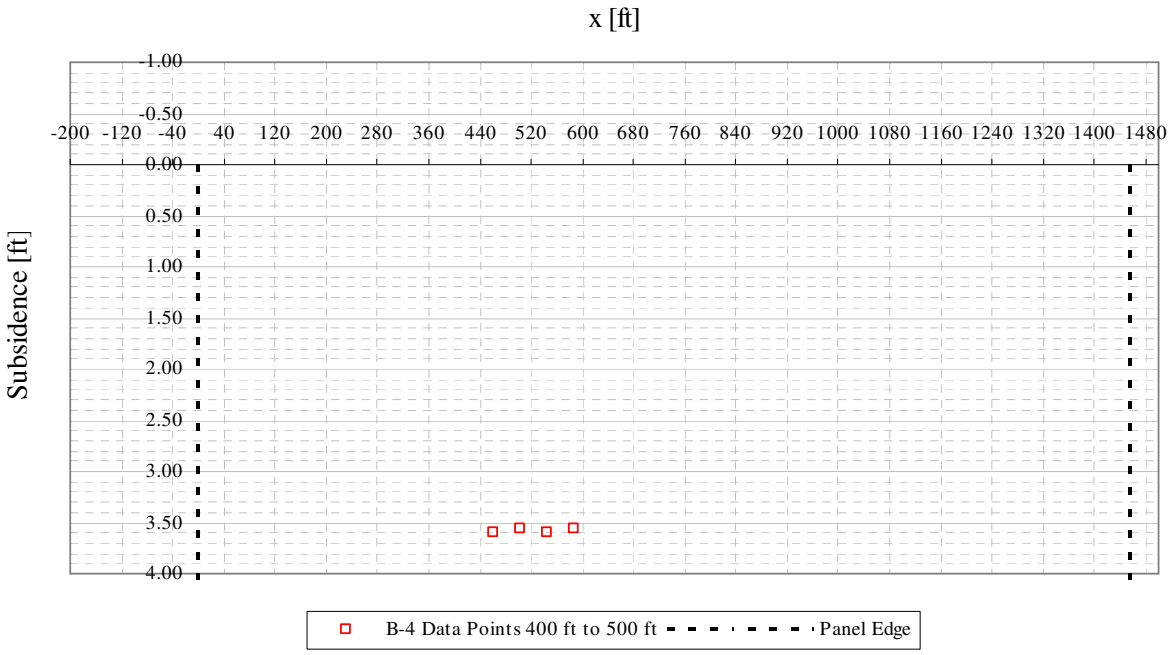

Figure A1- 9 B-4 transverse view of data points from 400 ft to 500 ft from mine face

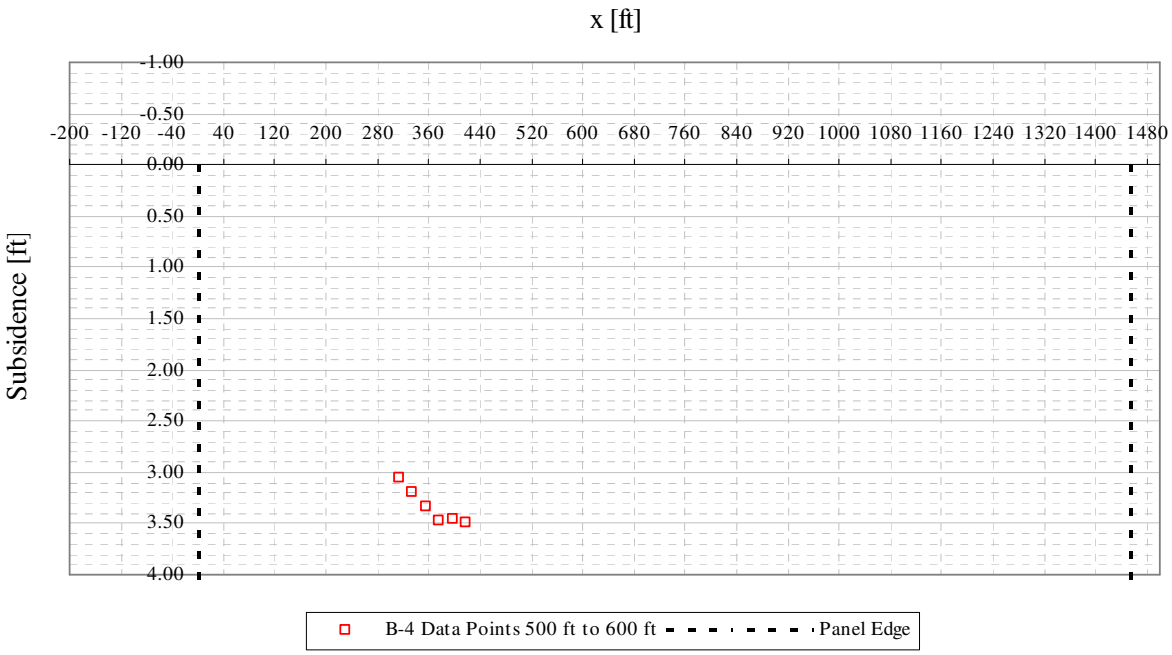

Figure A1- 10 B-4 transverse view of data points from 500 ft to 600 ft from mine face

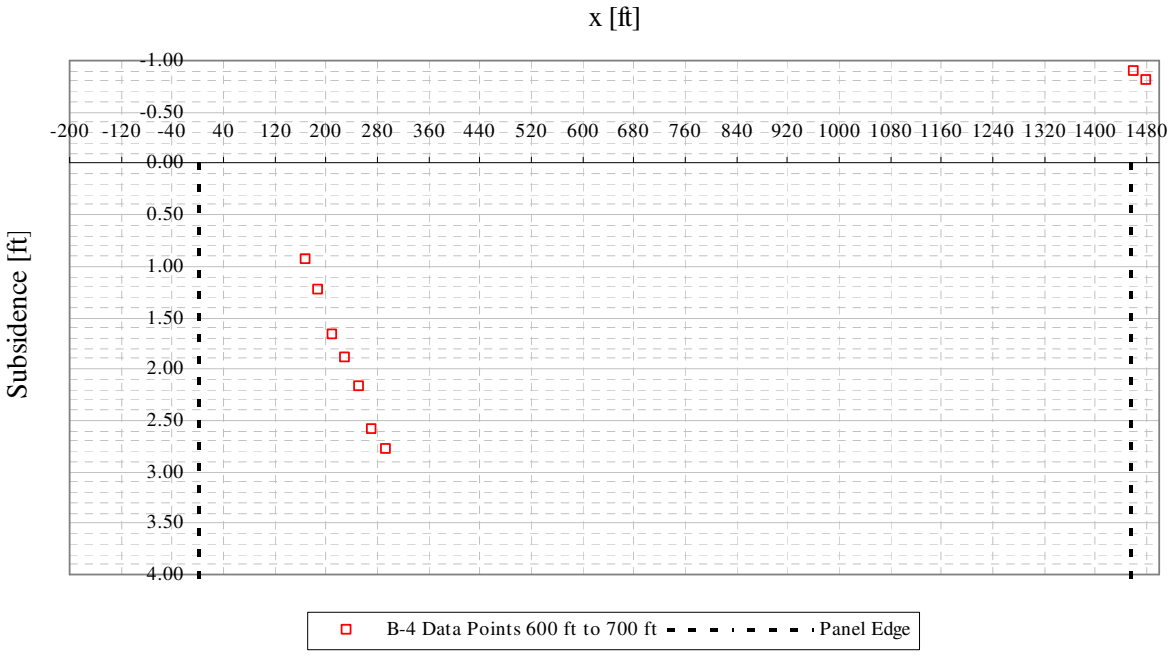

Figure A1- 11 B-4 transverse view of data points from 600 ft to 700 ft from mine face

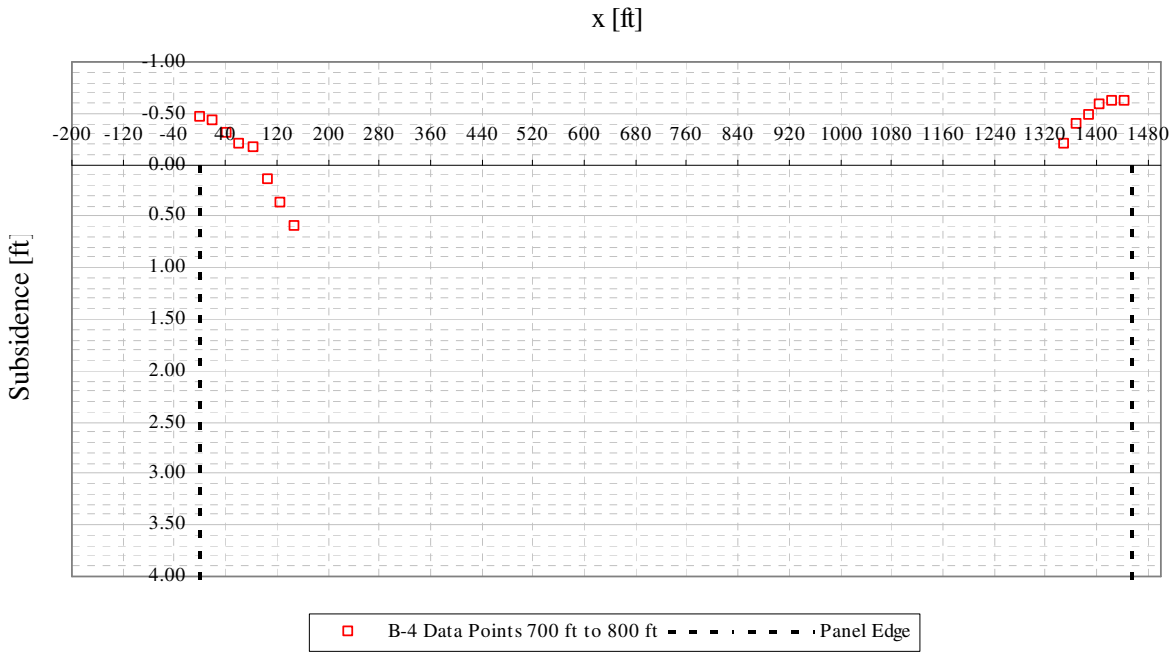

Figure A1- 12 B-4 transverse view of data points from 700 ft to 800 ft from mine face

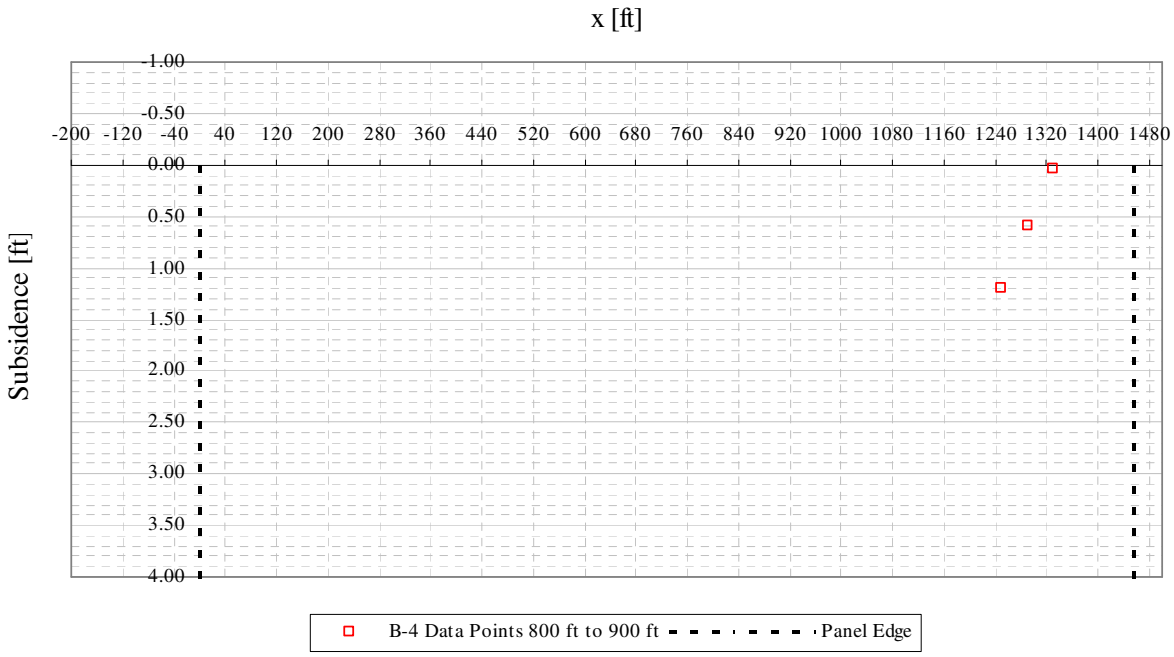

Figure A1- 13 B-4 transverse view of data points from 800 ft to 900 ft from mine face

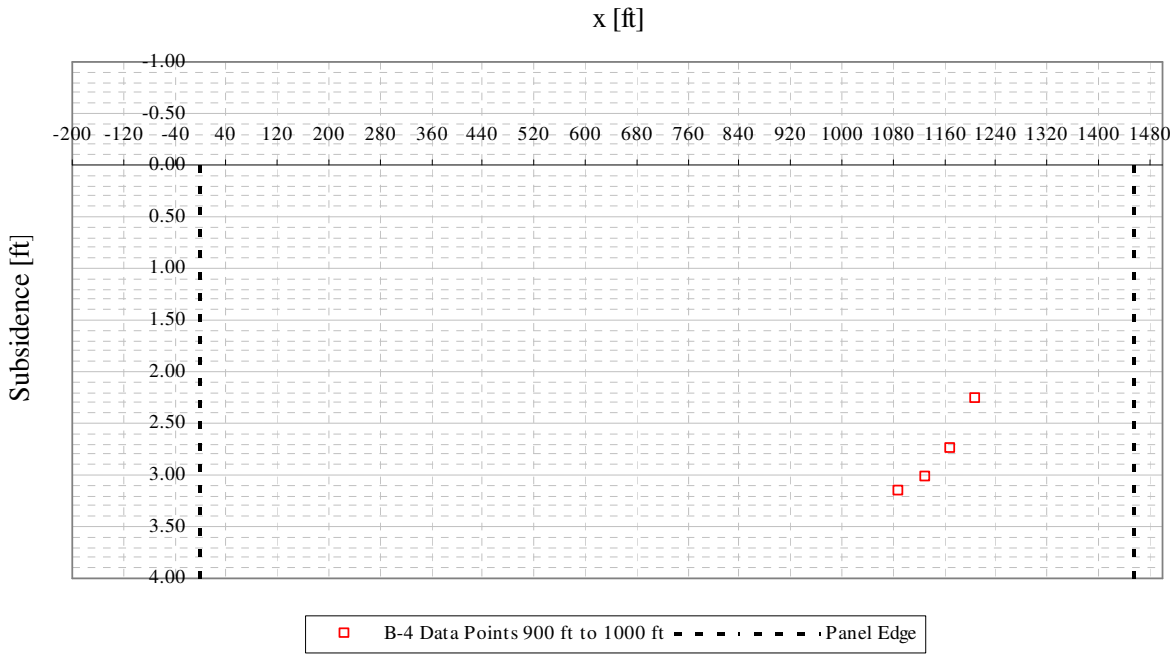

Figure A1- 14 B-4 transverse view of data points from 900 ft to 1000 ft from mine face

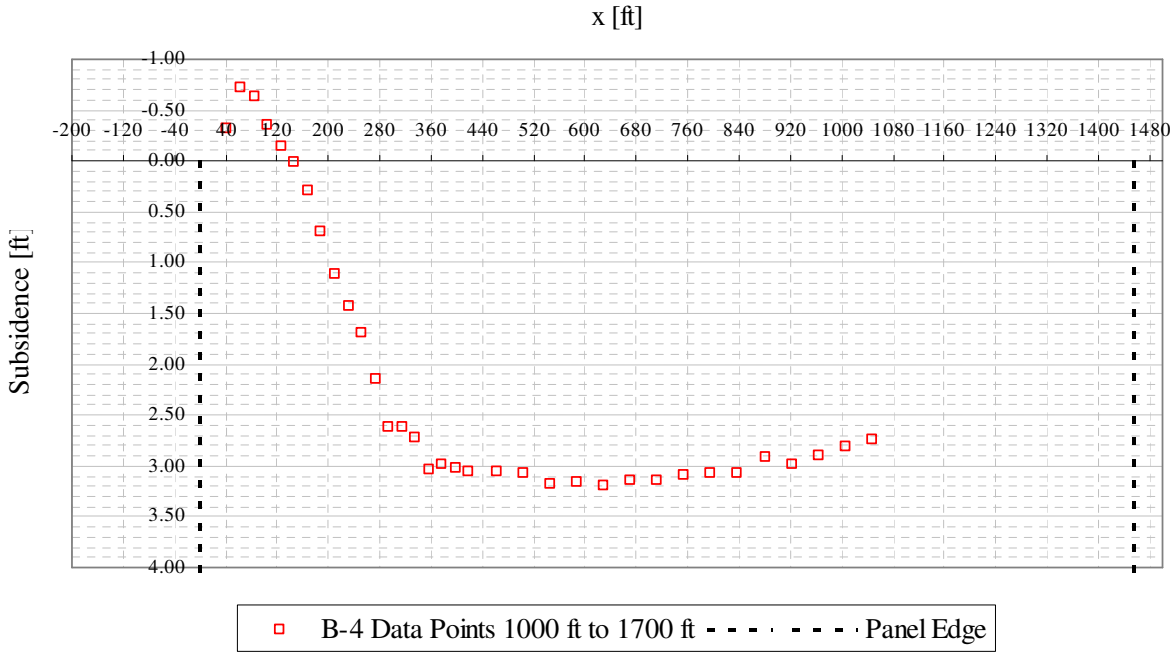

Figure A1- 15 B-4 transverse view of data points from 1000 ft to 1700 ft from mine face

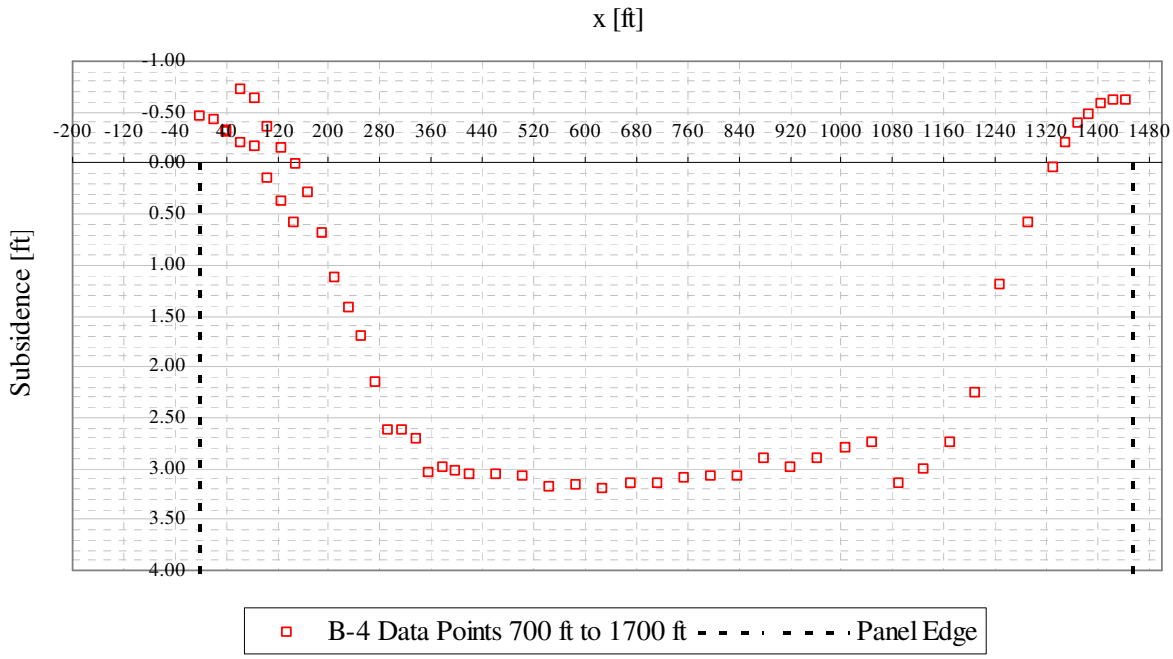

Figure A1- 16 B-4 transverse view of data points from 700 ft to 1700 ft from mine face

A.2 EMERALD MINE PANEL LW-49 TRANSFORMED DATA

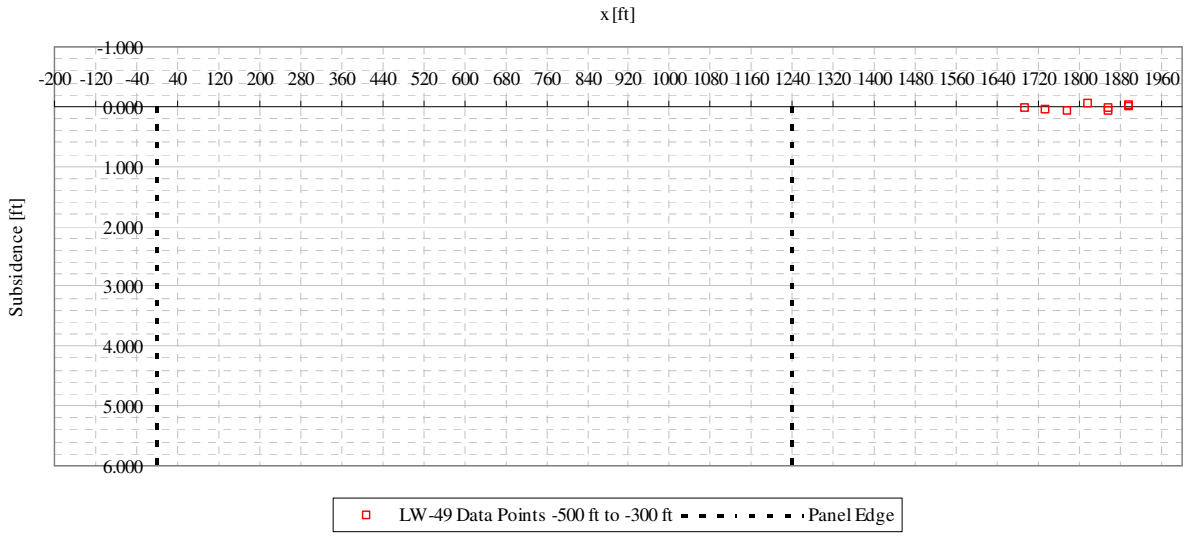

Figure A2- 1 LW-49 transverse view of data points from -500 ft to -300 ft from mine face

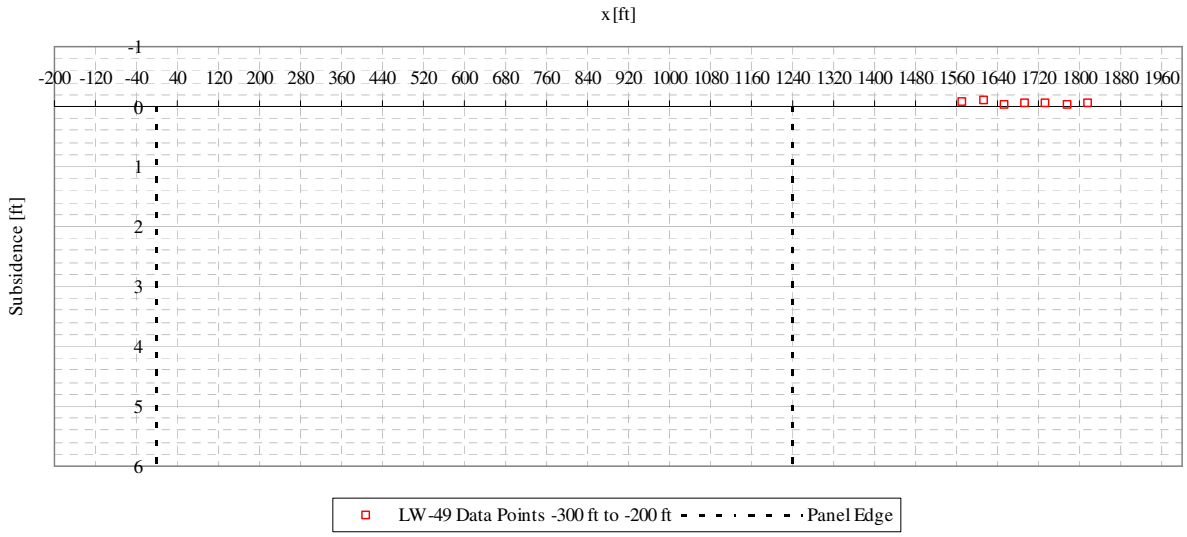

Figure A2- 2 LW-49 transverse view of data points from -300 ft to -200 ft from mine face

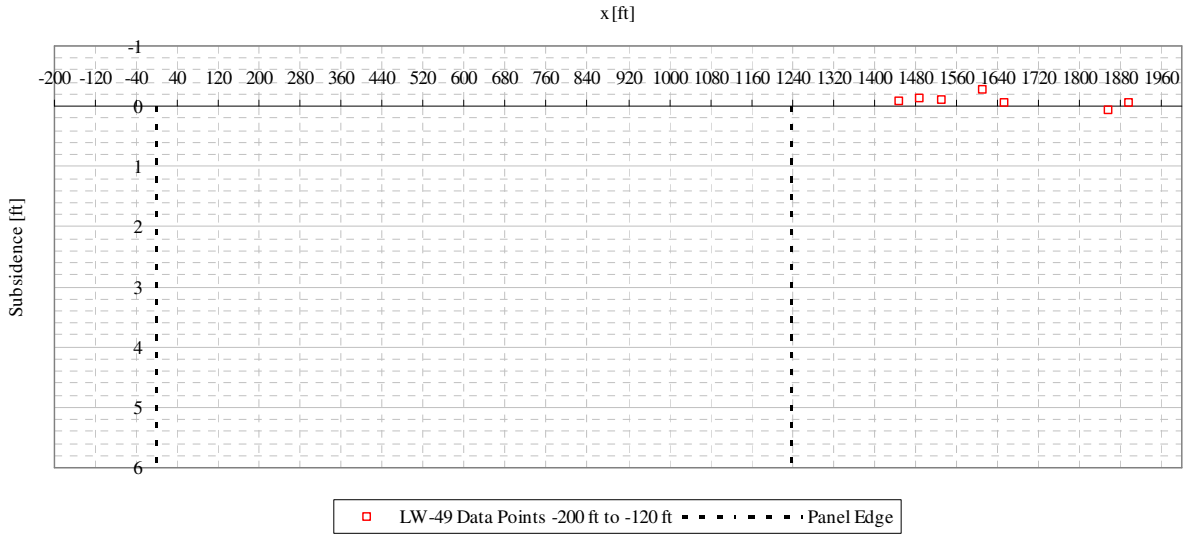

Figure A2- 3 LW-49 transverse view of data points from -200 ft to -120 ft from mine face

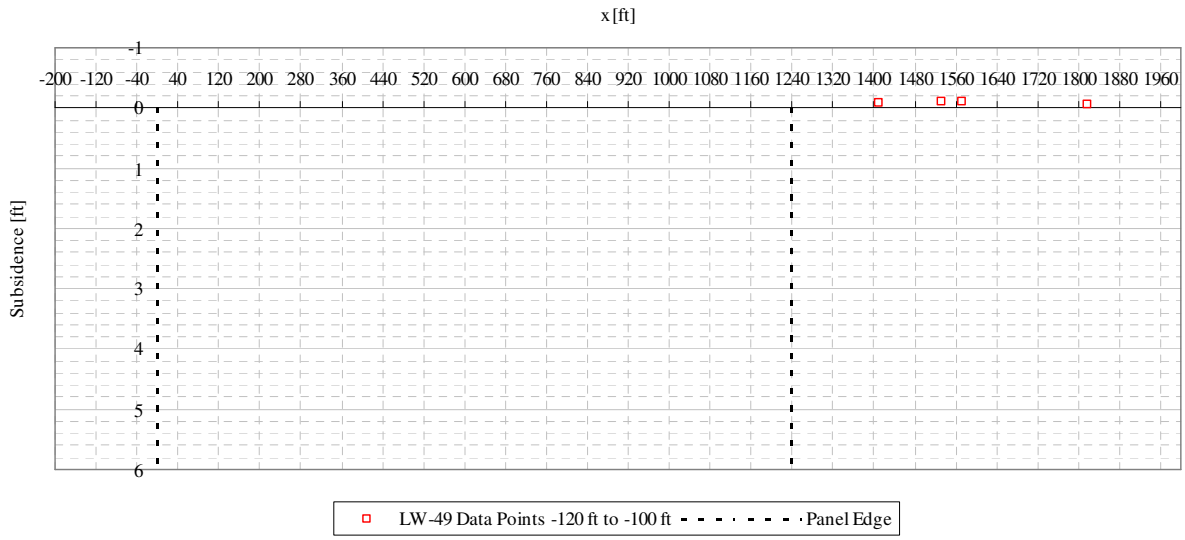

Figure A2- 4 LW-49 transverse view of data points from -120 ft to -100 ft from mine face

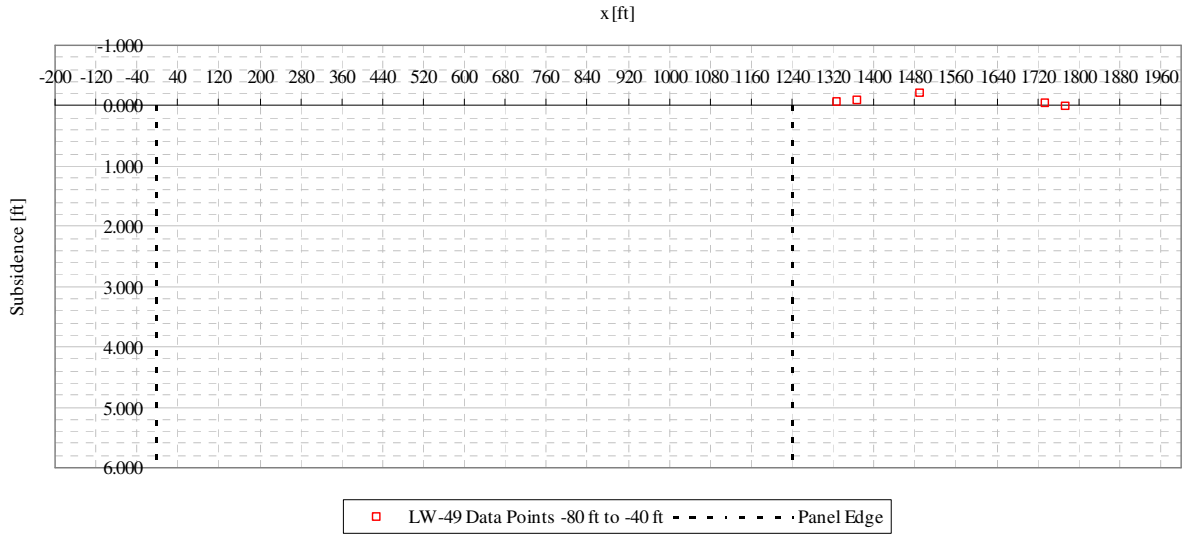

Figure A2- 5 LW-49 transverse view of data points from -80 ft to -40 ft from mine face

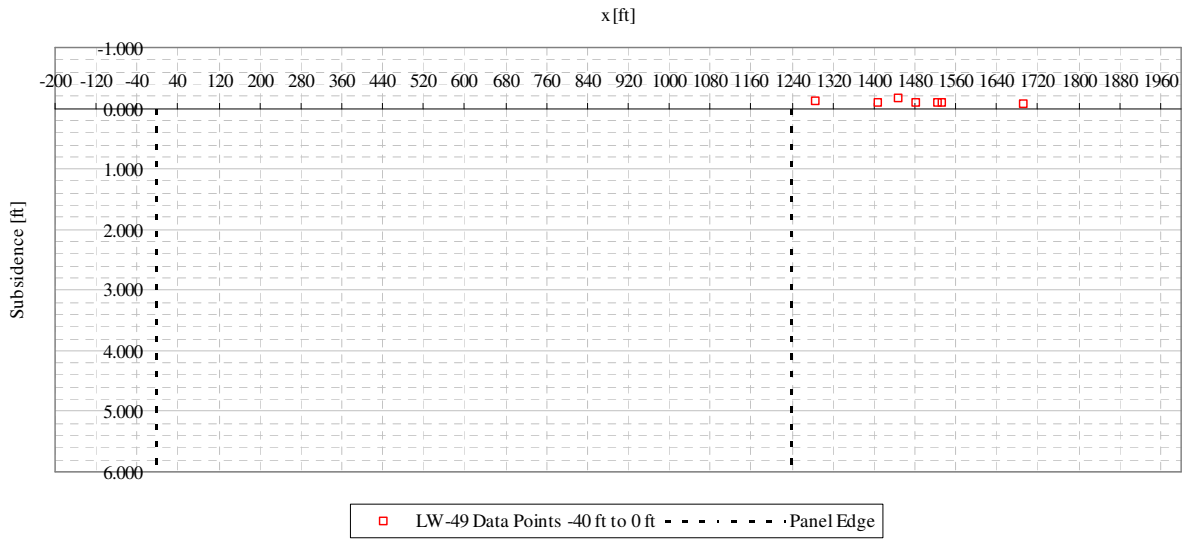

Figure A2- 6 LW-49 transverse view of data points from -40 ft to 0 ft from mine face

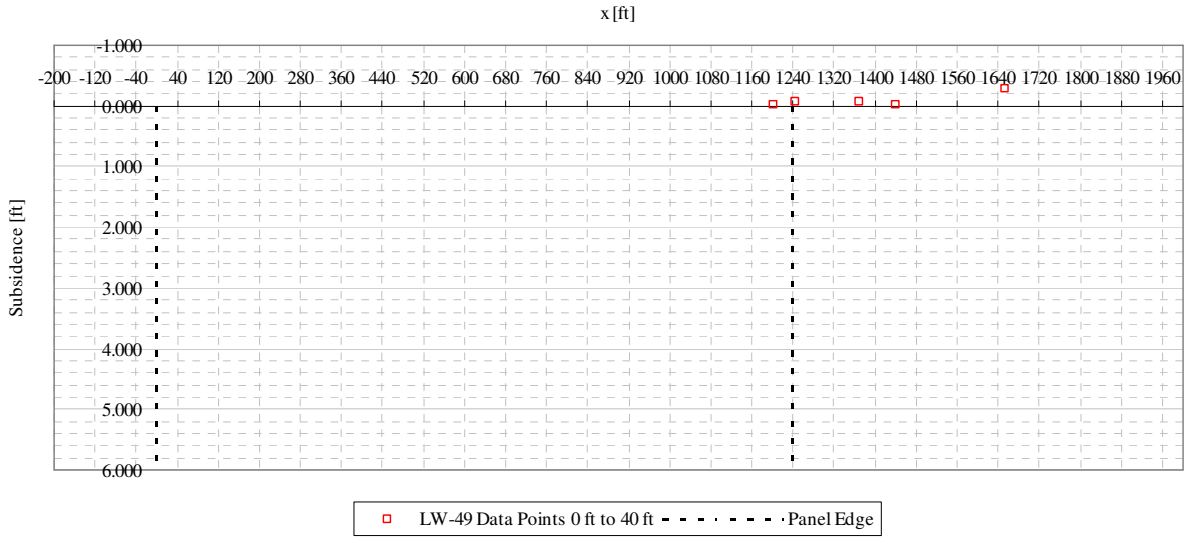

Figure A2- 7 LW-49 transverse view of data points from 0 ft to 40 ft from mine face

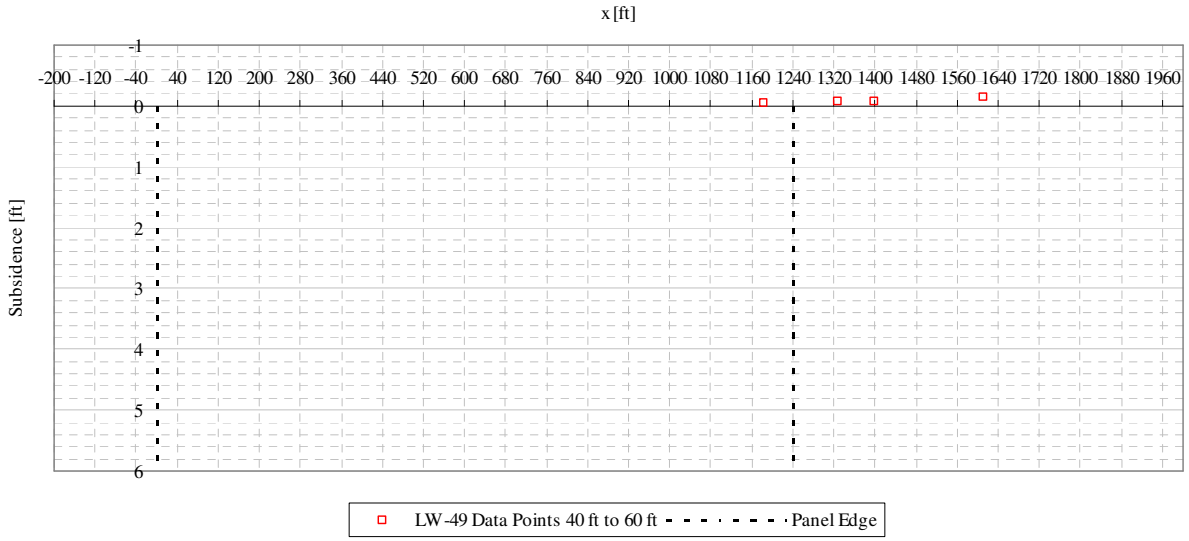

Figure A2- 8 LW-49 transverse view of data points from 40 ft to 60 ft from mine face

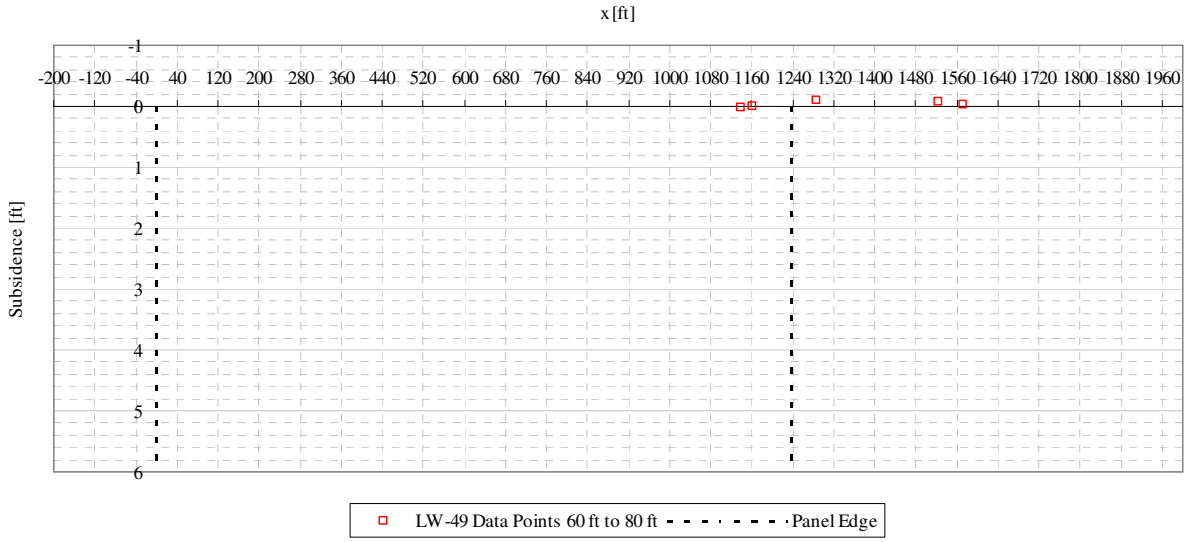

Figure A2- 9 LW-49 transverse view of data points from 60 ft to 80 ft from mine face

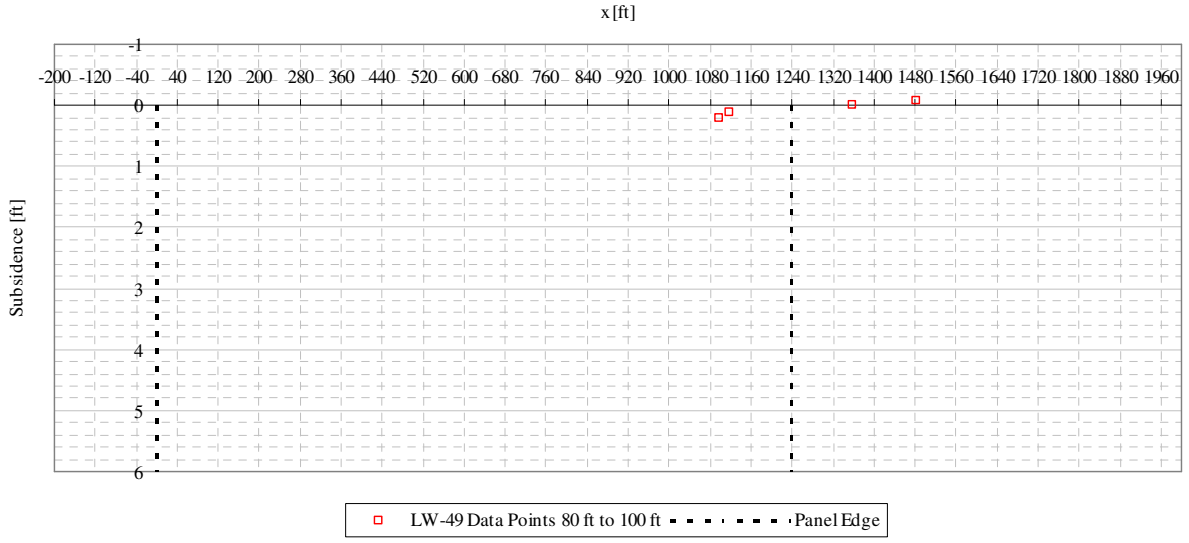

Figure A2- 10 LW-49 transverse view of data points from 80 ft to 100 ft from mine face

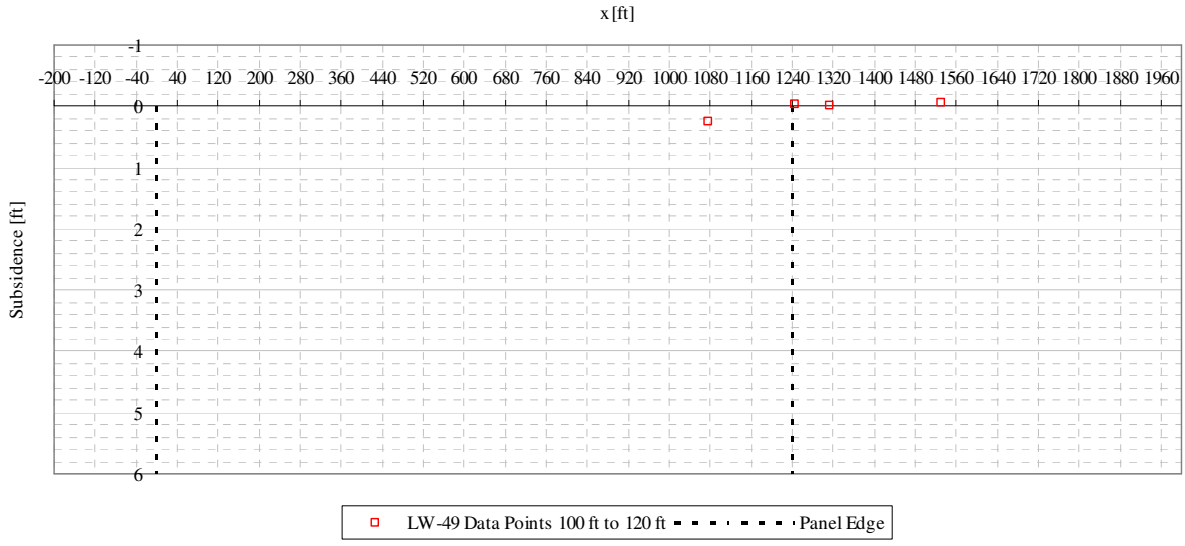

Figure A2- 11 LW-49 transverse view of data points from 100 ft to 120 ft from mine face

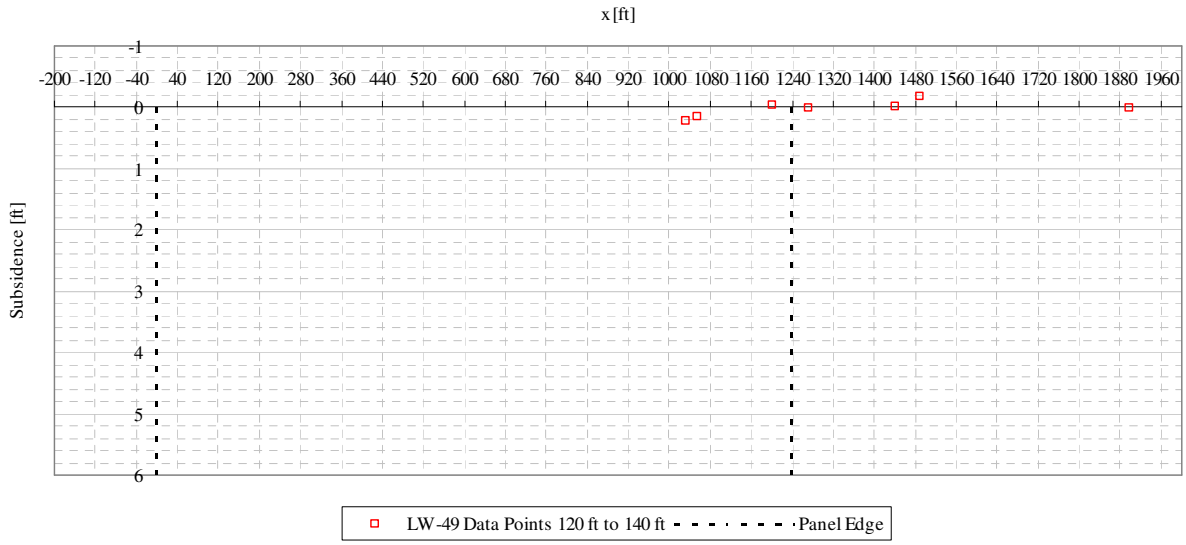

Figure A2- 12 LW-49 transverse view of data points from 120 ft to 140 ft from mine face

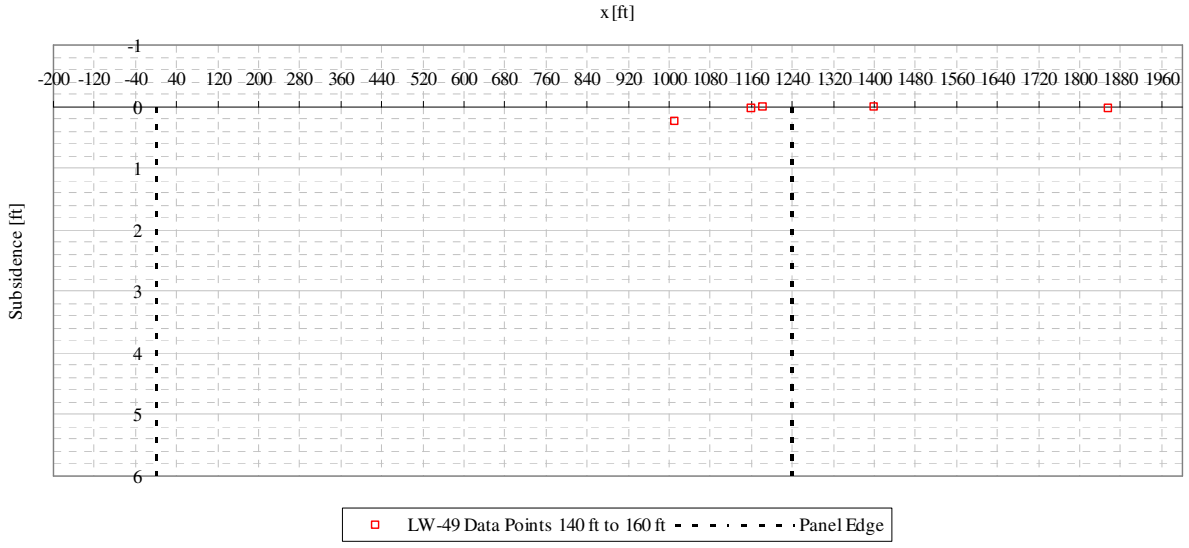

Figure A2- 13 LW-49 transverse view of data points from 140 ft to 160 ft from mine face

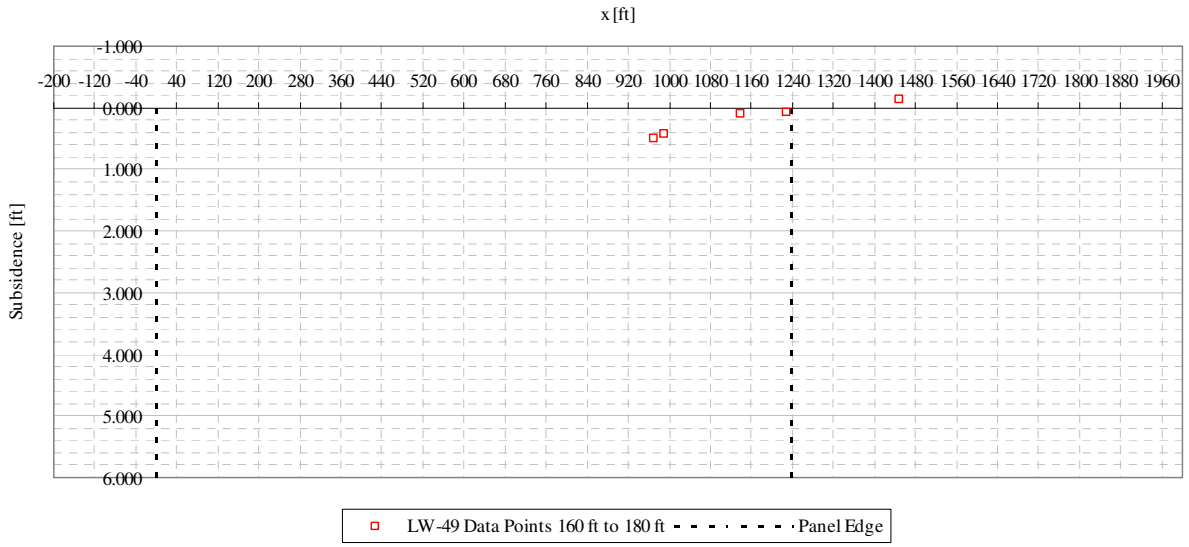

Figure A2- 14 LW-49 transverse view of data points from 160 ft to 180 ft from mine face

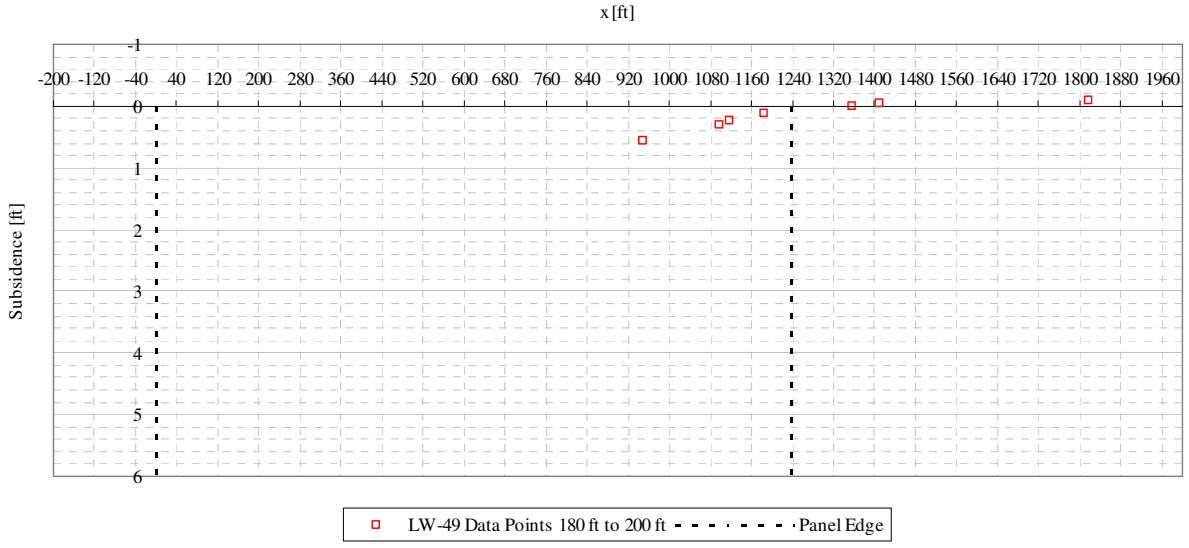

Figure A2- 15 LW-49 transverse view of data points from 180 ft to 200 ft from mine face

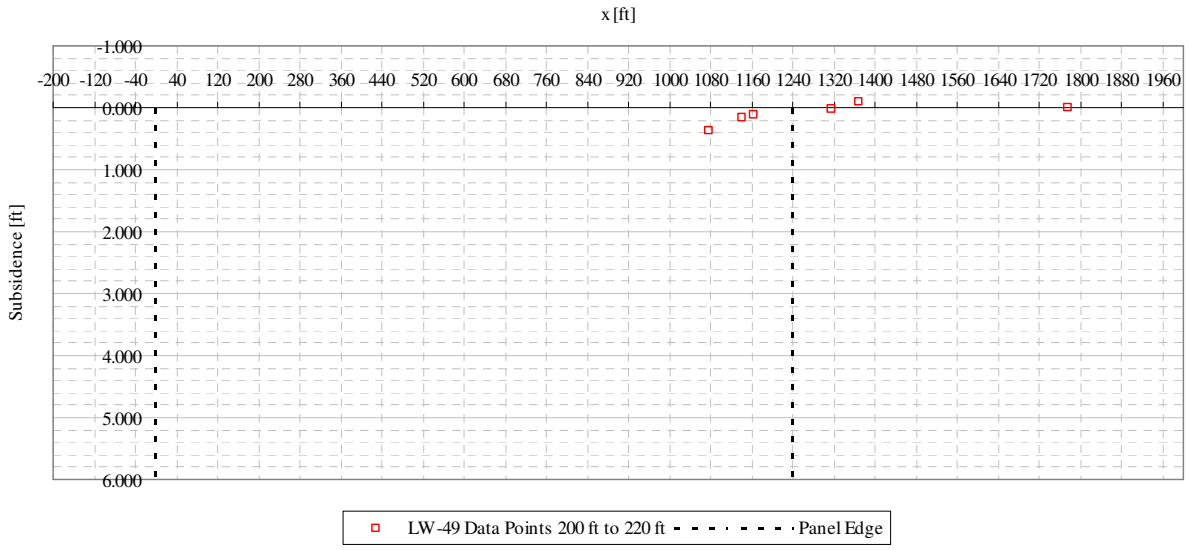

Figure A2- 16 LW-49 transverse view of data points from 200 ft to 220 ft from mine face

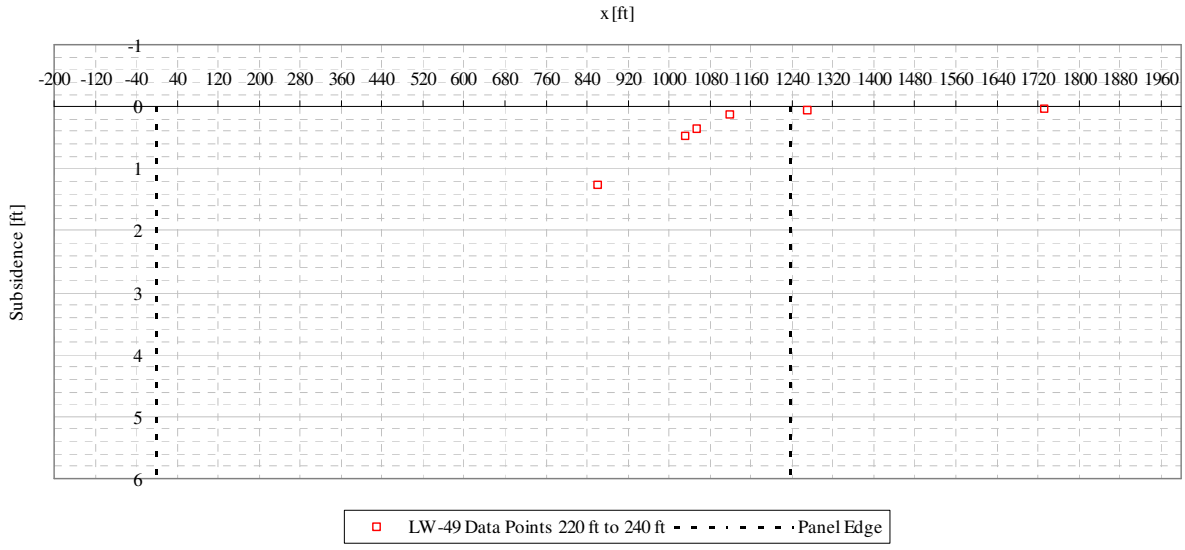

Figure A2- 17 LW-49 transverse view of data points from 220 ft to 240 ft from mine face

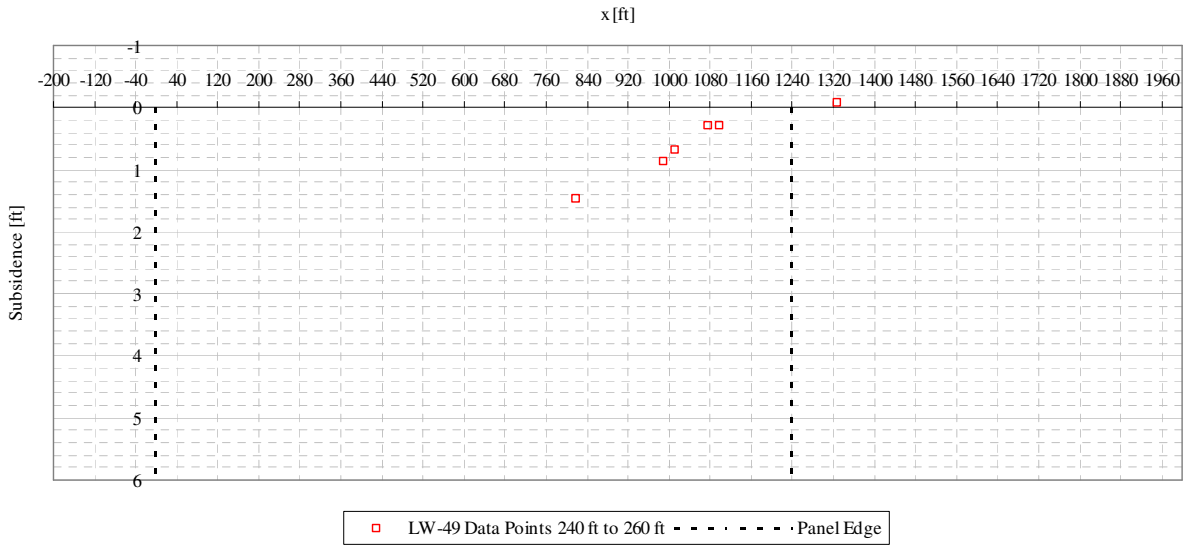

Figure A2- 18 LW-49 transverse view of data points from 240 ft to 260 ft from mine face

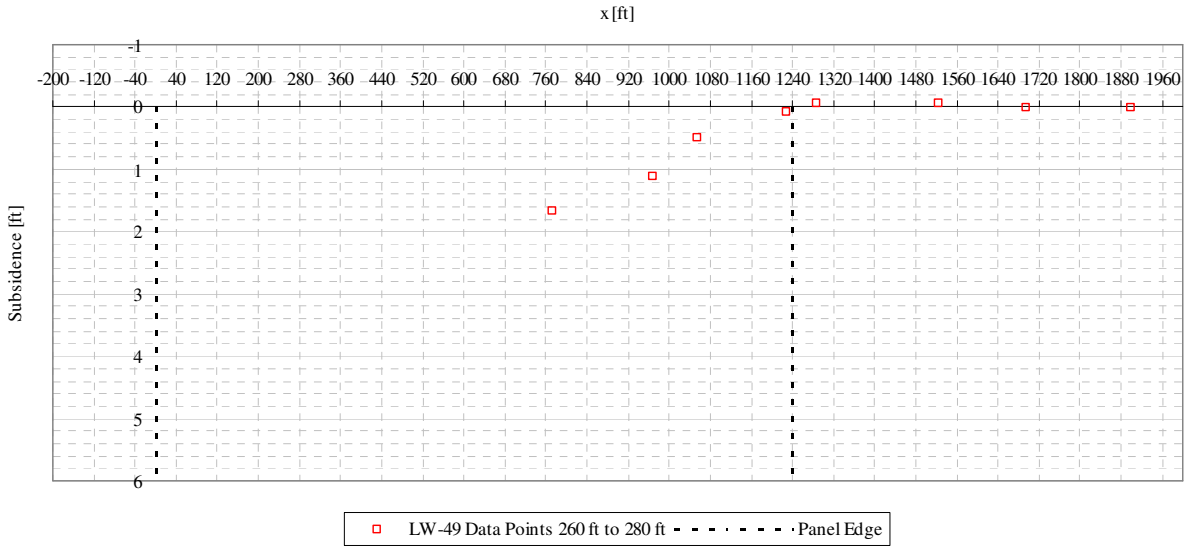

Figure A2- 19 LW-49 transverse view of data points from 260 ft to 280 ft from mine face

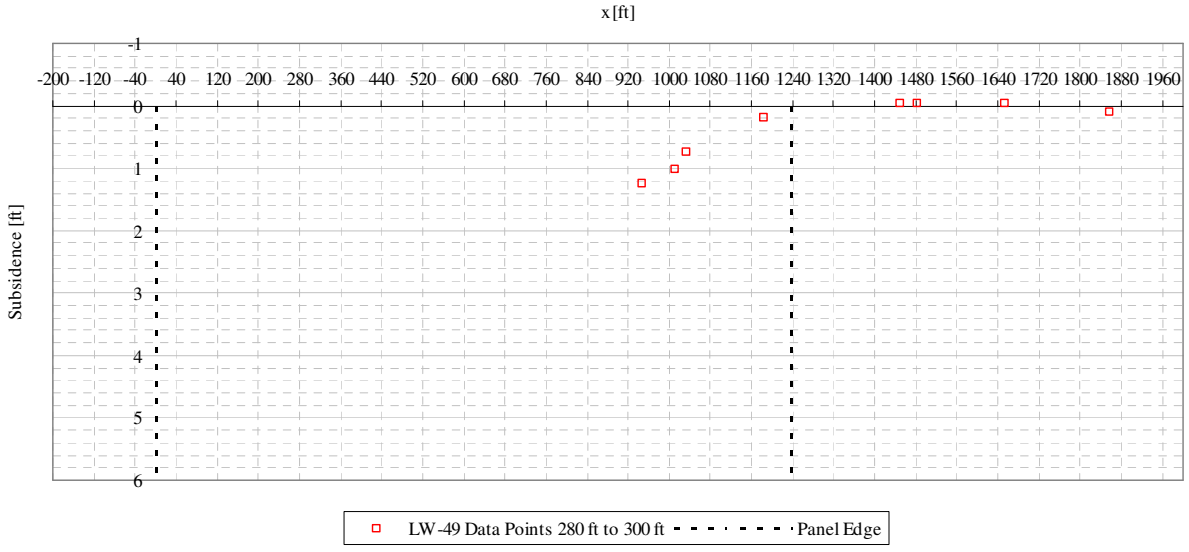

Figure A2- 20 LW-49 transverse view of data points from 280 ft to 300 ft from mine face

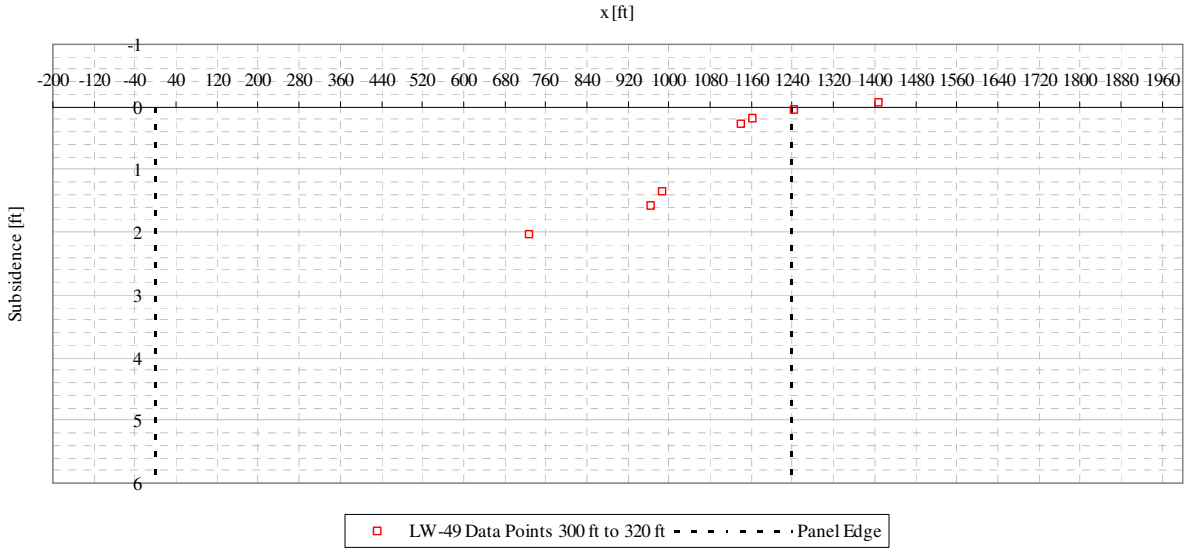

Figure A2- 21 LW-49 transverse view of data points from 300 ft to 320 ft from mine face

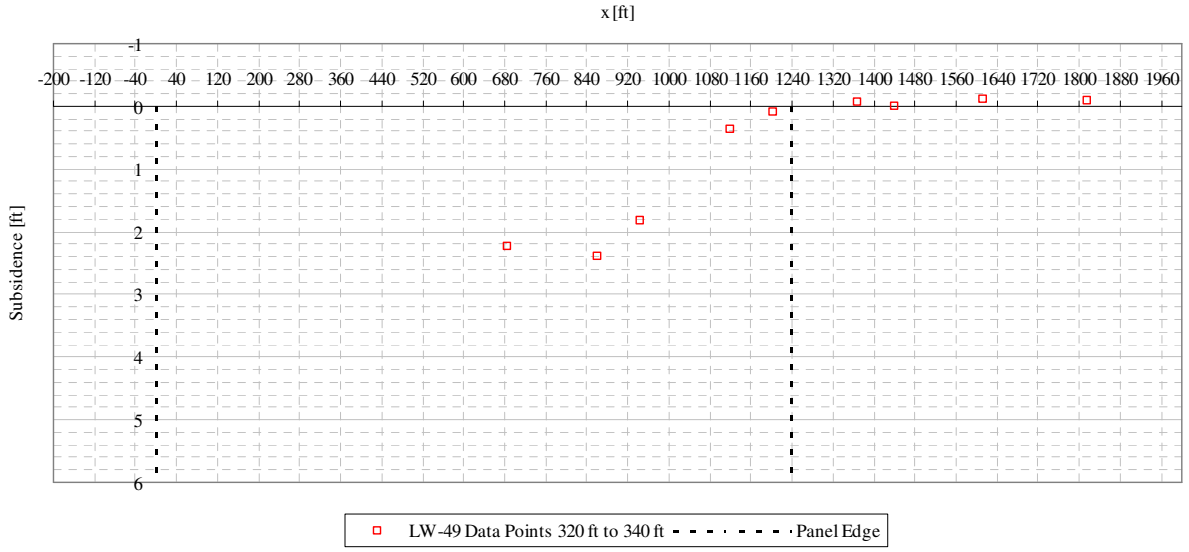

Figure A2- 22 LW-49 transverse view of data points from 320 ft to 340 ft from mine face

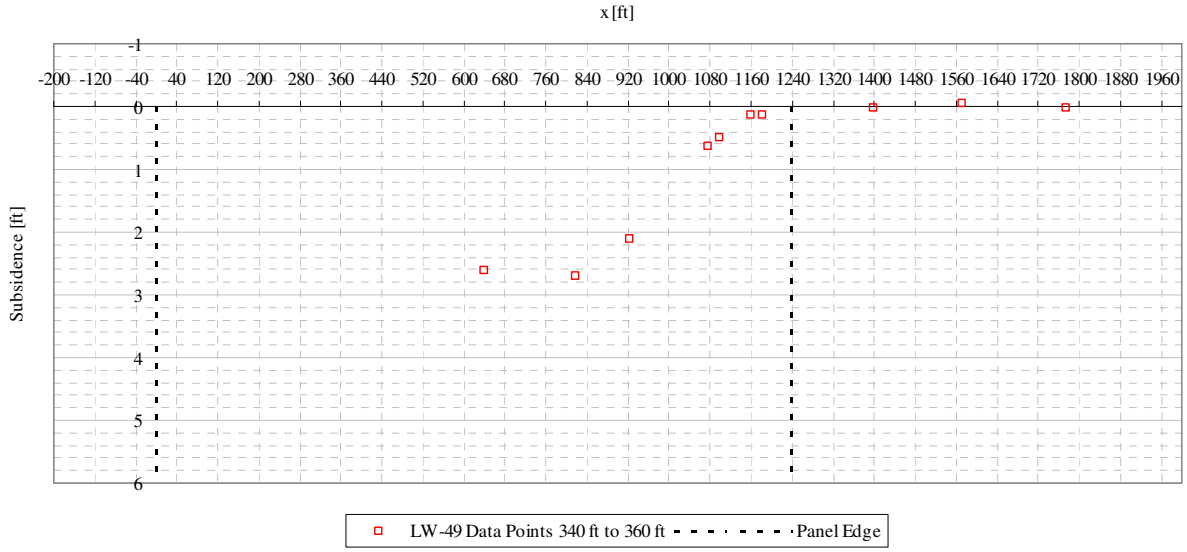

Figure A2- 23 LW-49 transverse view of data points from 340 ft to 360 ft from mine face

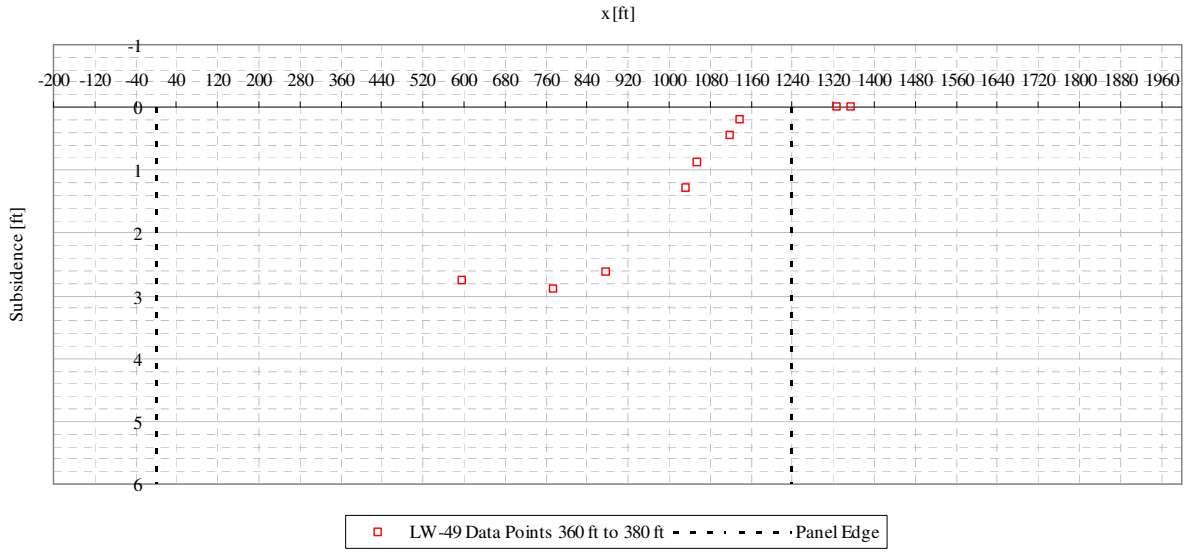

Figure A2- 24 LW-49 transverse view of data points from 360 ft to 380 ft from mine face

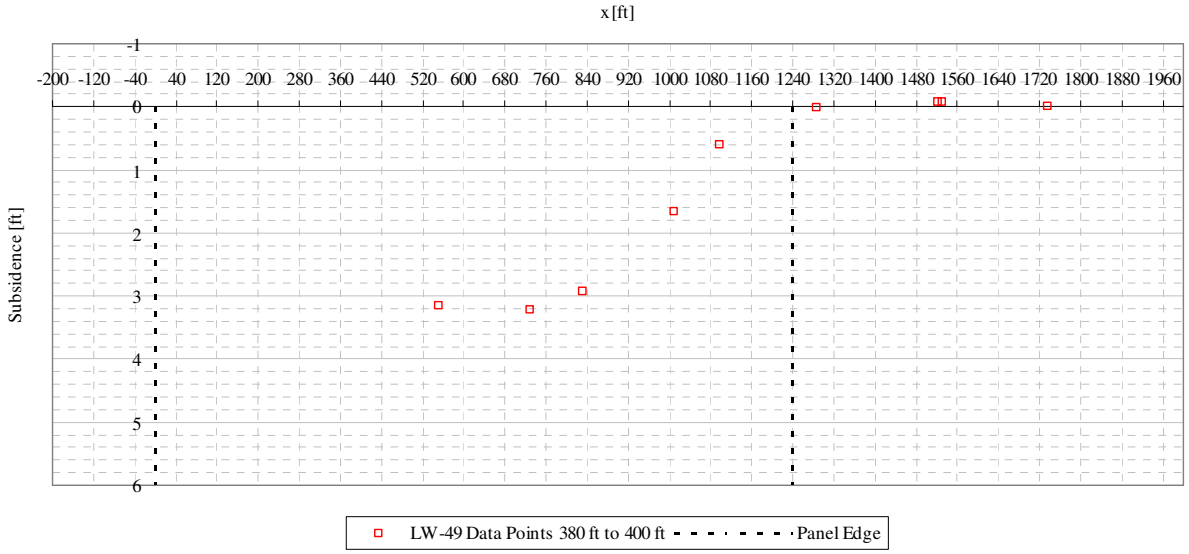

Figure A2- 25 LW-49 transverse view of data points from 380 ft to 400 ft from mine face

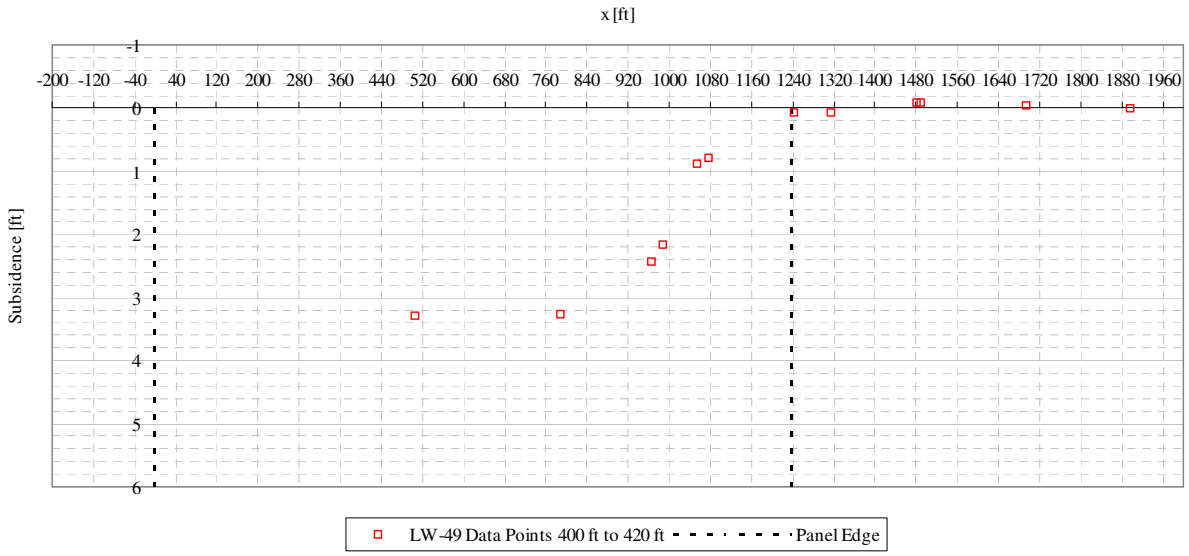

Figure A2- 26 LW-49 transverse view of data points from 400 ft to 420 ft from mine face

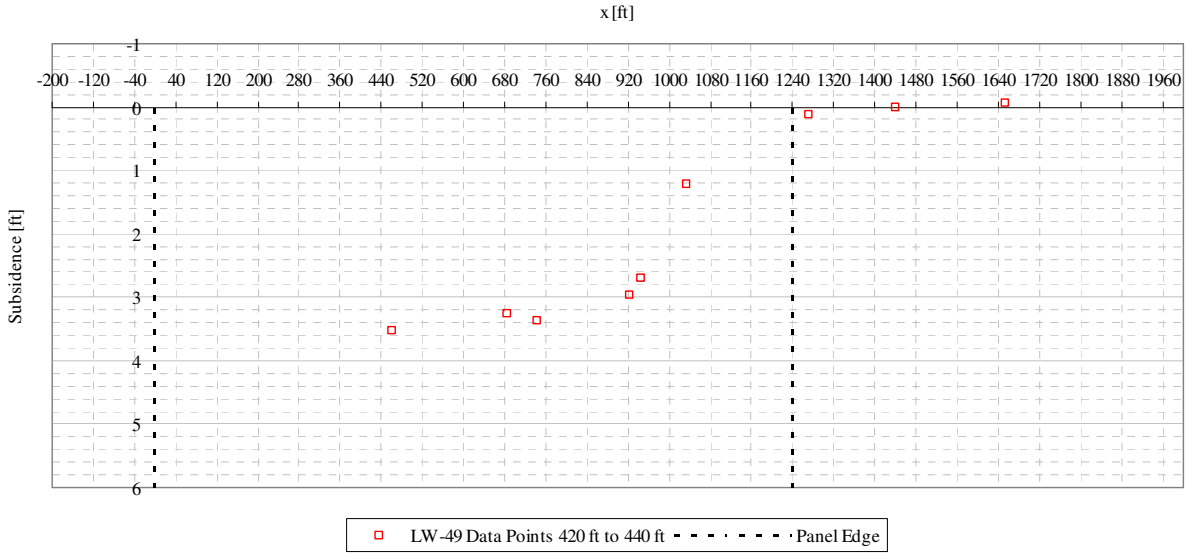

Figure A2- 27 LW-49 transverse view of data points from 420 ft to 440 ft from mine face

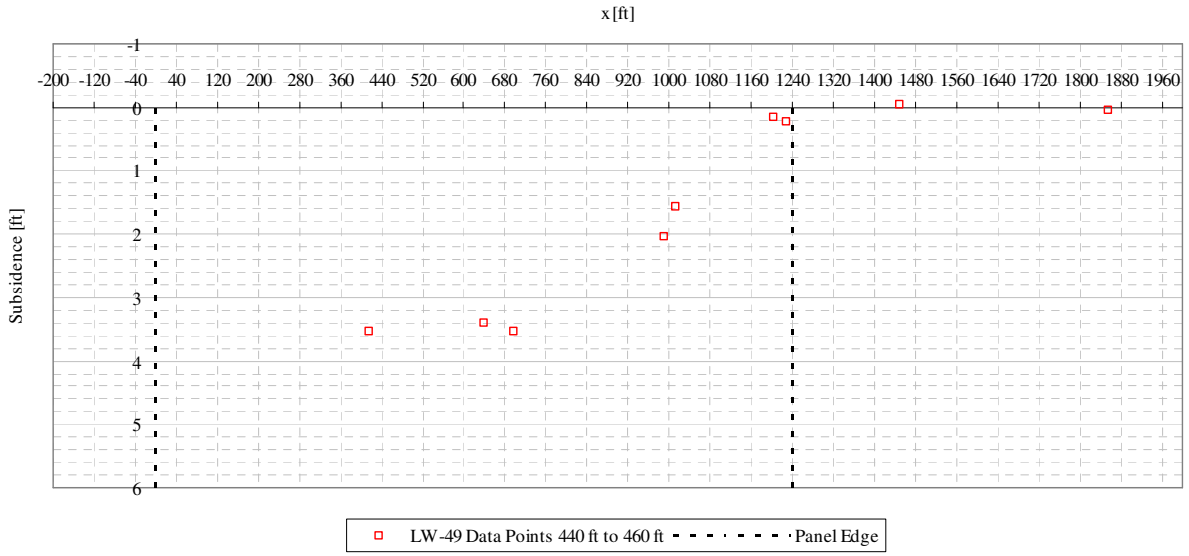

Figure A2- 28 LW-49 transverse view of data points from 440 ft to 460 ft from mine face

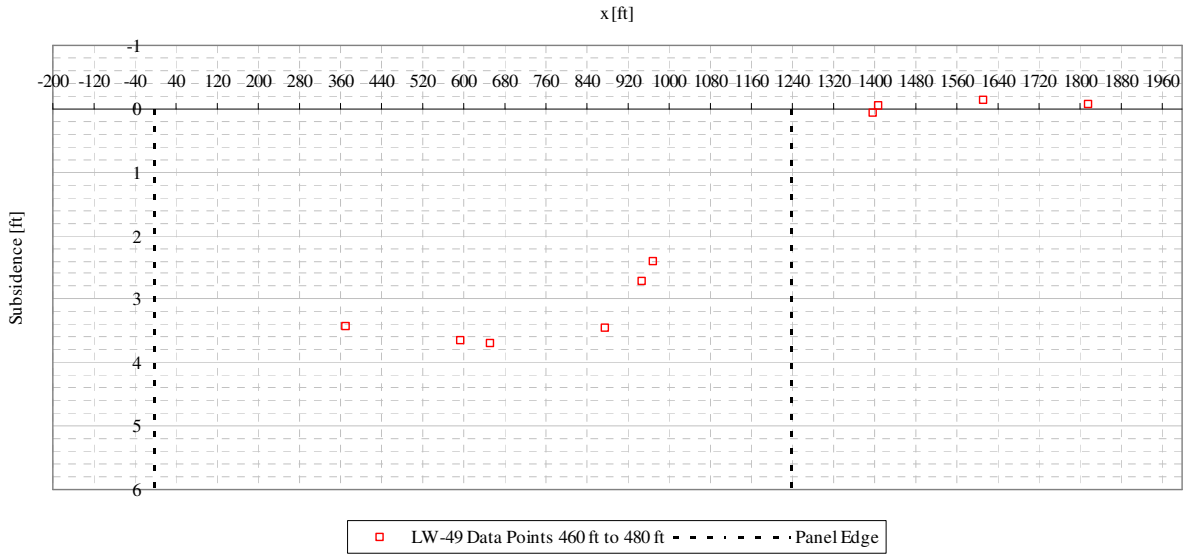

Figure A2- 29 LW-49 transverse view of data points from 460 ft to 480 ft from mine face

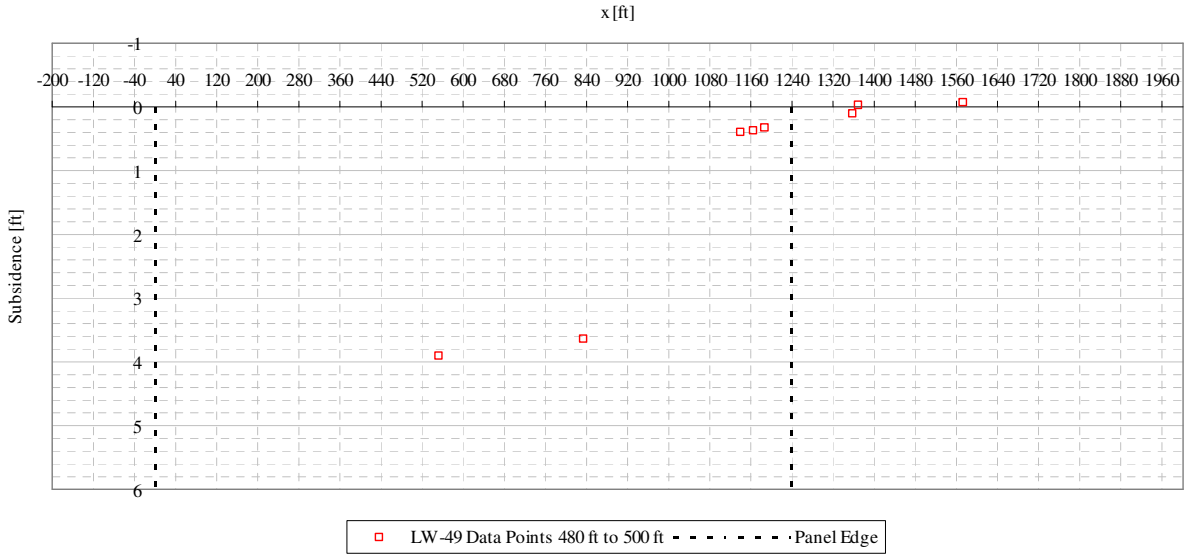

Figure A2- 30 LW-49 transverse view of data points from 480 ft to 500 ft from mine face

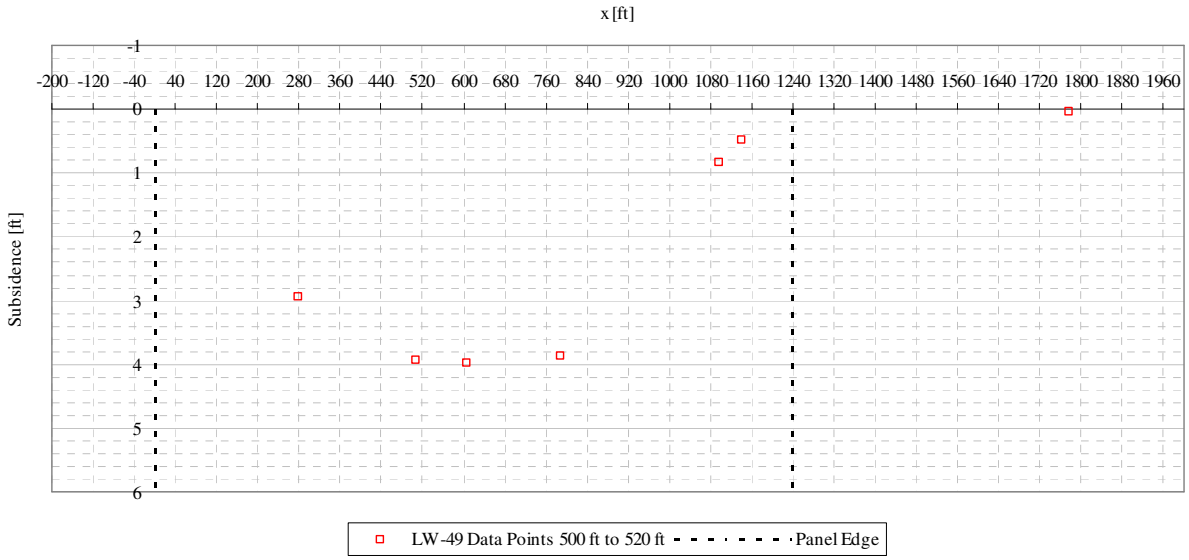

Figure A2- 31 LW-49 transverse view of data points from 500 ft to 520 ft from mine face

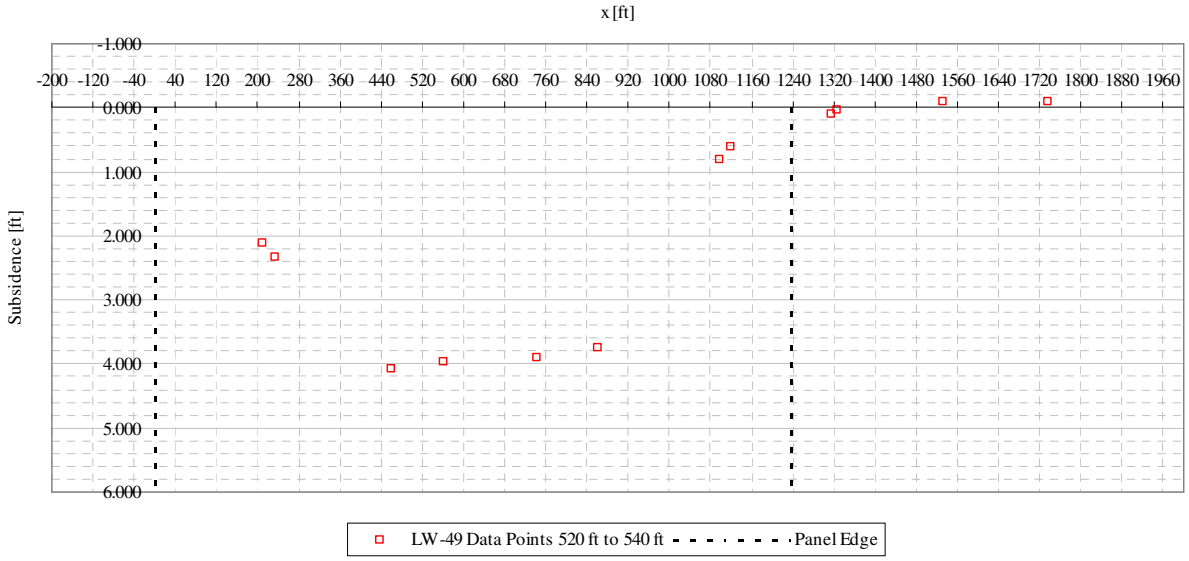

Figure A2- 32 LW-49 transverse view of data points from 520 ft to 540 ft from mine face

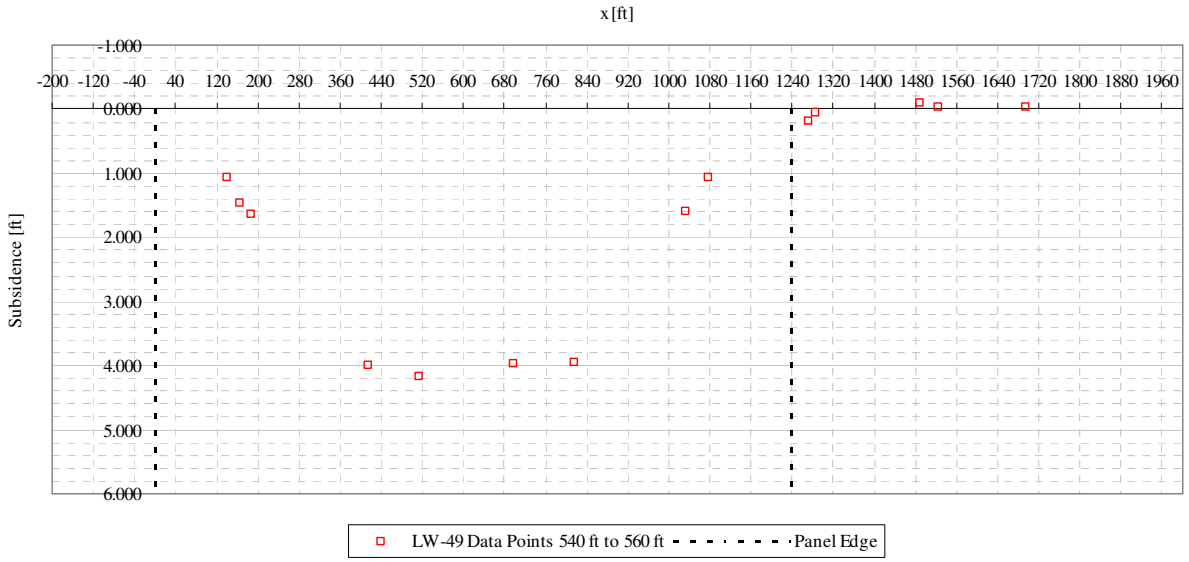

Figure A2- 33 LW-49 transverse view of data points from 540 ft to 560 ft from mine face

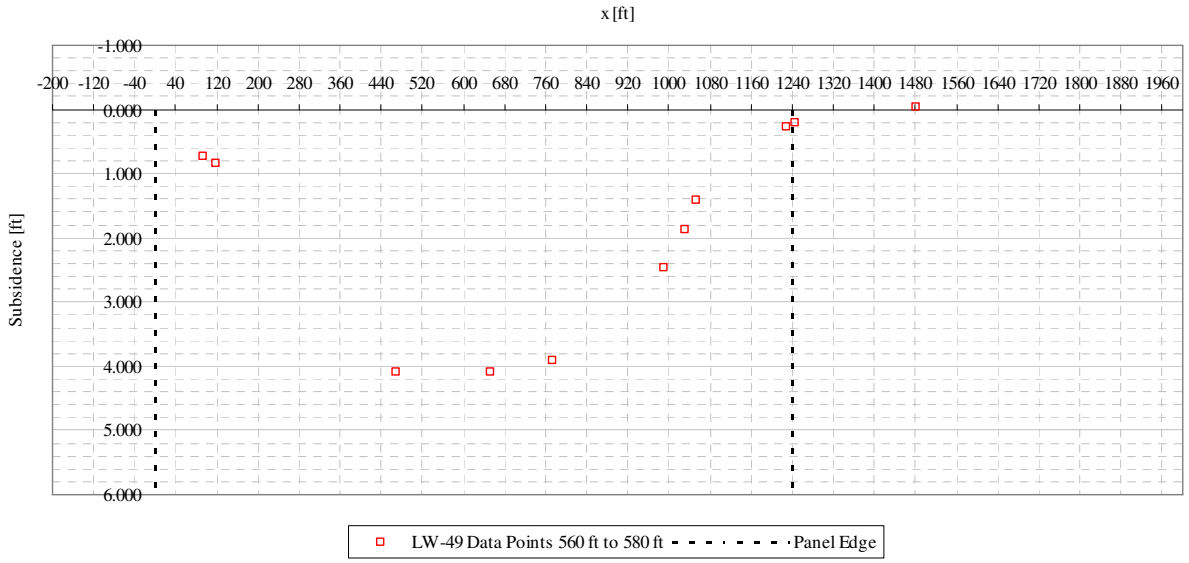

Figure A2- 34 LW-49 transverse view of data points from 560 ft to 580 ft from mine face

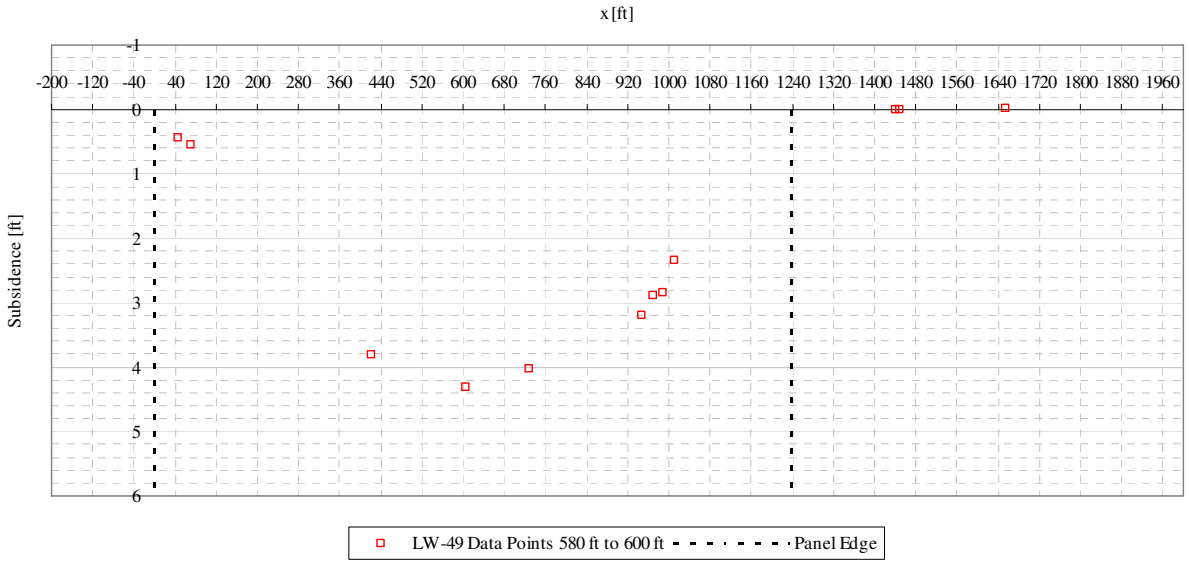

Figure A2- 35 LW-49 transverse view of data points from 580 ft to 600 ft from mine face

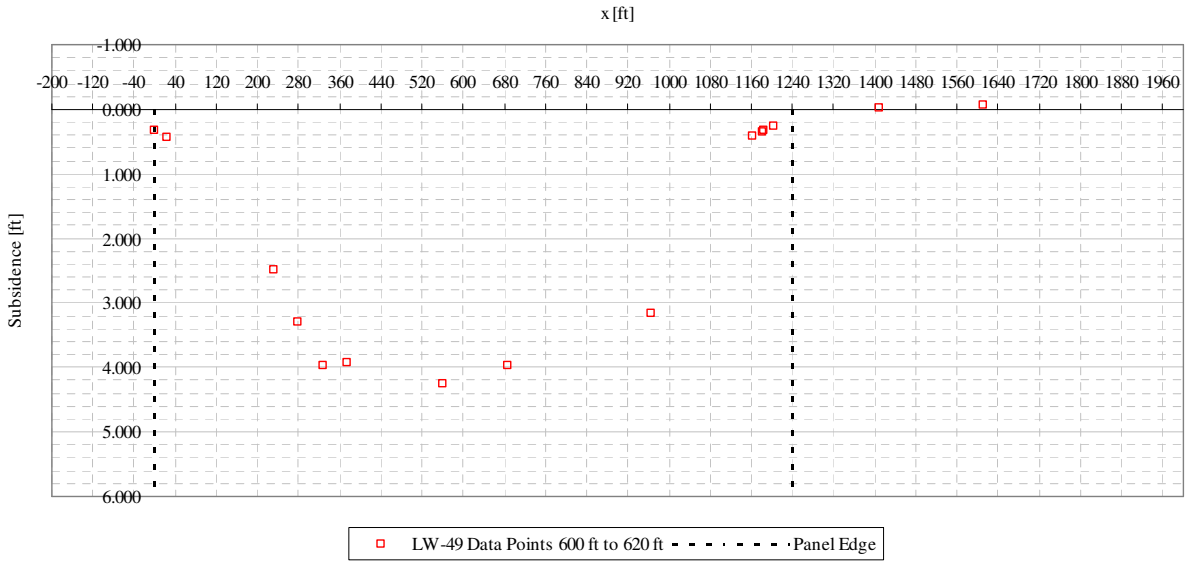

Figure A2- 36 LW-49 transverse view of data points from 600 ft to 620 ft from mine face

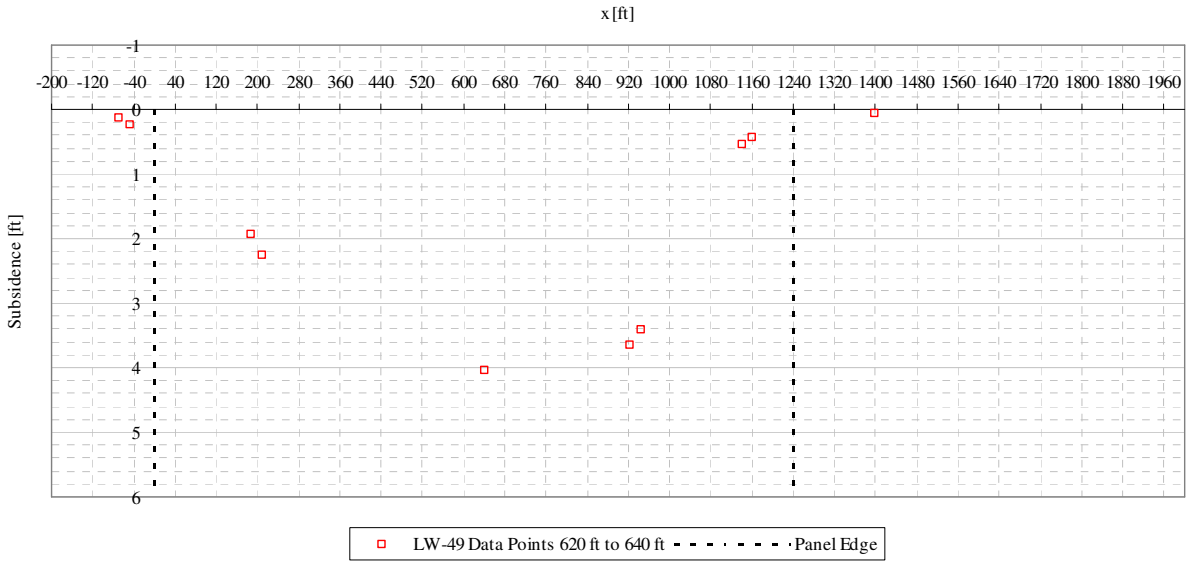

Figure A2- 37 LW-49 transverse view of data points from 620 ft to 640 ft from mine face

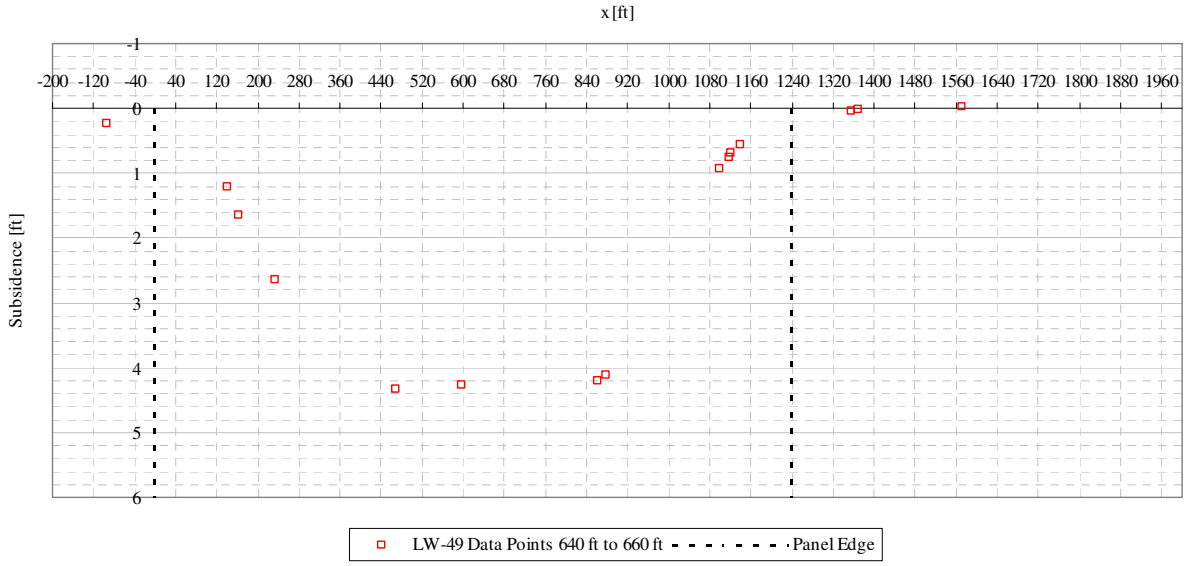

Figure A2- 38 LW-49 transverse view of data points from 640 ft to 660 ft from mine face

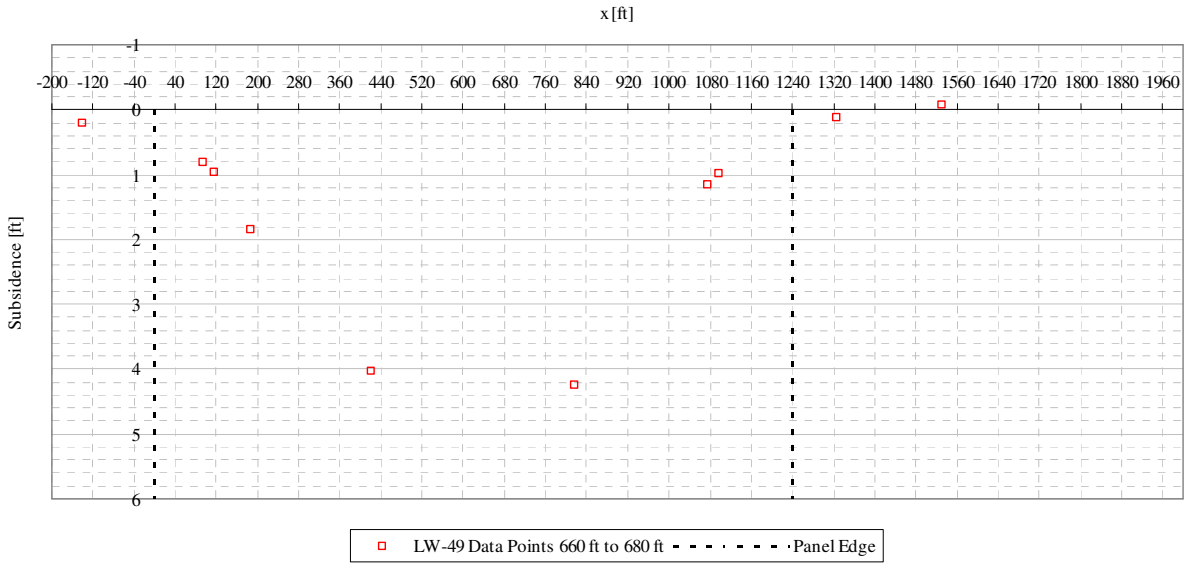

Figure A2- 39 LW-49 transverse view of data points from 660 ft to 680 ft from mine face

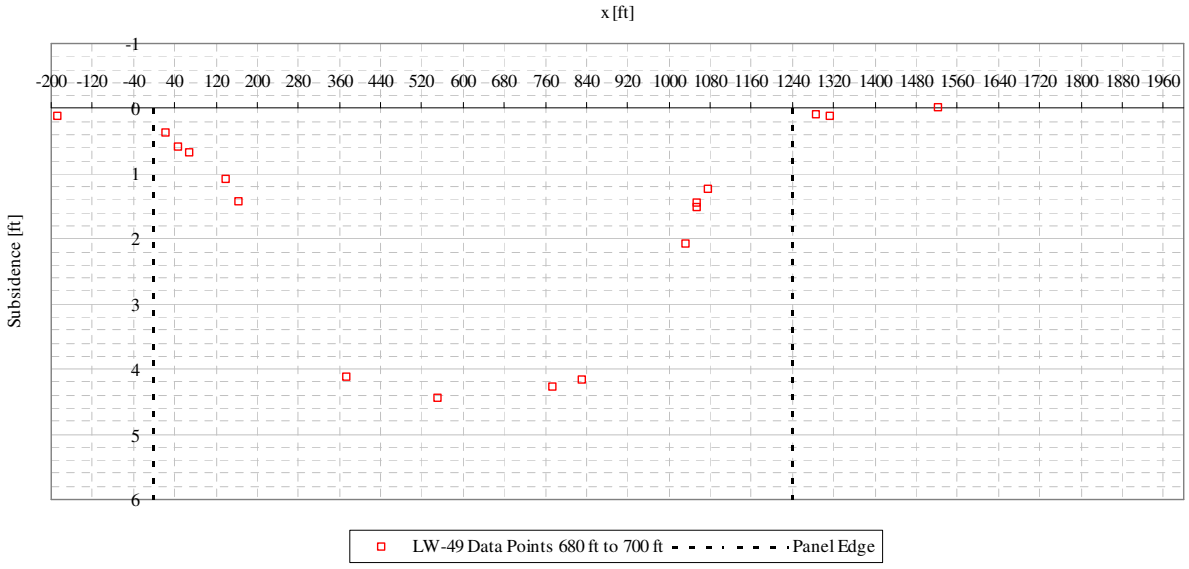

Figure A2- 40 LW-49 transverse view of data points from 680 ft to 700 ft from mine face

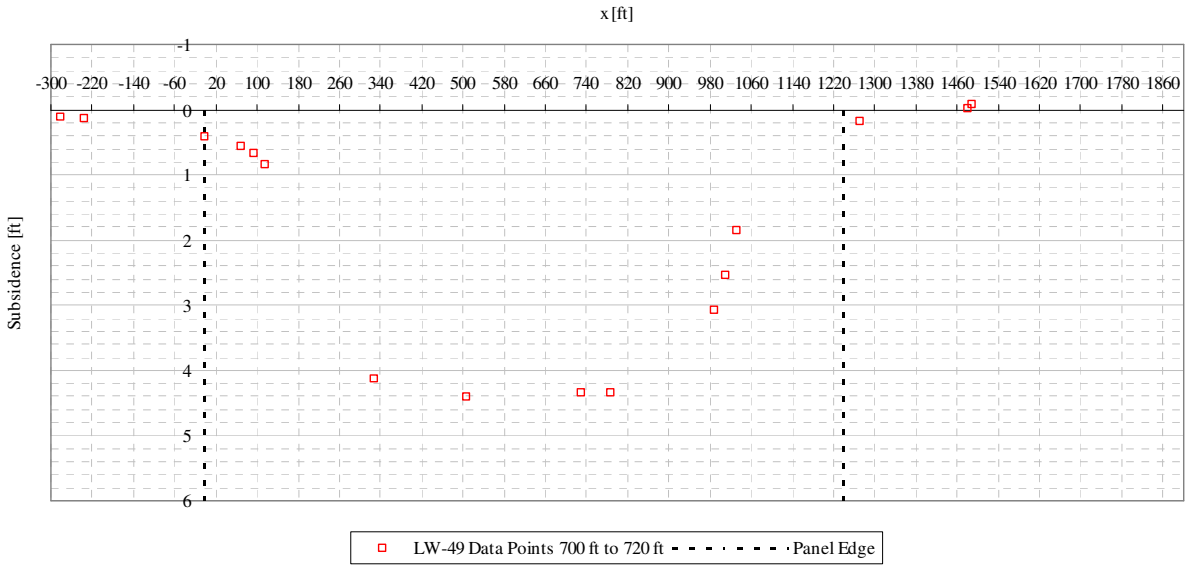

Figure A2- 41 LW-49 transverse view of data points from 700 ft to 720 ft from mine face

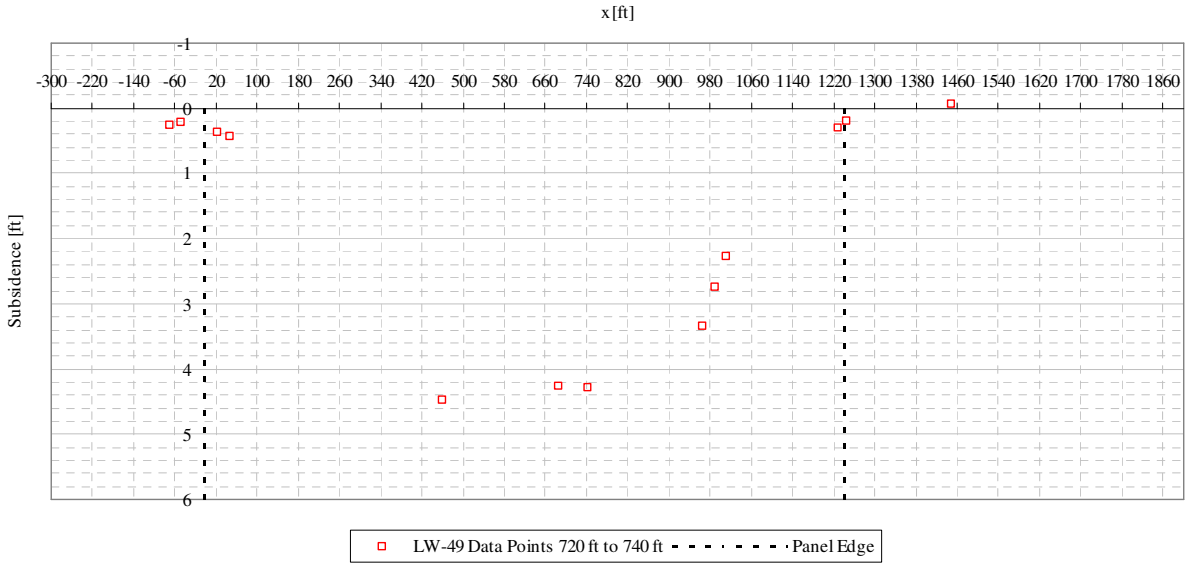

Figure A2- 42 LW-49 transverse view of data points from 720 ft to 740 ft from mine face

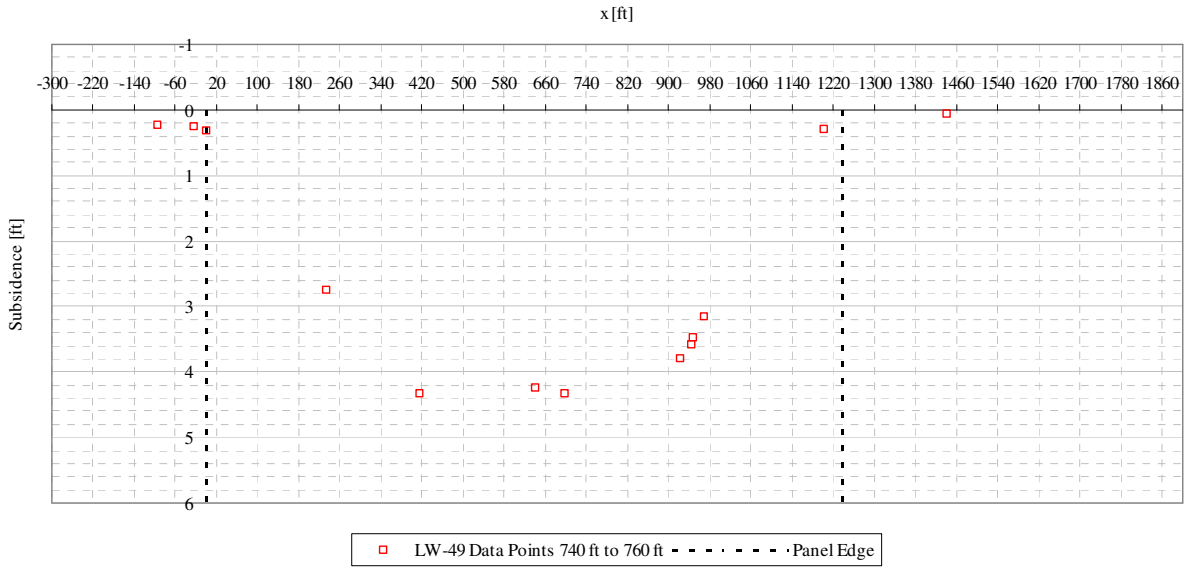

Figure A2- 43 LW-49 transverse view of data points from 740 ft to 760 ft from mine face

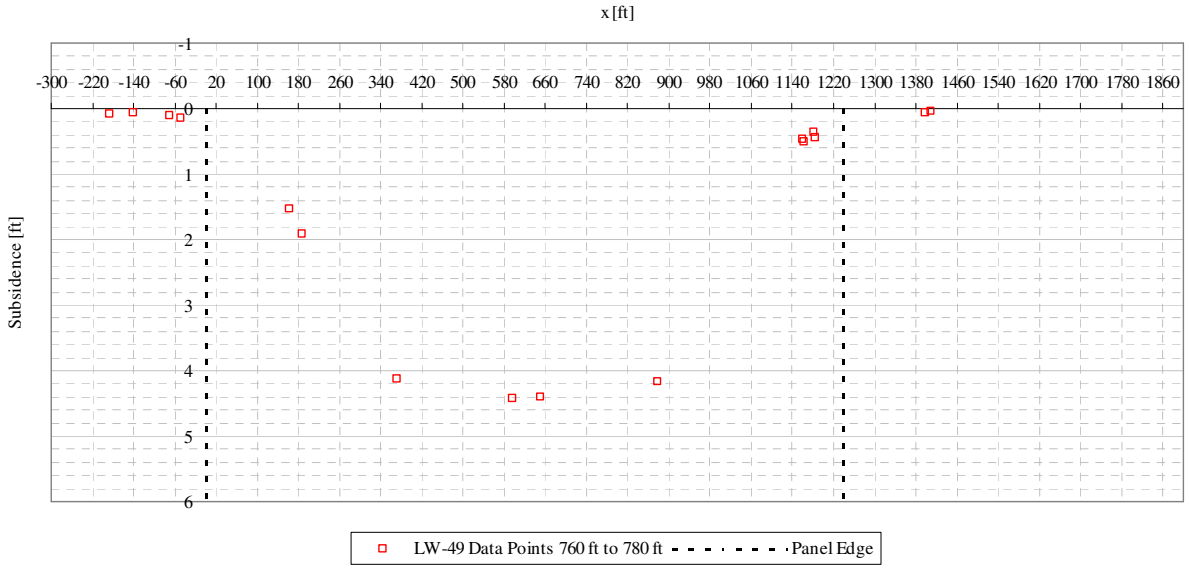

Figure A2- 44 LW-49 transverse view of data points from 760 ft to 780 ft from mine face

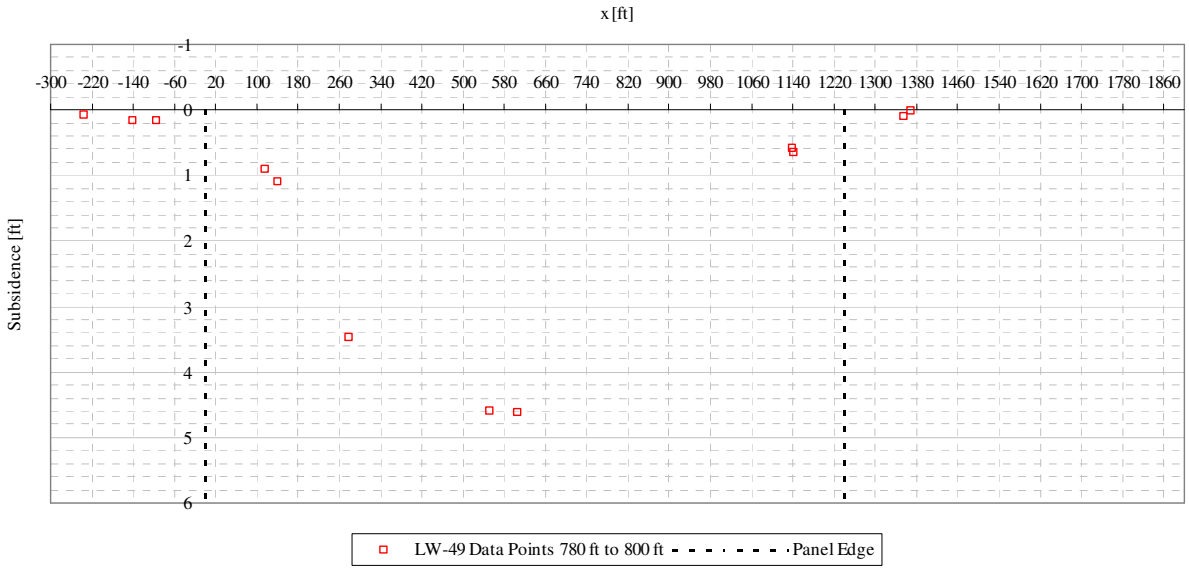

Figure A2- 45 LW-49 transverse view of data points from 780 ft to 800 ft from mine face

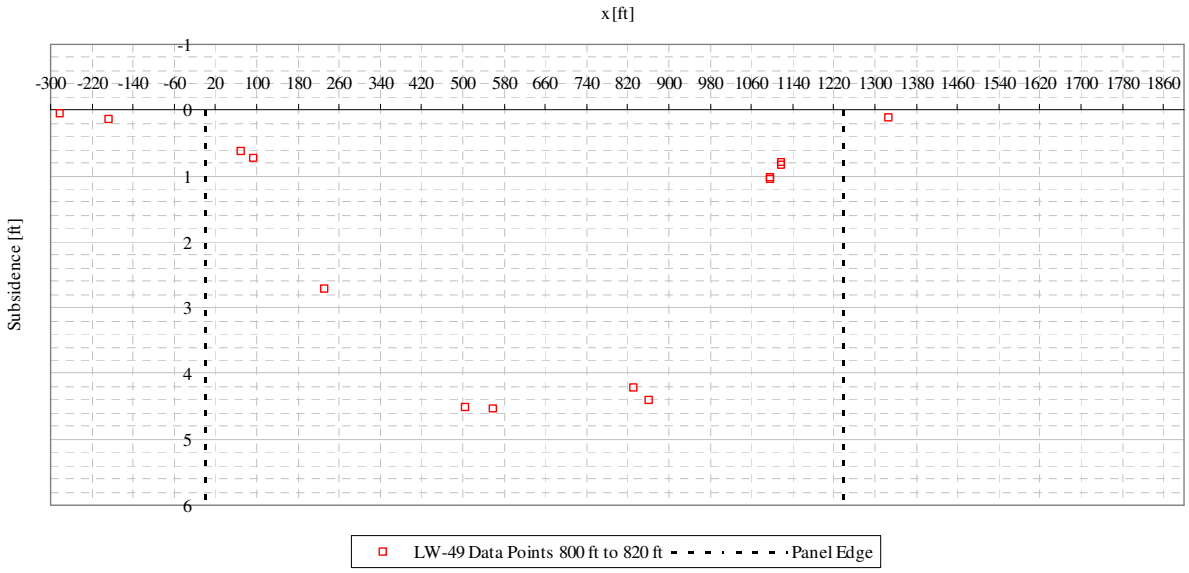

Figure A2- 46 LW-49 transverse view of data points from 800 ft to 820 ft from mine face

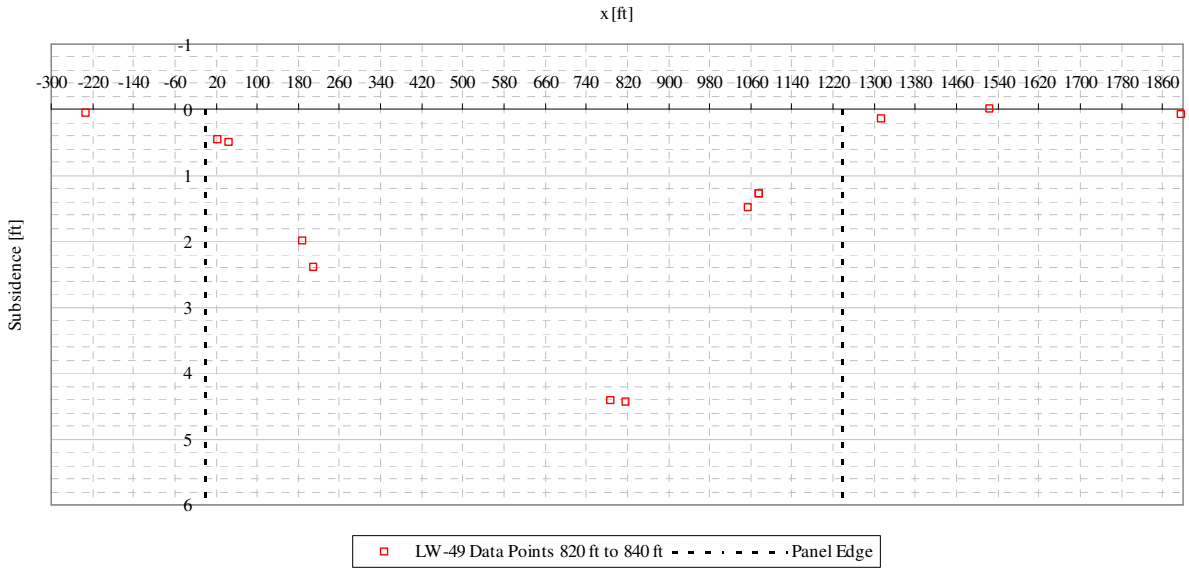

Figure A2- 47 LW-49 transverse view of data points from 820 ft to 840 ft from mine face

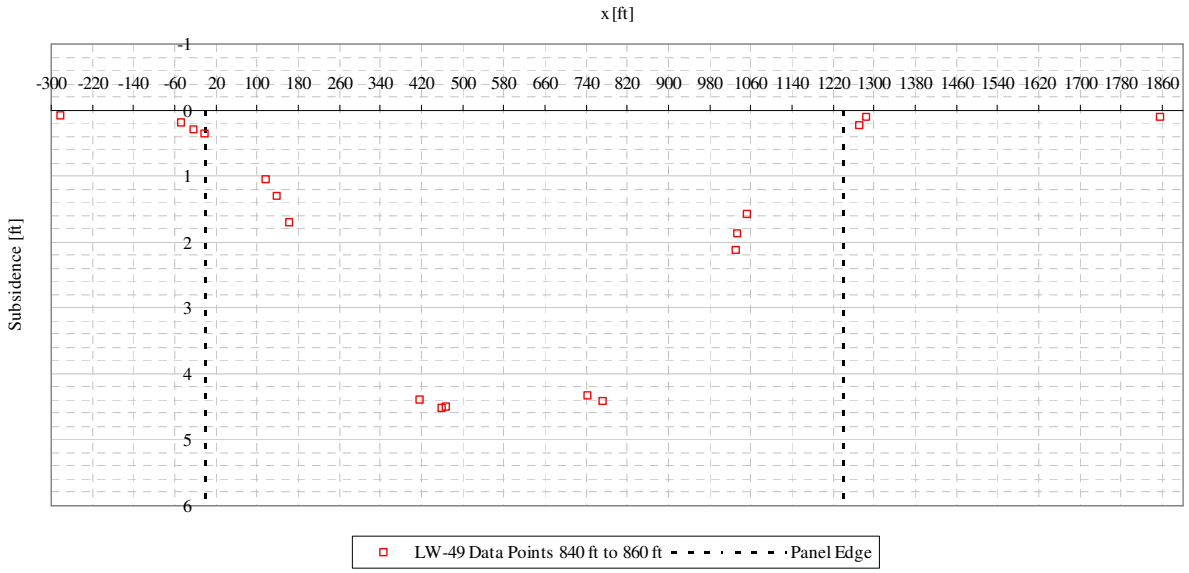

Figure A2- 48 LW-49 transverse view of data points from 840 ft to 860 ft from mine face

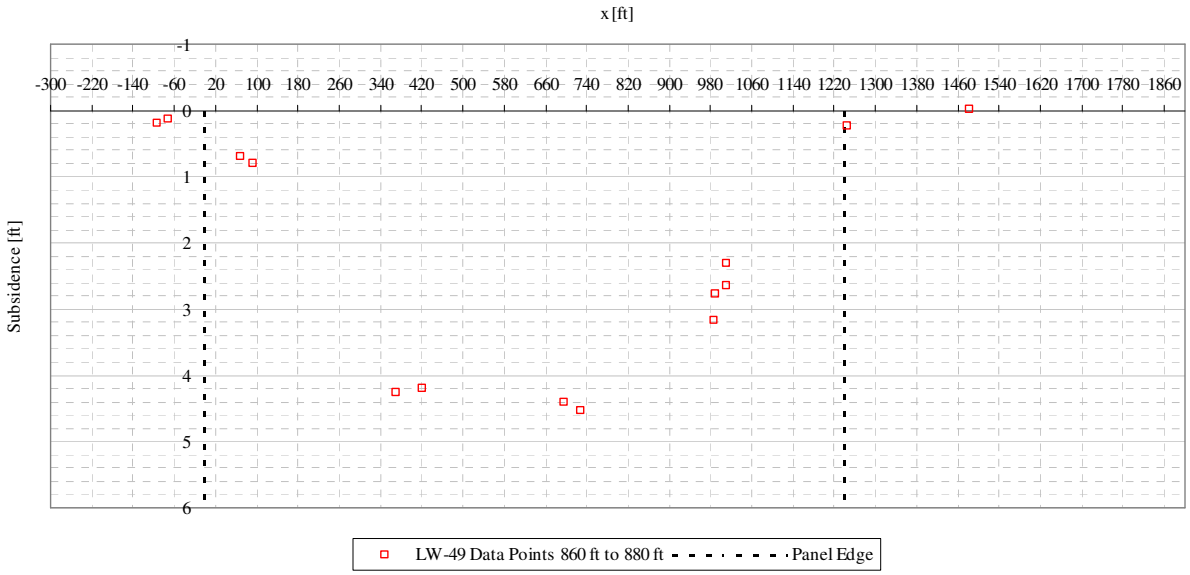

Figure A2- 49 LW-49 transverse view of data points from 860 ft to 880 ft from mine face

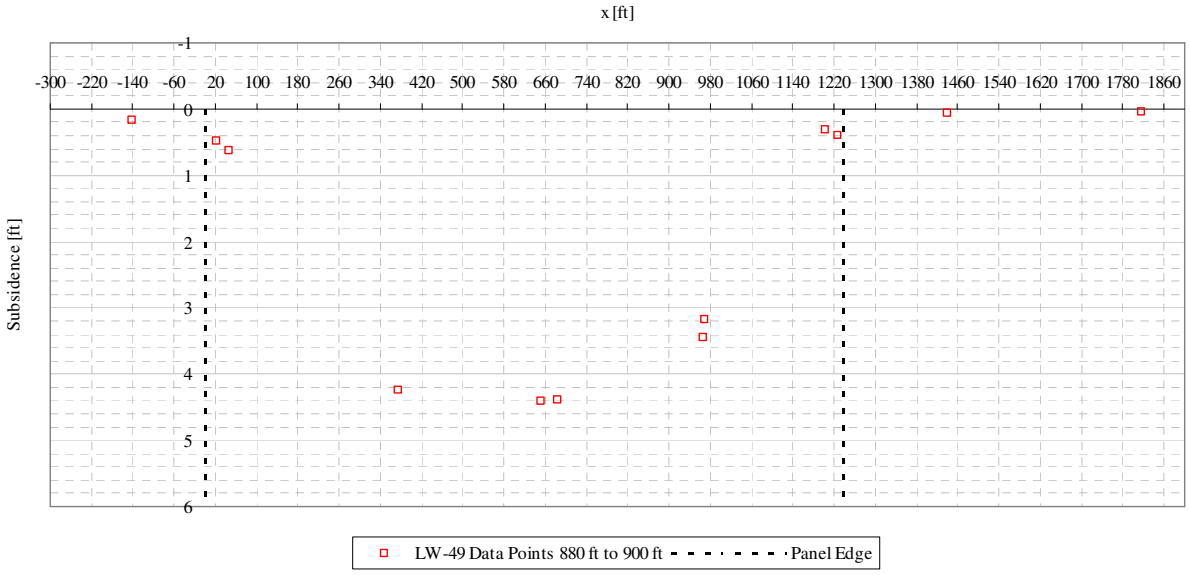

Figure A2- 50 LW-49 transverse view of data points from 880 ft to 900 ft from mine face

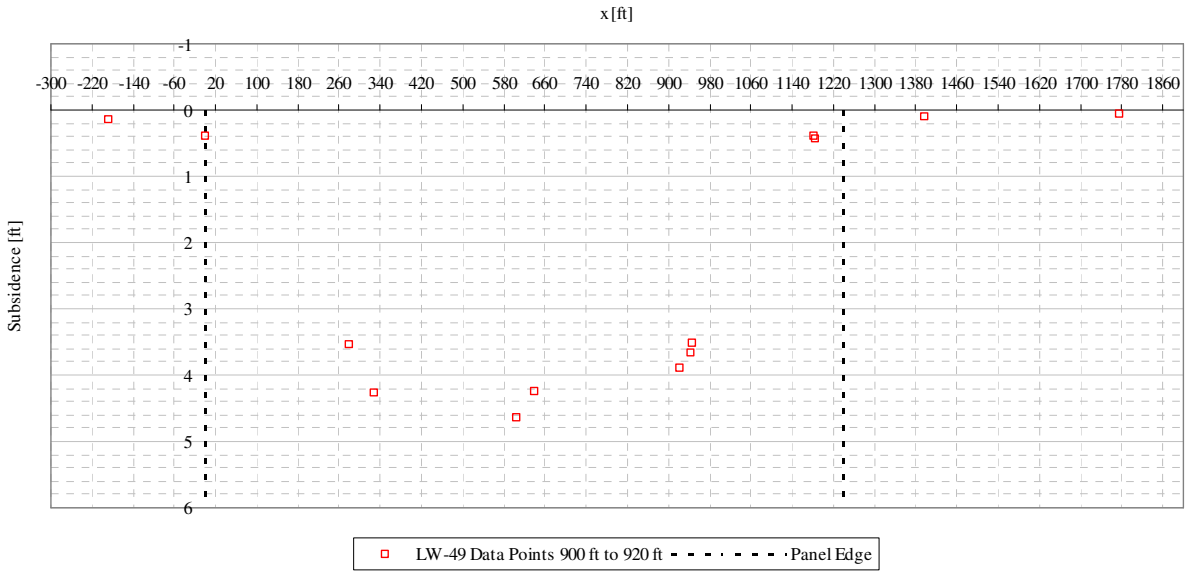

Figure A2- 51 LW-49 transverse view of data points from 900 ft to 920 ft from mine face

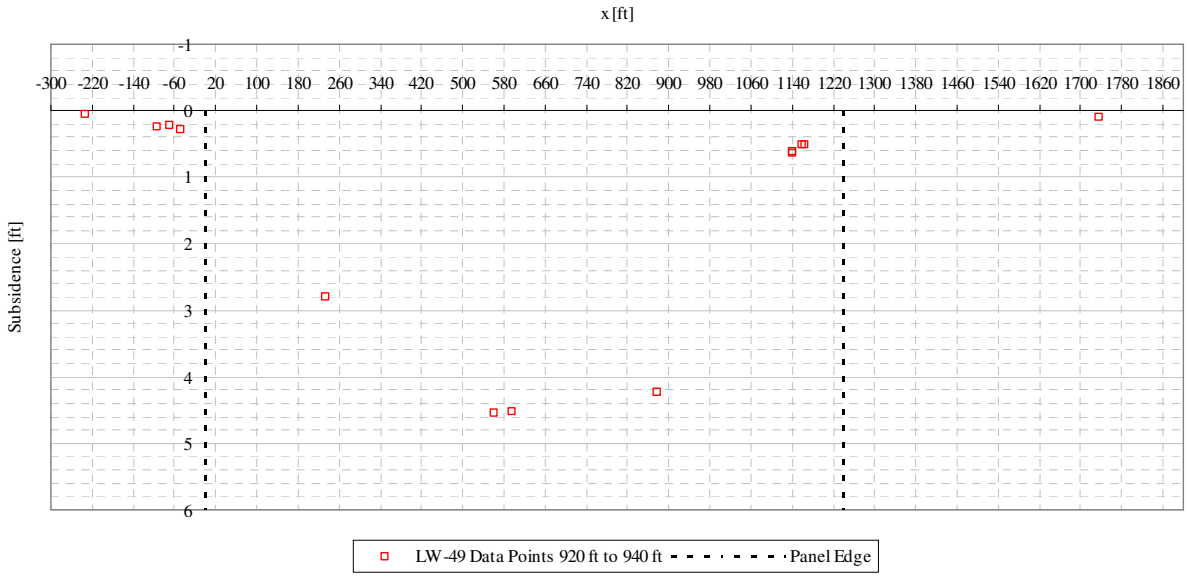

Figure A2- 52 LW-49 transverse view of data points from 920 ft to 940 ft from mine face

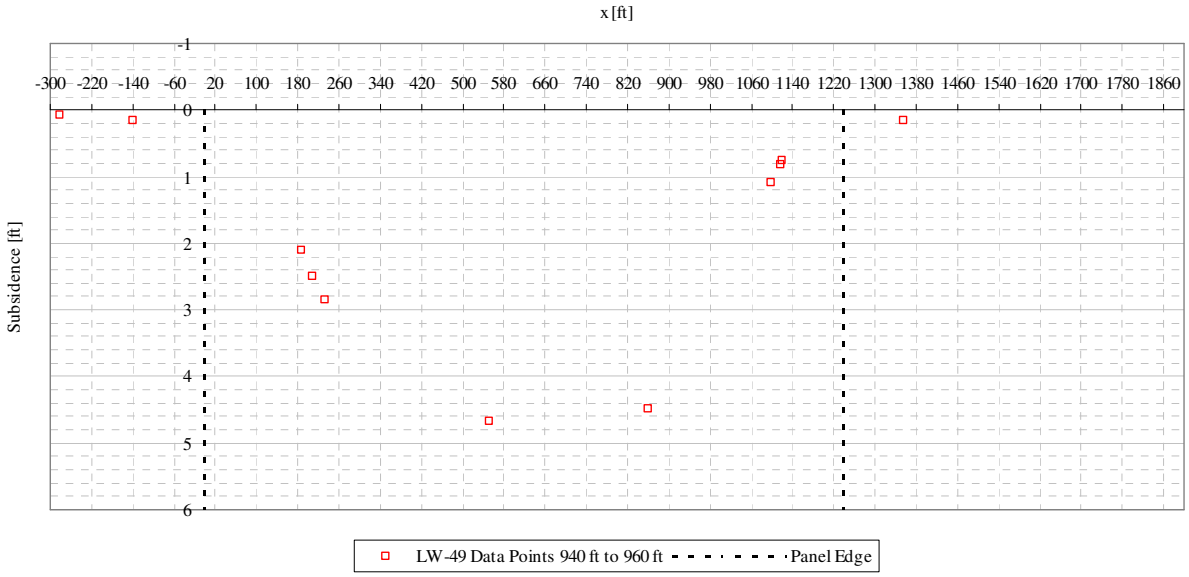

Figure A2- 53 LW-49 transverse view of data points from 940 ft to 960 ft from mine face

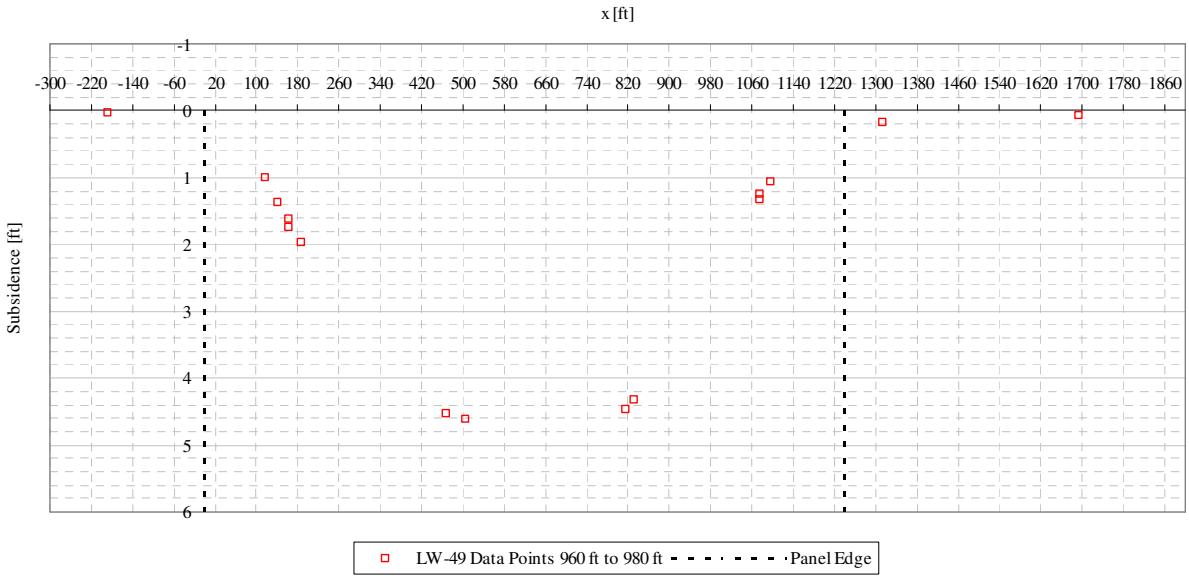

Figure A2- 54 LW-49 transverse view of data points from 960 ft to 980 ft from mine face

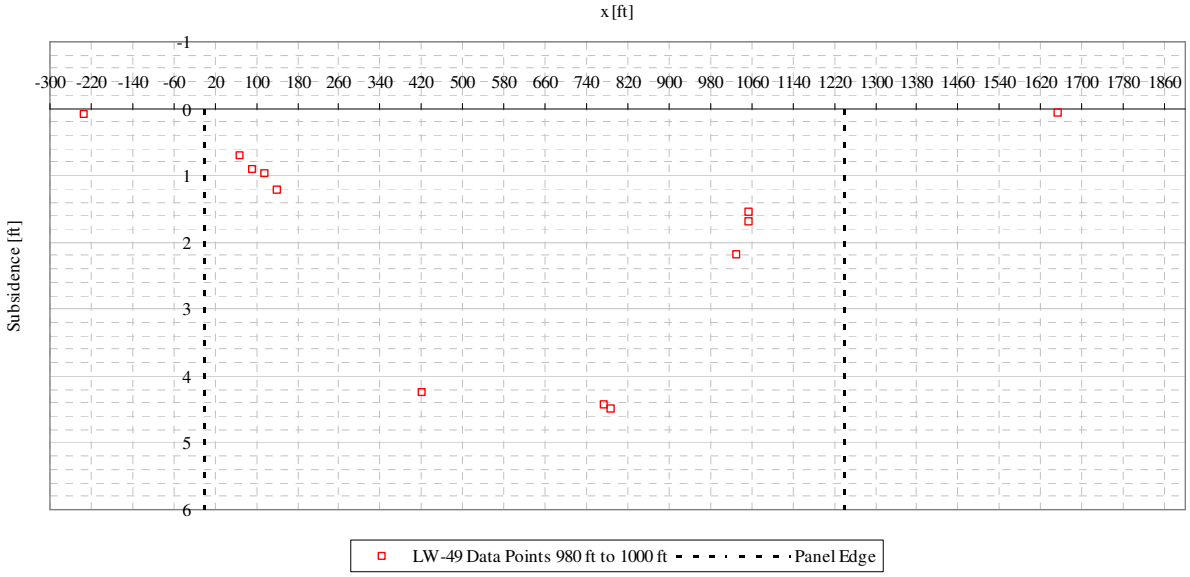

Figure A2- 55 LW-49 transverse view of data points from 980 ft to 1000 ft from mine face

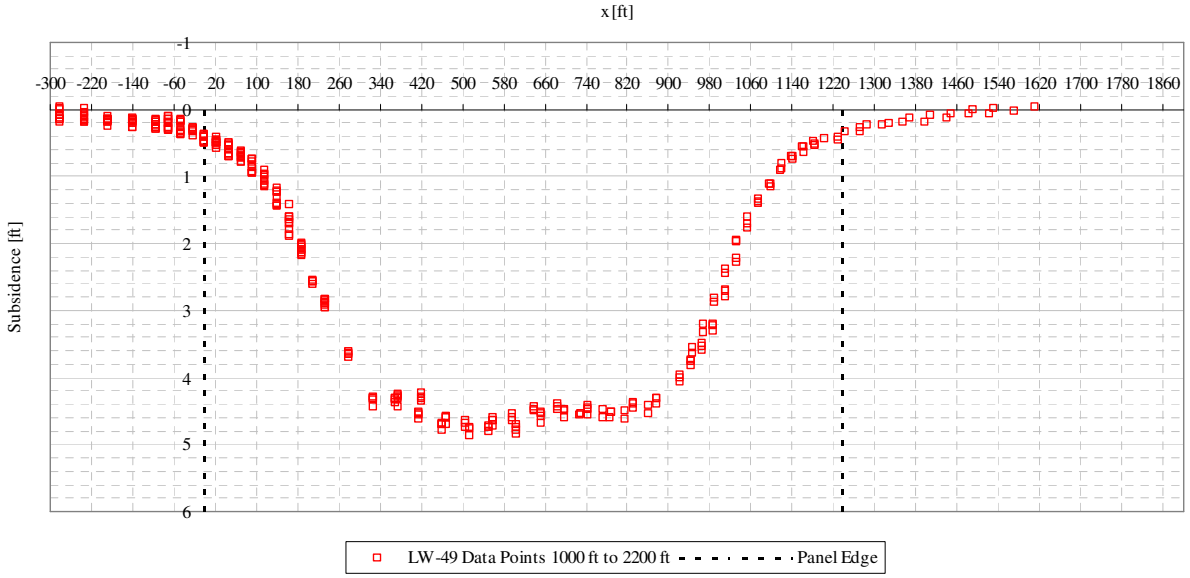

Figure A2- 56 LW-49 transverse view of data points from 1000 ft to 2200 ft from mine face

A.3 EMERALD MINE PANEL LW-51 TRANSFORMED DATA

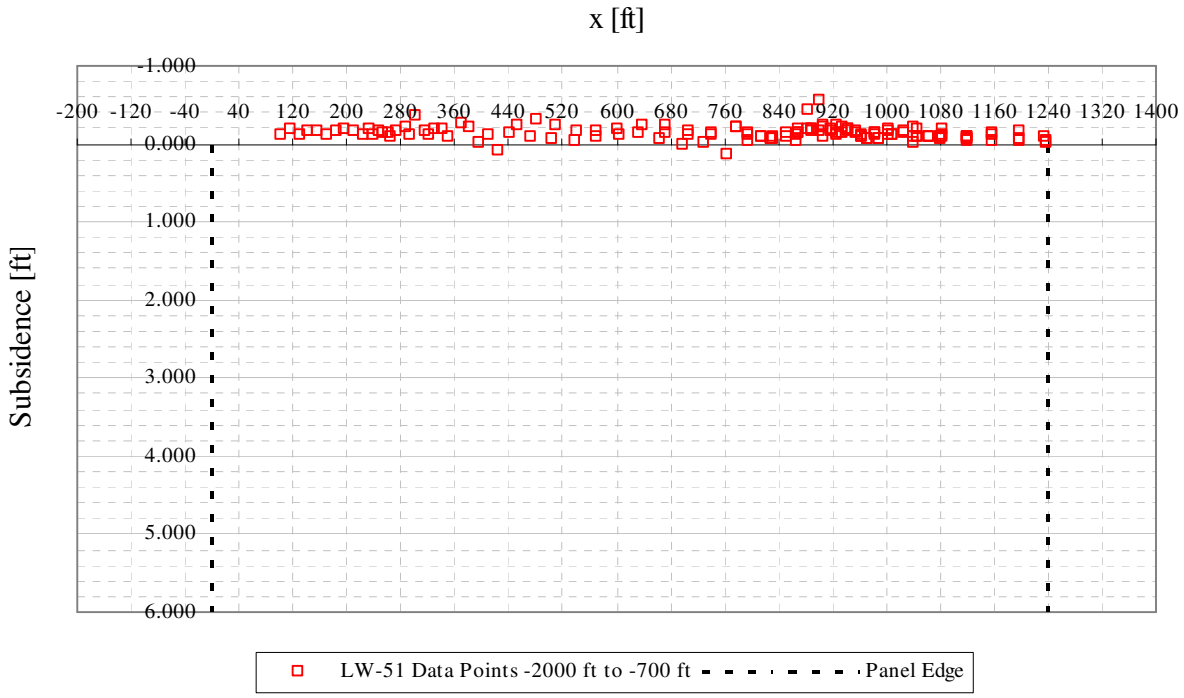

Figure A3- 1 LW-51 transverse view of data points from -2000 ft to -700 ft from mine face

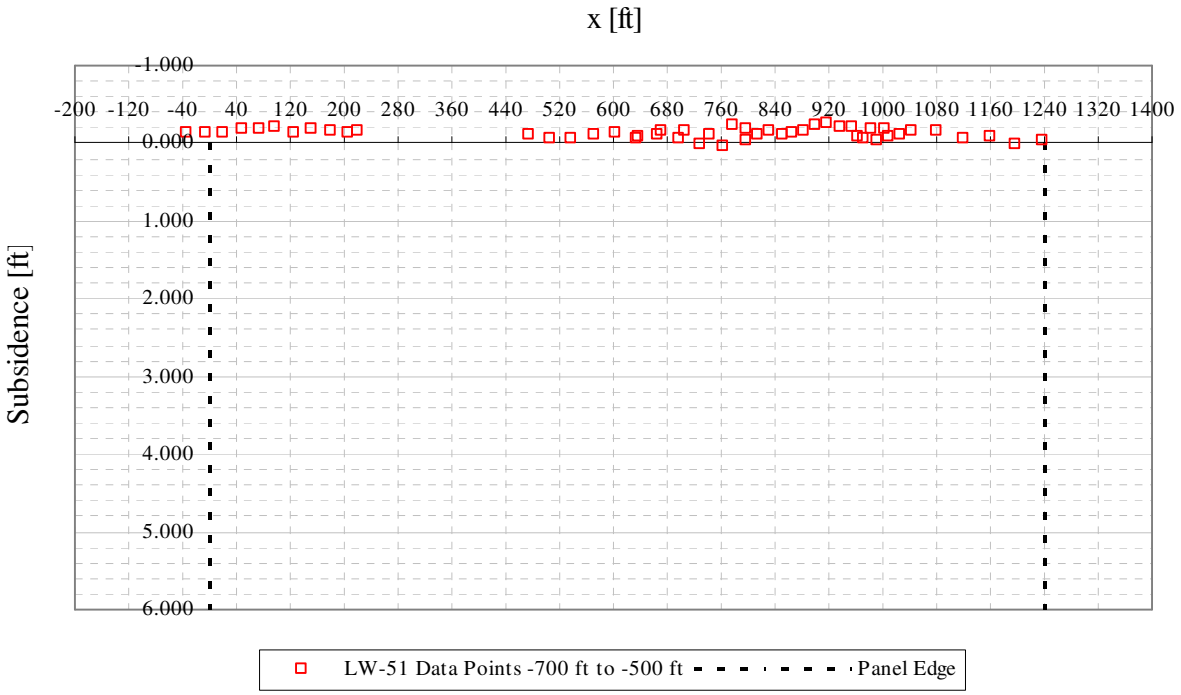

Figure A3- 2 LW-51 transverse view of data points from -700 ft to -500 ft from mine face

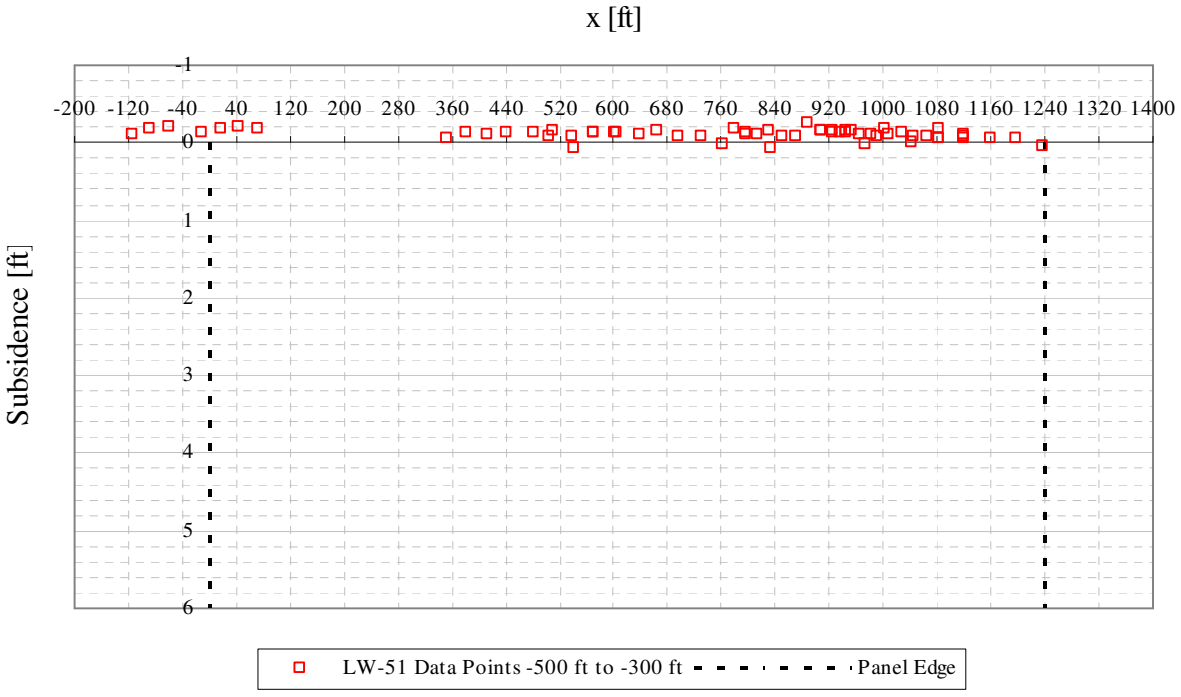

Figure A3- 3 LW-51 transverse view of data points from -500 ft to -300 ft from mine face

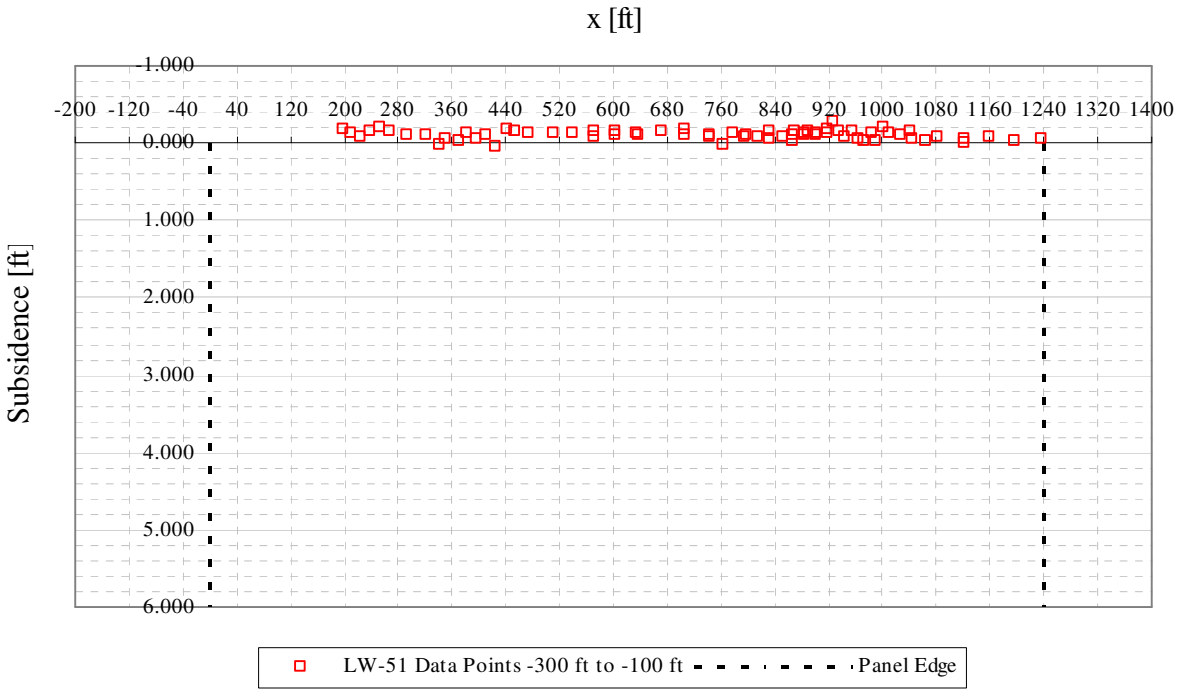

Figure A3- 4 LW-51 transverse view of data points from -300 ft to -100 ft from mine face

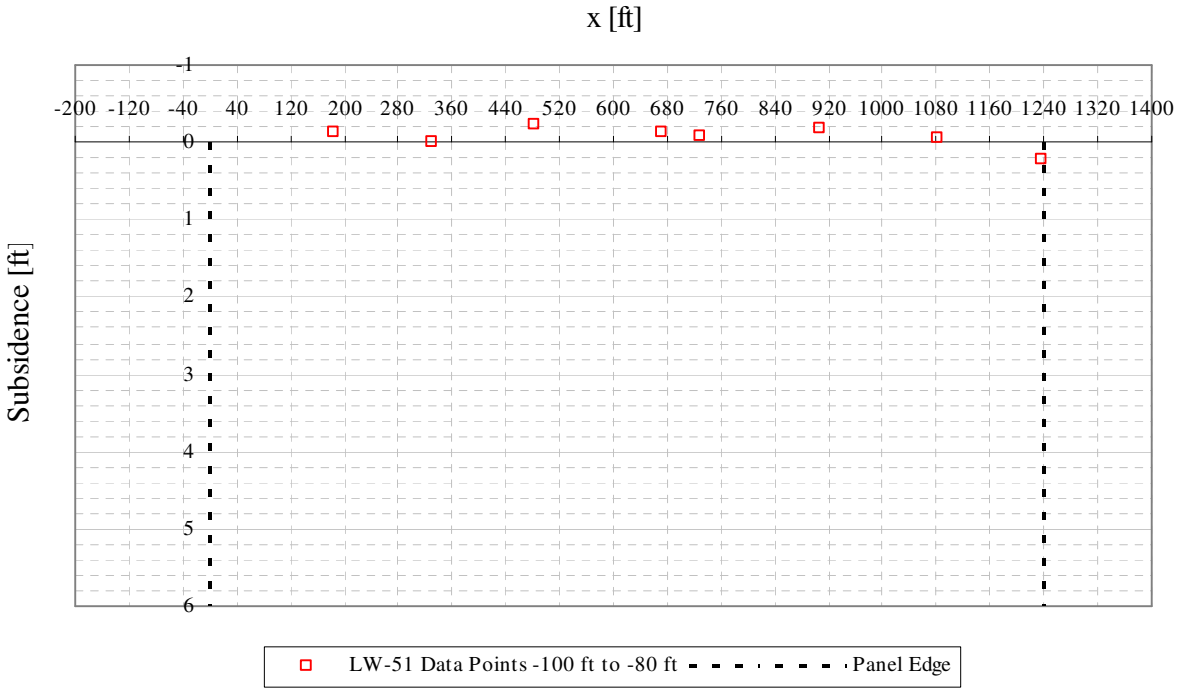

Figure A3- 5 LW-51 transverse view of data points from -100 ft to -80 ft from mine face

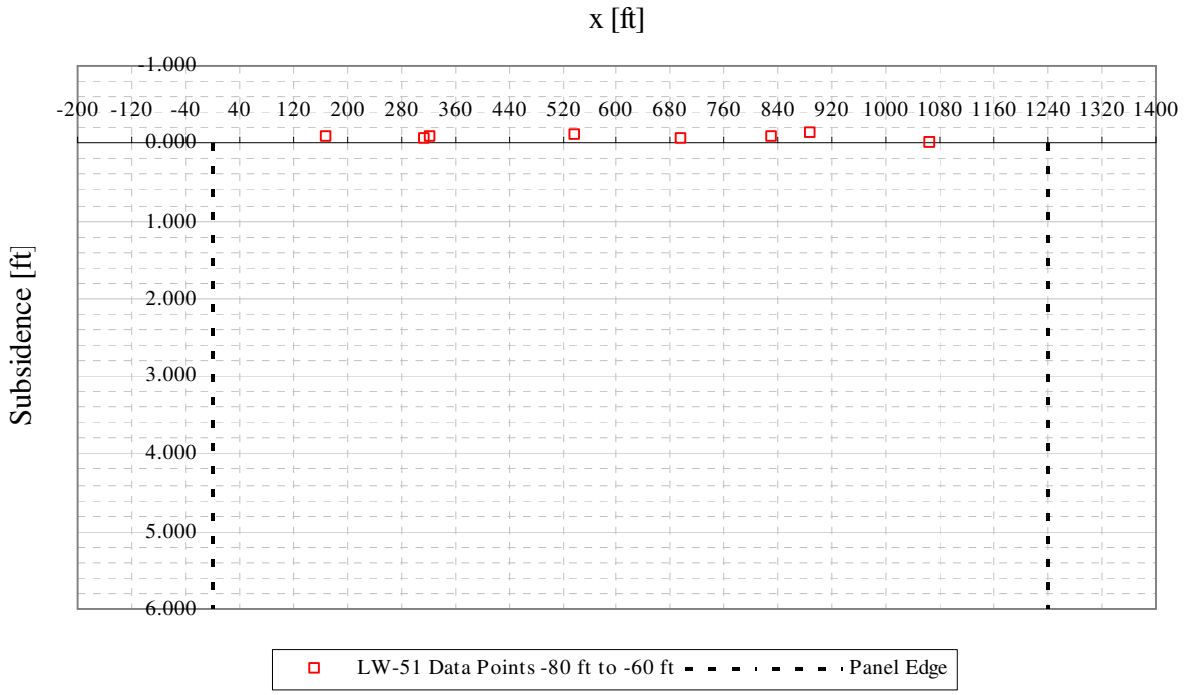

Figure A3- 6 LW-51 transverse view of data points from -80 ft to -60 ft from mine face

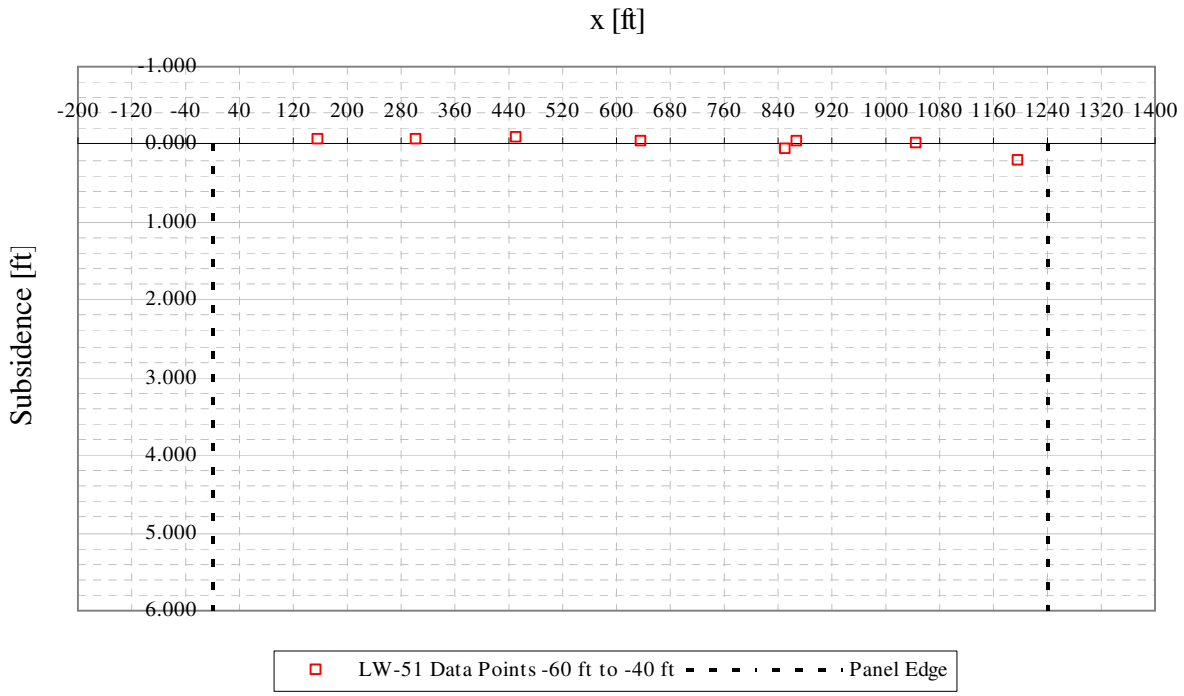

Figure A3- 7 LW-51 transverse view of data points from -60 ft to -40 ft from mine face

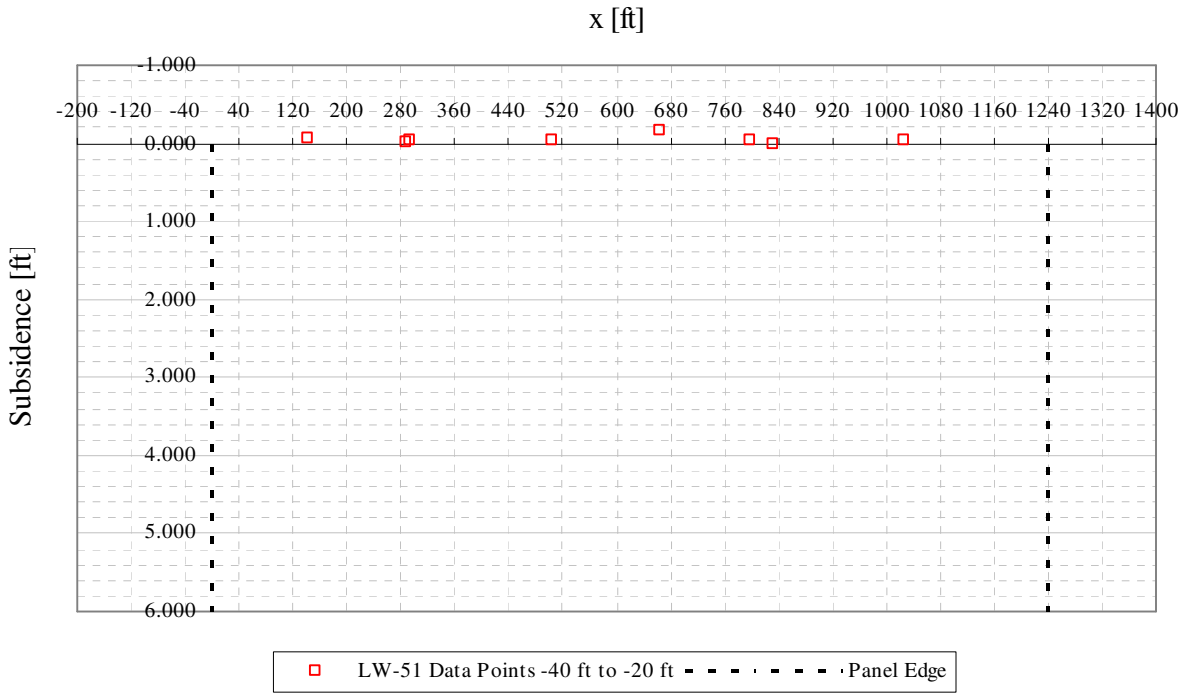

Figure A3- 8 LW-51 transverse view of data points from -40 ft to -20 ft from mine face

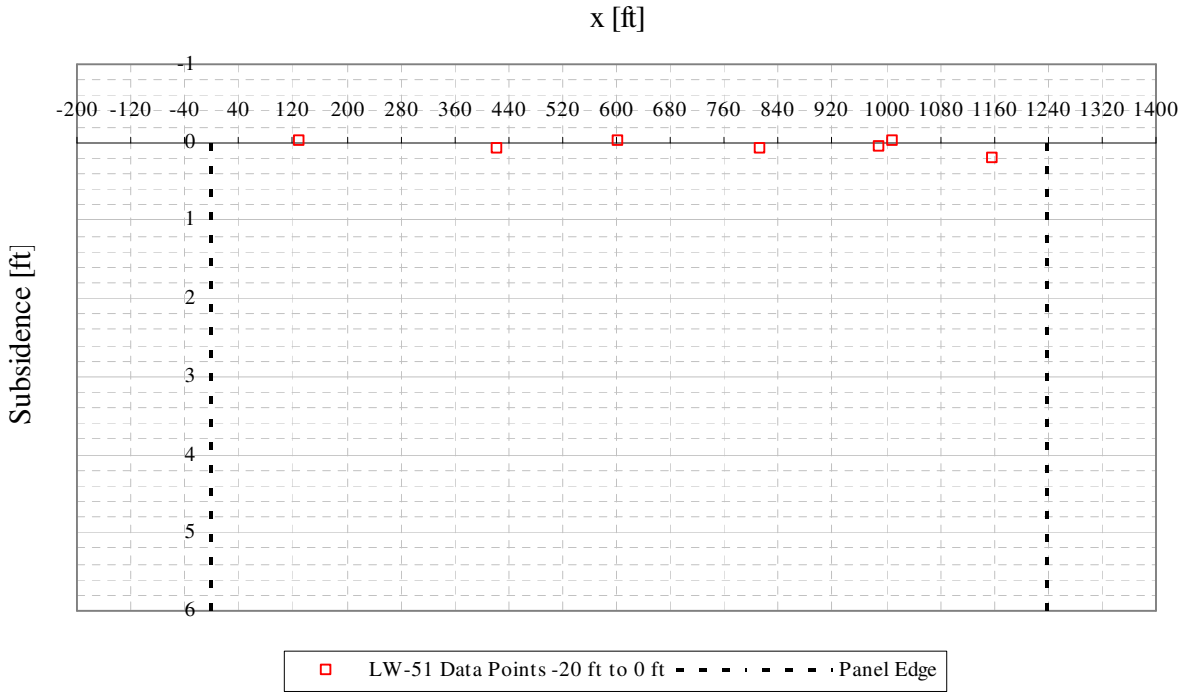

Figure A3- 9 LW-51 transverse view of data points from -20 ft to 0 ft from mine face

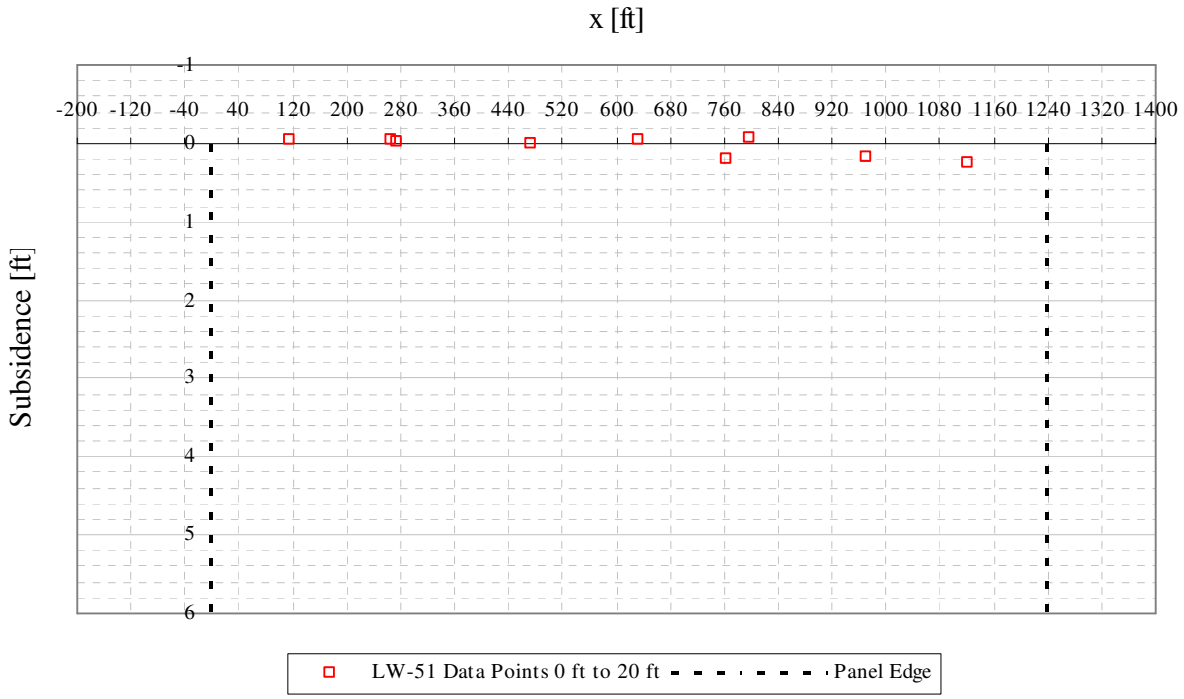

Figure A3- 10 LW-51 transverse view of data points from 0 ft to 20 ft from mine face

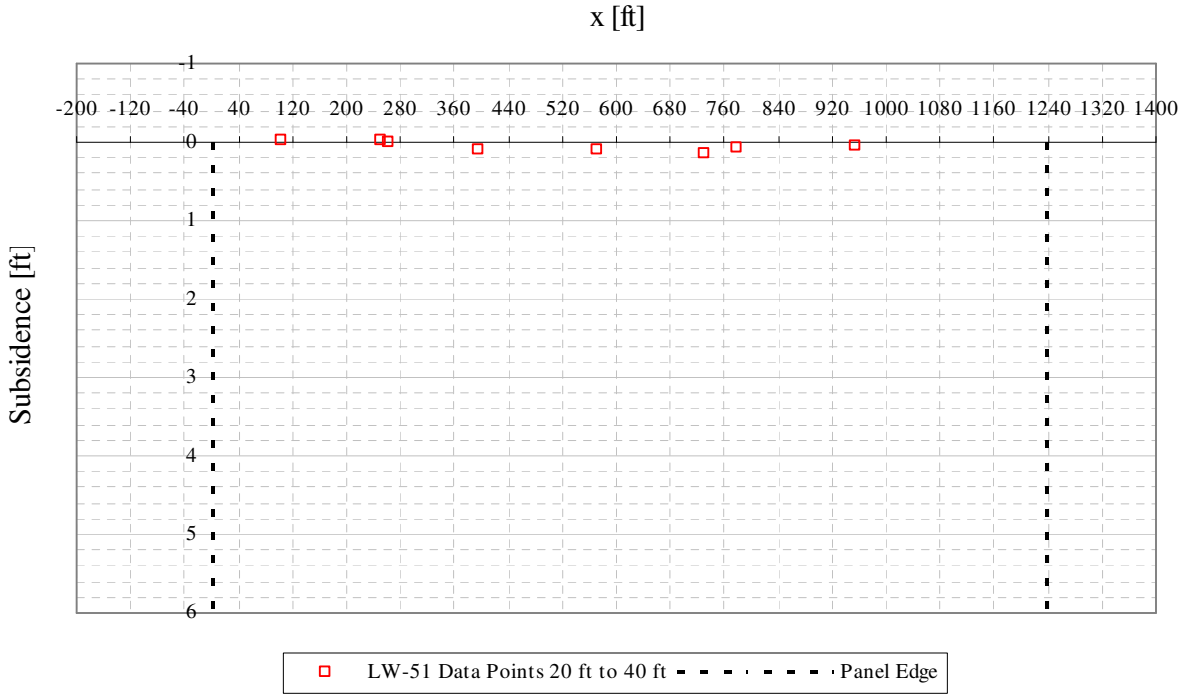

Figure A3- 11 LW-51 transverse view of data points from 20 ft to 40 ft from mine face

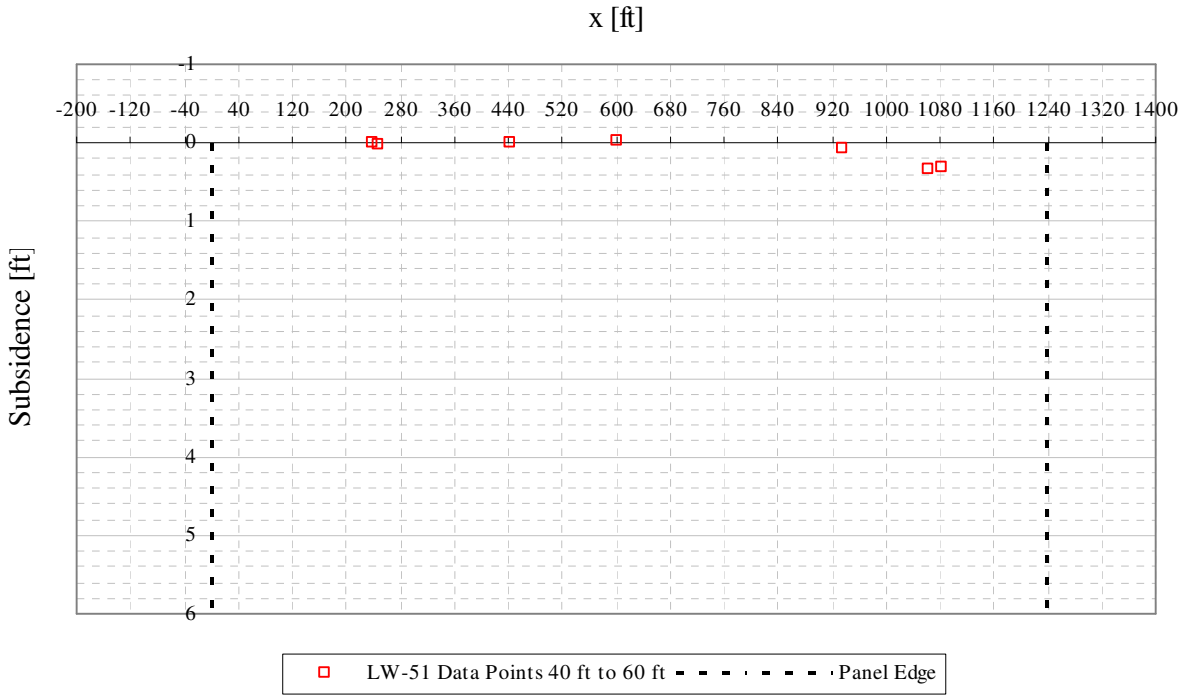

Figure A3- 12 LW-51 transverse view of data points from 40 ft to 60 ft from mine face

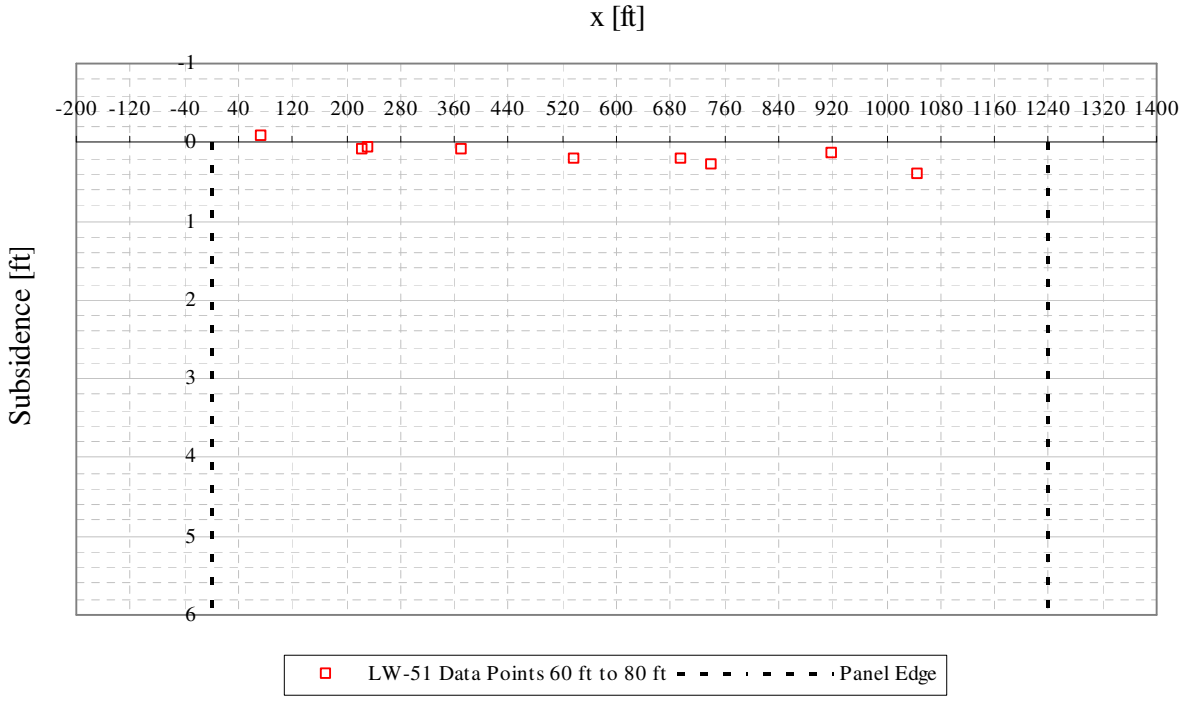

Figure A3- 13 LW-51 transverse view of data points from 60 ft to 80 ft from mine face

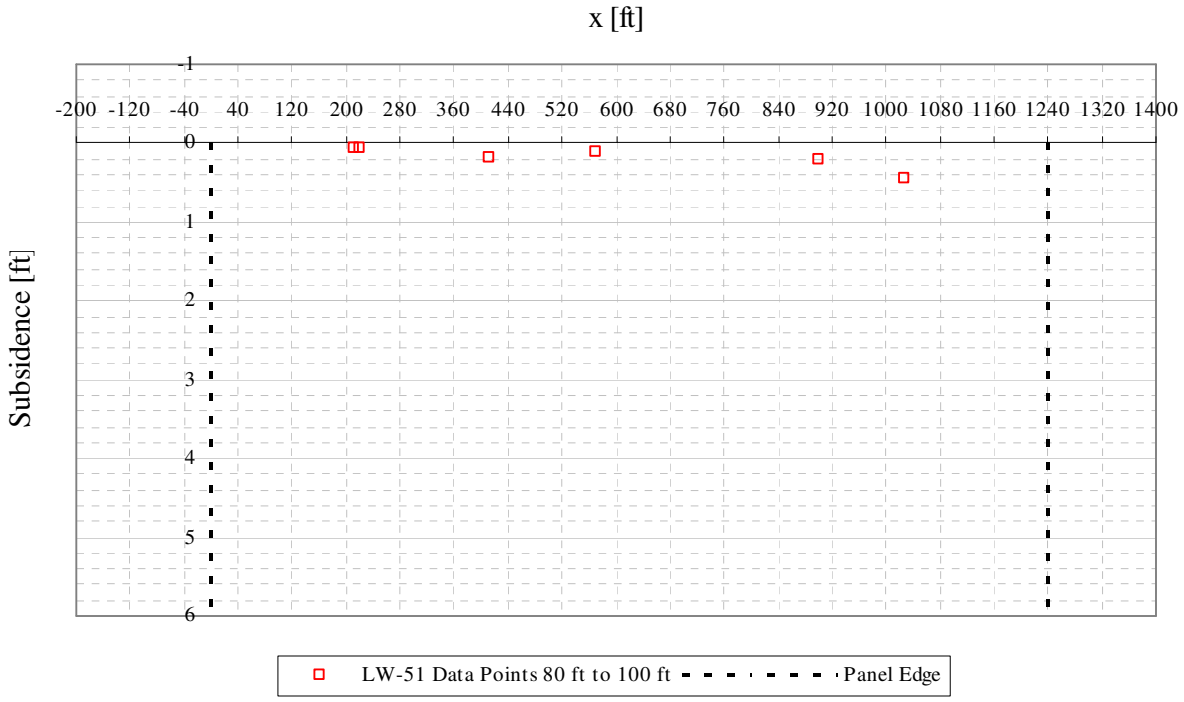

Figure A3- 14 LW-51 transverse view of data points from 80 ft to 100 ft from mine face

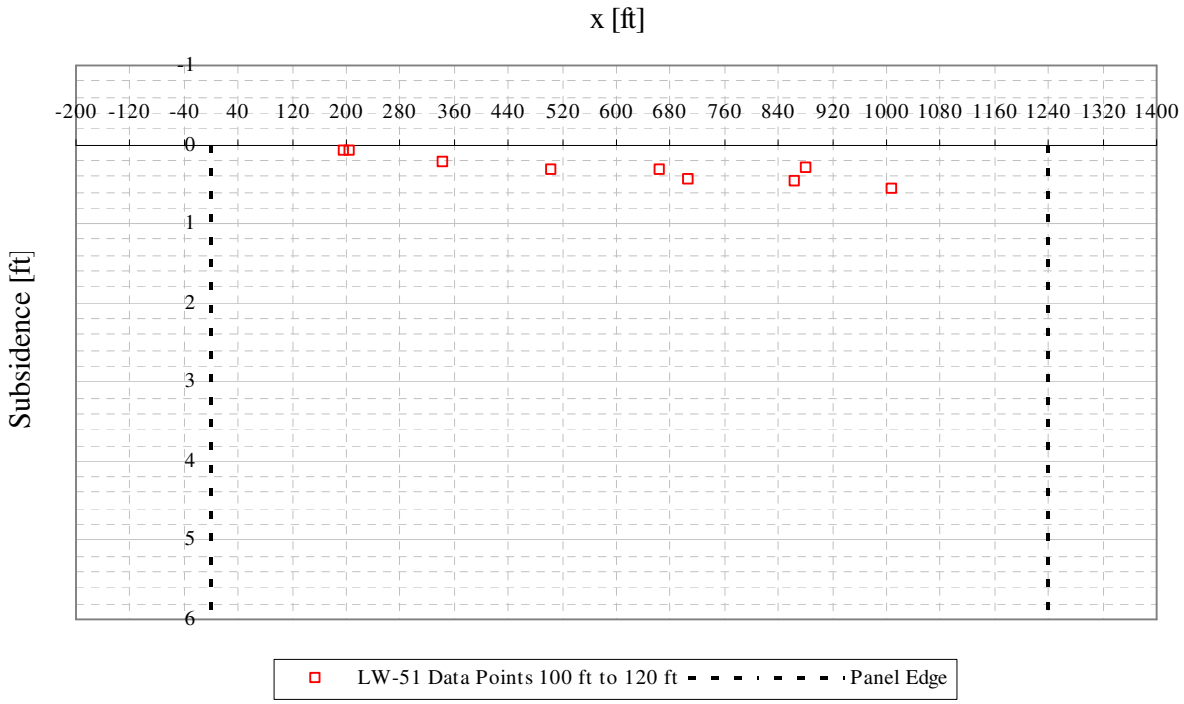

Figure A3- 15 LW-51 transverse view of data points from 100 ft to 120 ft from mine face

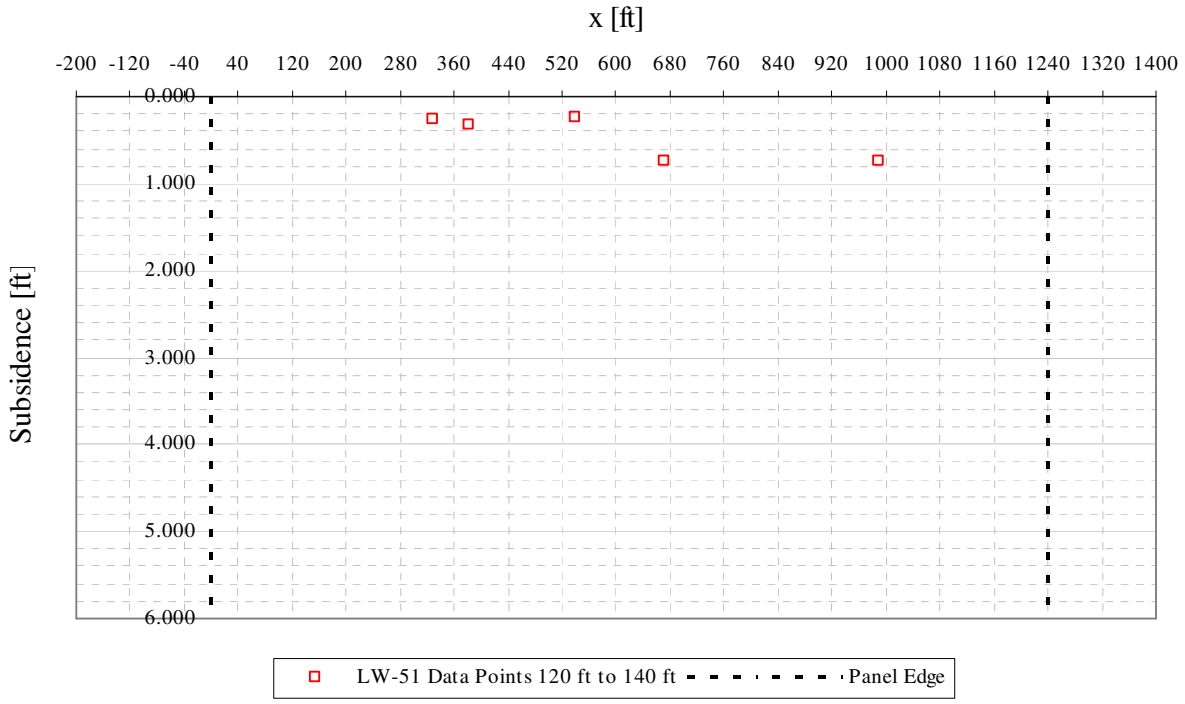

Figure A3- 16 LW-51 transverse view of data points from 120 ft to 140 ft from mine face

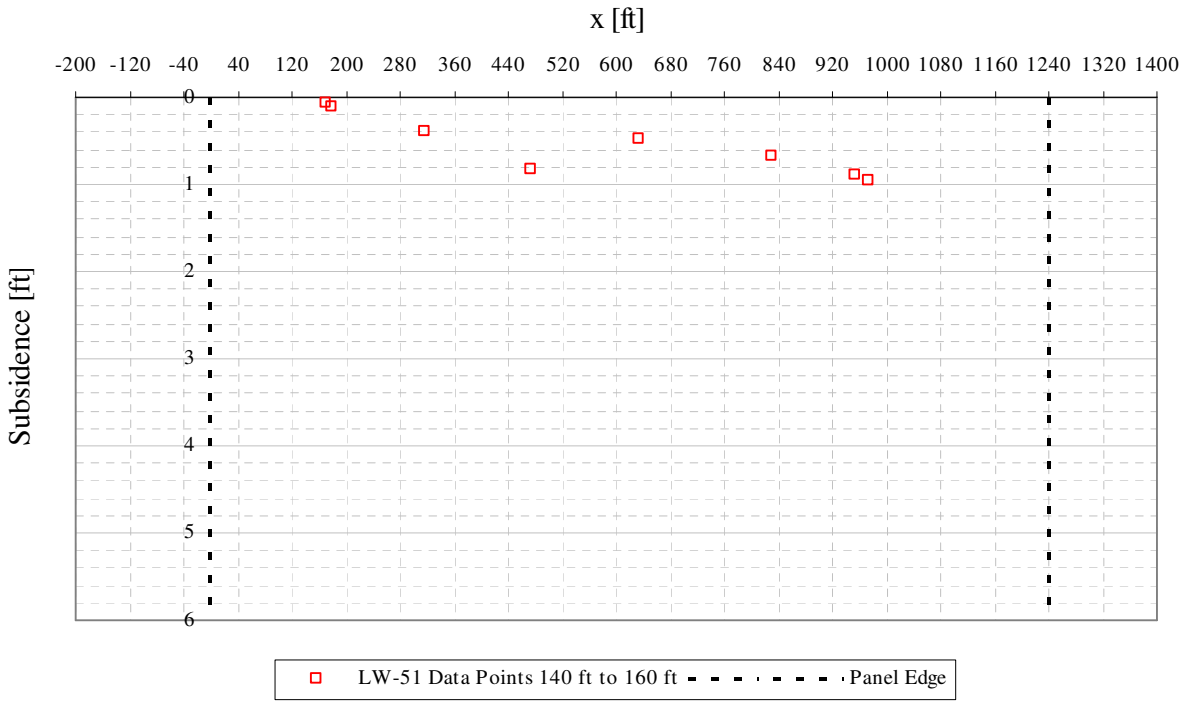

Figure A3- 17 LW-51 transverse view of data points from 140 ft to 160 ft from mine face

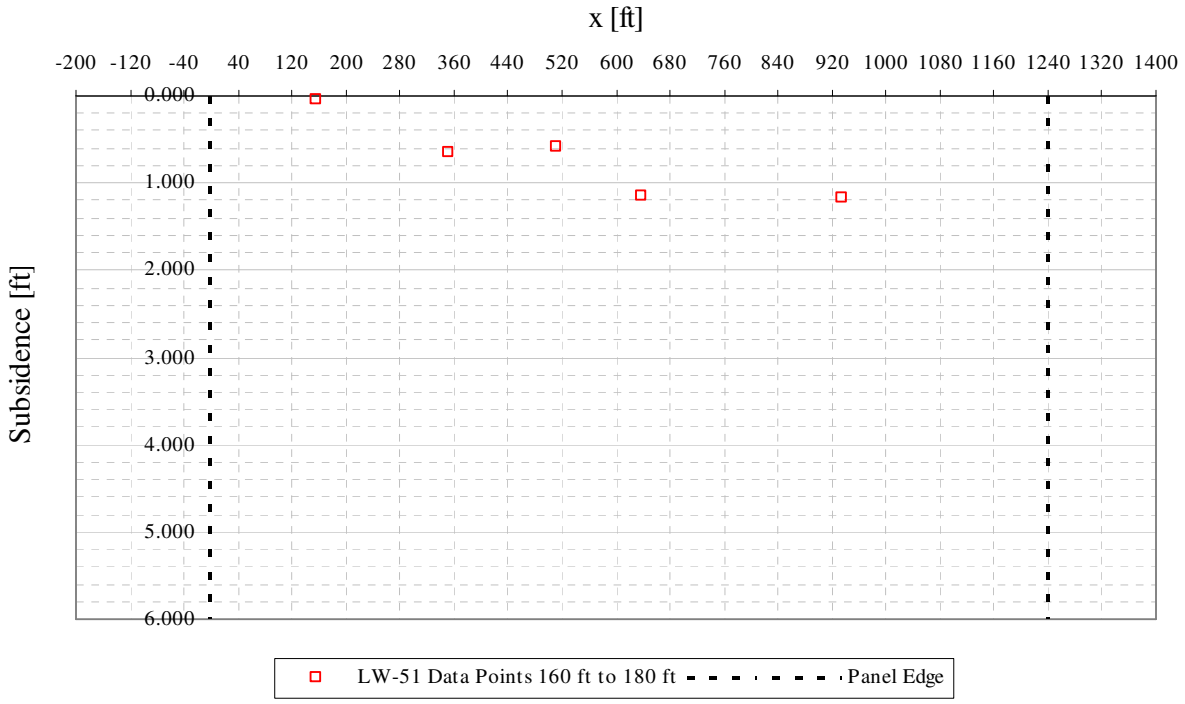

Figure A3- 18 LW-51 transverse view of data points from 160 ft to 180 ft from mine face

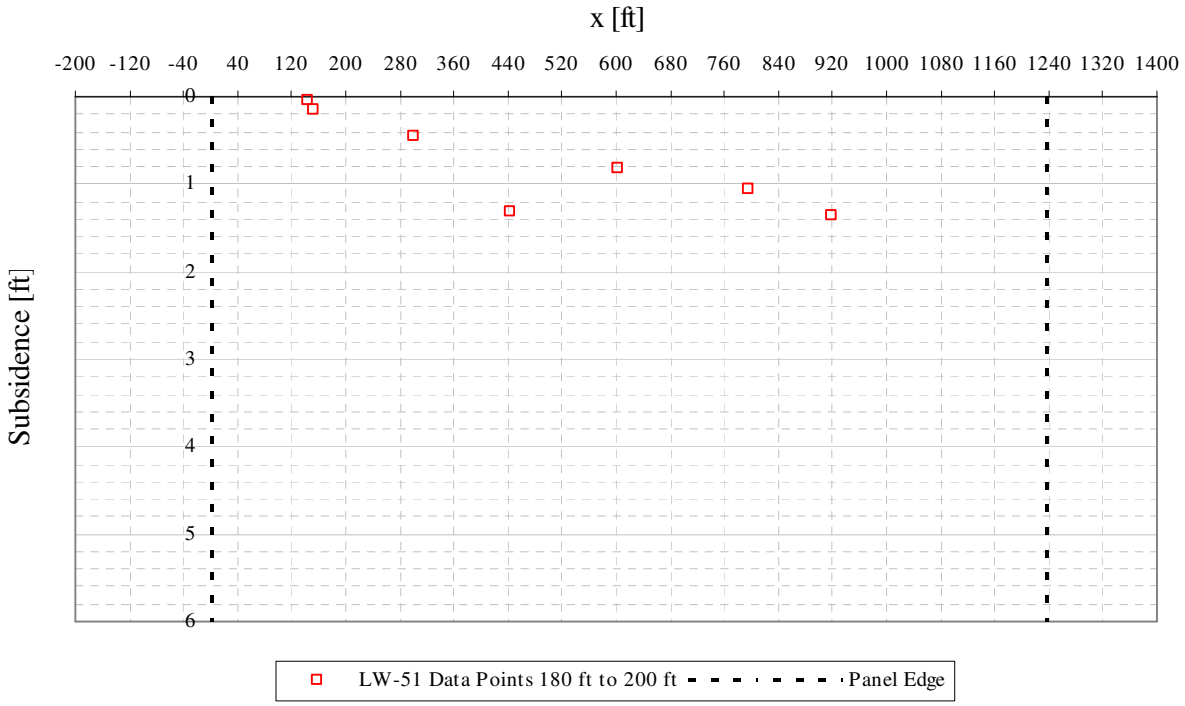

Figure A3- 19 LW-51 transverse view of data points from 180 ft to 200 ft from mine face

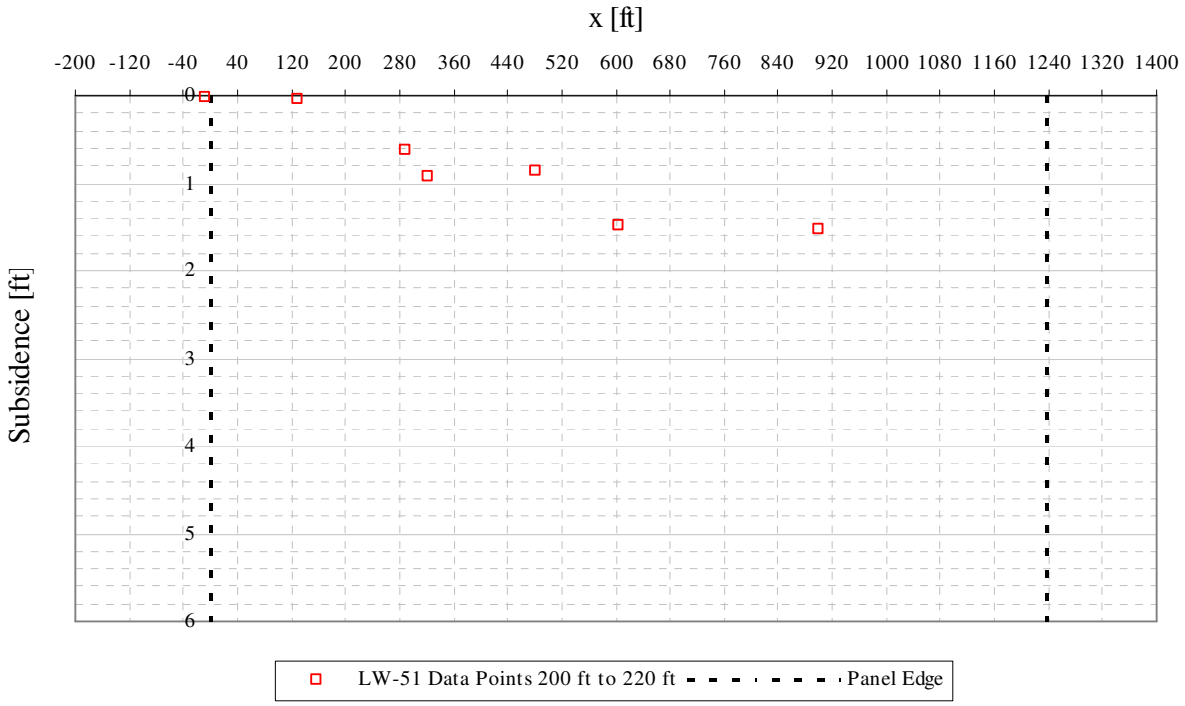

Figure A3- 20 LW-51 transverse view of data points from 200 ft to 220 ft from mine face

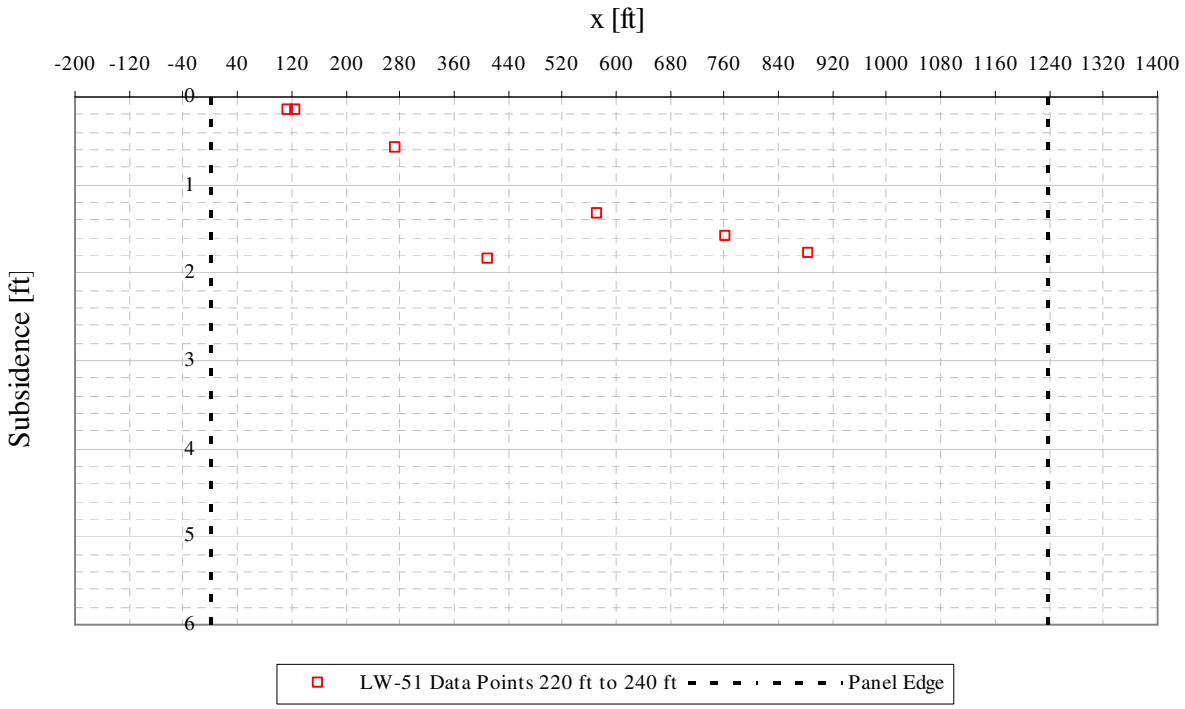

Figure A3- 21 LW-51 transverse view of data points from 220 ft to 240 ft from mine face

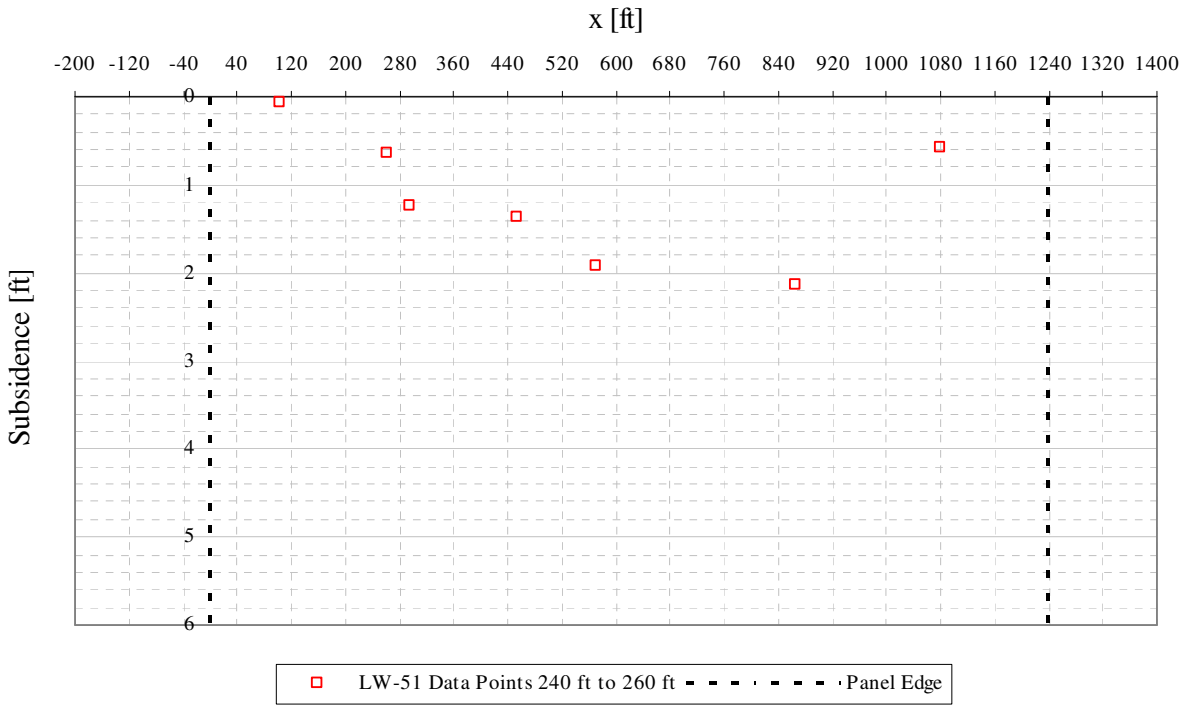

Figure A3- 22 LW-51 transverse view of data points from 240 ft to 260 ft from mine face

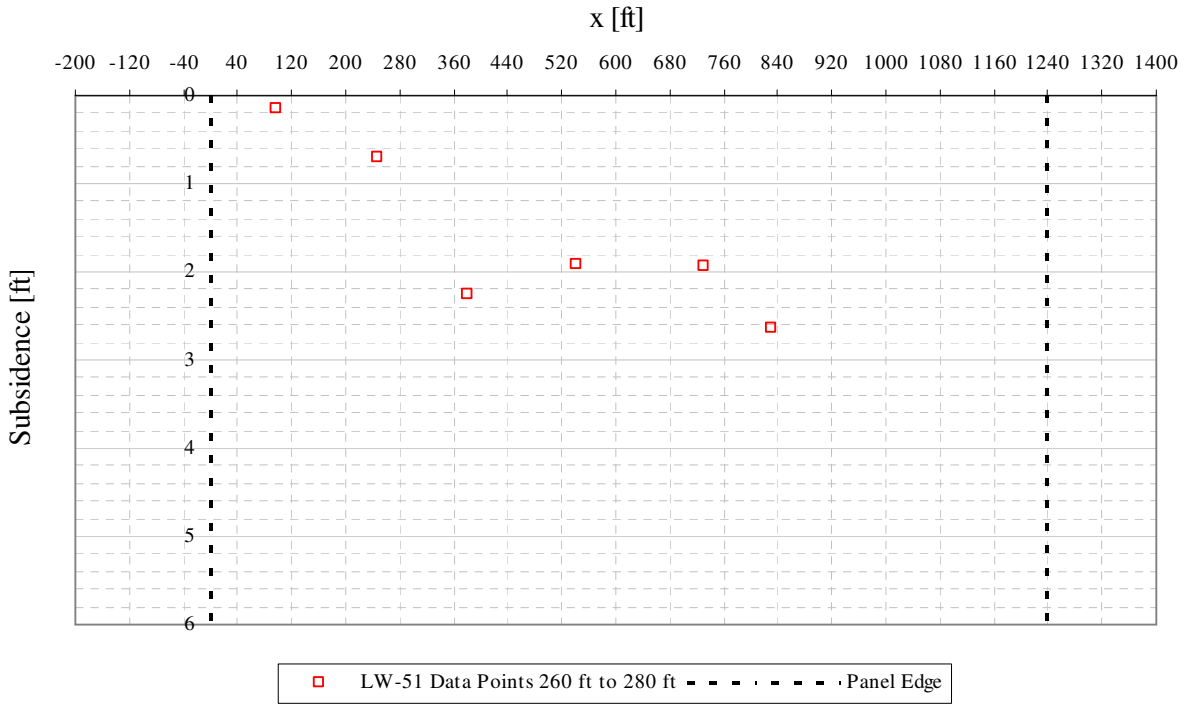

Figure A3- 23 LW-51 transverse view of data points from 260 ft to 280 ft from mine face

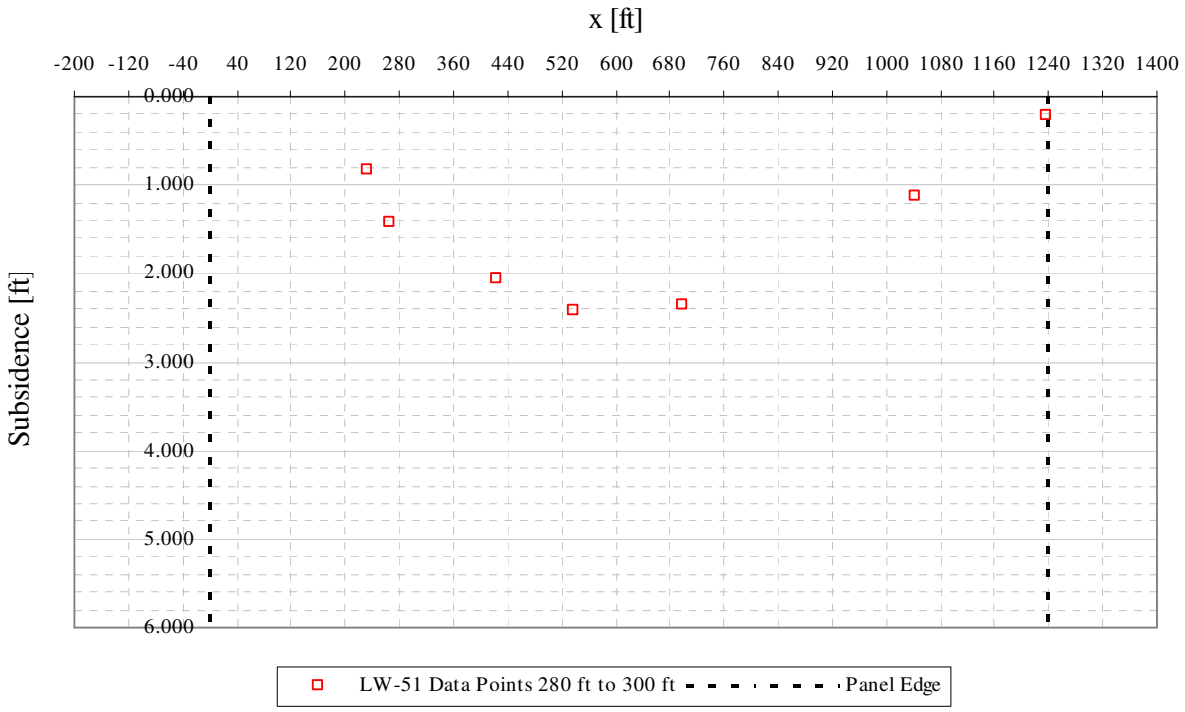

Figure A3- 24 LW-51 transverse view of data points from 280 ft to 300 ft from mine face

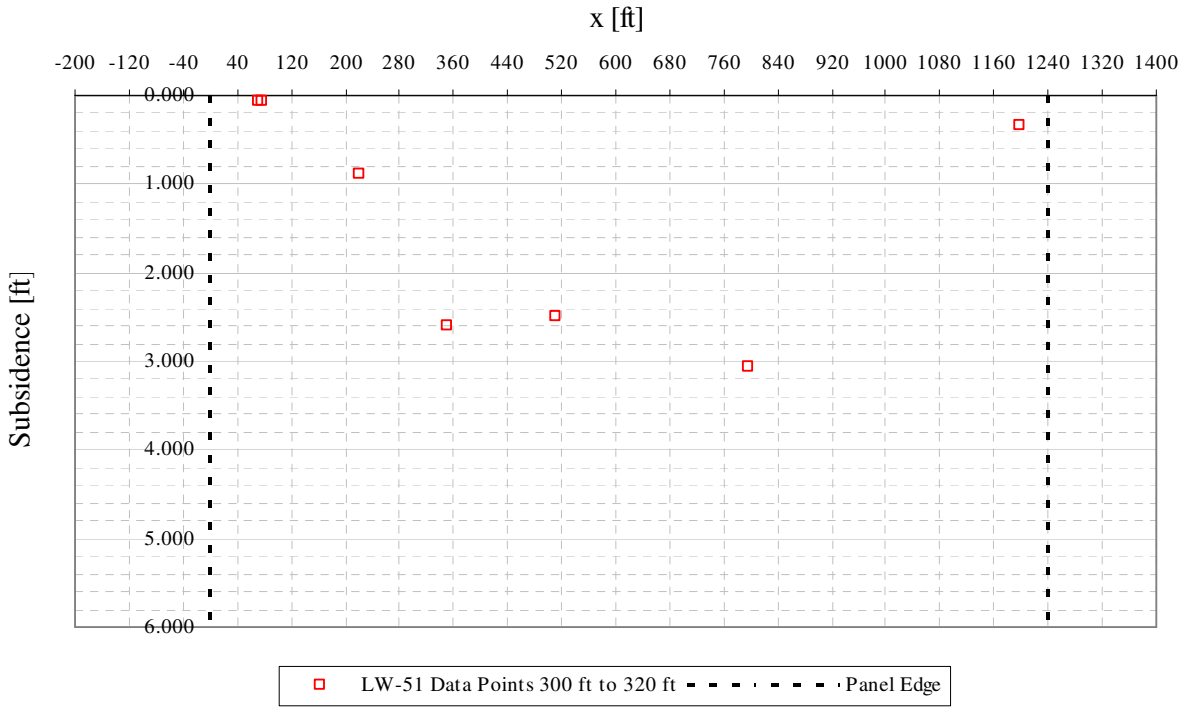

Figure A3- 25 LW-51 transverse view of data points from 300 ft to 320 ft from mine face

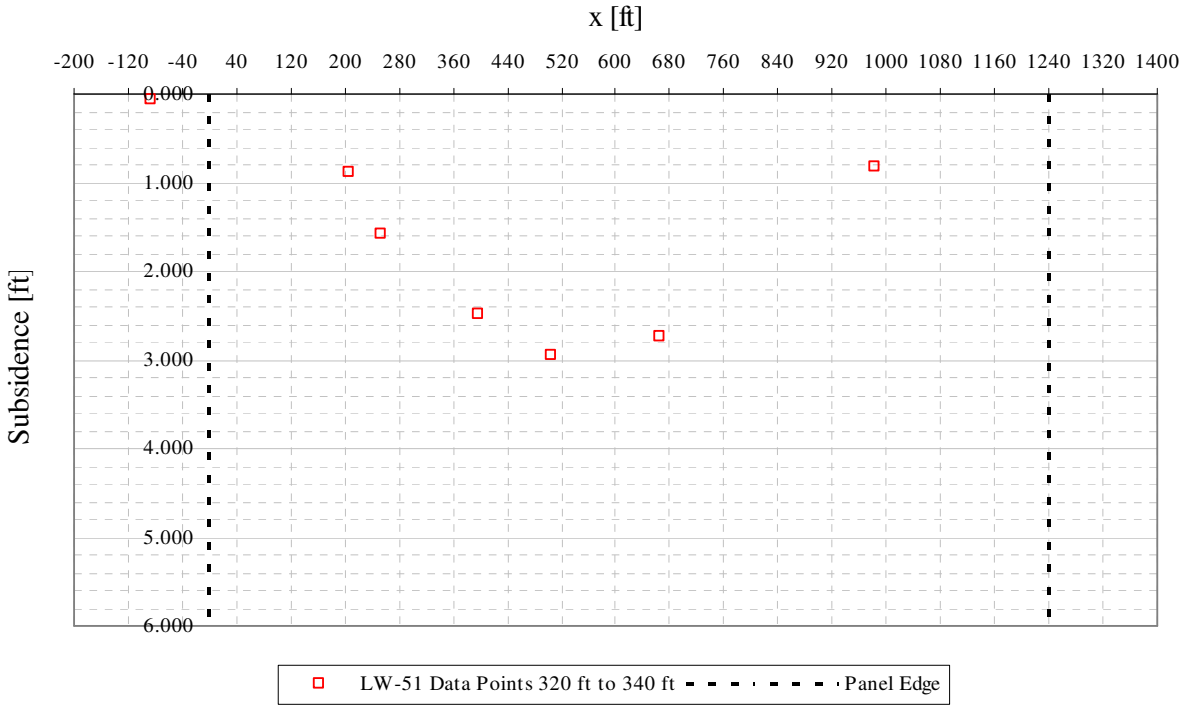

Figure A3- 26 LW-51 transverse view of data points from 320 ft to 340 ft from mine face

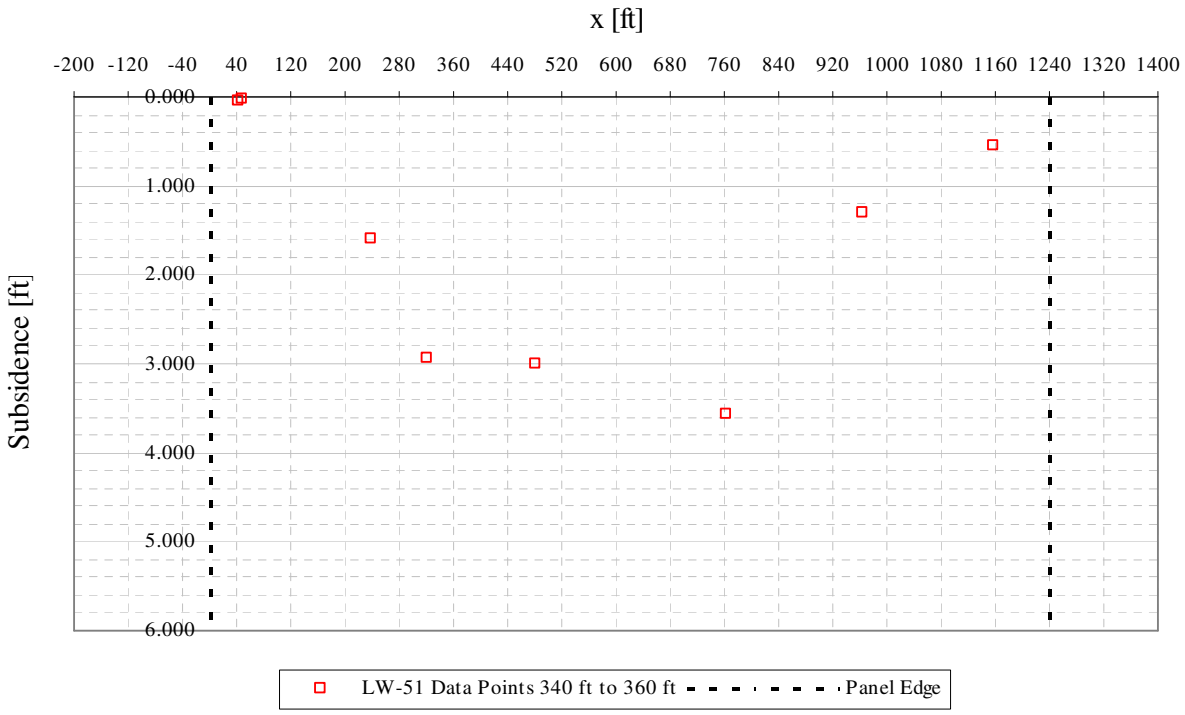

Figure A3- 27 LW-51 transverse view of data points from 340 ft to 360 ft from mine face

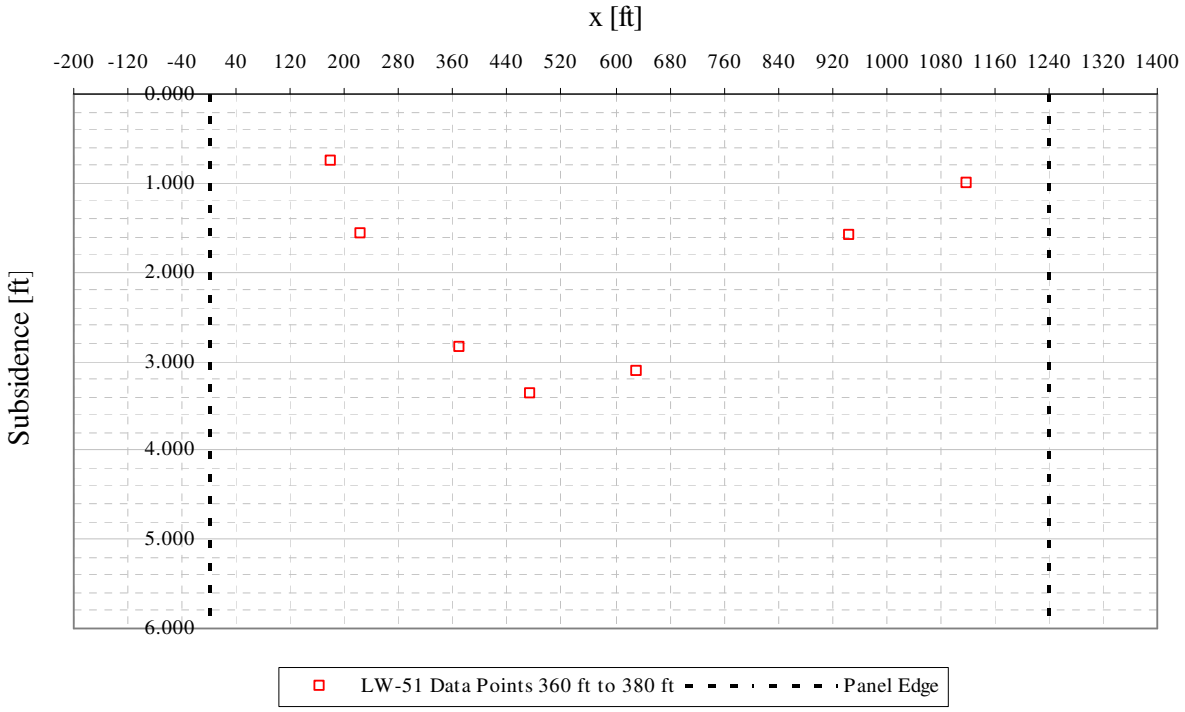

Figure A3- 28 LW-51 transverse view of data points from 360 ft to 380 ft from mine face

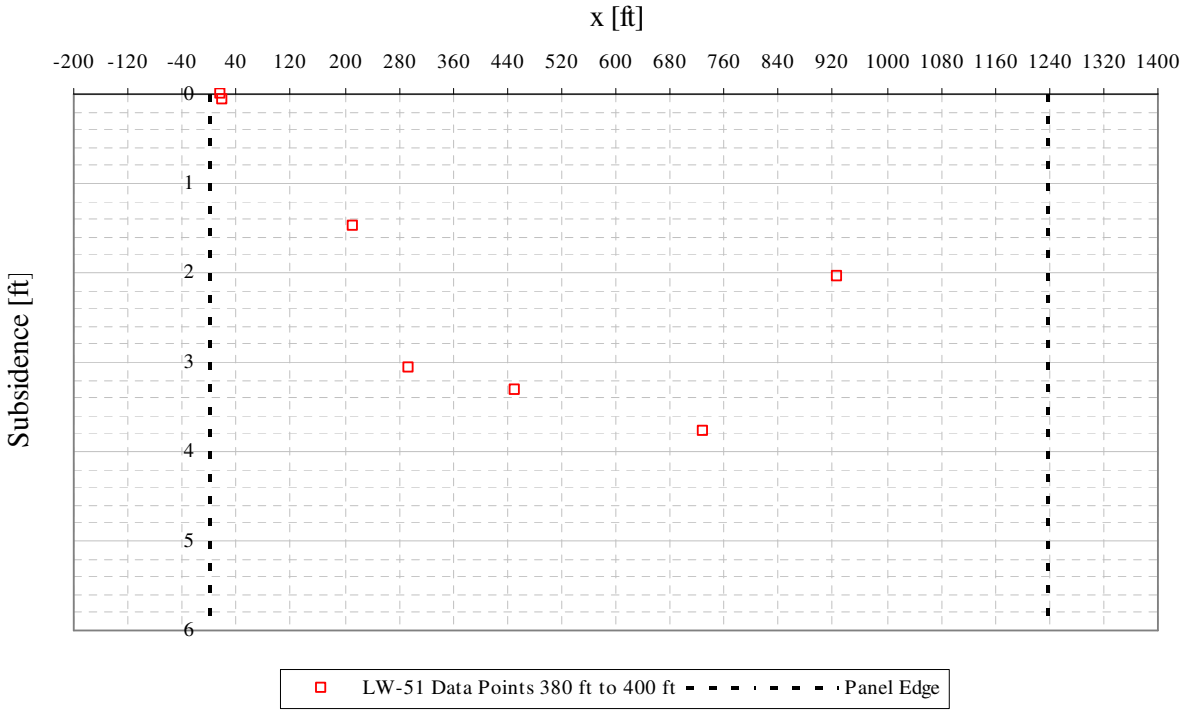

Figure A3- 29 LW-51 transverse view of data points from 380 ft to 400 ft from mine face

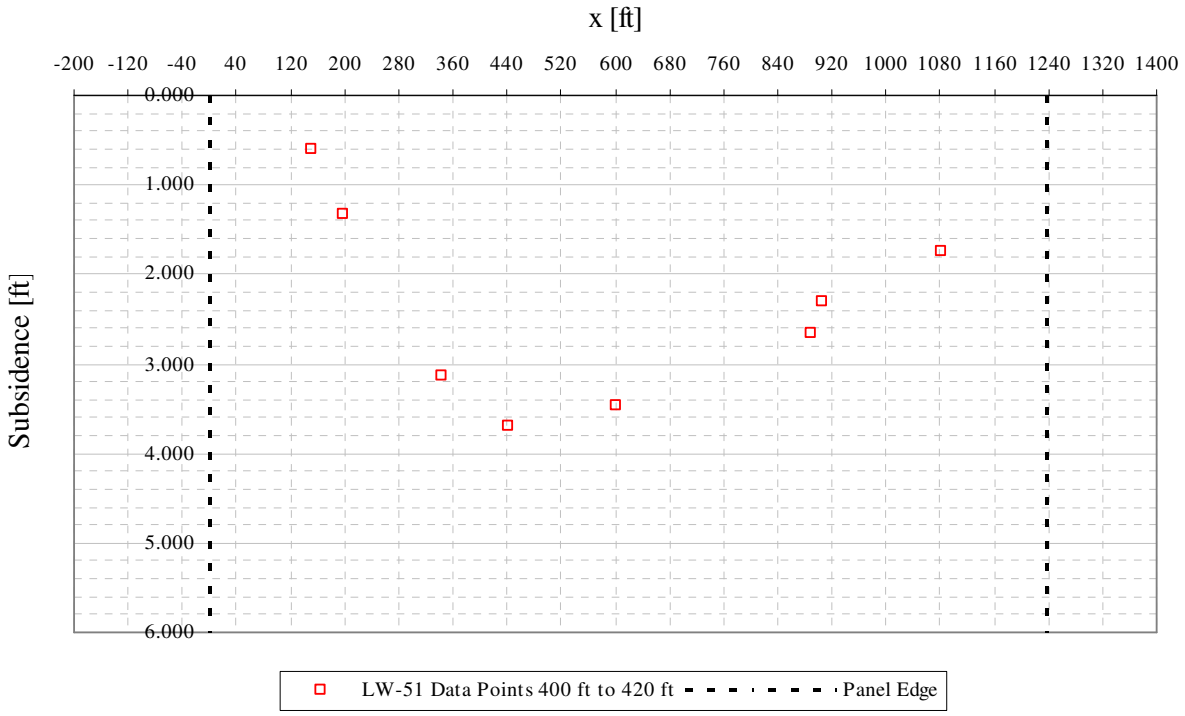

Figure A3- 30 LW-51 transverse view of data points from 400 ft to 420 ft from mine face

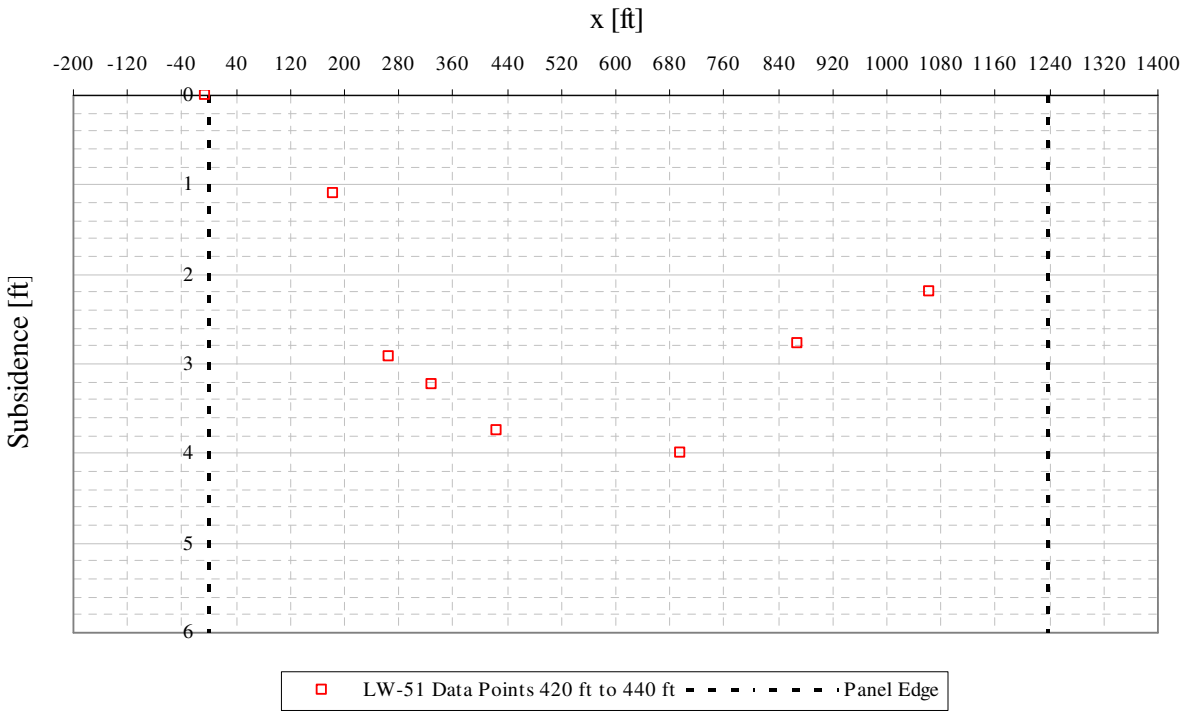

Figure A3- 31 LW-51 transverse view of data points from 420 ft to 440 ft from mine face

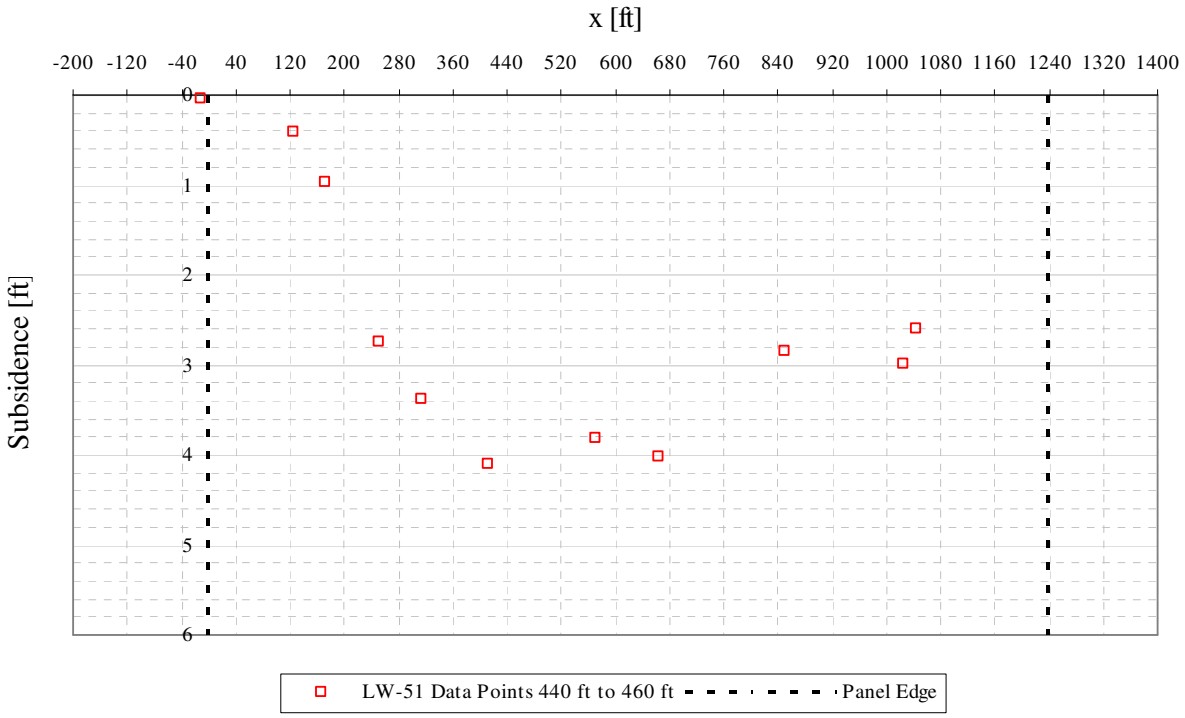

Figure A3- 32 LW-51 transverse view of data points from 440 ft to 460 ft from mine face

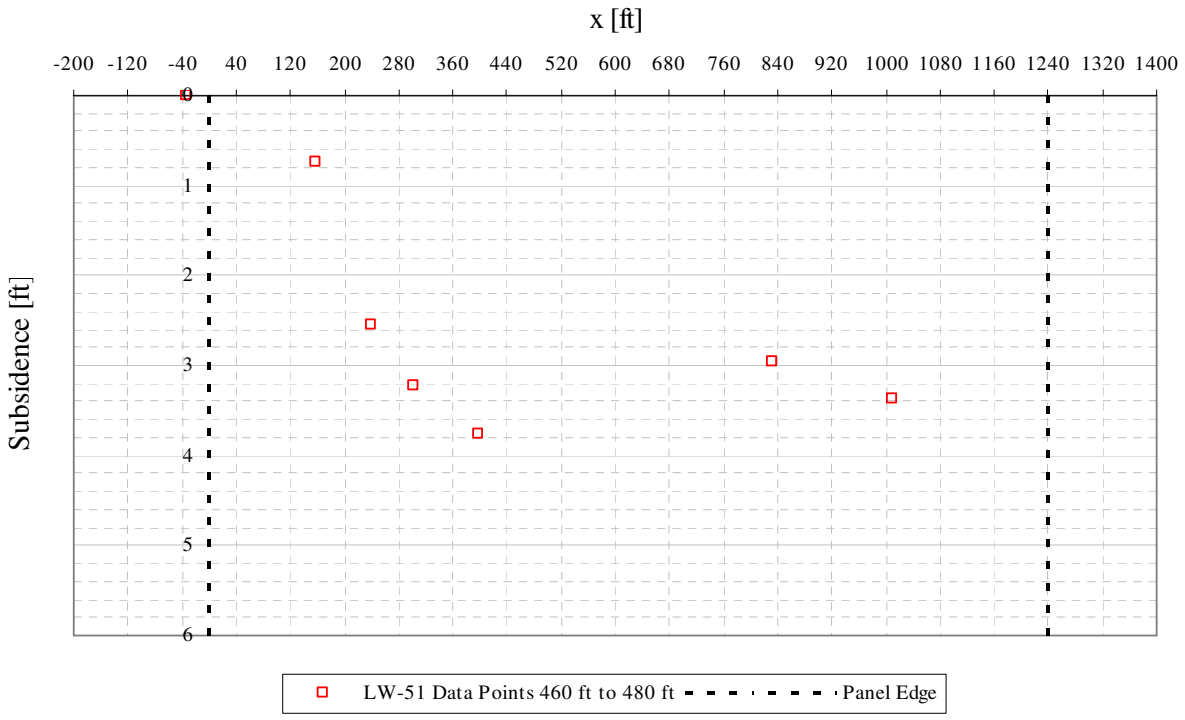

Figure A3- 33 LW-51 transverse view of data points from 460 ft to 480 ft from mine face

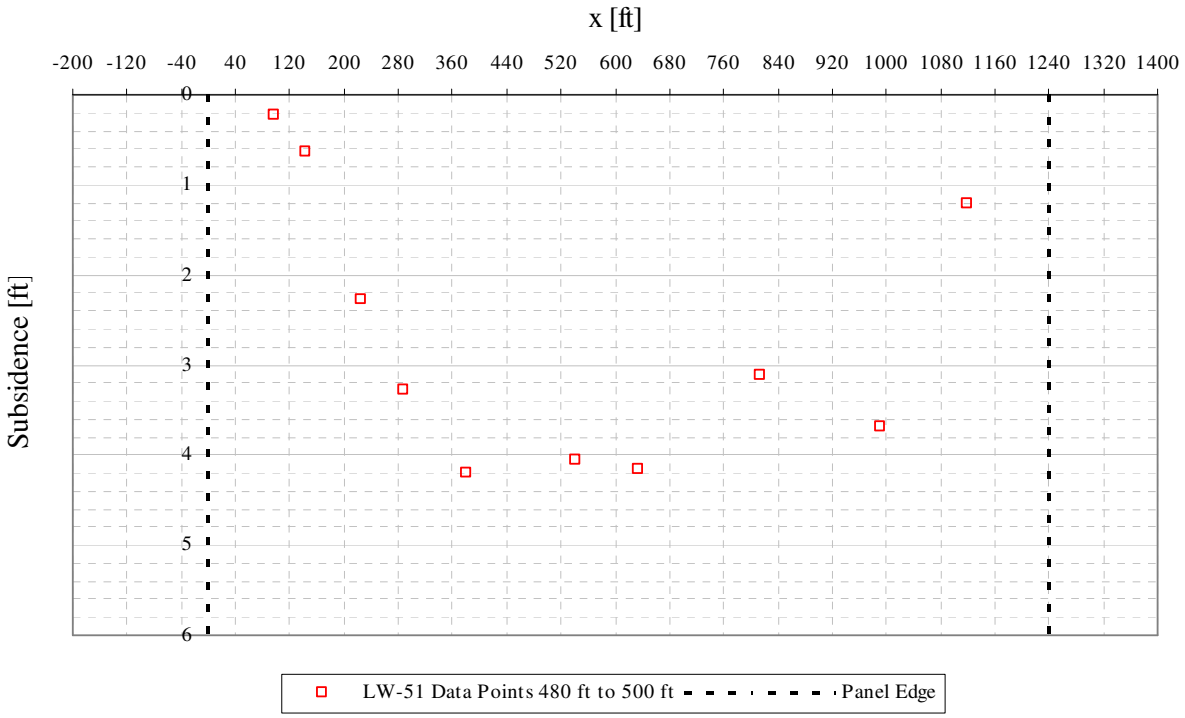

Figure A3- 34 LW-51 transverse view of data points from 480 ft to 500 ft from mine face

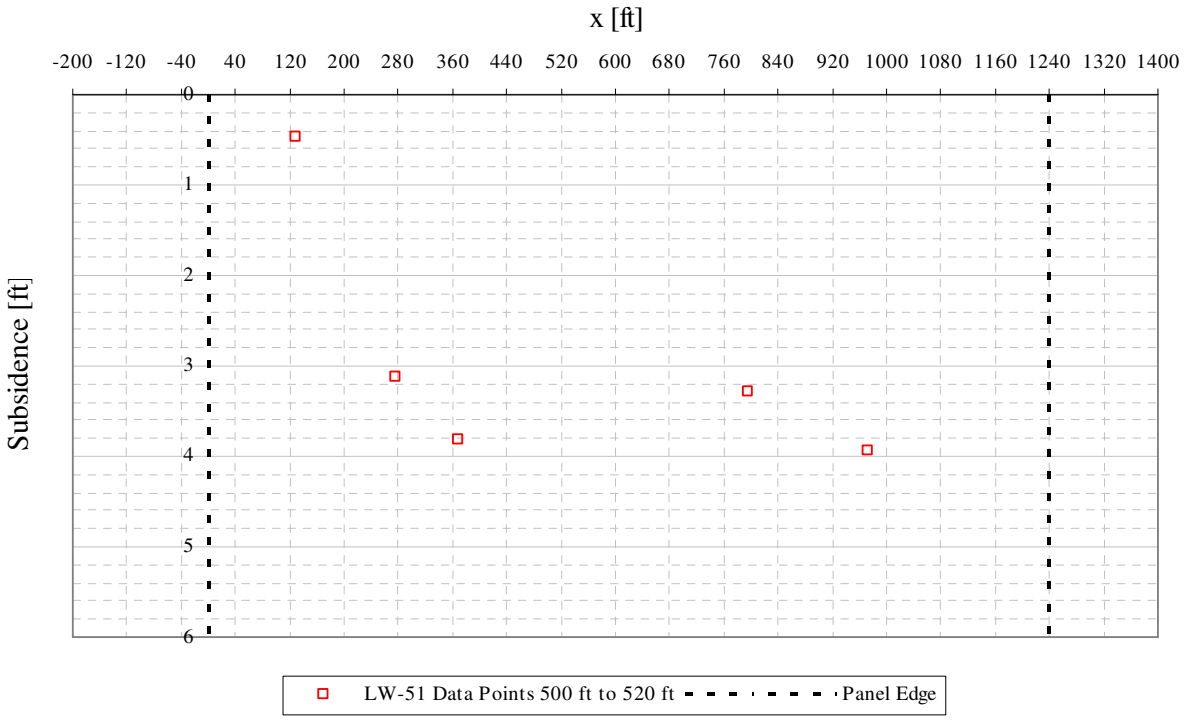

Figure A3- 35 LW-51 transverse view of data points from 500 ft to 520 ft from mine face

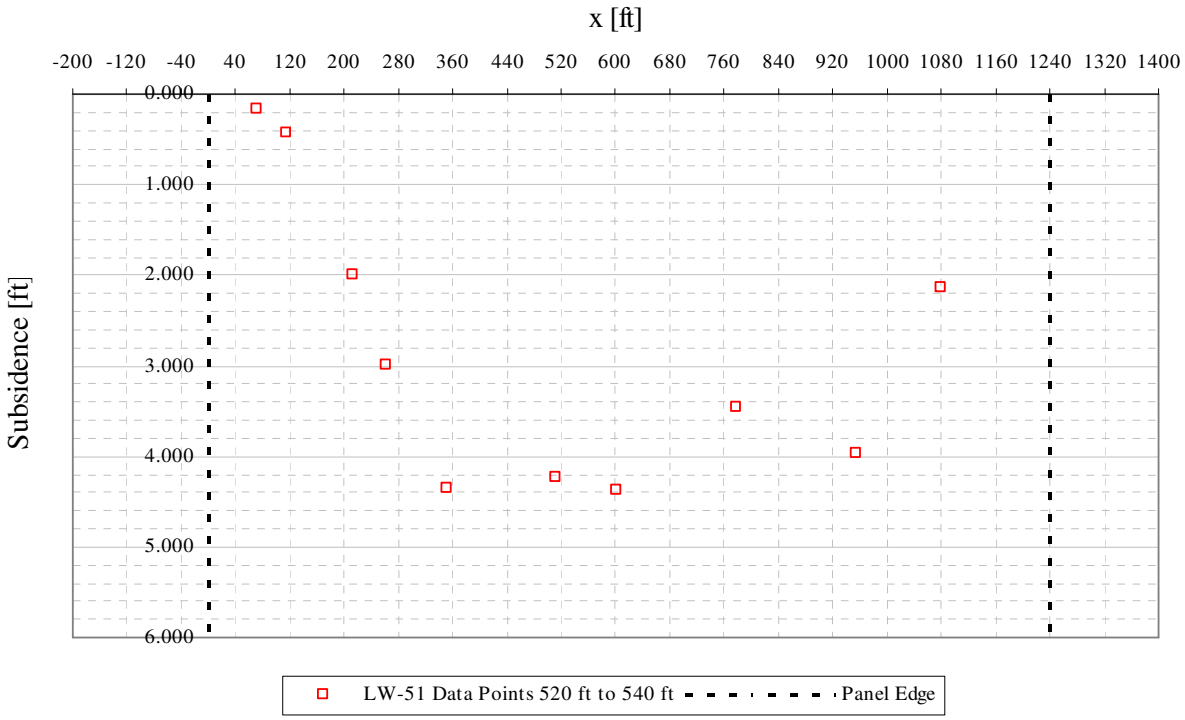

Figure A3- 36 LW-51 transverse view of data points from 520 ft to 540 ft from mine face

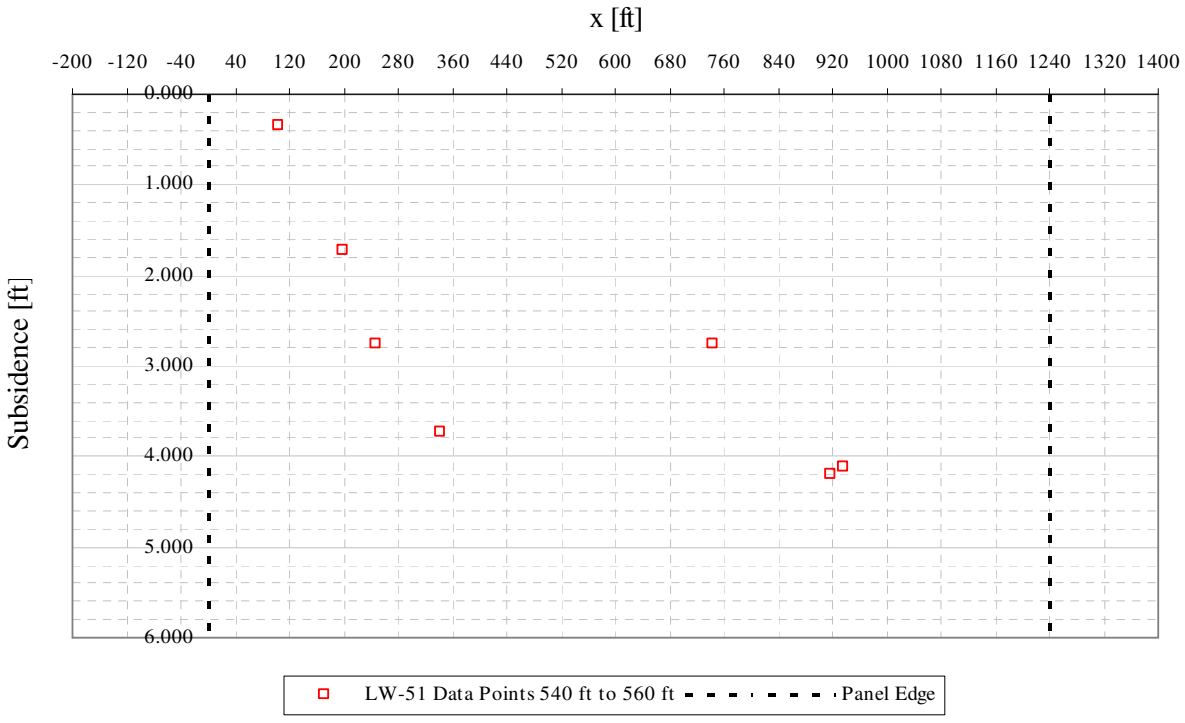

Figure A3- 37 LW-51 transverse view of data points from 540 ft to 560 ft from mine face

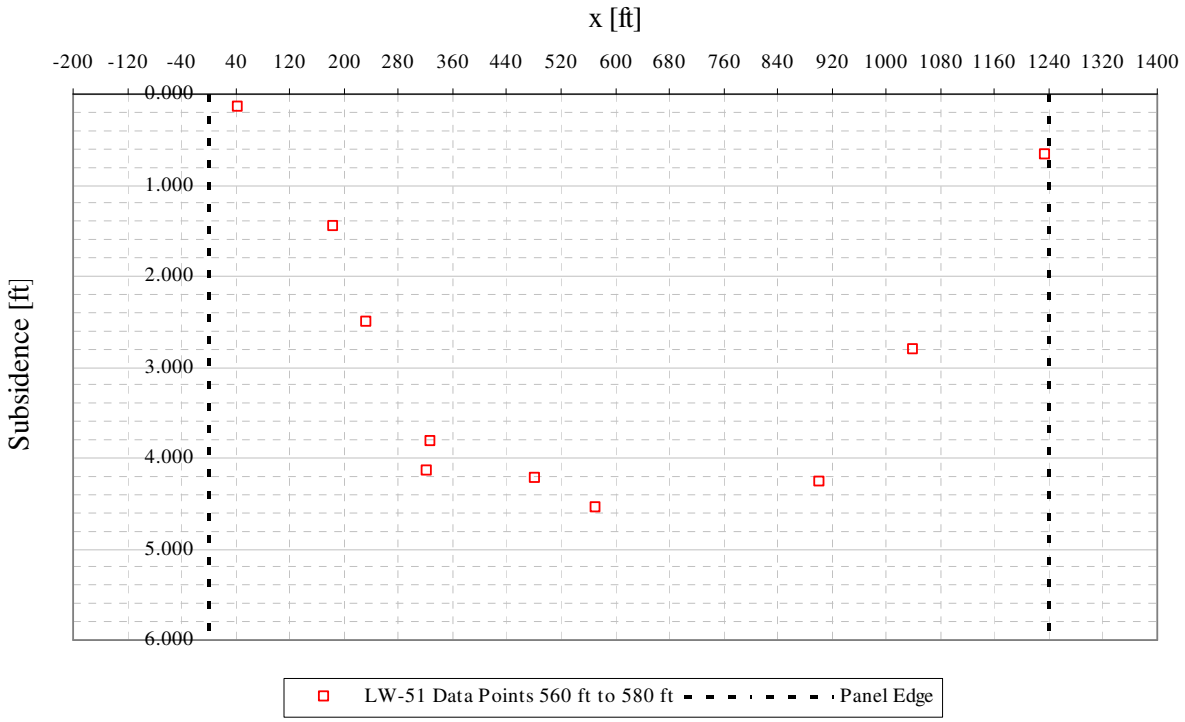

Figure A3- 38 LW-51 transverse view of data points from 560 ft to 580 ft from mine face

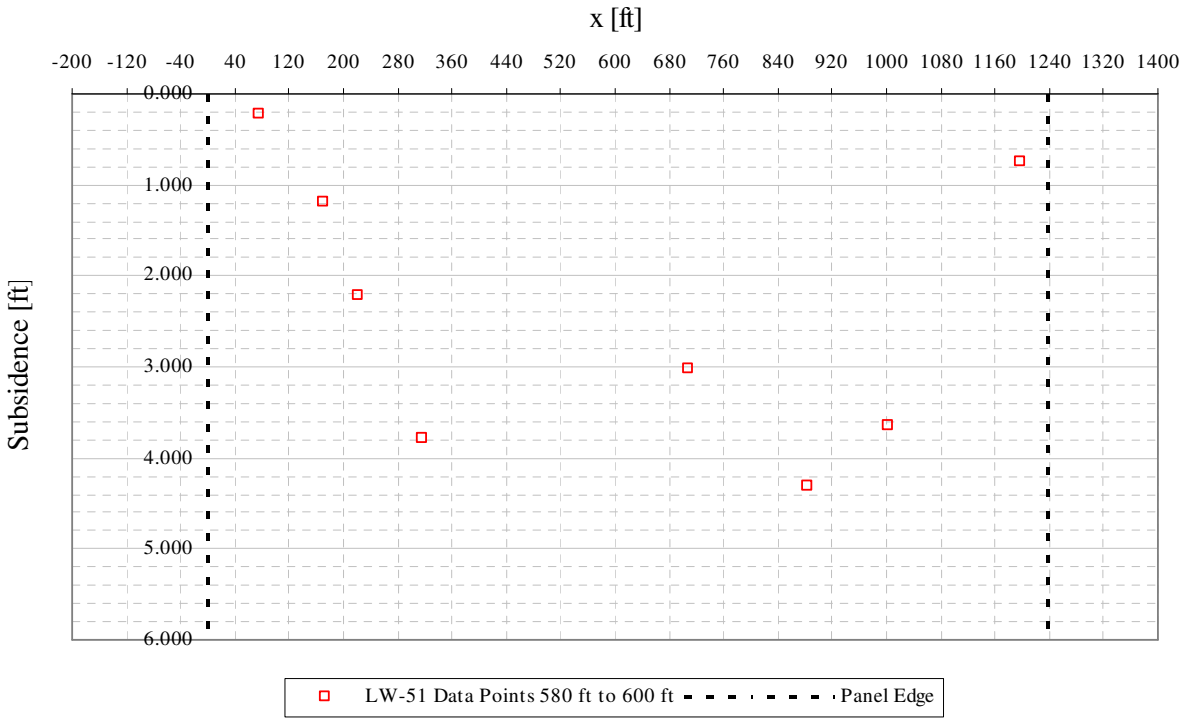

Figure A3- 39 LW-51 transverse view of data points from 580 ft to 600 ft from mine face

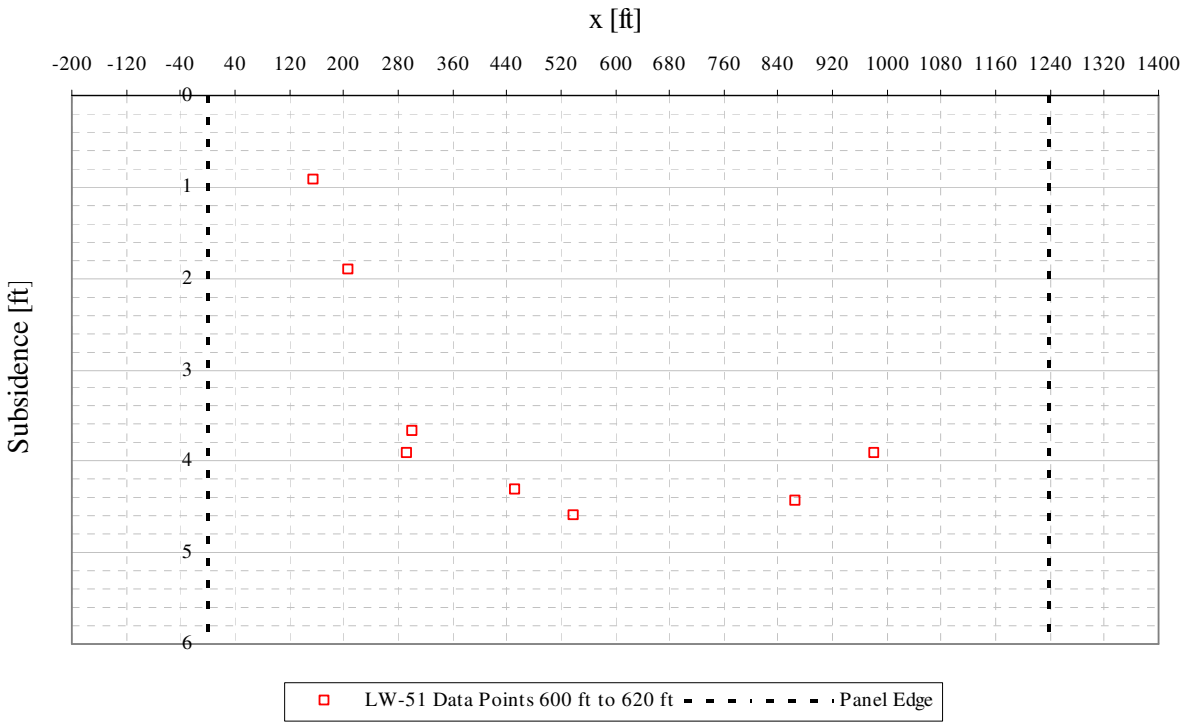

Figure A3- 40 LW-51 transverse view of data points from 600 ft to 620 ft from mine face

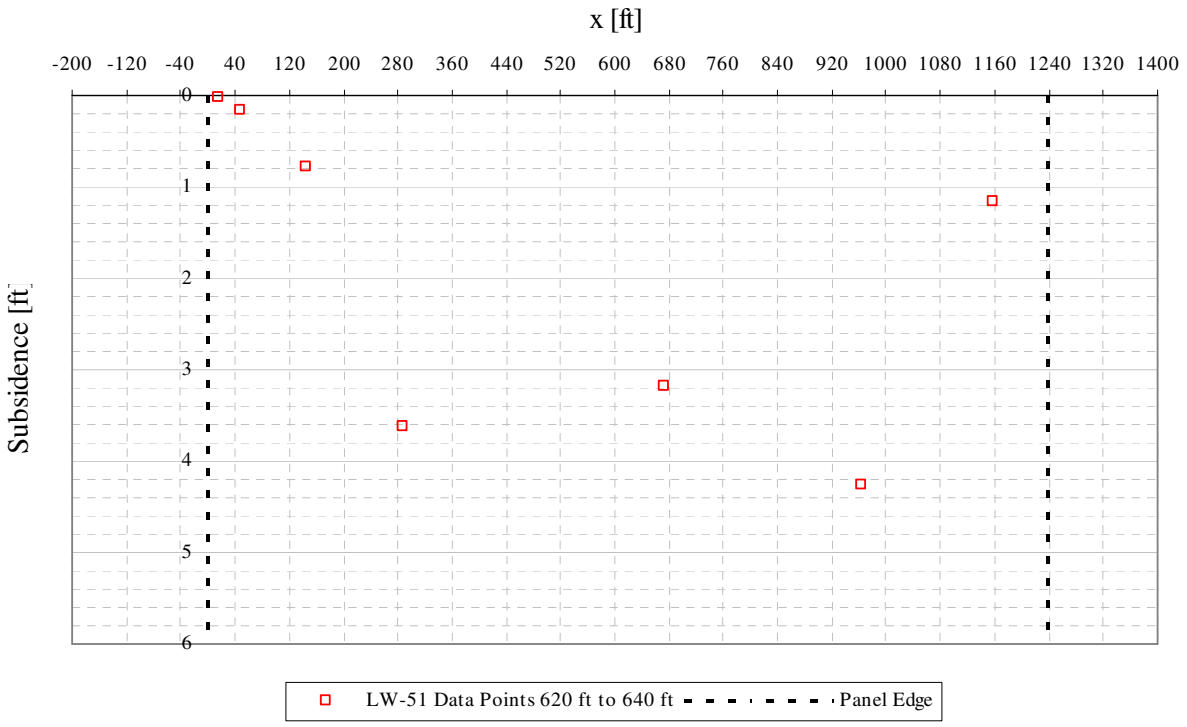

Figure A3- 41 LW-51 transverse view of data points from 620 ft to 640 ft from mine face

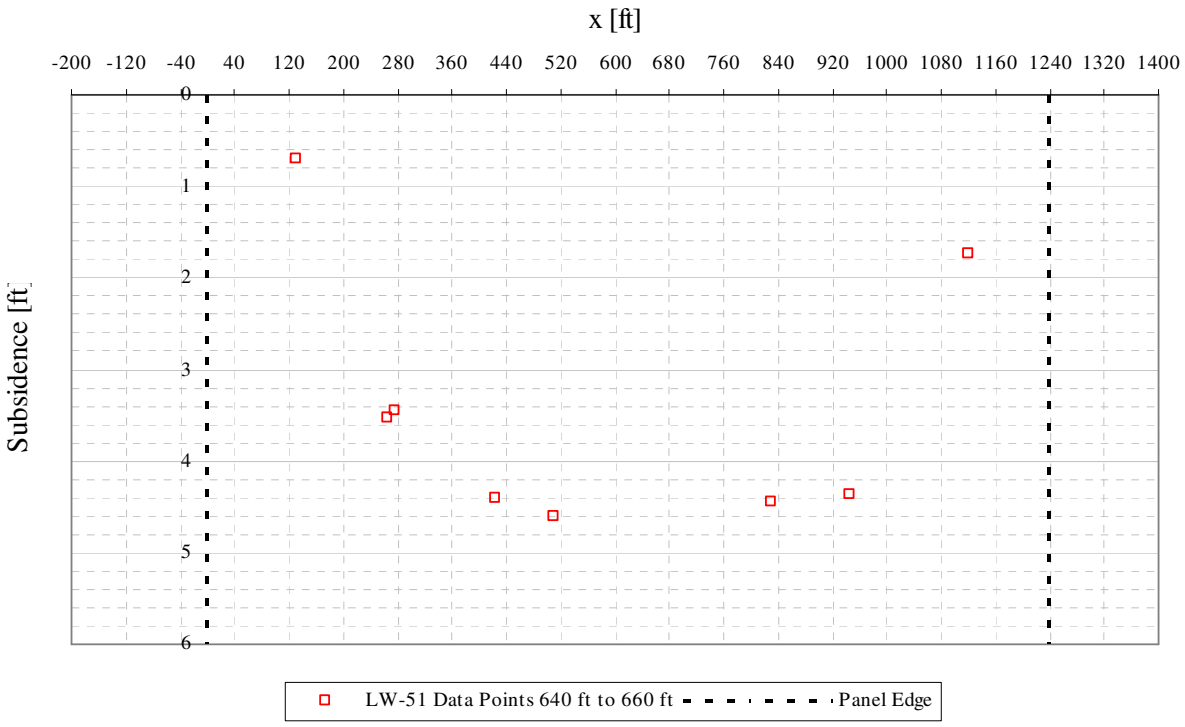

Figure A3- 42 LW-51 transverse view of data points from 640 ft to 660 ft from mine face

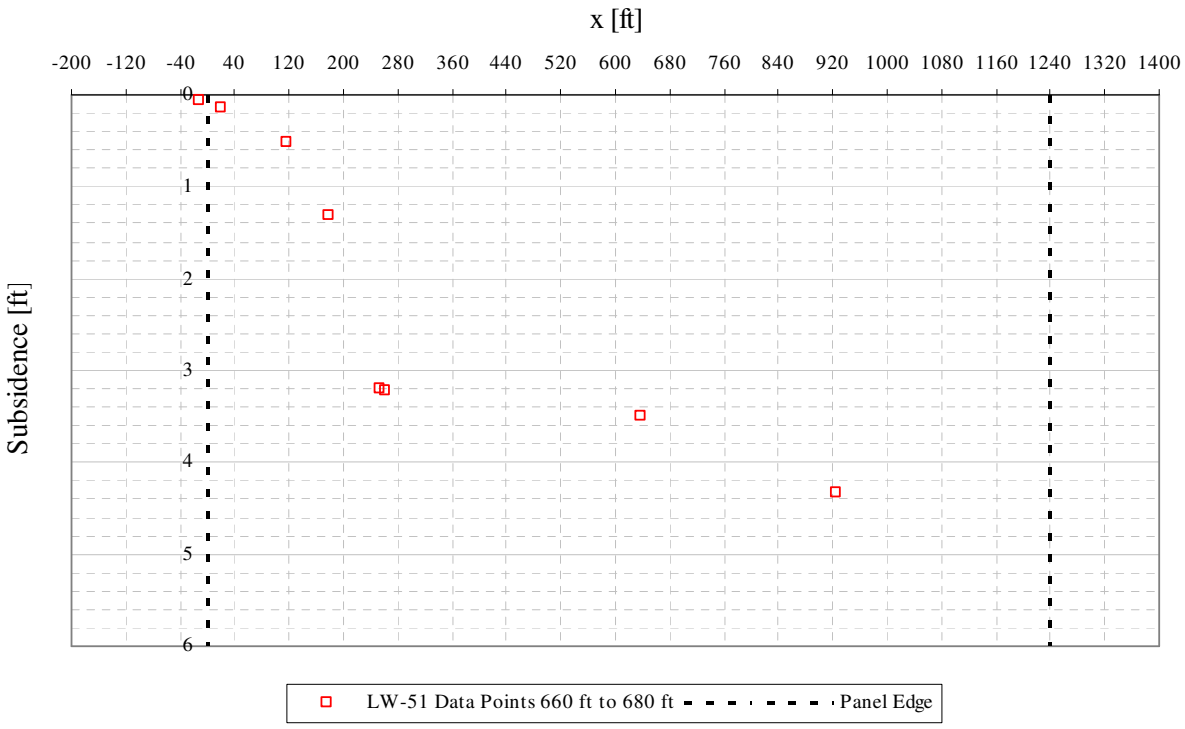

Figure A3- 43 LW-51 transverse view of data points from 660 ft to 680 ft from mine face

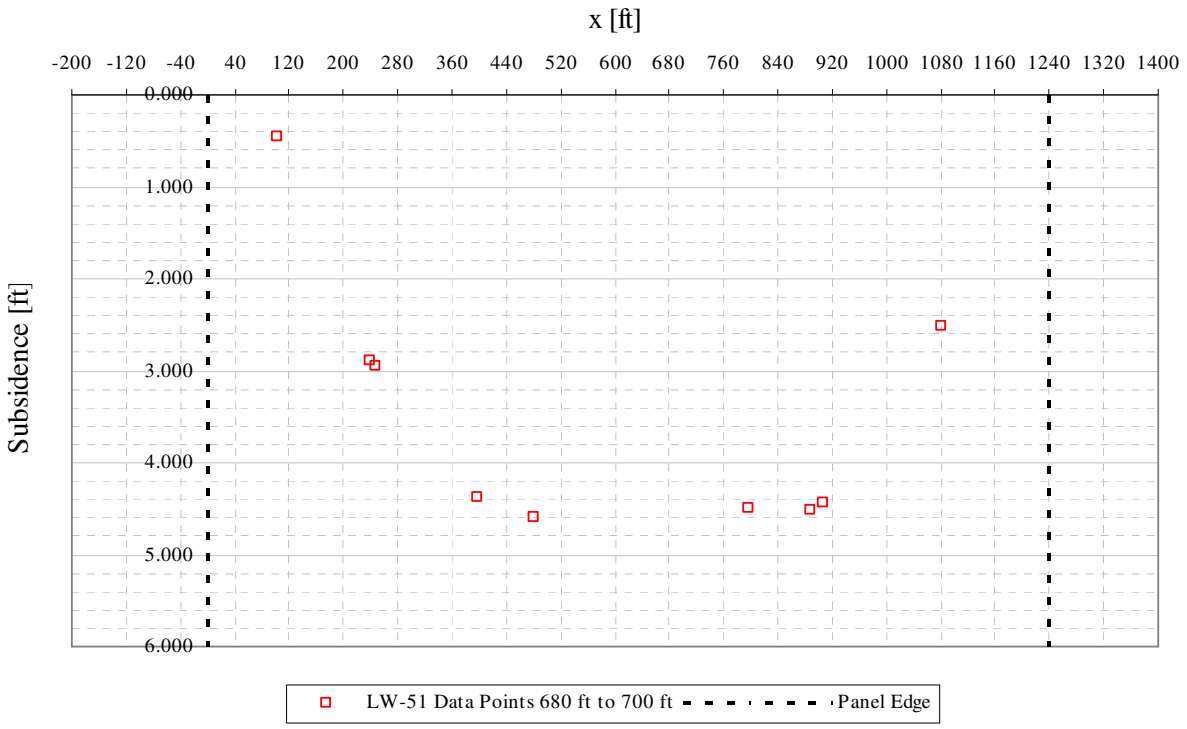

Figure A3- 44 LW-51 transverse view of data points from 680 ft to 700 ft from mine face

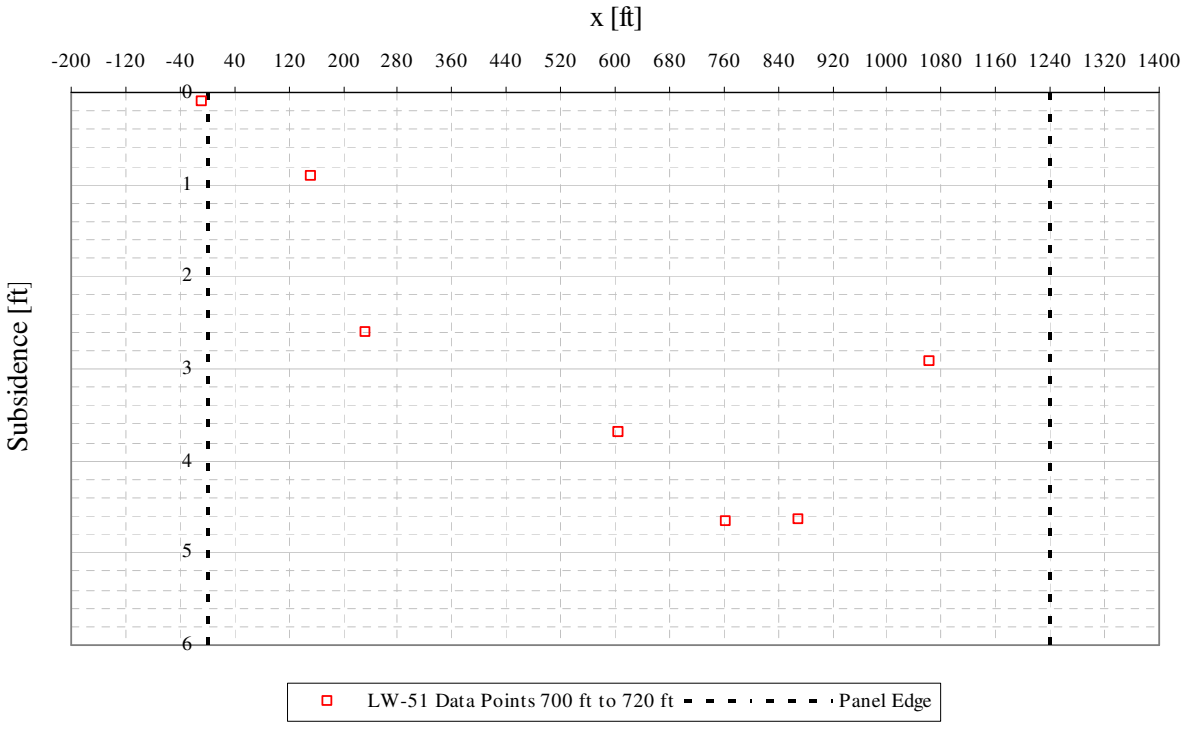

Figure A3- 45 LW-51 transverse view of data points from 700 ft to 720 ft from mine face

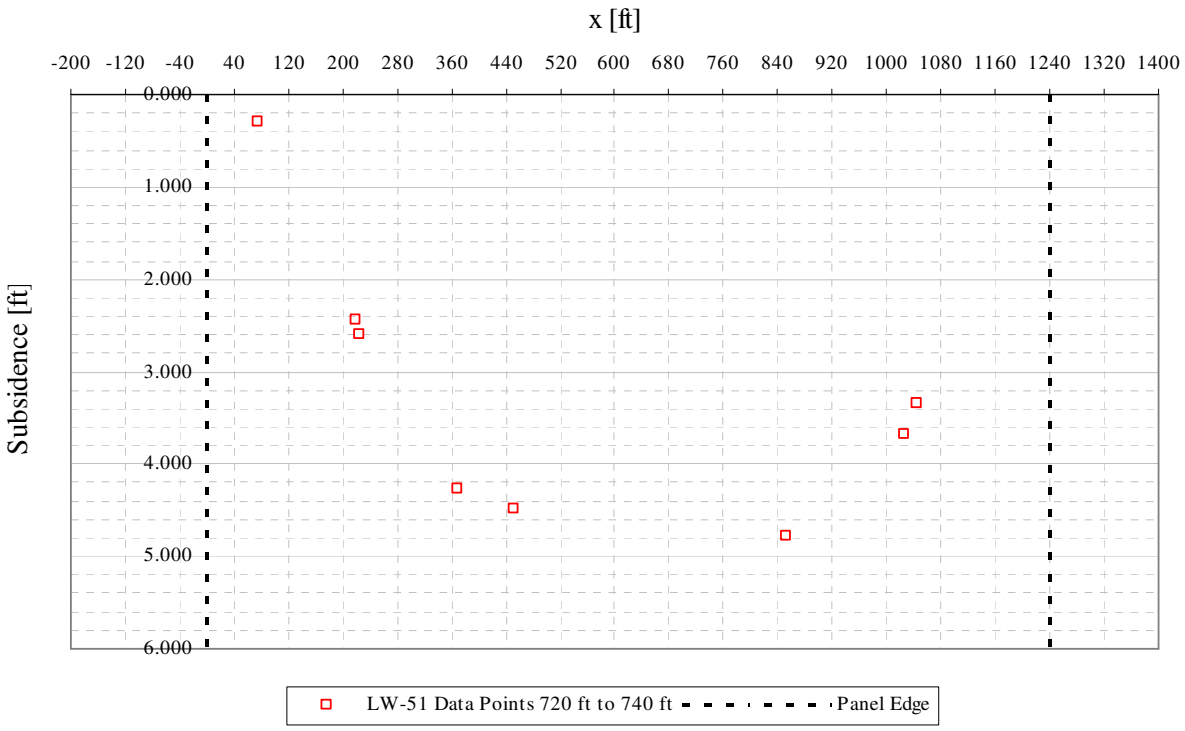

Figure A3- 46 LW-51 transverse view of data points from 720 ft to 740 ft from mine face

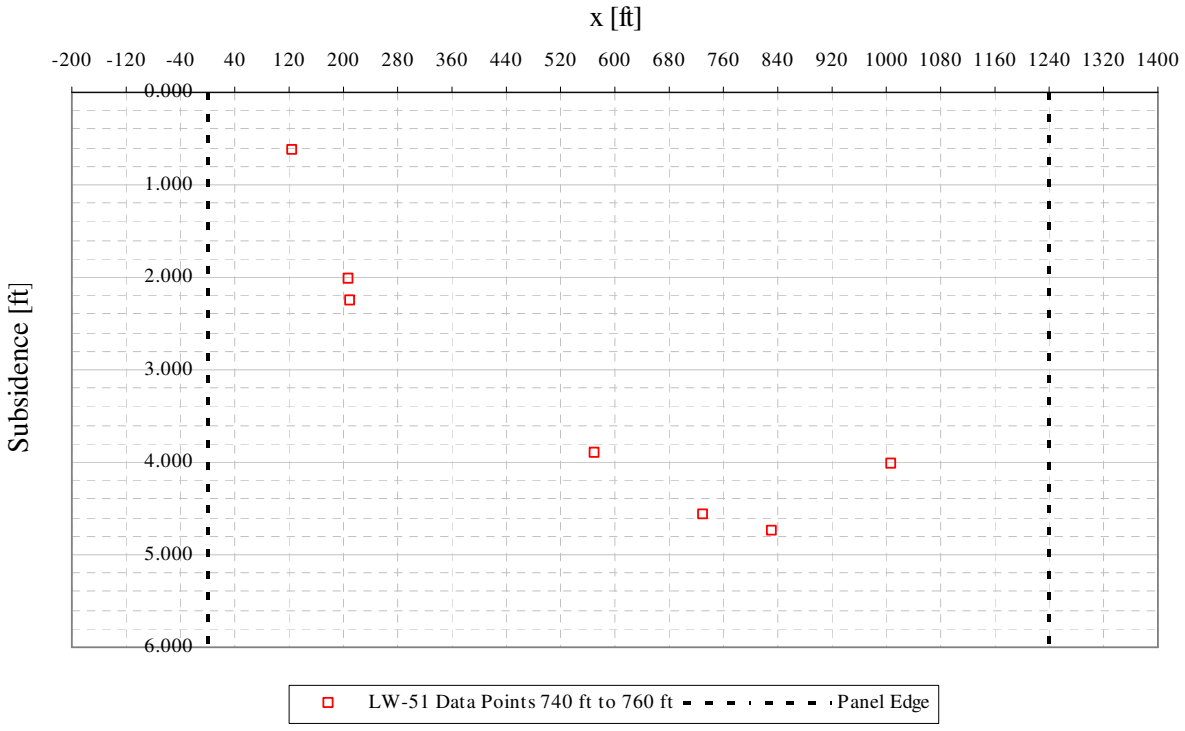

Figure A3- 47 LW-51 transverse view of data points from 740 ft to 760 ft from mine face

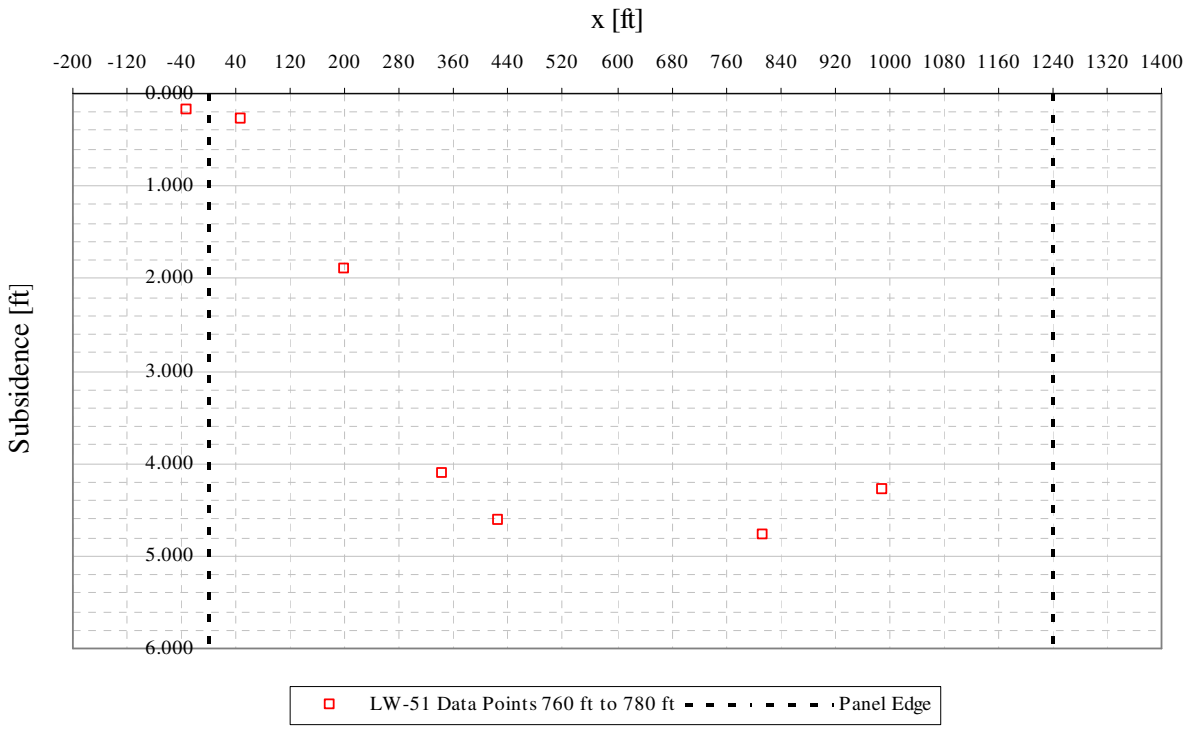

Figure A3- 48 LW-51 transverse view of data points from 760 ft to 780 ft from mine face

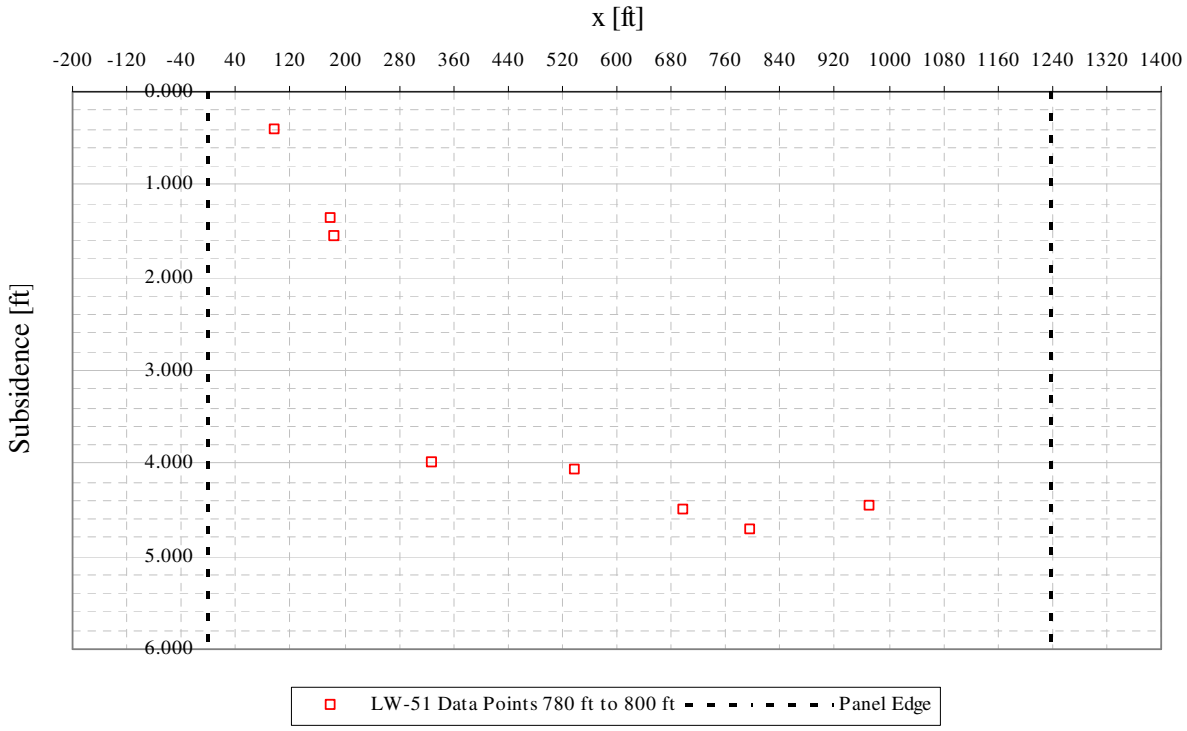

Figure A3- 49 LW-51 transverse view of data points from 780 ft to 800 ft from mine face

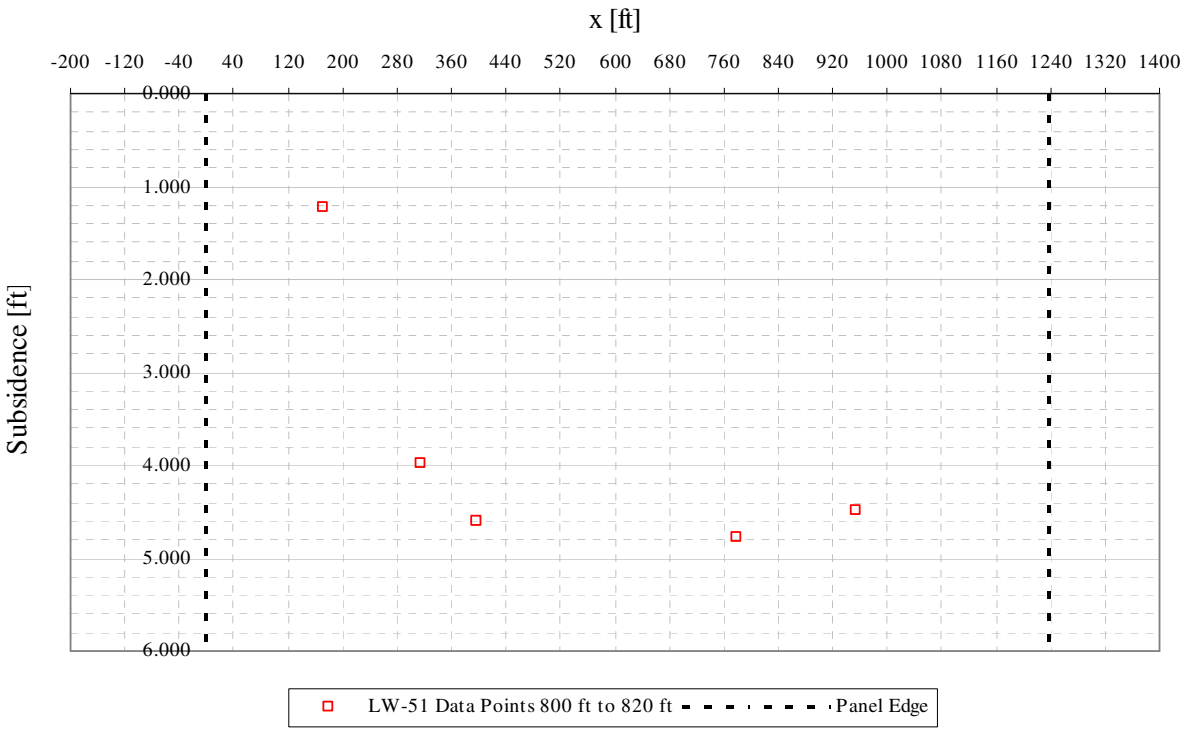

Figure A3- 50 LW-51 transverse view of data points from 800 ft to 820 ft from mine face

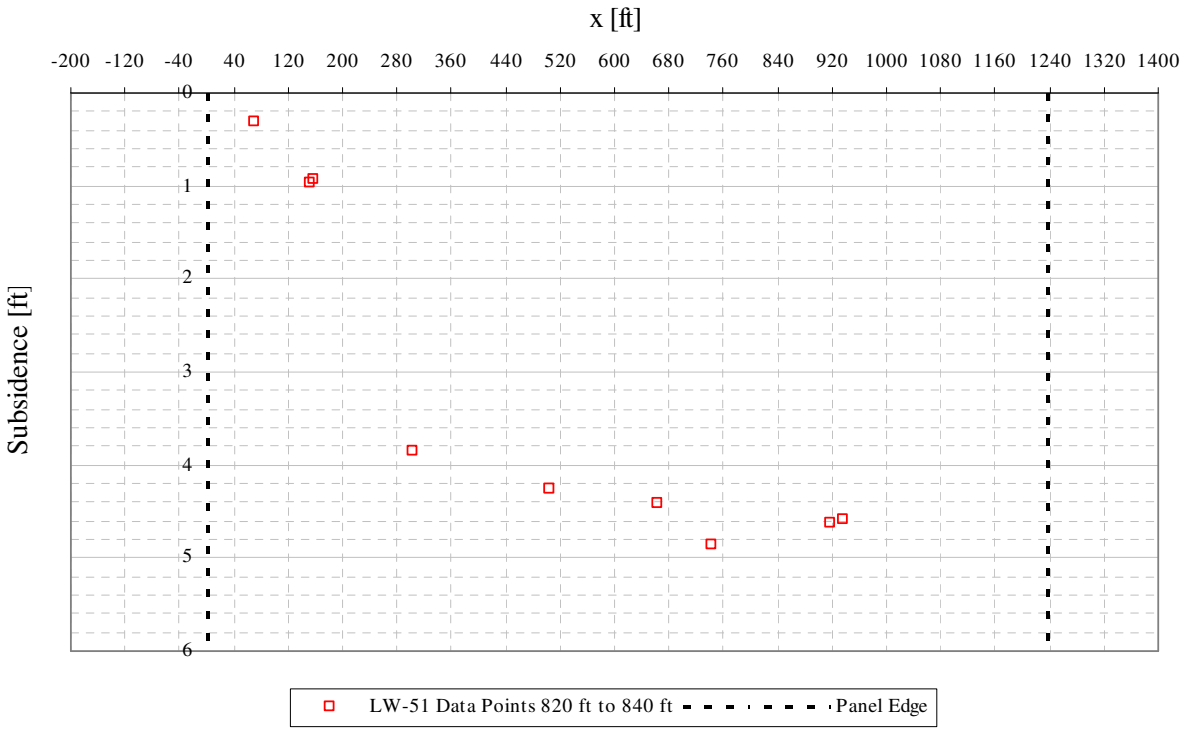

Figure A3- 51 LW-51 transverse view of data points from 820 ft to 840 ft from mine face

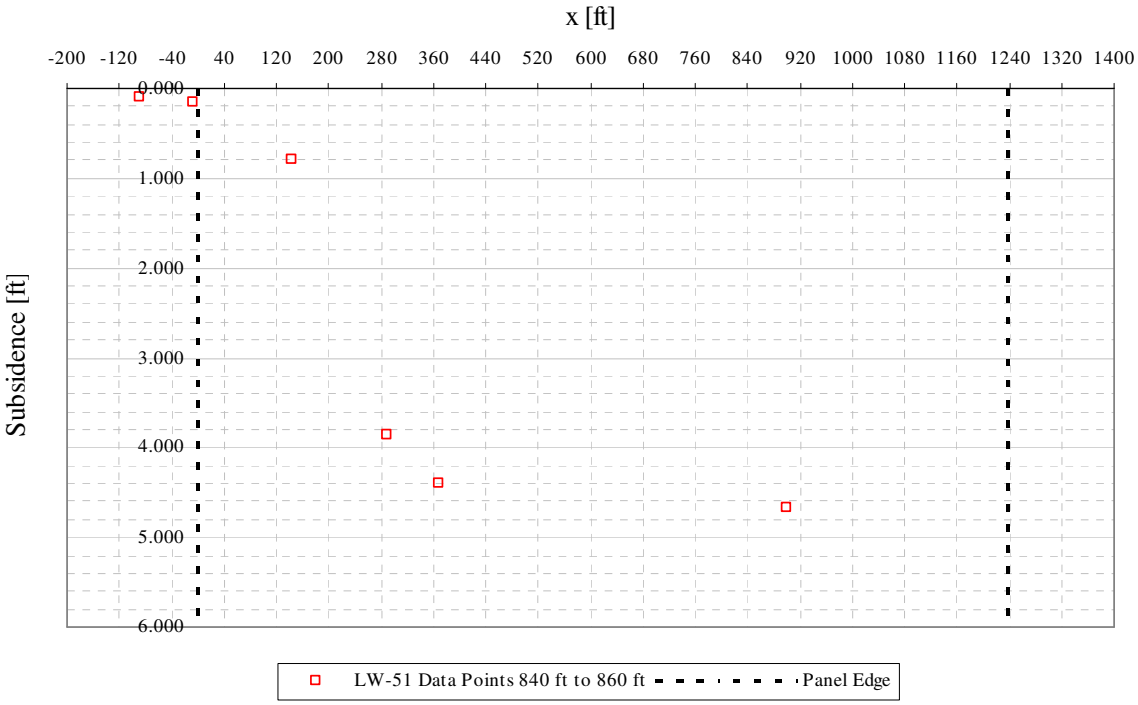

Figure A3- 52 LW-51 transverse view of data points from 840 ft to 860 ft from mine face

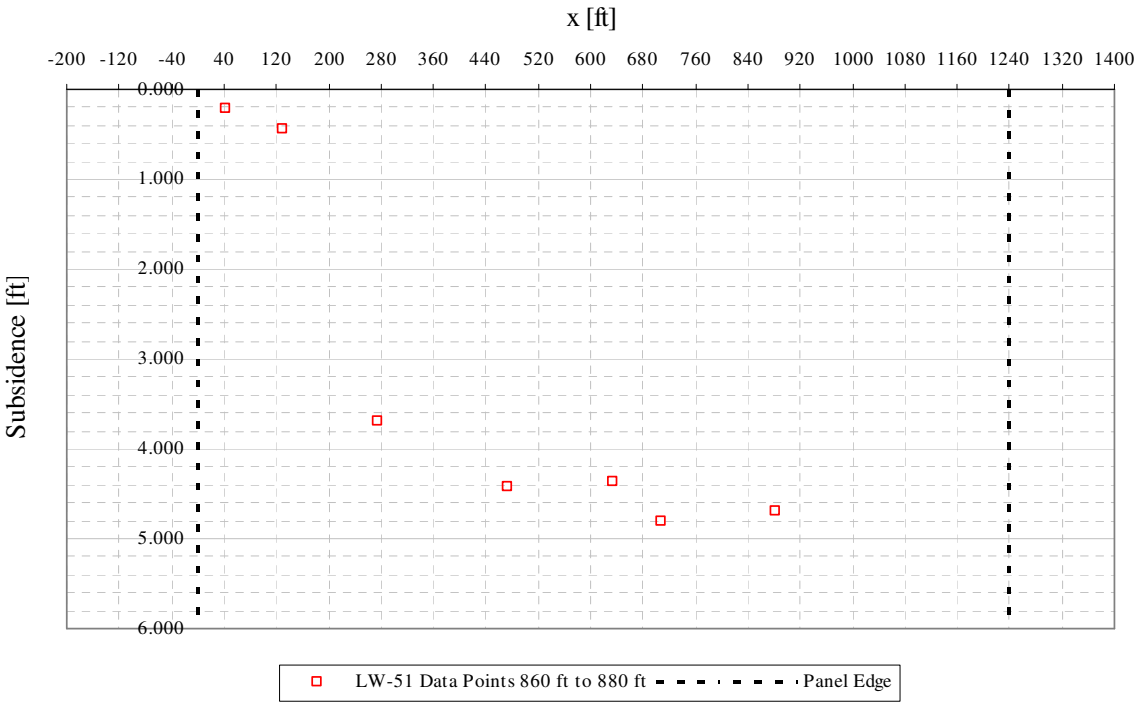

Figure A3- 53 LW-51 transverse view of data points from 860 ft to 880 ft from mine face

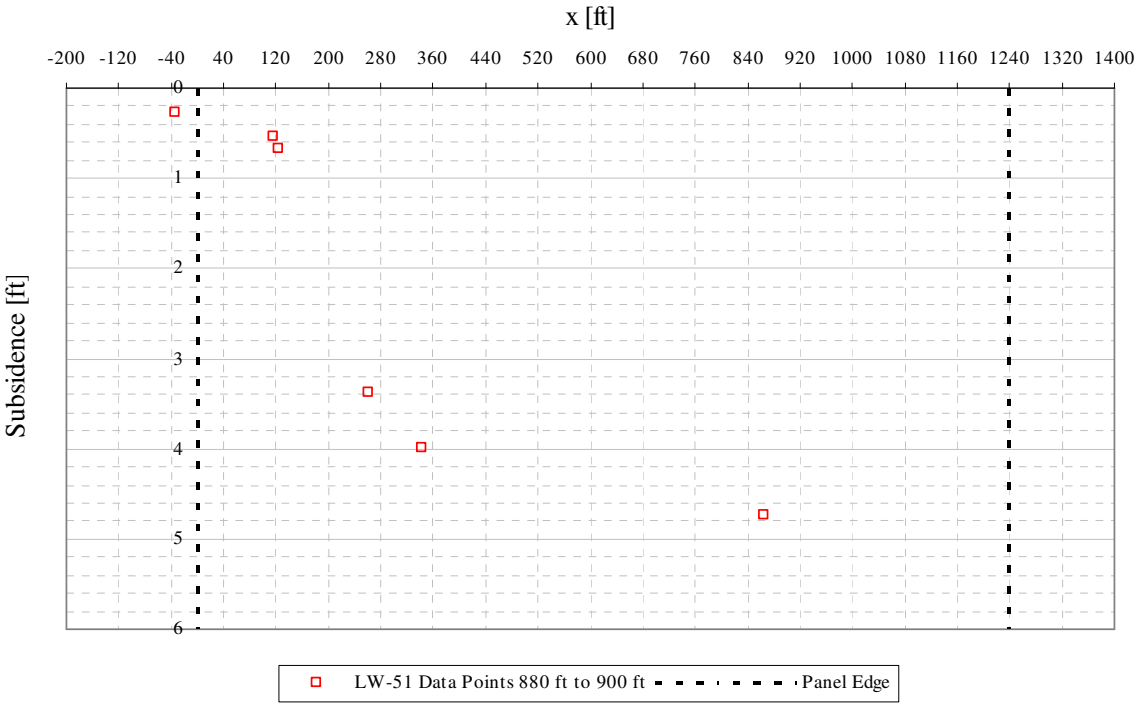

Figure A3- 54 LW-51 transverse view of data points from 880 ft to 900 ft from mine face

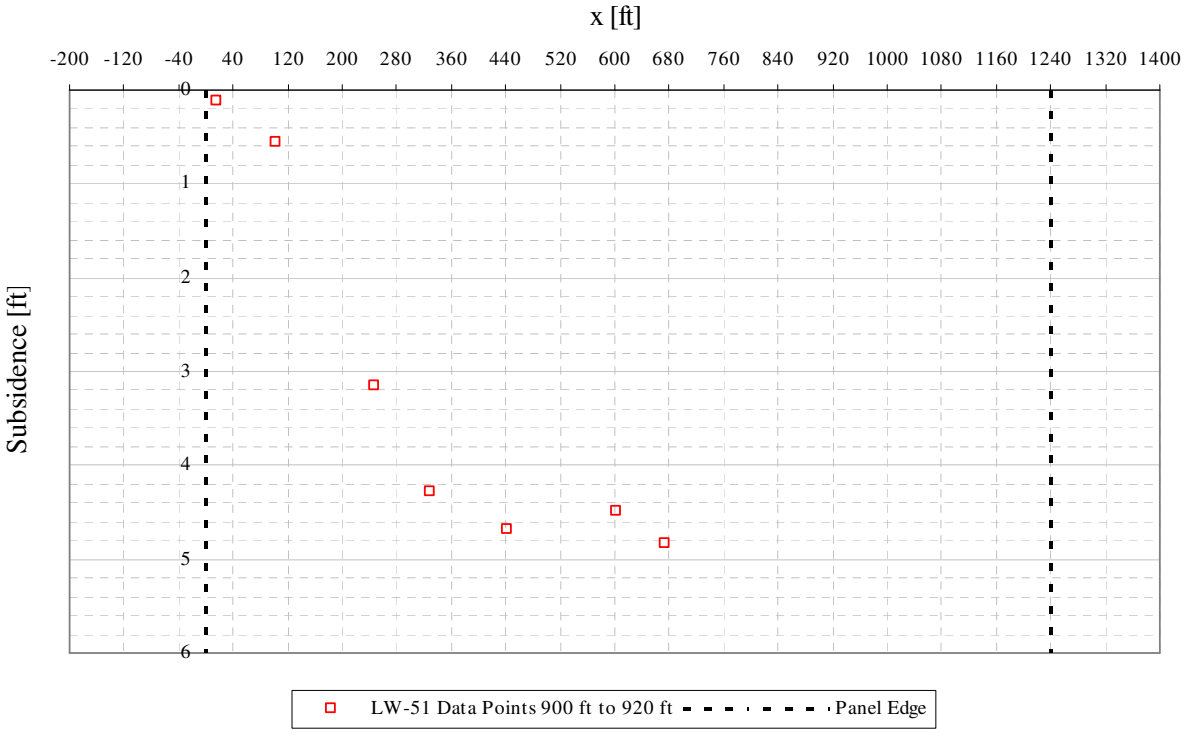

Figure A3- 55 LW-51 transverse view of data points from 900 ft to 920 ft from mine face

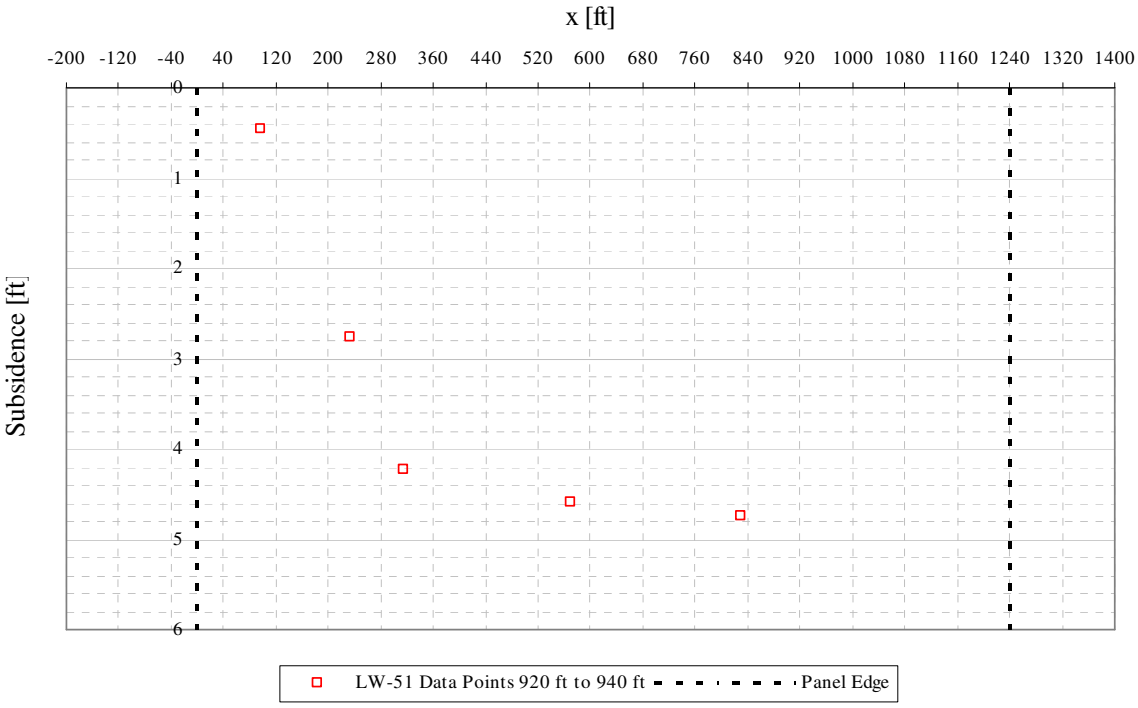

Figure A3- 56 LW-51 transverse view of data points from 920 ft to 940 ft from mine face

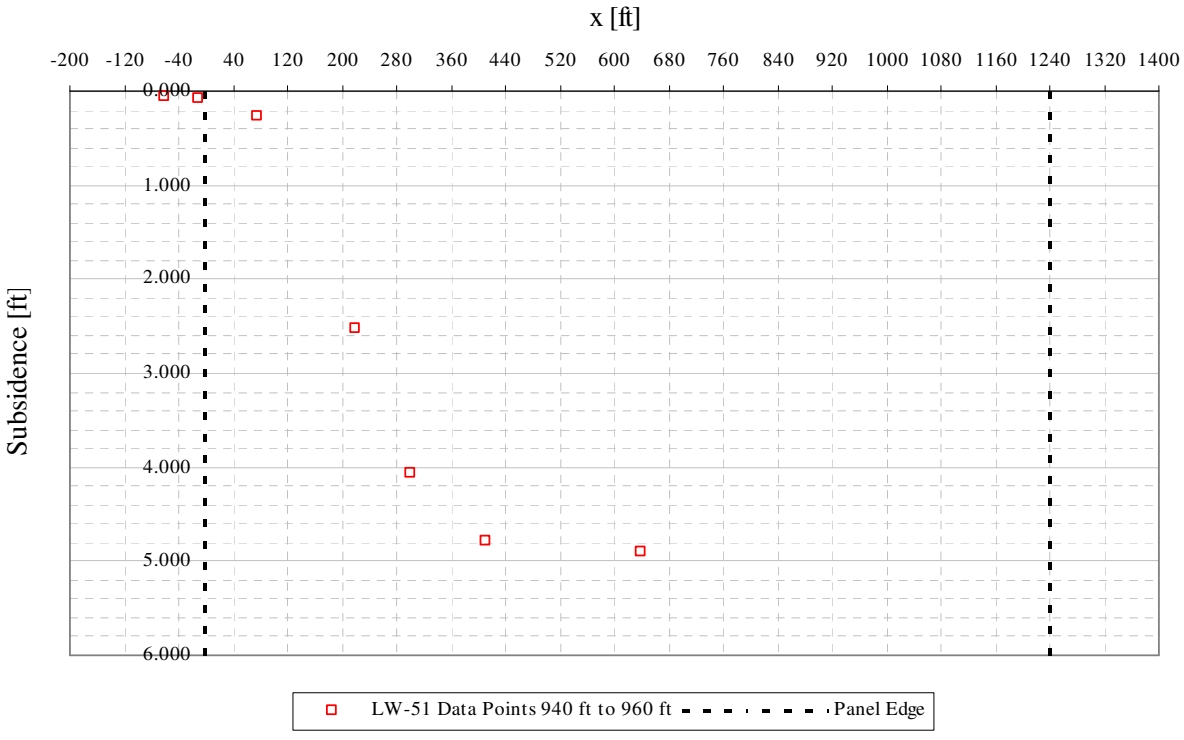

Figure A3- 57 LW-51 transverse view of data points from 940 ft to 960 ft from mine face

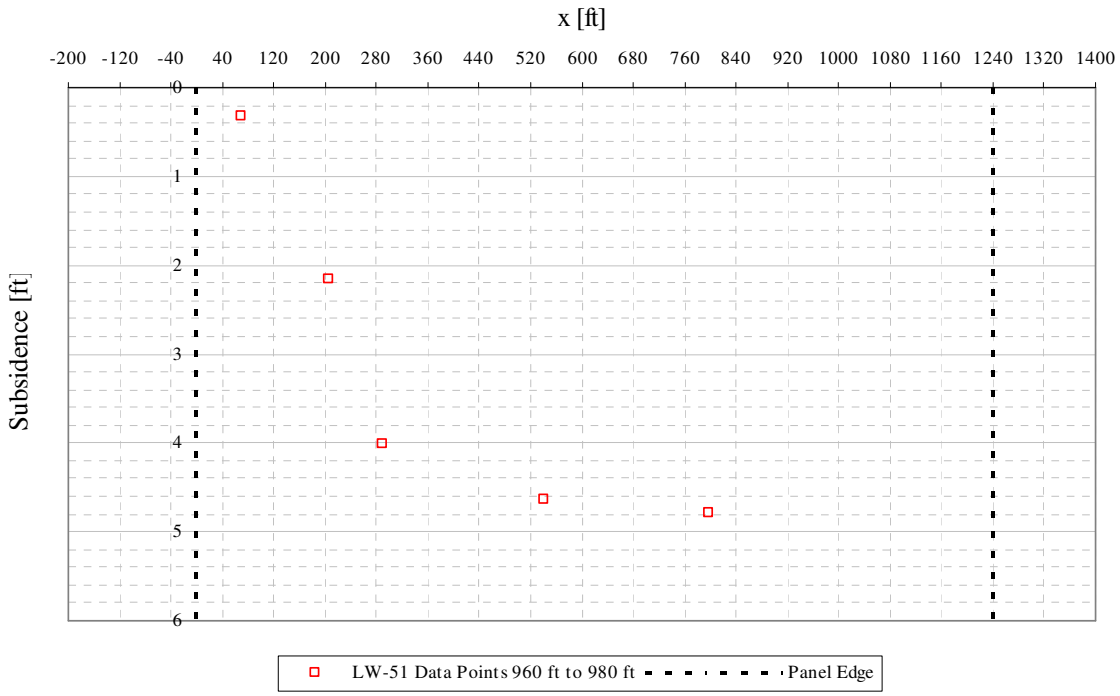

Figure A3- 58 LW-51 transverse view of data points from 960 ft to 980 ft from mine face

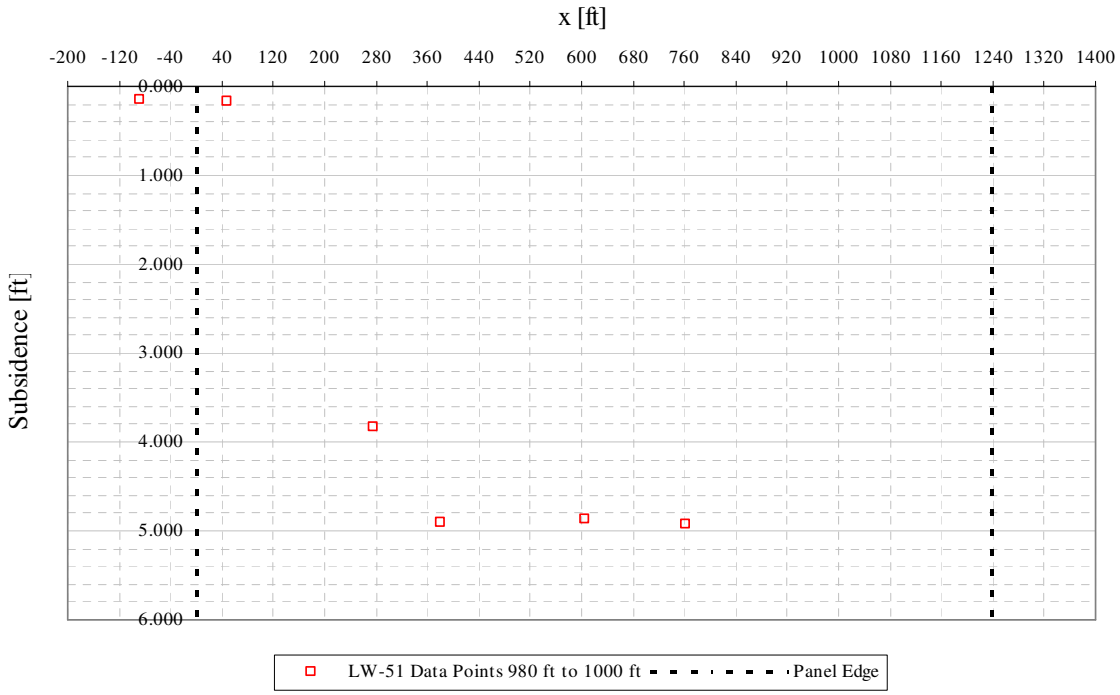

Figure A3- 59 LW-51 transverse view of data points from 980 ft to 1000 ft from mine face

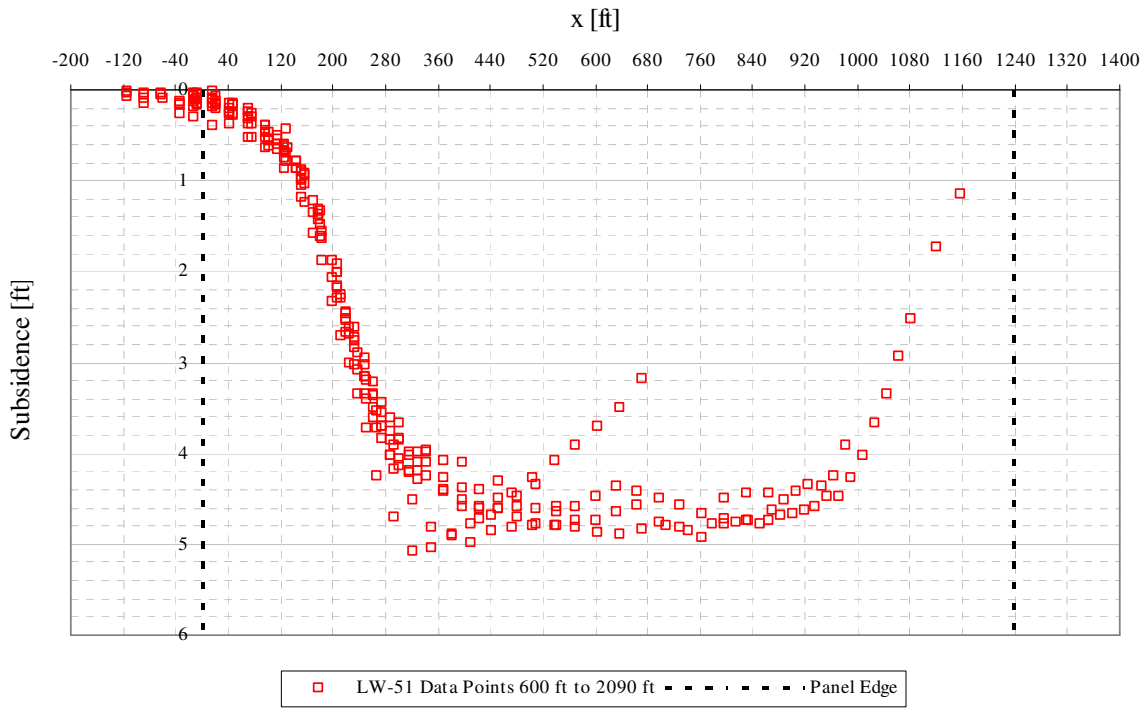

Figure A3- 60 LW-51 transverse view of data points from 600 ft to 2090 ft from mine face

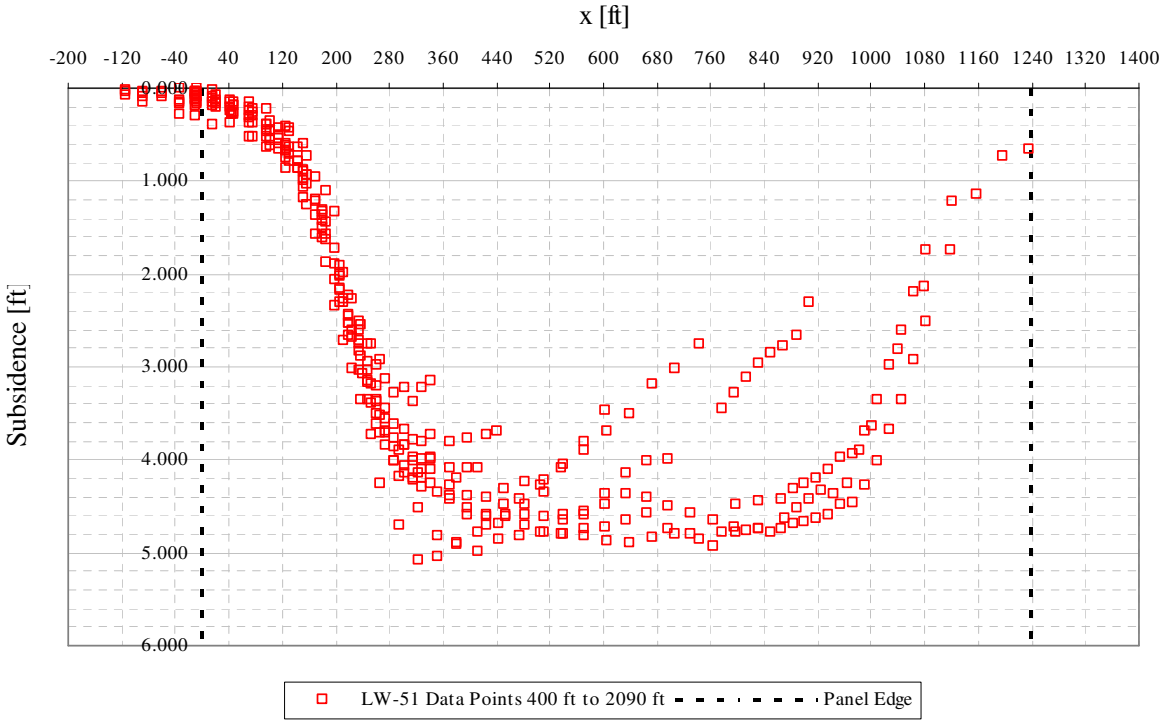

Figure A3- 61 LW-51 transverse view of data points from 400 ft to 2090 ft from mine face

A.4 EMERALD MINE PANEL LW-52 TRANSFORMED DATA

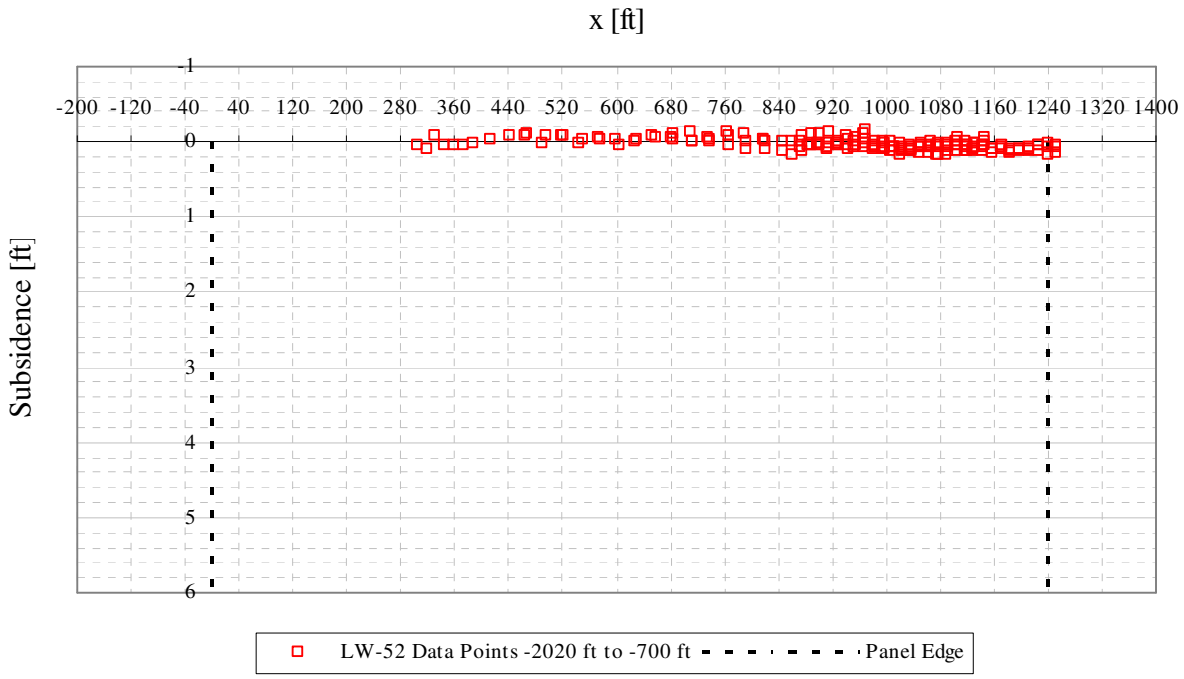

Figure A4- 1 LW-52 transverse view of data points from -2020 ft to -700 ft from mine face

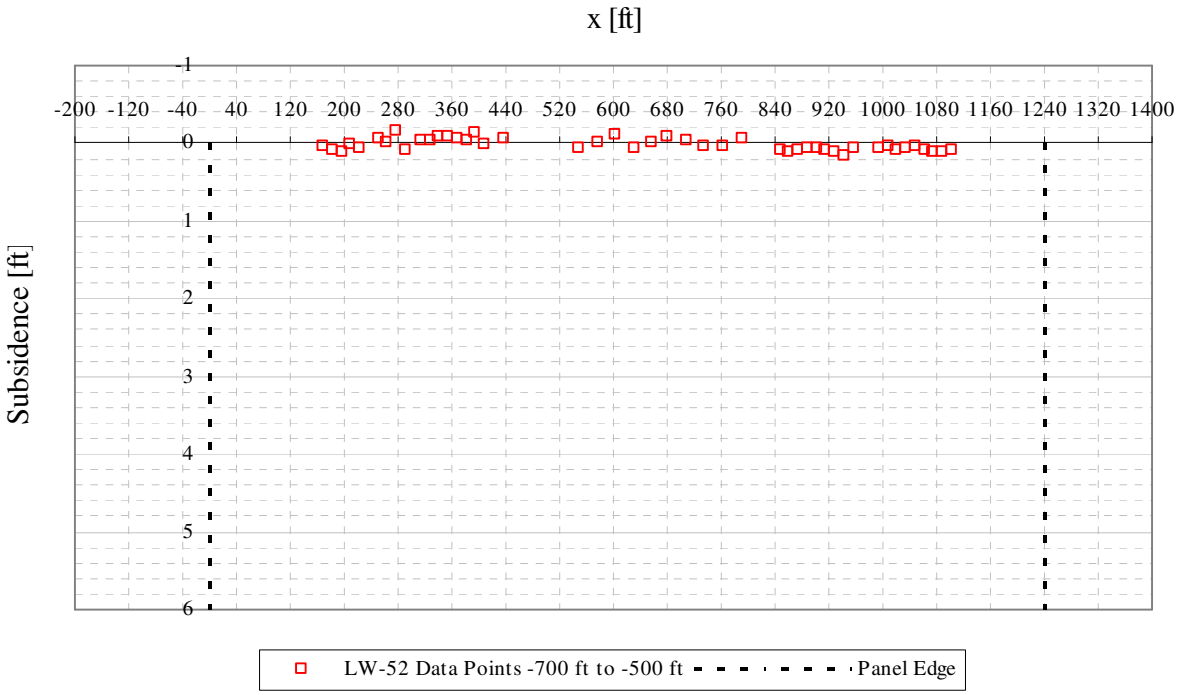

Figure A4- 2 LW-52 transverse view of data points from -700 ft to -500 ft from mine face

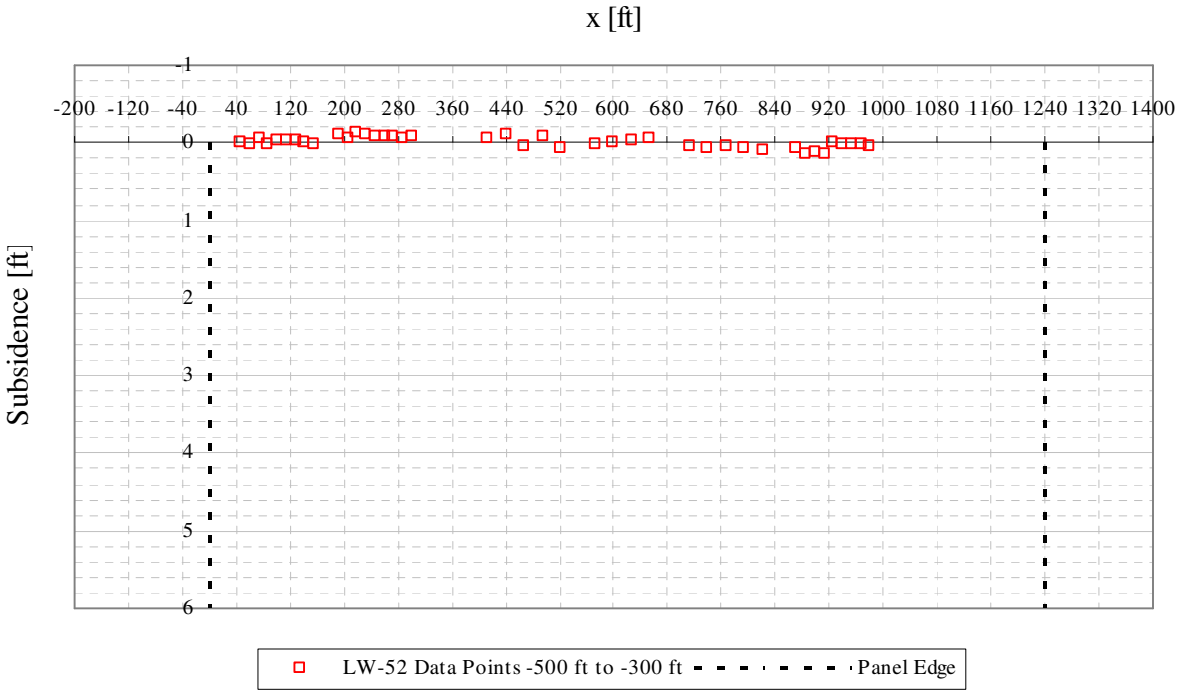

Figure A4- 3 LW-52 transverse view of data points from -500 ft to -300 ft from mine face

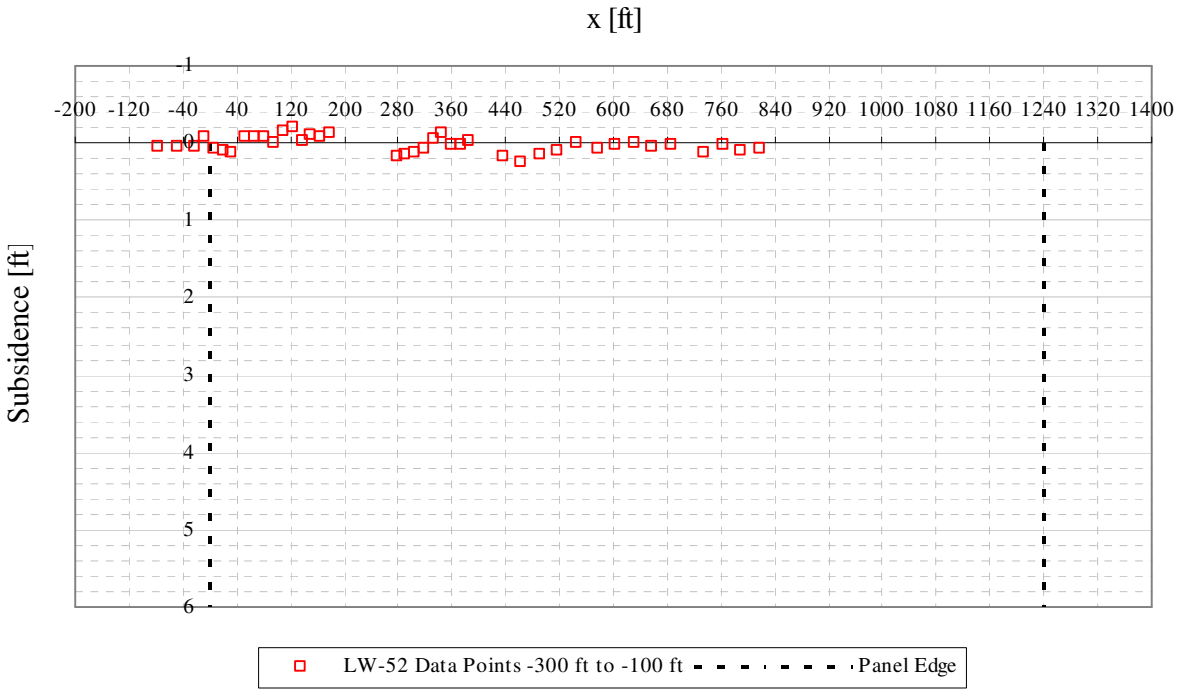

Figure A4- 4 LW-52 transverse view of data points from -300 ft to -100 ft from mine face

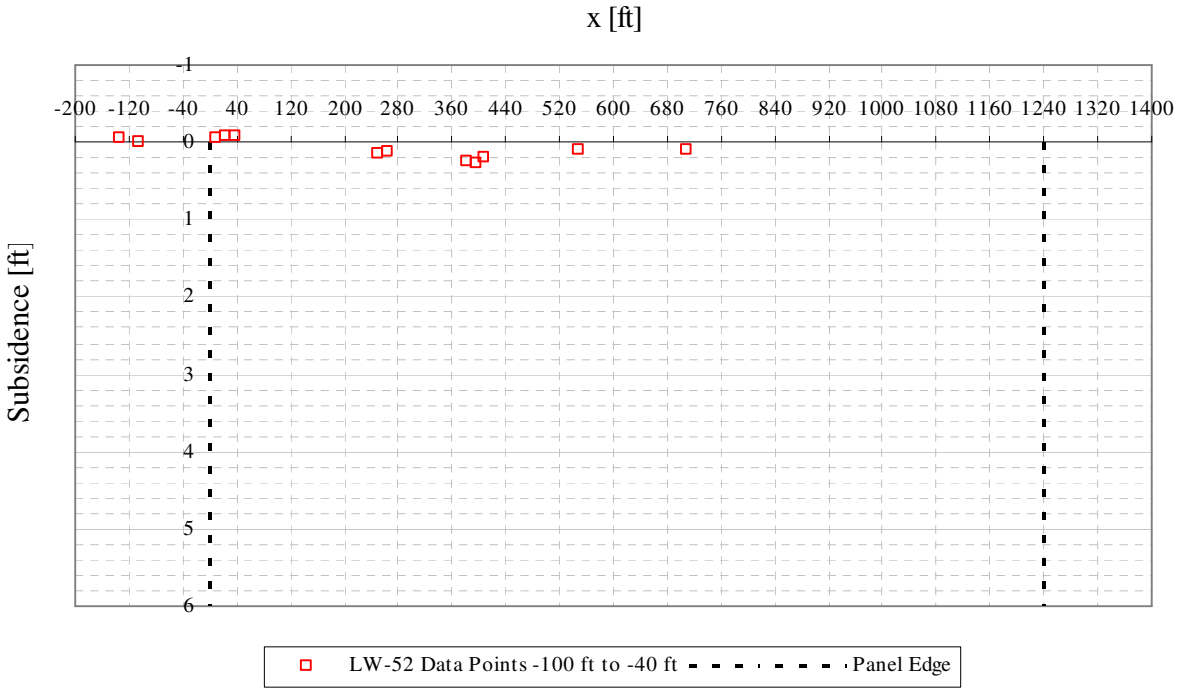

Figure A4- 5 LW-52 transverse view of data points from -100 ft to -40 ft from mine face

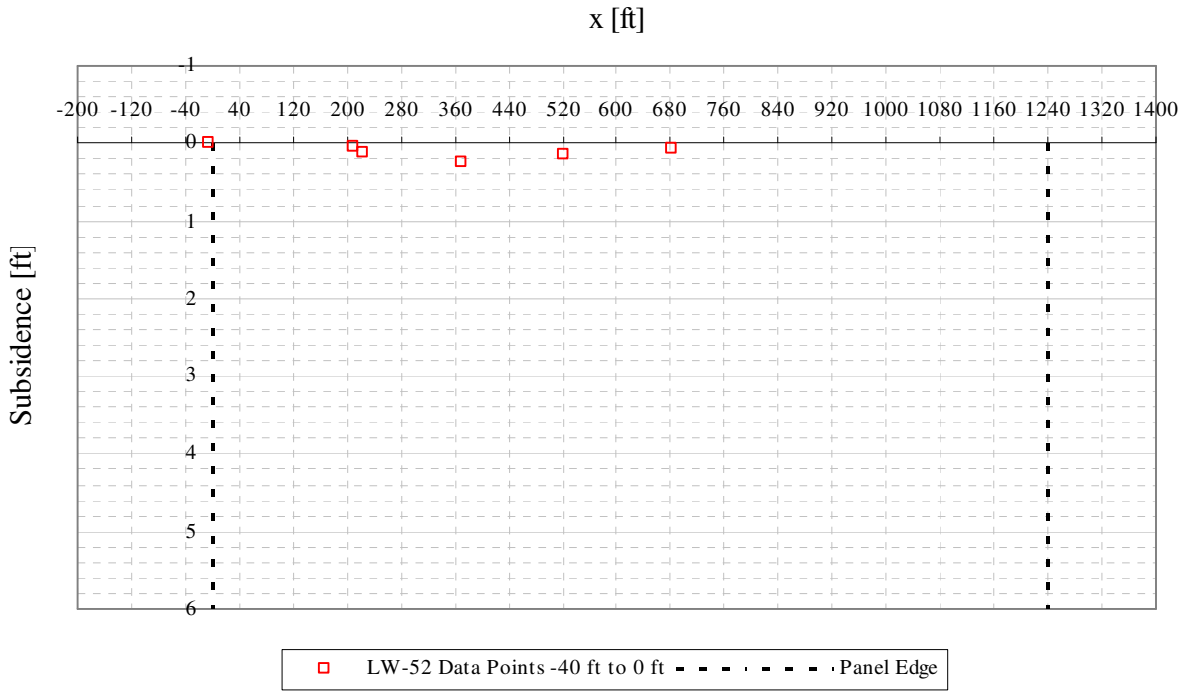

Figure A4- 6 LW-52 transverse view of data points from -40 ft to 0 ft from mine face

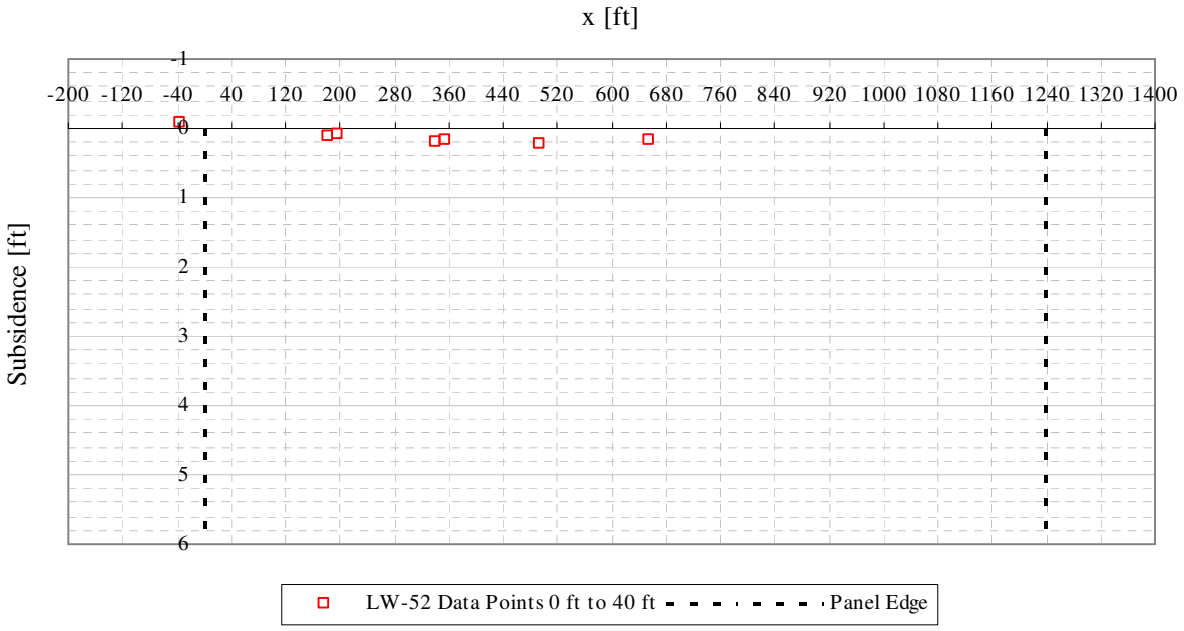

Figure A4- 7 LW-52 transverse view of data points from 0 ft to 40 ft from mine face

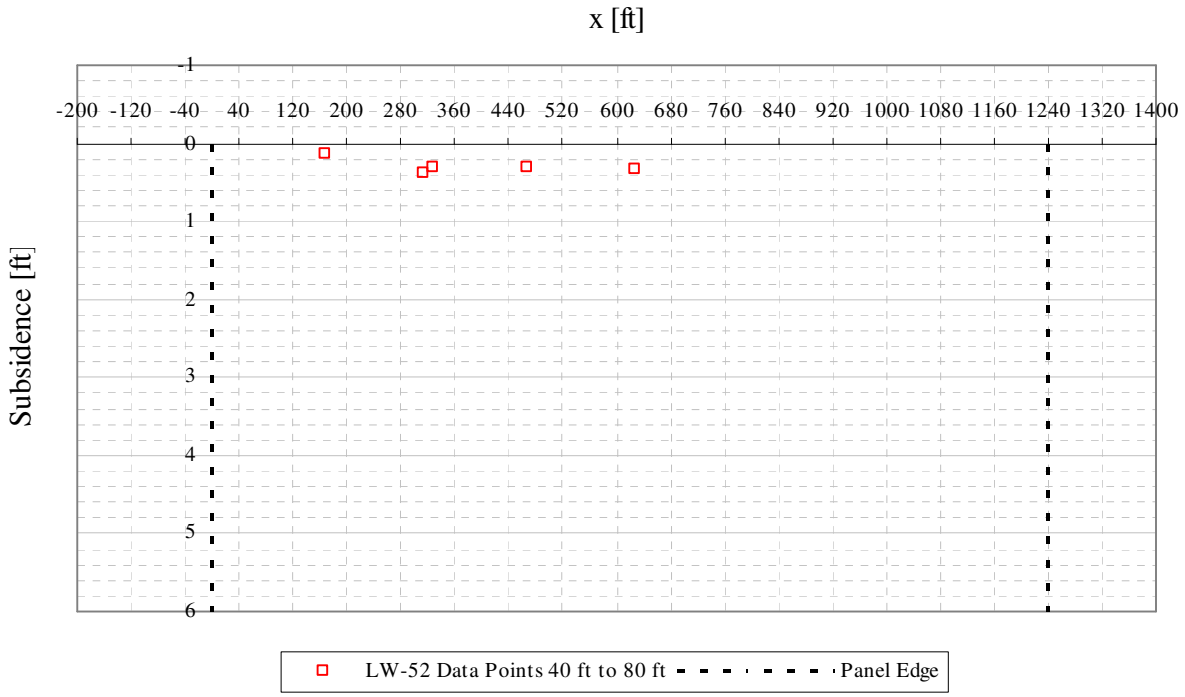

Figure A4- 8 LW-52 transverse view of data points from 40 ft to 80 ft from mine face

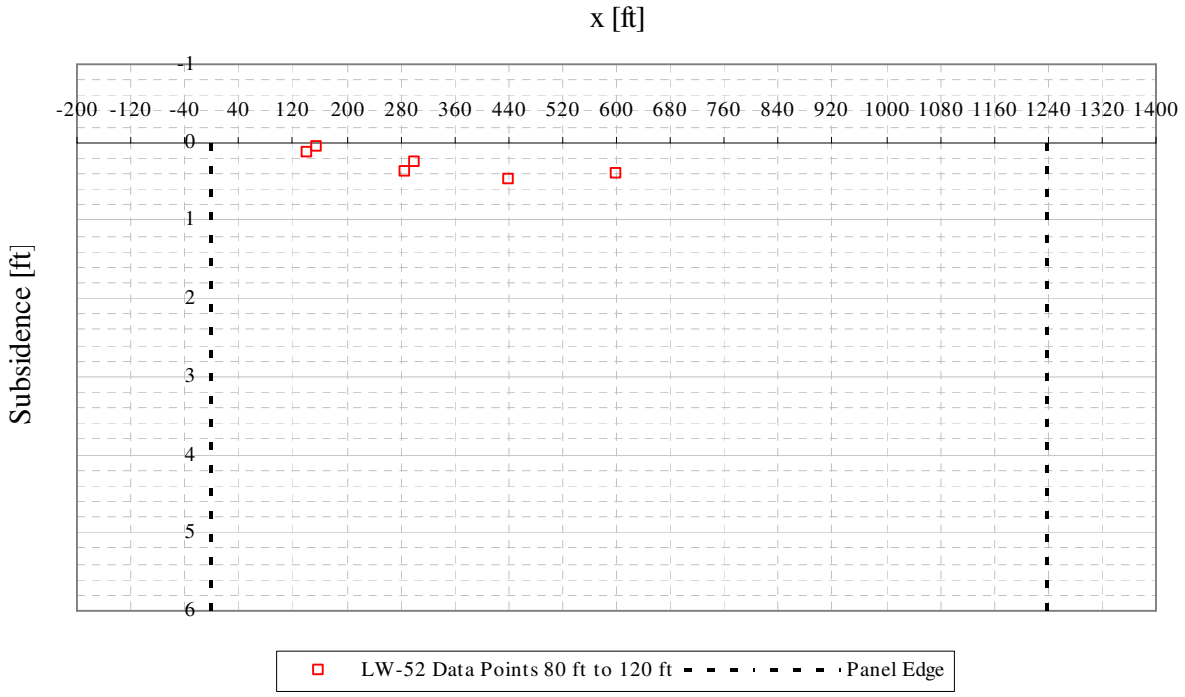

Figure A4- 9 LW-52 transverse view of data points from 80 ft to 120 ft from mine face

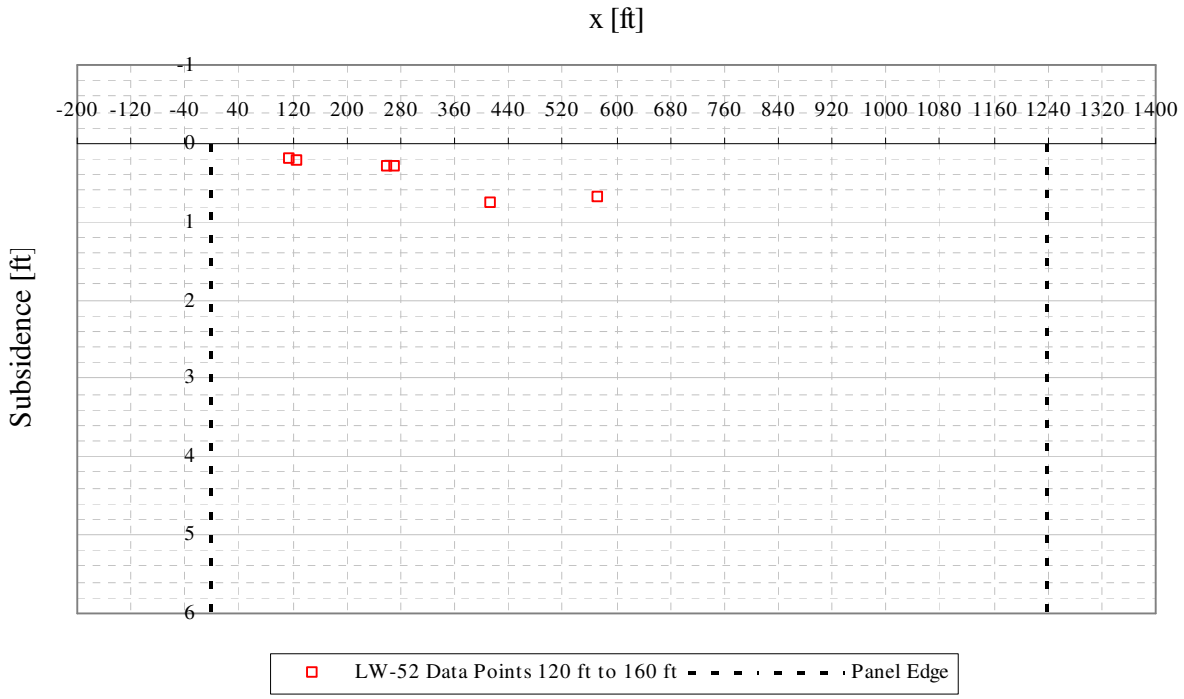

Figure A4- 10 LW-52 transverse view of data points from 120 ft to 160 ft from mine face

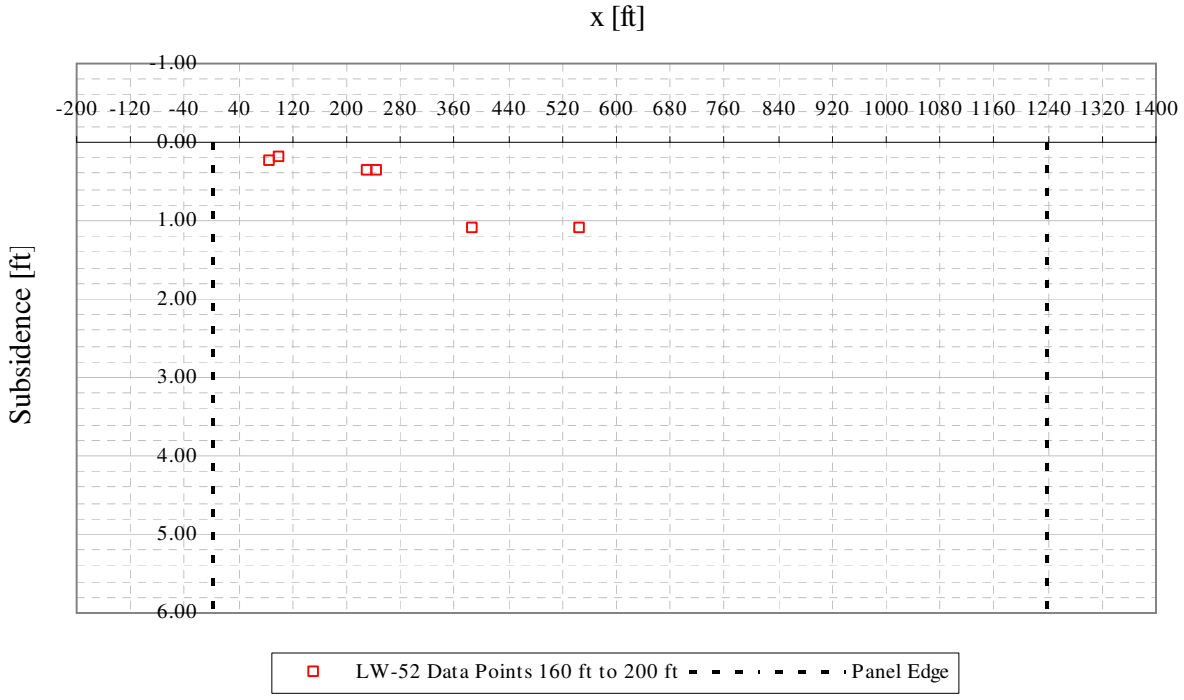

Figure A4- 11 LW-52 transverse view of data points from 160 ft to 200 ft from mine face

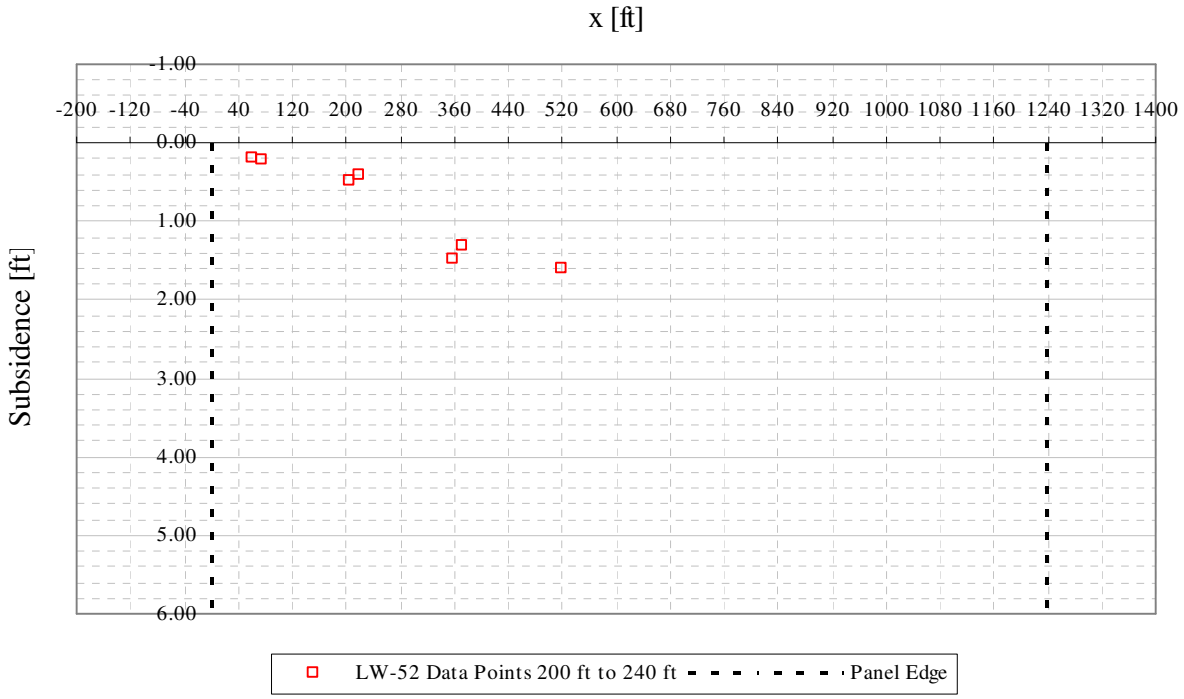

Figure A4- 12 LW-52 transverse view of data points from 200 ft to 240 ft from mine face

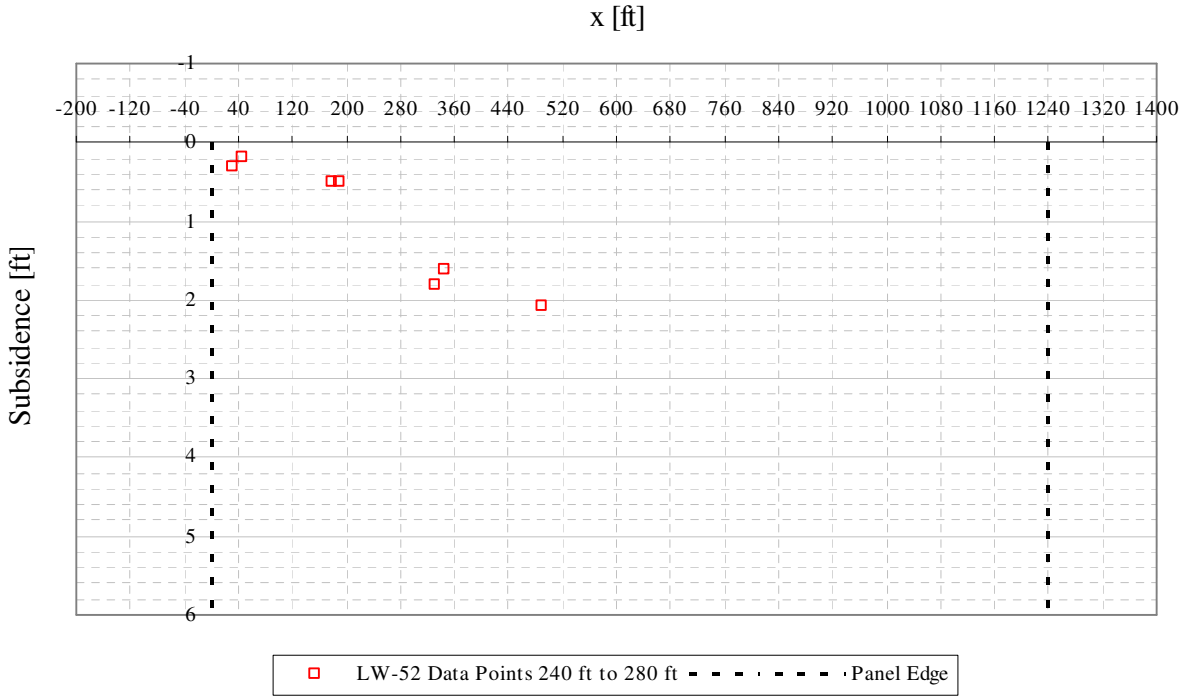

Figure A4- 13 LW-52 transverse view of data points from 240 ft to 280 ft from mine face

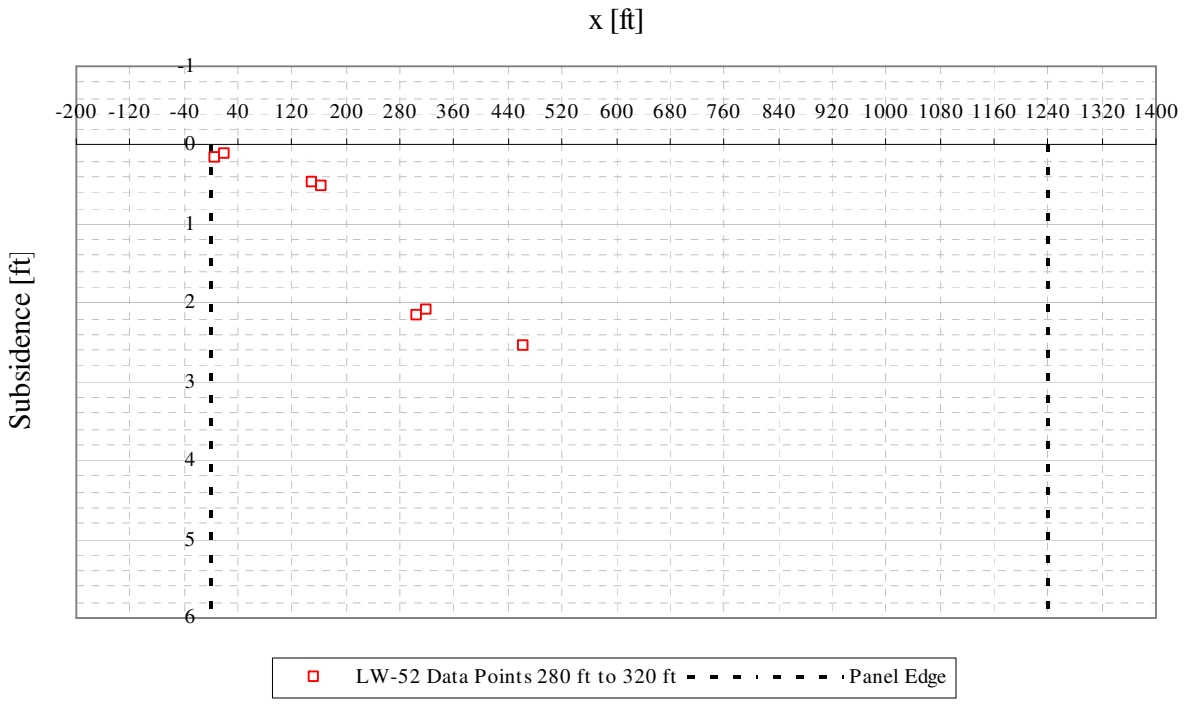

Figure A4- 14 LW-52 transverse view of data points from 280 ft to 320 ft from mine face

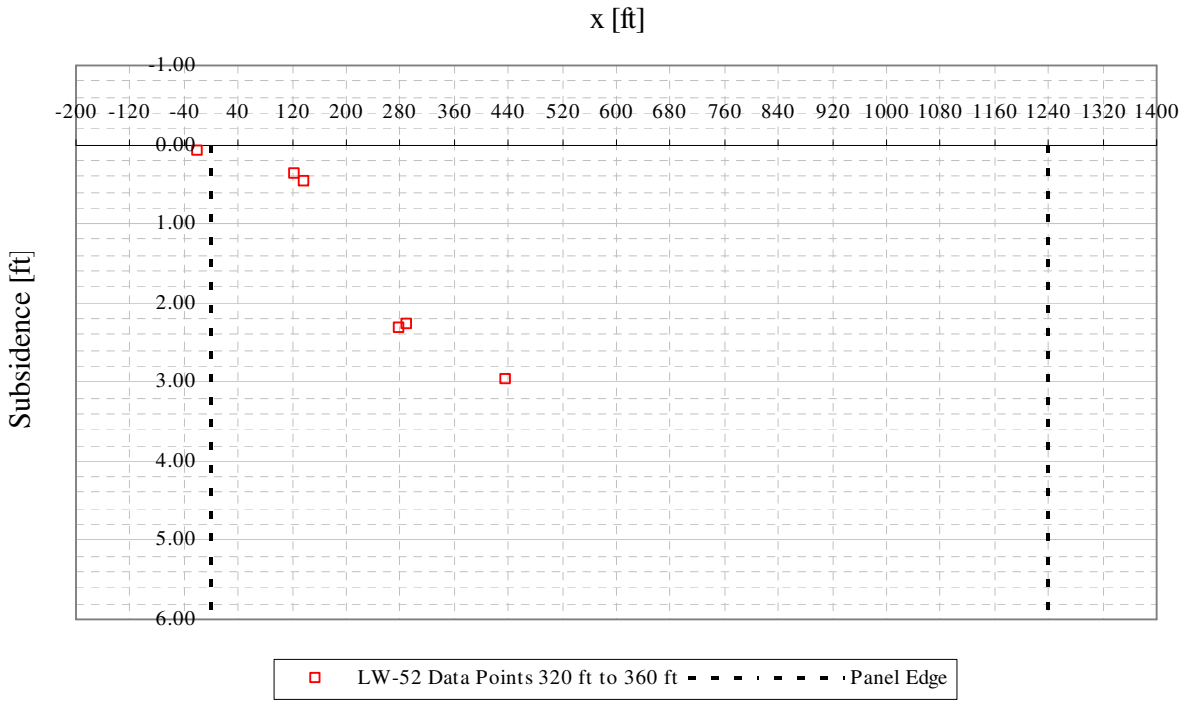

Figure A4- 15 LW-52 transverse view of data points from 320 ft to 360 ft from mine face

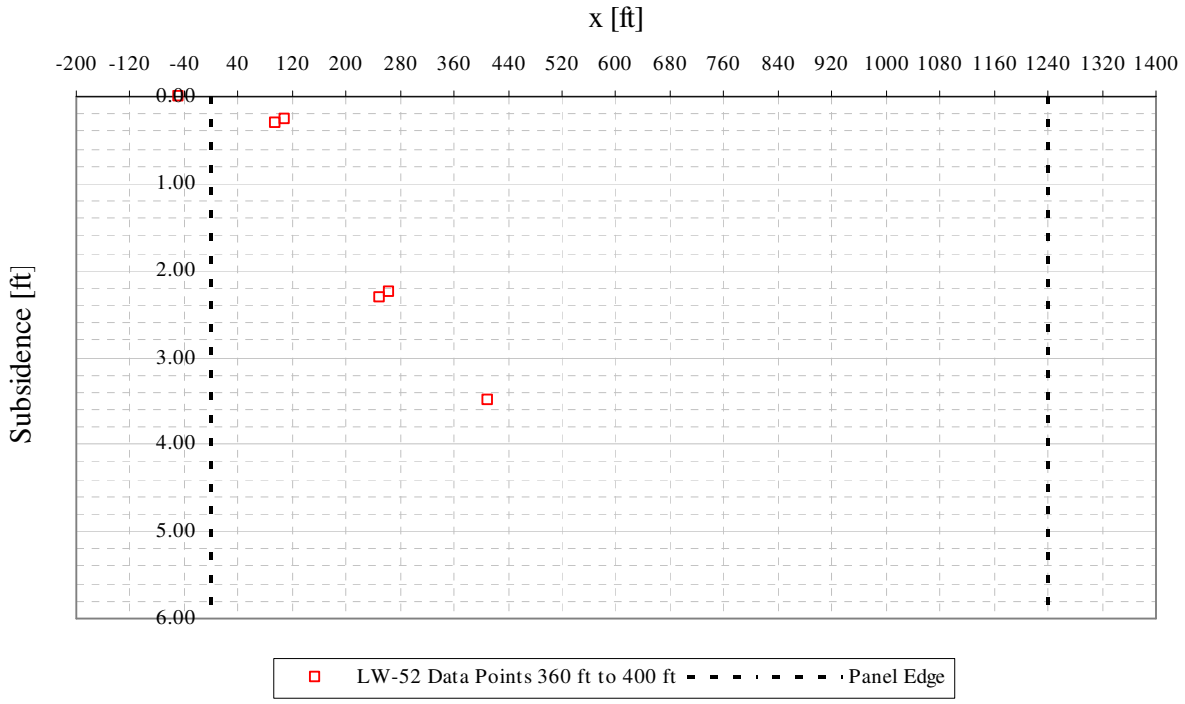

Figure A4- 16 LW-52 transverse view of data points from 360 ft to 400 ft from mine face

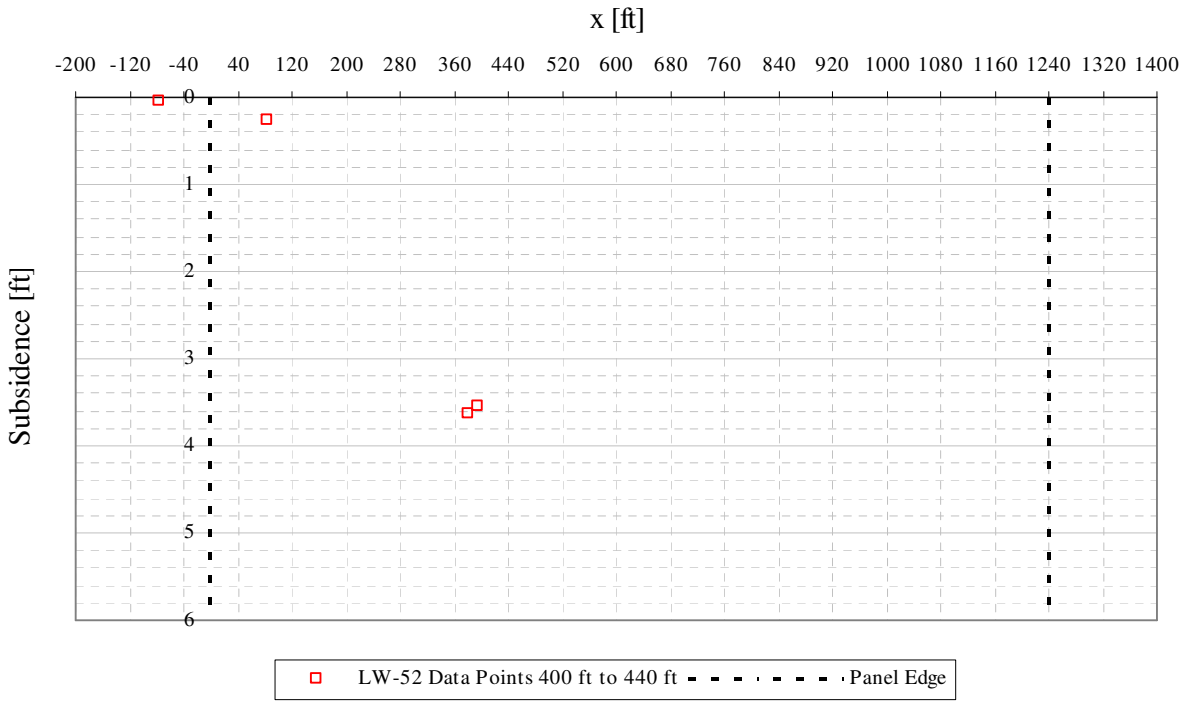

Figure A4- 17 LW-52 transverse view of data points from 400 ft to 440 ft from mine face

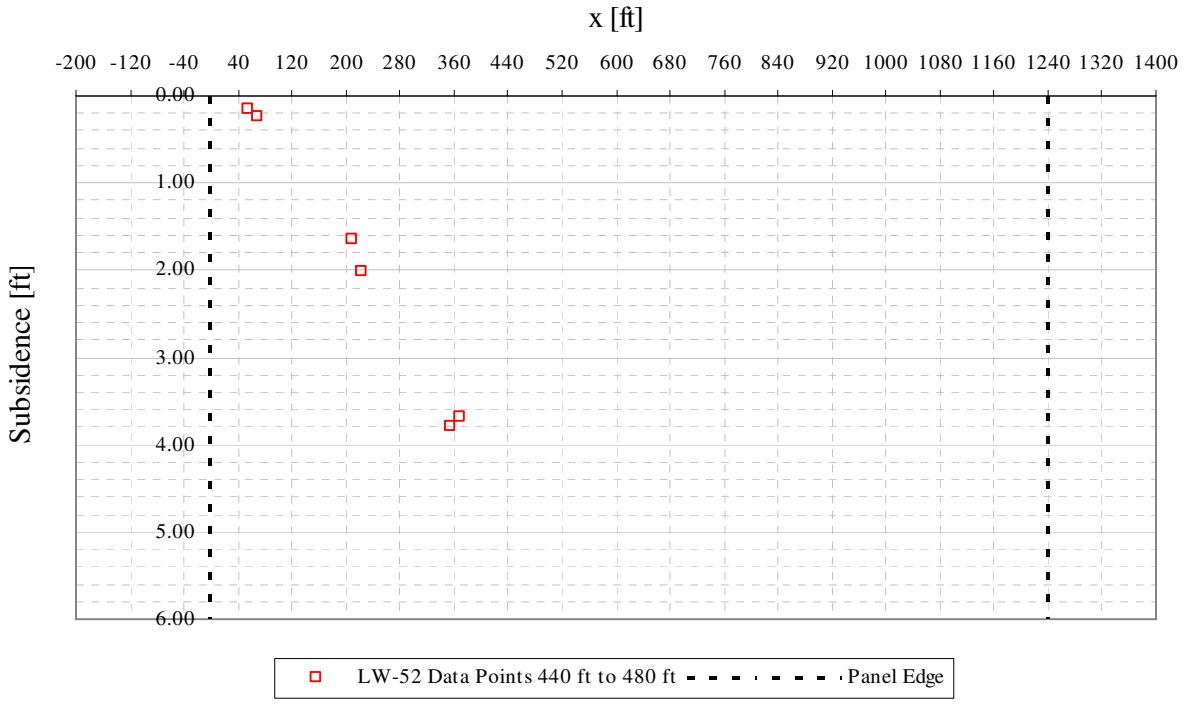

Figure A4- 18 LW-52 transverse view of data points from 440 ft to 480 ft from mine face

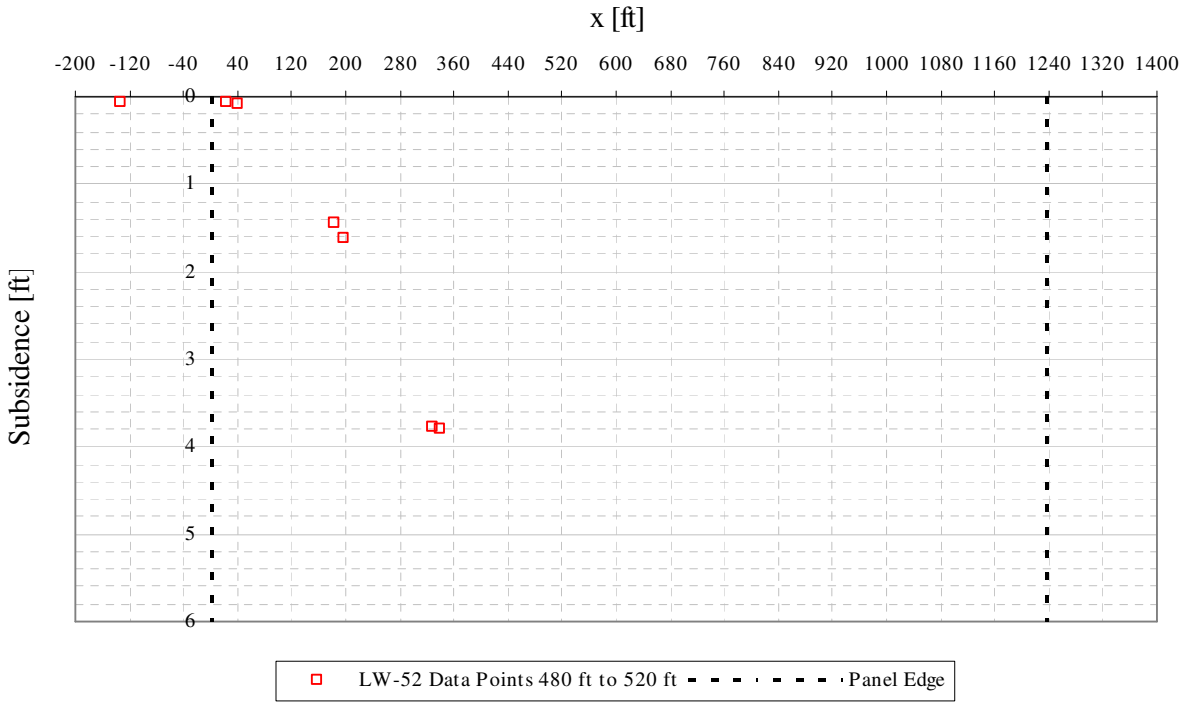

Figure A4- 19 LW-52 transverse view of data points from 480 ft to 520 ft from mine face

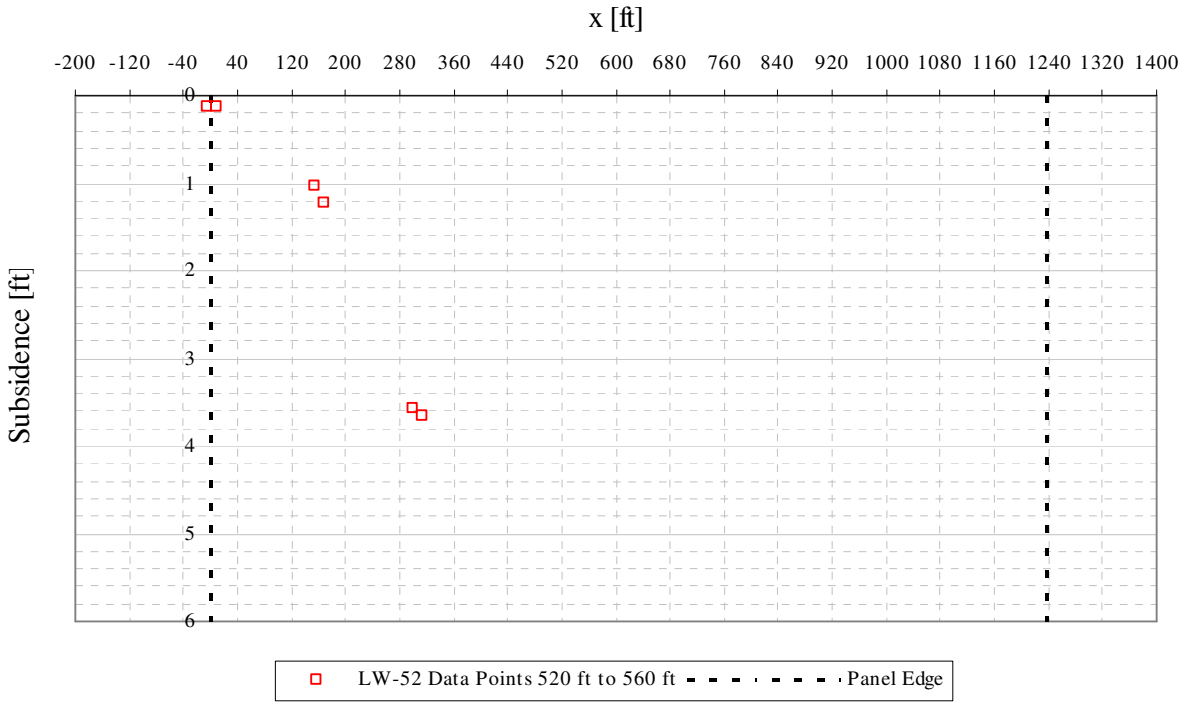

Figure A4- 20 LW-52 transverse view of data points from 520 ft to 560 ft from mine face

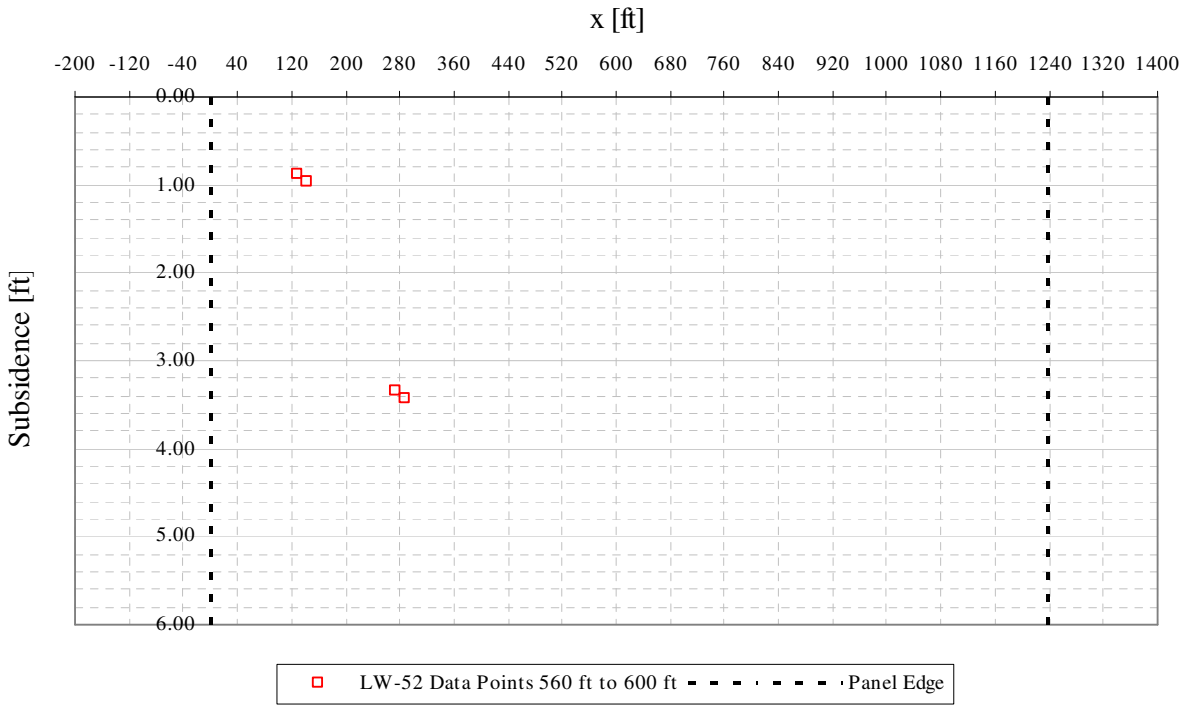

Figure A4- 21 LW-52 transverse view of data points from 560 ft to 600 ft from mine face

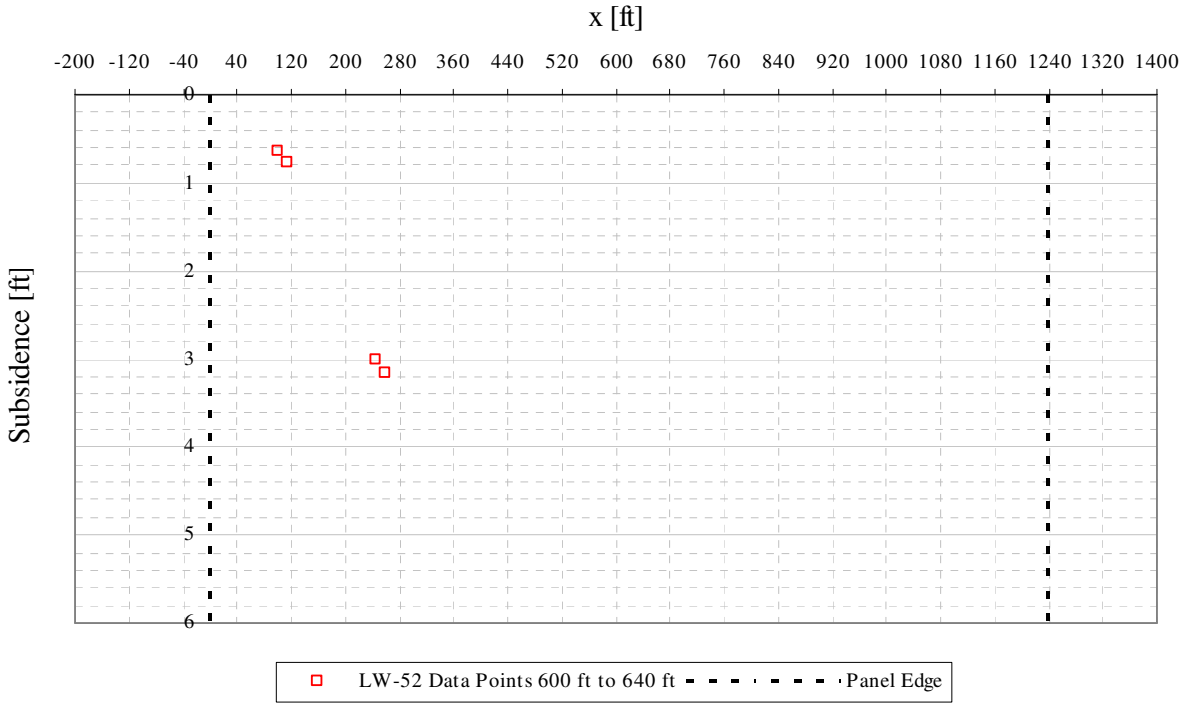

Figure A4- 22 LW-52 transverse view of data points from 600 ft to 640 ft from mine face

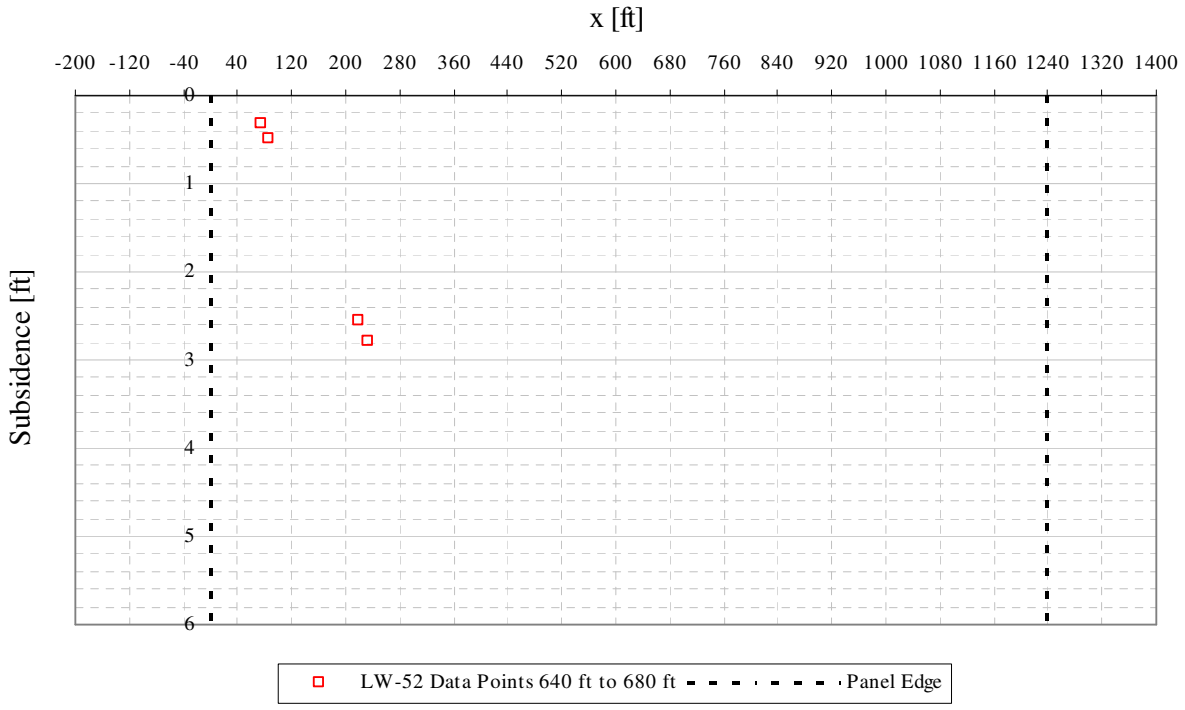

Figure A4- 23 LW-52 transverse view of data points from 640 ft to 680 ft from mine face

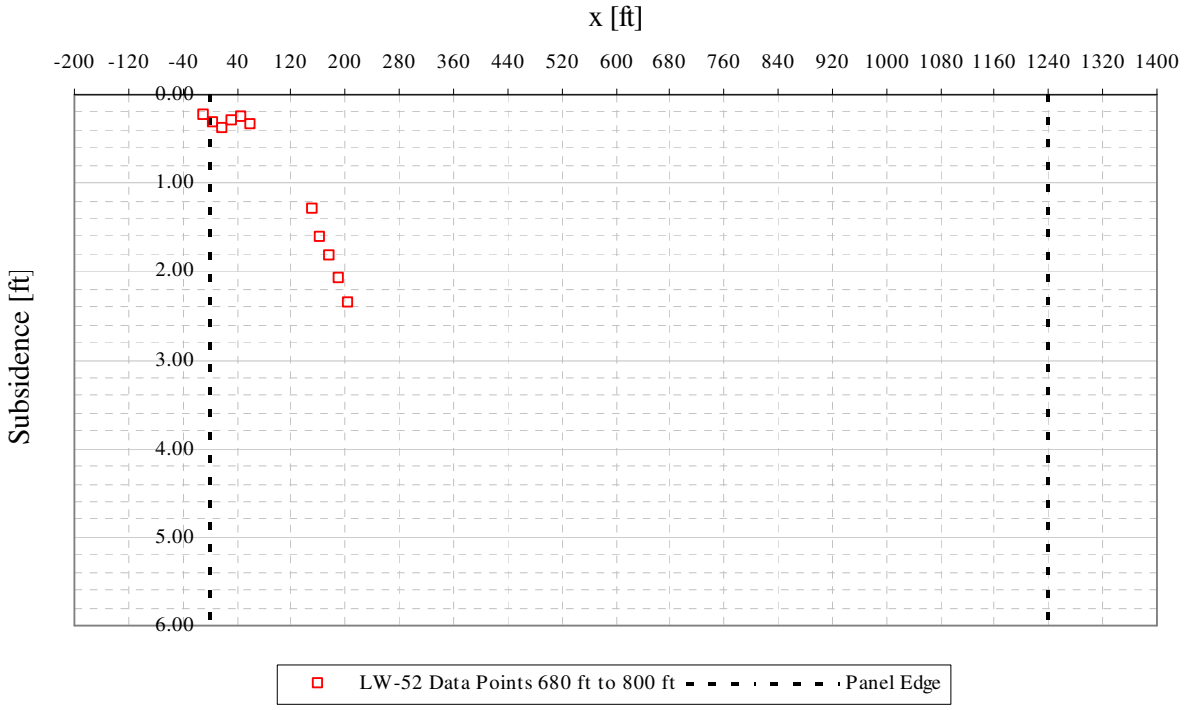

Figure A4- 24 LW-52 transverse view of data points from 680 ft to 800 ft from mine face

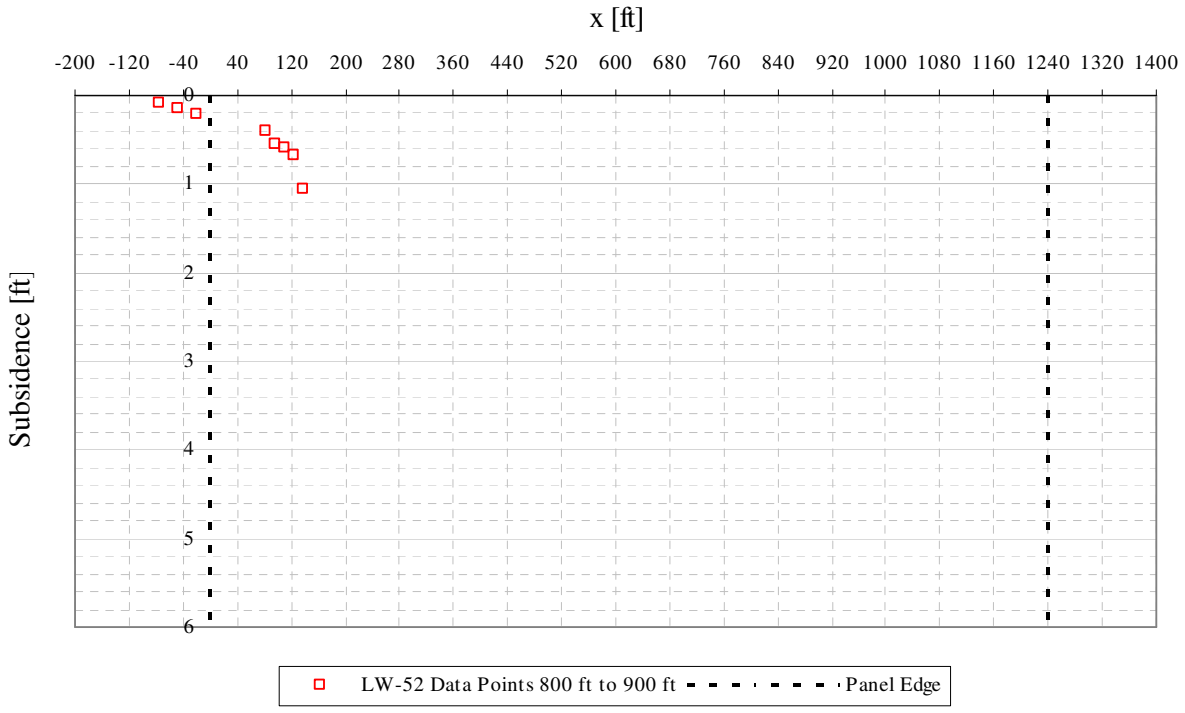

Figure A4- 25 LW-52 transverse view of data points from 800 ft to 900 ft from mine face

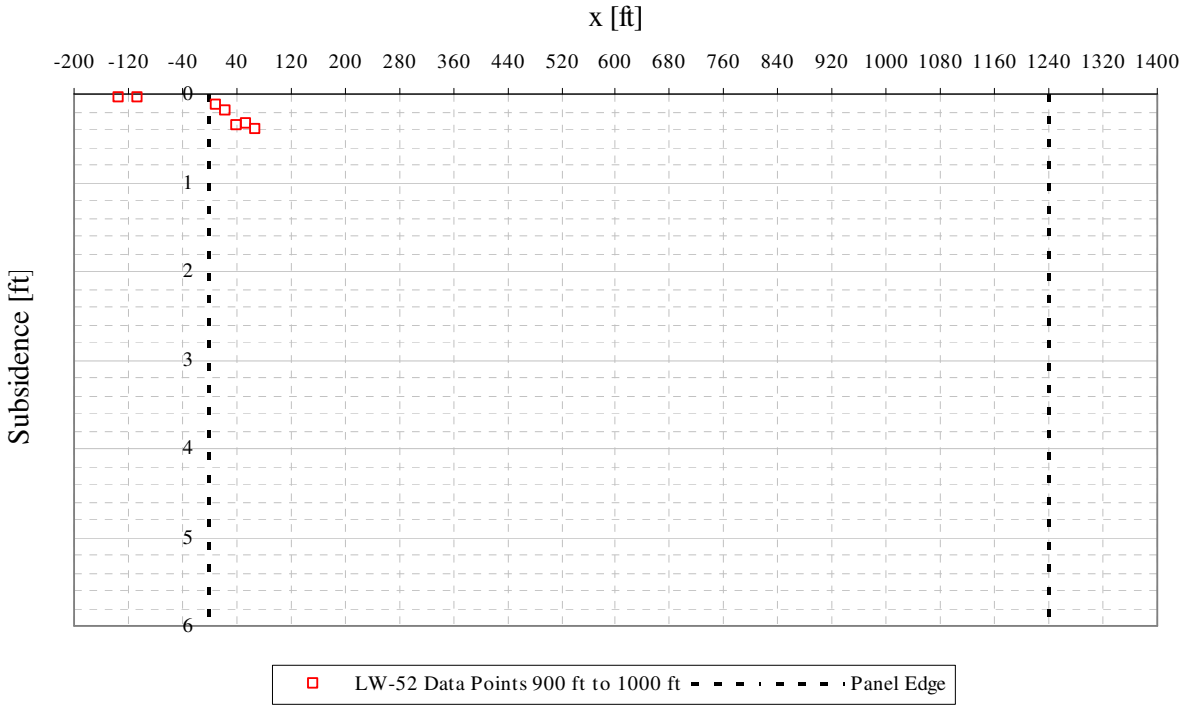

Figure A4- 26 LW-52 transverse view of data points from 900 ft to 1000 ft from mine face

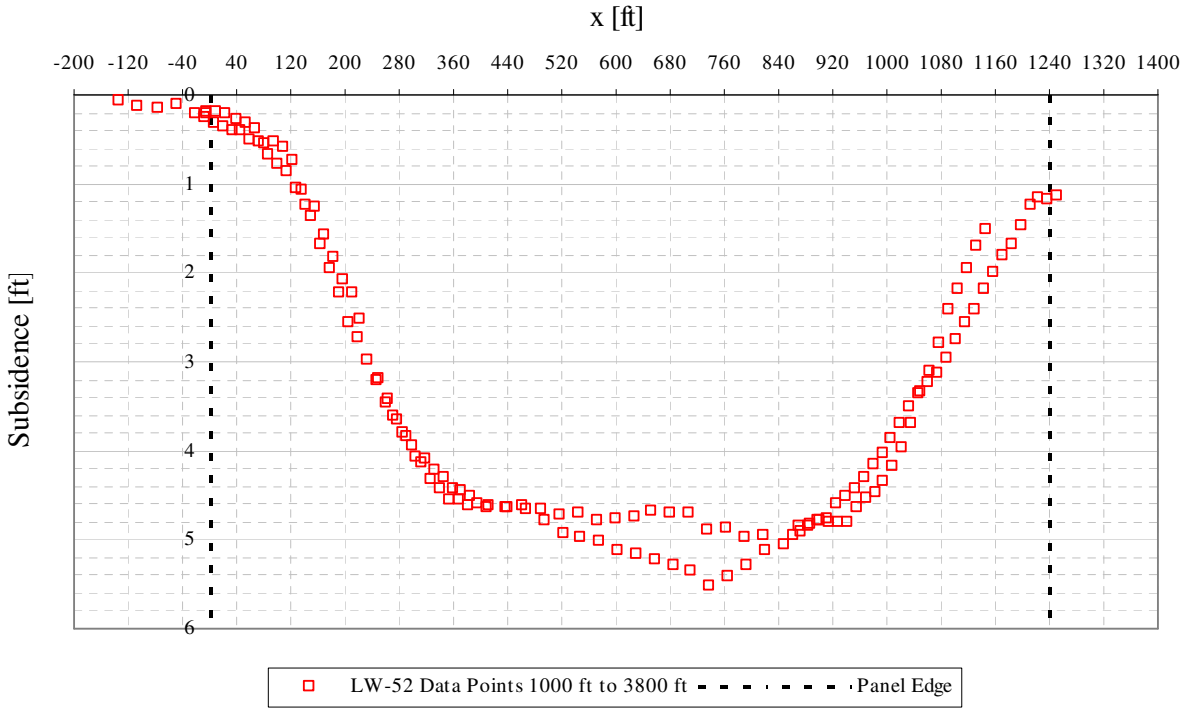

Figure A4- 27 LW-52 transverse view of data points from 1000 ft to 3800 ft from mine face

A.5 EMERALD MINE PANEL LW-49 SDPS INFLUENCE FUNCTION PREDICTION

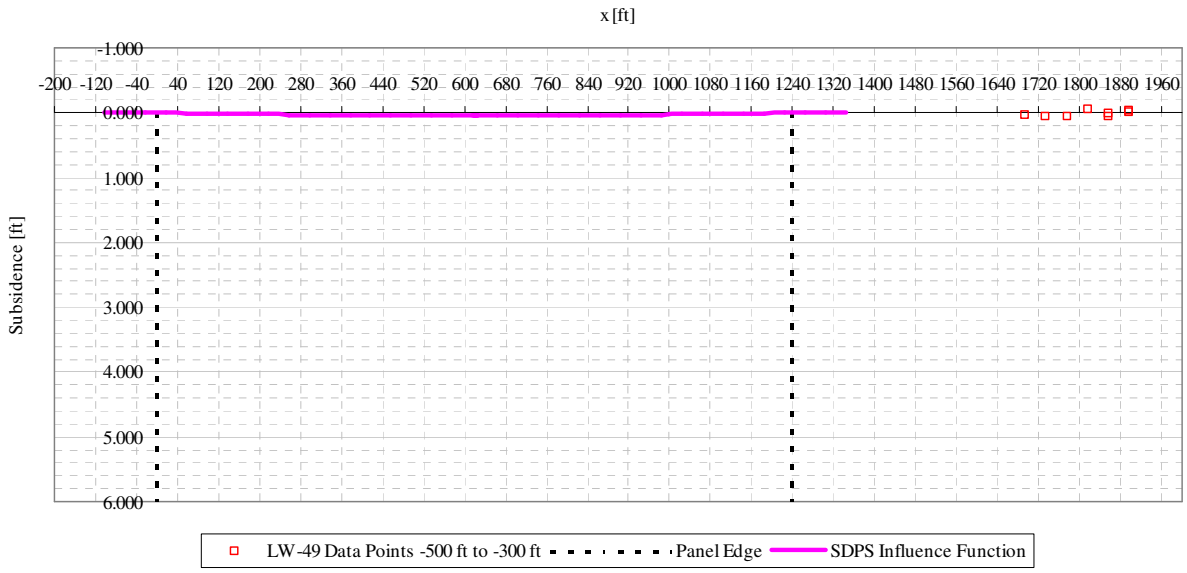

Figure A5- 1 LW-49 transverse view of data points from -500 ft to -300 ft from mine face and SDPS prediction

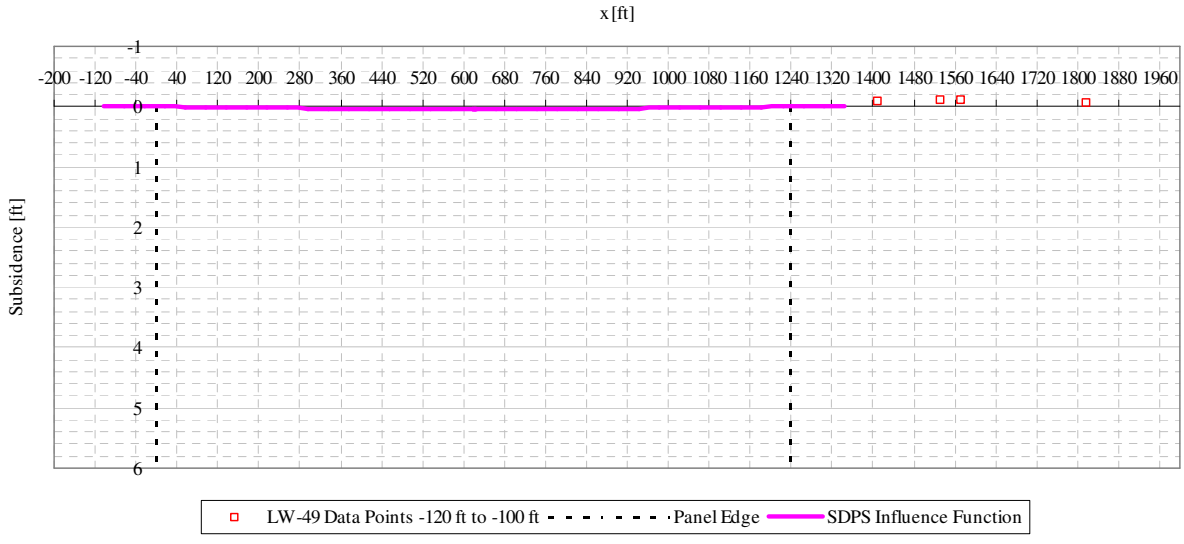

Figure A5- 2 LW-49 transverse view of data points from -120 ft to -100 ft from mine face and SDPS prediction

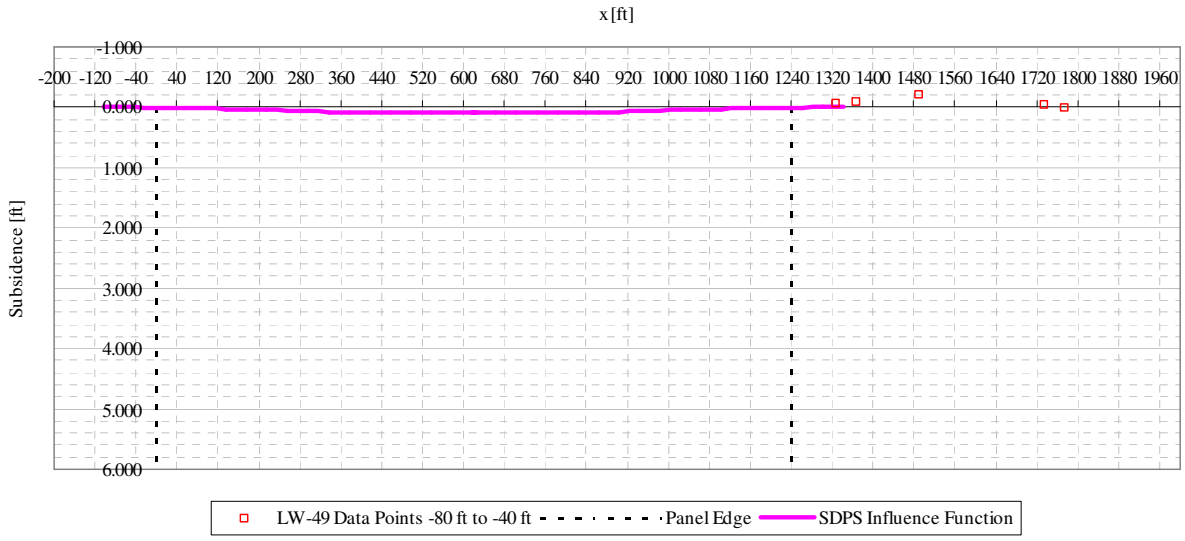

Figure A5- 3 LW-49 transverse view of data points from -80 ft to -40 ft from mine face and SDPS prediction

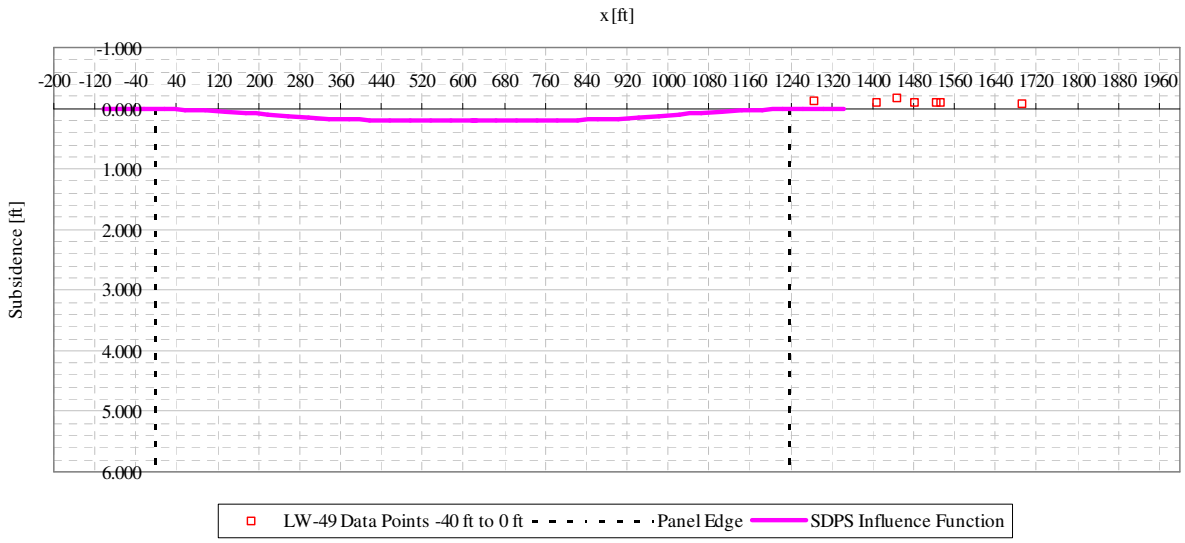

Figure A5- 4 LW-49 transverse view of data points from -40 ft to 0 ft from mine face and SDPS prediction

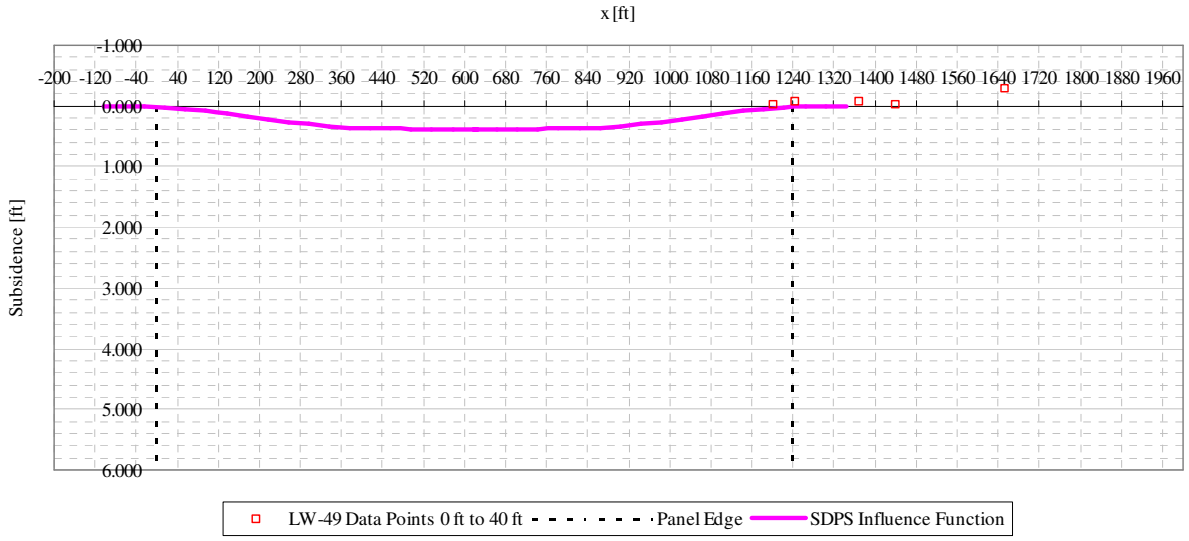

Figure A5- 5 LW-49 transverse view of data points from 0 ft to 40 ft from mine face and SDPS prediction

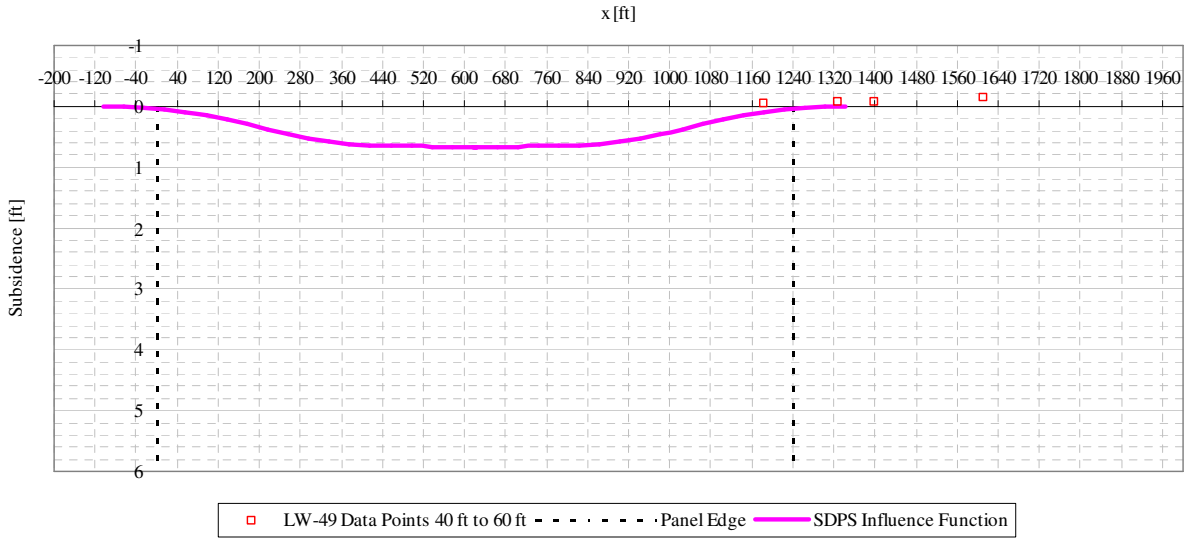

Figure A5- 6 LW-49 transverse view of data points from 40 ft to 60 ft from mine face and SDPS prediction

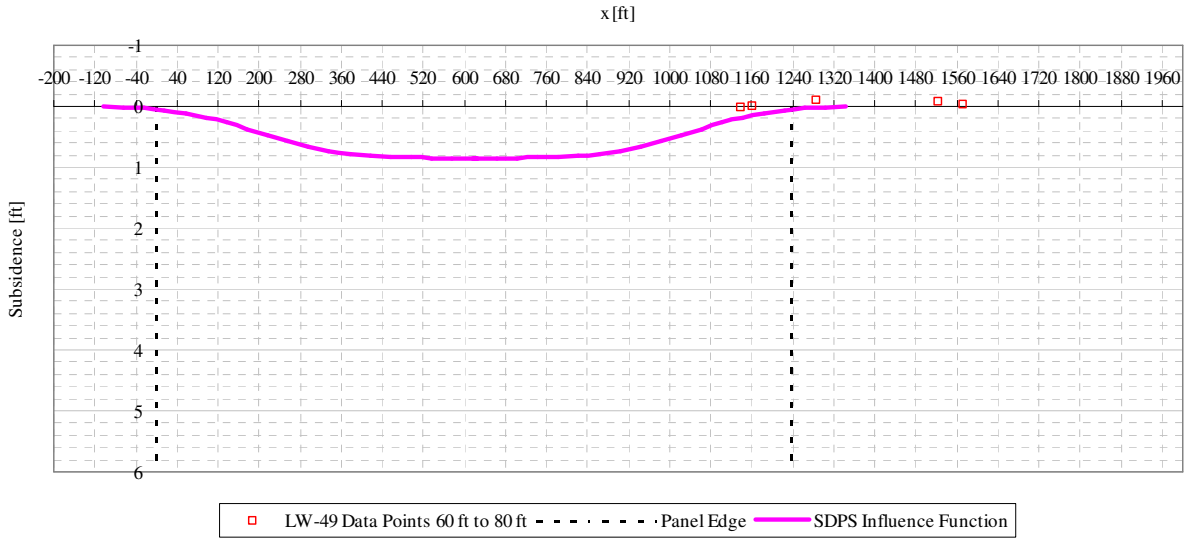

Figure A5- 7 LW-49 transverse view of data points from 60 ft to 80 ft from mine face and SDPS prediction

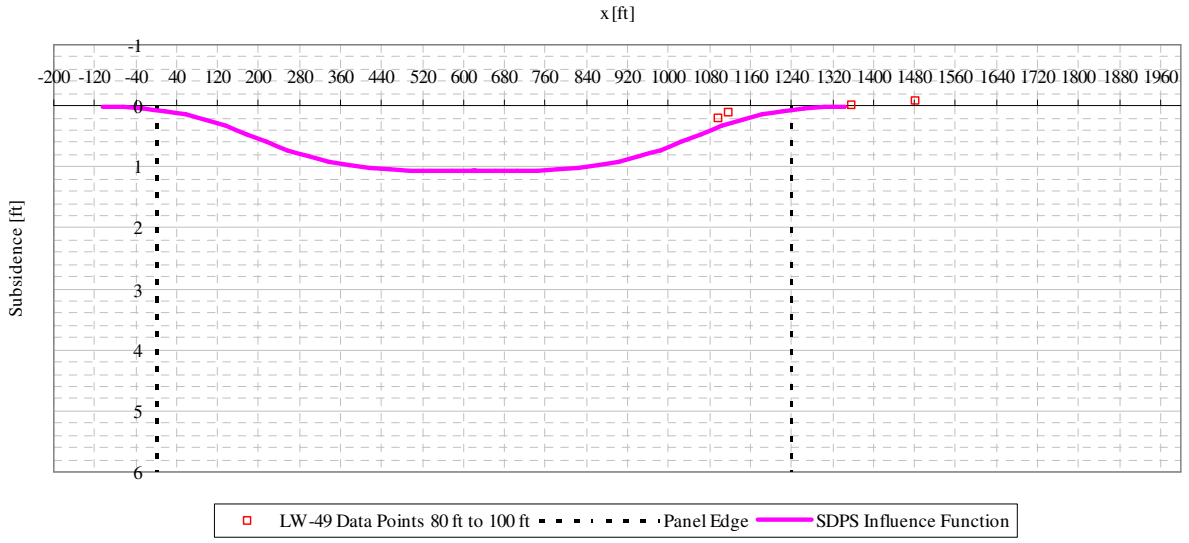

Figure A5- 8 LW-49 transverse view of data points from 80 ft to 100 ft from mine face and SDPS prediction

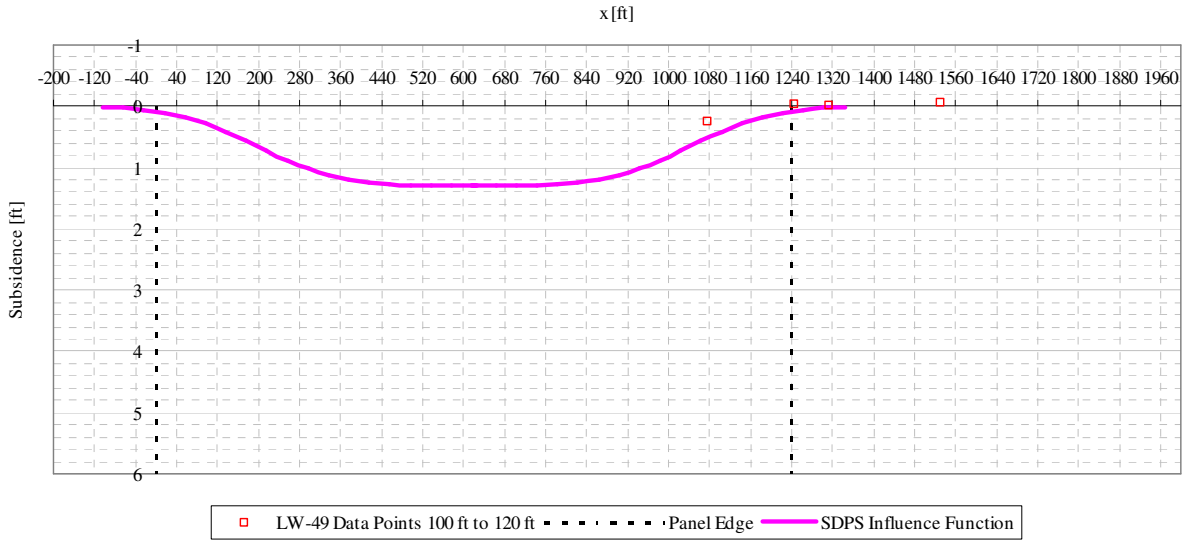

Figure A5- 9 LW-49 transverse view of data points from 100 ft to 120 ft from mine face and SDPS prediction

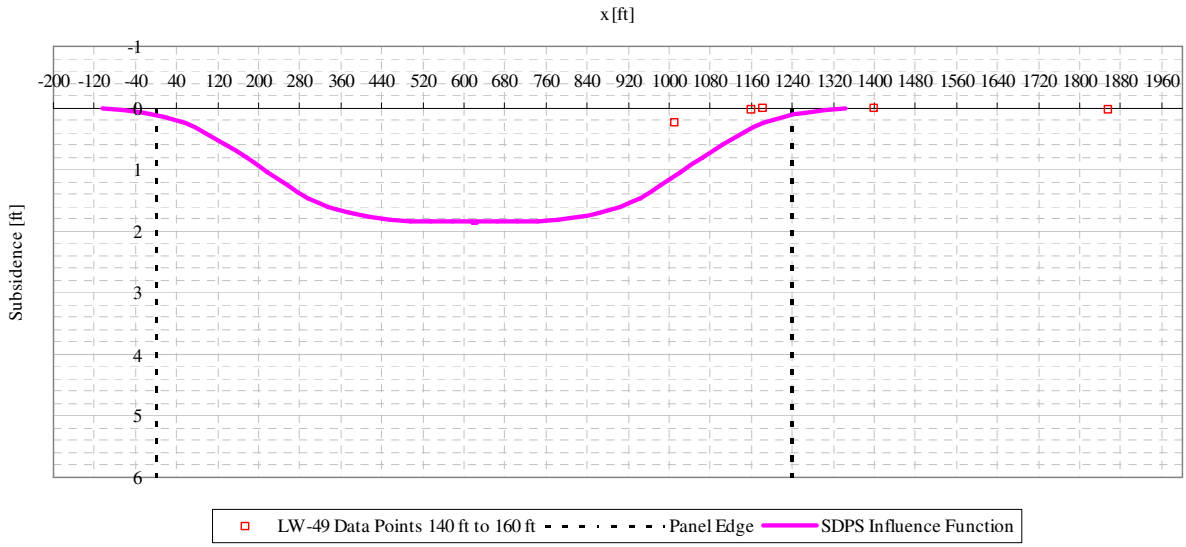

Figure A5- 10 LW-49 transverse view of data points from 140 ft to 160 ft from mine face and SDPS prediction

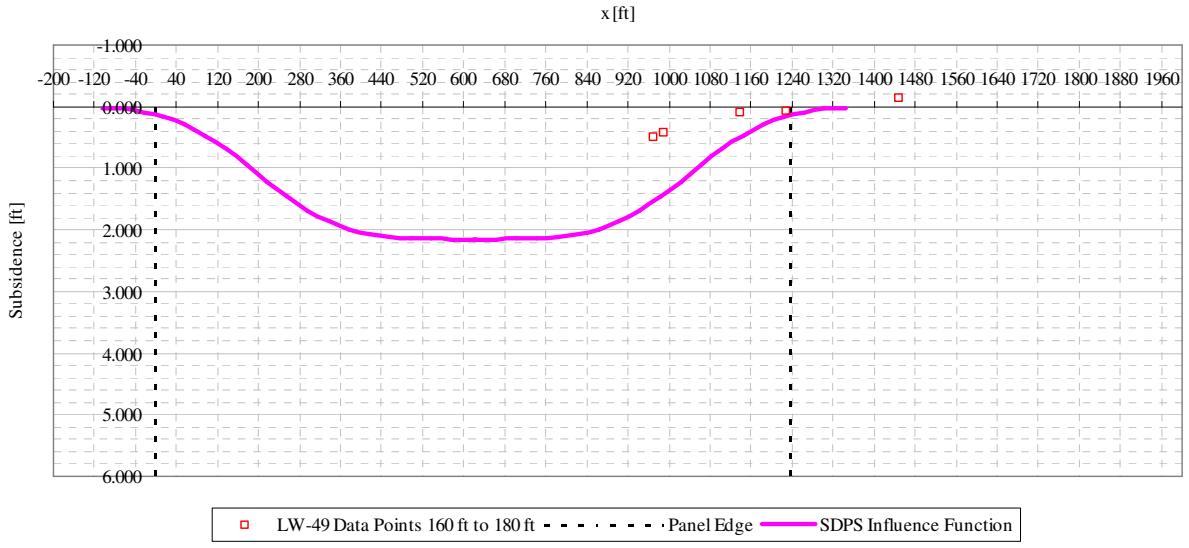

Figure A5- 11 LW-49 transverse view of data points from 160 ft to180 ft from mine face and SDPS prediction

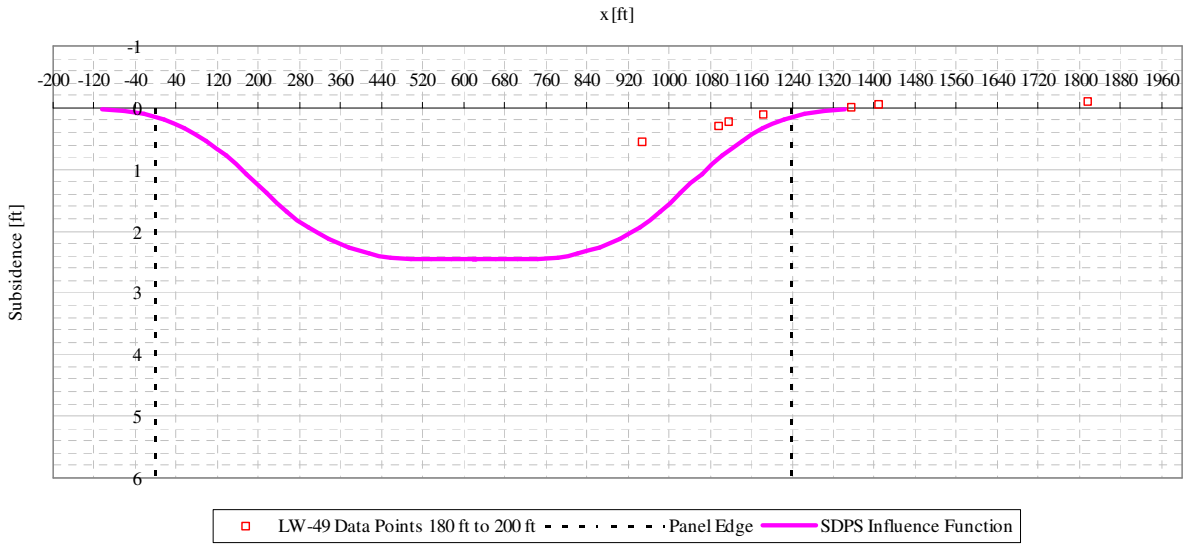

Figure A5- 12 LW-49 transverse view of data points from 180 ft to 200 ft from mine face and SDPS prediction

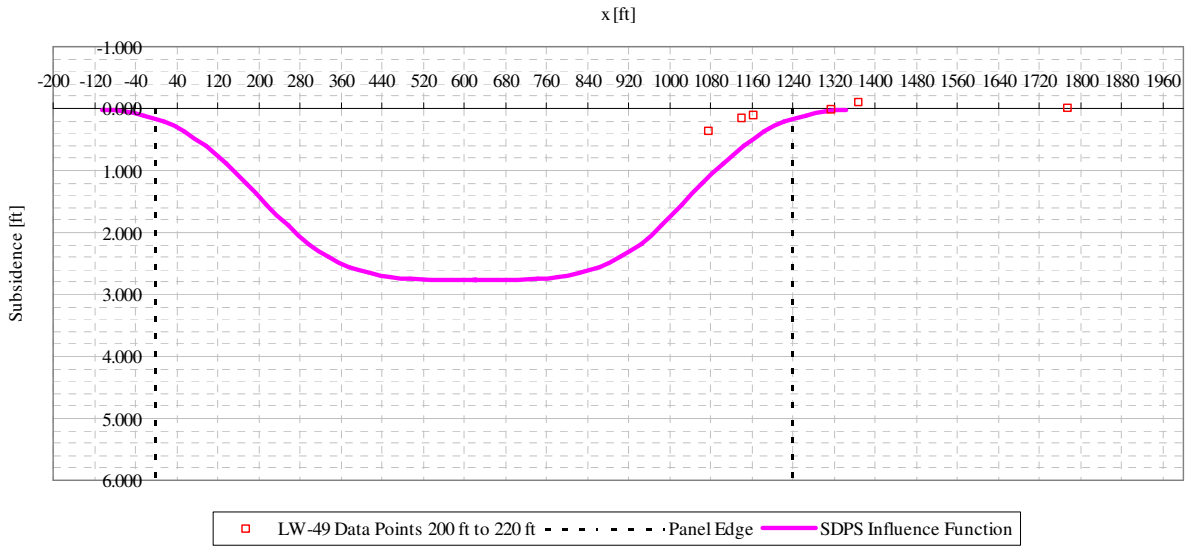

Figure A5- 13 LW-49 transverse view of data points from 200 ft to 220 ft from mine face and SDPS prediction

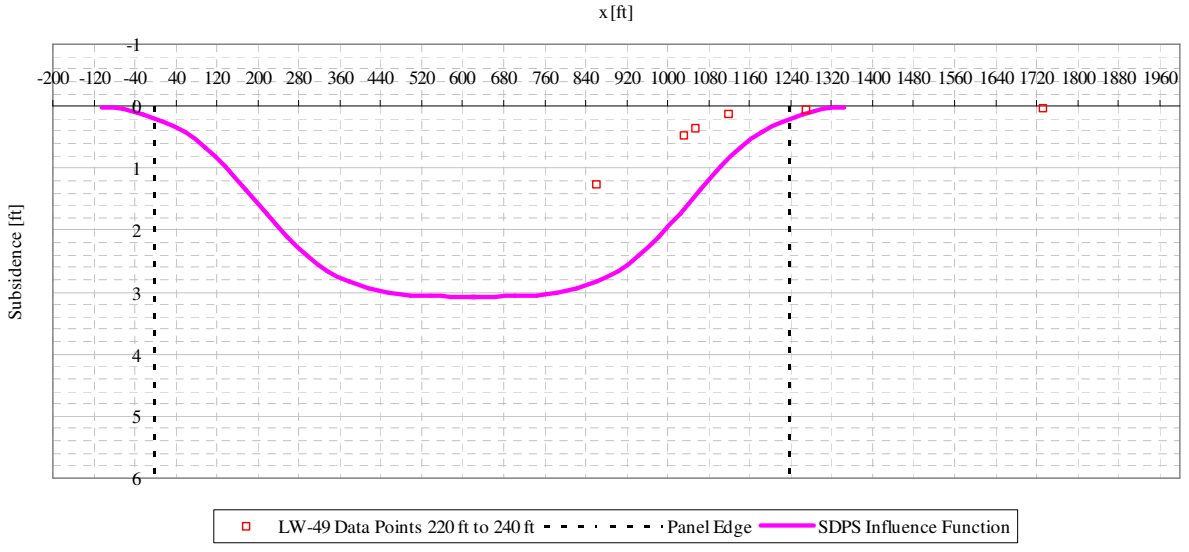

Figure A5- 14 LW-49 transverse view of data points from 220 ft to 240 ft from mine face and SDPS prediction

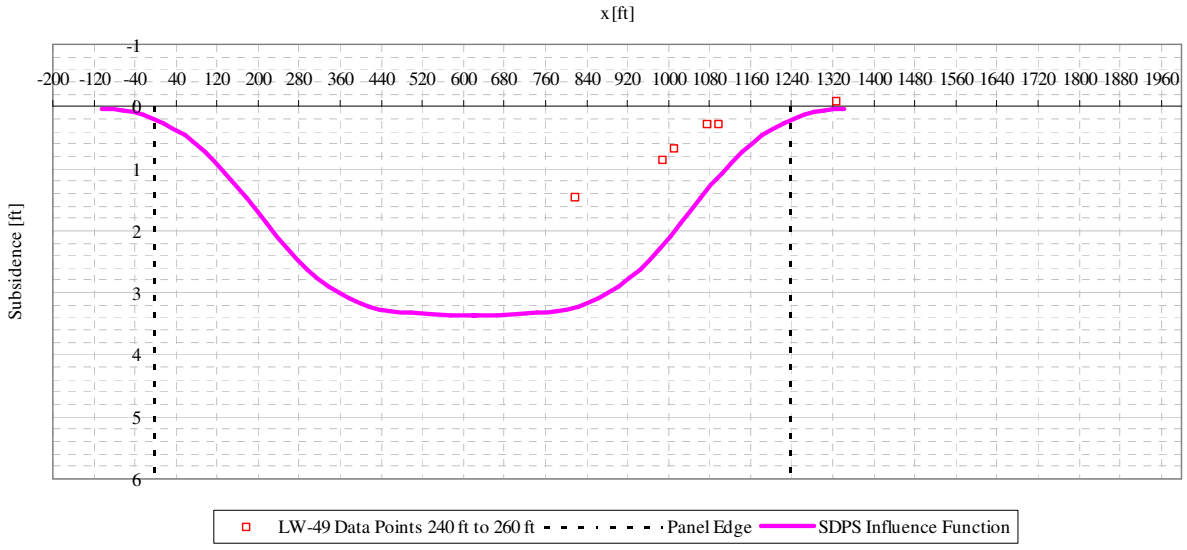

Figure A5- 15 LW-49 transverse view of data points from 240 ft to 260 ft from mine face and SDPS prediction

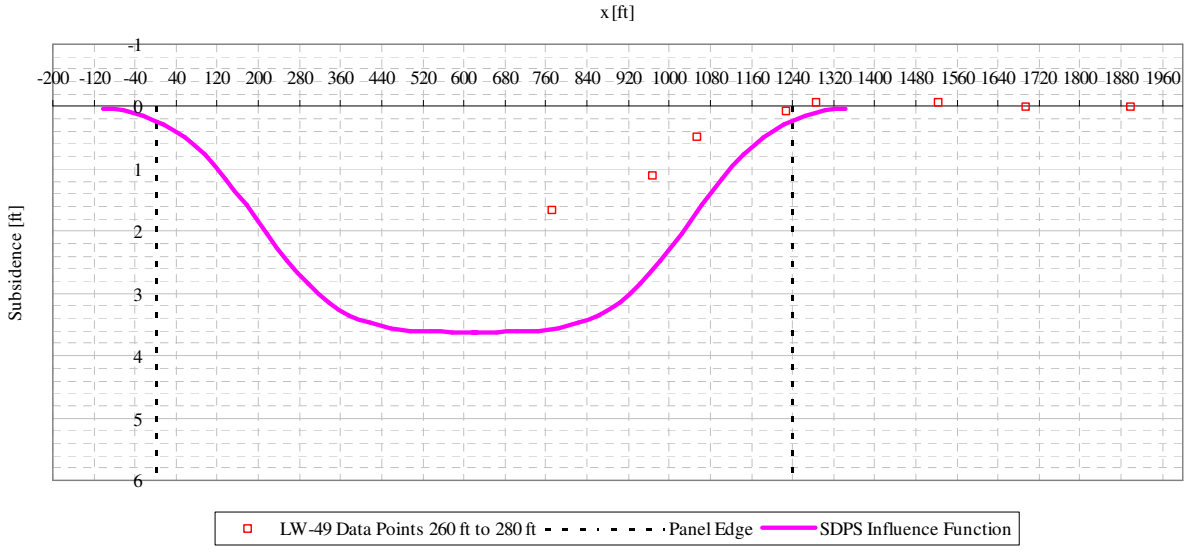

Figure A5- 16 LW-49 transverse view of data points from 260 ft to 280 ft from mine face and SDPS prediction

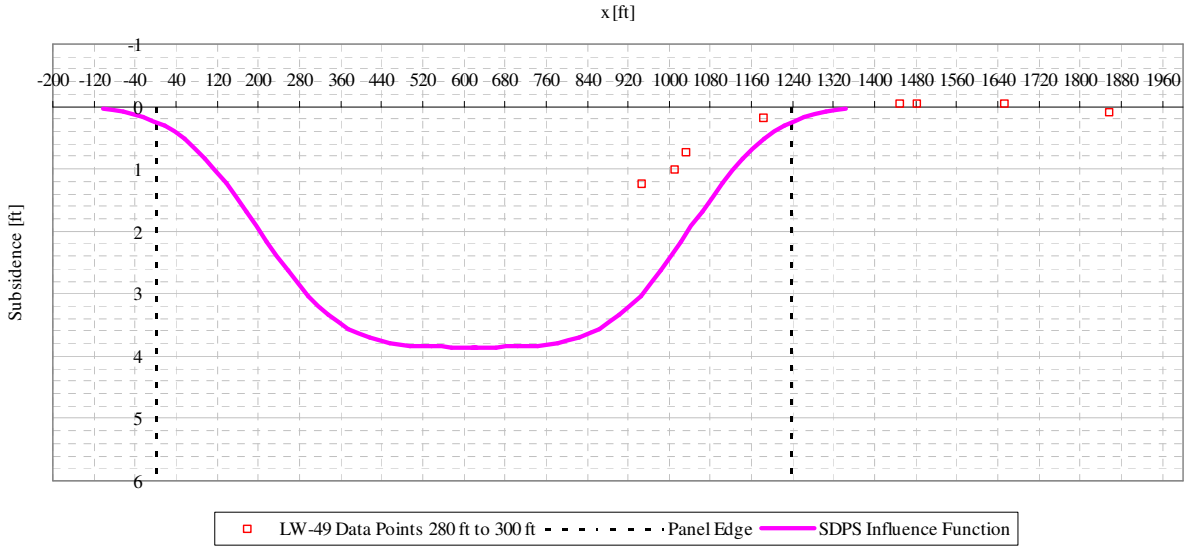

Figure A5- 17 LW-49 transverse view of data points from 280 ft to 300 ft from mine face and SDPS prediction

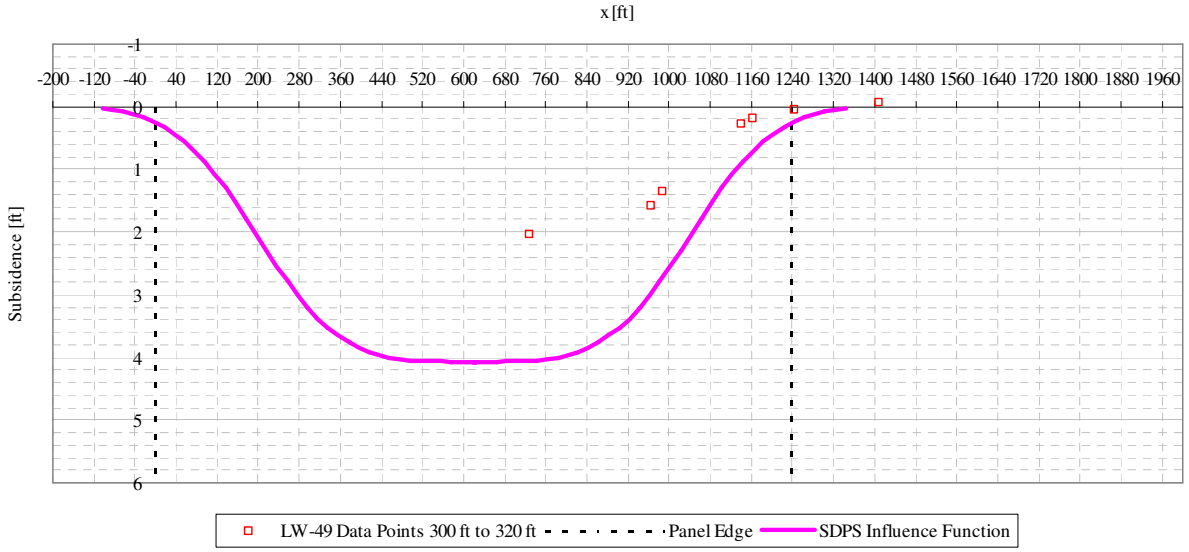

Figure A5- 18 LW-49 transverse view of data points from 300 ft to 320 ft from mine face and SDPS prediction

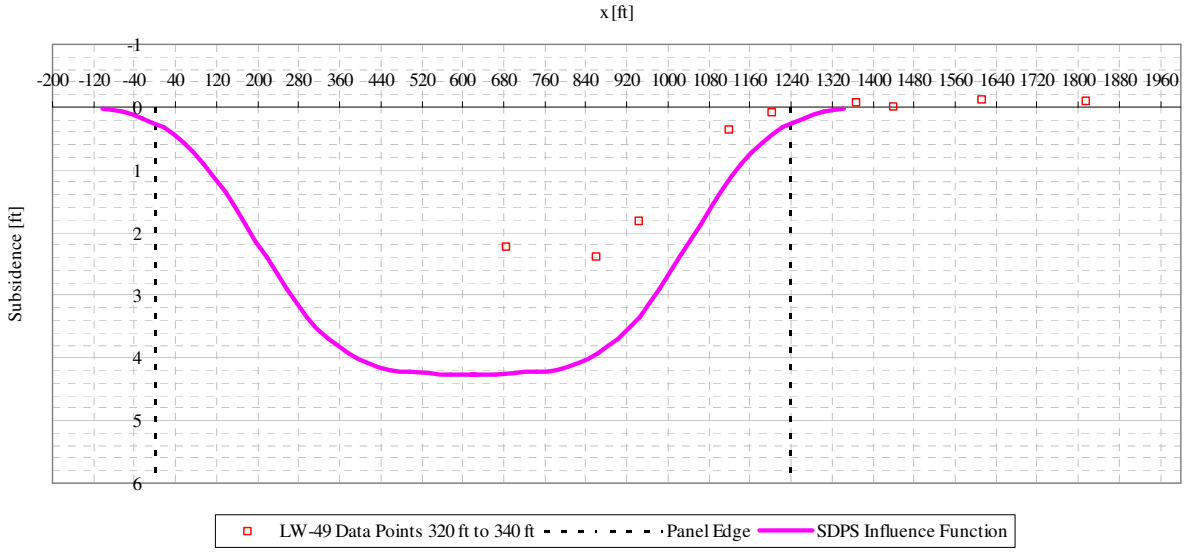

Figure A5- 19 LW-49 transverse view of data points from 320 ft to 340 ft from mine face and SDPS prediction

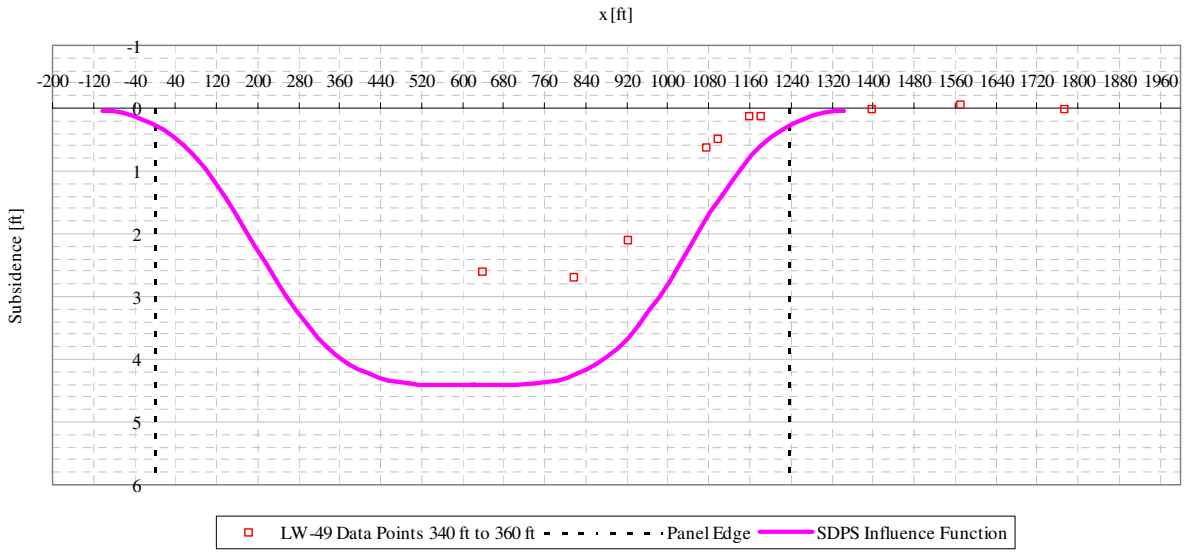

Figure A5- 20 LW-49 transverse view of data points from 340 ft to 360 ft from mine face and SDPS prediction

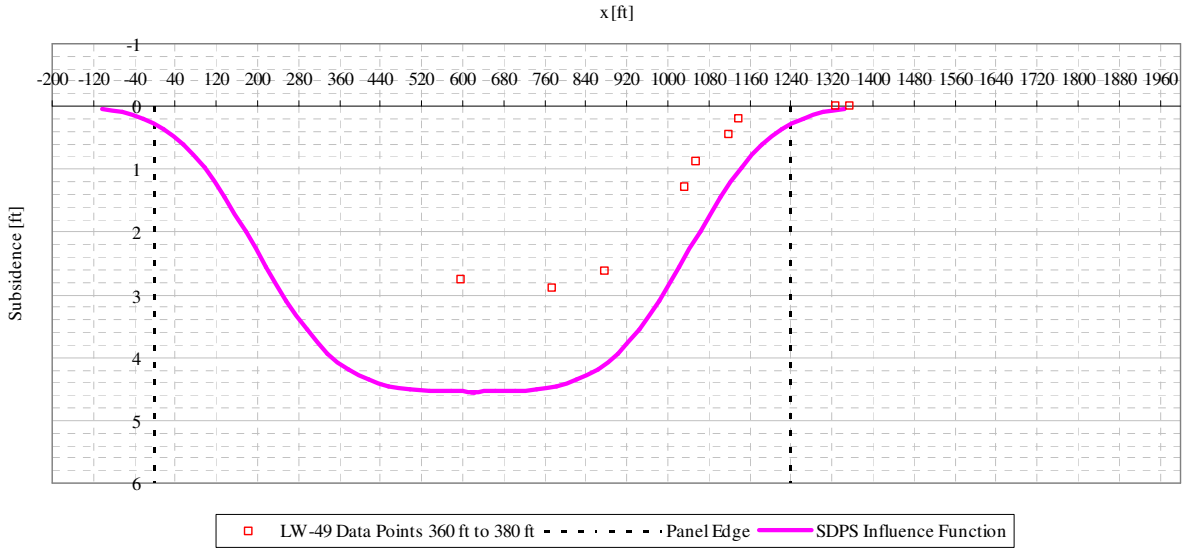

Figure A5- 21 LW-49 transverse view of data points from 360 ft to 380 ft from mine face and SDPS prediction

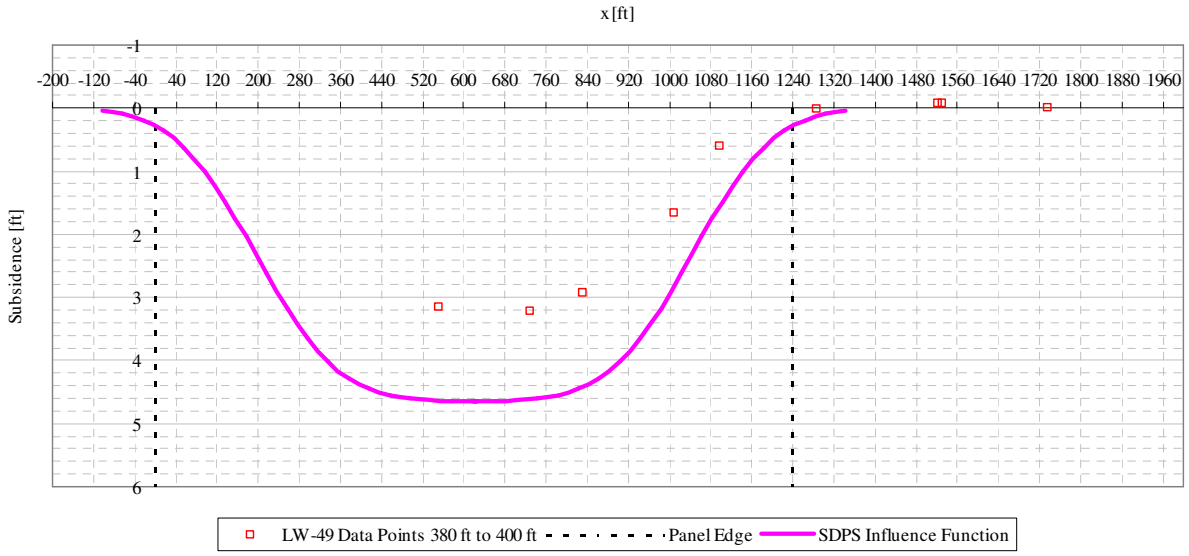

Figure A5- 22 LW-49 transverse view of data points from 380 ft to 400 ft from mine face and SDPS prediction

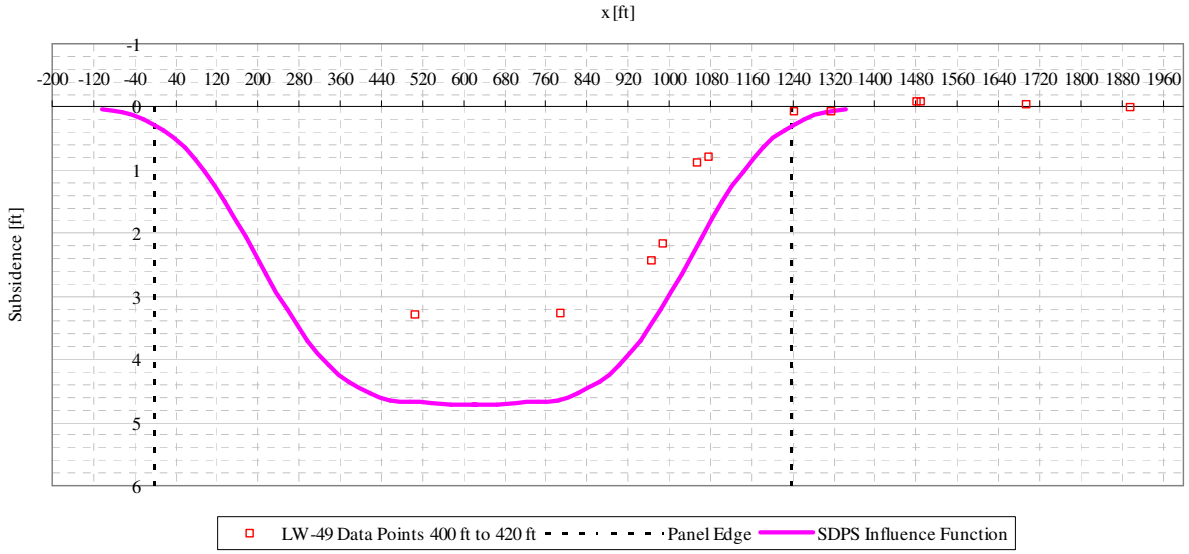

Figure A5- 23 LW-49 transverse view of data points from 400 ft to 420 ft from mine face and SDPS prediction

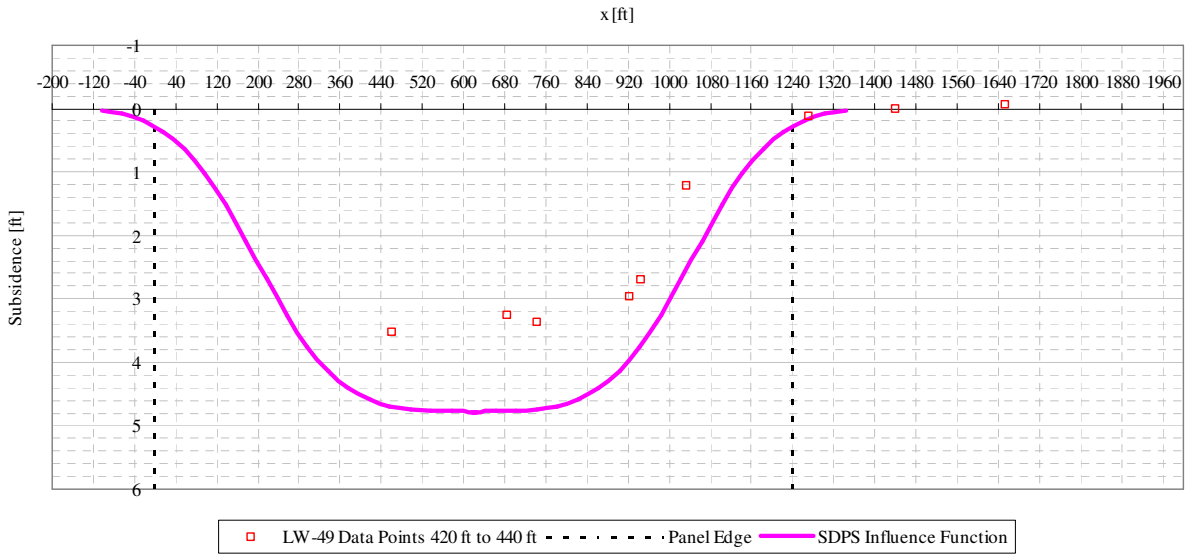

Figure A5- 24 LW-49 transverse view of data points from 420 ft to 440 ft from mine face and SDPS prediction

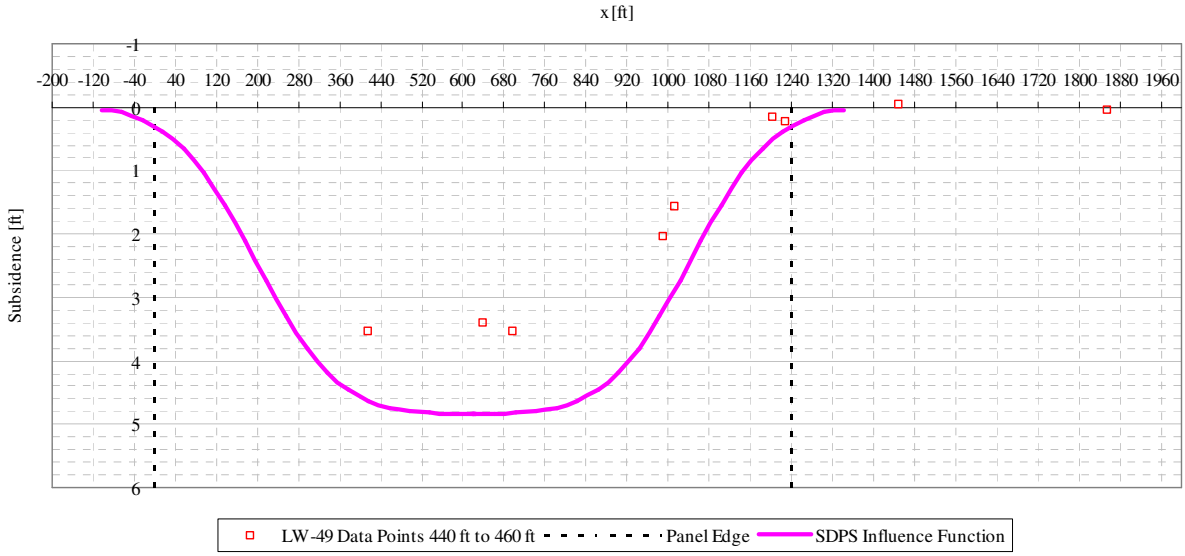

Figure A5- 25 LW-49 transverse view of data points from 440 ft to 460 ft from mine face and SDPS prediction

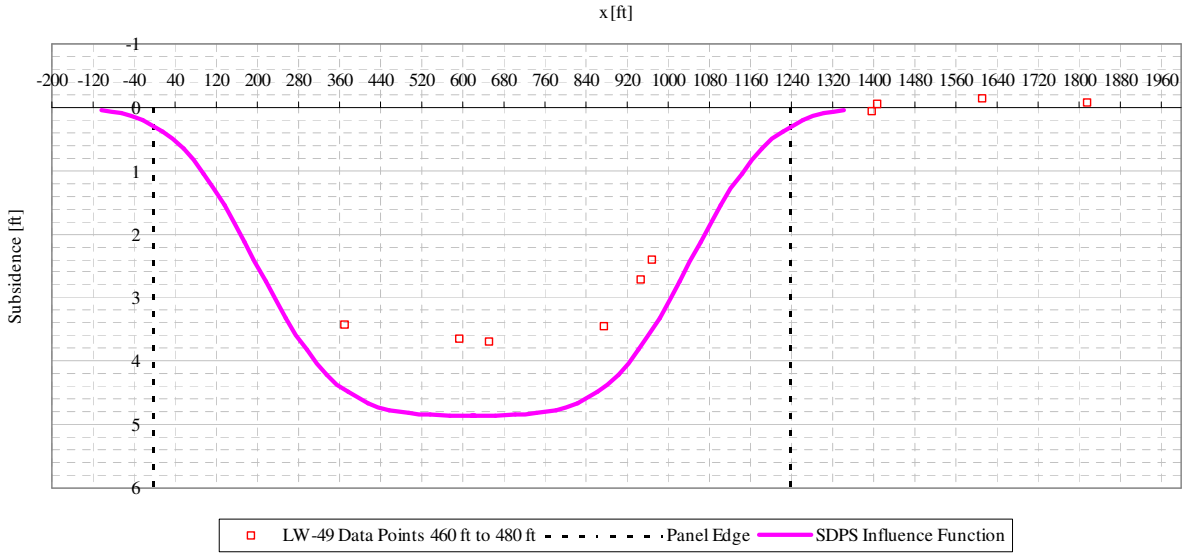

Figure A5- 26 LW-49 transverse view of data points from 460 ft to 480 ft from mine face and SDPS prediction

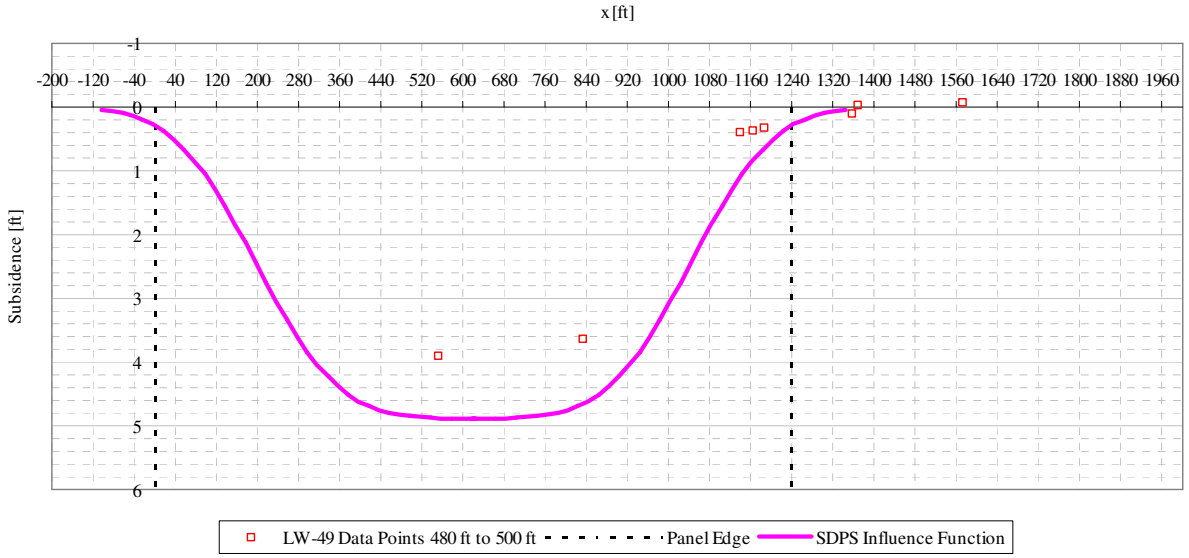

Figure A5- 27 LW-49 transverse view of data points from 480 ft to 500 ft from mine face and SDPS prediction

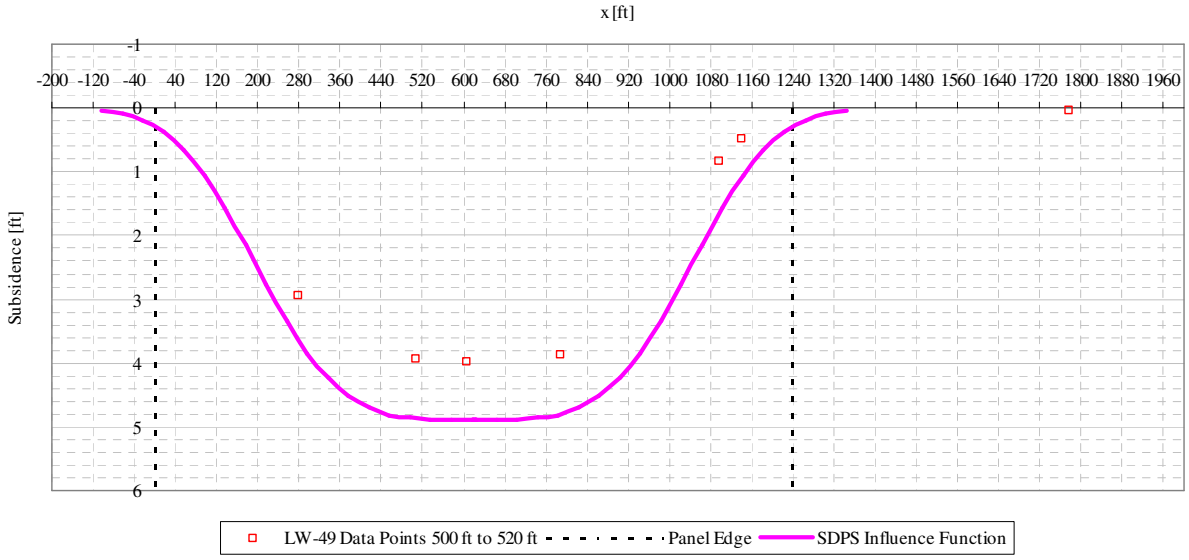

Figure A5- 28 LW-49 transverse view of data points from 500 ft to 520 ft from mine face and SDPS prediction

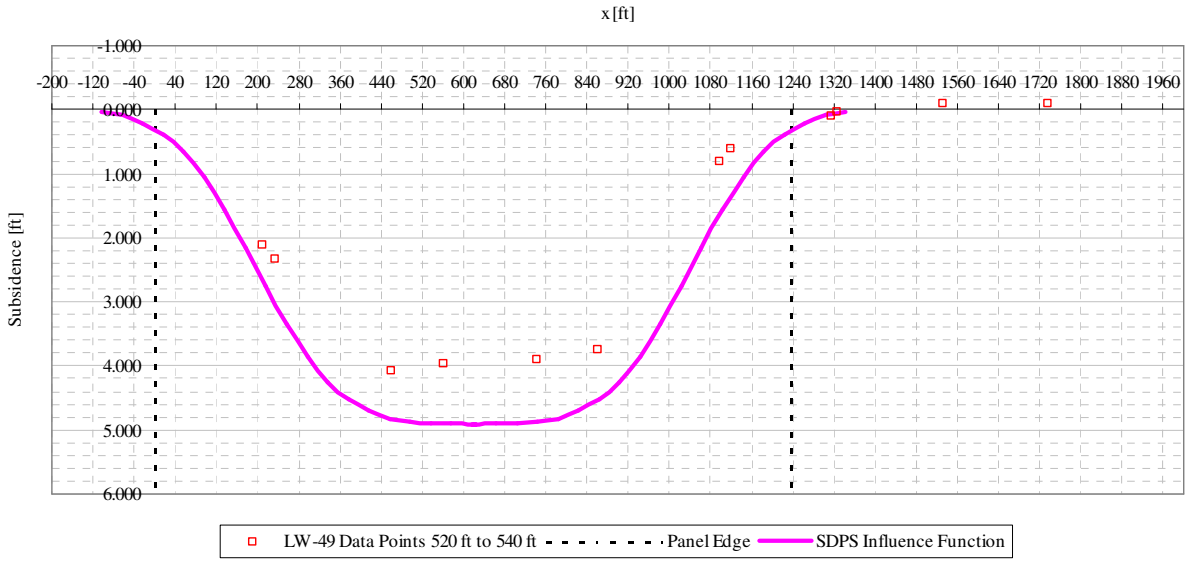

Figure A5- 29 LW-49 transverse view of data points from 520 ft to 540 ft from mine face and SDPS prediction

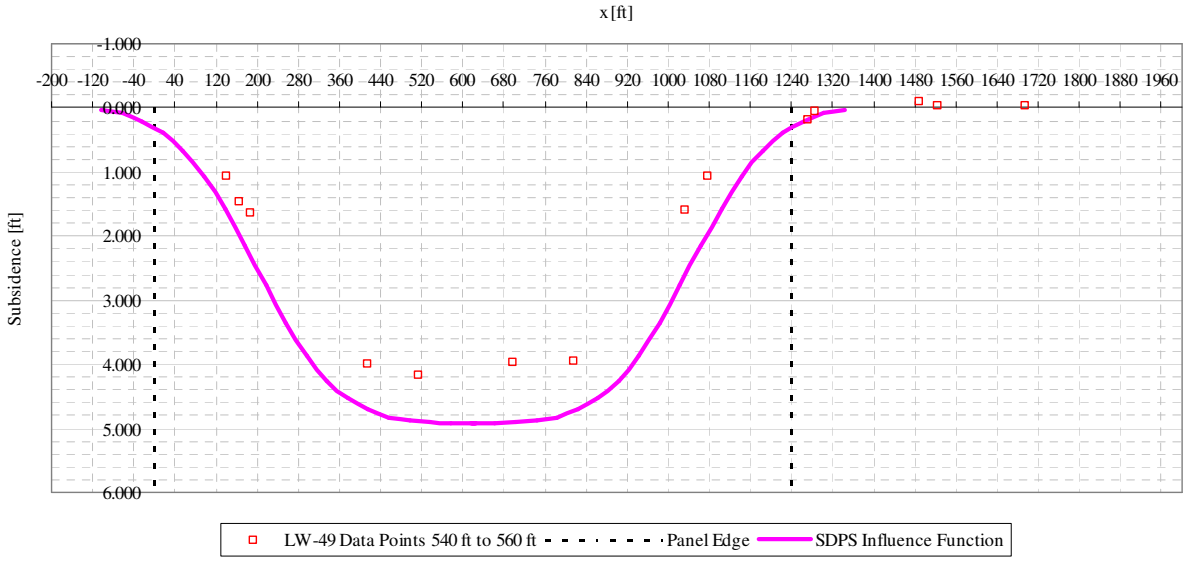

Figure A5- 30 LW-49 transverse view of data points from 540 ft to 560 ft from mine face and SDPS prediction

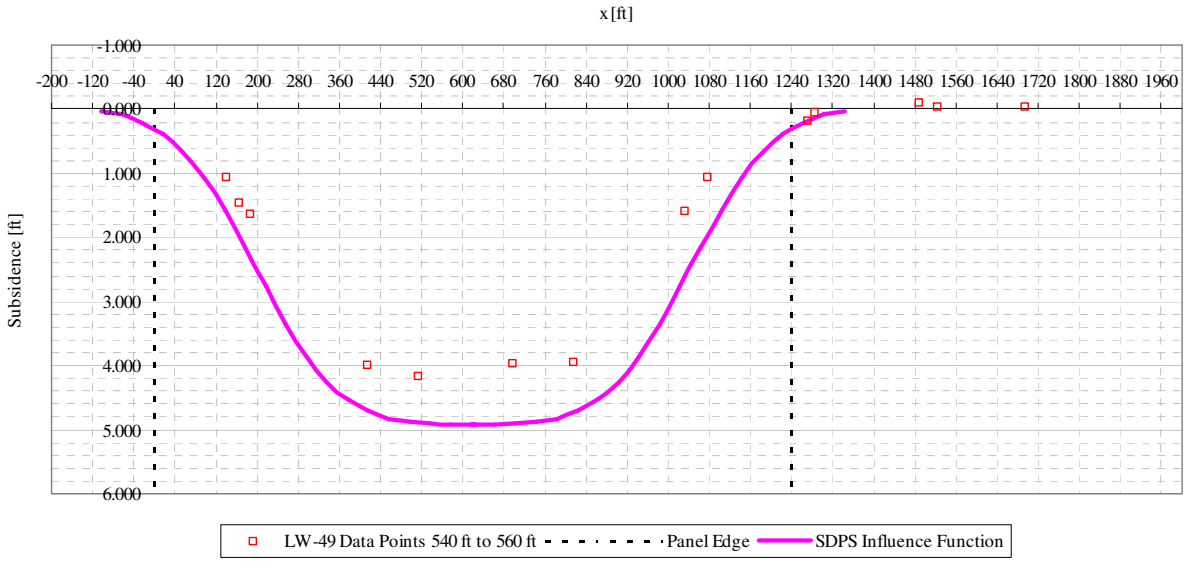

Figure A5- 31 LW-49 transverse view of data points from 560 ft to 580 ft from mine face and SDPS prediction

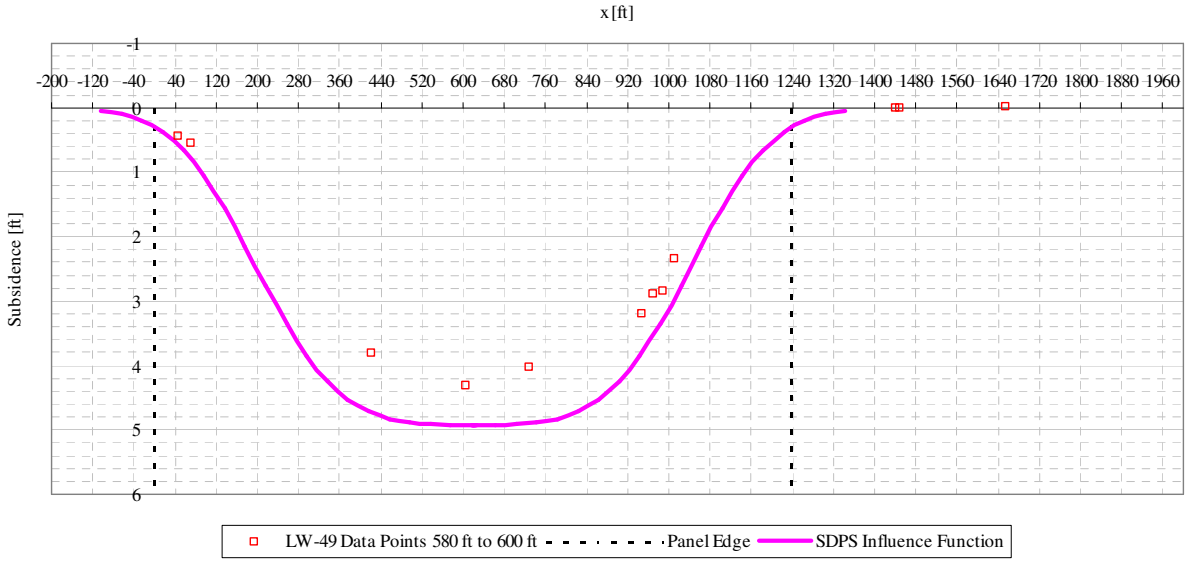

Figure A5- 32 LW-49 transverse view of data points from 580 ft to 600 ft from mine face and SDPS prediction

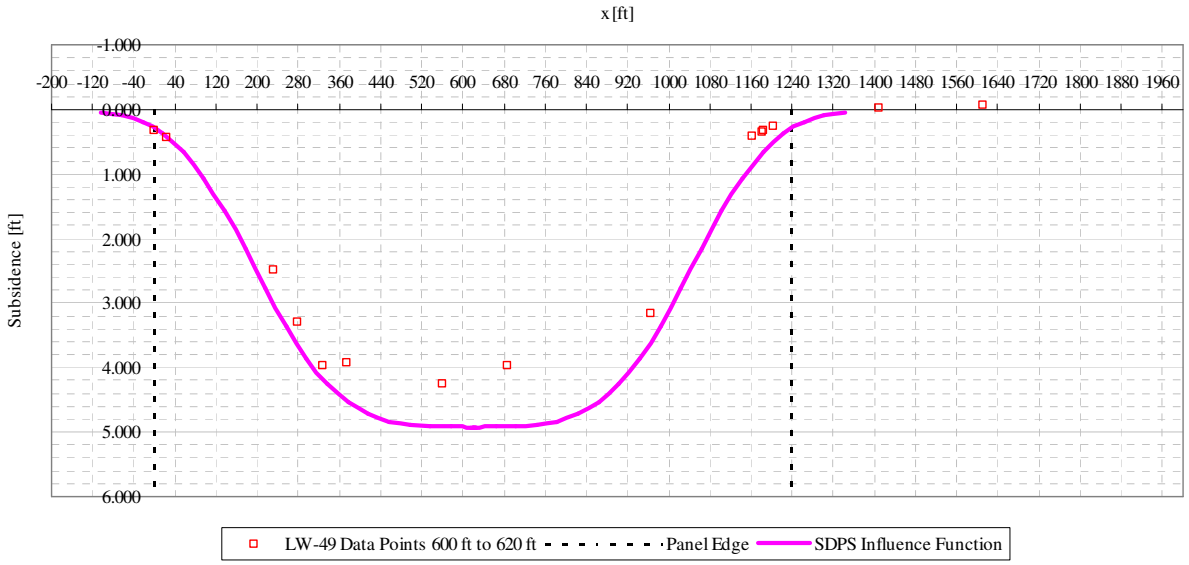

Figure A5- 33 LW-49 transverse view of data points from 600 ft to 620 ft from mine face and SDPS prediction

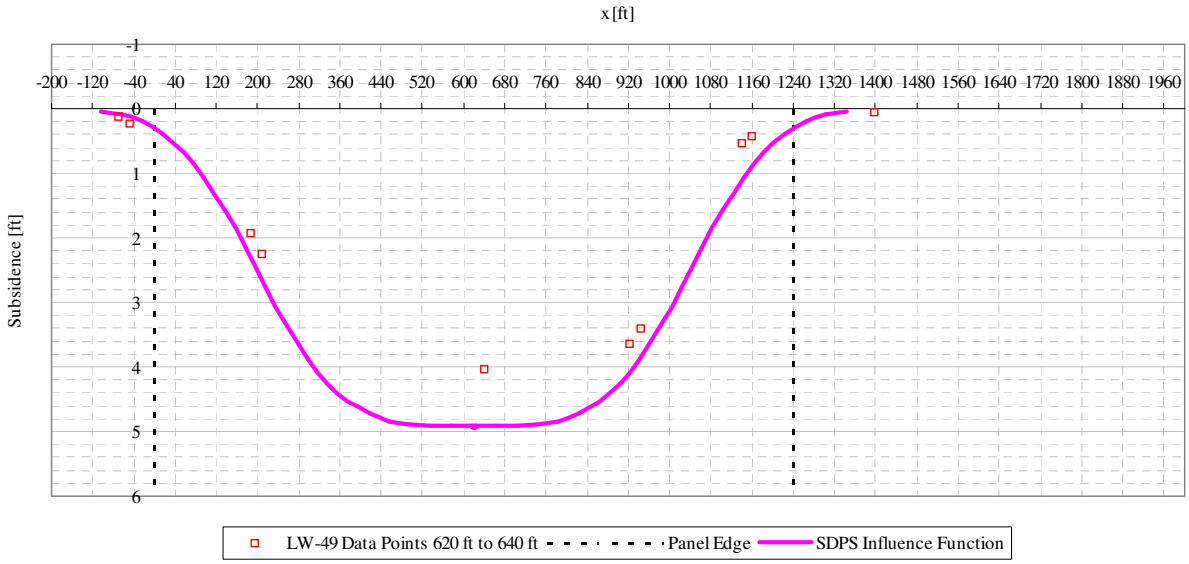

Figure A5- 34 LW-49 transverse view of data points from 620 ft to 640 ft from mine face and SDPS prediction

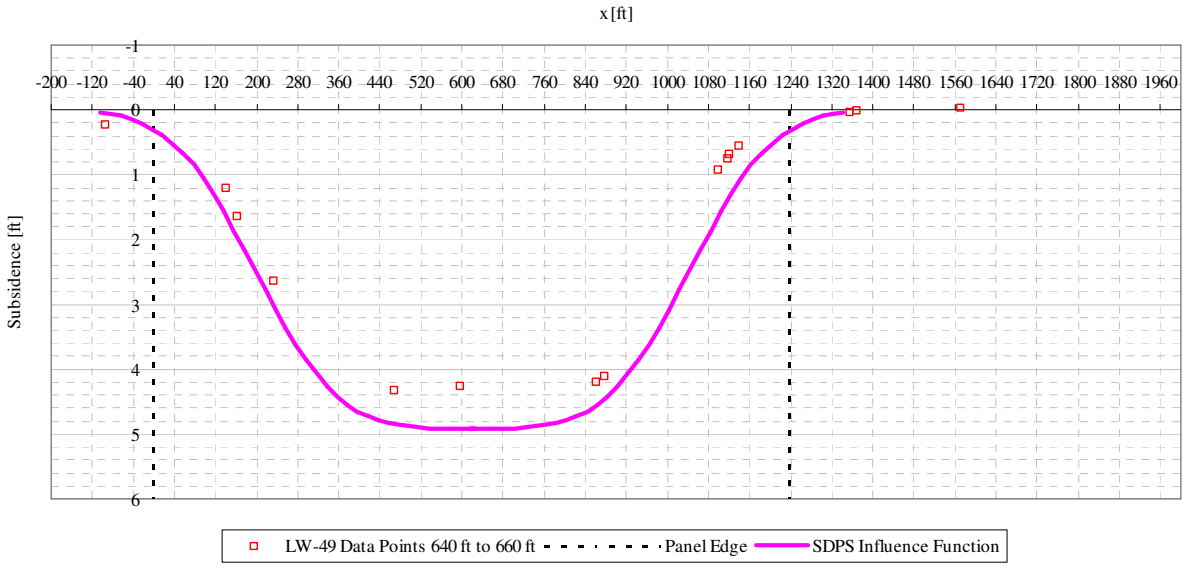

Figure A5- 35 LW-49 transverse view of data points from 640 ft to 660 ft from mine face and SDPS prediction

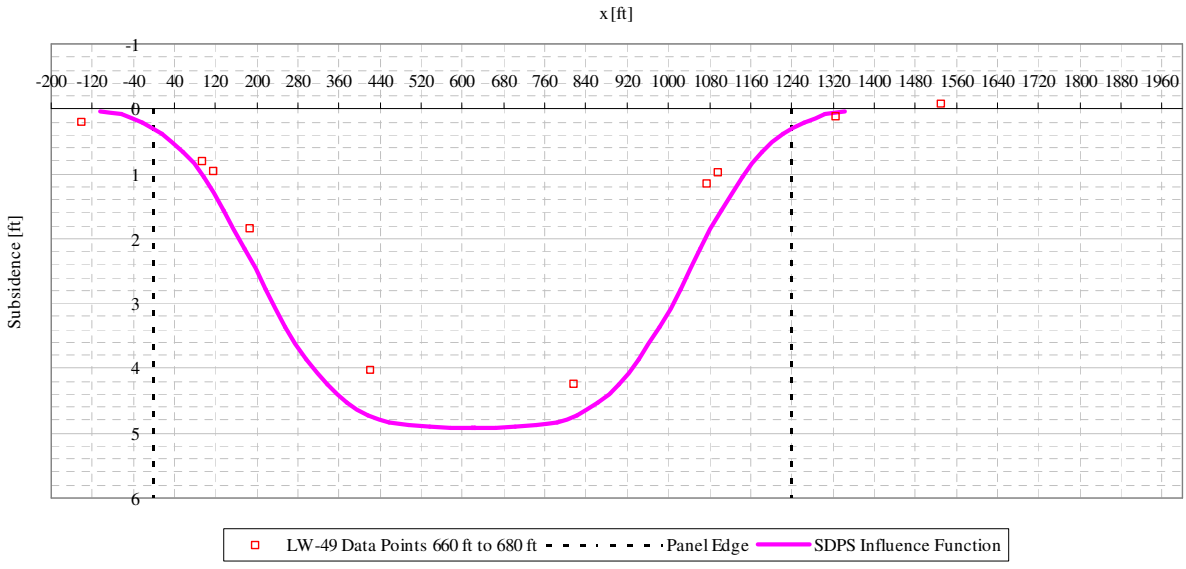

Figure A5- 36 LW-49 transverse view of data points from 660 ft to 680 ft from mine face and SDPS prediction

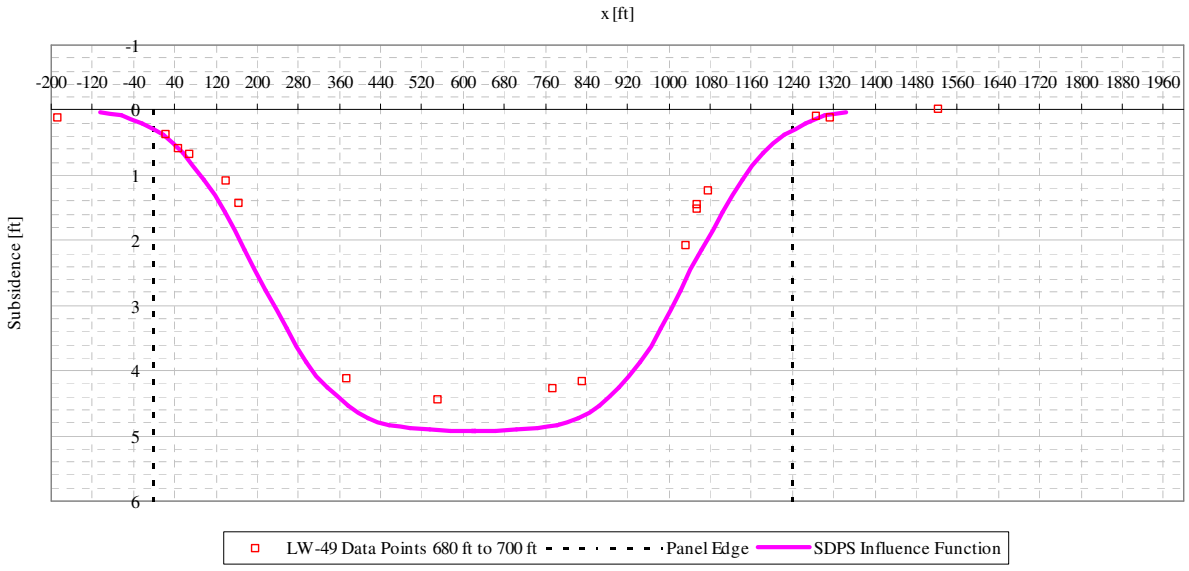

Figure A5- 37 LW-49 transverse view of data points from 680 ft to 700 ft from mine face and SDPS prediction

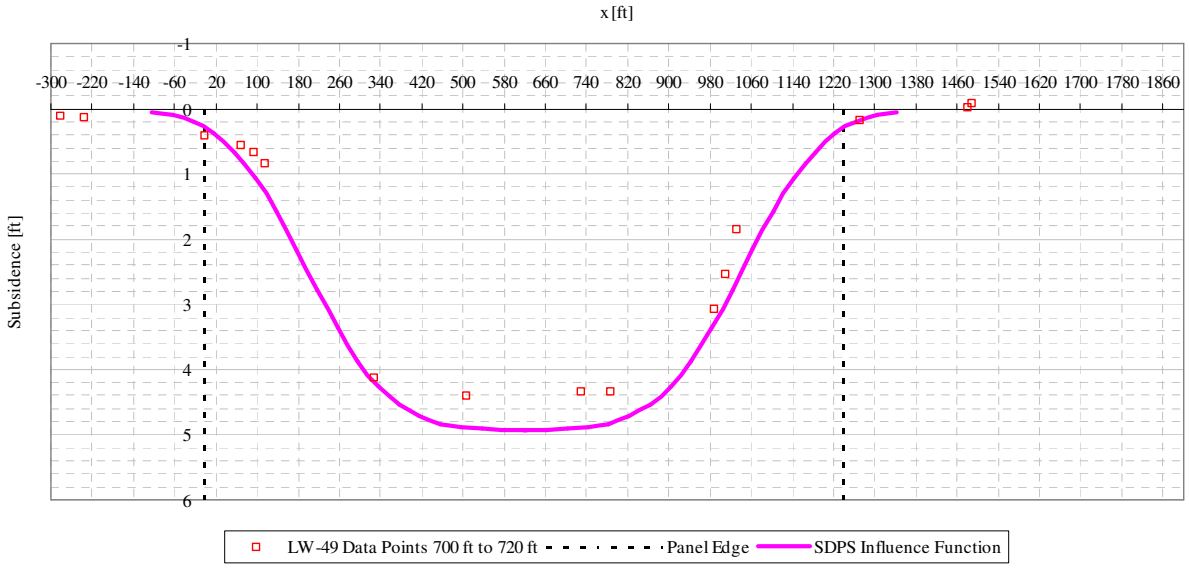

Figure A5- 38 LW-49 transverse view of data points from 700 ft to 720 ft from mine face and SDPS prediction

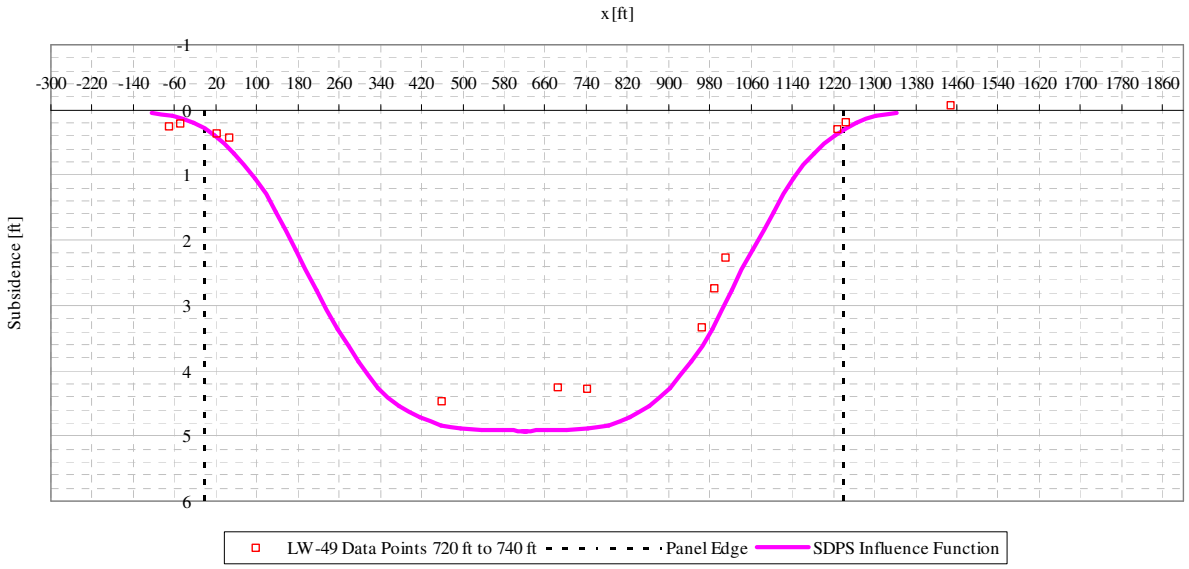

Figure A5- 39 LW-49 transverse view of data points from 720 ft to 740 ft from mine face and SDPS prediction

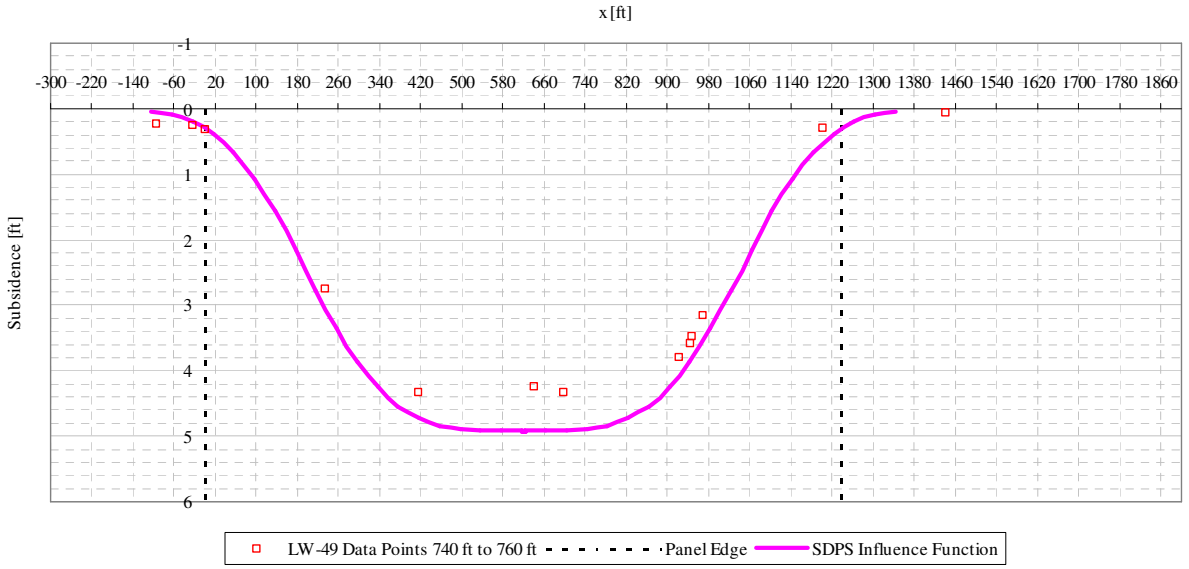

Figure A5- 40 LW-49 transverse view of data points from 740 ft to 760 ft from mine face and SDPS prediction

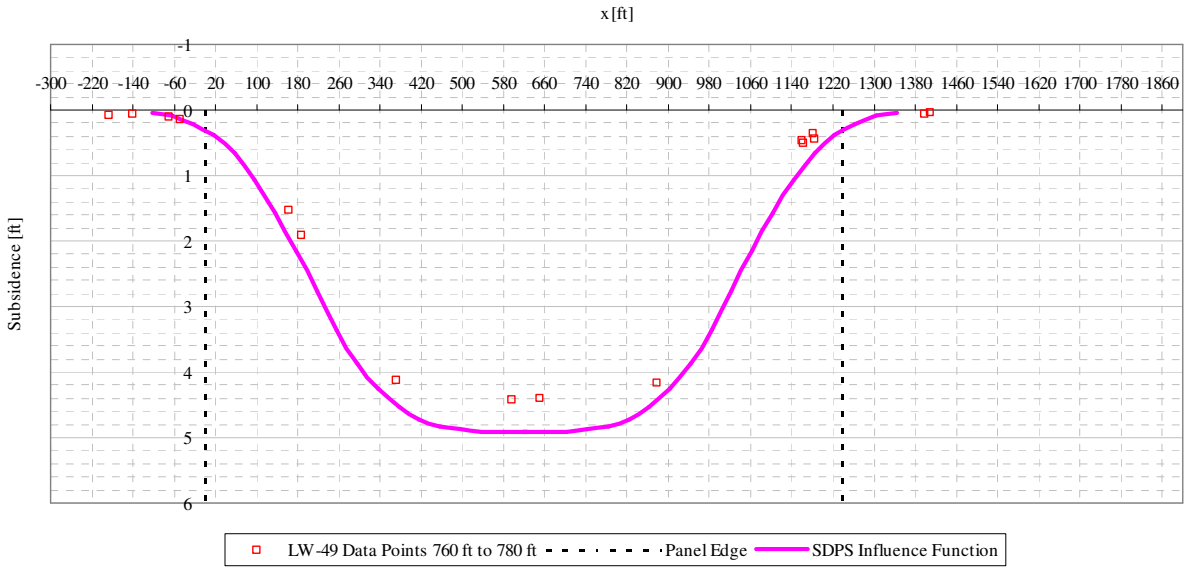

Figure A5- 41 LW-49 transverse view of data points from 760 ft to 780 ft from mine face and SDPS prediction

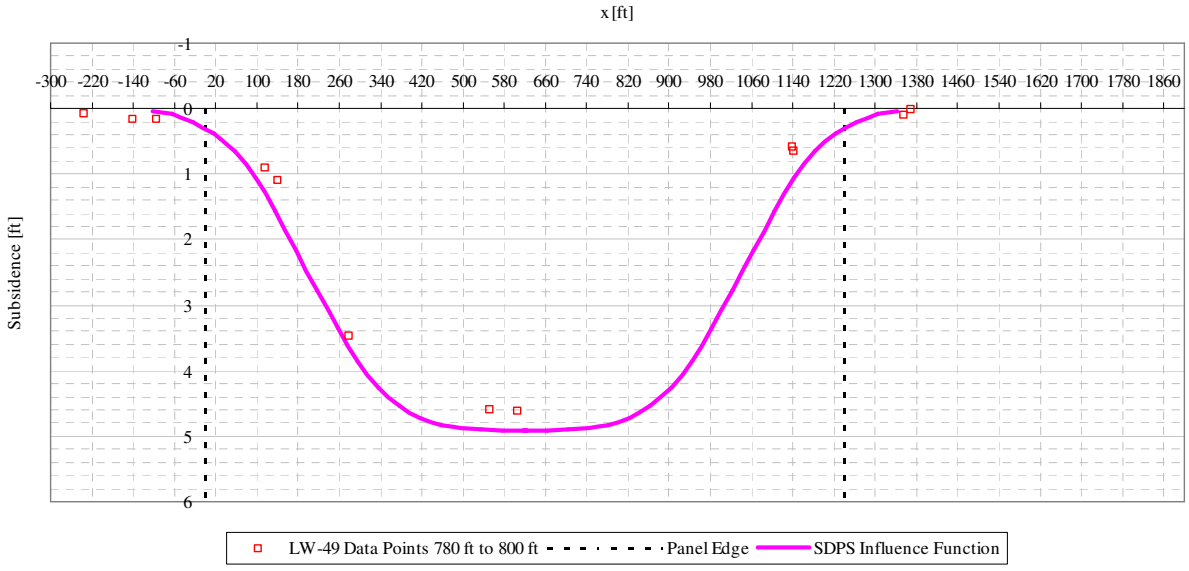

Figure A5- 42 LW-49 transverse view of data points from 780 ft to 800 ft from mine face and SDPS prediction

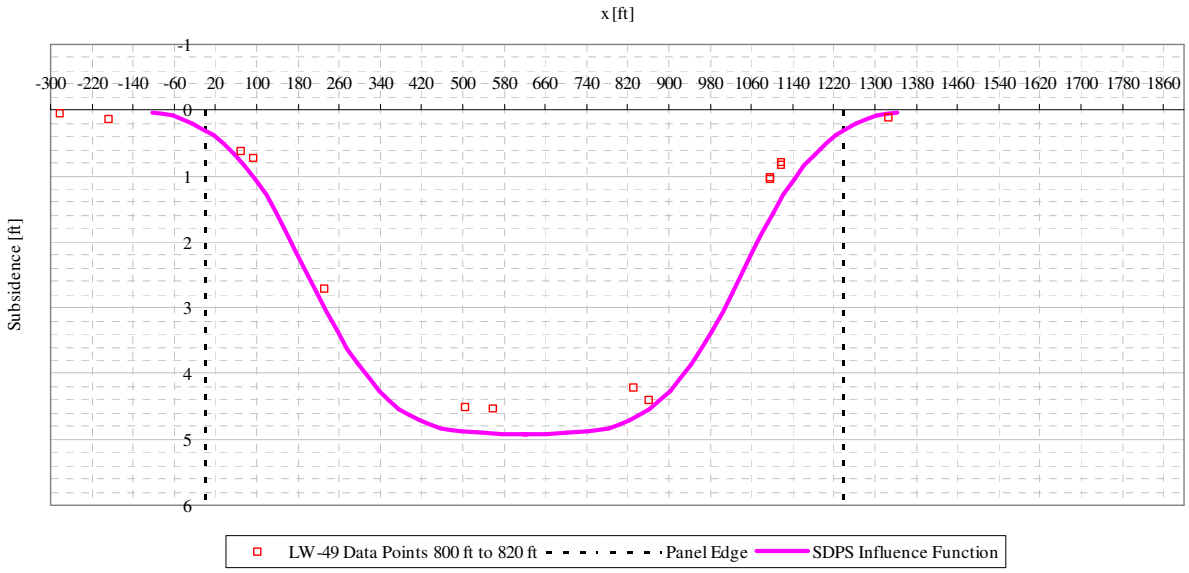

Figure A5- 43 LW-49 transverse view of data points from 800 ft to 820 ft from mine face and SDPS prediction

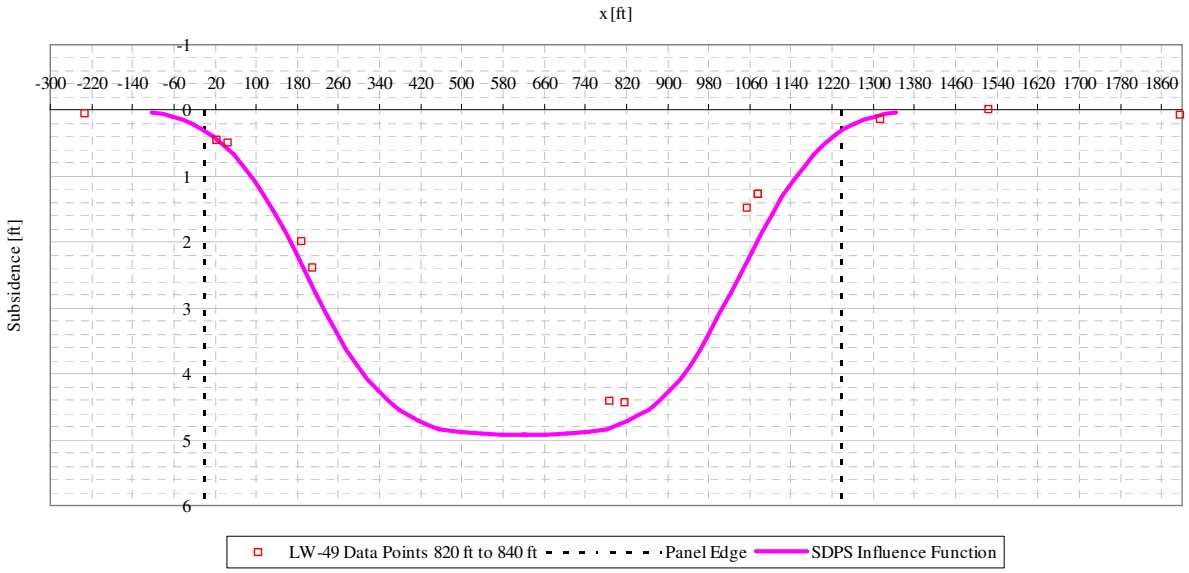

Figure A5- 44 LW-49 transverse view of data points from 820 ft to 840 ft from mine face and SDPS prediction

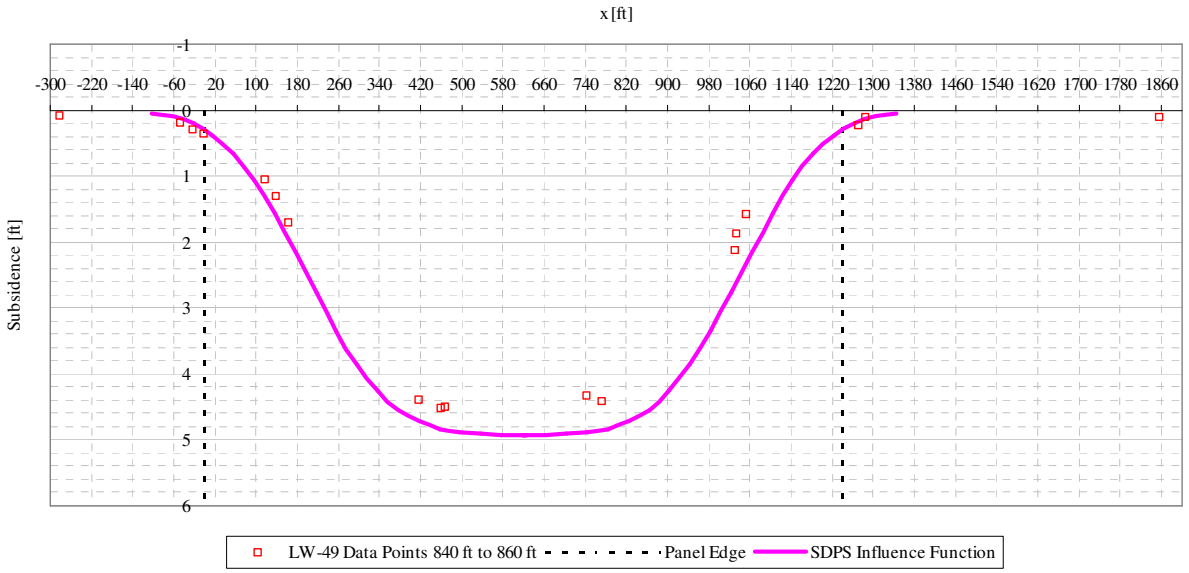

Figure A5- 45 LW-49 transverse view of data points from 840 ft to 860 ft from mine face and SDPS prediction

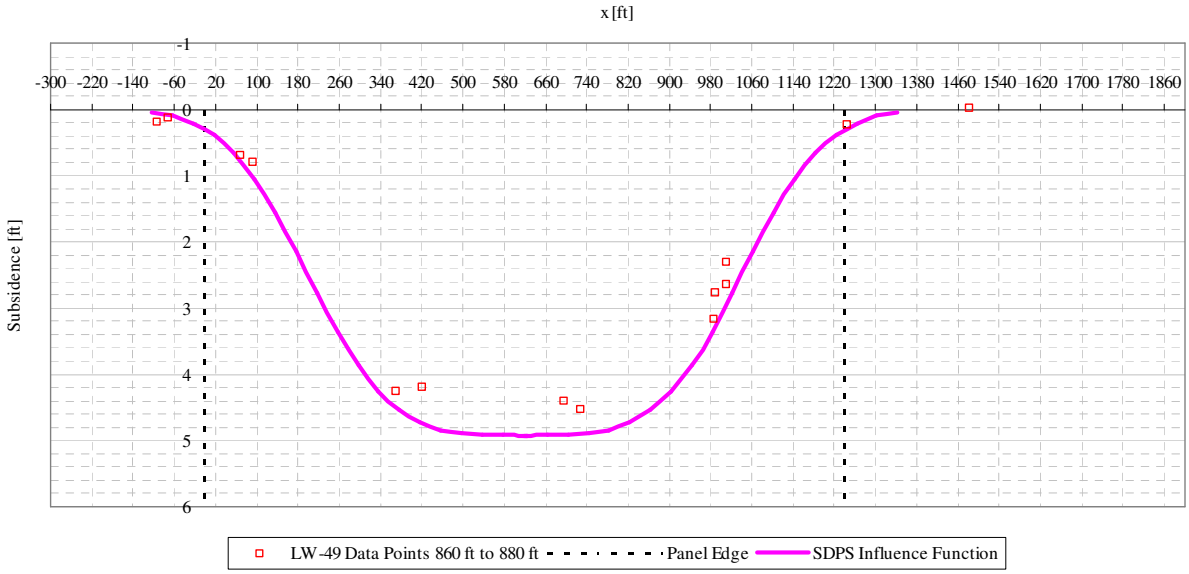

Figure A5- 46 LW-49 transverse view of data points from 860 ft to 880 ft from mine face and SDPS prediction

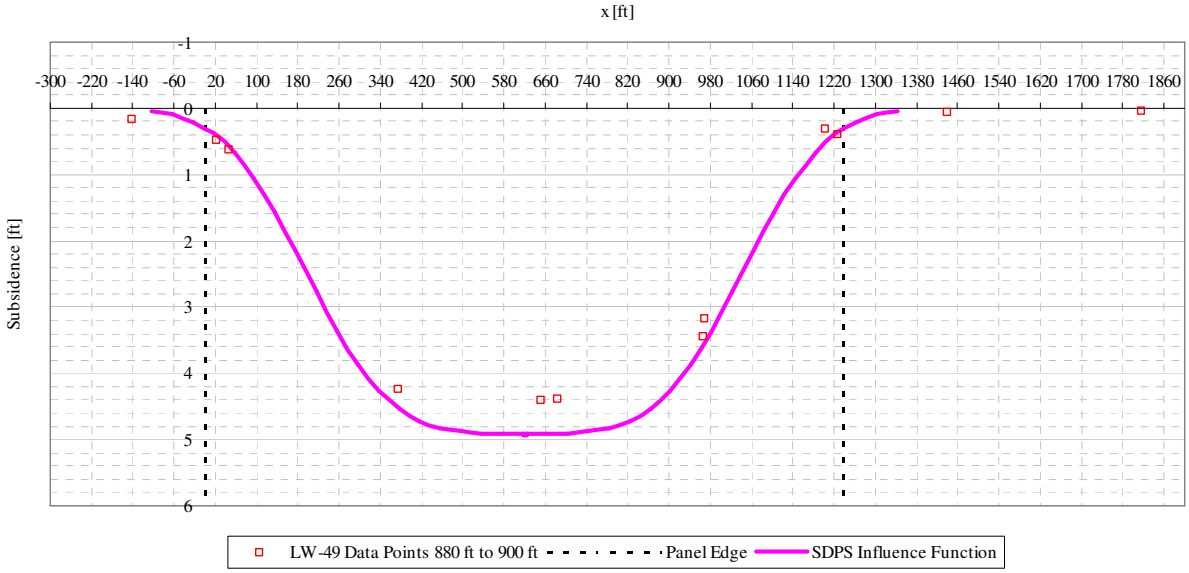

Figure A5- 47 LW-49 transverse view of data points from 880 ft to 900 ft from mine face and SDPS prediction

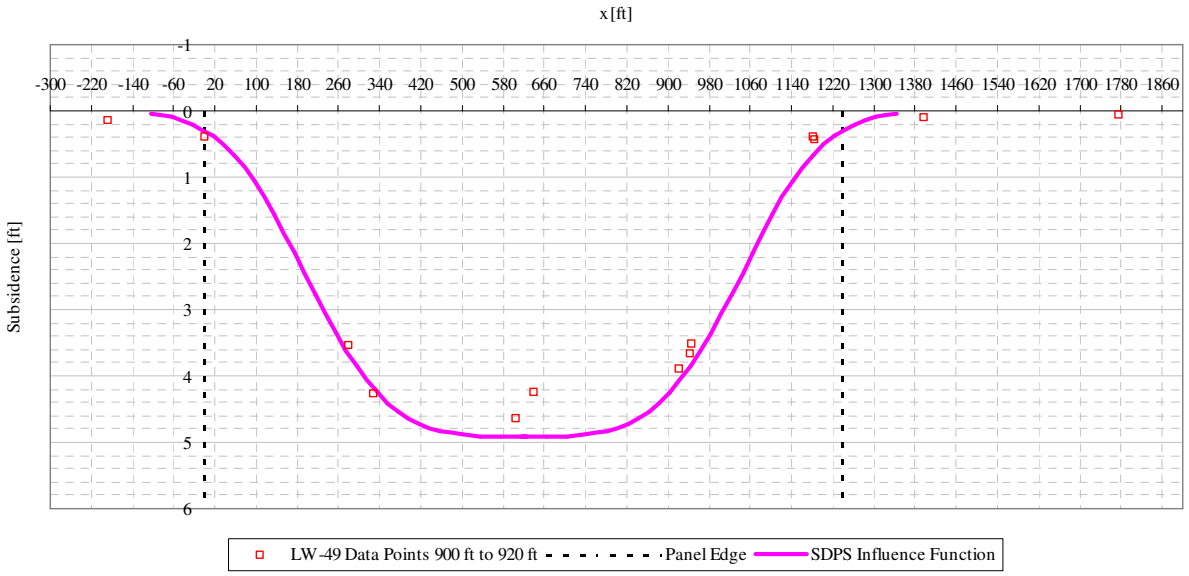

Figure A5- 48 LW-49 transverse view of data points from 900 ft to 920 ft from mine face and SDPS prediction

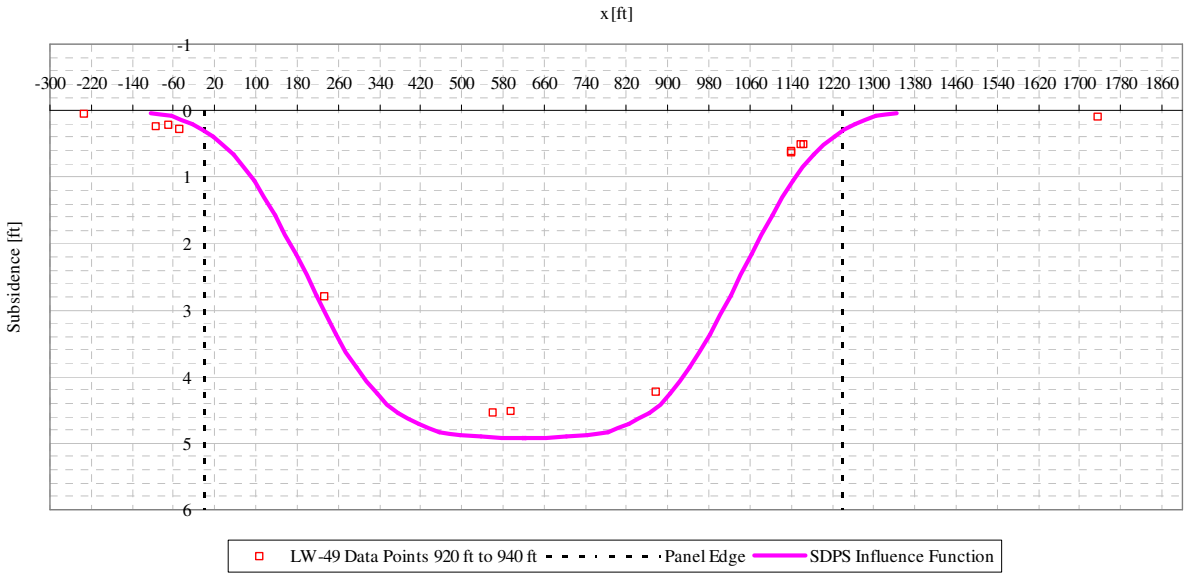

Figure A5- 49 LW-49 transverse view of data points from 920 ft to 940 ft from mine face and SDPS prediction

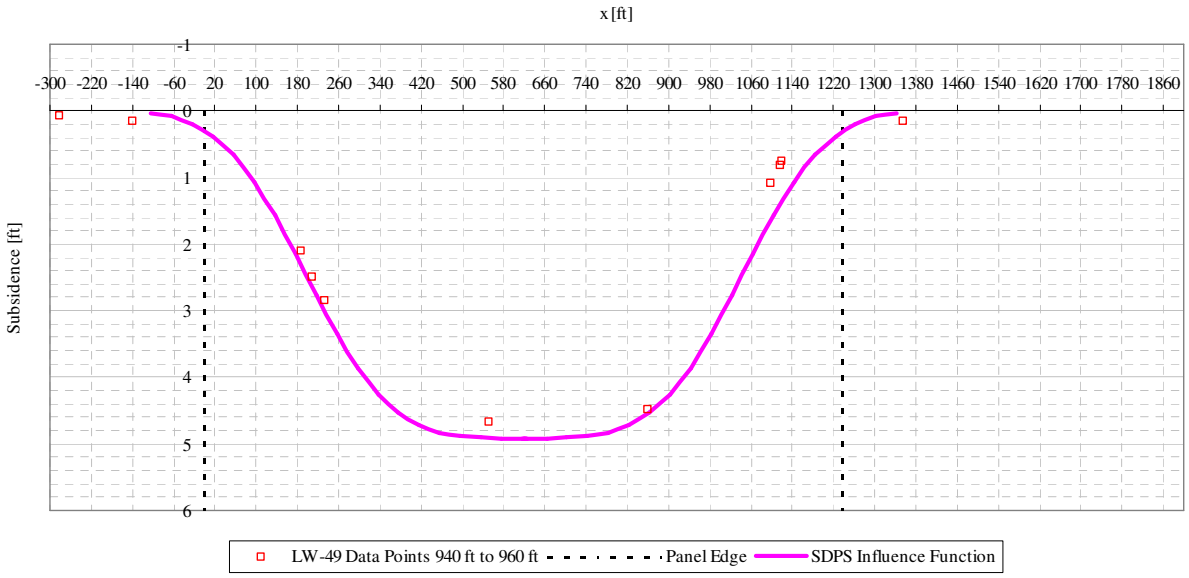

Figure A5- 50 LW-49 transverse view of data points from 940 ft to 960 ft from mine face and SDPS prediction

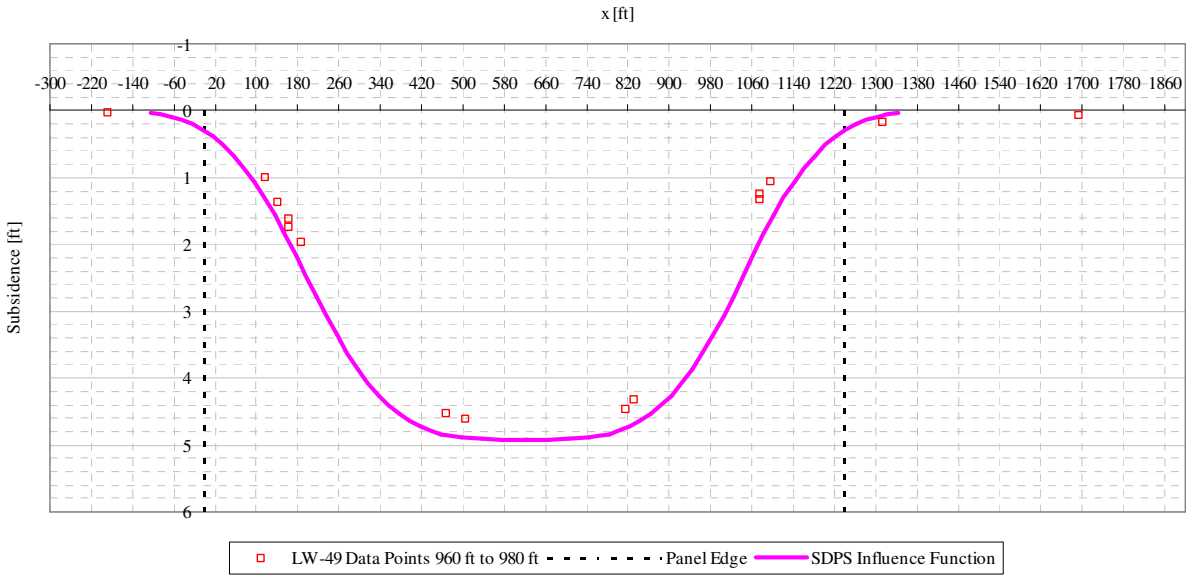

Figure A5- 51 LW-49 transverse view of data points from 960 ft to 980 ft from mine face and SDPS prediction

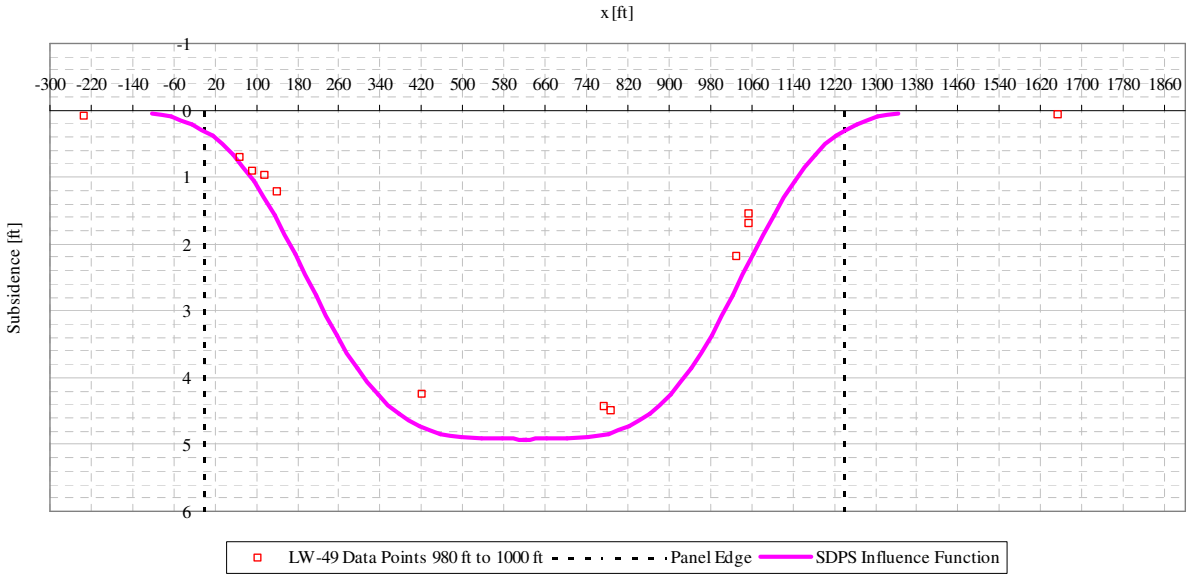

Figure A5- 52 LW-49 transverse view of data points from 980 ft to 1000 ft from mine face and SDPS prediction

A.6 EMERALD MINE PANEL LW-51 SDPS INFLUENCE FUNCTION PREDICTION

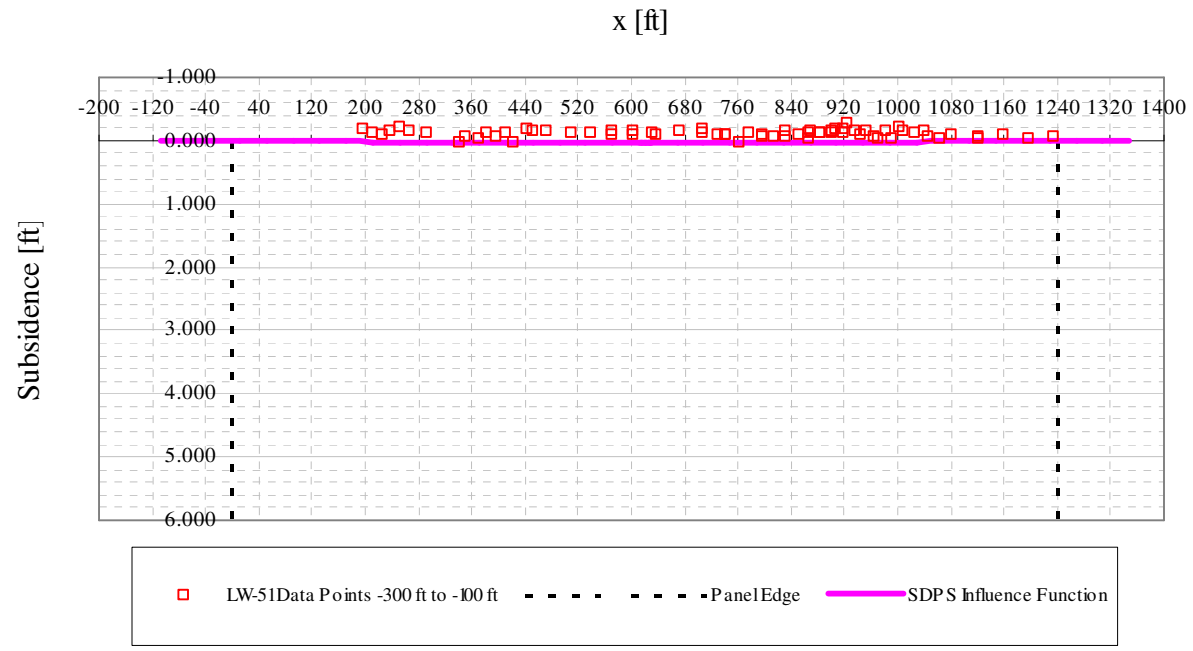

Figure A6- 1 LW-51 transverse view of data points from -300 ft to -100 ft from mine face and SDPS prediction

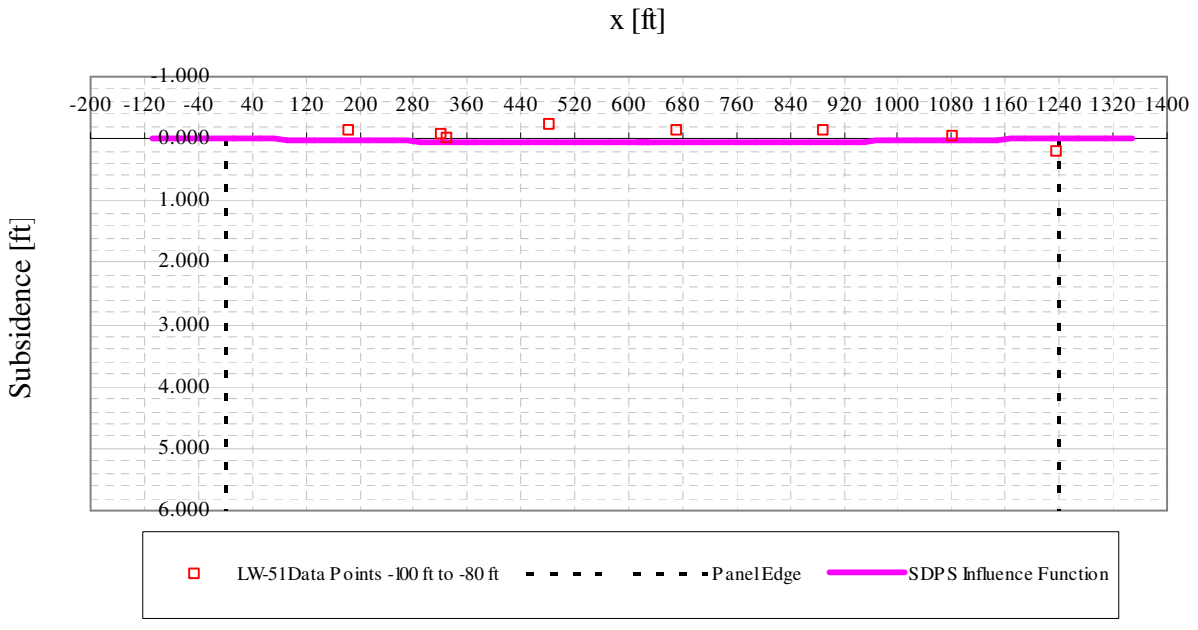

Figure A6- 2 LW-51 transverse view of data points from -100 ft to -80 ft from mine face and SDPS prediction

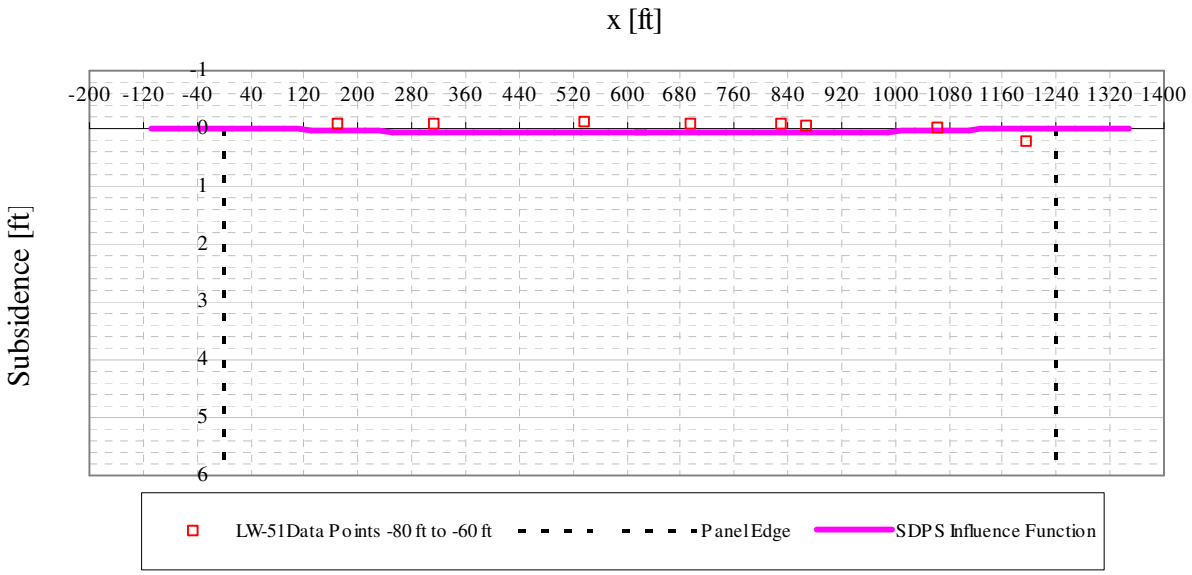

Figure A6- 3 LW-51 transverse view of data points from -80 ft to -60 ft from mine face and SDPS prediction

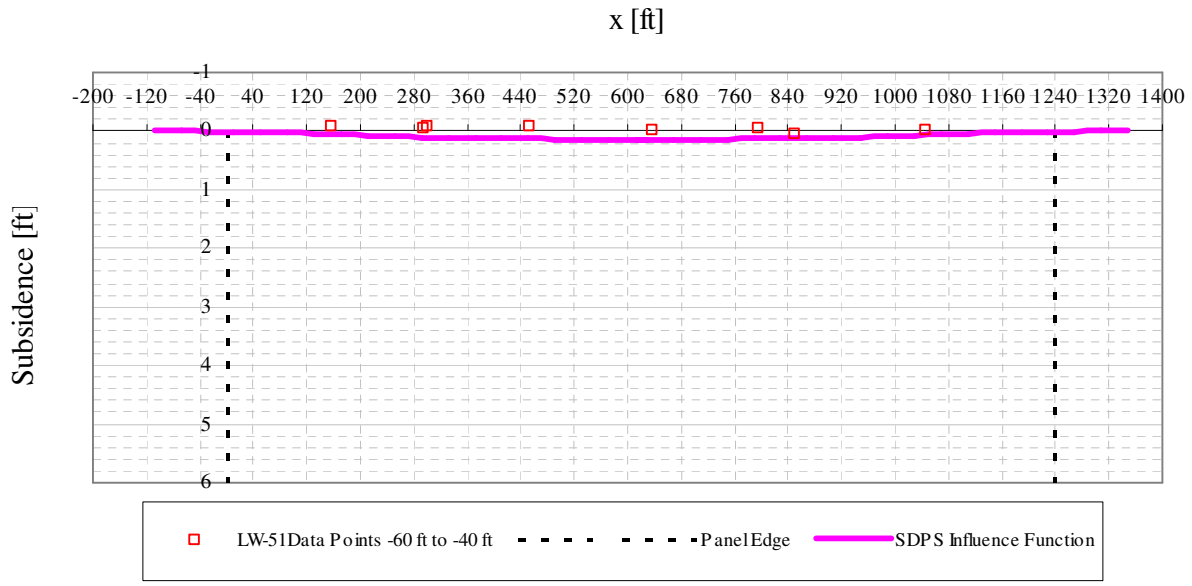

Figure A6- 4 LW-51 transverse view of data points from -60 ft to -40 ft from mine face and SDPS prediction

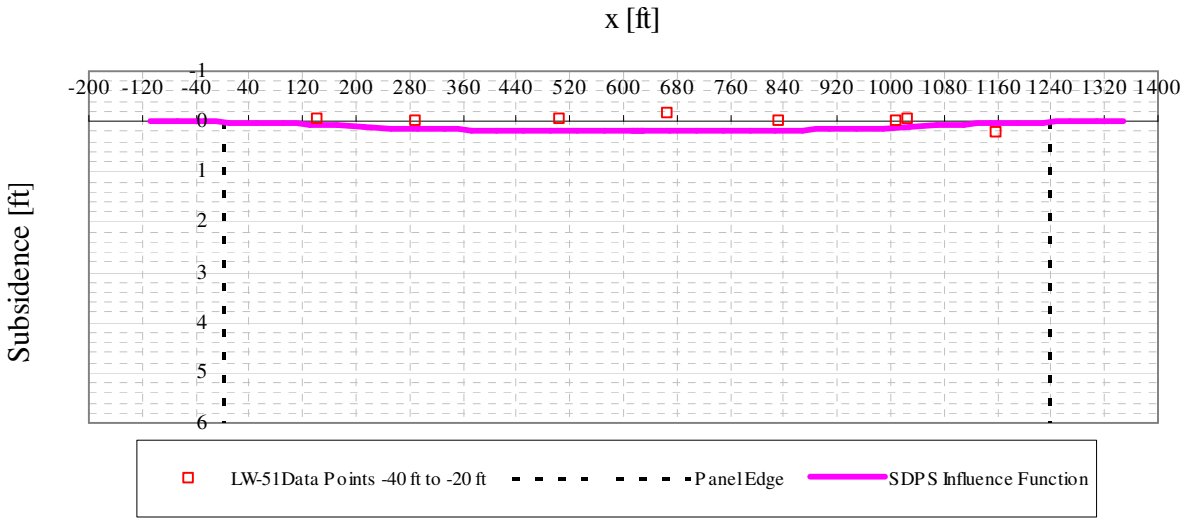

Figure A6- 5 LW-51 transverse view of data points from -40 ft to -20 ft from mine face and SDPS prediction

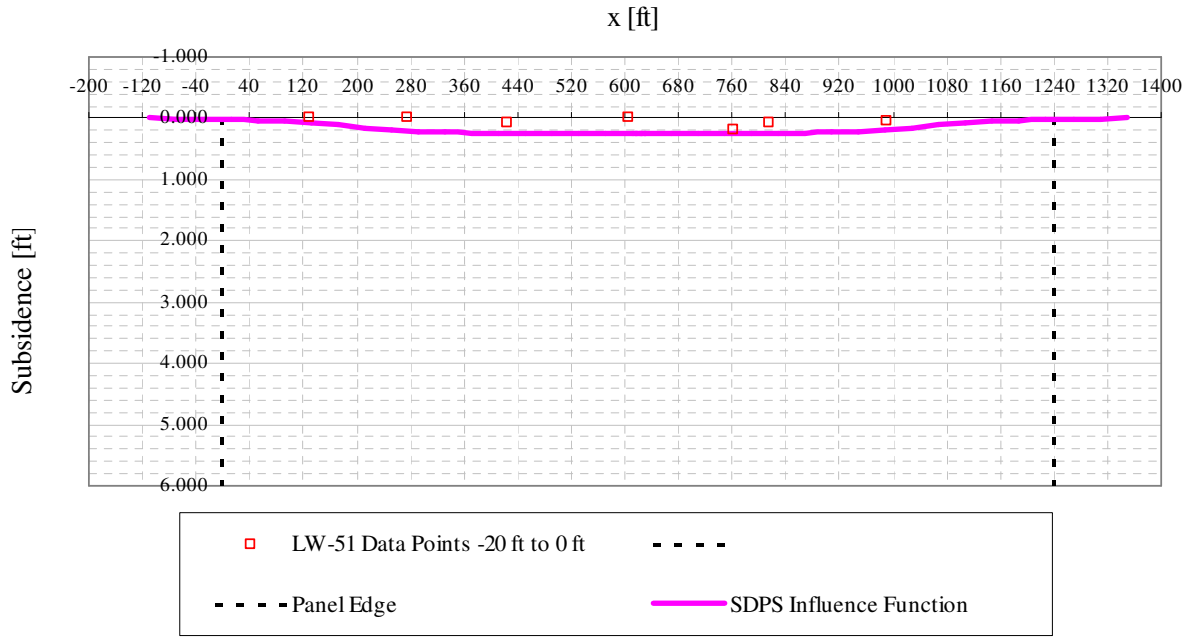

Figure A6- 6 LW-51 transverse view of data points from -20 ft to 0 ft from mine face and SDPS prediction

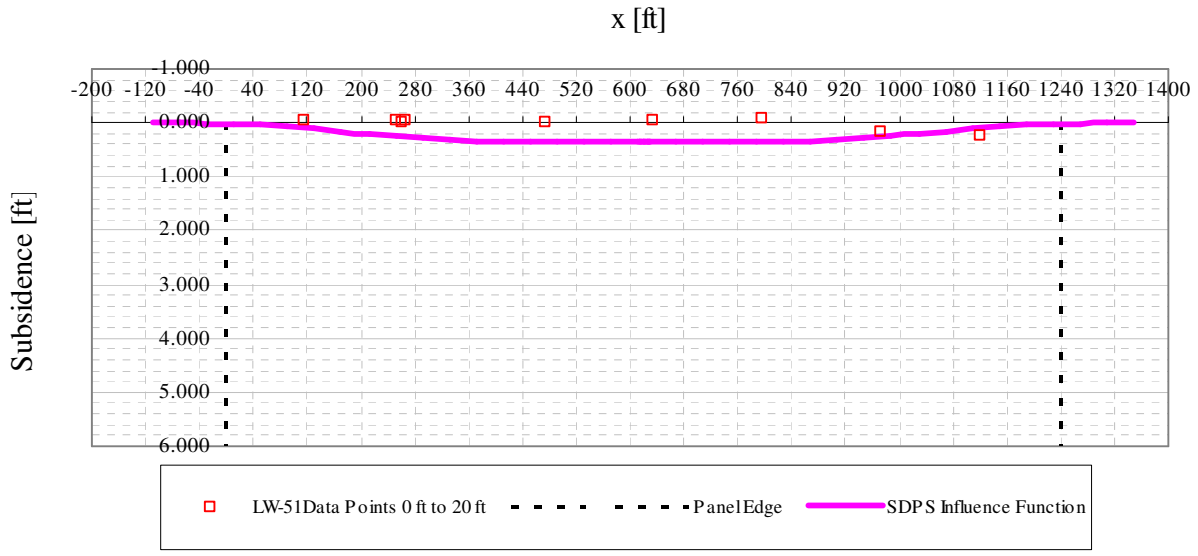

Figure A6- 7 LW-51 transverse view of data points from 0 ft to 20 ft from mine face and SDPS prediction

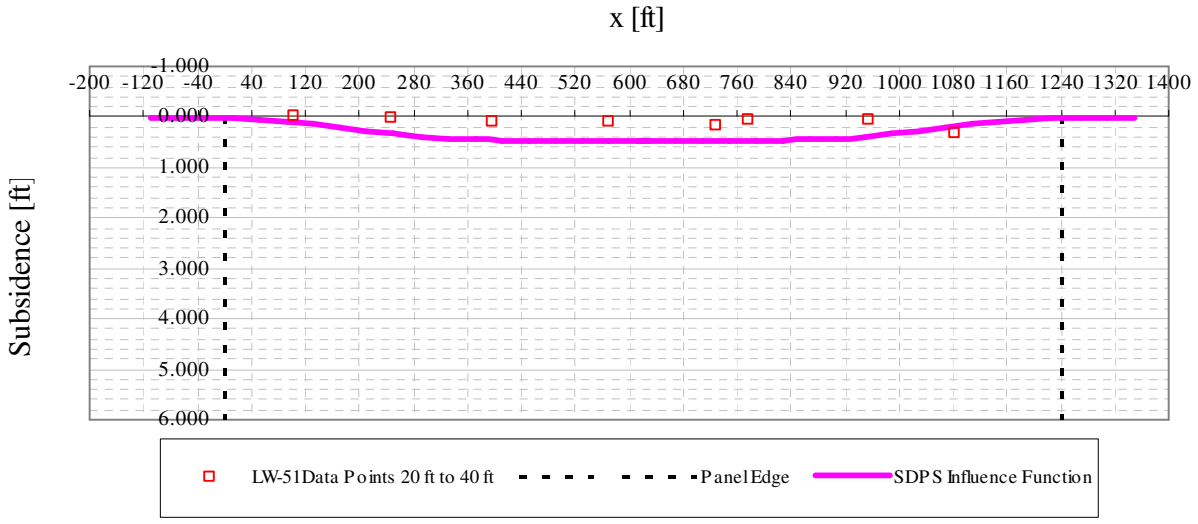

Figure A6- 8 LW-51 transverse view of data points from 20 ft to 40 ft from mine face and SDPS prediction

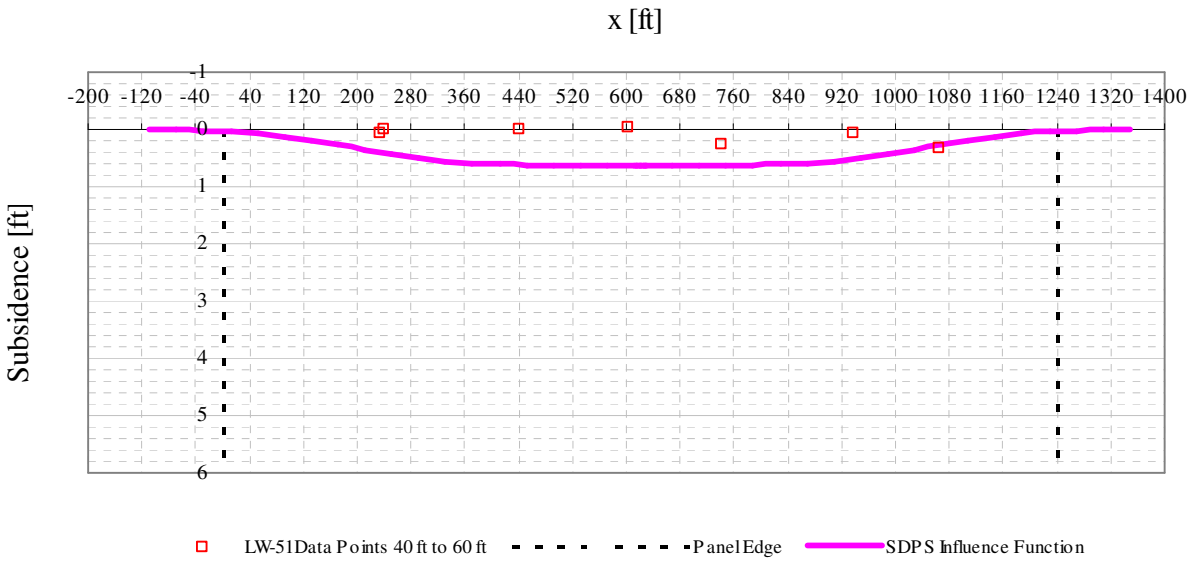

Figure A6- 9 LW-51 transverse view of data points from 40 ft to 60 ft from mine face and SDPS prediction

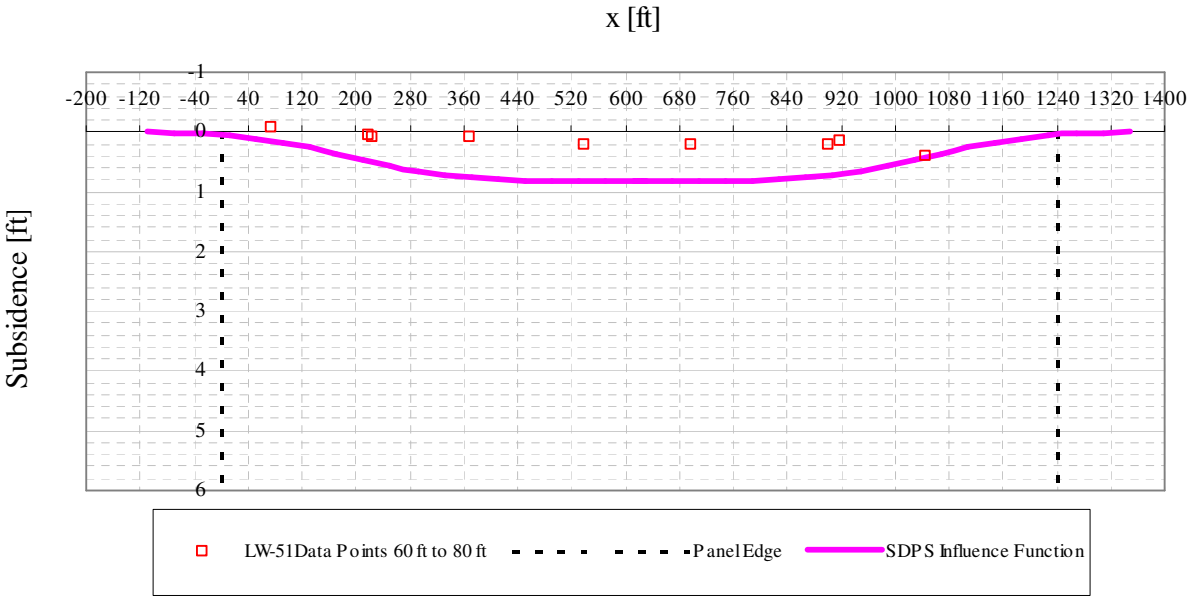

Figure A6- 10 LW-51 transverse view of data points from 60 ft to 80 ft from mine face and SDPS prediction

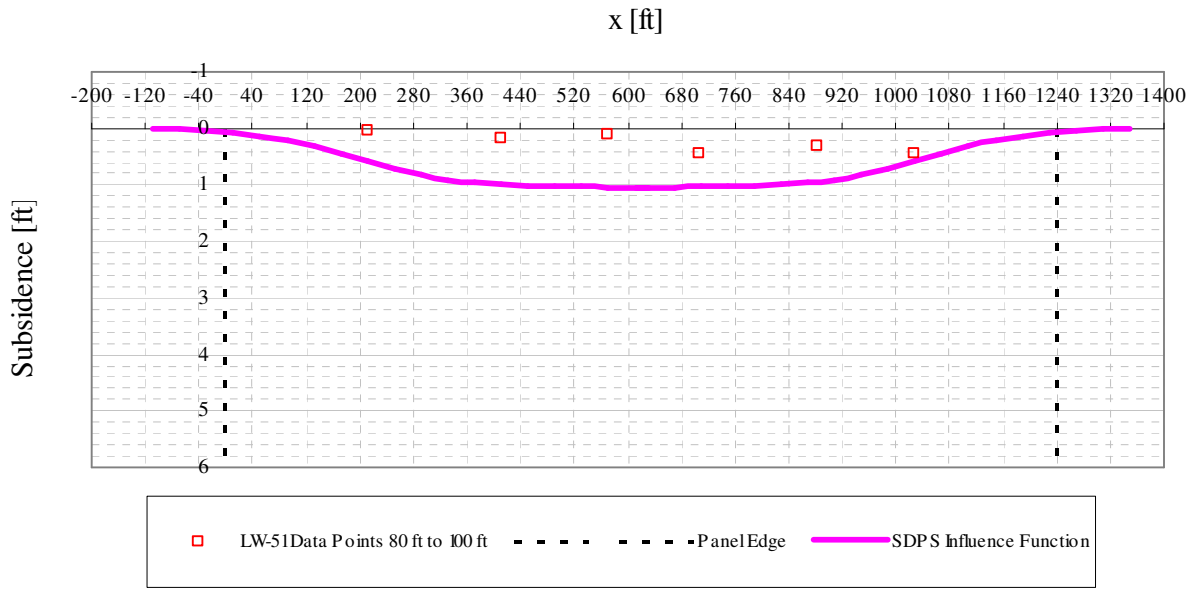

Figure A6- 11 LW-51 transverse view of data points from 80 ft to 100 ft from mine face and SDPS prediction

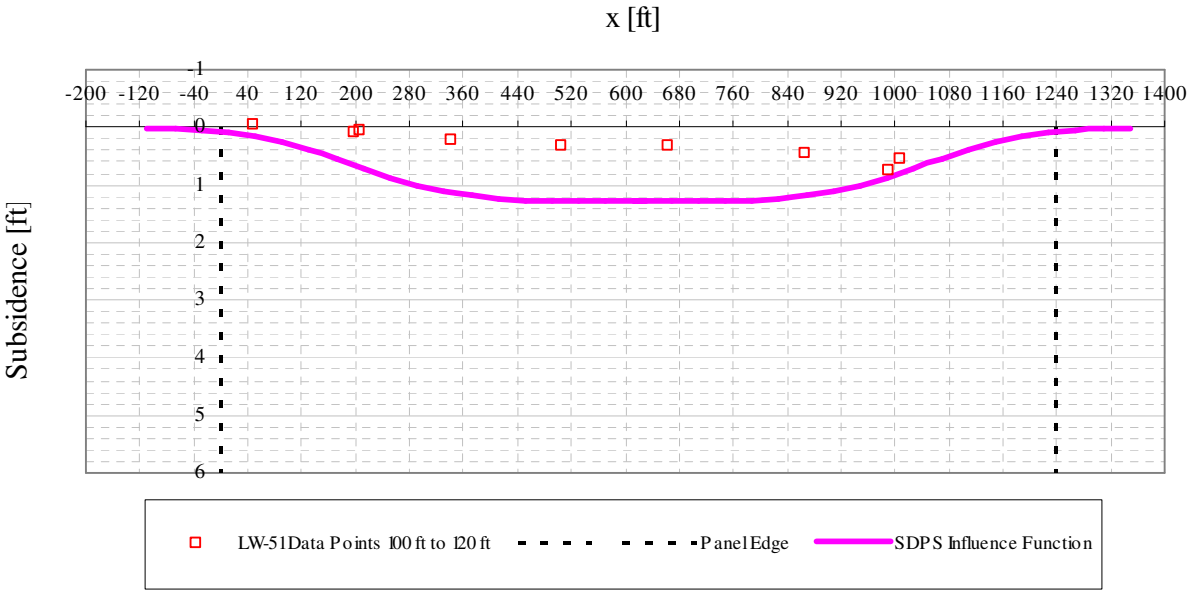

Figure A6- 12 LW-51 transverse view of data points from 100 ft to 120 ft from mine face and SDPS prediction

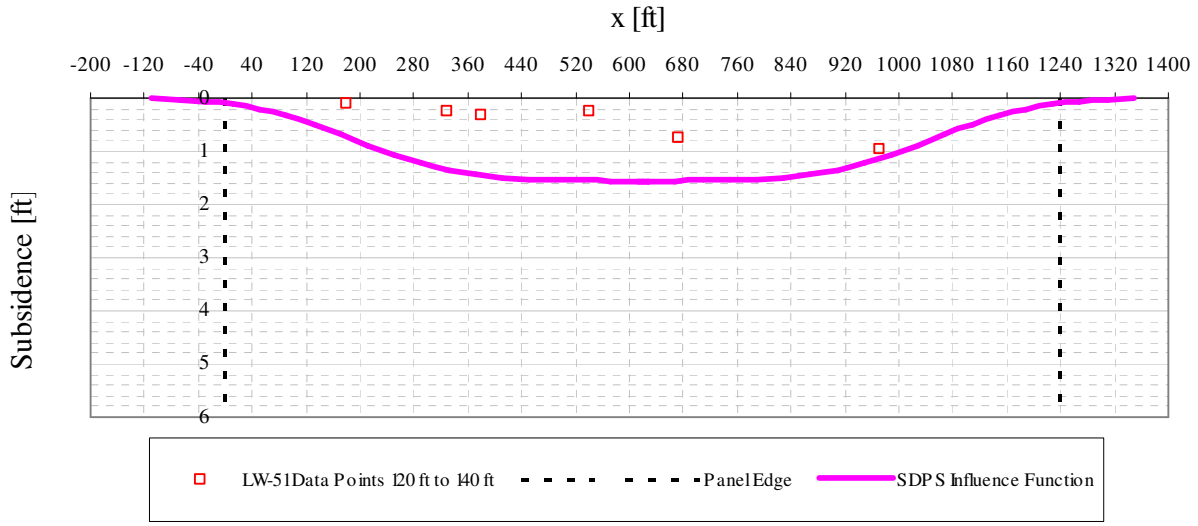

Figure A6- 13 LW-51 transverse view of data points from 120 ft to 140 ft from mine face and SDPS prediction

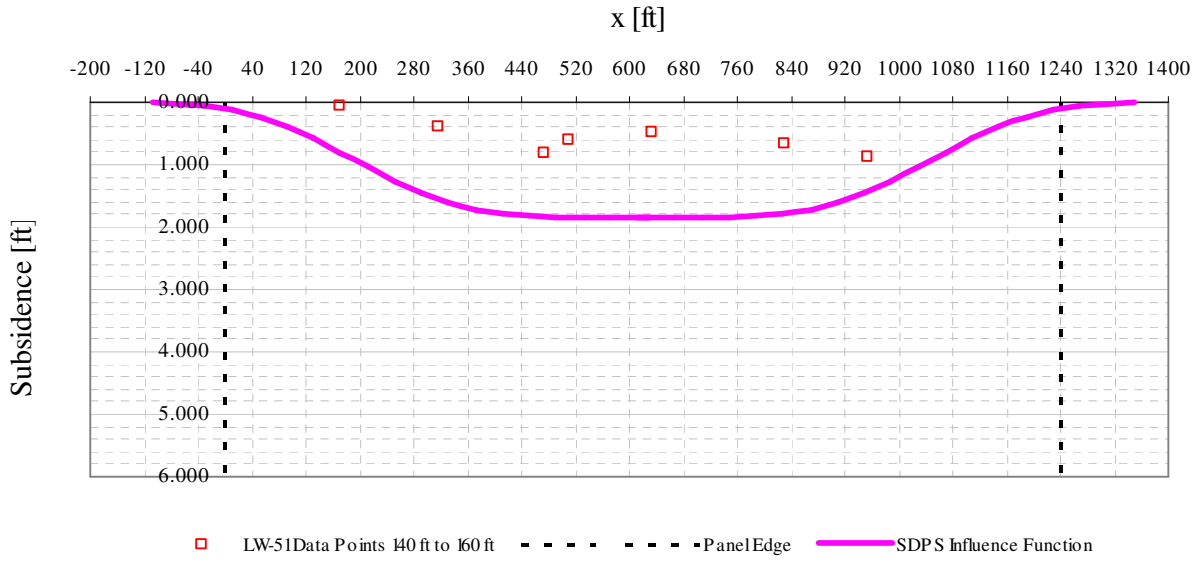

Figure A6- 14 LW-51 transverse view of data points from 140 ft to 160 ft from mine face and SDPS prediction

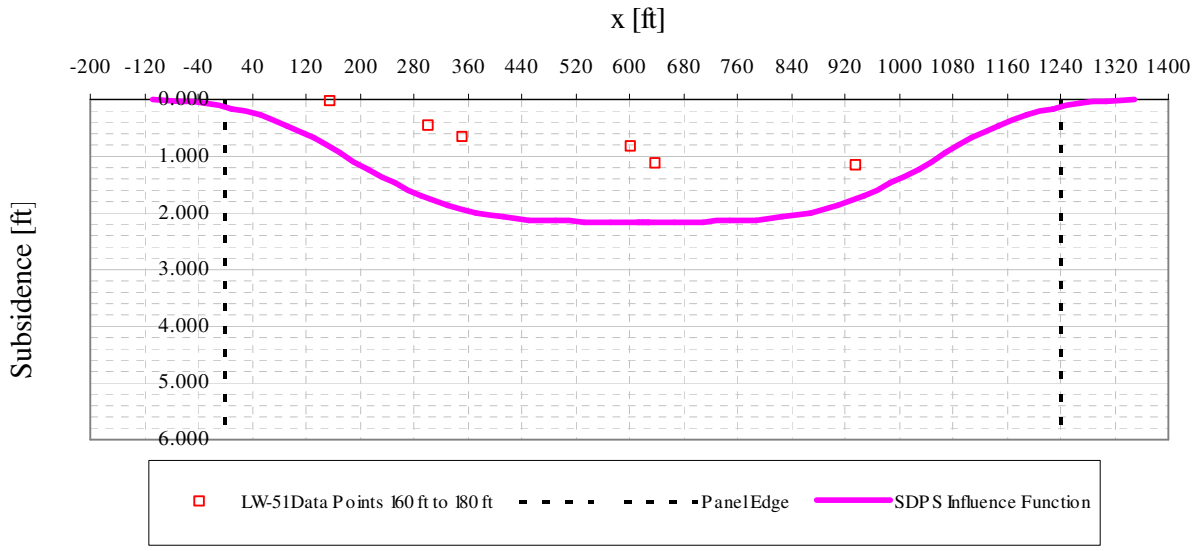

Figure A6- 15 LW-51 transverse view of data points from 160 ft to 180 ft from mine face and SDPS prediction

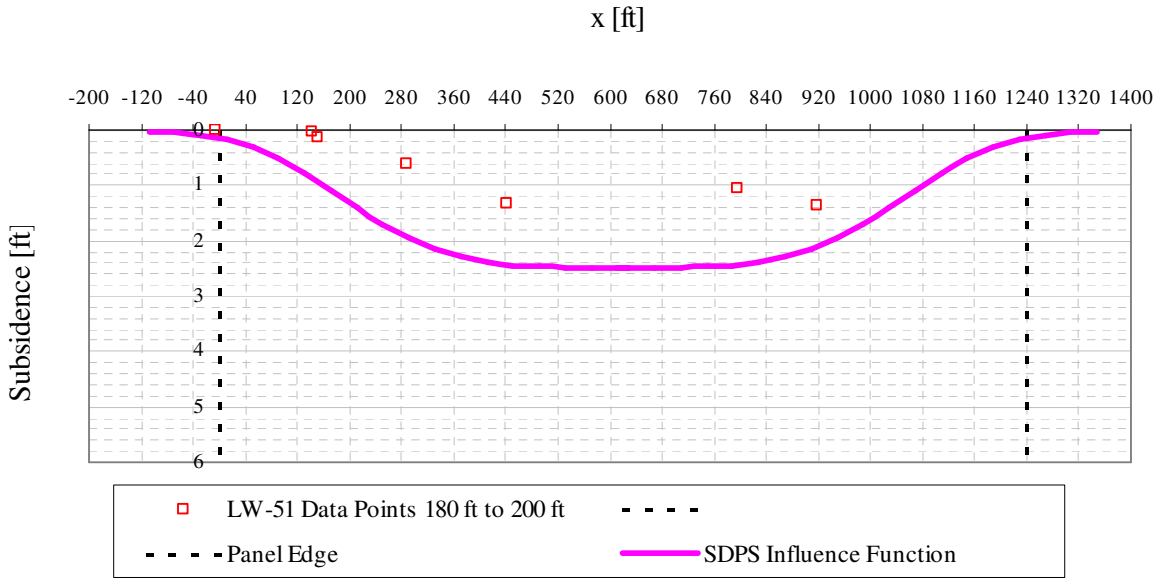

Figure A6- 16 LW-51 transverse view of data points from 180 ft to 200 ft from mine face and SDPS prediction

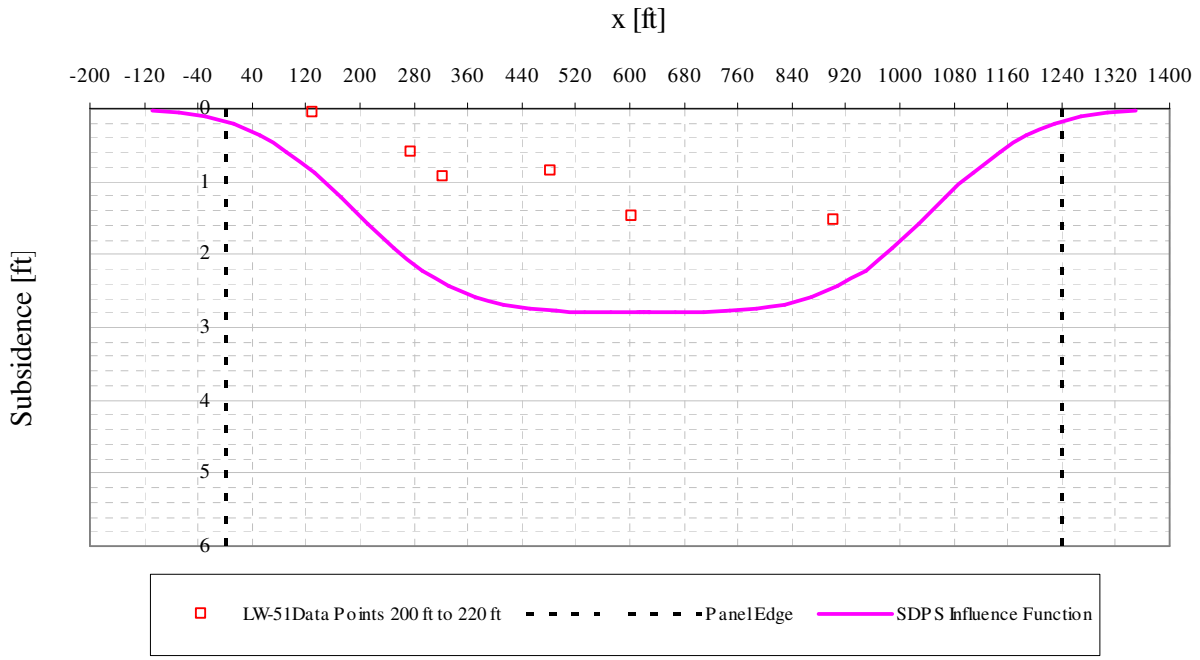

Figure A6- 17 LW-51 transverse view of data points from 200 ft to 220 ft from mine face and SDPS prediction

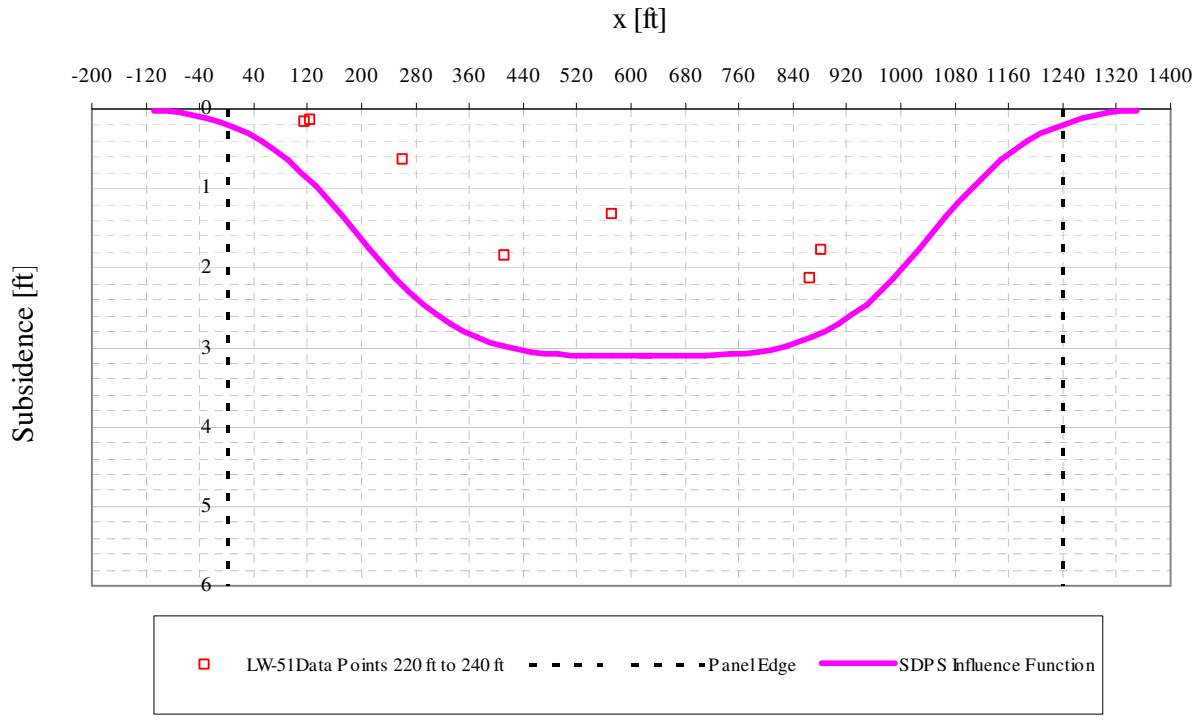

Figure A6- 18 LW-51 transverse view of data points from 220 ft to 240 ft from mine face and SDPS prediction

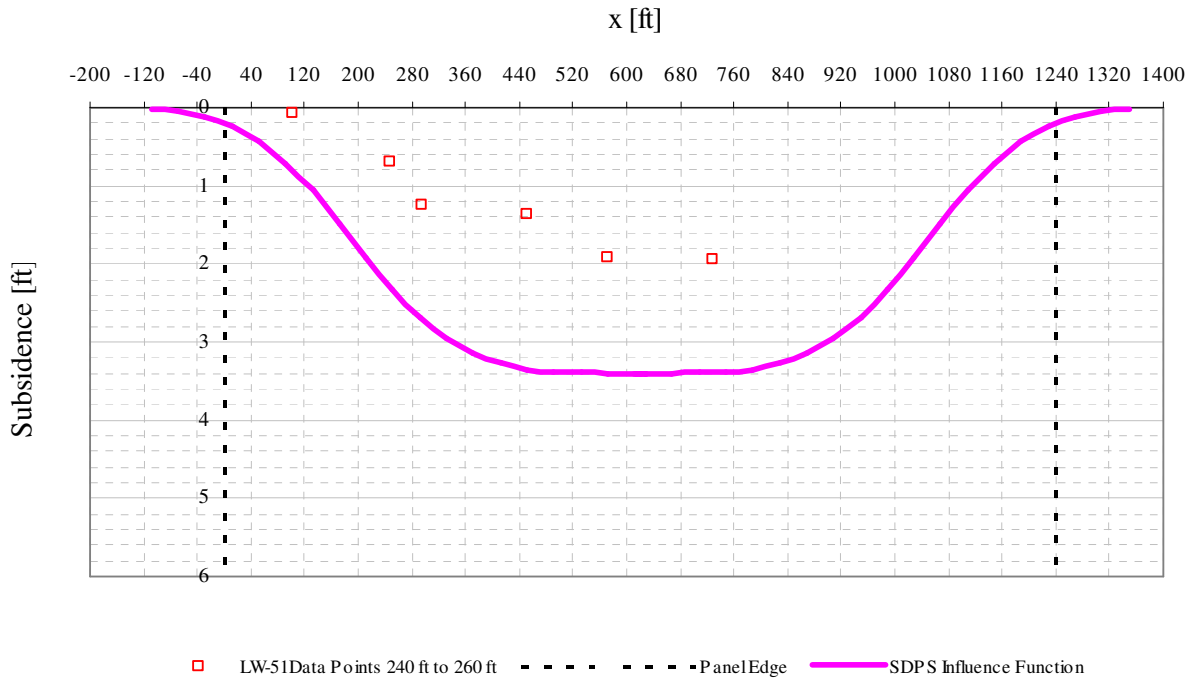

Figure A6- 19 LW-51 transverse view of data points from 240 ft to 260 ft from mine face and SDPS prediction

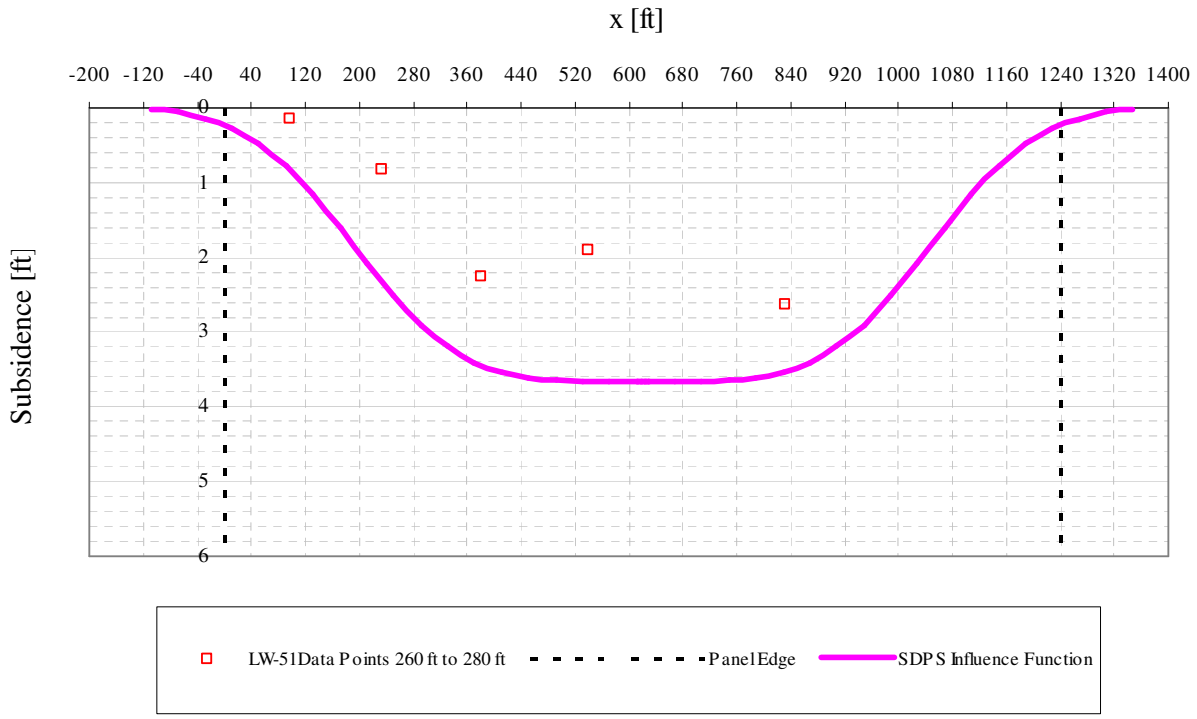

Figure A6- 20 LW-51 transverse view of data points from 260 ft to 280 ft from mine face and SDPS prediction

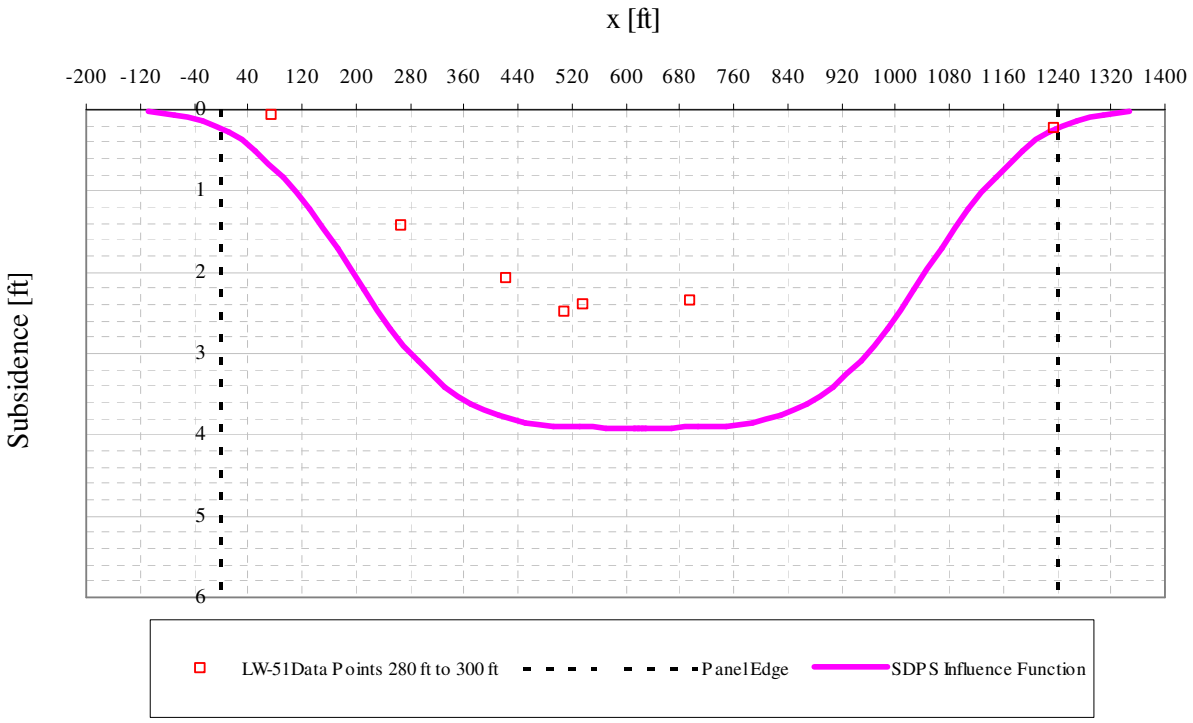

Figure A6- 21 LW-51 transverse view of data points from 280 ft to 300 ft from mine face and SDPS prediction

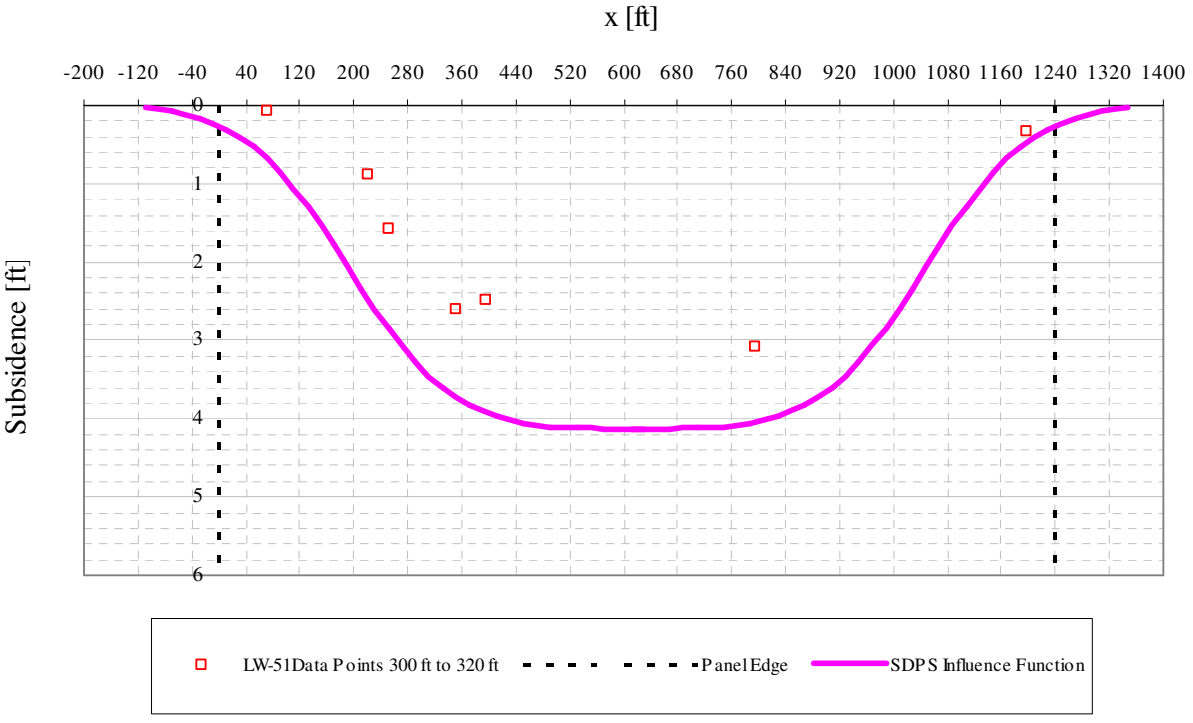

Figure A6- 22 LW-51 transverse view of data points from 300 ft to 320 ft from mine face and SDPS prediction

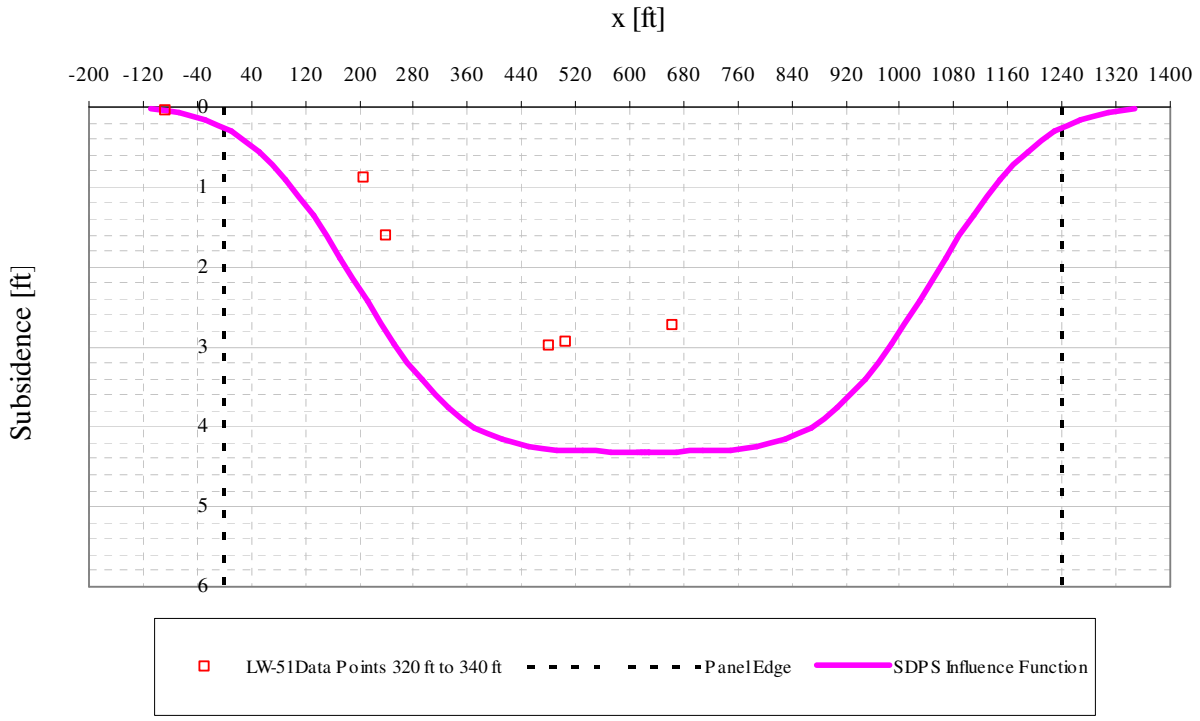

Figure A6- 23 LW-51 transverse view of data points from 320 ft to 340 ft from mine face and SDPS prediction

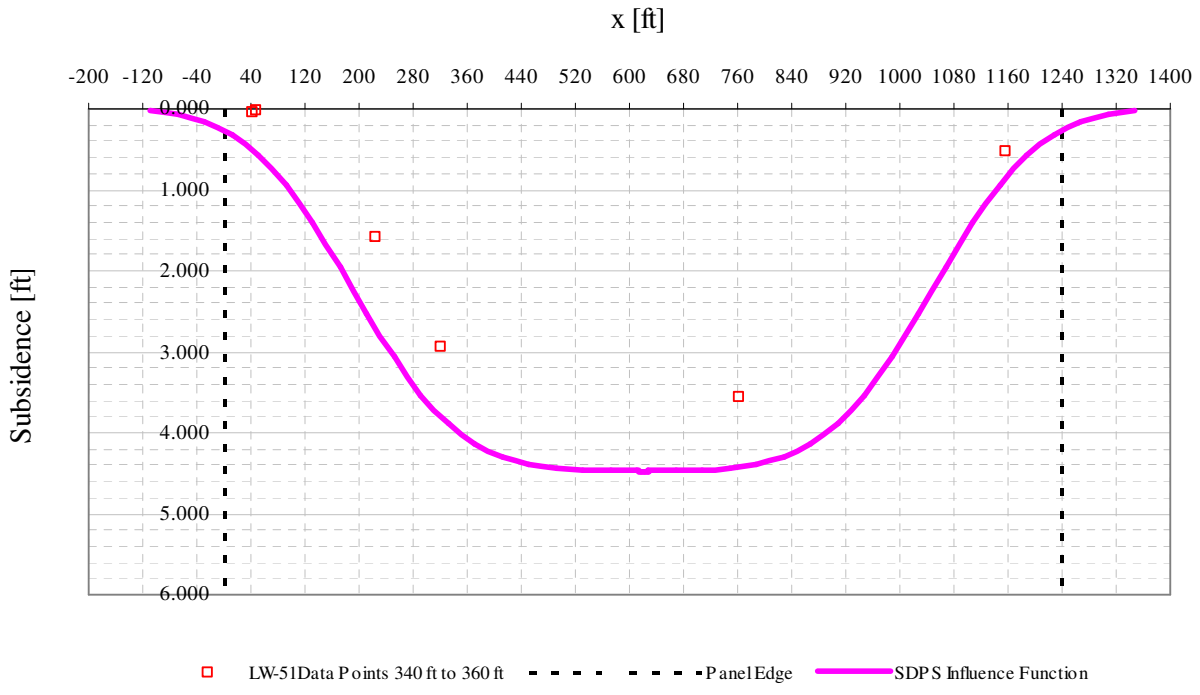

Figure A6- 24 LW-51 transverse view of data points from 340 ft to 360 ft from mine face and SDPS prediction

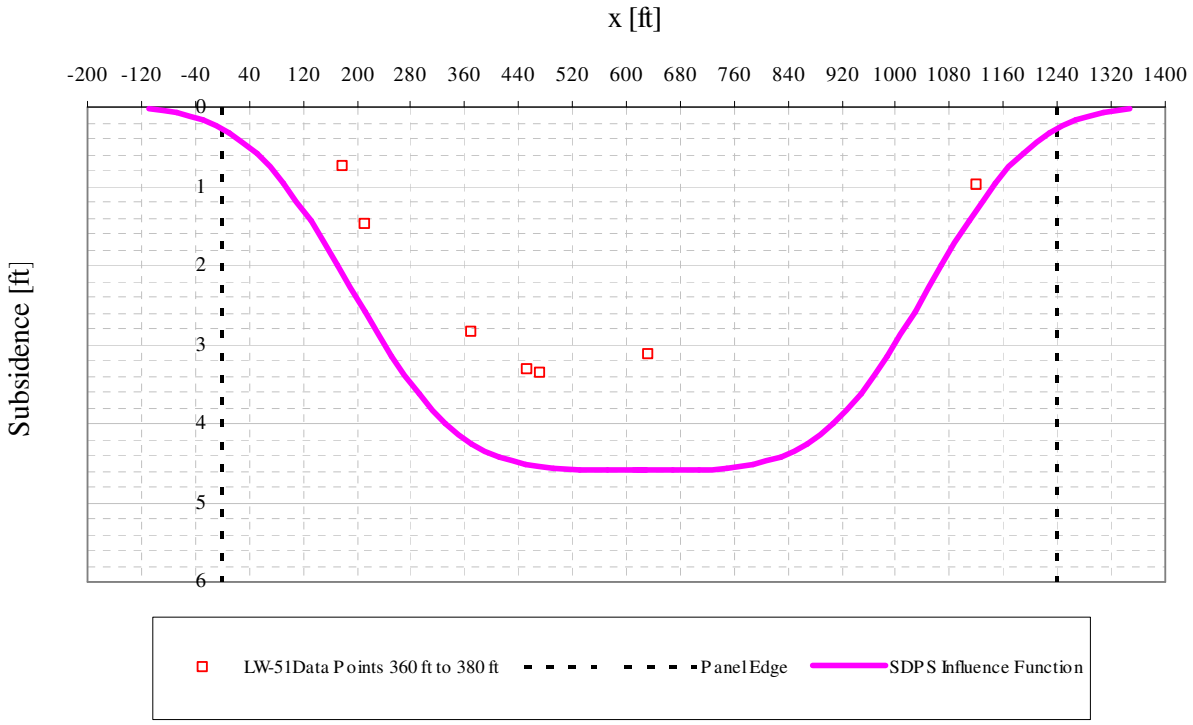

Figure A6- 25 LW-51 transverse view of data points from 360 ft to 380 ft from mine face and SDPS prediction

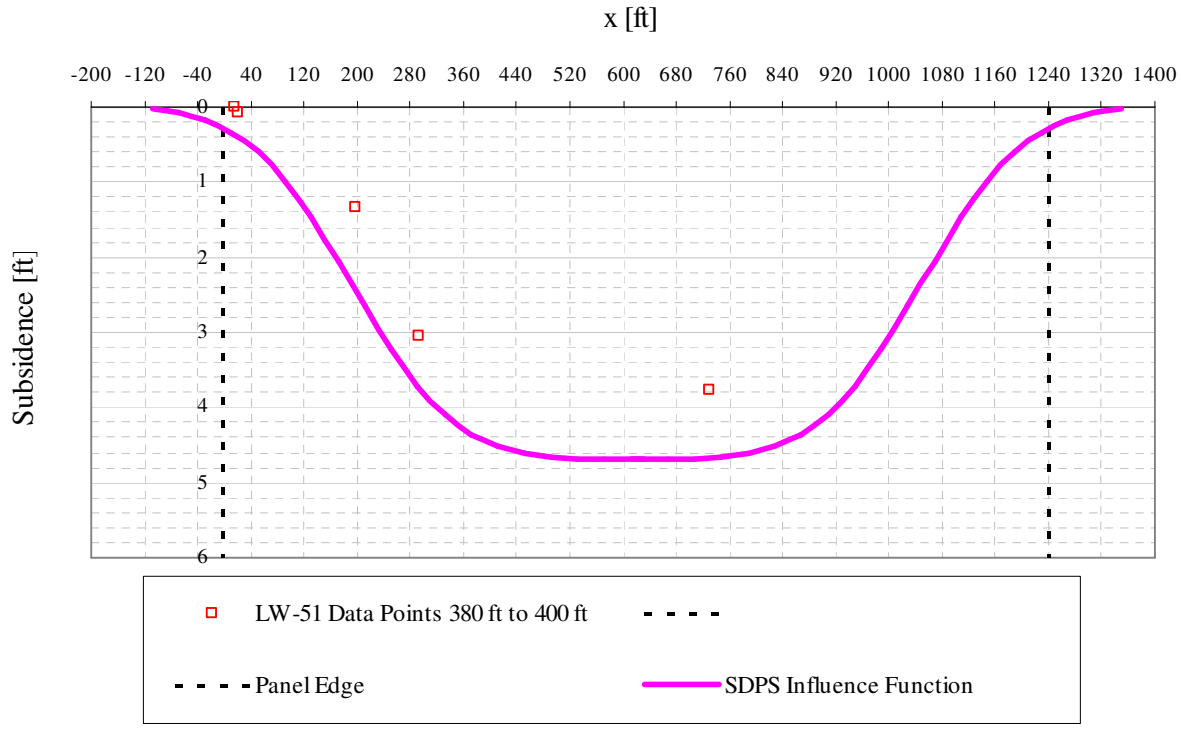

Figure A6- 26 LW-51 transverse view of data points from 380 ft to 400 ft from mine face and SDPS prediction

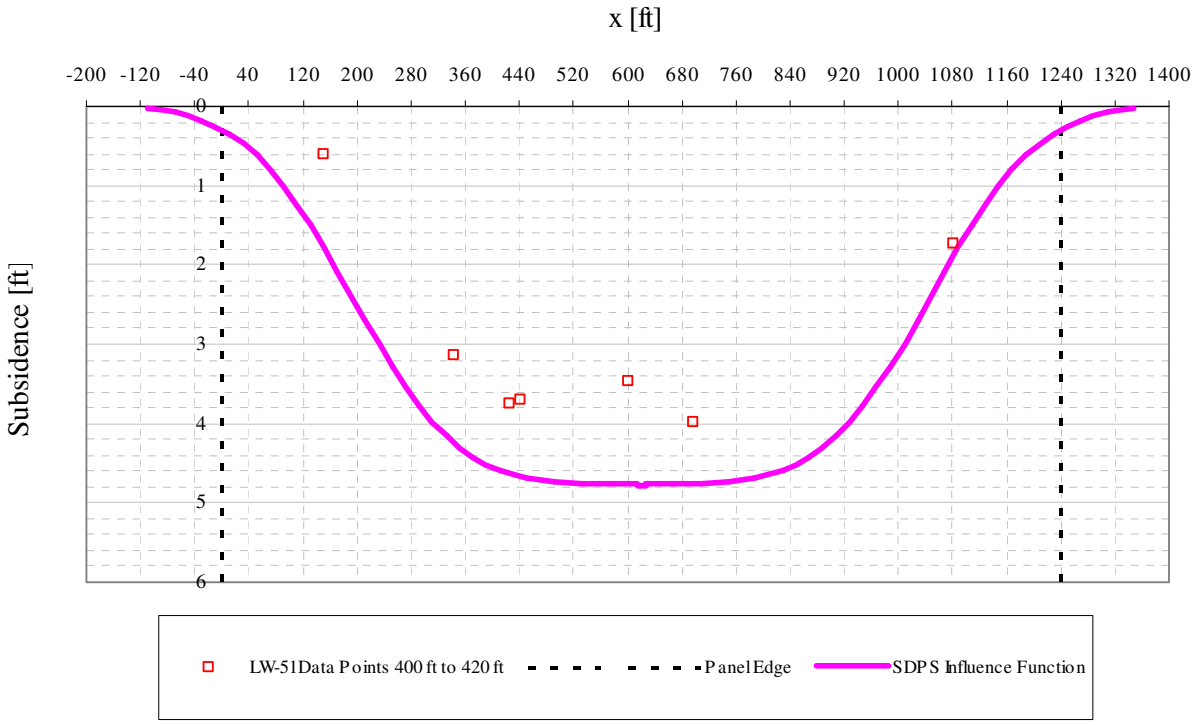

Figure A6- 27 LW-51 transverse view of data points from 400 ft to 420 ft from mine face and SDPS prediction

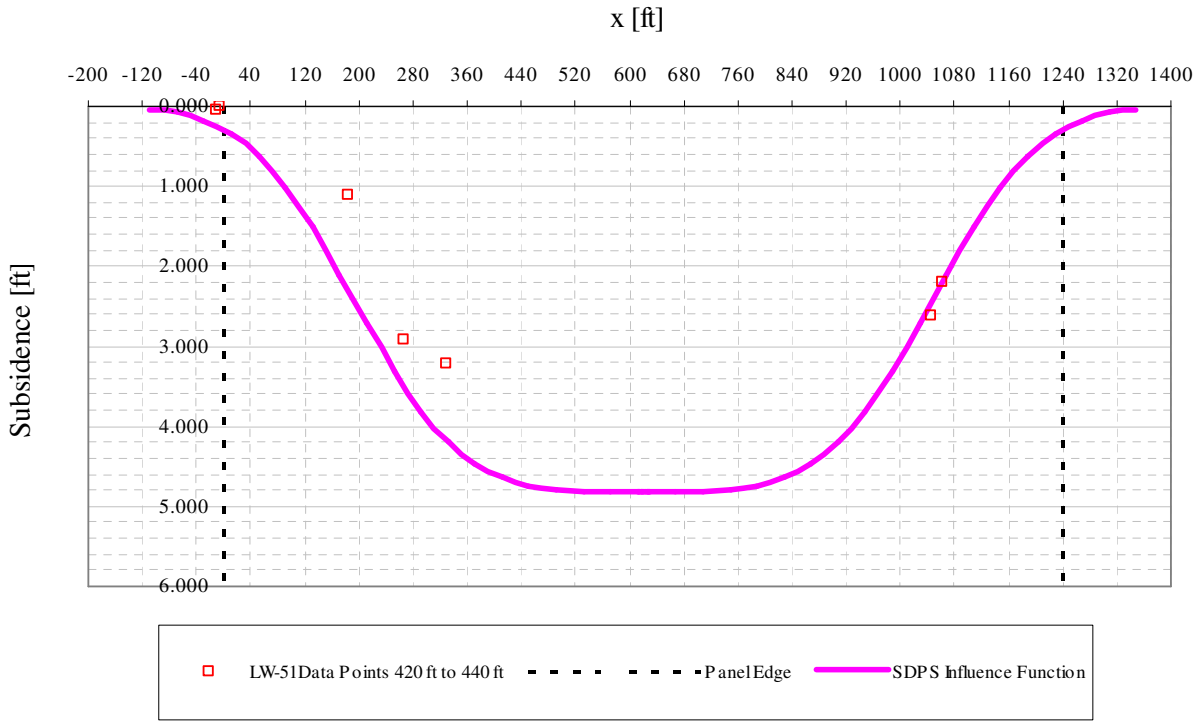

Figure A6- 28 LW-51 transverse view of data points from 420 ft to 440 ft from mine face and SDPS prediction

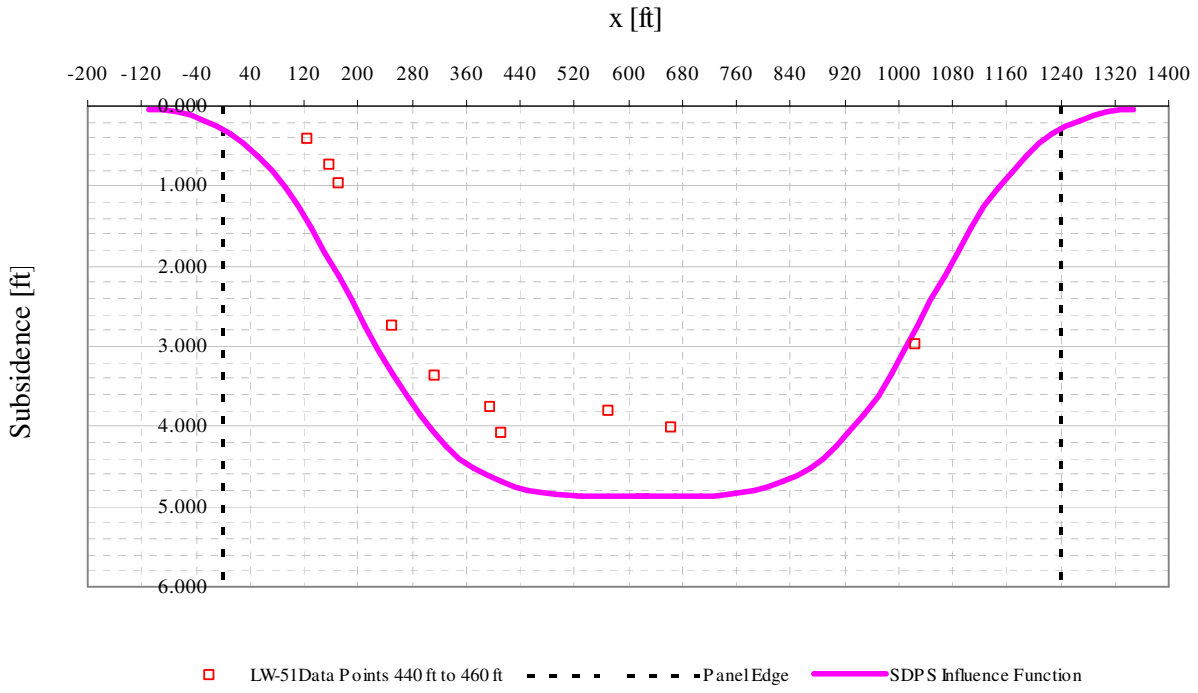

Figure A6- 29 LW-51 transverse view of data points from 440 ft to 460 ft from mine face and SDPS prediction

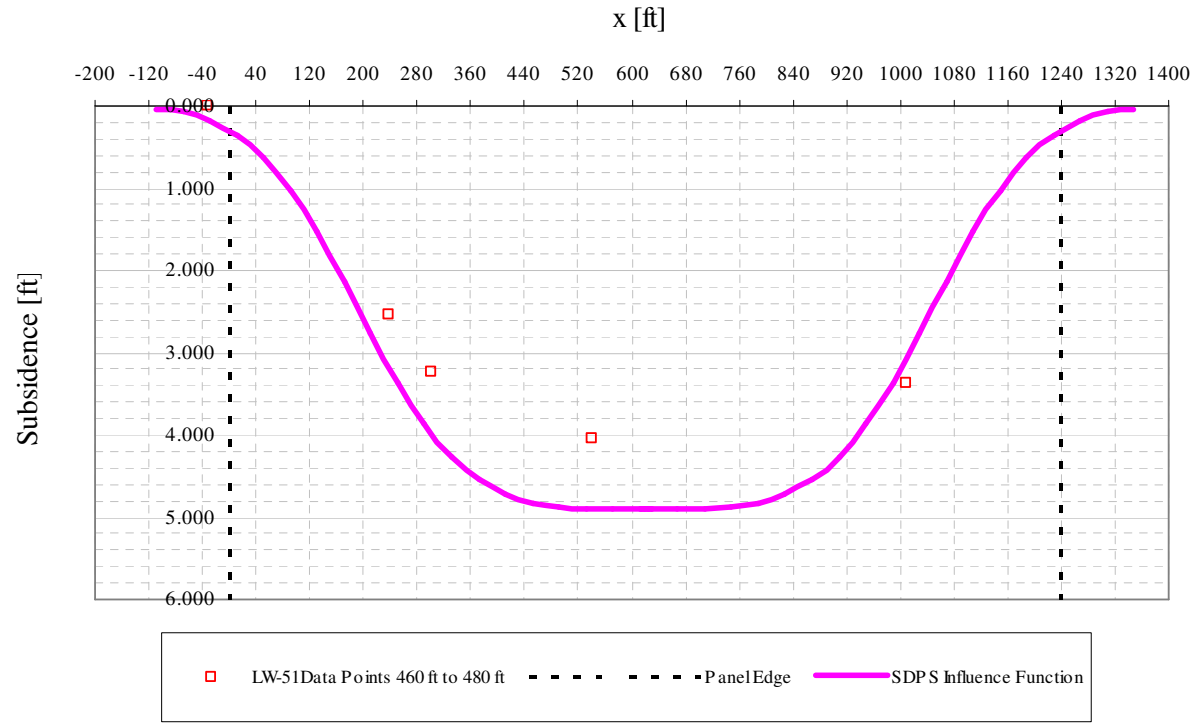

Figure A6- 30 LW-51 transverse view of data points from 460 ft to 480 ft from mine face and SDPS prediction

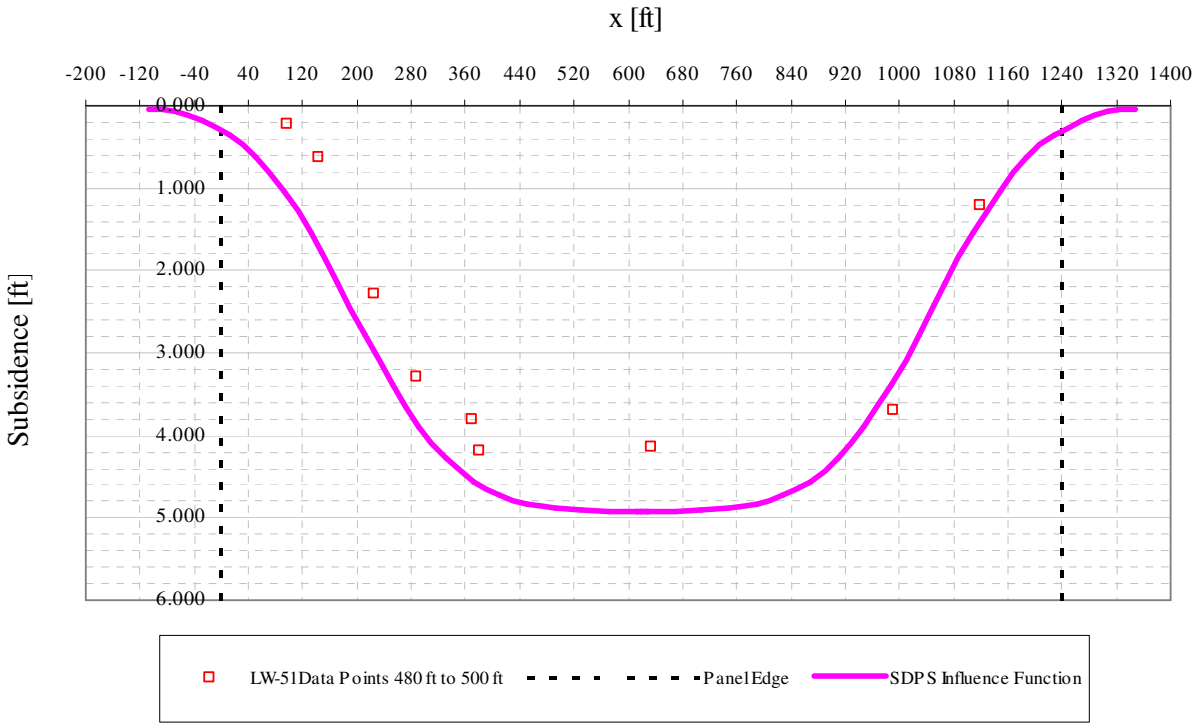

Figure A6- 31 LW-51 transverse view of data points from 480 ft to 500 ft from mine face and SDPS prediction

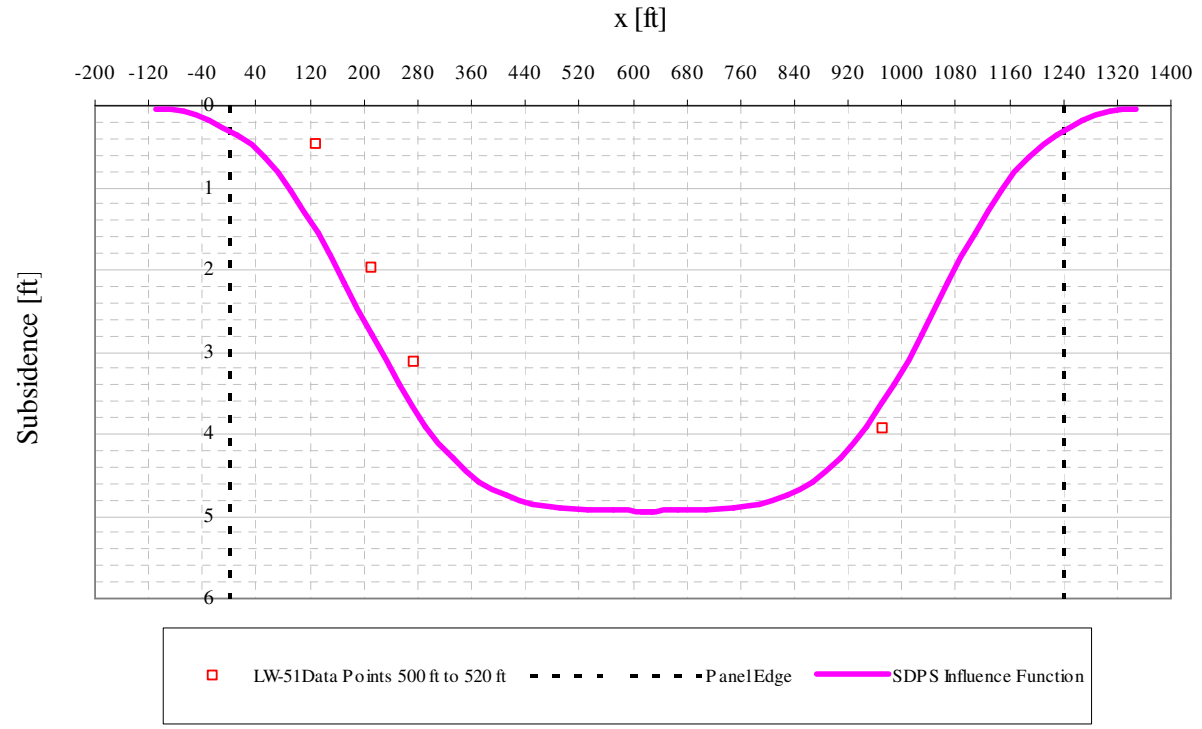

Figure A6- 32 LW-51 transverse view of data points from 500 ft to 520 ft from mine face and SDPS prediction

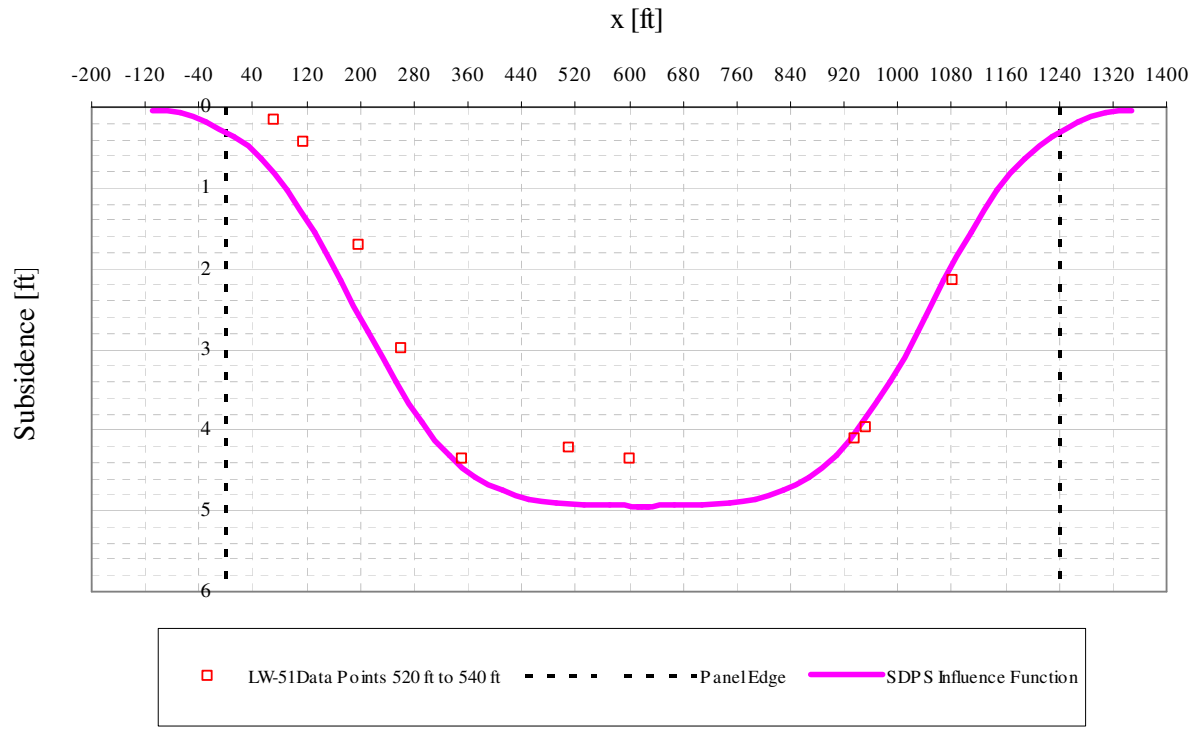

Figure A6- 33 LW-51 transverse view of data points from 520 ft to 540 ft from mine face and SDPS prediction

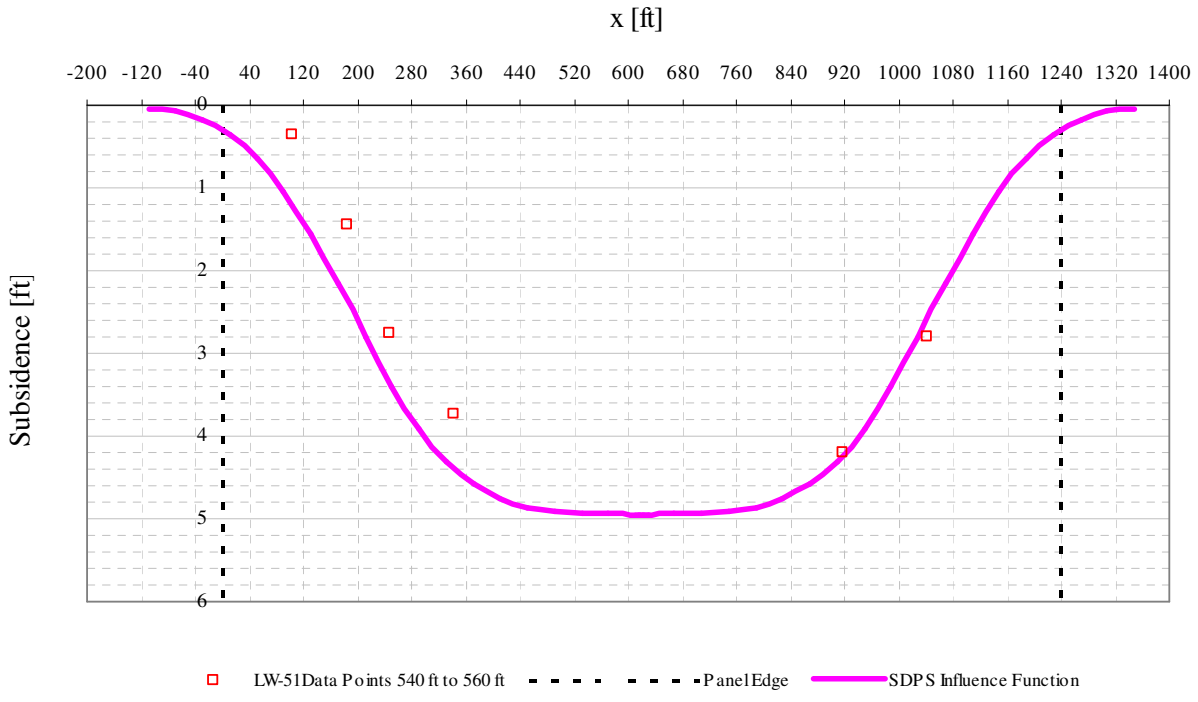

Figure A6- 34 LW-51 transverse view of data points from 540 ft to 560 ft from mine face and SDPS prediction

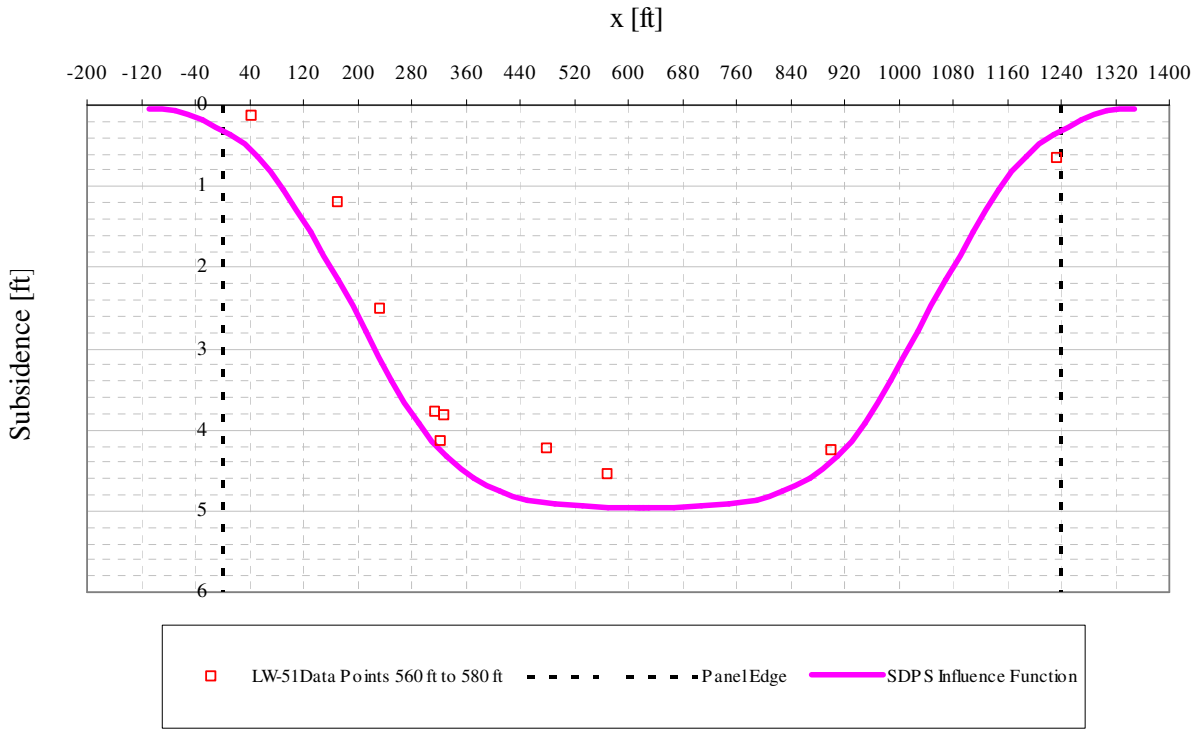

Figure A6- 35 LW-51 transverse view of data points from 560 ft to 580 ft from mine face and SDPS prediction

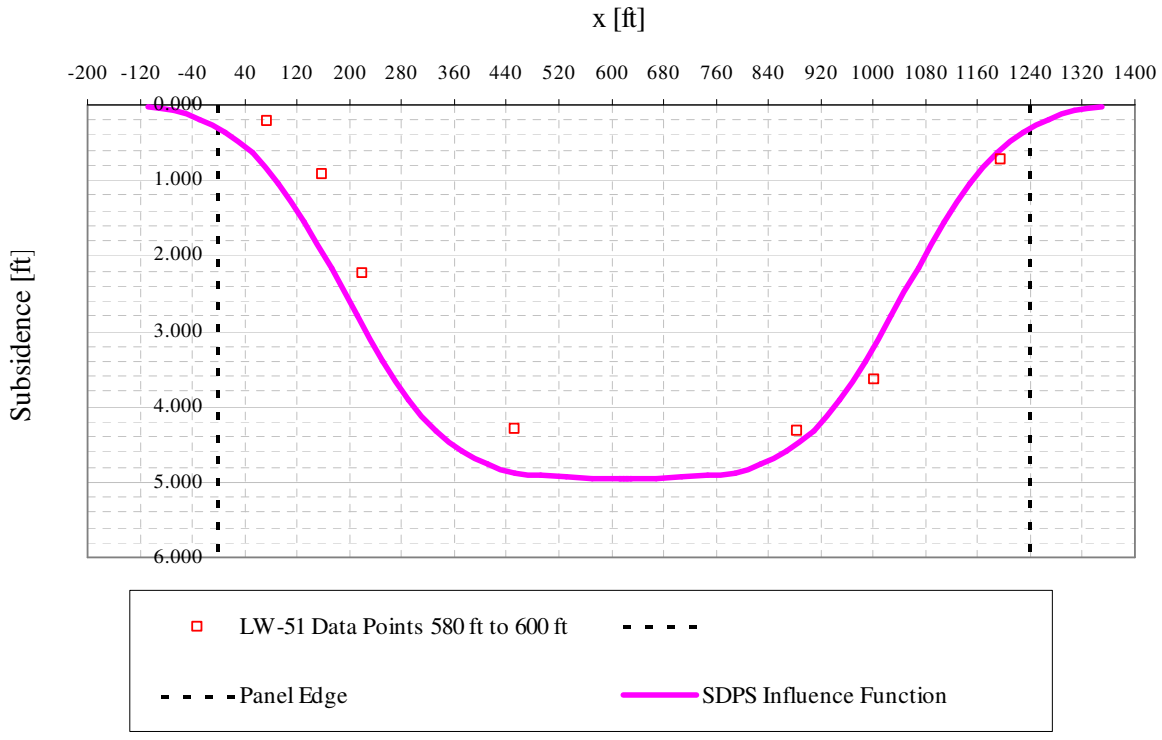

Figure A6- 36 LW-51 transverse view of data points from 580 ft to 600 ft from mine face and SDPS prediction

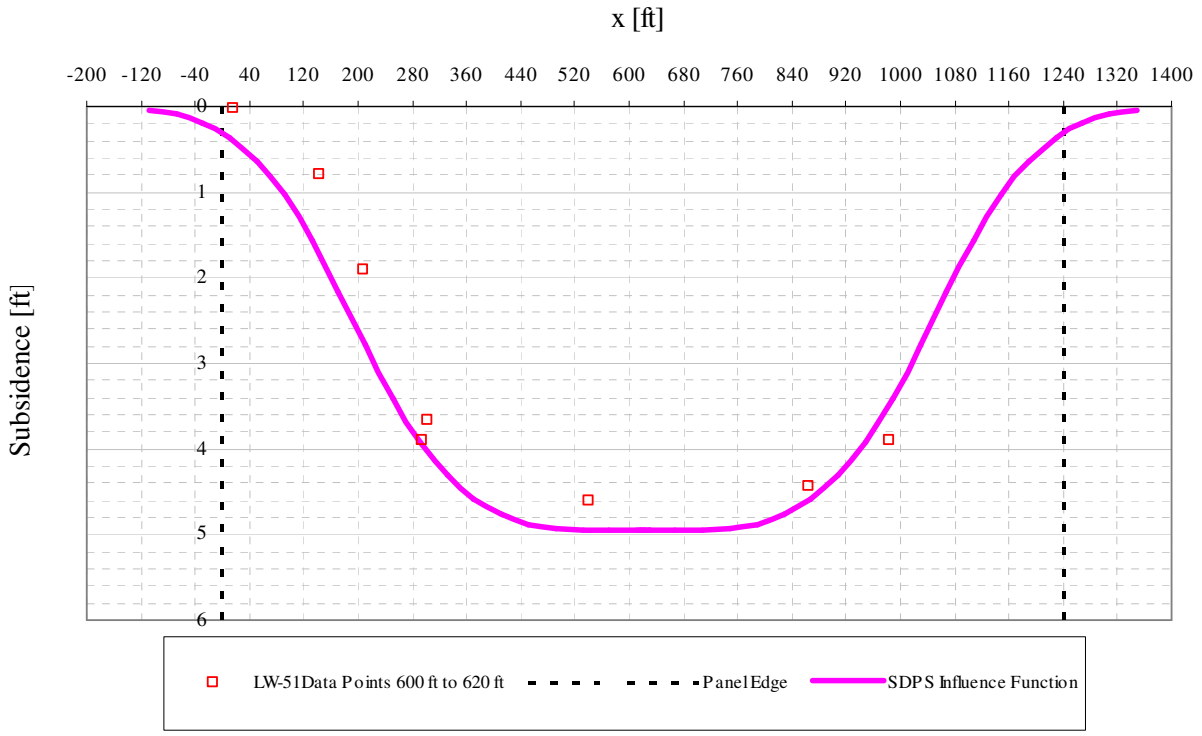

Figure A6- 37 LW-51 transverse view of data points from 600 ft to 620 ft from mine face and SDPS prediction

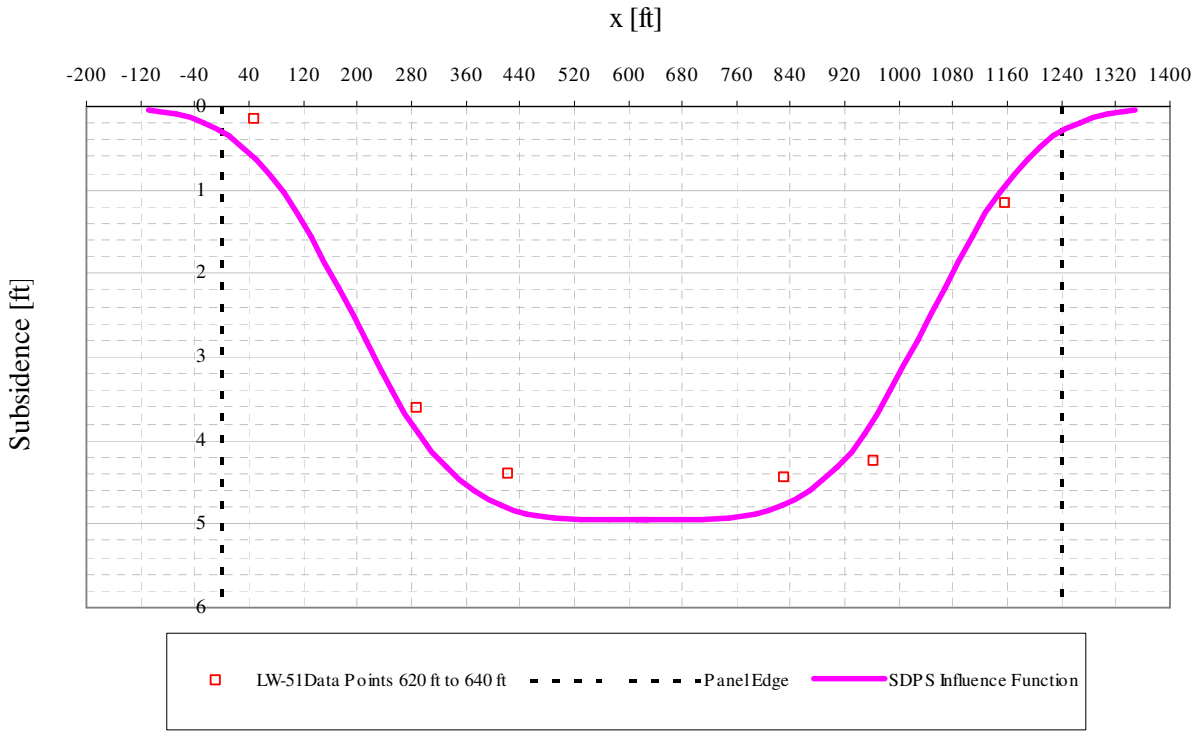

Figure A6- 38 LW-51 transverse view of data points from 620 ft to 640 ft from mine face and SDPS prediction

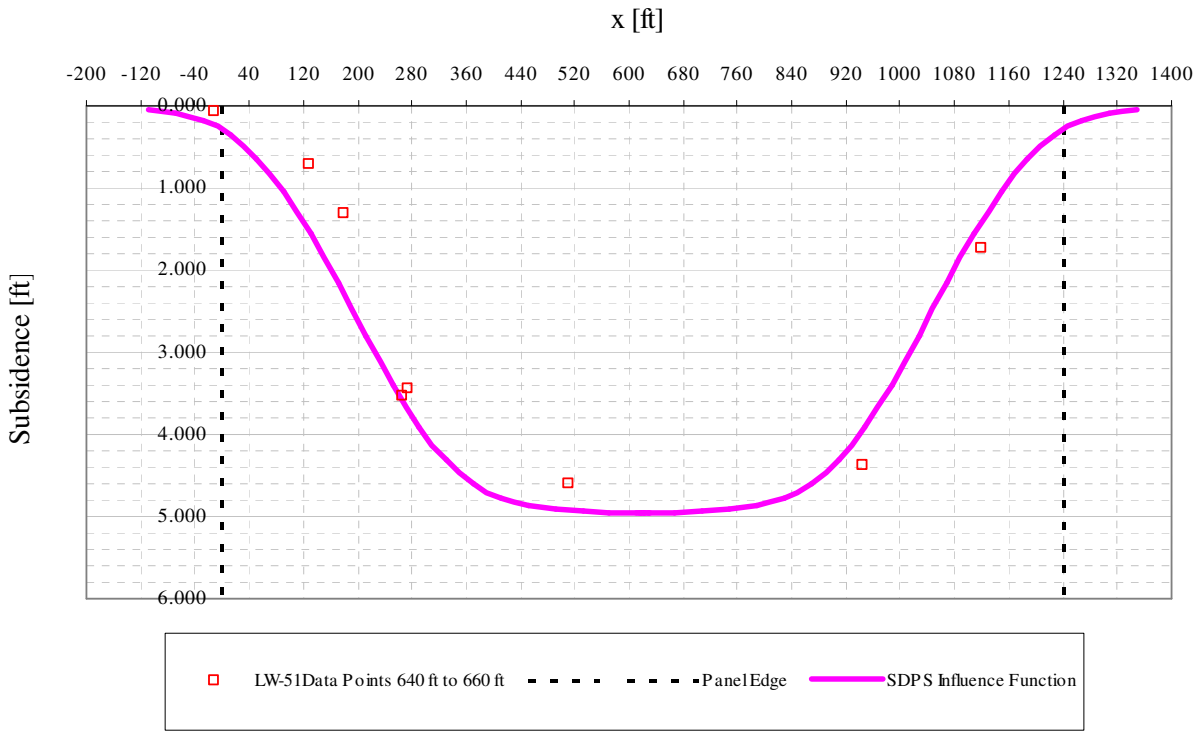

Figure A6- 39 LW-51 transverse view of data points from 640 ft to 660 ft from mine face and SDPS prediction

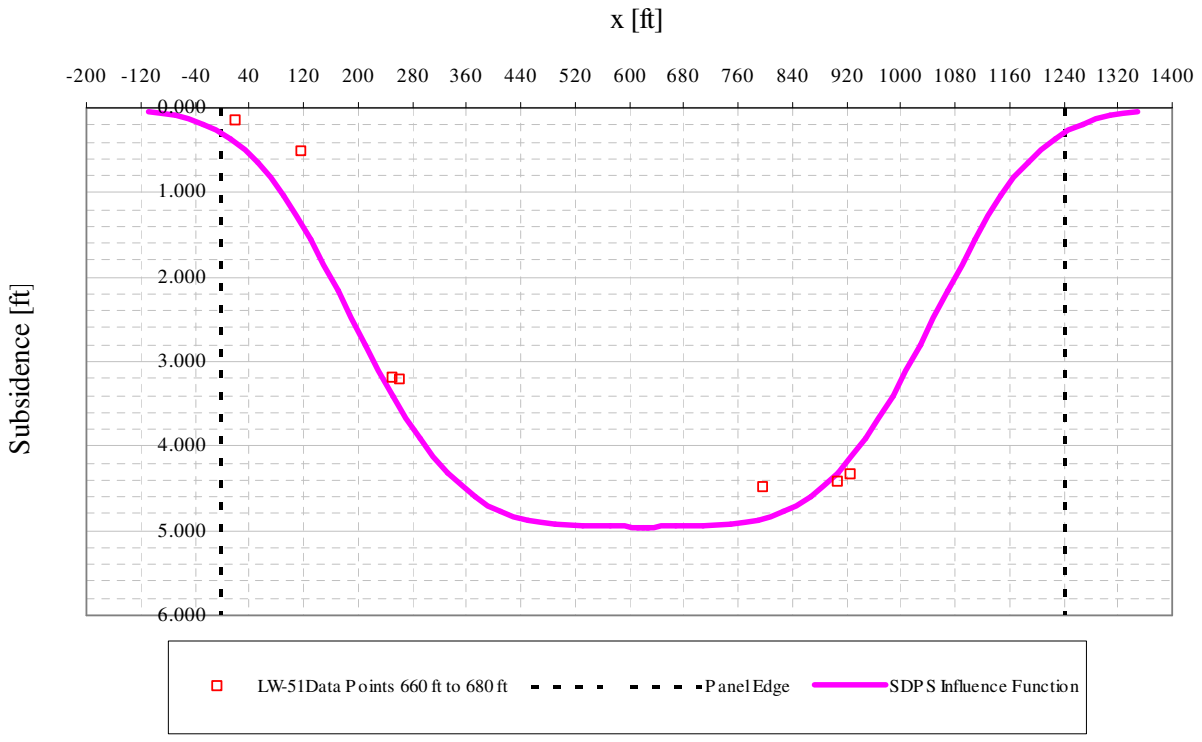

Figure A6- 40 LW-51 transverse view of data points from 660 ft to 680 ft from mine face and SDPS prediction

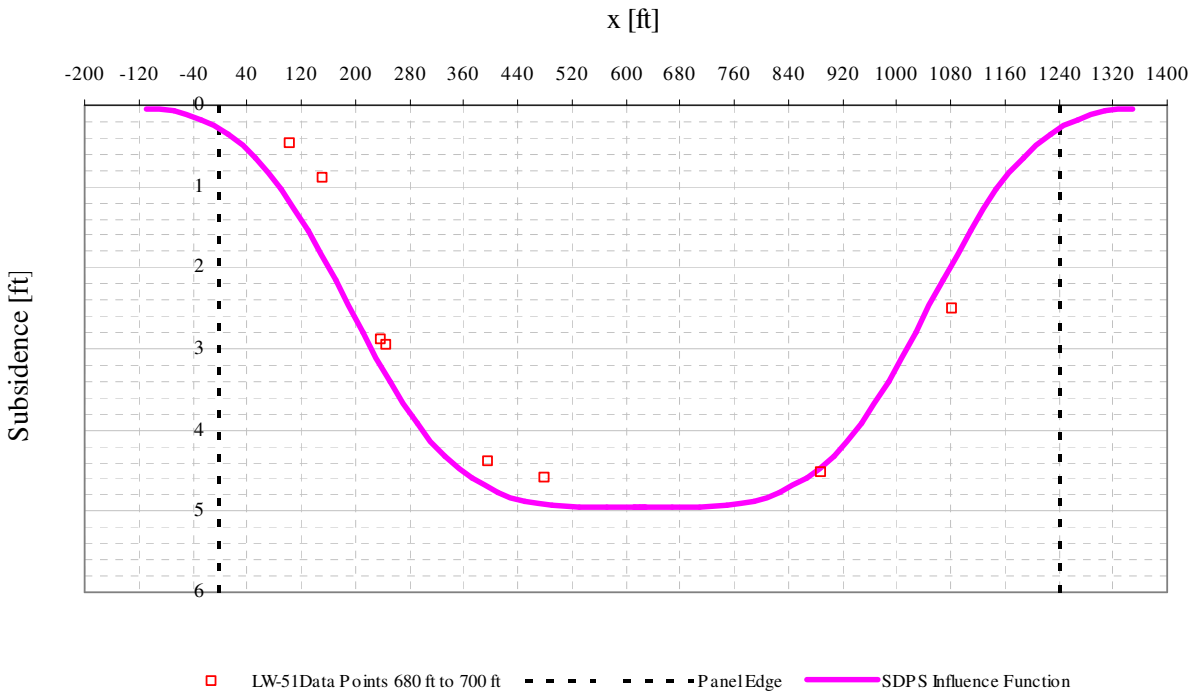

Figure A6- 41 LW-51 transverse view of data points from 680 ft to 700 ft from mine face and SDPS prediction

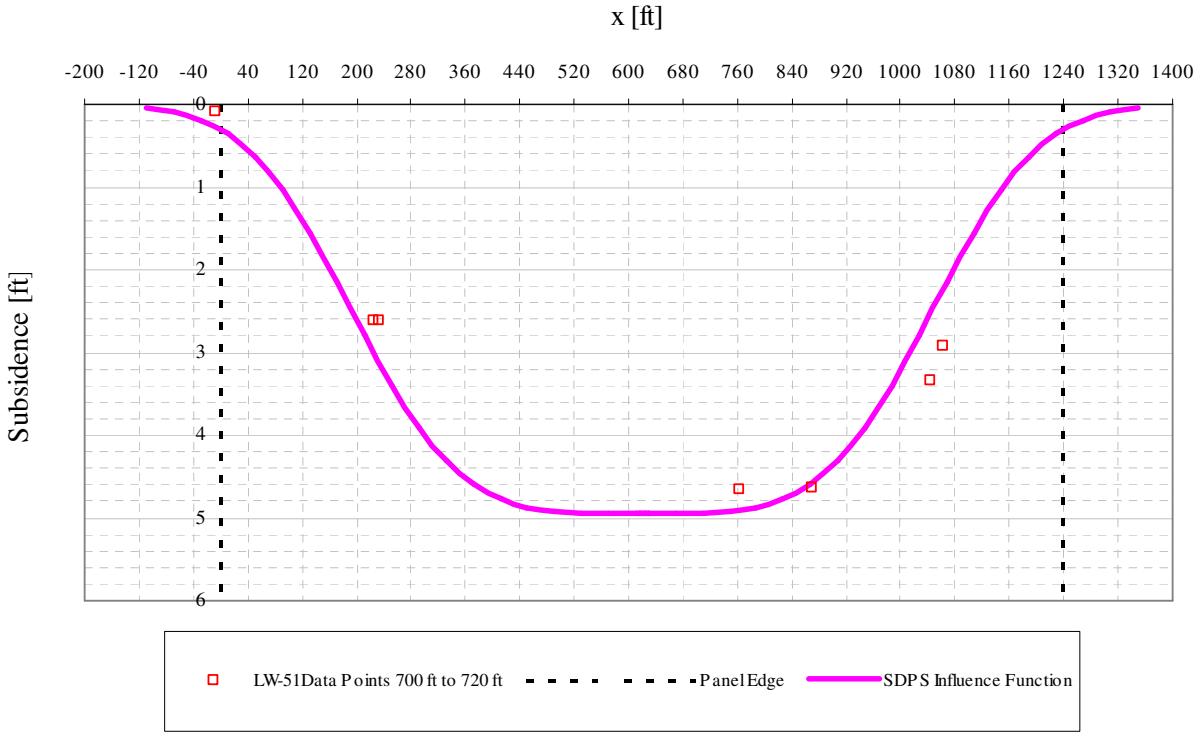

Figure A6- 42 LW-51 transverse view of data points from 700 ft to 720 ft from mine face and SDPS prediction

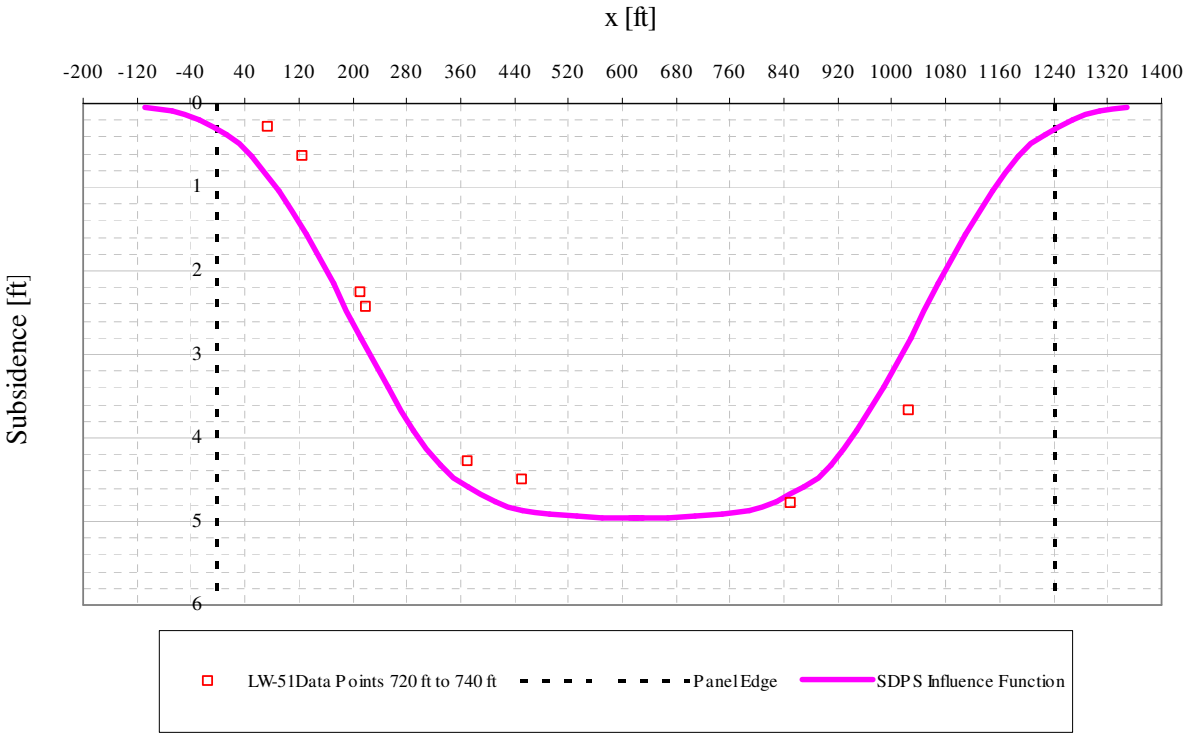

Figure A6- 43 LW-51 transverse view of data points from 720 ft to 740 ft from mine face and SDPS prediction

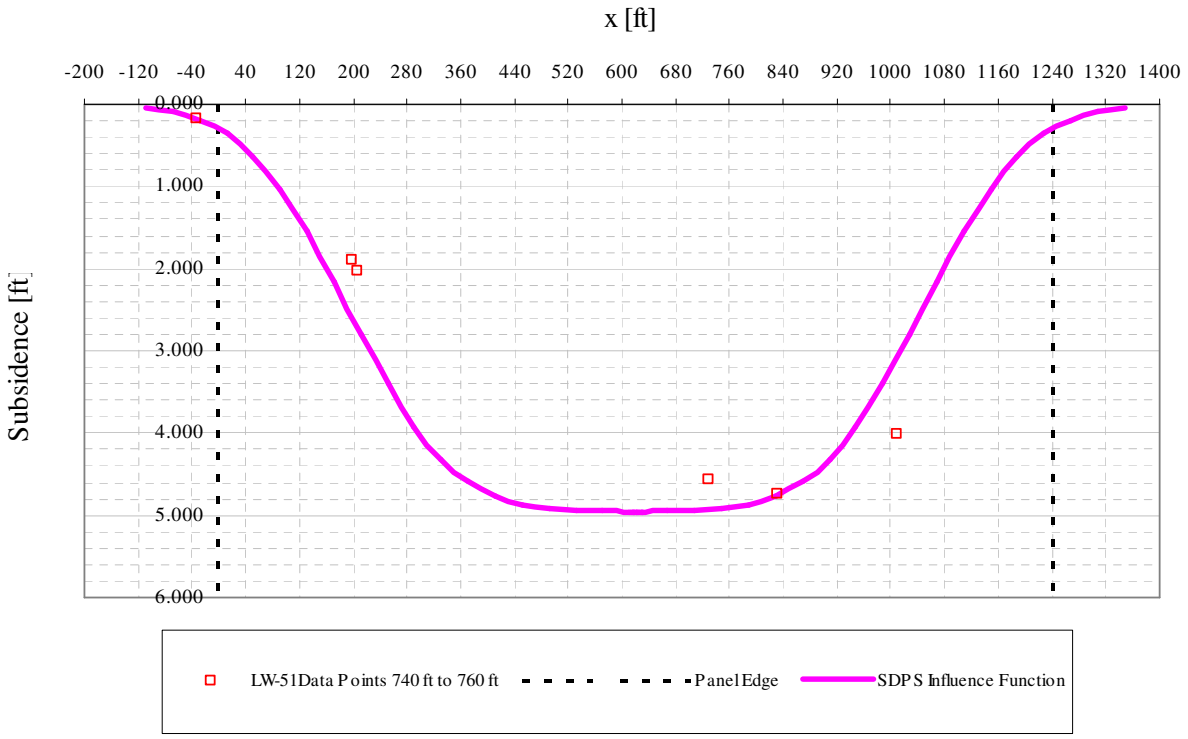

Figure A6- 44 LW-51 transverse view of data points from 740 ft to 760 ft from mine face and SDPS prediction

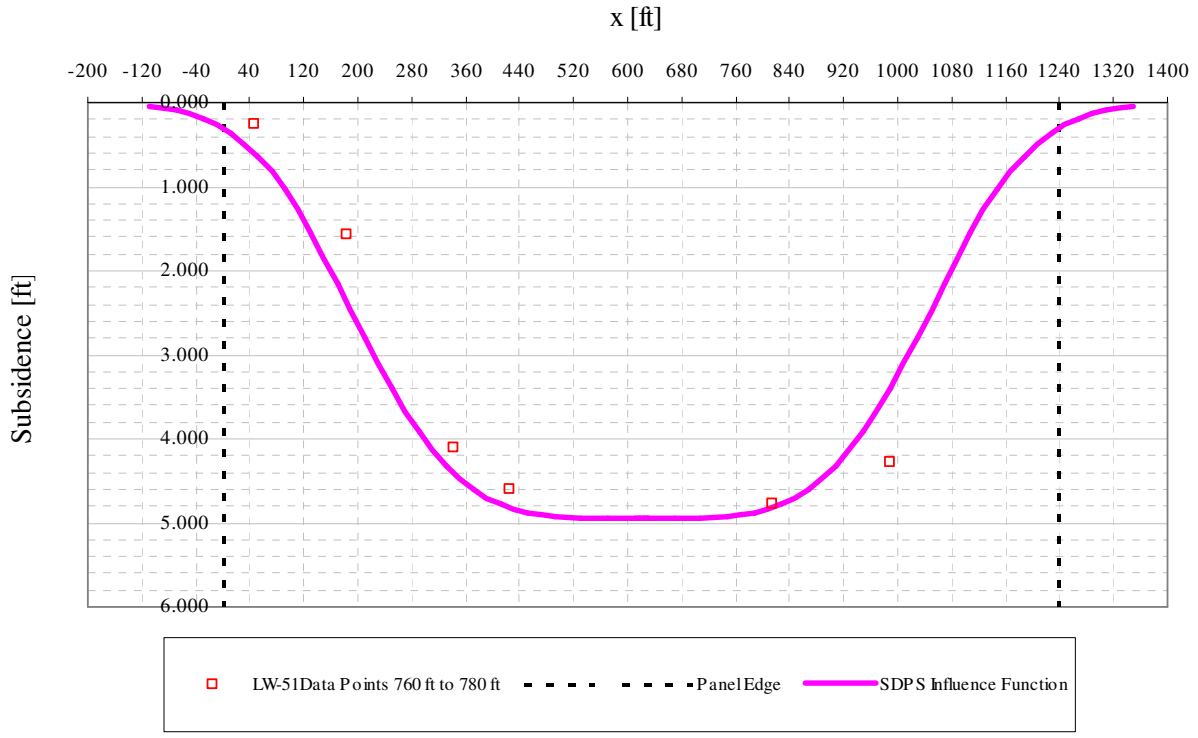

Figure A6- 45 LW-51 transverse view of data points from 760 ft to 780 ft from mine face and SDPS prediction

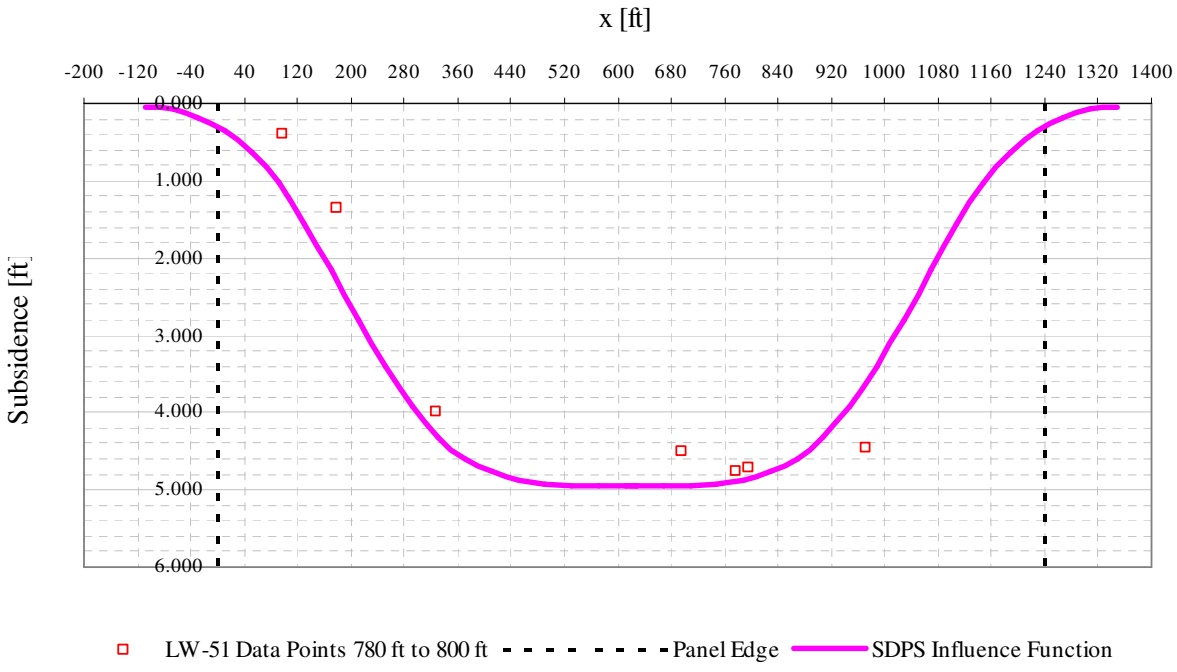

Figure A6- 46 LW-51 transverse view of data points from 780 ft to 800 ft from mine face and SDPS prediction

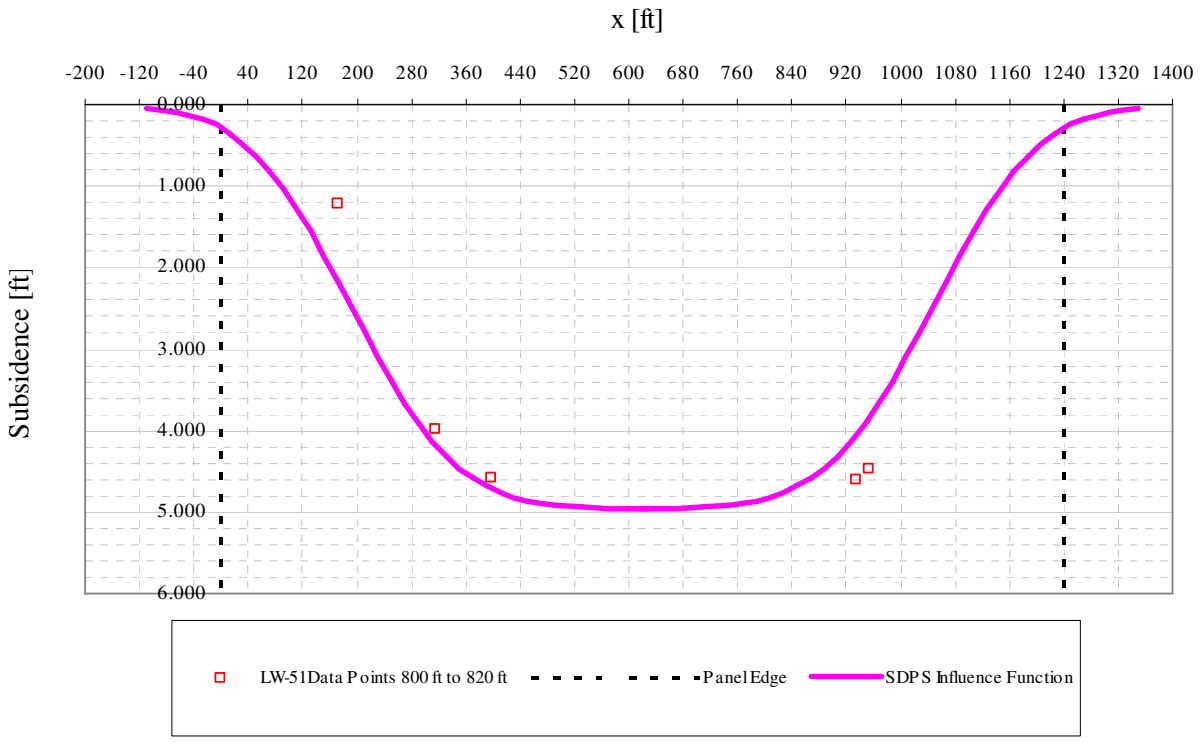

Figure A6- 47 LW-51 transverse view of data points from 800 ft to 820 ft from mine face and SDPS prediction

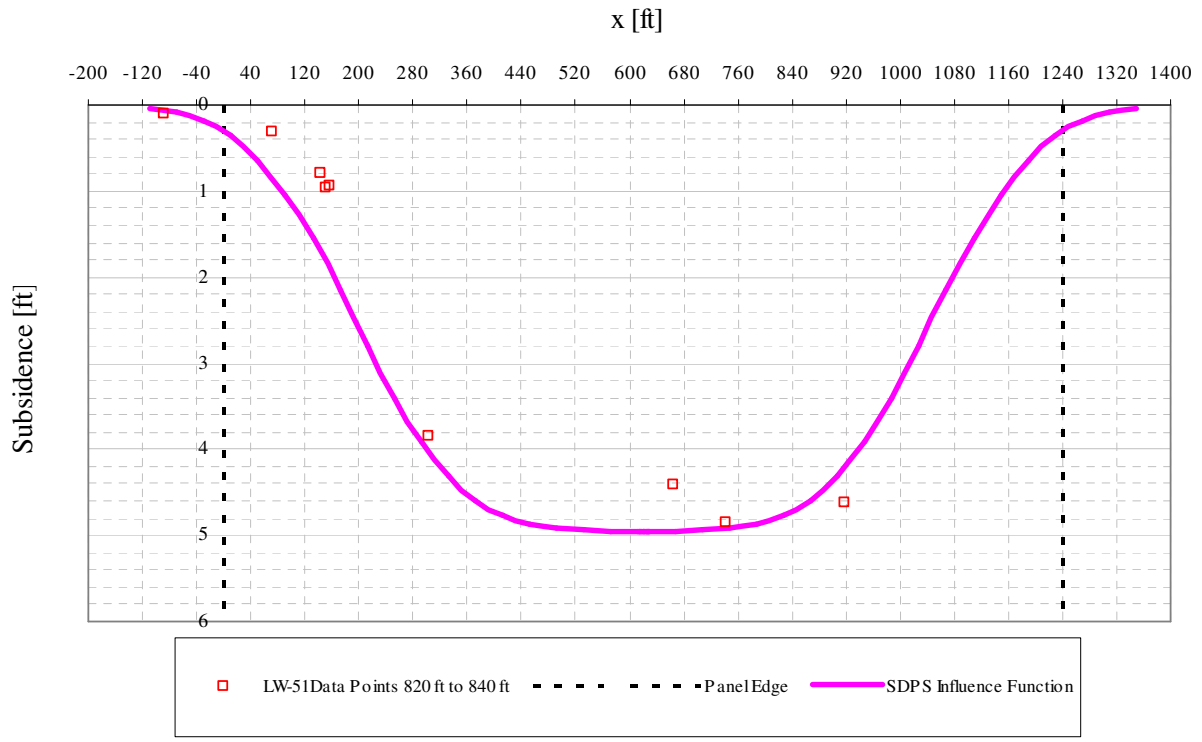

Figure A6- 48 LW-51 transverse view of data points from 820 ft to 840 ft from mine face and SDPS prediction

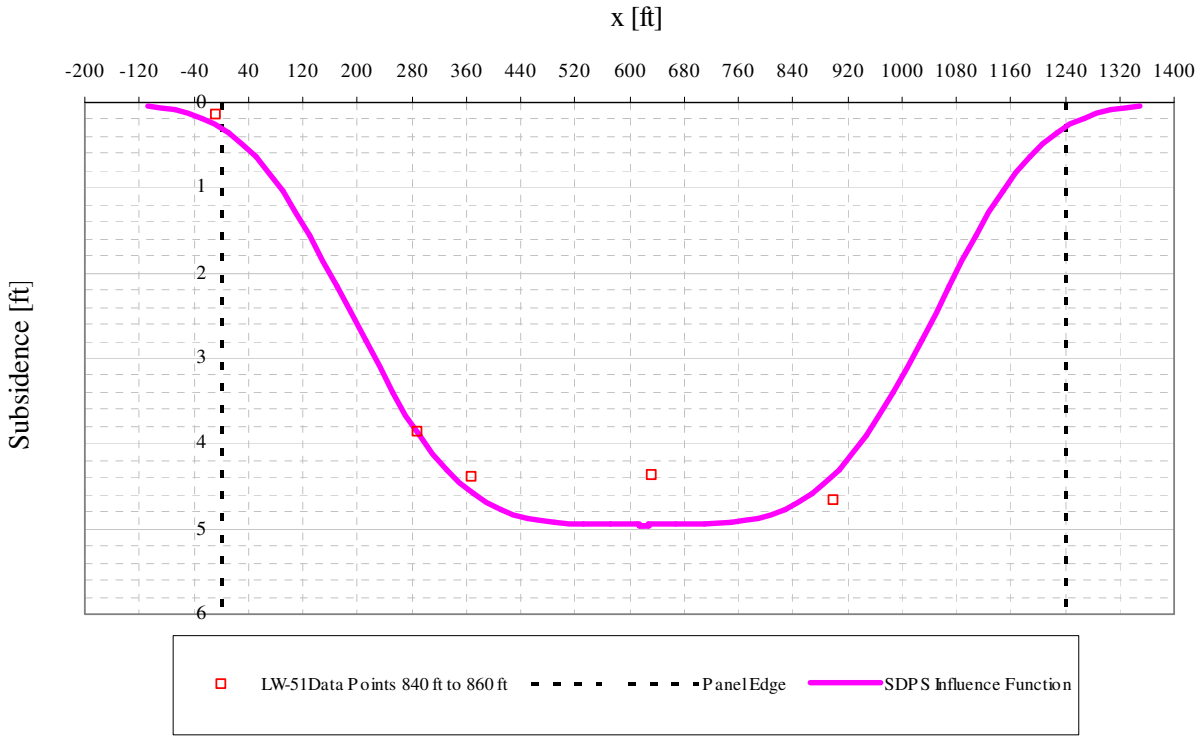

Figure A6- 49 LW-51 transverse view of data points from 840 ft to 860 ft from mine face and SDPS prediction

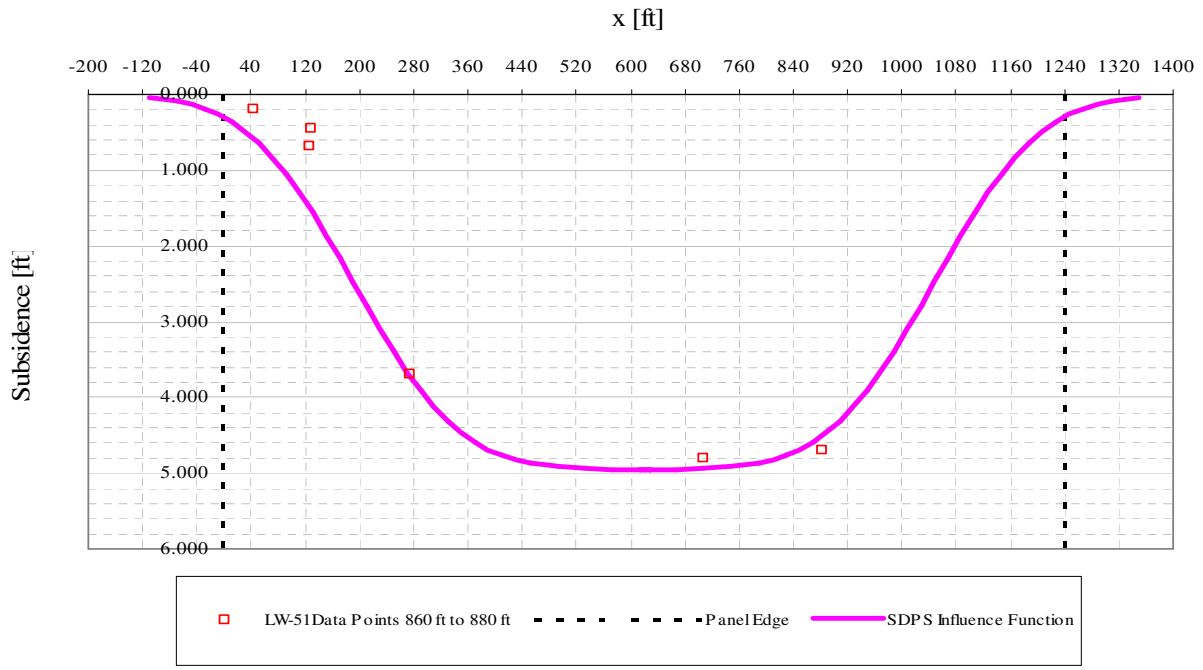

Figure A6- 50 LW-51 transverse view of data points from 860 ft to 880 ft from mine face and SDPS prediction

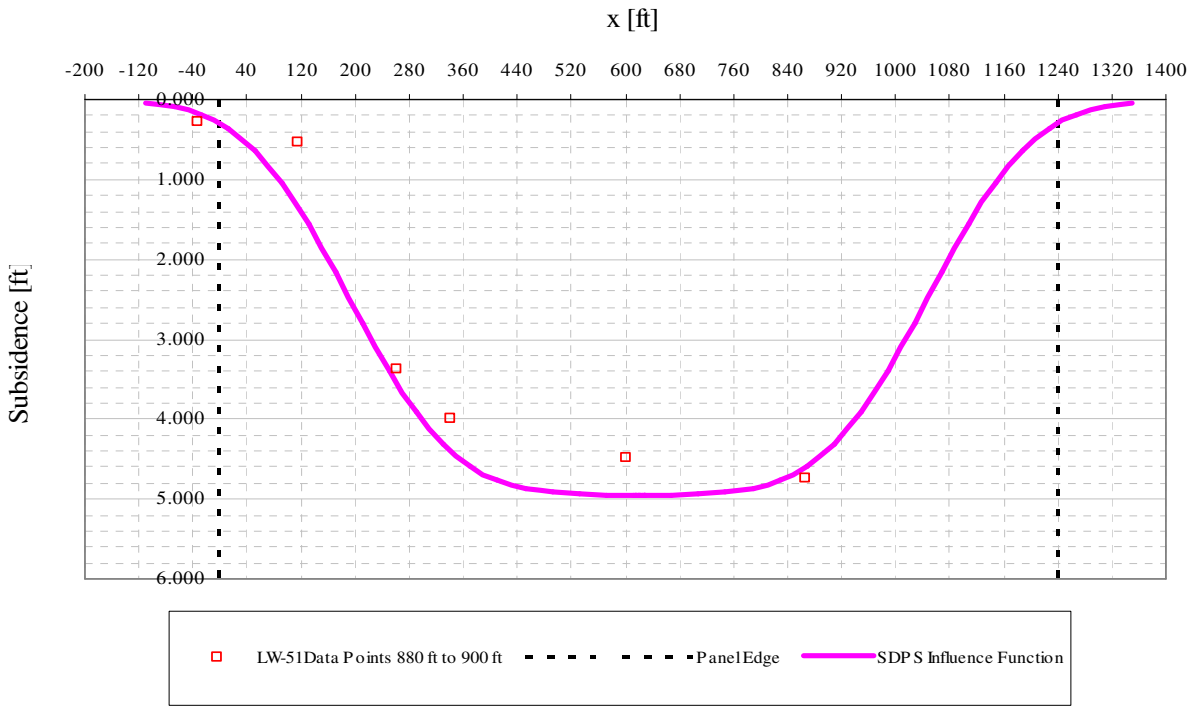

Figure A6- 51 LW-51 transverse view of data points from 880 ft to 900 ft from mine face and SDPS prediction

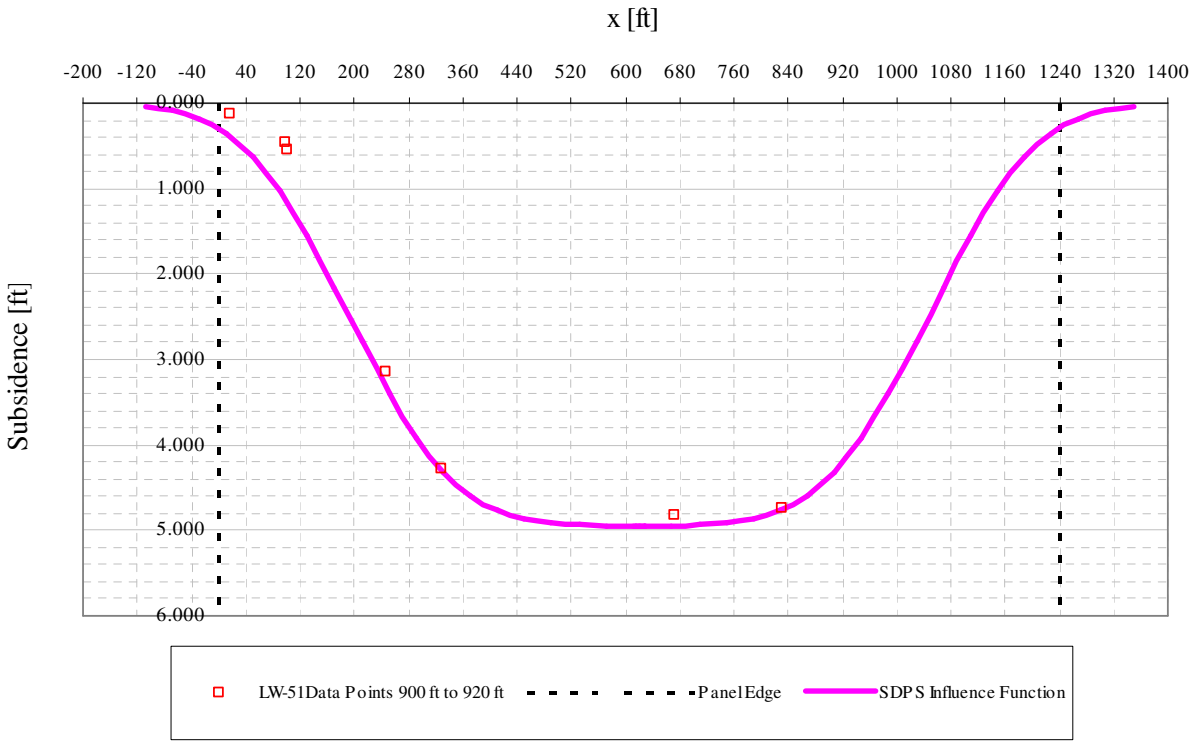

Figure A6- 52 LW-51 transverse view of data points from 900 ft to 920 ft from mine face and SDPS prediction

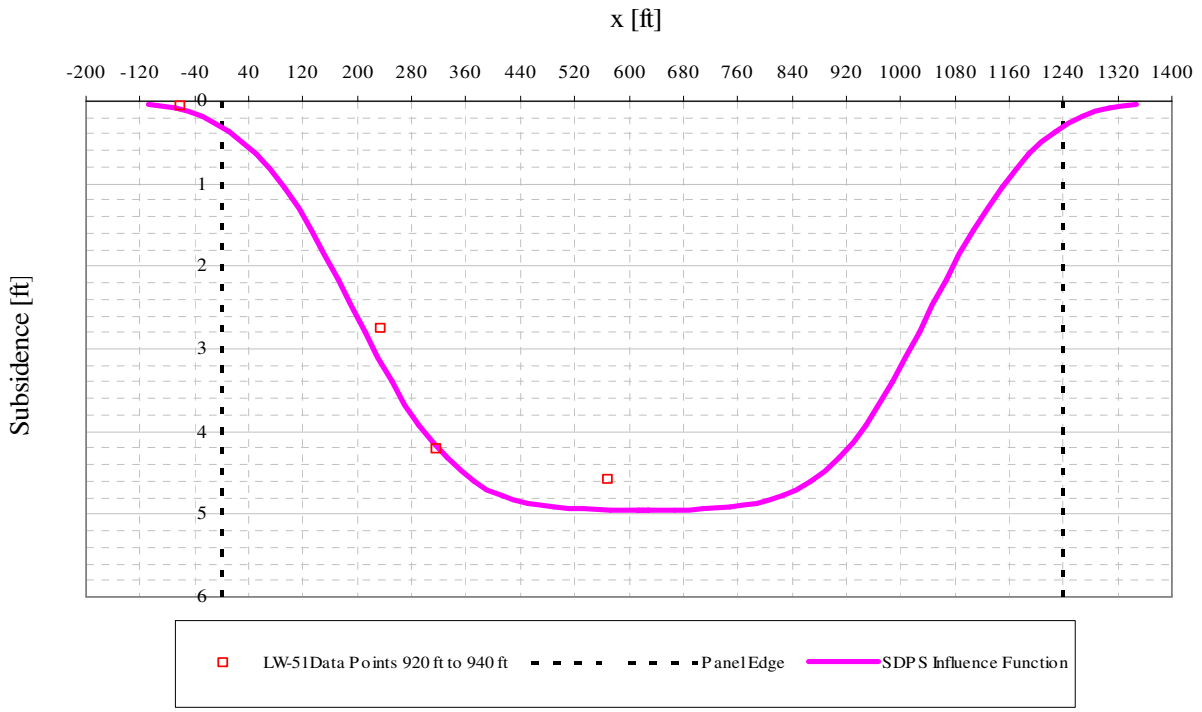

Figure A6- 53 LW-51 transverse view of data points from 920 ft to 940 ft from mine face and SDPS prediction

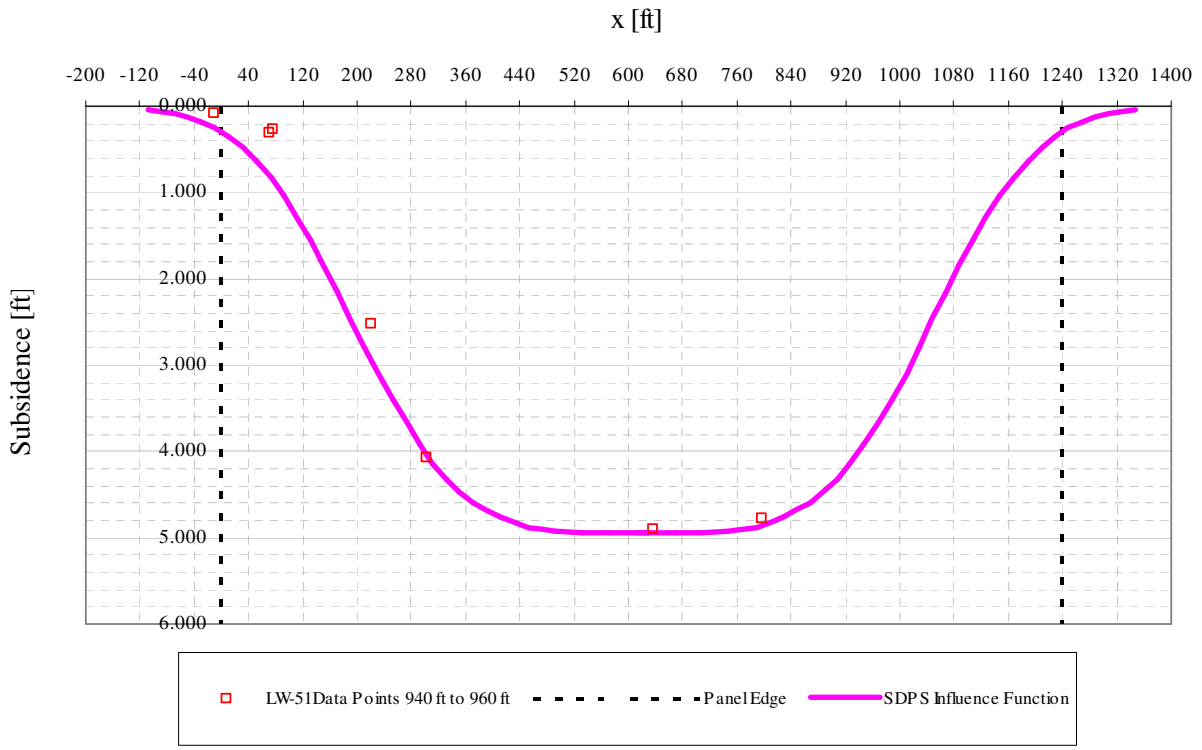

Figure A6- 54 LW-51 transverse view of data points from 940 ft to 960 ft from mine face and SDPS prediction

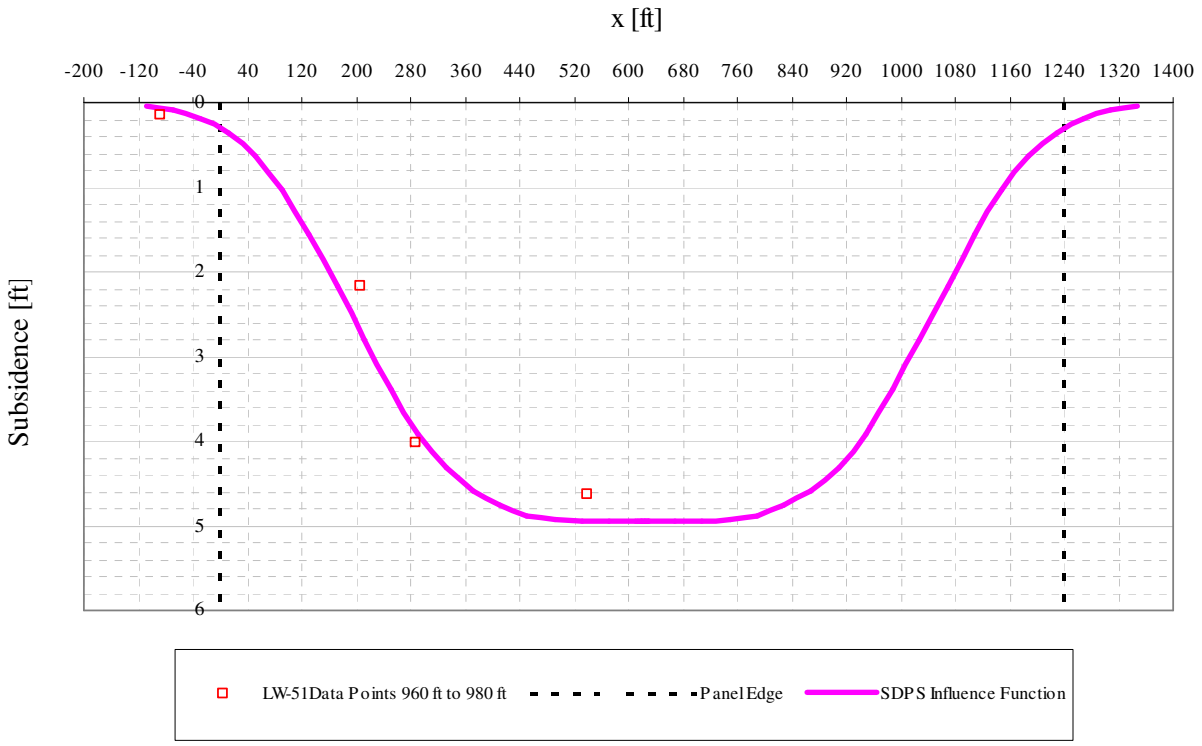

Figure A6- 55 LW-51 transverse view of data points from 960 ft to 980 ft from mine face and SDPS prediction

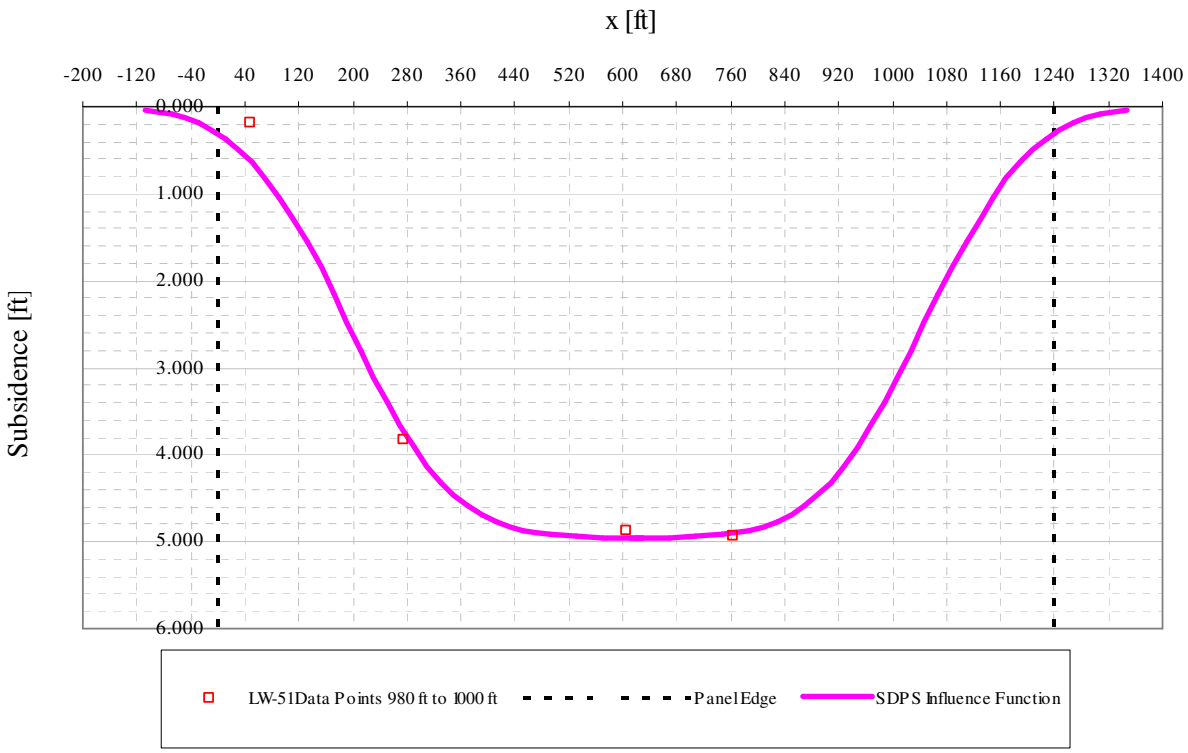

Figure A6- 56 LW-51 transverse view of data points from 980 ft to 1000 ft from mine face and SDPS prediction

A.7 EMERALD MINE PANEL LW-52 SDPS INFLUENCE FUNCTION PREDICTION

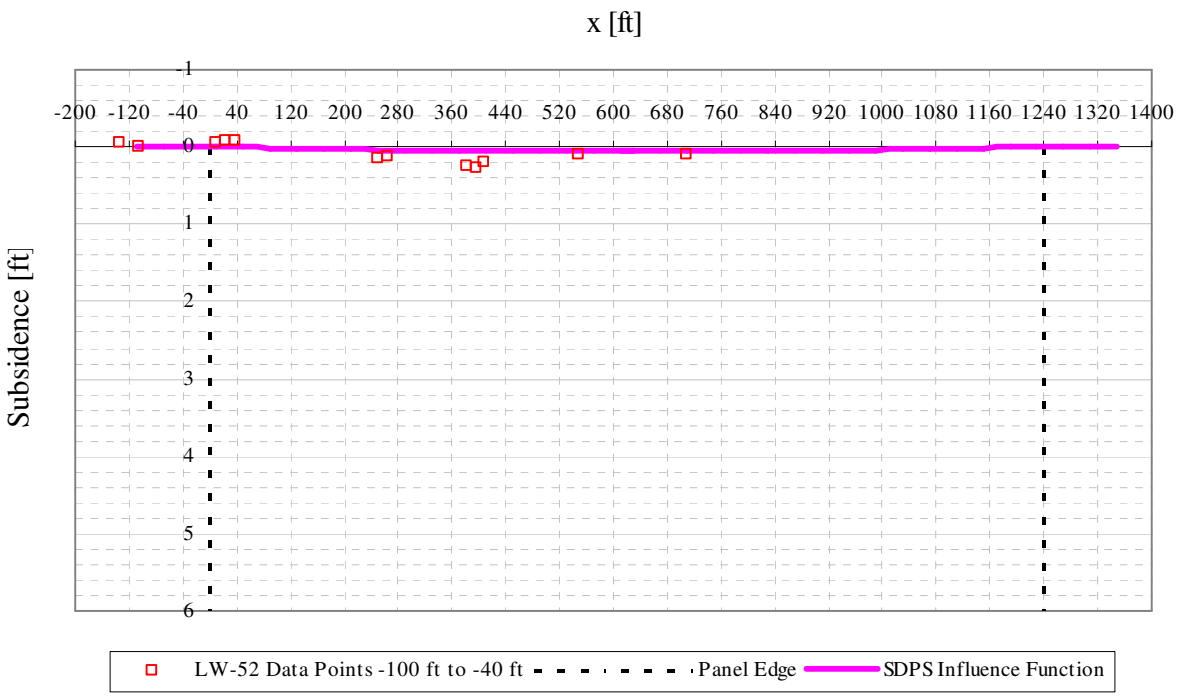

Figure A7- 1 LW-52 transverse view of data points from -100 ft to -40 ft from mine face and SDPS prediction

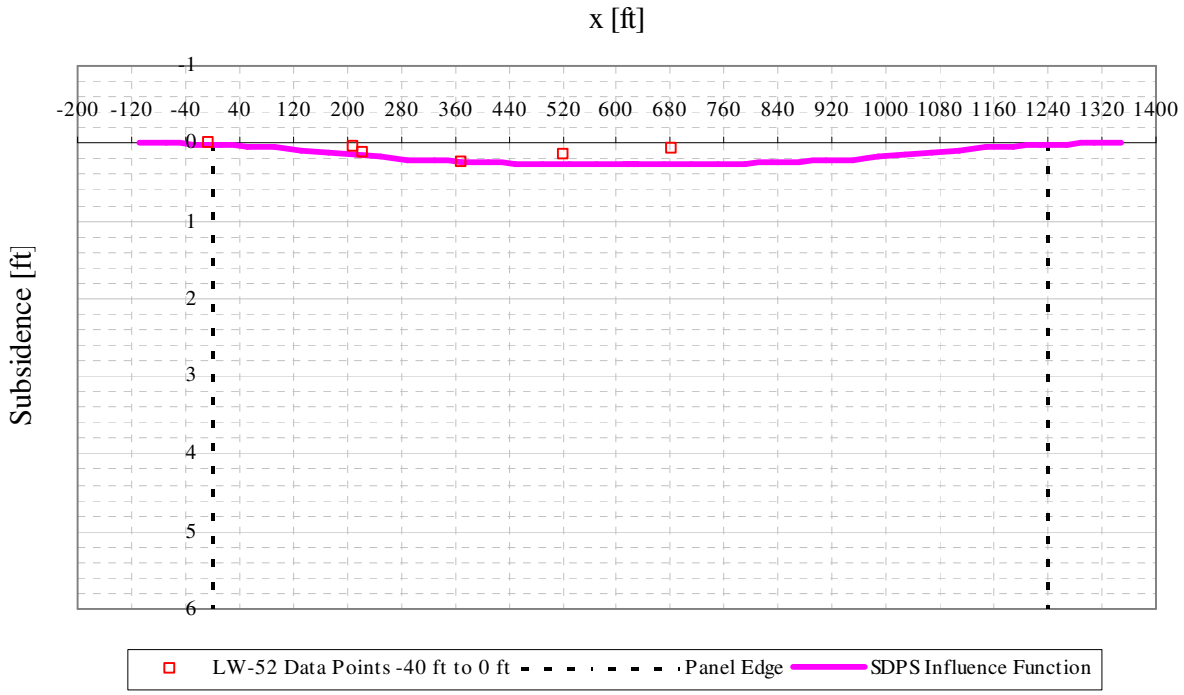

Figure A7- 2 LW-52 transverse view of data points from -40 ft to 0 ft from mine face and SDPS prediction

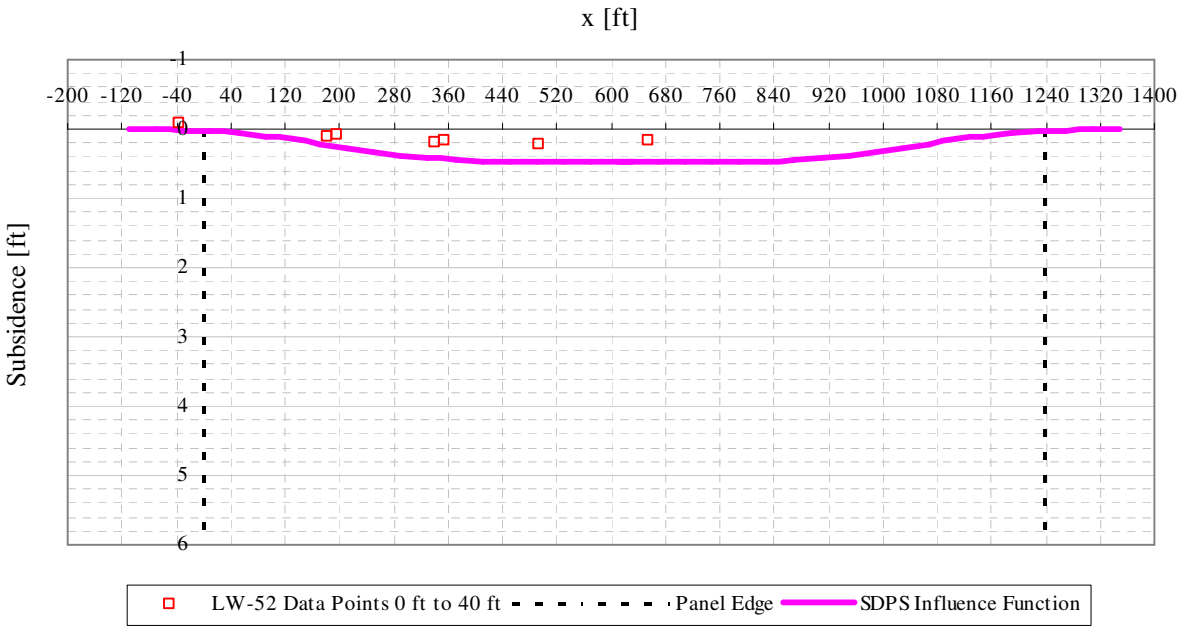

Figure A7- 3 LW-52 transverse view of data points from 0 ft to 40 ft from mine face and SDPS prediction

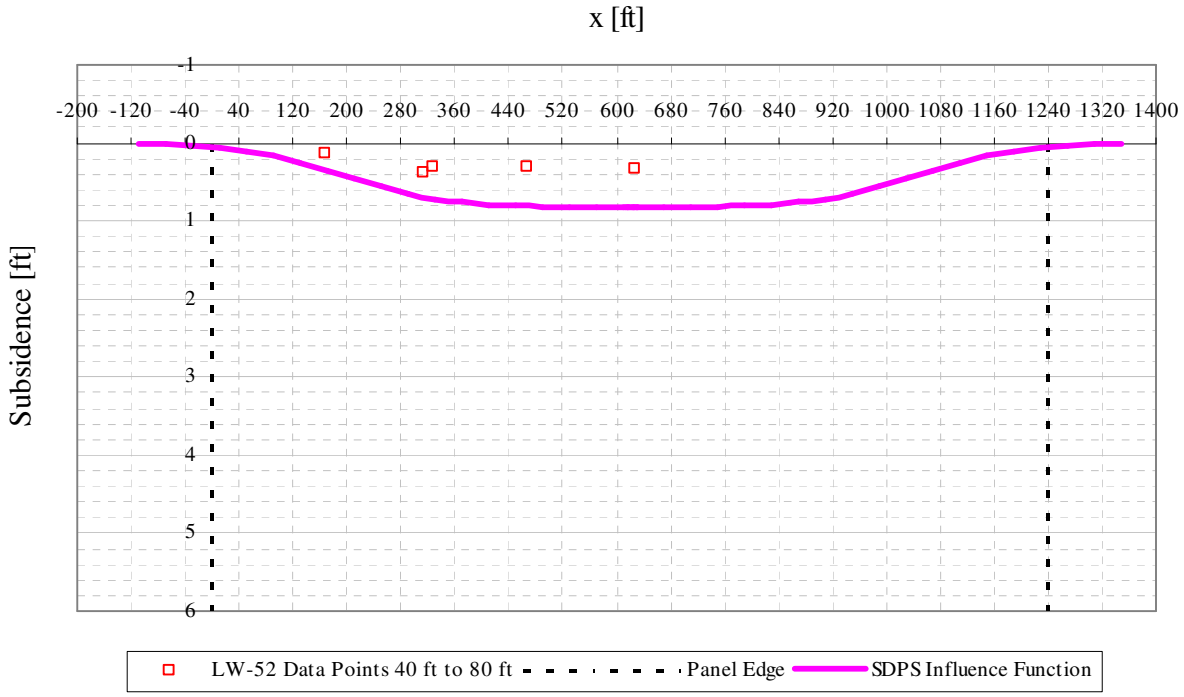

Figure A7- 4 LW-52 transverse view of data points from 40 ft to 80 ft from mine face and SDPS prediction

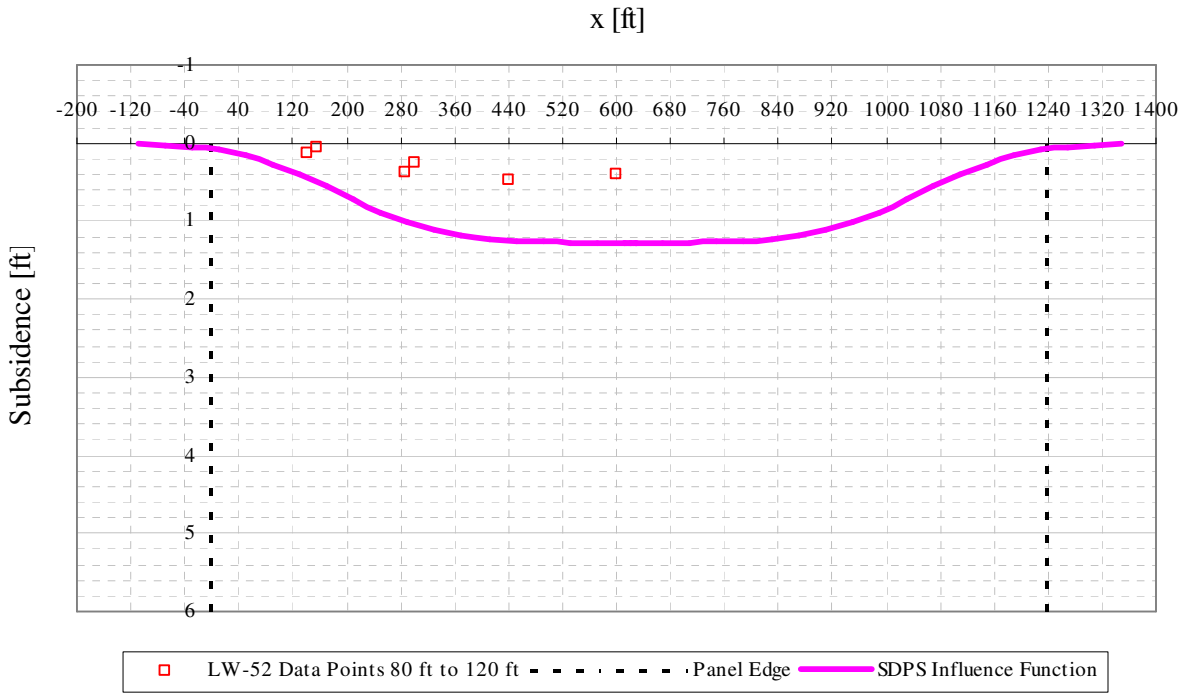

Figure A7- 5 LW-52 transverse view of data points from 80 ft to 120 ft from mine face and SDPS prediction

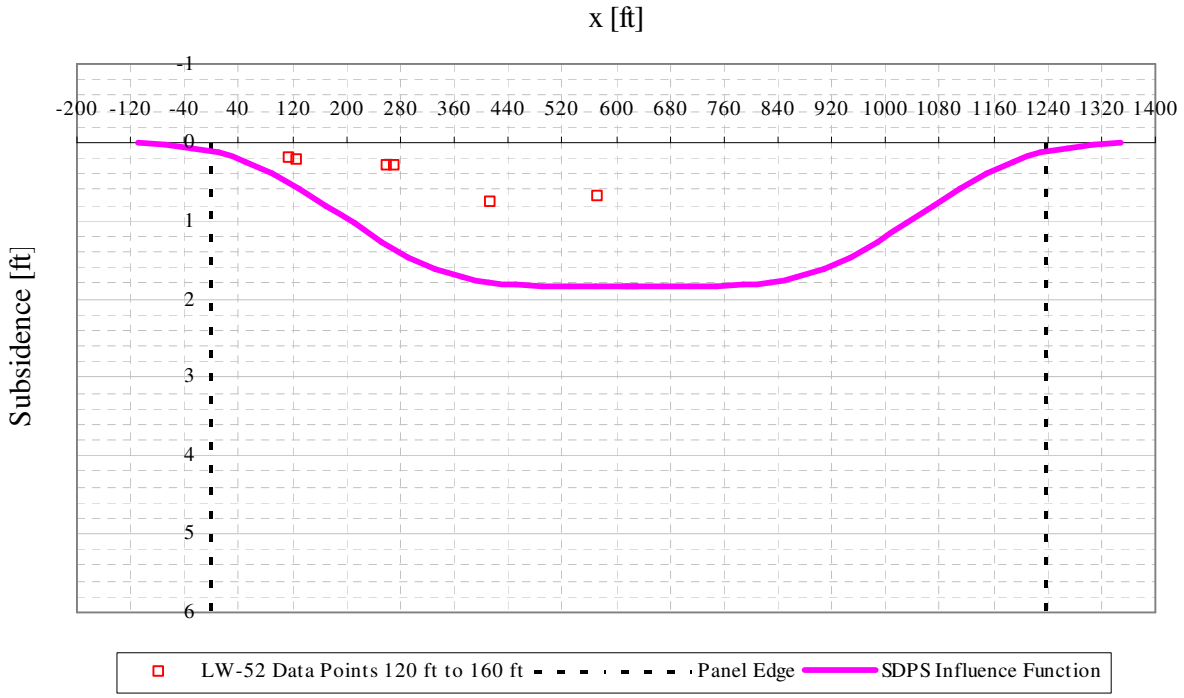

Figure A7- 6 LW-52 transverse view of data points from 120 ft to 160 ft from mine face and SDPS prediction

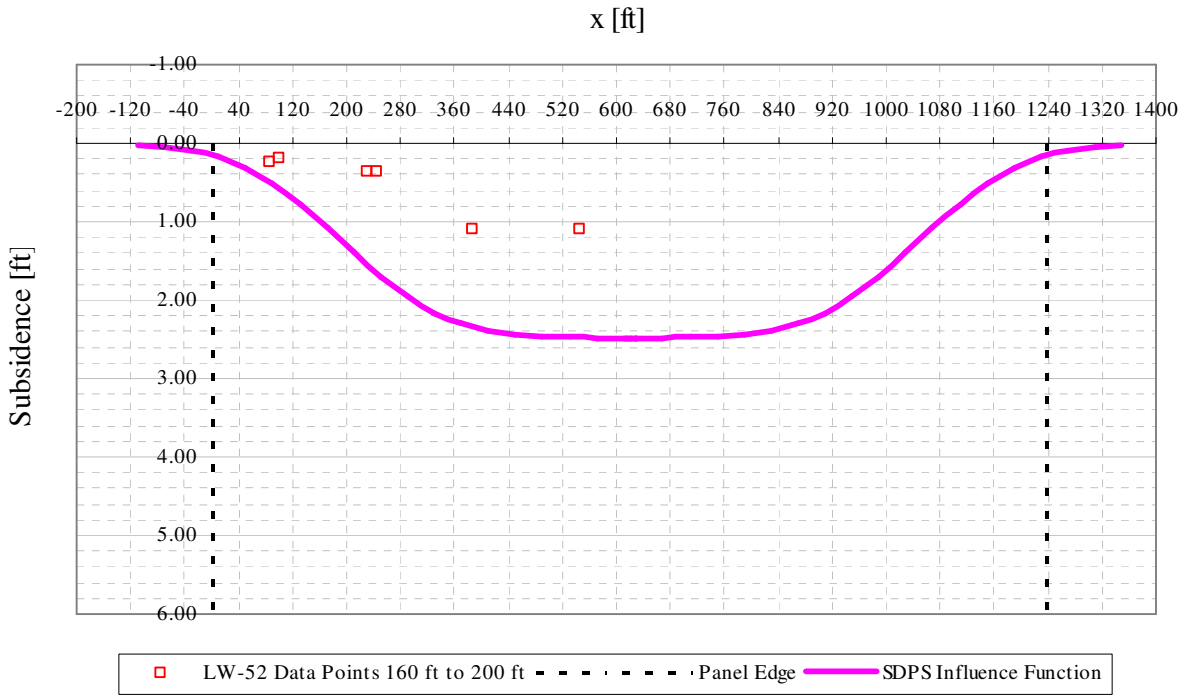

Figure A7- 7 LW-52 transverse view of data points from 160 ft to 200 ft from mine face and SDPS prediction

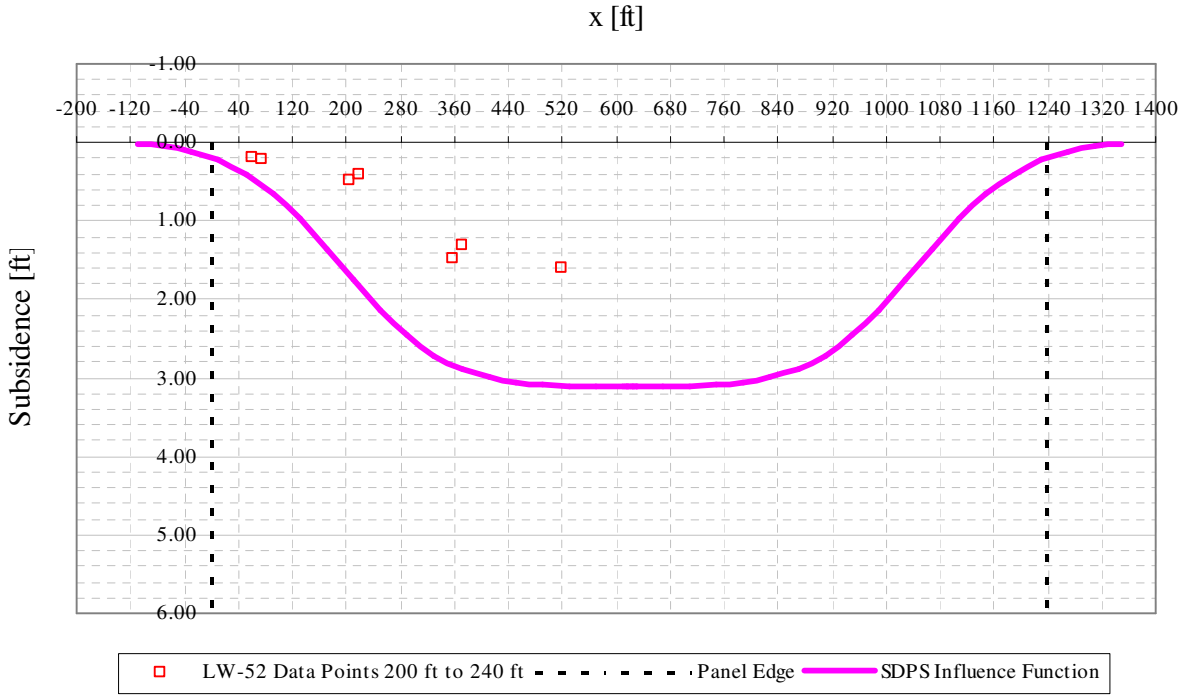

Figure A7- 8 LW-52 transverse view of data points from 200 ft to 240 ft from mine face and SDPS prediction

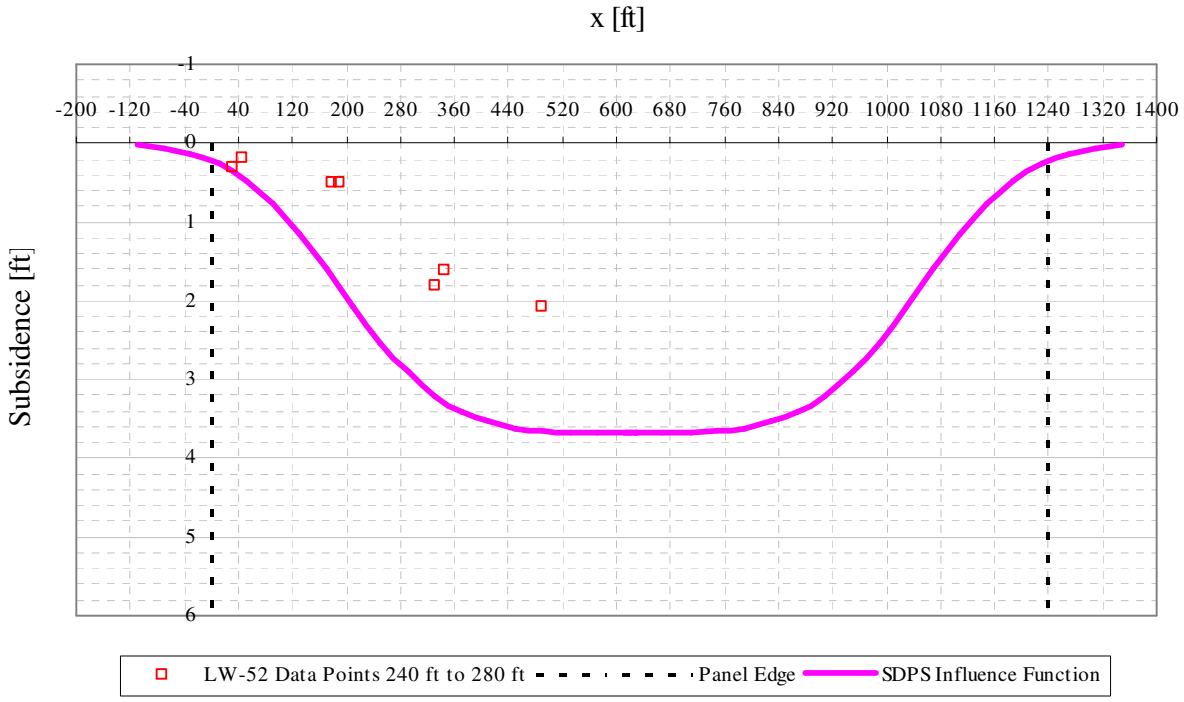

Figure A7- 9 LW-52 transverse view of data points from 240 ft to 280 ft from mine face and SDPS prediction

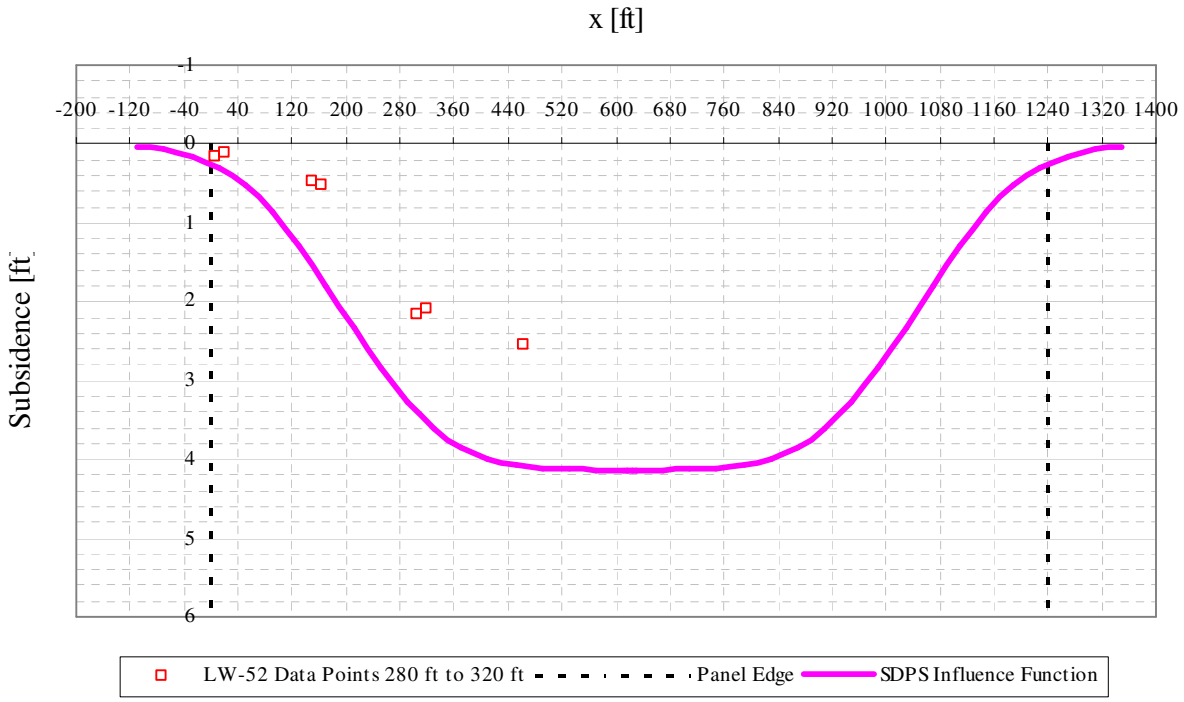

Figure A7- 10 LW-52 transverse view of data points from 280 ft to 320 ft from mine face and SDPS prediction

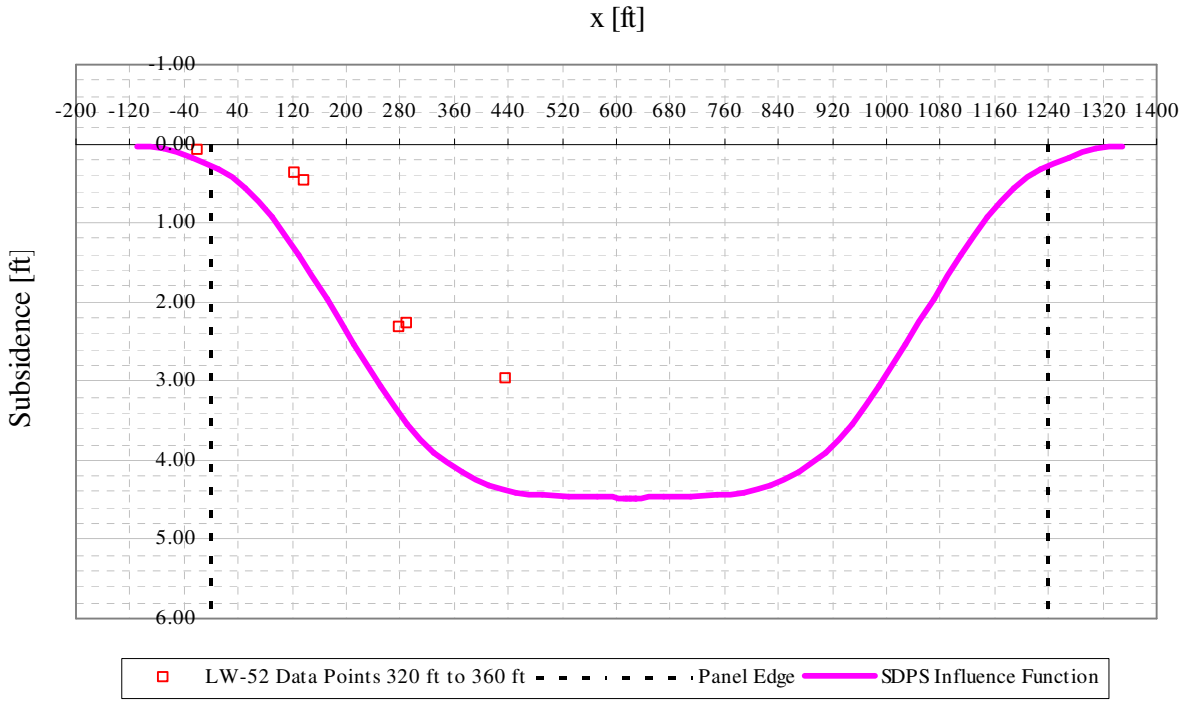

Figure A7- 11 LW-52 transverse view of data points from 320 ft to 360 ft from mine face and SDPS prediction

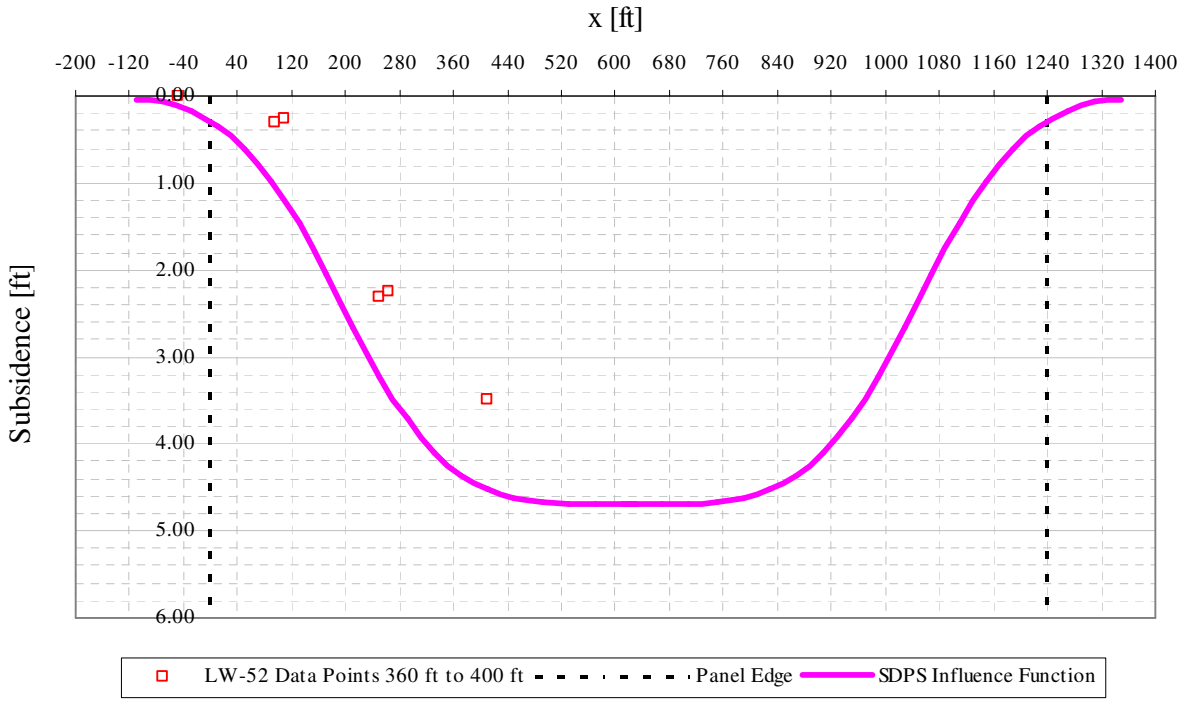

Figure A7- 12 LW-52 transverse view of data points from 360 ft to 400 ft from mine face and SDPS prediction

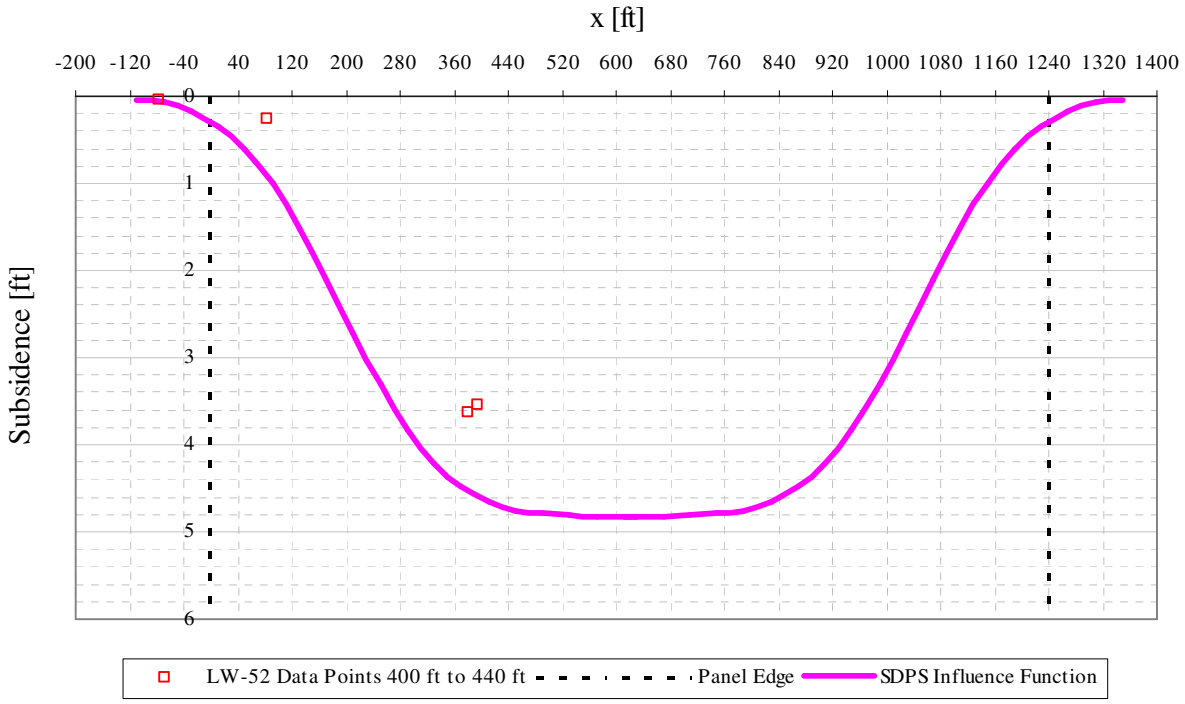

Figure A7- 13 LW-52 transverse view of data points from 400 ft to 440 ft from mine face and SDPS prediction

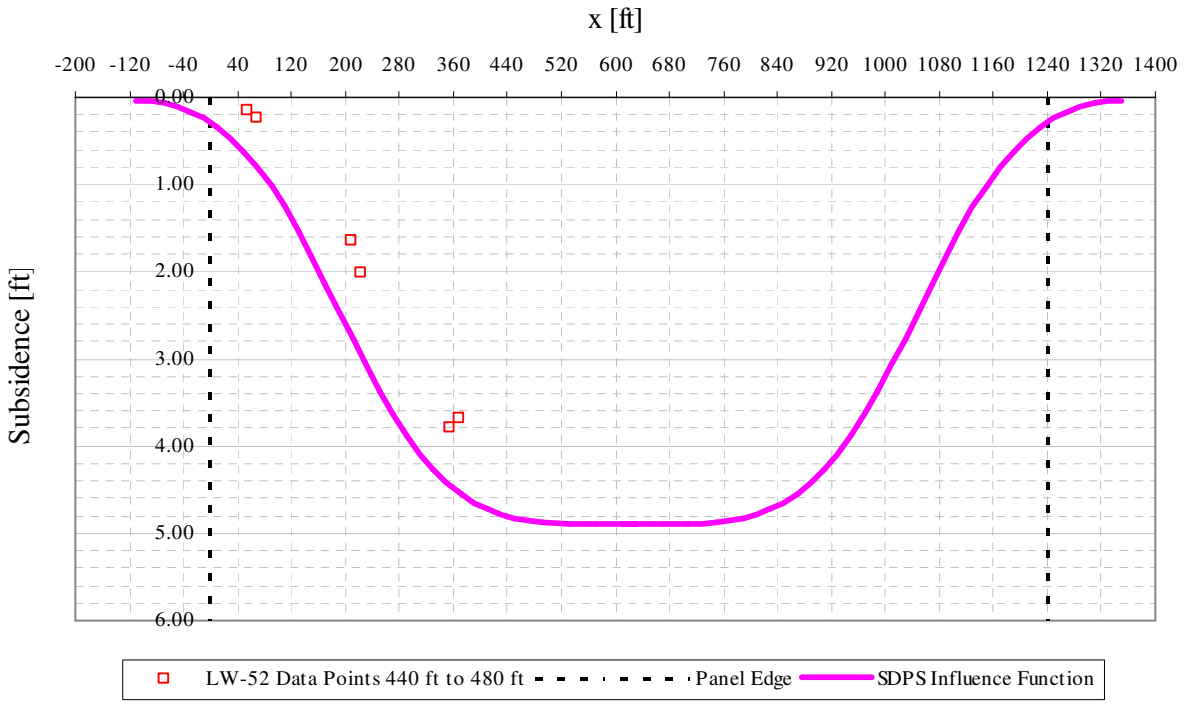

Figure A7- 14 LW-52 transverse view of data points from 440 ft to 480 ft from mine face and SDPS prediction

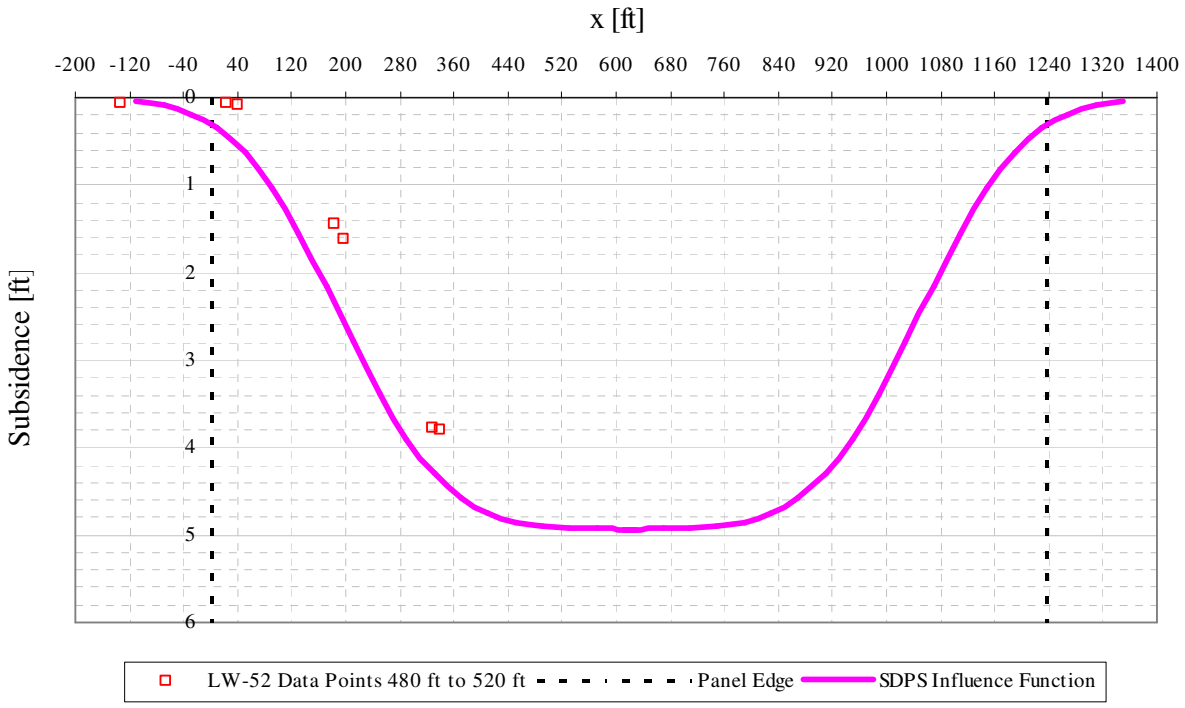

Figure A7- 15 LW-52 transverse view of data points from 480 ft to 520 ft from mine face and SDPS prediction

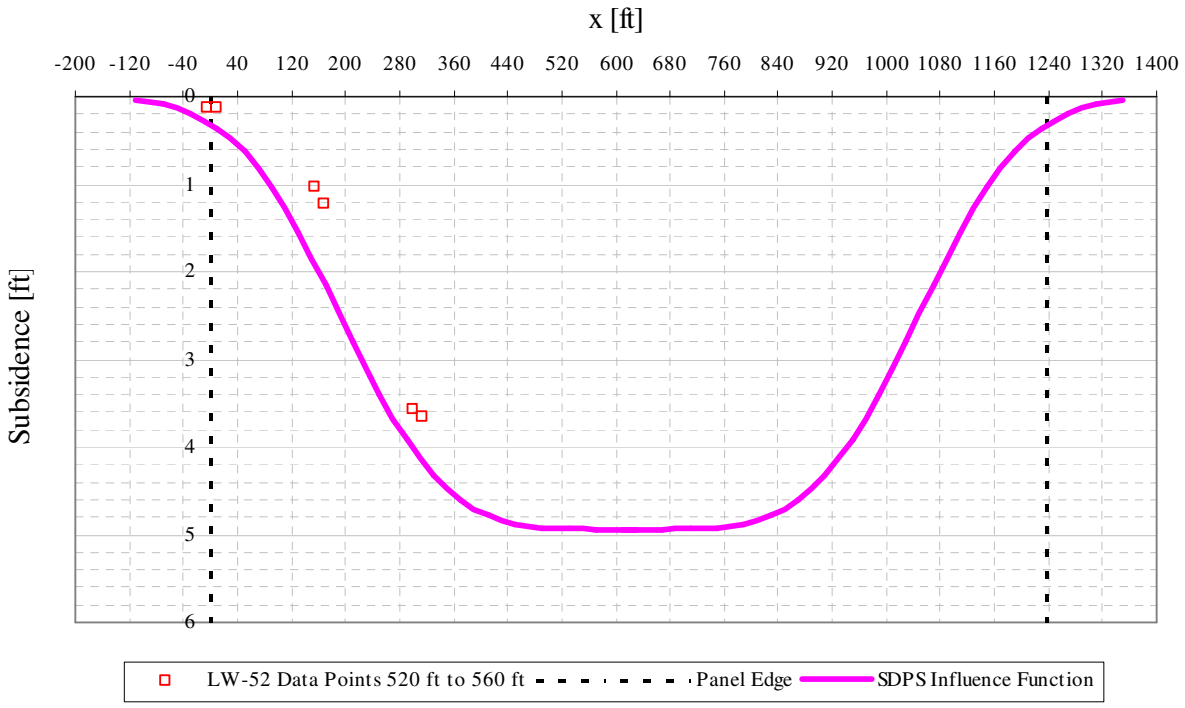

Figure A7- 16 LW-52 transverse view of data points from 520 ft to 560 ft from mine face and SDPS prediction

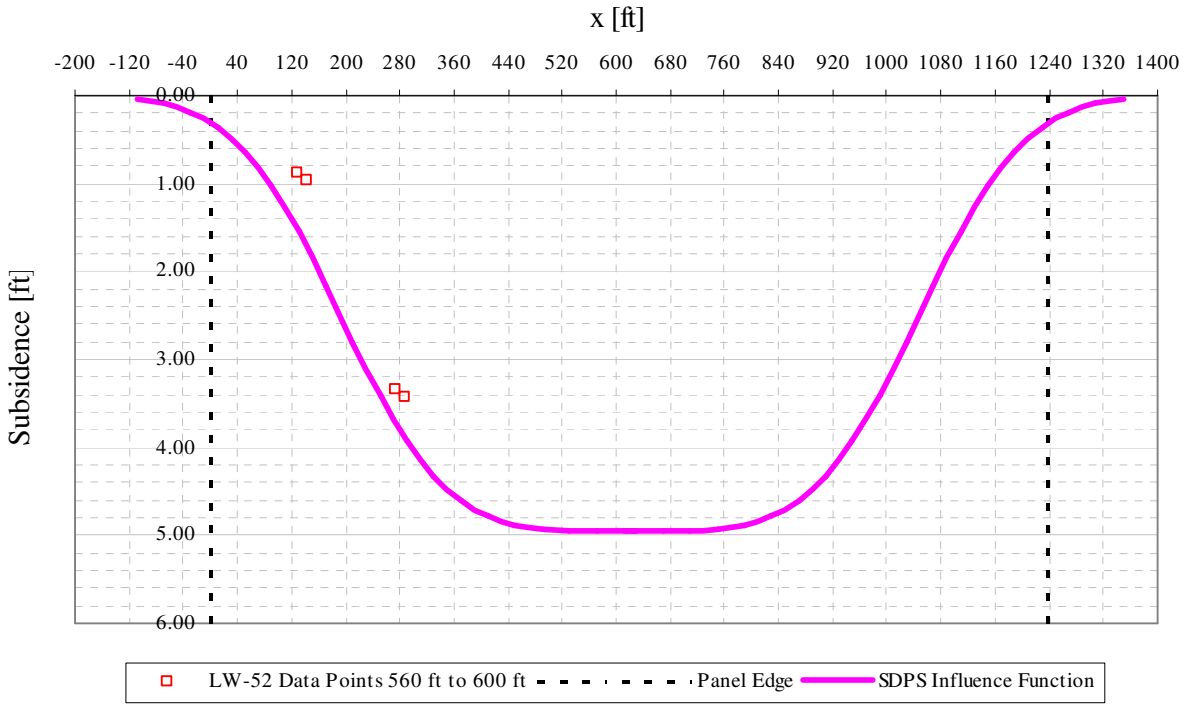

Figure A7- 17 LW-52 transverse view of data points from 560 ft to 600 ft from mine face and SDPS prediction

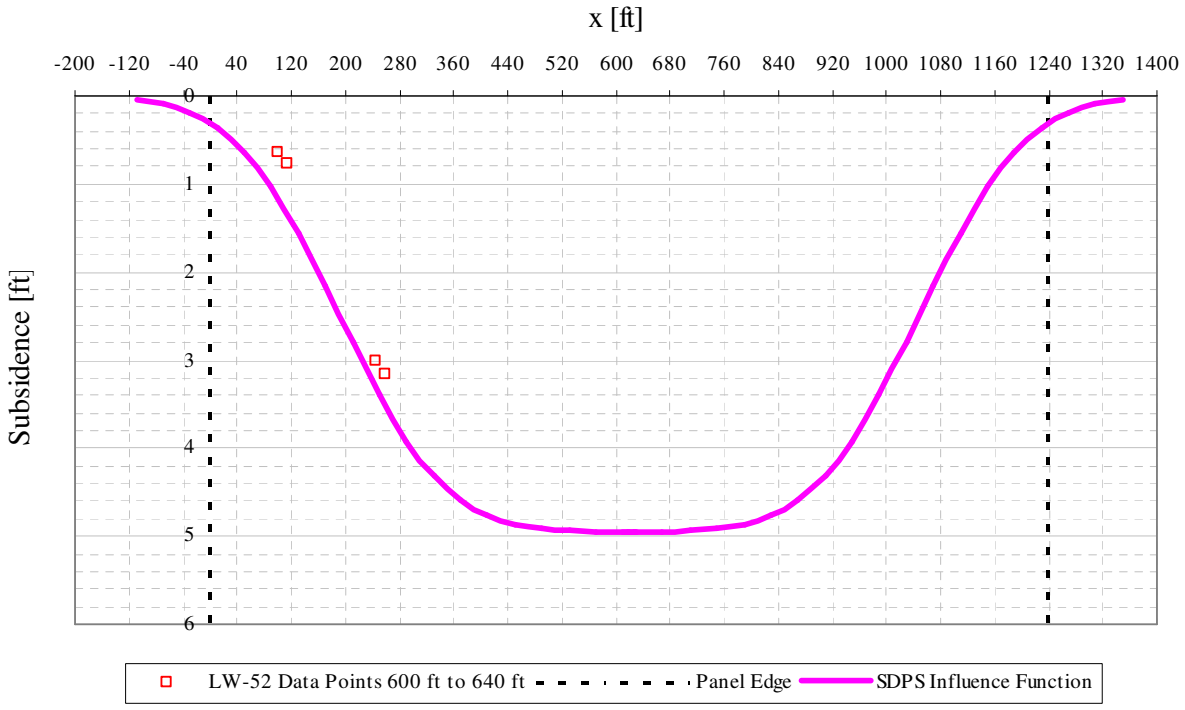

Figure A7- 18 LW-52 transverse view of data points from 600 ft to 640 ft from mine face and SDPS prediction

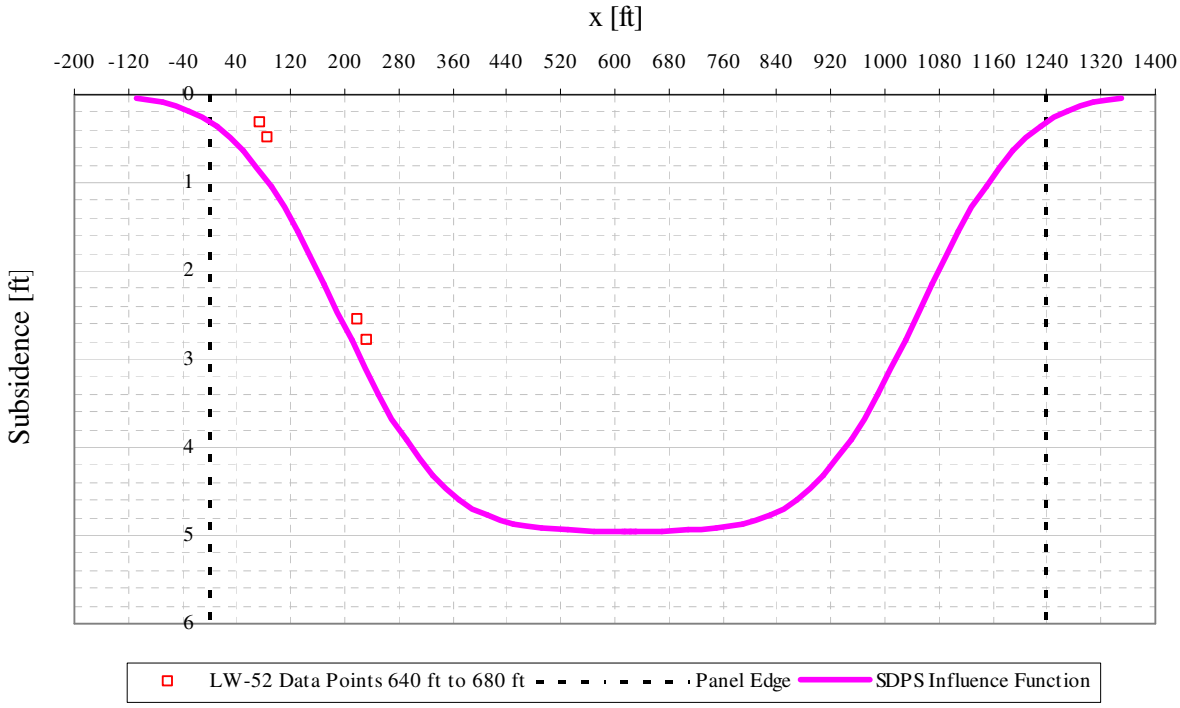

Figure A7- 19 LW-52 transverse view of data points from 640 ft to 680 ft from mine face and SDPS prediction

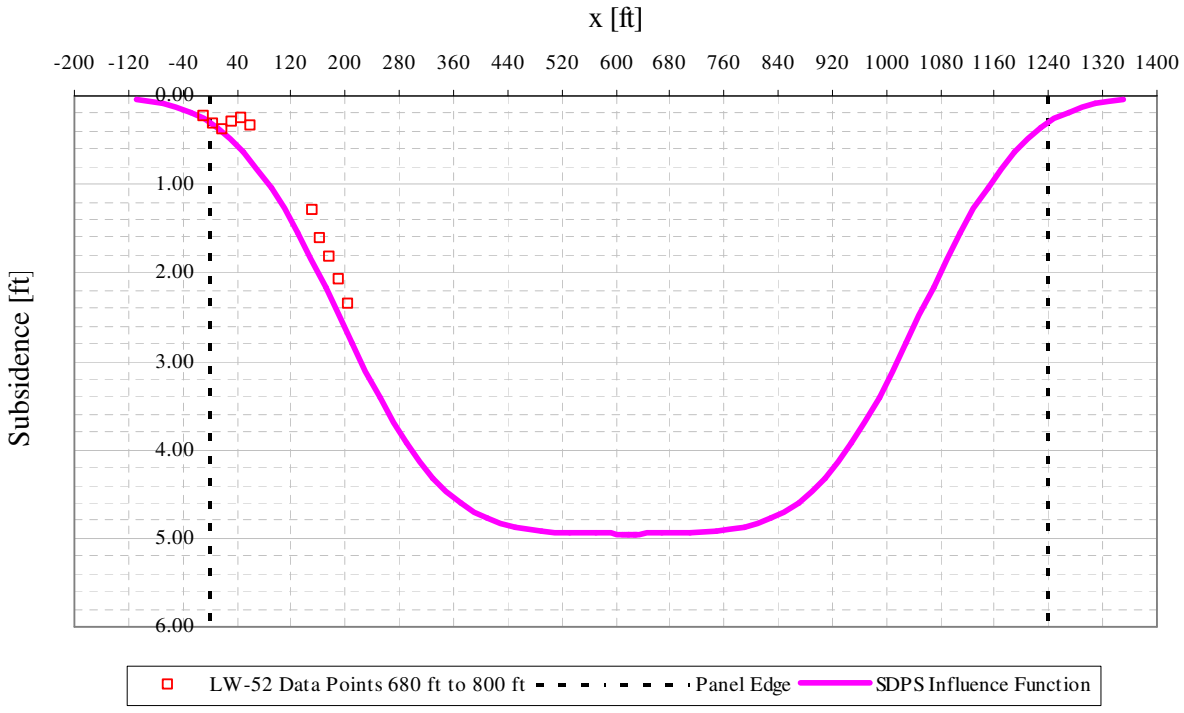

Figure A7- 20 LW-52 transverse view of data points from 680 ft to 800 ft from mine face and SDPS prediction

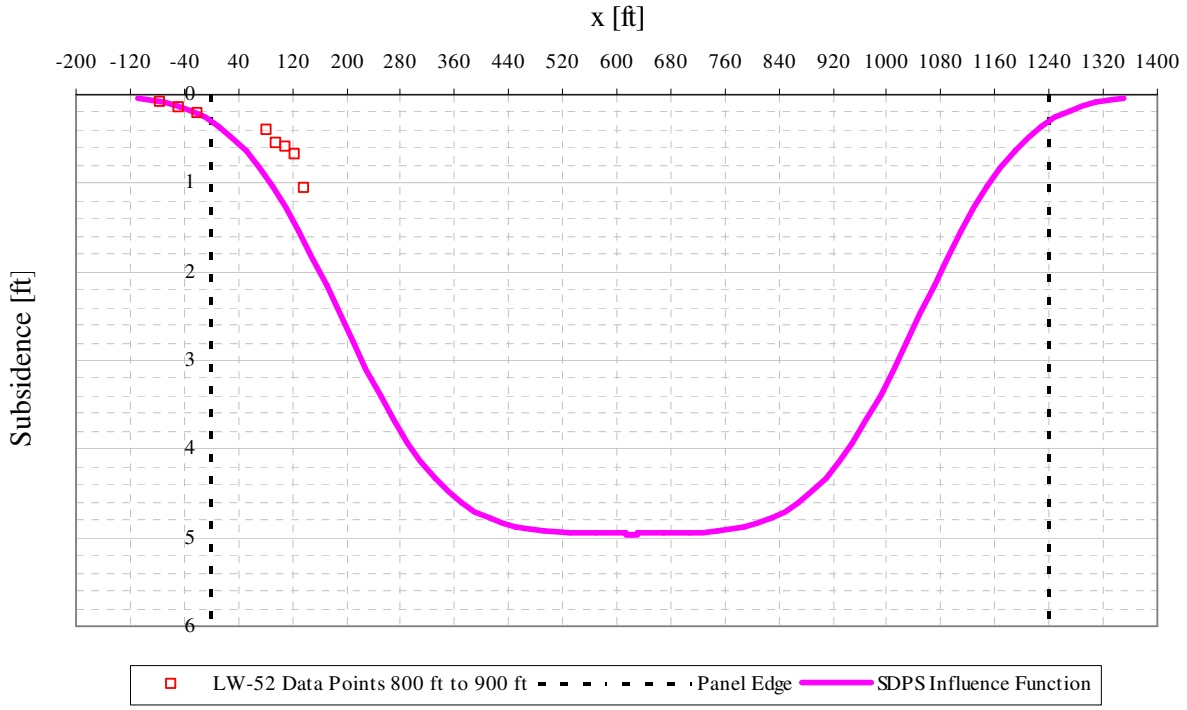

Figure A7- 21 LW-52 transverse view of data points from 800 ft to 900 ft from mine face and SDPS prediction

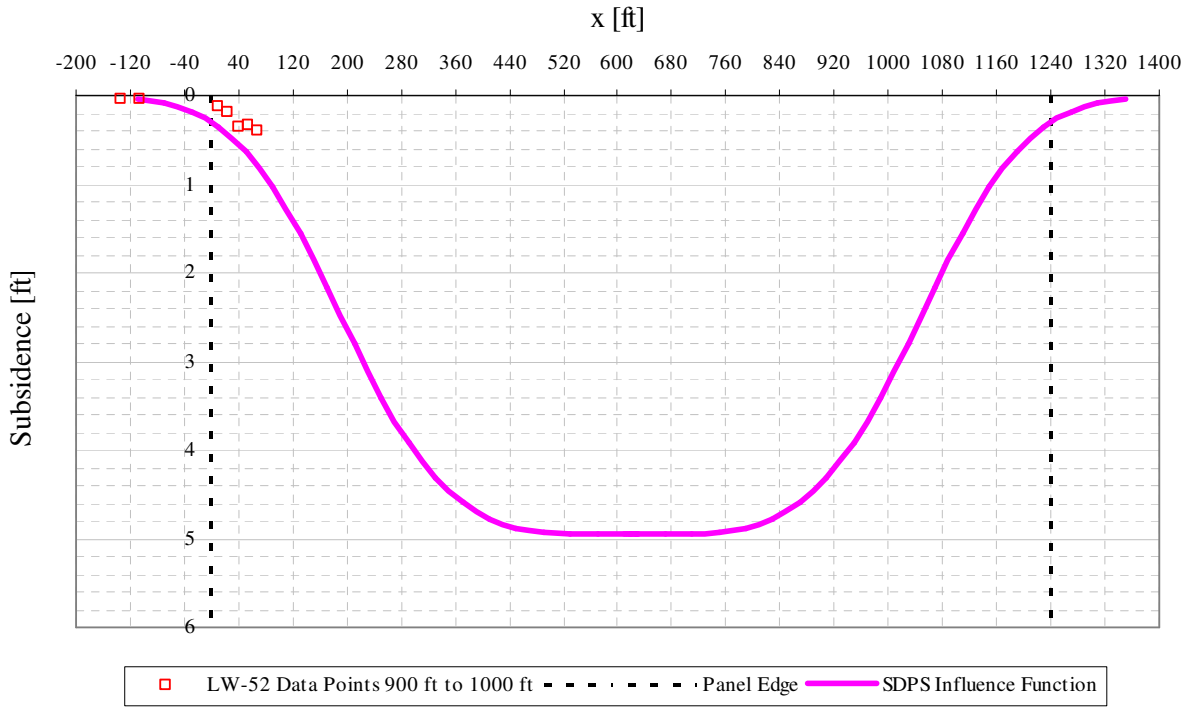

Figure A7- 22 LW-52 transverse view of data points from 900 ft to 1000 ft from mine face and SDPS prediction

A.8 SDPS PROFILE FUNCTION METHOD TABULAR OUTPUT

Table A4- 1 SDPS output of panel B-4 using profile function method

H.R. = 23%

[SUBSIDENCE CALCULATIONS]
Panel geometry.....Supercritical
Maximum subsidence (Smax).....-4.23 (ft)
Maximum subsidence factor (Smax/m)....0.669
Offset of inflection point from rib ..192.0 (ft) (inby)
Estimate of inflection point (I.P.)...Average
Distance of point of Smax from I.P....268.8 (ft)

Distance from Center Line (ft)	Subsidence (ft)	Angle from the rib (deg)
0	-4.235	
25	-4.234	
50	-4.232	
75	-4.229	
100	-4.226	
125	-4.221	
150	-4.214	
175	-4.204	
200	-4.191	
225	-4.173	
250	-4.148	
275	-4.113	
300	-4.065	
325	-4.000	
350	-3.912	
375	-3.796	
400	-3.645	
425	-3.452	
450	-3.215	
475	-2.933	
500	-2.614	
525	-2.268	
550	-1.914	
575	-1.571	
600	-1.257	
625	-0.982	
650	-0.752	
675	-0.567	
700	-0.422	
725	-0.310	
750	-0.227	1.678
775	-0.165	3.539
800	-0.119	5.393
825	-0.086	7.235
850	-0.062	9.063
875	-0.044	10.872
900	-0.032	12.659
925	-0.023	14.422
950	-0.016	16.157
975	-0.012	17.862
1000	-0.008	19.536
1025	-0.006	21.175
1050	-0.004	22.779
1075	-0.003	24.346
1100	-0.002	25.875
1125	-0.002	27.365
1150	-0.001	28.817
1175	-0.001	30.229

Table A4- 2 SDPS output of panel LW-49 using profile function method

H.R. = 23%

[SUBSIDENCE CALCULATIONS]
Panel geometry.....Supercritical
Maximum subsidence (Smax).....-4.92 (ft)
Maximum subsidence factor (Smax/m)....0.665
Offset of inflection point from rib ..196.5 (ft) (inby)
Estimate of inflection point (I.P.)...Average
Distance of point of Smax from I.P....275.1 (ft)

Distance from Center Line (ft)	Subsidence (ft)	Angle from the rib (deg)
0	-4.922	
25	-4.915	
50	-4.905	
75	-4.890	
100	-4.871	
125	-4.844	
150	-4.807	
175	-4.757	
200	-4.689	
225	-4.597	
250	-4.477	
275	-4.319	
300	-4.118	
325	-3.869	
350	-3.569	
375	-3.222	
400	-2.840	
425	-2.439	
450	-2.039	
475	-1.661	
500	-1.322	
525	-1.030	
550	-0.788	
575	-0.595	
600	-0.444	
625	-0.328	0.401
650	-0.241	2.222
675	-0.176	4.039
700	-0.128	5.848
725	-0.093	7.645
750	-0.068	9.427
775	-0.049	11.191
800	-0.035	12.933
825	-0.026	14.652
850	-0.018	16.344
875	-0.013	18.008
900	-0.010	19.640
925	-0.007	21.240
950	-0.005	22.806
975	-0.004	24.337
1000	-0.003	25.832
1025	-0.002	27.290
1050	-0.001	28.710
1075	-0.001	30.093

Table A4- 3 SDPS output of panel LW-51 using profile function method

H.R. = 23%

[SUBSIDENCE CALCULATIONS]
Panel geometry.....Supercritical
Maximum subsidence (Smax).....-4.93 (ft)
Maximum subsidence factor (Smax/m)....0.666
Offset of inflection point from rib ..191.5 (ft) (inby)
Estimate of inflection point (I.P.)...Average
Distance of point of Smax from I.P....268.1 (ft)

Distance from Center Line (ft)	Subsidence (ft)	Angle from the rib (deg)
0	-4.927	
25	-4.921	
50	-4.912	
75	-4.900	
100	-4.883	
125	-4.860	
150	-4.827	
175	-4.783	
200	-4.722	
225	-4.639	
250	-4.528	
275	-4.381	
300	-4.191	
325	-3.952	
350	-3.659	
375	-3.315	
400	-2.931	
425	-2.521	
450	-2.109	
475	-1.716	
500	-1.362	
525	-1.056	
550	-0.804	
575	-0.603	
600	-0.446	
625	-0.328	0.411
650	-0.239	2.280
675	-0.173	4.144
700	-0.125	5.999
725	-0.090	7.842
750	-0.065	9.668
775	-0.046	11.475
800	-0.033	13.259
825	-0.024	15.018
850	-0.017	16.747
875	-0.012	18.446
900	-0.009	20.112
925	-0.006	21.743
950	-0.004	23.339
975	-0.003	24.896
1000	-0.002	26.415
1025	-0.002	27.896
1050	-0.001	29.337
1075	-0.001	30.738

Table A4- 4 SDPS output of panel LW-52 using profile function method

H.R. = 23%

[SUBSIDENCE CALCULATIONS]
Panel geometry.....Supercritical
Maximum subsidence (Smax).....-4.93 (ft)
Maximum subsidence factor (Smax/m)....0.666
Offset of inflection point from rib ..190.8 (ft) (inby)
Estimate of inflection point (I.P.)...Average
Distance of point of Smax from I.P....267.1 (ft)

Distance from Center Line (ft)	Subsidence (ft)	Angle from the rib (deg)
0	-4.928	
25	-4.922	
50	-4.913	
75	-4.901	
100	-4.885	
125	-4.862	
150	-4.830	
175	-4.786	
200	-4.726	
225	-4.645	
250	-4.535	
275	-4.390	
300	-4.202	
325	-3.964	
350	-3.673	
375	-3.330	
400	-2.944	
425	-2.534	
450	-2.120	
475	-1.725	
500	-1.368	
525	-1.061	
550	-0.807	
575	-0.604	
600	-0.447	
625	-0.328	0.413
650	-0.238	2.289
675	-0.173	4.160
700	-0.124	6.023
725	-0.089	7.872
750	-0.064	9.706
775	-0.046	11.519
800	-0.033	13.310
825	-0.024	15.074
850	-0.017	16.810
875	-0.012	18.514
900	-0.009	20.185
925	-0.006	21.821
950	-0.004	23.420
975	-0.003	24.982
1000	-0.002	26.505
1025	-0.002	27.989
1050	-0.001	29.433
1075	-0.001	30.837

Table A4- 5 SDPS output of panel LW-55 using profile function method

H.R. = 20%

[SUBSIDENCE CALCULATIONS]
Panel geometry.....Supercritical
Maximum subsidence (Smax).....-5.15 (ft)
Maximum subsidence factor (Smax/m)....0.695
Offset of inflection point from rib ..160.0 (ft) (inby)
Estimate of inflection point (I.P.)...Average
Distance of point of Smax from I.P....224.0 (ft)

Distance from Center Line (ft)	Subsidence (ft)	Angle from the rib (deg)
0	-5.147	
25	-5.146	
50	-5.145	
75	-5.143	
100	-5.141	
125	-5.138	
150	-5.133	
175	-5.126	
200	-5.115	
225	-5.100	
250	-5.076	
275	-5.041	
300	-4.990	
325	-4.916	
350	-4.809	
375	-4.657	
400	-4.447	
425	-4.167	
450	-3.808	
475	-3.374	
500	-2.883	
525	-2.368	
550	-1.869	
575	-1.421	
600	-1.046	
625	-0.751	
650	-0.528	
675	-0.365	
700	-0.250	2.237
725	-0.170	4.467
750	-0.115	6.684
775	-0.078	8.881
800	-0.052	11.052
825	-0.035	13.191
850	-0.024	15.293
875	-0.016	17.354
900	-0.011	19.370
925	-0.007	21.337
950	-0.005	23.253
975	-0.003	25.115
1000	-0.002	26.922
1025	-0.001	28.673
1050	-0.001	30.368

A.9 PITT-PENNDOT HIGHWAY SUBSIDENCE MODEL IN TABULAR AND GRAPHICAL FORM

The Pitt-PennDOT highway subsidence method described in detail in chapter 4.0 can be used with the help of charts and tables, in two simple steps. These tables and charts are given here for both left and right side of a panel, for the ease of use. Also, the symmetric (no adjacent panel previously mined) and asymmetric (previously mined adjacent panel) prediction models in the form of charts are provided.

Step 1

Given the extracted thickness, *M*, and the overburden coal thickness, *H*:

Calculate the maximum subsidence, *S**, from equation A.9-1 or estimate *S** from Figure A9- 1.

$$\frac{S^*}{M} = -6.9988\left(\frac{H}{1000}\right)^2 + 9.3788\left(\frac{H}{1000}\right) - 2.4258 \qquad \textbf{A9 - 1}$$

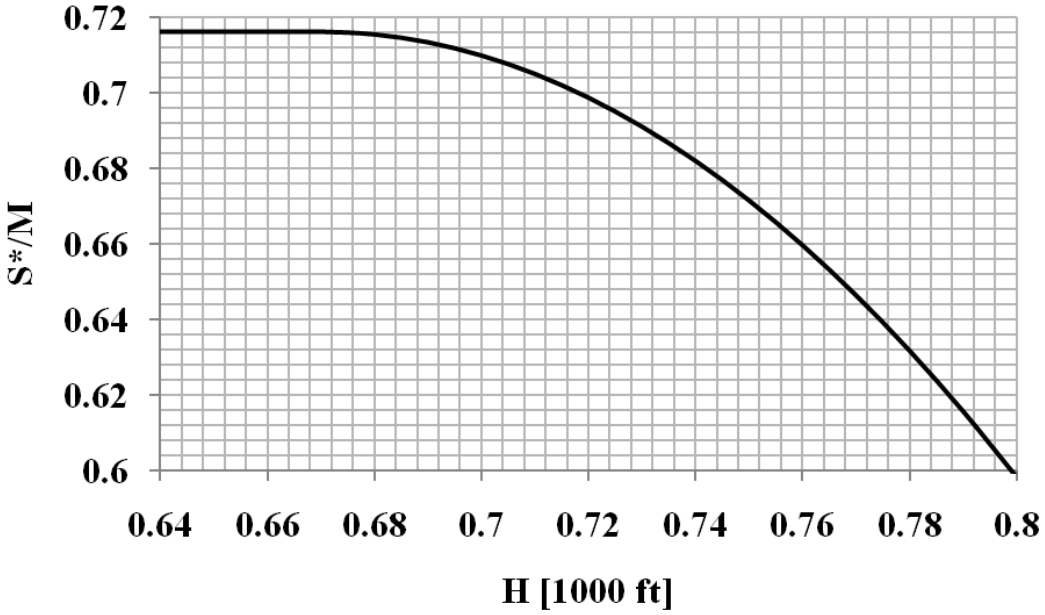

Figure A9- 1 Maximum Subsidence Model

Step 2

Given the overburden thickness, *H*, and the coordinates of interest, *x* (transversal) and *z* (longitudinal), calculate *S/S**. Since *S** is known from step 1, find *S* for any position *x*, *z*. within the panel or in zones adjacent to the panel, taking into account whether there is a previously mined adjacent panel to the panel of interest or not. For this, use Figure A9- 2 through Figure A9- 5 and Table A9- 1 through Table A9- 4, which contain the different cases (left and right, symmetric and asymmetric).

Prediction of subsidence as a function of time

The PITT-PennDOT model can give prediction of subsidence as a function of time as long as the rate of advance is similar to the rate at which the data were obtained, that is 56 ft/day. In that

case, the variable z can be replaced by $56t$, under the assumption of constant rate of advance, and the same charts and tables presented below can be used. To summarize, follow these steps:

Given time, in days, at which subsidence is to be predicted, calculate:

$$z = 56t \qquad \textbf{A9 - 2}$$

Then use the same charts and tables available below. Notice that, since $z = 0$ corresponds to the mine face position, the time $t = 0$ corresponds to the mine face being exactly below the point where subsidence is to be predicted. Therefore, negative times correspond to positions of the mine face behind the point of interest, whereas positive times correspond to positions ahead of the point of interest. For example, given a point of concern, a time of -5 days means that, given the assumption of a constant rate of advance of 56 ft/day, the mine face will reach the point of interest in 5 days. Consistently, +5days means 5 days have passed since the mine face reached the point of interest.

Table A9- 1 Normalized subsidence *S/S** for symmetric longwall panel, left side

		x/H																					
		-0.2	-0.1	-0.1	0	0.05	0.1	0.15	0.2	0.25	0.3	0.35	0.4	0.45	0.5	0.55	0.6	0.65	0.7	0.75	0.8	0.85
z/H	-0.40	0.00	0.00	0.00	0.00	0.00	0.00	0.00	0.00	0.00	0.00	0.00	0.00	0.00	0.00	0.00	0.00	0.00	0.00	0.00	0.00	0.00
	-0.35	0.00	0.00	0.00	0.00	0.00	0.00	0.00	0.00	0.00	0.00	0.01	0.01	0.01	0.01	0.01	0.01	0.01	0.01	0.01	0.01	0.01
	-0.30	0.00	0.00	0.00	0.00	0.00	0.00	0.00	0.00	0.00	0.01	0.01	0.01	0.01	0.01	0.01	0.01	0.01	0.01	0.01	0.01	0.01
	-0.25	0.00	0.00	0.00	0.00	0.00	0.00	0.00	0.00	0.01	0.01	0.01	0.01	0.01	0.01	0.01	0.01	0.01	0.01	0.01	0.01	0.01
	-0.20	0.00	0.00	0.00	0.00	0.00	0.00	0.00	0.01	0.01	0.01	0.01	0.02	0.02	0.02	0.02	0.02	0.02	0.02	0.02	0.02	0.02
	-0.15	0.00	0.00	0.00	0.00	0.00	0.00	0.01	0.01	0.01	0.02	0.02	0.02	0.03	0.03	0.03	0.03	0.03	0.03	0.03	0.03	0.03
	-0.10	0.00	0.00	0.00	0.00	0.00	0.00	0.01	0.01	0.02	0.02	0.03	0.03	0.04	0.04	0.04	0.04	0.04	0.04	0.04	0.04	0.04
	-0.05	0.00	0.00	0.00	0.00	0.00	0.01	0.01	0.02	0.03	0.03	0.04	0.05	0.05	0.05	0.05	0.06	0.06	0.06	0.06	0.06	0.06
	0.00	0.00	0.00	0.00	0.00	0.00	0.01	0.01	0.02	0.04	0.05	0.06	0.07	0.07	0.07	0.08	0.08	0.08	0.08	0.08	0.08	0.08
	0.05	0.00	0.00	0.00	0.00	0.01	0.01	0.02	0.03	0.05	0.06	0.08	0.09	0.10	0.10	0.10	0.10	0.11	0.11	0.11	0.11	0.11
	0.10	0.00	0.00	0.00	0.00	0.01	0.02	0.03	0.04	0.07	0.09	0.11	0.12	0.13	0.14	0.14	0.14	0.14	0.14	0.14	0.14	0.14
	0.15	0.00	0.00	0.00	0.01	0.01	0.02	0.04	0.06	0.09	0.12	0.14	0.16	0.17	0.18	0.19	0.19	0.19	0.19	0.19	0.19	0.19
	0.20	0.00	0.00	0.00	0.01	0.01	0.03	0.05	0.08	0.11	0.15	0.18	0.21	0.22	0.23	0.24	0.24	0.25	0.25	0.25	0.25	0.25
	0.25	0.00	0.00	0.00	0.01	0.02	0.03	0.06	0.10	0.14	0.19	0.23	0.26	0.28	0.30	0.30	0.31	0.31	0.31	0.31	0.31	0.31
	0.30	0.00	0.00	0.01	0.01	0.02	0.04	0.07	0.12	0.18	0.24	0.29	0.32	0.35	0.37	0.38	0.38	0.39	0.39	0.39	0.39	0.39
	0.35	0.00	0.00	0.01	0.01	0.03	0.05	0.09	0.14	0.21	0.28	0.34	0.39	0.42	0.44	0.45	0.46	0.46	0.46	0.47	0.47	0.47
	0.40	0.00	0.00	0.01	0.02	0.03	0.06	0.10	0.17	0.25	0.33	0.40	0.46	0.49	0.52	0.53	0.54	0.54	0.54	0.54	0.55	0.55
	0.45	0.00	0.00	0.01	0.02	0.04	0.07	0.12	0.19	0.28	0.38	0.46	0.52	0.56	0.59	0.60	0.61	0.62	0.62	0.62	0.62	0.62
	0.50	0.00	0.01	0.01	0.02	0.04	0.07	0.13	0.21	0.31	0.42	0.51	0.58	0.62	0.65	0.67	0.68	0.69	0.69	0.69	0.69	0.69
	0.55	0.00	0.01	0.01	0.02	0.04	0.08	0.14	0.23	0.34	0.46	0.55	0.63	0.68	0.71	0.73	0.74	0.75	0.75	0.75	0.75	0.75
	0.60	0.00	0.01	0.01	0.02	0.05	0.09	0.15	0.25	0.36	0.49	0.59	0.67	0.73	0.76	0.78	0.79	0.80	0.80	0.80	0.80	0.81
	0.65	0.00	0.01	0.01	0.02	0.05	0.09	0.16	0.26	0.38	0.51	0.63	0.71	0.77	0.80	0.82	0.83	0.84	0.84	0.85	0.85	0.85
	0.70	0.00	0.01	0.01	0.03	0.05	0.09	0.17	0.27	0.40	0.53	0.65	0.74	0.80	0.83	0.85	0.87	0.87	0.88	0.88	0.88	0.88
	0.75	0.00	0.01	0.01	0.03	0.05	0.10	0.17	0.28	0.41	0.55	0.67	0.76	0.82	0.86	0.88	0.89	0.90	0.91	0.91	0.91	0.91
	0.80	0.00	0.01	0.01	0.03	0.05	0.10	0.17	0.29	0.42	0.56	0.69	0.78	0.84	0.88	0.90	0.92	0.92	0.93	0.93	0.93	0.93
	0.85	0.00	0.01	0.01	0.03	0.05	0.10	0.18	0.29	0.43	0.57	0.70	0.79	0.86	0.89	0.92	0.93	0.94	0.94	0.95	0.95	0.95
	0.90	0.00	0.01	0.01	0.03	0.05	0.10	0.18	0.29	0.44	0.58	0.71	0.80	0.87	0.91	0.93	0.94	0.95	0.96	0.96	0.96	0.96
	0.95	0.00	0.01	0.01	0.03	0.06	0.10	0.18	0.30	0.44	0.59	0.71	0.81	0.88	0.92	0.94	0.95	0.96	0.97	0.97	0.97	0.97
	1.00	0.00	0.01	0.01	0.03	0.06	0.10	0.18	0.30	0.44	0.59	0.72	0.82	0.88	0.92	0.95	0.96	0.97	0.97	0.98	0.98	0.98
	1.05	0.00	0.01	0.01	0.03	0.06	0.10	0.18	0.30	0.45	0.59	0.72	0.82	0.89	0.93	0.95	0.97	0.97	0.98	0.98	0.98	0.98
	1.10	0.00	0.01	0.01	0.03	0.06	0.10	0.19	0.30	0.45	0.60	0.73	0.82	0.89	0.93	0.96	0.97	0.98	0.98	0.99	0.99	0.99
	1.15	0.00	0.01	0.01	0.03	0.06	0.11	0.19	0.30	0.45	0.60	0.73	0.83	0.89	0.93	0.96	0.97	0.98	0.99	0.99	0.99	0.99
	1.20	0.00	0.01	0.01	0.03	0.06	0.11	0.19	0.30	0.45	0.60	0.73	0.83	0.89	0.94	0.96	0.97	0.98	0.99	0.99	0.99	0.99
	1.25	0.00	0.01	0.01	0.03	0.06	0.11	0.19	0.30	0.45	0.60	0.73	0.83	0.90	0.94	0.96	0.98	0.98	0.99	0.99	0.99	0.99
	1.30	0.00	0.01	0.01	0.03	0.06	0.11	0.19	0.30	0.45	0.60	0.73	0.83	0.90	0.94	0.96	0.98	0.99	0.99	0.99	0.99	1.00

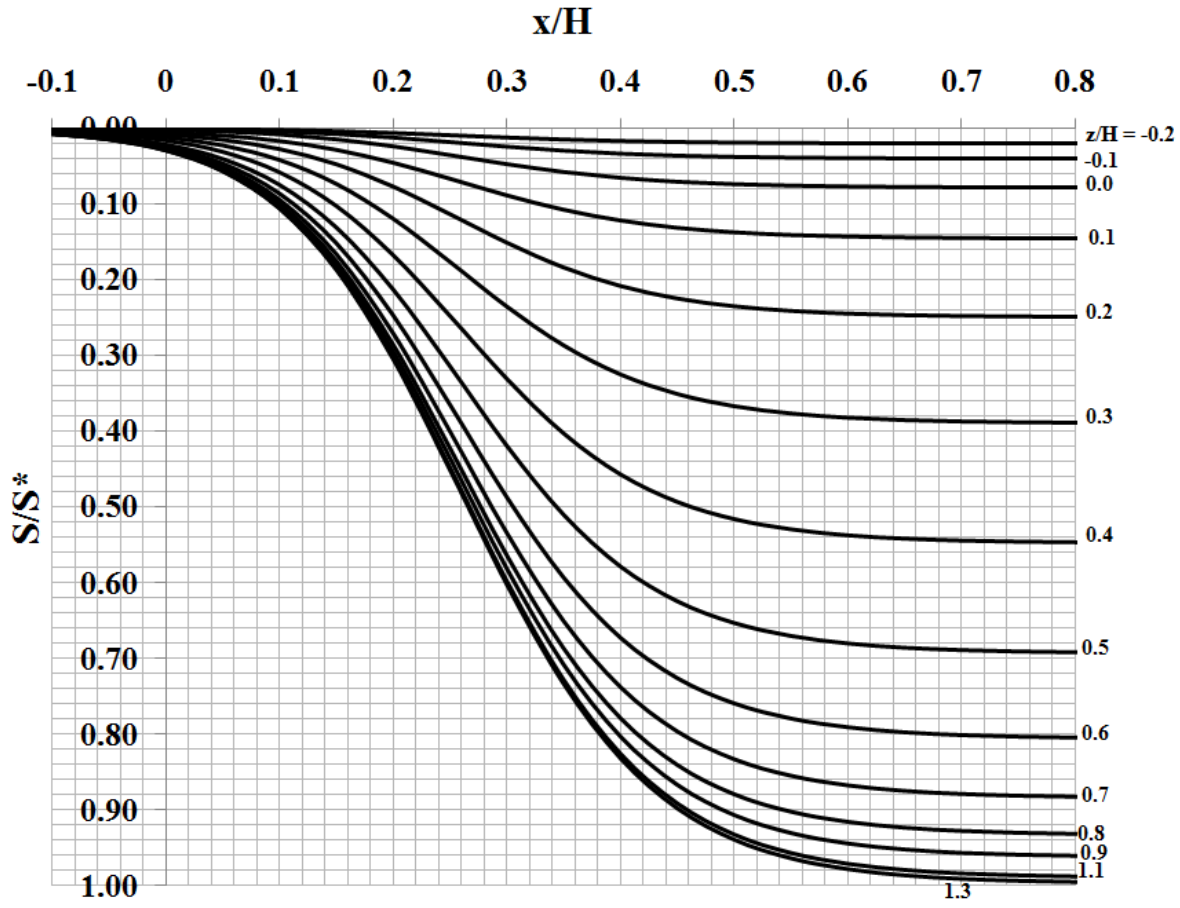

Figure A9- 2 Normalized subsidence *S/S** for symmetric longwall panel, left side

Table A9- 2 Normalized subsidence *S/S** for symmetric longwall panel, right side

x/H																						
0.85	0.80	0.75	0.70	0.65	0.60	0.55	0.50	0.45	0.40	0.35	0.30	0.25	0.20	0.15	0.10	0.05	0.00	-0.05	-0.10	-0.15		
0.00	0.00	0.00	0.00	0.00	0.00	0.00	0.00	0.00	0.00	0.00	0.00	0.00	0.00	0.00	0.00	0.00	0.00	0.00	0.00	0.00	-0.40	
0.01	0.01	0.01	0.01	0.01	0.01	0.01	0.01	0.01	0.01	0.01	0.00	0.00	0.00	0.00	0.00	0.00	0.00	0.00	0.00	0.00	-0.35	
0.01	0.01	0.01	0.01	0.01	0.01	0.01	0.01	0.01	0.01	0.01	0.01	0.00	0.00	0.00	0.00	0.00	0.00	0.00	0.00	0.00	-0.30	
0.01	0.01	0.01	0.01	0.01	0.01	0.01	0.01	0.01	0.01	0.01	0.01	0.01	0.00	0.00	0.00	0.00	0.00	0.00	0.00	0.00	-0.25	
0.02	0.02	0.02	0.02	0.02	0.02	0.02	0.02	0.02	0.02	0.01	0.01	0.01	0.01	0.00	0.00	0.00	0.00	0.00	0.00	0.00	-0.20	
0.03	0.03	0.03	0.03	0.03	0.03	0.03	0.03	0.03	0.02	0.02	0.02	0.01	0.01	0.01	0.00	0.00	0.00	0.00	0.00	0.00	-0.15	
0.04	0.04	0.04	0.04	0.04	0.04	0.04	0.04	0.04	0.03	0.03	0.02	0.02	0.01	0.01	0.00	0.00	0.00	0.00	0.00	0.00	-0.10	
0.06	0.06	0.06	0.06	0.06	0.06	0.05	0.05	0.05	0.05	0.04	0.03	0.03	0.02	0.01	0.01	0.00	0.00	0.00	0.00	0.00	-0.05	
0.08	0.08	0.08	0.08	0.08	0.08	0.08	0.07	0.07	0.07	0.06	0.05	0.04	0.02	0.01	0.01	0.00	0.00	0.00	0.00	0.00	0.00	
0.11	0.11	0.11	0.11	0.11	0.10	0.10	0.10	0.10	0.09	0.08	0.06	0.05	0.03	0.02	0.01	0.01	0.00	0.00	0.00	0.00	0.05	
0.14	0.14	0.14	0.14	0.14	0.14	0.14	0.14	0.13	0.12	0.11	0.09	0.07	0.04	0.03	0.02	0.01	0.00	0.00	0.00	0.00	0.10	
0.19	0.19	0.19	0.19	0.19	0.19	0.19	0.18	0.17	0.16	0.14	0.12	0.09	0.06	0.04	0.02	0.01	0.01	0.00	0.00	0.00	0.15	
0.25	0.25	0.25	0.25	0.25	0.24	0.24	0.23	0.22	0.21	0.18	0.15	0.11	0.08	0.05	0.03	0.01	0.01	0.00	0.00	0.00	0.20	
0.31	0.31	0.31	0.31	0.31	0.31	0.30	0.30	0.28	0.26	0.23	0.19	0.14	0.10	0.06	0.03	0.02	0.01	0.00	0.00	0.00	0.25	
0.39	0.39	0.39	0.39	0.39	0.38	0.38	0.37	0.35	0.32	0.29	0.24	0.18	0.12	0.07	0.04	0.02	0.01	0.01	0.00	0.00	0.30	
0.47	0.47	0.47	0.46	0.46	0.46	0.45	0.44	0.42	0.39	0.34	0.28	0.21	0.14	0.09	0.05	0.03	0.01	0.01	0.00	0.00	0.35	
0.55	0.55	0.54	0.54	0.54	0.54	0.53	0.52	0.49	0.46	0.40	0.33	0.25	0.17	0.10	0.06	0.03	0.02	0.01	0.00	0.00	0.40	
0.62	0.62	0.62	0.62	0.62	0.61	0.60	0.59	0.56	0.52	0.46	0.38	0.28	0.19	0.12	0.07	0.04	0.02	0.01	0.00	0.00	0.45	z/H
0.69	0.69	0.69	0.69	0.69	0.68	0.67	0.65	0.62	0.58	0.51	0.42	0.31	0.21	0.13	0.07	0.04	0.02	0.01	0.01	0.00	0.50	
0.75	0.75	0.75	0.75	0.75	0.74	0.73	0.71	0.68	0.63	0.55	0.46	0.34	0.23	0.14	0.08	0.04	0.02	0.01	0.01	0.00	0.55	
0.81	0.80	0.80	0.80	0.80	0.79	0.78	0.76	0.73	0.67	0.59	0.49	0.36	0.25	0.15	0.09	0.05	0.02	0.01	0.01	0.00	0.60	
0.85	0.85	0.85	0.84	0.84	0.83	0.82	0.80	0.77	0.71	0.63	0.51	0.38	0.26	0.16	0.09	0.05	0.02	0.01	0.01	0.00	0.65	
0.88	0.88	0.88	0.88	0.87	0.87	0.85	0.83	0.80	0.74	0.65	0.53	0.40	0.27	0.17	0.09	0.05	0.03	0.01	0.01	0.00	0.70	
0.91	0.91	0.91	0.91	0.90	0.89	0.88	0.86	0.82	0.76	0.67	0.55	0.41	0.28	0.17	0.10	0.05	0.03	0.01	0.01	0.00	0.75	
0.93	0.93	0.93	0.93	0.92	0.92	0.90	0.88	0.84	0.78	0.69	0.56	0.42	0.29	0.17	0.10	0.05	0.03	0.01	0.01	0.00	0.80	
0.95	0.95	0.95	0.94	0.94	0.93	0.92	0.89	0.86	0.79	0.70	0.57	0.43	0.29	0.18	0.10	0.05	0.03	0.01	0.01	0.00	0.85	
0.96	0.96	0.96	0.96	0.95	0.94	0.93	0.91	0.87	0.80	0.71	0.58	0.44	0.29	0.18	0.10	0.05	0.03	0.01	0.01	0.00	0.90	
0.97	0.97	0.97	0.97	0.96	0.95	0.94	0.92	0.88	0.81	0.71	0.59	0.44	0.30	0.18	0.10	0.06	0.03	0.01	0.01	0.00	0.95	
0.98	0.98	0.98	0.97	0.97	0.96	0.95	0.92	0.88	0.82	0.72	0.59	0.44	0.30	0.18	0.10	0.06	0.03	0.01	0.01	0.00	1.00	
0.98	0.98	0.98	0.98	0.97	0.97	0.95	0.93	0.89	0.82	0.72	0.59	0.45	0.30	0.18	0.10	0.06	0.03	0.01	0.01	0.00	1.05	
0.99	0.99	0.99	0.98	0.98	0.97	0.96	0.93	0.89	0.82	0.73	0.60	0.45	0.30	0.19	0.10	0.06	0.03	0.01	0.01	0.00	1.10	
0.99	0.99	0.99	0.99	0.98	0.97	0.96	0.93	0.89	0.83	0.73	0.60	0.45	0.30	0.19	0.11	0.06	0.03	0.01	0.01	0.00	1.15	
0.99	0.99	0.99	0.99	0.98	0.97	0.96	0.94	0.89	0.83	0.73	0.60	0.45	0.30	0.19	0.11	0.06	0.03	0.01	0.01	0.00	1.20	
0.99	0.99	0.99	0.99	0.98	0.98	0.96	0.94	0.90	0.83	0.73	0.60	0.45	0.30	0.19	0.11	0.06	0.03	0.01	0.01	0.00	1.25	
1.00	0.99	0.99	0.99	0.99	0.98	0.96	0.94	0.90	0.83	0.73	0.60	0.45	0.30	0.19	0.11	0.06	0.03	0.01	0.01	0.00	1.30	

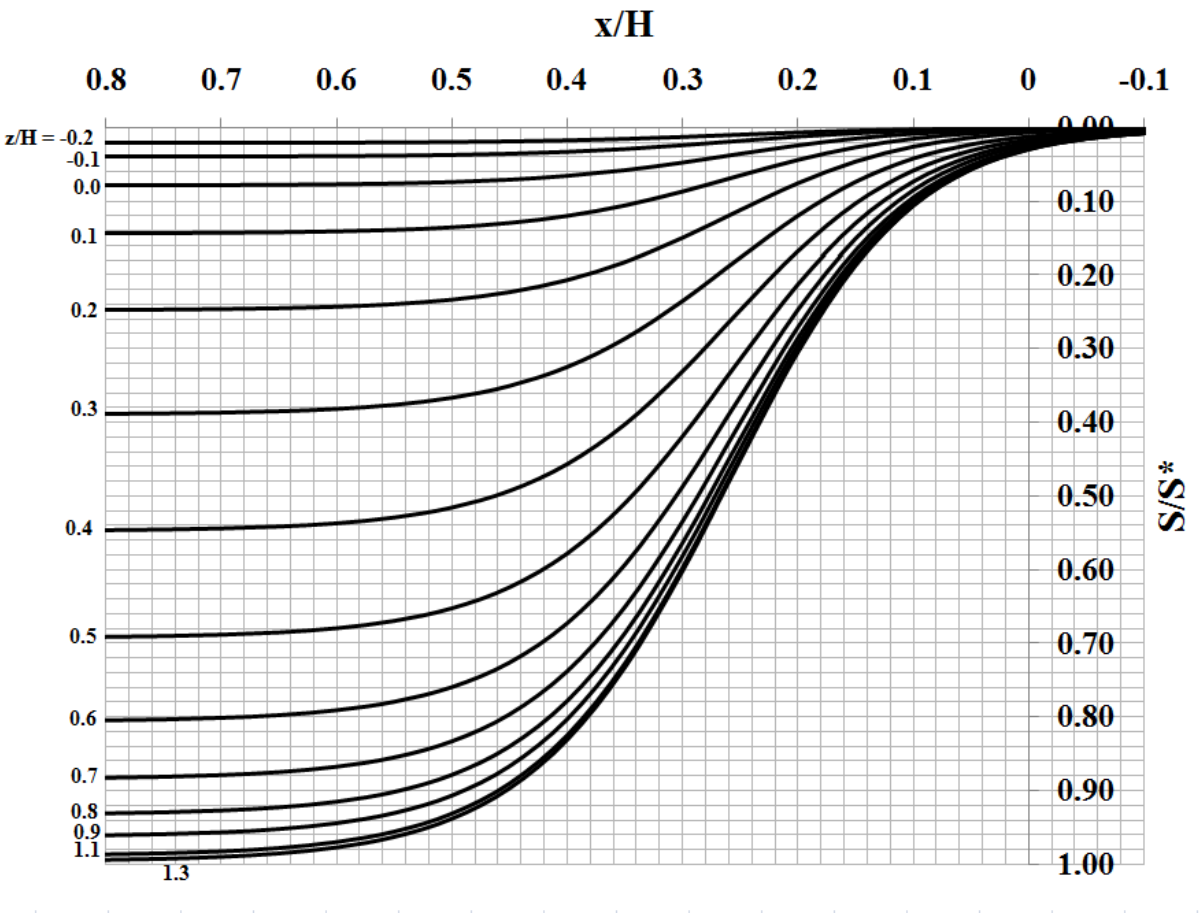

Figure A9- 3 Normalized subsidence *S/S** for symmetric longwall panel, right side

Table A9- 3 Normalized subsidence *S/S** for asymmetric longwall panel, left side

		x/H																					
		-0.15	-0.10	-0.05	0.00	0.05	0.10	0.15	0.20	0.25	0.30	0.35	0.40	0.45	0.50	0.55	0.60	0.65	0.70	0.75	0.80	0.85
z/H	-0.40	0.00	0.00	0.00	0.00	0.00	0.00	0.00	0.00	0.00	0.00	0.00	0.00	0.00	0.00	0.00	0.00	0.00	0.00	0.00	0.00	0.00
	-0.35	0.00	0.00	0.00	0.00	0.00	0.00	0.00	0.00	0.00	0.01	0.01	0.01	0.01	0.01	0.01	0.01	0.01	0.01	0.01	0.01	0.01
	-0.30	0.00	0.00	0.00	0.00	0.00	0.00	0.00	0.01	0.01	0.01	0.01	0.01	0.01	0.01	0.01	0.01	0.01	0.01	0.01	0.01	0.01
	-0.25	0.00	0.00	0.00	0.00	0.00	0.00	0.01	0.01	0.01	0.01	0.01	0.01	0.01	0.01	0.01	0.01	0.01	0.01	0.01	0.01	0.01
	-0.20	0.00	0.00	0.00	0.00	0.00	0.01	0.01	0.01	0.01	0.02	0.02	0.02	0.02	0.02	0.02	0.02	0.02	0.02	0.02	0.02	0.02
	-0.15	0.00	0.00	0.00	0.00	0.01	0.01	0.01	0.01	0.02	0.02	0.02	0.03	0.03	0.03	0.03	0.03	0.03	0.03	0.03	0.03	0.03
	-0.10	0.00	0.00	0.00	0.01	0.01	0.01	0.02	0.02	0.03	0.03	0.03	0.04	0.04	0.04	0.04	0.04	0.04	0.04	0.04	0.04	0.04
	-0.05	0.00	0.00	0.00	0.01	0.01	0.02	0.02	0.03	0.04	0.04	0.05	0.05	0.05	0.05	0.06	0.06	0.06	0.06	0.06	0.06	0.06
	0.00	0.00	0.00	0.01	0.01	0.01	0.02	0.03	0.04	0.05	0.06	0.07	0.07	0.07	0.08	0.08	0.08	0.08	0.08	0.08	0.08	0.08
	0.05	0.00	0.01	0.01	0.01	0.02	0.03	0.04	0.06	0.07	0.08	0.09	0.10	0.10	0.10	0.11	0.11	0.11	0.11	0.11	0.11	0.11
	0.10	0.01	0.01	0.01	0.02	0.03	0.04	0.06	0.08	0.09	0.11	0.12	0.13	0.14	0.14	0.14	0.14	0.14	0.14	0.14	0.14	0.14
	0.15	0.01	0.01	0.02	0.02	0.04	0.05	0.07	0.10	0.12	0.15	0.16	0.18	0.18	0.19	0.19	0.19	0.19	0.19	0.19	0.19	0.19
	0.20	0.01	0.01	0.02	0.03	0.05	0.07	0.10	0.13	0.16	0.19	0.21	0.23	0.24	0.24	0.24	0.25	0.25	0.25	0.25	0.25	0.25
	0.25	0.01	0.02	0.03	0.04	0.06	0.09	0.12	0.16	0.21	0.24	0.27	0.29	0.30	0.31	0.31	0.31	0.31	0.31	0.31	0.31	0.32
	0.30	0.01	0.02	0.03	0.05	0.07	0.11	0.15	0.20	0.25	0.30	0.33	0.36	0.37	0.38	0.38	0.39	0.39	0.39	0.39	0.39	0.39
	0.35	0.02	0.03	0.04	0.06	0.09	0.13	0.18	0.24	0.31	0.36	0.40	0.43	0.44	0.45	0.46	0.46	0.47	0.47	0.47	0.47	0.47
	0.40	0.02	0.03	0.05	0.07	0.10	0.15	0.21	0.28	0.36	0.42	0.47	0.50	0.52	0.53	0.54	0.54	0.54	0.55	0.55	0.55	0.55
	0.45	0.02	0.03	0.05	0.08	0.12	0.17	0.24	0.32	0.41	0.48	0.53	0.57	0.59	0.61	0.61	0.62	0.62	0.62	0.62	0.62	0.62
	0.50	0.02	0.04	0.06	0.09	0.13	0.19	0.27	0.36	0.45	0.53	0.59	0.63	0.66	0.67	0.68	0.69	0.69	0.69	0.69	0.69	0.69
	0.55	0.03	0.04	0.06	0.10	0.14	0.21	0.29	0.39	0.49	0.58	0.64	0.69	0.72	0.73	0.74	0.75	0.75	0.75	0.75	0.75	0.75
	0.60	0.03	0.04	0.07	0.10	0.15	0.22	0.31	0.42	0.53	0.62	0.69	0.74	0.77	0.78	0.79	0.80	0.80	0.80	0.81	0.81	0.81
	0.65	0.03	0.05	0.07	0.11	0.16	0.24	0.33	0.44	0.55	0.65	0.73	0.78	0.81	0.83	0.84	0.84	0.85	0.85	0.85	0.85	0.85
	0.70	0.03	0.05	0.07	0.11	0.17	0.24	0.34	0.46	0.58	0.68	0.76	0.81	0.84	0.86	0.87	0.88	0.88	0.88	0.88	0.88	0.88
	0.75	0.03	0.05	0.08	0.12	0.17	0.25	0.36	0.47	0.60	0.70	0.78	0.83	0.87	0.89	0.90	0.90	0.91	0.91	0.91	0.91	0.91
	0.80	0.03	0.05	0.08	0.12	0.18	0.26	0.36	0.49	0.61	0.72	0.80	0.85	0.89	0.91	0.92	0.93	0.93	0.93	0.93	0.93	0.93
	0.85	0.03	0.05	0.08	0.12	0.18	0.26	0.37	0.49	0.62	0.73	0.81	0.87	0.90	0.92	0.93	0.94	0.95	0.95	0.95	0.95	0.95
	0.90	0.03	0.05	0.08	0.12	0.18	0.27	0.37	0.50	0.63	0.74	0.82	0.88	0.91	0.94	0.95	0.95	0.96	0.96	0.96	0.96	0.96
	0.95	0.03	0.05	0.08	0.12	0.18	0.27	0.38	0.51	0.63	0.75	0.83	0.89	0.92	0.94	0.96	0.96	0.97	0.97	0.97	0.97	0.97
	1.00	0.03	0.05	0.08	0.12	0.19	0.27	0.38	0.51	0.64	0.75	0.84	0.89	0.93	0.95	0.96	0.97	0.97	0.98	0.98	0.98	0.98
	1.05	0.03	0.05	0.08	0.12	0.19	0.27	0.38	0.51	0.64	0.76	0.84	0.90	0.94	0.96	0.97	0.98	0.98	0.98	0.98	0.98	0.98
	1.10	0.03	0.05	0.08	0.13	0.19	0.27	0.39	0.51	0.64	0.76	0.85	0.90	0.94	0.96	0.97	0.98	0.98	0.99	0.99	0.99	0.99
	1.15	0.04	0.05	0.08	0.13	0.19	0.27	0.39	0.52	0.65	0.76	0.85	0.91	0.94	0.96	0.98	0.98	0.99	0.99	0.99	0.99	0.99
	1.20	0.04	0.05	0.08	0.13	0.19	0.28	0.39	0.52	0.65	0.76	0.85	0.91	0.94	0.97	0.98	0.99	0.99	0.99	0.99	0.99	0.99
	1.25	0.04	0.05	0.08	0.13	0.19	0.28	0.39	0.52	0.65	0.76	0.85	0.91	0.95	0.97	0.98	0.99	0.99	0.99	0.99	0.99	0.99
	1.30	0.04	0.05	0.08	0.13	0.19	0.28	0.39	0.52	0.65	0.77	0.85	0.91	0.95	0.97	0.98	0.99	0.99	0.99	1.00	1.00	1.00

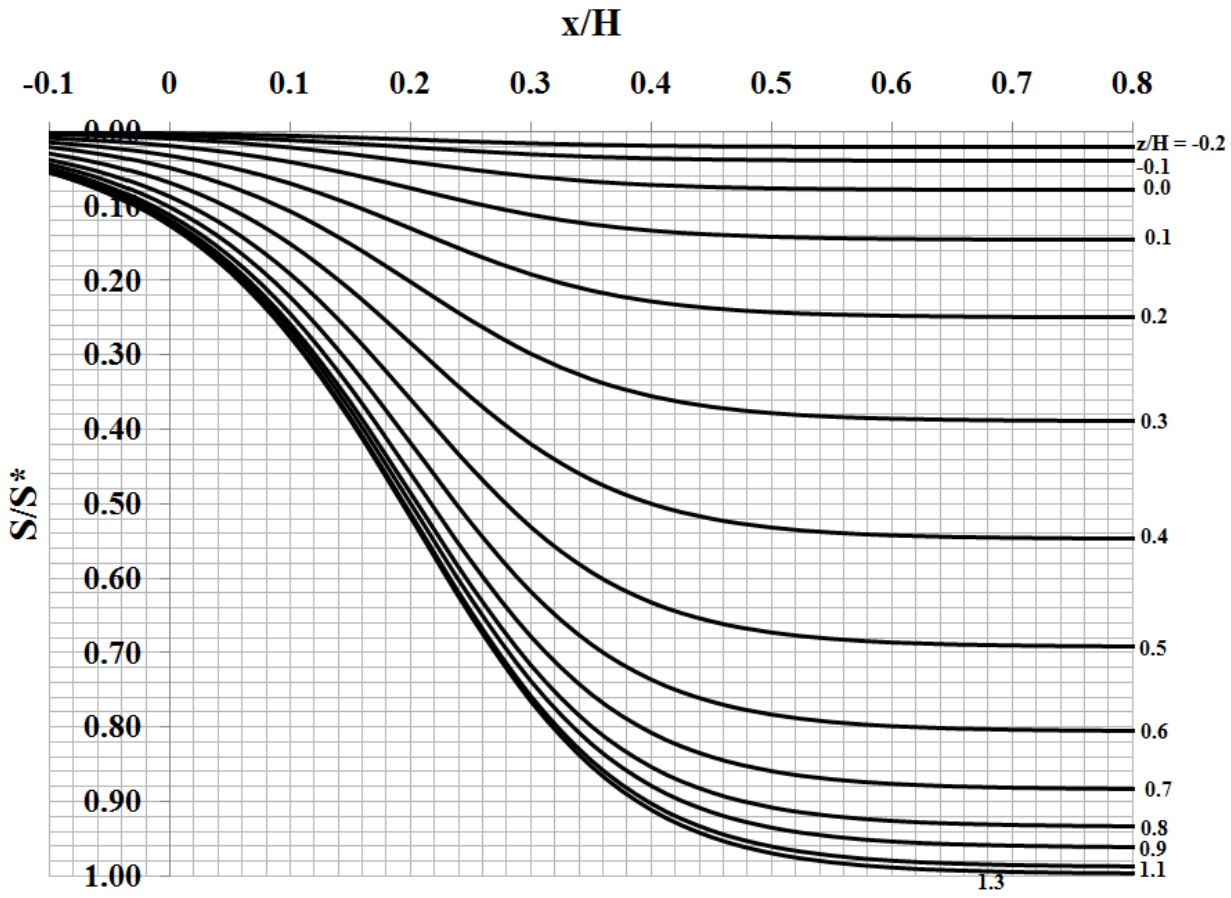

Figure A9- 4 Normalized subsidence *S/S** for asymmetric longwall panel, left side

Table A9- 4 Normalized subsidence *S/S** for asymmetric longwall panel, right side

x/H																						
0.85	0.80	0.75	0.70	0.65	0.60	0.55	0.50	0.45	0.40	0.35	0.30	0.25	0.20	0.15	0.10	0.05	0.00	-0.05	-0.10	-0.15		
0.00	0.00	0.00	0.00	0.00	0.00	0.00	0.00	0.00	0.00	0.00	0.00	0.00	0.00	0.00	0.00	0.00	0.00	0.00	0.00	0.00	-0.40	
0.01	0.01	0.01	0.01	0.01	0.01	0.01	0.01	0.01	0.01	0.01	0.01	0.00	0.00	0.00	0.00	0.00	0.00	0.00	0.00	0.00	-0.35	
0.01	0.01	0.01	0.01	0.01	0.01	0.01	0.01	0.01	0.01	0.01	0.01	0.01	0.01	0.00	0.00	0.00	0.00	0.00	0.00	0.00	-0.30	
0.01	0.01	0.01	0.01	0.01	0.01	0.01	0.01	0.01	0.01	0.01	0.01	0.01	0.01	0.01	0.00	0.00	0.00	0.00	0.00	0.00	-0.25	
0.02	0.02	0.02	0.02	0.02	0.02	0.02	0.02	0.02	0.02	0.02	0.02	0.01	0.01	0.01	0.01	0.00	0.00	0.00	0.00	0.00	-0.20	
0.03	0.03	0.03	0.03	0.03	0.03	0.03	0.03	0.03	0.03	0.02	0.02	0.02	0.01	0.01	0.01	0.01	0.00	0.00	0.00	0.00	-0.15	
0.04	0.04	0.04	0.04	0.04	0.04	0.04	0.04	0.04	0.04	0.03	0.03	0.03	0.02	0.02	0.01	0.01	0.01	0.00	0.00	0.00	-0.10	
0.06	0.06	0.06	0.06	0.06	0.06	0.06	0.05	0.05	0.05	0.05	0.04	0.04	0.03	0.02	0.02	0.01	0.01	0.00	0.00	0.00	-0.05	
0.08	0.08	0.08	0.08	0.08	0.08	0.08	0.08	0.07	0.07	0.07	0.06	0.05	0.04	0.03	0.02	0.01	0.01	0.01	0.00	0.00	0.00	
0.11	0.11	0.11	0.11	0.11	0.11	0.11	0.10	0.10	0.10	0.09	0.08	0.07	0.06	0.04	0.03	0.02	0.01	0.01	0.01	0.00	0.05	
0.14	0.14	0.14	0.14	0.14	0.14	0.14	0.14	0.14	0.13	0.12	0.11	0.09	0.08	0.06	0.04	0.03	0.02	0.01	0.01	0.01	0.10	
0.19	0.19	0.19	0.19	0.19	0.19	0.19	0.19	0.18	0.18	0.16	0.15	0.12	0.10	0.07	0.05	0.04	0.02	0.02	0.01	0.01	0.15	
0.25	0.25	0.25	0.25	0.25	0.25	0.24	0.24	0.24	0.23	0.21	0.19	0.16	0.13	0.10	0.07	0.05	0.03	0.02	0.01	0.01	0.20	
0.32	0.31	0.31	0.31	0.31	0.31	0.31	0.31	0.30	0.29	0.27	0.24	0.21	0.16	0.12	0.09	0.06	0.04	0.03	0.02	0.01	0.25	
0.39	0.39	0.39	0.39	0.39	0.39	0.38	0.38	0.37	0.36	0.33	0.30	0.25	0.20	0.15	0.11	0.07	0.05	0.03	0.02	0.01	0.30	
0.47	0.47	0.47	0.47	0.47	0.46	0.46	0.45	0.44	0.43	0.40	0.36	0.31	0.24	0.18	0.13	0.09	0.06	0.04	0.03	0.02	0.35	
0.55	0.55	0.55	0.55	0.54	0.54	0.54	0.53	0.52	0.50	0.47	0.42	0.36	0.28	0.21	0.15	0.10	0.07	0.05	0.03	0.02	0.40	
0.62	0.62	0.62	0.62	0.62	0.62	0.61	0.61	0.59	0.57	0.53	0.48	0.41	0.32	0.24	0.17	0.12	0.08	0.05	0.03	0.02	0.45	z/H
0.69	0.69	0.69	0.69	0.69	0.69	0.68	0.67	0.66	0.63	0.59	0.53	0.45	0.36	0.27	0.19	0.13	0.09	0.06	0.04	0.02	0.50	
0.75	0.75	0.75	0.75	0.75	0.75	0.74	0.73	0.72	0.69	0.64	0.58	0.49	0.39	0.29	0.21	0.14	0.10	0.06	0.04	0.03	0.55	
0.81	0.81	0.81	0.80	0.80	0.80	0.79	0.78	0.77	0.74	0.69	0.62	0.53	0.42	0.31	0.22	0.15	0.10	0.07	0.04	0.03	0.60	
0.85	0.85	0.85	0.85	0.85	0.84	0.84	0.83	0.81	0.78	0.73	0.65	0.55	0.44	0.33	0.24	0.16	0.11	0.07	0.05	0.03	0.65	
0.88	0.88	0.88	0.88	0.88	0.88	0.87	0.86	0.84	0.81	0.76	0.68	0.58	0.46	0.34	0.24	0.17	0.11	0.07	0.05	0.03	0.70	
0.91	0.91	0.91	0.91	0.91	0.90	0.90	0.89	0.87	0.83	0.78	0.70	0.60	0.47	0.36	0.25	0.17	0.12	0.08	0.05	0.03	0.75	
0.93	0.93	0.93	0.93	0.93	0.93	0.92	0.91	0.89	0.85	0.80	0.72	0.61	0.49	0.36	0.26	0.18	0.12	0.08	0.05	0.03	0.80	
0.95	0.95	0.95	0.95	0.95	0.94	0.93	0.92	0.90	0.87	0.81	0.73	0.62	0.49	0.37	0.26	0.18	0.12	0.08	0.05	0.03	0.85	
0.96	0.96	0.96	0.96	0.96	0.95	0.95	0.94	0.91	0.88	0.82	0.74	0.63	0.50	0.37	0.27	0.18	0.12	0.08	0.05	0.03	0.90	
0.97	0.97	0.97	0.97	0.97	0.96	0.96	0.94	0.92	0.89	0.83	0.75	0.63	0.51	0.38	0.27	0.18	0.12	0.08	0.05	0.03	0.95	
0.98	0.98	0.98	0.98	0.97	0.97	0.96	0.95	0.93	0.89	0.84	0.75	0.64	0.51	0.38	0.27	0.19	0.12	0.08	0.05	0.03	1.00	
0.98	0.98	0.98	0.98	0.98	0.98	0.97	0.96	0.94	0.90	0.84	0.76	0.64	0.51	0.38	0.27	0.19	0.12	0.08	0.05	0.03	1.05	
0.99	0.99	0.99	0.99	0.98	0.98	0.97	0.96	0.94	0.90	0.85	0.76	0.64	0.51	0.39	0.27	0.19	0.13	0.08	0.05	0.03	1.10	
0.99	0.99	0.99	0.99	0.99	0.98	0.98	0.96	0.94	0.91	0.85	0.76	0.65	0.52	0.39	0.27	0.19	0.13	0.08	0.05	0.04	1.15	
0.99	0.99	0.99	0.99	0.99	0.99	0.98	0.97	0.94	0.91	0.85	0.76	0.65	0.52	0.39	0.28	0.19	0.13	0.08	0.05	0.04	1.20	
0.99	0.99	0.99	0.99	0.99	0.99	0.98	0.97	0.95	0.91	0.85	0.76	0.65	0.52	0.39	0.28	0.19	0.13	0.08	0.05	0.04	1.25	
1.00	1.00	1.00	0.99	0.99	0.99	0.98	0.97	0.95	0.91	0.85	0.77	0.65	0.52	0.39	0.28	0.19	0.13	0.08	0.05	0.04	1.30	

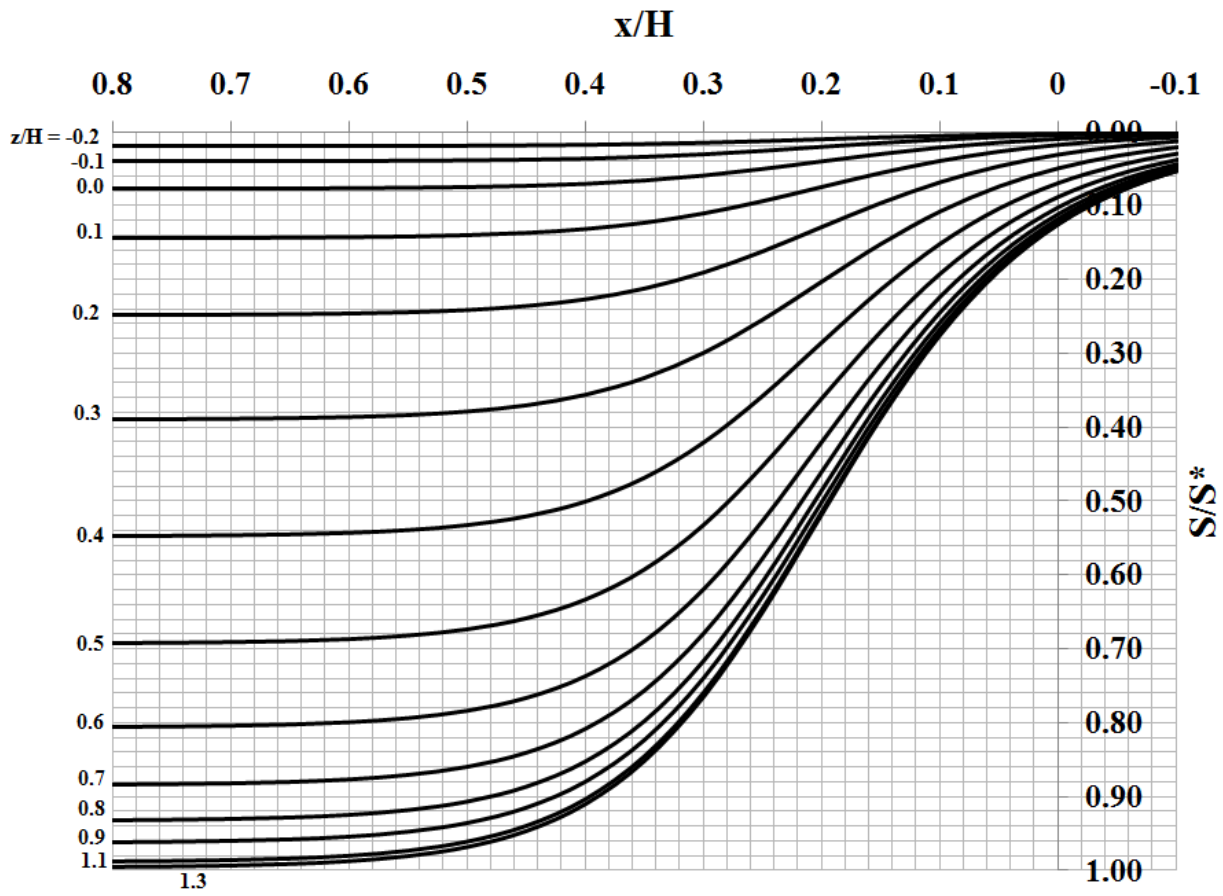

Figure A9- 5 Normalized subsidence *S/S** for asymmetric longwall panel, right side